CORROSION PROTECTION OF 2024-T351 BY A MG-RICH PRIMER

A Dissertation

Presented to the Faculty of the School of Engineering and Applied Science
University of Virginia

In Partial Fulfillment of the
Requirements for the Degree of
Doctor of Philosophy (Materials Science and Engineering)

by

Andrew Darrell King
May 2014

APPROVAL SHEET

The dissertation is submitted in partial fulfillment of the

requirements for the degree of

Doctor of Philosophy (Materials Science and Engineering)

Andrew D. King
(Author)

This dissertation has been read and approved by the examining Committee:

Dr. John R. Scully
(Dissertation Advisor)

Dr. Elizabeth J. Opila
(Committee Chairmen)

Dr. William C. Keene
(Committee Member)

Dr. Jason S. Lee
(Committee Member)

Dr. Robert G. Kelly
(Committee Member)

Accepted for the School of Engineering and Applied Science:

Dr. James H. Aylor
Dean, School of Engineering and Applied Science
May 2014

Abstract

An organic coating system containing an Mg-pigmented organic primer (MgRP) engineered for corrosion protection of precipitation age hardened Al alloy 2024-T351 used in aerospace applications has been developed as a candidate to replace chromate-containing surface pretreatments and primers. This work addresses the primary mechanisms of protection, analysis of function and performance of the coating system in standard lab accelerated tests compared to field environments. The effects of atmospheric CO_2 on degradation of the coating, the mechanisms and valence state of Mg anodic dissolution pertinent to understanding pigment charge capacity depletion, and the detailed current and potential distribution across a defect during atmospheric exposure are also examined. Some of the challenges include defining the primary protection mechanisms afforded by the MgRP, identifying remaining life assessment methods and residual protection, and understanding the cathodic protection current and potential distributions across a scratch or defect during atmospheric exposure.

The primary protection mechanisms afforded by the MgRP and which methods to use for remaining life assessment, were unclear. For instance, the corrosion community understands how to assess the life of barrier coatings and properties like adhesion but not local and global cathodic protection functions. The sacrificial and barrier mechanisms of protection afforded to the AA2024-T351 substrate by a magnesium rich primer (MgRP) were investigated including residual protection mechanisms after Mg pigment depletion. Test methods were developed to estimate the total residual barrier properties of the

coating, the stored Mg anode charge capacity, and the electrically “well connected” Mg in the primer, as sensed electrochemically. The residual barrier properties after depletion of the Mg primer were also assessed using electrochemical impedance spectroscopy. A full immersion testing protocol was designed. The testing regimen included an open circuit hold to assess galvanic coupled potentials between the MgRP and 2024-T351, electrochemical impedance spectroscopy to assess coating barrier properties, potentiostatic holds to asses Mg anodic dissolution charge and calibrated X-ray diffraction to assess the total elemental Mg remaining in the MgRP. An initial understanding of the evolution of these parameters was developed in full immersion in 50 mM NaCl solution as a function of MgRP pigment volume fraction (PVC) with or without a topcoat. The topcoat was observed to protect the Mg pigment from self-corrosion in saline solutions. This work found that residual Mg pigment remained stored in the coating. Preliminary findings suggest two possible modes of protection; long range protection of remote defects and local or short range Mg pigment-based protection of local and buried defects when stored, insulated Mg pigment in a polymer resin is activated. Both modes of protection are mediated by the high ionic and electrical resistance of the coating system as a function of MgPVC, primer polymer and topcoat properties

There are discrepancies between the rates of degradation in standard lab accelerated tests compared to field environments owing to different environmental severity factors based on differences in chemistry, relative humidity, and time of wetness, among others. Field and lab exposures of MgRP in a non-topcoated and topcoated condition were conducted

at a coastal marine site, Kennedy Space Center, FL (KSC); as well as at an inland rural site, Birdwood Golf Course in Charlottesville, VA; in ASTM B-117 with 5% NaCl, in the same standard test modified with ASTM Artificial Seawater as well as in full immersion in ambiently aerated 5% NaCl solution. Mg pigment depletion rate, galvanic protection potential and coating barrier properties were tracked throughout exposure periods in both field and laboratory environments. Preliminary acceleration factors with respect to pigment depletion and residual barrier properties were developed. Analysis near and far from the scribe was performed. Post-mortem characterization with SEM/EDS was conducted to elucidate coating and scribe morphology, corrosion products present, corrosion of the AA2024-T351 substrate, as well as in an attempt to determine the "throwing power" of the MgRP coating system based on cathodic protection of a scratch exposing bare AA2024-T351. The topcoat was observed to severely mediate the depletion of Mg pigment from the primer due to high self-corrosion of unprotected Mg pigment in the MgRP. The Mg pigment was depleted monotonically in all environments but the differences in rate of Mg depletion from the coating upon environmental exposure were rationalized to stem from differences in time-of-wetness and in rates of polymer degradation, specifically resistivity, due to certain environmental severity factors such as precipitation, pH, and UV exposure. Mg pigment was observed to deplete the fastest in field and lab environments with lowest pH levels such as at Birdwood Golf Course in Charlottesville, VA. In contrast, the barrier properties of the epoxy polymer were shown to severely degrade at sites which include UV radiation such as at Kennedy Space Center, FL. A key result from these studies is that the newer generation coating formulations

display consistent degradation characteristics in lab and field environments, albeit at different rates.

The so-called “negative difference effect” is well known to cause discrepancies in the estimated anodic dissolution of bare, pure Mg determined from traditional electrochemical measurements and remains a significant topic of debate in the corrosion community. For this reason, in addition to full immersion polarization tests, it was important to corroborate independent measurements of the dissolution of bare, commercially pure Mg at open circuit as well as under anodic polarization utilizing multiple techniques such as electrochemical impedance spectroscopy, mass loss, H_2 collection, and inductively coupled plasma optical emission spectrometry. EIS was successfully utilized to assess the charge capacity of the Mg anode and supports the notion that Mg is primarily oxidized to Mg^{+2}. This issue was hotly debated in the literature and these findings provided significant clarification for the corrosion community. An important clarification highlighted in these studies is that the applied current measured on the Mg anode by traditional electrochemical techniques accurately accounts for the current available for protection of the AA2024-T351 cathode, and is appropriate to use as E-i electrochemical boundary conditions for mixed potential and finite element modeling of the galvanic couple and throwing power of the MgRP system. However, in order to accurately predict the physical depletion of the Mg anode material from the MgRP coating, the actual anodic dissolution behavior was characterized.

The “galvanic throwing power” (TP) of the coating system pertains to the perpendicular distance extending away from the edge of the MgRP coating exposing bare AA2024-T351 over which the MgRP coating system can protect bare AA2024-T351 by sacrificial anode based cathodic protection. Differences in throwing power in lab and field environments were presumed to stem from differences in electrolyte geometries; continuous thin-layer electrolyte in salt fog cabinet exposures compared to isolated droplets which do not form a connected path in field exposures. It was found that during a given episodic drying or wetting event, throwing power was temporarily increased or diminished, making a definitive determination of throwing power by post-mortem sample evaluation difficult. As such, in addition to post-mortem sample evaluation, the galvanic throwing power of the MgRP was studied via finite element analysis modeling in conjunction with diagnostic multi-electrode arrays (MEAs), which enable the spatial distribution of cathodic protection to be elucidated. The galvanic protection capabilities of the coating in various full immersion, thin layer, and droplet electrolyte geometries relevant to field service explain long misunderstood field behavior.

Current and potential distributions extended across simulated defects when electrolyte layer was thick, continuous and more conductive (higher concentration) and in the absence of a polymer coating. Current and potential distributions did not extend across simulated defects when the electrolyte became discontinuous or the ionic path became tortuous due to drying or the addition of a polymer coating. Additionally, galvanic protection is shown to intensify during drying and re-wetting over short distances rationalized to be caused by changing solution conductivity, E-i behavior, and electrode

area effects. The drying characteristics of individual salts was also shown to have an effect on the evolution of throwing power as $MgCl_2$ (due to its low deliquescence point of ~35% at STP) was shown to be less susceptible to drying at low RH, thus extending the time of which the galvanic couple was active compared to pure NaCl or ASTM Artificial Sea Water.

The technological significance of this dissertation is that it develops a detailed understanding of the protection mechanisms afforded by a top candidate primer coating for the corrosion protection of precipitation age hardened Al alloy 2024-T351 and demonstrates a suite of field deployable electrochemical and characterization techniques that can be used to track coating degradation with respect to Mg pigment depletion rate, global galvanic protection potential and coating barrier properties throughout exposure periods in both field and laboratory environments. Additionally, the corrosion protection functions have been verified from studying corrosion processes at the micrometer scale up to the size of scribed test panels used in aerospace applications and the protection mechanisms were assessed before and after the Mg pigment was depleted.

The scientific significance of this work is that it considers and elucidates some of the electrochemical, physical, and geometric factors that govern the detailed corrosion performance (such as galvanic protection potential and throwing power) of such a coating in atmospheric exposure. This has never been accomplished before using an instrumented approach. This dissertation provides some guidance on what factors or attributes of the coating formulation are important and suggests means to tune the coating to optimize

performance. It also provides quantitative tools to study atmospheric corrosion protection. Further scientific inquiry is suggested to more fully understand how the details of a particular service environment or varying coating formulation (such as with the use of different pretreatments) may control the corrosion performance of the coating.

Acknowledgements

First I would like to thank my advisor, Dr. John Scully, for providing me the opportunity and endless support to pursue my degree. His guidance and mentorship extend far beyond the technical knowledge he bestowed upon me. In addition to being a great friend he has taught me countless intangible lessons on how to be a capable researcher and a responsible, productive member of the scientific community. I would also like to thank the members of my thesis committee: Dr. Opila, Dr. Kelly, Dr. Keene, and Dr. Lee for their invaluable discussions and guidance. I would like to thank Dr. Jason Lee in particular for his support with finite element modeling. Without his expertise, that work would not have been possible.

I appreciate the help of all of my colleagues within CESE and the MSE department. In particular, Tomo and Nicki proved to be invaluable mentors when I first arrived. With seemingly infinite patience, they showed me the ropes. Derek was an incredible friend and mentor during the last three years of my time at UVa. Sam, Rebecca, TJ, Mary Lyn, and Balaji have all provided an infinite amount of help around the labs, shoulders to lean on in difficult times, and countless evenings of stress relief.

Most of all, I would like to thank my family; all of it. My best friend and wife, Hillary, for sticking with me through the long distance, late nights and short weekends over the past 6 years and her constant ability to make me smile. My parents, Ann and Darrell, for always having no doubt in my abilities and for always supporting me without question. My in-laws Claudia and Dave for their amazing support and for truly treating me like a member of the family. Finally, I would like to thank my third set of parents, roommates, and landlords Donna and Bobbie. The warm meals, welcoming home, and unwavering support will always make my time in Charlottesville a happy memory.

Table of Contents

List of Tables

List of Figures

List of Symbols

β_a	anodic Tafel slope
β_a	cathodic Tafel slope
C	capacitance
CPE	constant phase element
E_{app}	applied potential
E_{couple}	galvanic couple potential
E_{SCE}	potential measured vs. SCE
E^0	equilibrium half-cell potential
F	frequency
F	Faraday's constant
i	current density (A/cm^2)
i_0	exchange current density
I	current (Amps)
i_{lim}	limited current density
n	number of electrons transferred in a reaction
PVC	Pigment volume concentration
PVC_{Mg}	Mg Pigment volume concentration
R	universal gas constant
R	resistance (Ω)
R_P	polarization resistance
σ	conductivity (S/m)
ρ	resistivity (Ω·m)
Q	charge
t	time
T	temperature
η	over-potential
W	Wagner number
Z	impedance

1 Introduction: Background, Significance and Objectives

The high strength-to-weight characteristics of aluminum alloys make them ideal structural metals and have led to their broad use in aerospace applications. Additionally, even though aluminum is an active metal in terms of its low Nernst potential, aluminum alloys are able to form stable aluminum-oxide surface films which generally afford them good atmospheric corrosion resistance.[1] These protective oxides tend to possess a two-layer, amorphous structure of a thin, dense inner layer of Al_2O_3 and thicker, porous outer layer of hydrated oxide[2] which, together, only grow to a total thickness of 20 nm in 52% RH and 170 nm in 100% RH after 5 years of atmospheric exposure but generally provide significant barrier protection.[2, 3] However, high strength Al alloys have many microstructural heterogeneities leading to micro-galvanic coupling in corrosive environments producing several modes of local corrosion. The mode of localized corrosion depends on the details of the local alloy microstructure and chemical environment, but such attack requires the application of corrosion mitigation strategies.

1.1 AA2024-T351 Metallurgy and the Susceptibility of Aerospace Al-Cu-Mg Alloys to Localized Corrosion

The Al-oxide films that naturally form on Al-based precipitation age hardened alloys exposed to aqueous, pure H_2O are thermodynamically stable, under standard operating temperature and pressure, in the pH range of 4 to 8.5 (Figure 1.1). The Al-oxide films significantly impede general, uniform corrosion of the Al-rich matrix of the alloy. However, even though these oxides are thermodynamically stable over a relatively large

range of pH, these surface films often break down locally in service, due to the presence of Cl^- or other anions, and leave the aluminum alloy susceptible to non-uniform, localized pitting corrosion.[4-6]

Al-Cu-Mg Al-alloys, such as AA2024-T351, contain significant amounts of Cu and Mg-rich intermetallic compounds within a solute-lean, α-Al matrix[7-30] (AA2024 chemistry specification shown in Table 1.1) along with several types of constituent particles, Cu solute depletion zones, precipitates, and dispersoids. This, inhomogeneous, non-uniform microstructure leads to the formation of localized galvanic cells (Figure 1.2 and Figure 1.3) as each phase possesses a different corrosion potential in chloride containing environments (Table 1.3 and Table 1.4).[9] The formation of these galvanic cells leads to localized attack of the alloy.[7, 8] All of the various phases found in Al-based precipitation age hardened alloys possess threshold potentials at which localized breakdown and attack of the particular phase occurs (Table 1.5).[9] When a localized galvanic cell is formed between two or more phases in an inhomogeneous alloy, any phase which is subsequently polarized above its threshold breakdown potential will become a site of pit initiation. Such a potential window is termed a "window of susceptibility" and is determined by the physical and electrochemical properties of the phases in the galvanic couple.

Some intermetallic compounds, such as the predominant Al_2CuMg (S-phase), are less noble than the Al-rich matrix (Figure 1.2 and Figure 1.3) and act as local anodes. These anodic sites are preferentially attacked and, upon localized breakdown of the barrier oxide, become sites of pit initiation which can propagate with prolonged anodic

polarization (Figure 1.4). Additionally, Cu solute-depleted zones surrounding grain boundaries in aged Al–Cu–X alloys are anodic to the Cu-rich IMC's and the non-Cu-depleted Al matrix (Figure 1.5) leading to pit initiation along grain boundaries which, upon spreading, leads to intergranular corrosion (IGC) and intergranular stress corrosion cracking. [6, 31, 32] Moreover, Cu that is dealloyed from these active intermetallic compounds and released into solution often travels to, and replates at, cathodic sites on the metal's surface.[33] Other intermetallic phases, particularly Cu-rich phases such as Al_2Cu, are more noble than the Al-rich matrix (Figure 1.2 and Figure 1.3) and these sites, along with sites of re-plated Cu, act as local cathodes, leading to alkaline attack and trenching of the more active Al-matrix around their perimeter.[33] Without additional protection during prolonged environmental exposure accumulated, non-uniform damage can eventually result in material failure. [7-12]

1.2 Corrosion Protection Methods Utilized in Protecting Aerospace Al Alloys

Many different methods are employed to minimize corrosion of Al-based precipitation age hardened alloys in service. Passive protection methods involve either thickening a barrier oxide film on the surface of the metal or applying a barrier organic polymer to the metal surface prior to service. Active protection methods possess the capability to protect the substrate even after a defect has formed that penetrates the barrier layer. Some of the most common passive and active protection schemes are discussed below where active corrosion inhibition is used to describe the protection of a bare defect or scratch. A scratch is defined as a site where the coating or pretreatment is removed or otherwise absent.

1.2.1 Limitations of Barrier Protection

Passive barrier layers, such as polymer coatings or conversion coatings, do not typically prevent electrolyte from wetting the metal surface as most organic polymers are significantly water permeable and most oxide layers become hydrated upon exposure to humid or aqueous environments.[34] Passive barrier layers reduce corrosion by simply limiting current flow between local anodes and cathodes, acting to suppress the driving force for corrosion on the surface of the metal. In service, however, defects in the barrier are formed by a nearly infinite list of environmental stresses such as abrasion, UV degradation, chemical attack, and many others. Once these defects form, the barrier oxide or coating does not possess the capability to protect the bare substrate where the coating is absent. Therefore, active corrosion protection schemes are necessary for the long term protection of valuable assets. The two primary active protection methods utilized in service are sacrificial anode based cathodic prevention[(1)35] and/or the incorporation of soluble chemical species inhibitors in pretreatments and primer coating systems applied to the substrate.

[1] Sacrificial anode based, cathodic corrosion "prevention" is not to be confused with similarly termed sacrificial cathodic "protection". The traditional concept of cathodic protection, classically applied to immersed steel structures, involves achieving a galvanic couple potential substantially below the OCP or near the reversible potential of the corroding metal such that uniform corrosion is significantly reduced. In the case of aluminum-based materials, this is not desired, as significant cathodic polarization can lead to cathodic corrosion of the Al-rich matrix when the pH shifts alkaline due to increased cathodic reaction rate, as Al is amphoteric. Instead, the proper goal is to cathodically polarize the Al alloy below a threshold potential associated with localized corrosion such as a critical pitting potential, critical potential for intergranular corrosion, or critical potential for S-phase dissolution, etc.

1.2.2 Sacrificial Anode-Based, Cathodic Prevention

One of the protection schemes utilized in aerospace applications is sacrificial anode based, cathodic corrosion prevention by sacrificial anodic coatings. Some sacrificial coatings commonly used on Al alloys are mechanical Al-cladding (Alclad^{TM})[36] or, more recently, Al-Co-Ce metallic coatings[37-39]. In this protection scheme a material that is more active than the Al alloy substrate is applied as a coating and, in absence of an insulating pretreatment layer, is galvanically coupled to the substrate in the presence of an electrolyte. The cladding layer consists of a roll-bonded layer that is usually commercially pure aluminum or an aluminum alloy that is anodic to the base metal. Usually, the thickness of the cladding is approximately 1.5-10 % of that of the base metal depending on the characteristics of the cladding alloy, base metal and the environment.[40] The more active, sacrificial coating material preferentially corrodes and provides current to the cathodic, Al-alloy substrate. This cathodic polarization of the substrate, ideally, is sufficient enough below the threshold potentials (Table 1.5) of the matrix phase and any constituent particles which make up the AA2024-T351 substrate to decrease both localized and uniform attack. Moreover, coatings which utilize the sacrificial galvanic protection mechanism have the ability to protect bare areas of the substrate that are both ionically and electrically well-connected to the anodic material in the coating (Figure 1.10).

The distance over which the coating system can protect a defect by sacrificial anode based cathodic protection, is termed the “galvanic throwing power”. The cathodic protection, as measured by galvanic throwing power, available to a defect depends on

many things such as the electrochemical driving force (ΔE_{OCP}) between anodes and cathodes, the area ratios between anodes and cathodes, electrolyte geometry and chemistry, electrical resistances between anodes and cathodes, as well as others. In the case of Al-cladding, which has been used for many decades, the galvanic couple potential that is achieved is often only 80 – 100 mV below the OCP of the substrate alloy it is being used to protect.[37-39] This modest cathodic polarization of the substrate provides limited driving force for galvanic throwing power to protect bare defects or scratches. Additionally, this galvanic couple potential is often above the critical pitting potential of the cladding material, resulting in non-uniform degradation of the cladding and inefficient anode utilization.

The cathodic current distribution that is spread across a scribe or coating defect exposing bare AA2024-T351 will be controlled by various factors and can be relatively summarized qualitatively by examining the Wagner number or Wagner polarization factor pertaining to various geometric and chemical exposure scenarios. [41, 42]The Wagner number can be used to evaluate the relative degree of uniformity of the galvanic current distribution. The Wagner number (W) is described by the ratio of the electrochemical polarization resistance of the anode and cathode (K) to the resistance to ionic conduction in the electrolyte path separating the anode and cathode (L).[42] If for any reason, the ionic pathway becomes tortuous (L is large) the Wagner number becomes small ($W \rightarrow 0$) and the current distribution over the scribe is expected to be more non-uniform.

Finite element analysis, or similar spatially resolved computational methods, of potential and current distribution in galvanic systems has long been studied in the literature.[41-47] Such studies are often carried out to investigate fundamental effects of electrolyte geometry[46, 48], electrode kinetics[45, 49, 50], unique part geometries[42], crevice corrosion[44, 51], and sacrificial anode based, cathodic protection schemes[38]. However, these studies do not involve the addition of restive polymer layers or study the effects of volume concentration of electrode material in a semi-permeable matrix.

1.2.3 Chemical Film-Forming Inhibitors

Another common protection scheme utilized to minimize corrosion of aluminum alloys in aerospace applications is the use of chemical inhibitor-containing coatings and pretreatments. Most chemical inhibitors utilized for the corrosion protection of Al alloys, such as hexavalent chromates, are either passivating or precipitation-type, film-forming, chemical species which function by promoting the formation of a passive film or deposit layer on the metal surface or IMCs. The formation of a passivating film on the surface of the metal serves to increase the pitting potential of the material while a passivating film covering the IMC's lowers the galvanic driving force (ΔE_{couple}) between the IMC and the matrix. Other chemical inhibitors, such as vanadates, function by forming a layer of adsorbed anionic species which are hypothesized to reduce oxygen reduction kinetics and may also displace Cl- ions on the Al matrix, increasing the stability of the passive film and reducing the breakdown of S-phase particles.[52-55] Both functions reduce the alloy's susceptibility to localized corrosion in hopes of prolonging its life in service. Hexavalent chromate is currently the primary inhibitor used for the protection of Al-alloys due to its

high efficacy and ability to protect a wide range of metals, making it suitable for the protection of inhomogeneous materials.[25, 56, 57] Chromate is an oxidizing inhibitor and produces a protective mixed oxide of chromium and aluminum oxides on the surface of the Al alloy in addition to being both and anodic and cathodic inhibitor. [25, 56, 57] Hexavalent chromium is commonly incorporated into pretreatments, sometimes into conversion coatings and as soluble pigments in organic polymer primers within coating systems where it is actively leached out (because it is soluble) to provide protection by inhibitor transport to a coating defect when it occurs service.[58, 59] Such factors such as electrolyte layer thickness, concentration, or pH, scratch size, even anodic and cathodic kinetics govern the throwing power of the chemical inhibitor across a bare defect.[43] Due to their low weight (as compared to sacrificial metallic coatings), high efficacy, ease of application, and long lifetimes, inhibitive, hexavalent chromium-containing conversion coatings and/or organic polymer paints have, for decades, been the primary active protection scheme utilized in aerospace applications.

1.3 The Need for a New Protection Technology for Aerospace Alloys

Unfortunately, due to their extreme carcinogenicity[60] and high handling costs, protection schemes which utilize hexavalent chromium are becoming increasingly burdensome and costly for industry and the US DoD[61] to implement in service. In April 2009 the US Under Secretary of Defense for Acquisition, Technology, and Logistics issued a memorandum[61] requiring an accelerated phase-out of hexavalent chromium, concurrent with a push to find effective alternatives. The memo states that the "serious human health and environmental risks" related to the use of hexavalent chromium, as well as the

growing number of international restrictions that threaten the supply chain "continue to increase the regulatory burdens and life cycle costs for DoD and decrease materiel availability". Therefore, there exists a need for a superior replacement corrosion protection technology for use on aerospace aluminum alloys that is not only effective at protecting aluminum alloys from corrosion by either a passive barrier or, preferably, active mitigation function or active inhibition of corrosion at scratches, but which is also safe, cost effective and weight competitive.

1.4 Mg-Rich Primer, a Promising Commercial Technology for Corrosion Protection

Over the past few years, a commercial organic coating system containing a Mg-pigmented polymer primer (MgRP) has been developed for the corrosion prevention of aluminum alloys, such as precipitation age hardened 2024-T351, and has shown good performance in the field.[59, 62-73] Additionally, the MgRP is weight competitive (~1.2 - 1.6 g/cm^3 dry weight) to existing, industry-standard, strontium chromate-containing polymer technologies, which is important where aircraft fuel efficiency is a primary concern. For these reasons, this coating system is a front-running candidate to replace widely used, chromate type surface pretreatments and chromate pigmented primers commonly used in aerospace applications.[59, 60, 74] The MgRP is designed to be applied to an aluminum alloy substrate as a primer layer, above any pretreatments, but below any topcoats which may be used (shown schematically in Figure 1.6). The MgRP is designed to galvanically couple the Mg pigment in the primer to the substrate and provide sacrificial anode based cathodic prevention to the aluminum alloy (AA2024-T351).

The concept of sacrificial anode based cathodic prevention by a metal-rich polymer is well established in the design of zinc-rich primers for use on various steels and has been well documented.[75-90] Protection by Zn-rich primers is afforded primarily by sacrificial anode based cathodic prevention and secondarily by precipitation of $Zn(OH)_2$ at bare sites after migration of Zn^{2+}.[84, 85] Zinc also has a low self-corrosion rate which leads to an acceptable protection lifetime. In the case of MgRP, magnesium is also less noble than all of the precipitation age hardened aluminum alloys it might be used to protect (Table 1.2) and is readily available and actively corrodes in most electrolytes.[65, 66, 91]

Complicating the use of Mg as a sacrificial anode is the so-called "negative difference effect" (NDE). The NDE on Mg dissolution remains a significant topic of debate in the corrosion community as the NDE is well known to cause discrepancies in the estimated anodic dissolution of bare, pure Mg determined from traditional electrochemical measurements and to produce a low anode efficiency for Mg of 60% or less.[92] For this reason, in addition to full immersion polarization tests, it is important to corroborate independent measurements of the dissolution of bare, commercially pure Mg at open circuit as well as under anodic polarization utilizing multiple techniques such as electrochemical impedance spectroscopy, mass loss, H_2 collection, and inductively coupled plasma optical emission spectrometry.

1.5 Current Understanding of Corrosion Protection Mechanisms afforded by MgRP to Al

When coupled to the AA2024-T351 (or similar alloy) substrate, the Mg pigment becomes an electron donor, and mixed potential theory can be used to explain the open circuit of

the system when exposed to full immersion. Results in the literature support the notion of mixed potential theory describing the galvanic coupling behavior between the primer and substrate.[62-67, 91, 93] Potentiodynamic scans (Figure 1.7) and open circuit measurements (Figure 1.8) in the literature show a bare Mg electrode having an open circuit potential, in 0.1 wt. % NaCl solution, of about -1.55 V vs. SCE while bare AA2024-T351 has an open circuit potential of about -0.6 V vs. SCE.[65] These potentiodynamic scans also show that the anodic reaction rate on Mg is relatively fast and that the cathodic reaction rate on AA2024-T351 is relatively slow.[65] The combination of a fast anodic reaction rate on Mg and a slow cathodic reaction rate on AA2024-T351 results in a polarizable cathode that enables a negative galvanic couple potential between bare AA2024-T351 and bare Mg electrodes of as low as -1.5 V vs. SCE in 0.1 wt. % NaCl solution.[65] However, when coated with MgRP, the open circuit potential of the AA2024-T351 is mediated and approaches -1.1 V vs. SCE (Figure 1.8).

The galvanic couple potential between the Mg and AA2024-T351 will depend on the surface area ratio between the two electrodes exposed to immersion, the geometric arrangement, electrochemical boundary conditions, and electrolyte chemistry, among others.[38, 43, 46, 48-50, 94, 95] Hence, when the sacrificial Mg is placed in an organic polymer, the galvanic couple potential between the Mg pigment and AA2024-T351 substrate becomes a function of the wetted surface area ratio of the two materials actually exposed to an aqueous environment (e.g. Mg pigment volume concentration that is wetted; AA2024-T351 that is wetted such as at scratch site), the kinetic properties of the anode and cathode, the electrolyte each is exposed to, the resistive path length and geometry as

well as the electrical and ionic conductivities of the system. The Mg pigment volume concentration (PVC) will affect both the resistive paths through the organic coating between the Mg pigment and the underlying AA2024-T351 substrate as well as the path through the organic coating and the electrolyte to any exposed AA2024-T351. All of these factors will mediate the galvanic couple potential existing at each metal surface.

Work on metal-rich coatings in the past has predicted and shown a direct dependence of a coating's conductance on the PVC of conducting pigment.[96-104] These studies have shown that there exists a critical pigment volume concentration (CPVC) that marks a composite coating's sharp transition from non-conductive to conductive behavior.[96, 97, 103, 105] The CPVC of MgRP with 20 μm diameter Mg pigment has been estimated by other groups to be about 50-60%.[65, 91] For this reason, it is predicted that samples with an Mg PVC of 45%, will have a pronounced drop in conductivity through the primer layer. This modest conductivity along the electrical pathway between the anode and cathode (Figure 1.9) limits the cathodic polarization afforded to the substrate by the Mg pigment at exposed areas in addition to the presence of a resistive ionic path through the electrolyte.

The resistive properties of the polymer used in the MgRP system also affect the total resistivity of the MgRP. Changing the resistivity of the polymer, via water uptake or other characteristics; will also affect the galvanic coupling potential of the system. The resistivity of the system will also change if the organic polymer degrades as a result of an environmental exposure due to effects of UV radiation, temperature, chemical damage, or other environmental effects. The resistivities of the organic polymers may be an

overlooked aspect of the factors governing the galvanic couple potential ultimately achieved in this system which is likely mediated by these resistances. Lastly, any resistive layer between the 2024-T351 and MgRP brought about by anodizing or adding a conversion coating could also serve to mediate the galvanic coupling potential of the system.

1.6 Length Scales of Key Phenomena Pertinent to Understanding MgRP and Atmospheric Corrosion

During atmospheric exposure, many length scales play a role in determining the protection mechanisms afforded to the AA2024-T351 substrate by the MgRP system and the subsequent degradation of the coating and substrate with prolonged exposure. Various length scales of interest are depicted schematically in Figure 1.10. Length scales of particular importance to the MgRP/2024 system are the size and distribution of constituent particles in the AA2024-T351 microstructure, the size, shape, and distribution of the metallic Mg pigment in the MgRP, the applied thickness of the primer and topcoat polymer coatings, the size and deposition density of aerosol salts in various exposure environments, the resulting electrolyte layer geometry, and the characteristic length scale of any coating defect, among others.

The microstructure of the AA2024-T351 substrate plays an important role in governing the corrosion morphology. As discussed earlier in this chapter, Al-Cu-Mg alloys such as AA2040-T351, typically corrode by non-uniform, localized pitting corrosion brought about by the breakdown of the 1 – 10 nm thick oxide film and subsequent galvanic interaction between the Al matrix and more noble Cu-rich intermetallic compounds

(IMCs).[4-6, 12, 14, 15, 17-24, 106] These local galvanic cells induce acid pitting proximate to the anode and alkaline attack proximate to the cathode. In AA2024-T3, pit initiation sites include Al-Cu-Mg particles and the matrix adjacent to Al-Cu and Al-Cu-Fe-Mn constituent particles.[12, 15, 17, 19, 22-24, 107] 2 – 4% of the LT surface of AA2024-T351 is covered by constituent particles with a mean nearest neighbor centroid distance of 5 – 10 μm (Figure 1.11). The Al-Cu-Mg type is the most active constituent particle and as much as 60% of the intermetallics on the surface of an AA2024-T3 sample are of the Al-Cu-Mg type.[15, 108, 109] The Al-Cu-Mg type IMC is anodic to the Al alloy-matrix and is present as 1 to 10 μm diameter particles.[33] The spacing and size distribution of these particles is important, as it will determine the distribution of anodes and cathodes under a water layer formed in environmental exposure, and subsequently play a large role in determining the morphology of attack of the alloy.

Aerosol salts range from 0.5 – 30 μm in size[110, 111] and their mean deposition density and chemistry depend largely on geographic location and rinsing frequency. Mean salt deposition densities at a particular geographic location result from the buildup of aerosol species according to the aerosol impingement rate at the exposure location less any salt removal by events such as wind, rain, immersion, or abrasion. Chloride impingement rates are historically measured by chloride candles.[112] Statistical distributions of mean salt deposition densities, which statistically account for salt removal events, at various environmental exposure sites are typically measured by rinse off conductivity techniques. Based on these measurements, mean salt deposition densities can range in the field from less than 1 μg/cm^2 at very benign rural inland sites to more than 100 μg/cm^2 in severe

coastal regions and can surpass 1,000 μg/cm^2 in outdoor sheltered or lab accelerate life environments such as ASTM B-117 salt spray (Figure 1.12).

The mean salt deposition density, along with ambient relative humidity, significantly affects the electrolyte layer geometry and coverage on the surface of a material during an environmental exposure. During exposure, in addition to periodic wetting events by dew, rainfall, or immersion, deposited salts can deliquesce and equilibrate to a thermodynamically stable electrolyte concentration (generally 0.1 to 1.0 M for NaCl) to form individual droplets and/or a continuous electrolyte layer. In field and lab environments, these droplets can have a significant range in diameter, generally from 1 to 10,000 μm, depending on the size of the deposited salt crystal (1 – 10 μm, Figure 1.10), the ambient RH, and the deposition density which determines whether the droplets touch and coalesce into larger droplets. As a result, these deliquesced droplets can cover as little as zero or up to thousands of constituent particles on the AA2024-T351 substrate, inducing galvanic interaction between the constituent particles and Al-rich matrix. In the context of a galvanic couple between Mg pigment in the MgRP and the AA2024-T351 substrate, the chemistry of such an electrolyte layer determines the E-i electrochemical boundary conditions of the Mg pigment and the AA2024-T351 substrate. The electrolyte geometry will dictate the relative area ratios of MgRP and AA2024-T351 in the galvanic couple as well as control the geometric bounds of a galvanic couple between Mg pigment in the MgRP and bare AA2024-T351 extending away from the interface of a coating defect, such as a scratch or scribe. A limitation in the cathodic protection distance extending away from the edge of a coating defect (termed “throwing power”) can be

brought about by a tortuous electrolyte and is discussed thoroughly later in chapters 4, 5, and 7 of this thesis.

The MgRP-coated AA2024-T351 panels studied throughout this thesis are considered to be dimensionally representative of the actual application scenarios used in service on aircraft. The samples were comprised of AA2024-T351 sheet, pretreated with Prekote surface pretreatment, and primed with a 30 ± 10 μm thick layer of magnesium rich primer, "MgRP" (Product and lot numbers ID'ed in Figure 1.10) and topcoated with a 60 ± 10 μm thick layer of high performance organic polyurethane polymer (Product and lot numbers ID'ed in Figure 1.10). All tested panels were provided and painted by collaborators at Akzo Nobel Aerospace Coatings or at NAVAIR.[113, 114] After curing for approximately 4 weeks in a dry box, a 50.8 mm (2") by 101.6 mm (4") "X" with a width of approximately 700 μm was machine scribed through the coating layers of the panel, exposing bare AA2024-T351, to simulate a scratch prior to environmental exposure. In general, the scribe penetrated 10 to 50 μm into the substrate. The right side of Figure 1.10 shows an SEM micrograph of cross-sectioned, topcoated MgRP on AA2024-T351, before the sample has been exposed to any weathering environment. Mg pigment particles have an approximate diameter of 20 μm and flake geometry and comprises 40 – 45% of the as-applied, cured primer by volume. EDS spot scans conducted on the Mg particles in the cross-sectioned MgRP also indicated low O levels, which suggest the Mg is largely unoxidized prior to weathering.

1.7 Critical Unresolved Issues in Current Research

Conceptual understandings of the sacrificial galvanic and barrier protection strategies that are designed into the full-up MgRP coating system are widely held.[59, 63-67, 69, 70, 91, 93, 115, 116] There is also a growing set of data (mainly visual) from field exposures. However, there exists a need to fundamentally understand and explain how various parameters of the coating system quantitatively govern the particular protection behaviors observed under various exposure conditions such as secondary barrier protection mechanisms and remote and local galvanic protection modes. Most testing is by lesson-learned trial and error field exposures.

An opportunity exists in utilizing mixed potential modeling along with diagnostic electrochemical tests to gain a fundamental understanding of how each component in the full-up coating system affects the sacrificial anode based galvanic and barrier corrosion protection mechanisms. This foundation may be essential to understand the difference in performance between field and lab environmental exposures.

In limited field and lab exposures of early generation products, differences in corrosion behavior of the MgRP between field and laboratory environmental exposures has been observed. Blistering of early, first generation commercial coating systems is seen in ASTM B-117 laboratory tests but is typically not seen in field exposures such as at Daytona Beach or Kennedy Space Center.[113, 114] Therefore, it is important to determine if the blistering phenomena is significant in the current, third-generation products and, if so, to understand the factors controlling this blistering phenomenon in order to guide predictions of whether it will be seen in any type of field environments as well as to

reassess the relevancy of the ASTM B-117 test to field conditions. To date, there has been very little blister characterization on early generations of this coating system in the literature beyond macroscopic optical micrographs. Similarly, there has been very little work done to identify a corrosion cell with electrochemical half-cell reactions to serve as an explanation of the blisters' formation or any verification with diagnostic testing to prove such a model. There are competing theories as to the cause of the blistering. One theory claims the blisters are a result of anodic coating disbondment aided by H_2 gas produced by Al dissolution. This theory claims the blistering is more prevalent in Mg-pigment-lean or non-MgRP organic polymer coatings, and results in the formation of blisters along the defect or scribe [29, 117]. The competing theory claims the blisters along scribe lines are caused by cathodic corrosion of the Al substrate due to its amphoteric nature.[118-123] In the second theory, it is hypothesized that the presumed cathodic corrosion is caused by a local increase in solution pH as a result of the dissolution of the Mg pigment and/or increased cathodic reaction rates at sites of severe cathodic polarization of the Al substrate.[113, 114] An opportunity gap lies in providing such an explanation and experimental verification. Also, it has been proposed that increased concentrations of environmental CO_2 might act to mitigate the blistering phenomena.[62, 114, 124] Therefore there exists a complimentary opportunity to the general issue of field/lab discrepencies to gain a fundamental understanding of how CO_2 and other environmental gases might act to mitigate such blistering phenomena once an understanding of their mechanisms of formation is obtained.

Finally, there exists a need to determine the long term performance characteristics of the MgRP coating system in environments relevant to realistic deployment scenarios. Much of the previous work attempting to do this have utilized laboratory accelerated life testing (LALT), primarily ASTM B-117 salt fog cabinet testing.[59, 62, 91, 113, 114, 124-127] However, this testing environment makes no effort to realistically reproduce field exposure environments with respect to factors relevant to environmental severity such as electrolyte chemistry, atmosphere composition, time of wetness (TOW), relative humidity, or UV exposure. As such, the validity of the ASTM B-117 exposure environment has largely been questioned, particularly because unique failure modes of early generations of the MgRP coating system have been observed in the ASTM B-117 environment that are not typically seen in the field.[113, 114] Alternatively, field testing to date has only examined visual appearance and limited removal of coatings.[113, 114, 128] Newer generations of the coating system do not typically display these failure modes in field or LALT environments when applied to AA2024-T351 and serve as the primary products of focus in this thesis.[113, 114]

In a non-topcoated condition, as a result of remote pigment depletion from the MgRP, mainly by self-corrosion, the global galvanic protection potential of the coating system, with respect to remote scratches, became more positive with exposure time in each lab and field environment, from values approximately equal to that of bare Mg (-1.6 V vs. SCE) to those approximately equal to that of bare AA2024-T351 (-0.55 V vs. SCE). Barrier properties of the MgRP primer coating also degraded with time in each environment but corrosion of the AA2024-T351 substrate under the coating was not

observed.[72, 73] In a topcoated condition, the topcoat was observed to strongly mediate the depletion of Mg pigment from the MgRP, due to self-corrosion. Exposure in all field and lab environments studied resulted in only partial depletion of metallic Mg pigment in the MgRP after 1000 hrs in the lab salt spray test and after 1 yr in the field exposures. As a result of partial depletion of remote Mg pigment particles, the global galvanic protection potential of the coating system, with respect to remote scratches only, increased slightly with exposure time in each environment, from initial values of approximately -1.0 V vs. SCE to -0.7 V vs. SCE after extensive environmental exposure.[73]

Given the similarity of corrosion modes in the absence of any blistering phenomena in this environment, a determination of acceleration factors with respect to measurable, quantifiable properties, such as Mg depletion rate, galvanic protection potential and coating barrier properties, is a worthy goal. Rather than just report the relative performance of the MgRP coating system in various environments, there also exists a need to try and explain the observed evolution of these measurable, quantifiable properties in the context of environmental severity in order to identify environmental factors which have a primary impact on MgRP performance. Factors important to environmental severity include electrolyte chemistry, atmosphere composition, time of wetness (TOW), relative humidity, UV exposure, and others.

1.8 Specific MgRp/Topcoat Coating Systems of Interest

Over the course of this work, two generations of commercial MgRP coating formulations were studied. Very early work primarily focused on "2nd generation", experimental

formulations of the MgRP which contained varying percent volume concentrations (PVC) of metallic Mg pigment but which all had identical organic 2-part epoxy polymer chemistries; the explicit details of which were not divulged by the manufacturer other than what is provided in the Materials Safety and Data Sheet (MSDS). These "second generation" MgRP samples were supplied by Scott Hayes at Akzo Nobel Aerospace Coatings and provided a means to study the effects of varying MgPVC on sacrificial galvanic and barrier protection mechanisms and to study MgPVC's effects on coating characterization by SEM, EDS and XRD. These second generation coatings also provided an opportunity to briefly study unique failure modes that were observed in laboratory exposures of the 2nd generation product. Such failure modes were not observed in later, "3rd generation" commercial products (Figure 1.13). The 3rd generation product was the primary coating system studied the in later stages of this work. The more stable, uniform degradation characteristics of the 3rd generation product (Akzo Nobels Aerodur 2100P003) allowed for the study and comparison of coating performance in various environments of interest and for the study of various exposure variables relevant to environmental severity.

1.9 Critical Unresolved Issues and Objectives of Research

While the primary objective of this thesis is to physically and electrochemically characterize the MgRP coating system and its' performance in the two desired corrosion functions (local corrosion barrier and sacrificial anode based cathodic protection), there are several aspects of this coating, which require more complex analysis and are considered to be critical issues. Understanding these issues is key to understanding the

behavior of this coating in various environments. The purpose of this research is to utilize laboratory full immersion exposures, laboratory diagnostic experiments, pre- and post-mortem coating characterization, electrochemical mixed potential modeling and field and laboratory accelerated life testing (LALT) to tackle the objectives listed below.

The needs in understanding and focus of this research are to:

- Understand the sacrificial anode based cathodic and barrier protection functions afforded by the Mg-rich primer with regards to how each component in the full-up coating system (substrate, primer, and topcoat) affects the protection characteristics. It is a purpose of this work to establish an integrated electrochemical, electrical, and physical understanding of this protection function. This has not really been established in the literature to date which is mainly based on visual observation and baseline electrochemical lab investigations.
- Explore lab and field deployable methods for assessing the total *and* electrically "well connected" residual stored anode capacity in the coating after environmental exposure.
- Determine if the protection mechanisms and degradation characteristics of the coating are similar in field and lab environments. Newer, optimized generations of the coating system do not typically display unique failure modes in field or LALT environments when applied to AA2024-T351. Therefore, assuming a similarity of corrosion modes in the absence of any blistering phenomena in these accelerated environments, the determination of acceleration factors with respect to specific, measurable coating properties is a worthy goal.

- Better understand the self-corrosion rate, theoretical anode capacity, and anode behavior of Mg pertinent to sacrificial galvanic protection during atmospheric exposure (i.e. wet/dry cycling). The issue of Mg oxidation to Mg^{+} or Mg^{2+} is addressed as this effects the anode capacity available for protection.
- Understand the effects of the wet-dry cycle, and other factors associated with environmental severity, on anode-cathode galvanic couple characteristics, electrolyte path resistance, and galvanic throwing power as a first step towards determining the basis for acceleration factors with respect to Mg depletion rate, the galvanic protection potential and coating barrier properties during exposure in various field and LALT environments. Other factors of interest, relevant to environmental severity, include time of wetness (TOW), relative humidity, UV light, and electrolyte chemistry.
- Another important piece of information to know in order to predict the protection capabilities of the coating in natural environments, and a severe lack of understanding in the literature, is the "throwing power" of the MgRP coating system under various conditions. The "galvanic throwing power" (TP) of the coating system pertains to the distance extending away from the edge of the MgRP coating over bare AA2024-T351 over which the MgRP coating system can protect bare AA2024-T351 by sacrificial anode based cathodic protection. Diagnostic electrochemical experiments utilizing microelectrode arrays, field and laboratory environmental exposures of diagnostic samples, along with computational COMSOL modeling will independently conducted to explore the variables controlling galvanic throwing power.

1.10 Thesis Organization

This thesis is organized by these needs and/or critical issues pertaining to the performance characteristics and limitations of the MgRP coating technology.

Chapter 2 combines diagnostic electrochemical measurements such as OCP and EIS with materials characterization techniques, such as electron microscopy and X-Ray diffraction, to further elucidate the sacrificial anode based cathodic and barrier protection functions afforded by the Mg-rich primer with regards to how each component in the full-up coating system (substrate, primer, MgPVC, and topcoat) affects the sacrificial and barrier protection characteristics of the coating. A mixed potential model is developed and utilized to describe the effects of MgPVC and of various electrical and ionic resistances that exist between the AA2024-T351 substrate and Mg pigment in the primer. Moreover, Chapter 2 also develops lab and field deployable test methodologies for assessing coating degradation with regards to both the total and the electrically "well connected" residual stored anode capacity in the coating as well as the residual barrier properties of the coating after environmental exposure.

Chapters 3 and 4 closely track the degradation of a current generation MgRP coating formulation (Ch. 3 without a topcoat, Ch. 4 with a topcoat) using a suite of high level surveillance in various field and laboratory salt fog exposures in order to study the effects of electrolyte chemistry, time of wetness and UV variables relevant to environmental severity. The coating's degradation is tracked in various environments utilizing the methodology developed in Chapter 2 and, absent of any significant differences in degradation behavior, acceleration factors are elucidated.

Chapter 5 focuses on the foundational electrochemistry of AA2024-T351 and high purity Mg. It is the purpose of Chapter 5 to study the effects of electrolyte chemistry on the E-i electrochemical boundary conditions of both bare Mg and bare AA2024-T351 in the context of a galvanic couple between the two materials. In this work, diagnostic full immersion polarization tests were utilized in an effort to determine E-i electrochemical boundary conditions of both bare, commercially pure Mg and bare AA2024-T351 in various electrolyte chemistries that are relevant to realistic MgRP deployment scenarios. Moreover, the anodic inefficiencies of Mg as an anode are discussed and characterized in Chapter 5 with the use of multiple corrosion rate assessment techniques such as EIS, mass loss, H_2 gas collection, and ICP-OES to help understand the E-i behavior of high purity Mg. In an effort to circumvent the little-understood negative difference effect (NDE), in-situ EIS and H_2 collection and post-mortem mass loss and ICP-OES techniques were utilized to characterize the anodic dissolution rates of high purity Mg.

In Chapter 6 the galvanic throwing power of the MgRP is studied via post-mortem sample evaluation, finite element analysis modeling, and diagnostic multi-electrode arrays (MEAs), which enable the spatial distribution of cathodic protection to be elucidated. This was done in an effort to assess and predict the galvanic protection capabilities of the coating in various full immersion, thin layer, and droplet electrolyte geometries relevant to field service. Discussion rationalizes a basis for field effects seen by Bill Abbott at Daytona vs. Charlottesville, Virginia and/or Columbus, Ohio.

Chapter 7 presents the conclusions of this work and highlights key lessons learned relevant to utilizing MgRP in service. Remaining questions and discussion of ongoing and future work are also detailed.

Appendix A utilizes diagnostic electrochemical measurements, laboratory salt fog cabinet exposures, and materials characterization techniques to address the origins of specific discrepancies (i.e. blistering failure modes of anodic undermining and cathodic corrosion as effects of CO_2) seen between laboratory and field exposure results in order to define the electrochemical cells responsible.

Appendix B extends the laboratory environmental exposures studied in Chapters 3 and 4 to include ASTM B-117 modified with ASTM Sea Water + UV light and ASTM B-117 modified with acidified ASTM Sea Water + UV light. The coating's degradation is tracked in various environments utilizing the methodology developed in Chapter 2 and, absent of any significant differences in degradation behavior, acceleration factors are elucidated.

Appendix C provides step-by-step instructions, diagrams, and schematics for conducting simultaneous H_2 collection, EIS, and gravimetric mass loss for determination of anodic charge consumption of Mg in full immersion.

1.11 References

1. Asm International Handbook Committee., ASM Handbook Corrosion: Materials, vol. 13B, (Materials Park, OH: ASM International, 1990),
2. M. S. Hunter and P. Fowle, Natural and Thermally Formed Oxide Films on Aluminum, J Electrochem Soc, 103, 9 (1956), pp. 482-485.
3. H. P. Godard, Oxide Film Growth over Five Years on Some Aluminum Sheet Alloys in Air of Varying Humidity at Room Temperature, J Electrochem Soc, 114, 4 (1967), pp. 354-356.
4. H. Kaesche, Investigation of Uniform Dissolution and Pitting of Aluminum Electrodes, Werkst. Korros., 14, (1963), p. 557.
5. H. Böhni and H. H. Uhlig, Environmental Factors Affecting the Critical Pitting Potential of Aluminum, J Electrochem Soc, 116, 7 (1969), pp. 906-910.
6. J. R. Galvele, S. M. De De Micheli, I. L. Muller, S. B. De Wexler and I. L. Alanis, Critical Potentials for Localized Corrosion of Aluminum Alloys, U.R. Evans Conference on Localized Corrosion, NACE-3, p. 580-599, (Williamsburg, VA, National Association of Corrosion Engineers, 1971).
7. R. G. Buchheit, R. K. Boger, M. C. Carroll, R. M. Leard, C. Paglia and J. L. Searles, The electrochemistry of intermetallic particles and localized corrosion in Al alloys, Jom-J Min Met Mat S, 53, 7 (2001), p. 29.
8. R. G. Buchheit, R. P. Grant, P. F. Hlava, B. Mckenzie and G. L. Zender, Local dissolution phenomena associated with S phase (Al2CuMg) particles in aluminum alloy 2024-T3, J Electrochem Soc, 144, 8 (1997), pp. 2621-2628.
9. N. Birbilis and R. G. Buchheit, Electrochemical characteristics of intermetallic phases in aluminum alloys - An experimental survey and discussion, J Electrochem Soc, 152, 4 (2005), pp. B140-B151.
10. G. O. Ilevbare, O. Schneider, R. G. Kelly and J. R. Scully, In situ confocal laser scanning microscopy of AA 2024-T3 corrosion metrology - I. Localized corrosion of particles, J Electrochem Soc, 151, 8 (2004), pp. B453-B464.
11. O. Schneider, G. O. Ilevbare, J. R. Scully and R. G. Kelly, In situ confocal laser scanning microscopy of AA 2024-T3 corrosion metrology - II. Trench formation around particles, J Electrochem Soc, 151, 8 (2004), pp. B465-B472.
12. G. S. Chen, M. Gao and R. P. Wei, Microconstituent-Induced Pitting Corrosion in Aluminum Alloy 2024-T3, Corrosion, 52, 1 (1996), pp. 8-15.
13. R. R. Leard and R. G. Buchheit, Electrochemical Characterization of Copper-bearing Intermetallic Compounds and Localized Corrosion of Al-Cu-Mg-Mn Alloy 2024, Material Science Forum, 396-402, (2002), pp. 1491-1496.
14. R. G. Buchheit, Journal of Electrochemical Society, 142, (1995), p. 3994.
15. R. G. Buchheit, R. P. Grant, P. F. Hlava, B. Mckenzie and G. L. Zender, Local Dissolution Phenomena Associated with S Phase (Al_2CuMg) Particles in Aluminum Alloy 2024-T3, Journal of Electrochemical Society, 144, 8 (1997), pp. 2621-2628.
16. G. S. Chen, C.-M. Liao, K.-C. Wan, M. Gao and R. P. Wei, ASTM STP 1298, ASTM, p. 18, 1997).

17. M. A. Alodan and W. H. Smyrl, Detection of Localized Corrosion Using Fluorescence Microscopy, Journal of Electrochemical Society, 144, 10 (1997), pp. L282-L284.
18. M. A. Alodan and W. H. Smyrl, Journal of Electrochemical Society, 145, (1998), p. 1571.
19. M. Büchler, J. Kerimo, F. Guillaume and W. H. Smyrl, Journal of Electrochemical Society, 147, (2000), p. 3691.
20. M. J. Pryor and D. S. Keir, Journal of Electrochemical Society, 102, (1955), p. 605.
21. J. R. Scully, T. O. Knight, R. G. Buchheit and D. E. Peebles, Electrochemical Characteristics of the Al_2Cu, Al_3Ta and Al_3Zr Intermetallic Phases and Their Relevancy to the Localized Corrosion of Al Alloys, Corros Sci, 35, 1-4 (1993), pp. 185-195.
22. P. Schmutz and G. S. Frankel, Journal of Electrochemical Society, 145, (1998), p. 2295.
23. R. G. Buchheit, L. P. Montez, M. A. Martinez, J. Michael and J. Hlava, Journal of Electrochemical Society, 146, (1999), p. 4426.
24. V. Guillaumin and G. Mankowski, Localized Corrosion of 2024 T351 Aluminum Alloy in Chloride Media, Corros Sci, 41, (1999), pp. 421-438.
25. G. O. Ilevbare and J. R. Scully, Mass-Transport-Limited Oxygen Reduction Reaction on AA2024-T3 and Selected Intermetallic Compounds in Chromate-Containing Solutions, Corrosion, 57, 2 (2001), pp. 134-152.
26. G. O. Ilevbare, J. R. Scully, J. Yuan and R. G. Kelly, Inhibition of Pitting Corrosion on Aluminum Alloy 2024-T3: Effect of Soluble Chromate Additions vs. Chromate Conversion Coating, Corrosion, 56, 3 (2000), pp. 227-242.
27. D. A. Little, "Role(s) of Pretreatment, Inhibitors, and Other Process Steps That Effect Surface Composition On the Under-Paint Corrosion of An Al-Cu-Mg Alloy 2024-T3" University of Virginia, 2006),
28. D. A. Little, "An Electrochemical Framework to Explain the Intergranular Stress Corrosion Path in Two Al-Cu-Mg-Ag Alloys, C415 and C416" (MS Thesis, University of Virginia, 2001),
29. D. A. Little, M. A. Jakab and J. R. Scully, Effect of surface pretreatment on the underpaint corrosion of AA2024-T3 at various temperatures, Corrosion, 62, 4 (2006), pp. 300-315.
30. D. A. Little, J. R. Scully and J. R. Ferrell, The Effect of Pretreatment and Temper on the Under-paint Corrosion of AA2024, NACE CORROSION 2004, (New Orleans, LA, 2004).
31. J. R. Galvele and Demichel.Sm, Mechanism of Intergranular Corrosion of Al-Cu Alloys, Corros Sci, 10, 11 (1970), pp. 795-&.
32. I. L. Muller and J. R. Galvele, Pitting Potential of High Purity Binary Aluminum Alloys - I. Al-Cu Alloys. Pitting and Intergranular Corrosion, Corros Sci, 17, (1977), pp. 179-1936.
33. R. G. Buchheit and R. K. Boger, Cu Redistribution and Surface Enrichment Due to Dissolution of Al-Cu Alloys, Corrosion/2001 Research Topical Symposium - Localized Corrosion, p. 265-292, (Houston, TX, NACE, 2001).

34. Z. W. Wicks, Organic coatings : science and technology, 3rd, vol. (Hoboken, N.J.: Wiley-Interscience, 2007), p. xxiii, 722 p.
35. J. R. Scully, F. Presuel-Moreno, M. Goldman, R. G. Kelly and N. Tailleart, User-selectable barrier, sacrificial anode, and active corrosion inhibiting properties of Al-Co-Ce alloys for coating applications, Corrosion, 64, 3 (2008), pp. 210-229.
36. M. Cerny, Present State of Knowledge About Cathodic Protection of Aluminum, Protection of Metals, 11, 6 (1975), p. 645.
37. F. Presuel-Moreno, M. A. Jakab, N. Tailleart, M. Goldman and J. R. Scully, Corrosion-resistant metallic coatings, Mater Today, 11, 10 (2008), pp. 14-23.
38. F. J. Presuel-Moreno, M. E. Goldman, R. G. Kelly and J. R. Scully, Electrochemical sacrificial cathodic prevention provided by an Al-Co-Ce metal coating coupled to AA2024-T3, J Electrochem Soc, 152, 8 (2005), pp. B302-B310.
39. N. R. Tailleart, B. Gauthier, S. Eidelman and J. R. Scully, Metallurgical and Physical Factors Controlling the Multi-Functional Corrosion Properties of Pulsed Thermal-Sprayed Al-Co-Ce Coatings, Corrosion, 68, 3 (2012).
40. J. R. Davis, Corrosion of aluminum and aluminum alloys, vol. (Materials Park, OH: ASM International, 1999),
41. C. Wagner, Theoretical Analysis of the Current Density Distribution in Electrolytic Cells, J Electrochem Soc, 98, 3 (1951), pp. 116-128.
42. J. Scully and H. P. Hack, Prediction of tube-tubesheet galvanic corrosion using finite element and Wagner number analyses, ASTM STP 978 Galvanic Corrosion, (1988), p. 136.
43. F. J. Presuel-Moreno, H. Wang, M. A. Jakab, R. G. Kelly and J. R. Scully, Computational modeling of active corrosion inhibitor release from an Al-Co-Ce metallic coating - Protection of exposed AA2024-T3, J Electrochem Soc, 153, 11 (2006), pp. B486-B498.
44. J. S. Lee, M. L. Reed and R. G. Kelly, Combining rigorously controlled crevice geometry and computational modeling for study of crevice corrosion scaling factors, J Electrochem Soc, 151, 7 (2004), pp. B423-B433.
45. E. Kennard and J. T. Waber, Mathematical Study of Galvanic Corrosion - Equal Coplanar Anode and Cathode with Unequal Polarization Parameters, J Electrochem Soc, 117, 7 (1970), pp. 880-&.
46. J. T. Waber and B. Fagan, Mathematical Studies on Galvanic Corrosion: IV . Influence of Electrolyte Thickness on the Potential and Current Distributions over Coplanar Electrodes Using Polarization Parameters, J Electrochem Soc, 103, 1 (1956), pp. 64-72.
47. J. W. Fu, A Finite-Element Analysis of Corrosion Cells, Corrosion, 38, 5 (1982), pp. 295-296.
48. J. T. Waber, Mathematical Studies of Galvanic Corrosion: VI. . Limiting Case of Very Thin Films, J Electrochem Soc, 103, 10 (1956), pp. 567-570.
49. J. T. Waber, Mathematical Studies of Galvanic Corrosion: III . Semi-infinite Coplanar Electrodes with Equal Constant Polarization Parameters, J Electrochem Soc, 102, 7 (1955), pp. 420-429.

50. J. T. Waber and M. Rosenbluth, Mathematical Studies of Galvanic Corrosion: II . Coplanar Electrodes with One Electrode Infinitely Large and with Equal Polarization Parameters, J Electrochem Soc, 102, 6 (1955), pp. 344-353.
51. S. M. Sharland, C. P. Jackson and A. J. Diver, A finite-element model of the propagation of corrosion crevices and pits, Corros Sci, 29, 9 (1989), pp. 1149-1166.
52. M. Iannuzzi and G. S. Frankel, Inhibition of Aluminum Alloy 2024 Corrosion by Vanadates: An In Situ Atomic Force Microscopy Scratching Investigation, Corrosion, 63, 7 (2007), pp. 672-688.
53. M. Iannuzzi and G. S. Frankel, Mechanisms of corrosion inhibition of AA2024-T3 by vanadates, Corros Sci, 49, 5 (2007), pp. 2371-2391.
54. M. Iannuzzi, J. Kovac and G. S. Frankel, A study of the mechanisms of corrosion inhibition of AA2024-T3 by vanadates using the split cell technique, Electrochim Acta, 52, 12 (2007), pp. 4032-4042.
55. M. Iannuzzi, T. Young and G. S. Frankel, Aluminum alloy corrosion inhibition by vanadates, J Electrochem Soc, 153, 12 (2006), pp. B533-B541.
56. G. O. Ilevbare and J. R. Scully, Oxygen Reduction Reaction Kinetics on Chromate Conversion Coated Al-Cu, Al-Cu-Mg, and Al-Cu-Mn-Fe Intermetallic Compounds, J Electrochem Soc, 148, 5 (2001), pp. B196-B207.
57. G. O. Ilevbare, J. R. Scully, J. Yuan and R. G. Kelly, Inhibition of pitting corrosion on aluminum alloy 2024-T3: Effect of soluble chromate additions vs chromate conversion coating, Corrosion, 56, 3 (2000), pp. 227-242.
58. G. Bierwagen, R. Brown, D. Battocchi and S. Hayes, Observations on the testing of Mg-Rich Primers for Totally Chromate-free Corrosion Protection of Aerospace Alloys, NACE DoD 2009 Conference Proceedings, (Washing, DC, 2009).
59. G. P. Bierwagen, D. E. Tallman, M. Nanna, D. Battocchi, A. Stamness and V. J. Gelling, New developments in Cr-free primers for aerospace alloys., Abstr Pap Am Chem S, 228, (2004), pp. U360-U360.
60. U.S. Department of Health and Human Services., Report on Carcinogens, 12th Edition, U.S. Department of Health and Human Services, Public Health Services, National Toxicology Program, 2011.
61. J. J. Young, "Memorandum for Secratries of the Military Departments - Minimizing the Use of Hexavalent Chromium (Cr6+)", OUSD, Washington, DC, April 8, 2009
62. S. S. Pathak, M. D. Blanton, S. K. Mendon and J. W. Rawlins, Investigation on dual corrosion performance of magnesium-rich primer for aluminum alloys under salt spray test (ASTM B117) and natural exposure, Corros Sci, 52, 4 (2010), pp. 1453-1463.
63. A. Simoes, D. Battocchi, D. Tallman and G. Bierwagen, Assessment of the corrosion protection of aluminium substrates by a Mg-rich primer: EIS, SVET and SECM study, Prog Org Coat, 63, 3 (2008), pp. 260-266.
64. D. Battocchi, A. M. Simoes, D. E. Tallman and G. P. Bierwagen, Comparison of testing solutions on the protection of Al-alloys using a Mg-rich primer, Corros Sci, 48, 8 (2006), pp. 2226-2240.

65. D. Battocchi, A. M. Simoes, D. E. Tallman and G. P. Bierwagen, Electrochemical behaviour of a Mg-rich primer in the protection of Al alloys, Corros Sci, 48, 5 (2006), pp. 1292-1306.
66. H. Xu, D. Battocchi, D. E. Tallman and G. P. Bierwagen, Use of Magnesium Alloys as Pigments in Magnesium-Rich Primers for Protecting Aluminum Alloys, Corrosion, 65, 5 (2009), pp. 318-325.
67. G. Bierwagen, D. Battocchi, A. Simoes, A. Stamness and D. Tallman, The use of multiple electrochemical techniques to characterize Mg-rich primers for A1 alloys, Prog Org Coat, 59, 3 (2007), pp. 172-178.
68. A. D. King and J. R. Scully, Sacrificial Anode-Based Galvanic and Barrier Corrosion Protection of 2024-T351 by a Mg-Rich Primer and Development of Test Methods for Remaining Life Assessment, Corrosion, 67, 5 (2011), pp. 05500401-05500422.
69. B. Maier and G. S. Frankel, Behavior of Magnesium-Rich Primers on AA2024-T3, Corrosion, 67, 5 (2011), p. 055001.
70. A. D. King and J. R. Scully, Blistering Phenomena in Early Generation Mg-Rich Primer Coatings on AA2024-T351 and the Effects of CO_2, NACE DoD 2011 Conference Proceedings, (Palm Springs, CA, 2011).
71. J. Nie, M. C. Yan, J. Wang, D. E. Tallman, D. Battocchi and G. P. Bierwagen, Cathodic Corrosion Protection Performance of Mg-Rich Primers: Effect of Pigment Shape and Pigment Volume Concentration, ECS Transactions, 24, 1 (2010), pp. 261-275.
72. A. D. King, B. Kannan and J. R. Scully, Environmental Degradation of a Mg-Rich Primer in Selected Field and Laboratory Environments – Part I. Without a Topcoat, Corrosion, 70, 5 (2014).
73. A. D. King, B. Kannan and J. R. Scully, Environmental Degradation of a Mg-Rich Primer in Selected Field and Laboratory Environments – Part II. Primer and Topcoat, Corrosion, 70, 5 (2014).
74. R. G. Buchheit, Chromate and Chromate-Free Conversion Coatings, vol. 13A, ASM Handbook Volume 13A, Corrosion: Fundamentals, Testing, and Protection (ASM International) (Materials Park, Ohio, ASM International, 2003).
75. S. Feliu, R. Barajas, J. M. Bastidas and M. Morcillo, Ac Impedance Study About the Protection Mechanisms of Zinc-Rich Primers, Abstr Pap Am Chem S, 195, (1988), pp. 58-Pmse.
76. D. Pereira, J. D. Scantlebury, M. G. S. Ferreira and M. E. Almeida, The Application of Electrochemical Measurements to the Study and Behavior of Zinc-Rich Coatings, Corros Sci, 30, 11 (1990), pp. 1135-1147.
77. S. Feliu, M. Morcillo and S. Feliu, Deterioration of cathodic protection action of zinc-rich paint coatings in atmospheric exposure, Corrosion, 57, 7 (2001), pp. 591-597.
78. V. M. Rudoi, O. V. Yaroslavtseva, T. N. Ostanina, L. P. Yurkina and O. Y. Subbotina, Electrochemical behavior of protective anodic primers, Protection of Metals, 35, 3 (1999), pp. 277-281.
79. H. Marchebois, C. Savall, J. Bernard and S. Touzain, Electrochemical behavior of zinc-rich powder coatings in artificial sea water, Electrochim Acta, 49, 17-18 (2004), pp. 2945-2954.

80. C. M. Abreu, M. Izquierdo, M. Keddam, X. R. Novoa and H. Takenouti, Electrochemical behaviour of zinc-rich epoxy paints in 3% NaCl solution, Electrochim Acta, 41, 15 (1996), pp. 2405-2415.
81. S. G. Real, A. C. Elias, J. R. Vilche, C. A. Gervasi and A. Disarli, An Electrochemical Impedance Spectroscopy Study of Zinc Rich Paints on Steels in Artificial Sea-Water by a Transmission-Line Model, Electrochim Acta, 38, 14 (1993), pp. 2029-2035.
82. C. M. Abreu, M. Izquierdo, X. R. Novoa, C. Perez and A. Sanchez, Influence of different aggressive media on the protective behaviour of zinc rich paints, Rev Metal Madrid, 35, 3 (1999), pp. 182-189.
83. N. V. Kondrashova, S. A. Nesterenko, O. V. Naumenko and L. I. Antropov, Influence of Zinc and Magnesium Cations on the Electrochemical-Behavior of Steel with a Polymer Primer, Protection of Metals, 25, 1 (1989), pp. 73-75.
84. S. Feliu, R. Barajas, J. M. Bastidas and M. Morcillo, Mechanism of Cathodic Protection of Zinc-Rich Paints by Electrochemical Impedance Spectroscopy .1. Galvanic Stage, J Coating Technol, 61, 775 (1989), pp. 63-69.
85. S. Feliu, R. Barajas, J. M. Bastidas and M. Morcillo, Mechanism of Cathodic Protection of Zinc-Rich Paints by Electrochemical Impedance Spectroscopy .2. Barrier Stage, J Coating Technol, 61, 775 (1989), pp. 71-76.
86. C. M. Abreu, M. Izquierdo, P. Merino, X. R. Novoa and C. Perez, A new approach to the determination of the cathodic protection period in zinc-rich paints, Corrosion, 55, 12 (1999), pp. 1173-1181.
87. M. Morcillo, R. Barajas, S. Feliu and J. M. Bastidas, A-Sem Study on the Galvanic Protection of Zinc-Rich Paints, J Mater Sci, 25, 5 (1990), pp. 2441-2446.
88. R. A. Armas, C. A. Gervasi, A. Disarli, S. G. Real and J. R. Vilche, Zinc-Rich Paints on Steels in Artificial Seawater by Electrochemical Impedance Spectroscopy, Corrosion, 48, 5 (1992), pp. 379-383.
89. H. Marchebois, M. Keddam, C. Savall, J. Bernard and S. Touzain, Zinc-rich powder coatings characterisation in artificial sea water - EIS analysis of the galvanic action, Electrochim Acta, 49, 11 (2004), pp. 1719-1729.
90. O. O. Knudsen, U. Steinsmo and M. Bjordal, Zinc-rich primers - Test performance and electrochemical properties, Prog Org Coat, 54, 3 (2005), pp. 224-229.
91. M. E. Nanna and G. P. Bierwagen, Mg-rich coatings: A new paradigm for Cr-free corrosion protection of al aerospace alloys, Jct Research, 1, 2 (2004), pp. 69-80.
92. D. A. Jones, Principles and prevention of corrosion, 2nd, vol. (Upper Saddle River, NJ: Prentice Hall, 1996), p. xvi, 572 p.
93. D. H. Wang, D. Battocchi, K. N. Allahar, S. Balbyshev and G. P. Bierwagen, In situ monitoring of a Mg-rich primer beneath a topcoat exposed to Prohesion conditions, Corros Sci, 52, 2 (2010), pp. 441-448.
94. J. T. Waber, Mathematical Studies on Galvanic Corrosion: I . Coplanar Electrodes with Negligible Polarization, J Electrochem Soc, 101, 6 (1954), pp. 271-276.
95. J. T. Waber, J. Mobrissey and J. Ruth, Mathematical Studies on Galvanic Corrosion: V . Calculation of the Average Value of the Corrosion Current Parameter, J Electrochem Soc, 103, 2 (1956), pp. 138-147.

96. B. J. Last and D. J. Thouless, Percolation Theory and Electrical Conductivity, Phys Rev Lett, 27, 25 (1971), p. 1719.
97. G. R. Ruschau, S. Yoshikawa and R. E. Newnham, Resistivities of Conductive Composites, J Appl Phys, 72, 3 (1992), pp. 953-959.
98. M. T. Rodriguez, J. J. Gracenea, A. H. Kudama and J. J. Suay, The influence of pigment volume concentration (PVC) on the properties of an epoxy coating - Part I. Thermal and mechanical properties, Prog Org Coat, 50, 1 (2004), pp. 62-67.
99. M. T. Rodriguez, J. J. Gracenea, J. J. Saura and J. J. Suay, The influence of the critical pigment volume concentration (CPVC) on the properties of an epoxy coating - Part II. Anticorrosion and economic properties, Prog Org Coat, 50, 1 (2004), pp. 68-74.
100. G. R. Ruschau and R. E. Newnham, Critical Volume Fractions in Conductive Composites, J Compos Mater, 26, 18 (1992), pp. 2727-2735.
101. R. Y. Yang, R. P. Zou and A. B. Yu, Computer simulation of the packing of fine particles, Phys Rev E, 62, 3 (2000), pp. 3900-3908.
102. R. Y. Yang, R. P. Zou and A. B. Yu, Effect of material properties on the packing of fine particles, J Appl Phys, 94, 5 (2003), pp. 3025-3034.
103. G. P. Bierwagen, Cpvc Calculations, J Paint Technol, 44, 572 (1972), p. 28.
104. G. P. Bierwagen and T. E. Saunders, Studies of Effects of Particle-Size Distribution on Packing Efficiency of Particles, Powder Technol, 10, 3 (1974), pp. 111-119.
105. G. P. Bierwagen, Cpvc Calculations, J Paint Technol, 44, 574 (1972), p. 46.
106. G. S. Chen, C.-M. Liao, K.-C. Wan, M. Gao and R. P. Wei, Effects of Environment on Initiation of Crack Growth, W. A. Van Der Sluys, R. S. Piascik and R. Zawierucha, Eds., ASTM STP 1298 (West Conshohocken, American Society for Testing and Materials, 1997, p. 18).
107. T. Suter and R. C. Alkire, Microelectrochemical Studies of Pit Initiation at Single Inclusions in a 2024-T3 Al Alloy, Critical Factors in Localized Corrosion III, PV 98-17, p. 118-129, (Boston, MA, The Electrochemical Society, 1998).
108. C. Blanc, B. Lavelle and G. Mankowski, The Role of Precipitates Enriched with Copper on the Susceptibility to Pitting Corrosion of the 2024 Aluminum Alloy, Corros Sci, 39, 3 (1997), pp. 495-510.
109. R. R. Leard and R. G. Buchheit, Electrochemical Characterization of Copper-bearing Intermetallic Compounds and Localized Corrosion of Al-Cu-Mg-Mn Alloy 2024, Materials Science Forum, 396-402, (2002), pp. 1491-1496.
110. W. C. Keene, H. Maring, J. R. Maben, D. J. Kieber, A. a. P. Pszenny, E. E. Dahl, M. A. Izaguirre, A. J. Davis, M. S. Long, X. L. Zhou, L. Smoydzin and R. Sander, Chemical and physical characteristics of nascent aerosols produced by bursting bubbles at a model air-sea interface, J Geophys Res-Atmos, 112, D21 (2007).
111. A. Mészáros and K. Vissy, Concentration, size distribution and chemical nature of atmospheric aerosol particles in remote oceanic areas, Journal of Aerosol Science, 5, 1 (1974), pp. 101-109.
112. Astm, Determining Atmospheric Chloride Deposition Rate by Wet Candle method, ASTM G140 - 02, DOI: 10.1520/D1141-98R08 (2002).
113. C. Matzdorf, Personal correspondence with Mr. Craig Matzdorf of NAVAIR, (2009).

114. W. H. Abbott, Personal correspondence with Mr. William Abbott of Battelle Memorial Institute, (2009).
115. A. D. King and J. Scully, Sacrificial Anode based Galvanic and Barrier Corrosion Protection of AA2024-T351 by a Mg-Rich Primer and Development of Test Methods for Remaining Life Assessment Corrosion, 67, 5 (2011), p. 055004.
116. R. L. Twite and G. P. Bierwagen, Review of alternatives to chromate for corrosion protection of aluminum aerospace alloys, Prog Org Coat, 33, 2 (1998), pp. 91-100.
117. E. L. Koehler, U. R. Evans, B. F. Brown, J. Kruger, R. W. Staehle and National Association of Corrosion Engineers. Research Committee., Corrosion Under Organic Coatings, Localized Corrosion (Houston, Tex., National Association of Corrosion Engineers, 1974, p. 117-133).
118. M. Pourbaix, Atlas of electrochemical equilibria in aqueous solutions, 2d English, vol. (Houston, Tex.: National Association of Corrosion Engineers, 1974), p. 644.
119. G. S. Frankel and Y. Baek, Electrochemical quartz crystal microbalance study of corrosion of phases in AA2024, J Electrochem Soc, 150, 1 (2003), pp. B1-B9.
120. H. Kaesche, Studies on the Corrosion of Aluminum, Zeitschrift für physikalische Chemie, 14, 7 (1963), pp. 557-566.
121. A. R. Despic, J. Radosevic, P. Dabic and M. Kliskic, Abnormal Yields of Hydrogen and the Mechanism of Its Evolution during Cathodic Polarization of Aluminum, Electrochim Acta, 35, 11-12 (1990), pp. 1743-1746.
122. E. P. G. T. Vandeven and H. Koelmans, Cathodic Corrosion of Aluminum, J Electrochem Soc, 123, 1 (1976), pp. 143-144.
123. S. M. Moon and S. I. Pyun, The corrosion of pure aluminium during cathodic polarization in aqueous solutions, Corros Sci, 39, 2 (1997), pp. 399-408.
124. S. S. Pathak, M. D. Blanton, S. K. Mendon and J. W. Rawlins, Carbonation of Mg powder to enhance the corrosion resistance of Mg-rich primers, Corros Sci, 52, 11 (2010), pp. 3782-3792.
125. K. N. Allahar, D. Wang, D. Battocchi, G. P. Bierwagen and S. Balbyshev, Real-Time Monitoring of a United States Air Force Topcoat/Mg-Rich Primer System in ASTM B117 Exposure by Embedded Electrodes, Corrosion, 66, 7 (2010).
126. Astm, Standard Practice for Operating Salt Spray (Fog) Apparatus, ASTM B117 - 09, DOI: 10.1520/C0033-03, (2009).
127. J. Li, J. He, B. J. Chisholm, M. Stafslien, D. Battocchi and G. P. Bierwagen, An investigation of the effects of polymer binder compositional variables on the corrosion control of aluminum alloys using magnesium-rich primers, J Coat Technol Res, 7, 6 (2010), pp. 757-764.
128. W. H. Abbott, Performance of Chrome-Free Paint Systems In Field and Lab Environments: Summary of 4+ Years of Flight and Ground Exposures, NACE DoD 2011 Conference Proceedings, (Palm Springs, CA, 2011).

1.12 Tables

Table 1.1 The specified, nominal alloying element concentrations for 2024 on a weight percentage basis.
The alloy must not contain more than 0.05% of any other individual element, and the total of these elements must not exceed 0.15%.

Element	Cu	Mg	Mn	Si	Fe	Zn	Ti	Cr
Limit (wt. %)	3.8 to 4.9	1.2 to1.8	0.3 to 0.9	0.5	0.5	0.15	0.15	0.1

Table 1.2 Solution potentials of heat treatable commercial aluminum alloys and pure Mg in 0.9 M NaCl + 0.09 M H_2O_2 solution.
J. G. Kaufman, Corrosion of Aluminum and Aluminum Alloys. ASM Handbook 13B Corrosion: Materials, ASM International (2005) p. 97

Material	Temper	E (V vs. SCE)
AA 2014	T4	-0.6
	T6	-0.69
AA 2219	T3	-0.55
	T4	-0.55
	T6	-0.71
	T8	-0.73
AA 2024	T3	-0.6
	T4	-0.6
	T6	-0.72
	T8	-0.73
AA 2036	T4	-0.63
AA 2090	T8E41	-0.74
AA 6009	T4	-0.71
AA 6010	T4	-0.7
AA 6151	T6	-0.74
AA 6351	T5	-0.74
AA 6061	T4	-0.71
	T6	-0.74
AA 6063	T5	-0.74
	T6	-0.74
AA 7005	T6	-0.85
AA 7021	T6	-0.9
AA 7029	T6	-0.76
AA 7049	T73	-0.75
	T76	-0.75
AA 7050	T73	-0.75
	T76	-0.75
AA 7075	T6	-0.74
	T73	-0.75
	T76	-0.75
AA 7175	T6	-0.74
	T73	-0.75
	T76	-0.75
AA 7178	T6	-0.74
Pure Mg		-1.65

Table 1.3 Corrosion potentials for intermetallic compounds common in aluminum alloys. N. Birbilis and R. G. Buchheit, Electrochemical characteristics of intermetallic phases in aluminum alloys - An experimental survey and discussion, J Electrochem Soc, 152, 4 (2005), pp. B140-B151.

		Corrosion potential (mV_{SCE})			
Stoichiometry	Phase	0.01 M	0.1 M	0.6 M	Note
Al_3Fe	β	−493	−539	−566	
Al_2Cu	θ	−592	−665	−695	
Al_3Zr	β	−752	−776	−801	
Al_6Mn	-	−839	−779	−913	
Al_3Ti	β	−620	−603	−799	
$Al_{32}Zn_{49}$	T′	−1009	−1004	−1063	
Mg_2Al_3	β	−1124	−1013	−1162	
$MgZn_2$	M, η	−1001	−1029	−1095	
Mg_2Si	β	−1355	−1538	−1536	
Al_7Cu_2Fe	-	−549	−551	−654	
Mg(AlCu)	-	−898	−943	−936	
Al_2CuMg	S	−956	−883	−1061	
$Al_{20}Cu_2Mn_3$	-	−550	−565	−617	
$Al_{12}Mn_3Si$	-	−890	−810	−858	
Al (99.9999)	-	−679	−823	−849	A
Cu (99.9)	-	−177	−232	−220	A
Si (99.9995)	α	−450	−441	−452	A
Mg (99.9)	-	−1601	−1586	−1688	A
Mn (99.9)	-	−1315	−1323	−1318	A
Cr (99.0)	-	−495	−506	−571	A
Zn (99.99)	-	−985	−1000	−1028	A
Al-2%Cu	α	−813	−672	−744	B
Al-4%Cu	α	−750	−602	−642	B
7X75 Matrix	-	−699	−799	−812	M
AA 7075-T651	-	−816	−965	−1180	X

Notes:

A. Pure metal were obtained from Alfa-Aeser and tested using the micro-cell method.

B. These specimens are homogeneous solid solutions and tested using the microcell method.

M. The phase denoted as 7X75 matrix is the particle-free matrix-phase of AA7474.

X. Tests upon AA7075-T651 were done on bulk specimens using conventional electrochemical methods and an electrode area of 1 cm^2.

Table 1.4 Galvanic series for intermetallic compounds common in aluminum alloys in 0.1 M NaCl with pH = 6.
N. Birbilis and R. G. Buchheit, Electrochemical characteristics of intermetallic phases in aluminum alloys - An experimental survey and discussion, J Electrochem Soc, 152, 4 (2005), pp. B140-B151.

Stoichiometry	Phase	Corrosion potential (m V_{SCE})
Mg (99.9)	-	−1586
Mg_2Si	β	−1538
$MgZn_2$	M, η	−1029
Mg_2Al_3	β	−1013
$Al_{32}Zn_{49}$	T′	−1004
Zn (99.99)	-	−1000
AA 7075-T651	-	−965
Mg (AlCu)	-	−943
Al_2CuMg	S	−883
Al (99.9999)	-	−823
$Al_{12}Mn_3Si$	-	−810
7X75 Matrix	-	−799
Al_6Mn	-	−779
Al_3Zr	β	−776
Al-2%Cu	α	−672
Al_2Cu	θ	−665
Al_3Ti	β	−603
Al-4%Cu	α	−602
$Al_{20}Cu_2Mn_3$	-	−565
Al_7Cu_2Fe	-	−551
Al_3Fe	β	−539
Cu (99.9)	-	−232

Table 1.5 Pitting potentials for intermetallic compounds common in aluminum alloys. Reproduced with permission from N. Birbilis and R. G. Buchheit, Electrochemical characteristics of intermetallic phases in aluminum alloys - An experimental survey and discussion, J Electrochem Soc, 152, 4 (2005), pp. B140-B151.

		Pitting potential (mV_{SCE})			
Stoichiometry	Phase	0.01 M	0.1 M	0.6 M	Note
Al_3Fe	β	442	106	−382	
Al_2Cu	θ	−434	−544	−652	
Al_3Zr	β	−223	−275	−346	
Al_6Mn	-	−485	−755	−778	
Al_3Ti	β	−232	−225	−646	
$Al_{32}Zn_{49}$	T′	-	-	-	C
Mg_2Al_3	β	−818	−846	−959	
$MgZn_2$	M, η	-	-	-	C
Mg_2Si	β	-	-	-	C
Al_7Cu_2Fe	-	−447	−448	−580	
Mg (AlCu)	-	224	−2	-	D, E
Al_2CuMg	S	108	80	135	F
$Al_{20}Cu_2Mn_3$	-	−210	−428	−534	
$Al_{12}Mn_3Si$	-	−563	−621	−712	
Al (99.9999)	-	−545	−610	−696	A
Cu (99.9)	-	19	−30	−94	A
Si (99.9995)	α	-	-	-	A, C
Mg (99.9)	-	−1095	−1391	−1473	A, G
Mn (99.9)	-	-	-	-	A, C
Cr (99.0)	-	479	297	190	A
Zn (99.99)	-	-	-	-	A, C
Al-2%Cu	α	−447	−471	−529	B
Al-4%Cu	α	−418	−406	−465	B
7X75 Matrix	-	−633	−736	−768	M
AA 7075-T651	-	−684	−739	−810	X

Notes:

C. These compounds do not shows a breakdown of passivity, with active dissolution occurring at potentials more positive than E_{corr}.

D. Did not show a breakdown in all cases when tested at 0.1 M NaCl.

E. At the highest concentration of NaCl tested, this compound did not display a breakdown of passivity, with active dissolution occurring at potentials more positive than E_{corr}.

F. The breakdown potential (E_{pit}) of S-phase should be viewed with caution. The electrochemical behavior of this compound is complex[20] and incorporates dealloying of the Al and Mg, capable of generating a relatively large corrosion current density prior to ultimate breakdown. For more details regarding S-phase, see Ref. 20 and 30.

G. The quoted E_{pit} values of pure Mg correspond with the potential at which current density rapidly increases. Pure Mg, however, is generally unstable and freely corrodes in Cl-containing solution.

1.13 Figures

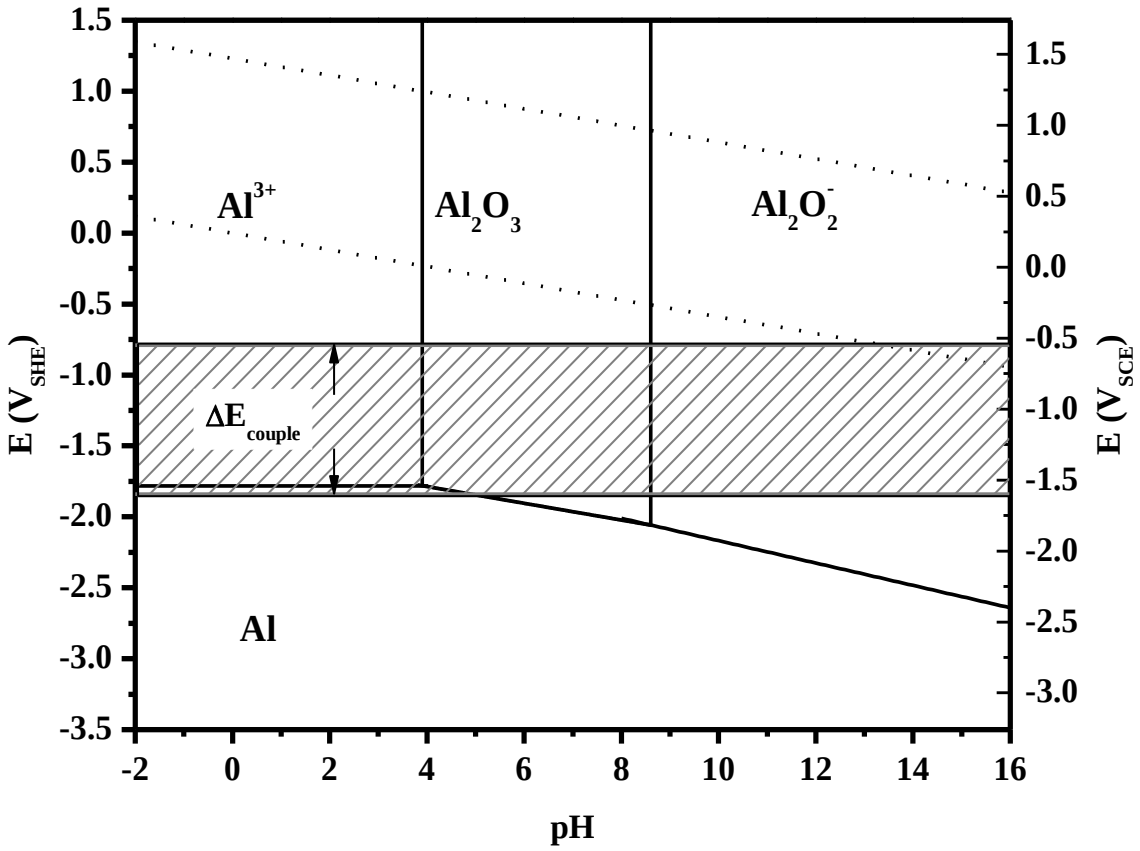

Figure 1.1. . Potential-pH equilibrium (Pourbaix) diagram for the Al-H_2O system at 25°C assuming an ion concentration of 10^{-6}.
Pontential values are for the standard hydrogen electrode (SHE) scale.
Reproduced with permission from M. Pourbaix, Atlas of Electrochemical Equilibrium in Aqueous Solutions, NACE International (1974) p. 171

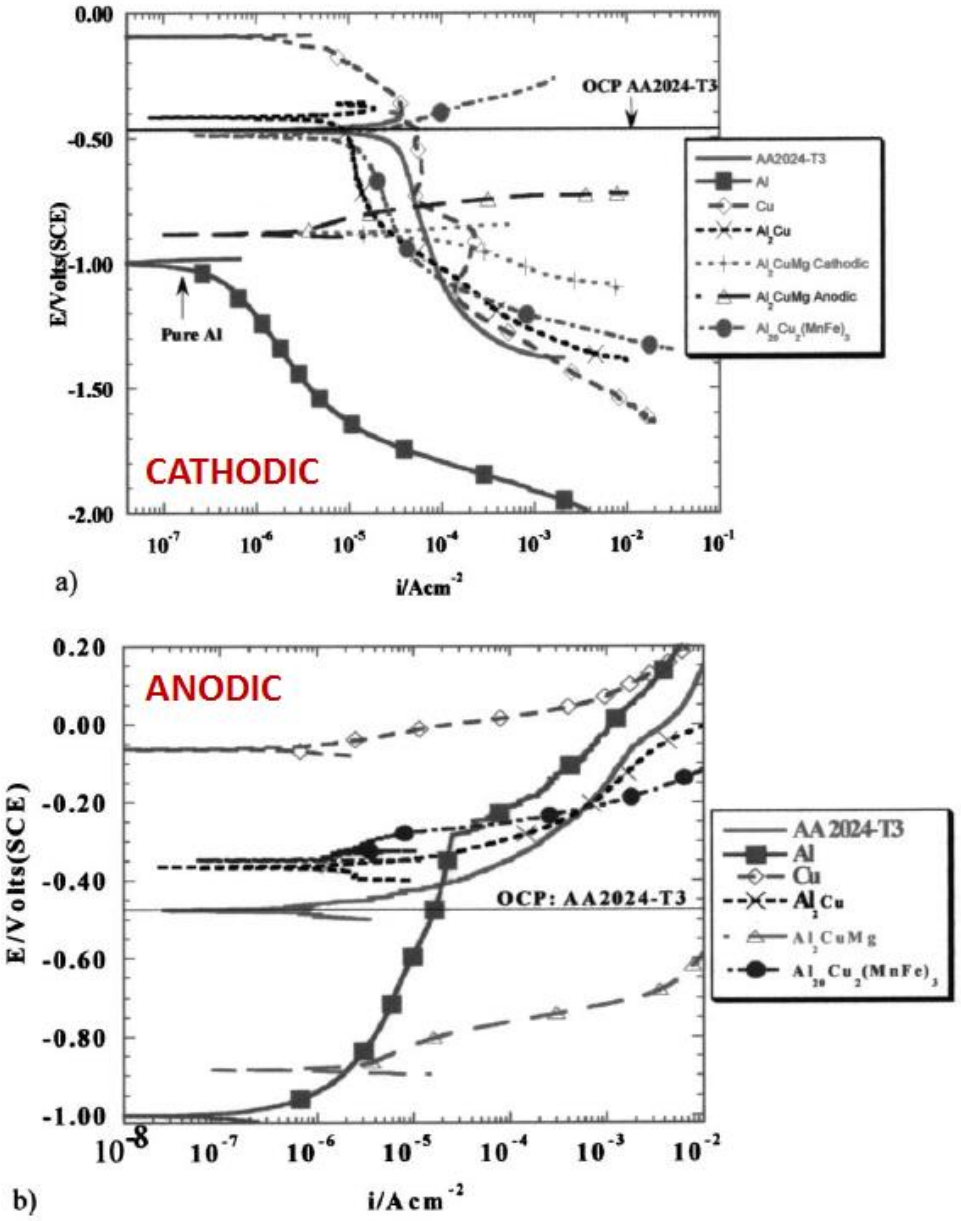

Figure 1.2. The E-log(i) behavior of stationary electrodes of 99.998% Al, S-Al_2CuMg, AA2024-T3, θ-Al_2Cu, $Al_{20}Cu_2(MnFe)_3$, and 99.999% Cu in 0.1 M Na_2SO_4 + 0.005 M NaCl at ambient aeration. (a) cathodic (including anodic S-Al_2CuMg curve) and (b) anodic; all recorded after a 2 h OCP

Reproduced with permission from G. O. Ilevbare, O. Schneider, R. G. Kelly, and J. R. Scully, J. Elec. Soc., 151(8). (2004) p. B453

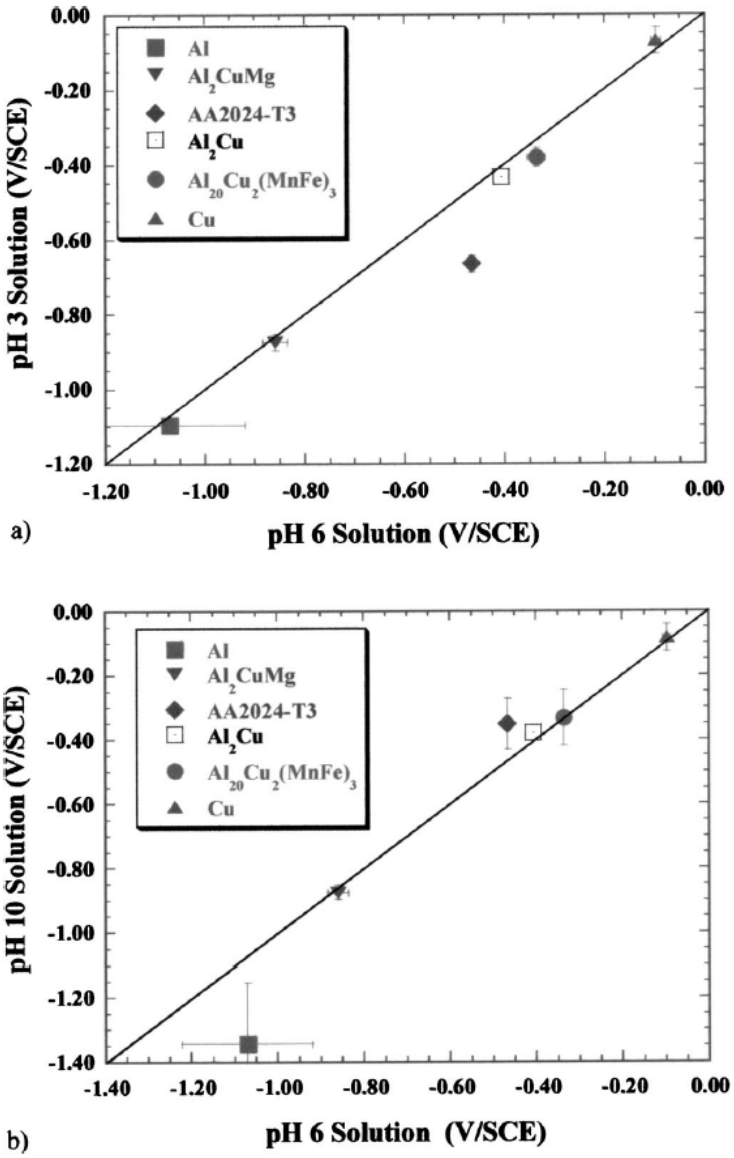

Figure 1.3. OCP's of 99.998% Al, S-Al_2CuMg, AA2024-T3, Al_2Cu, $Al_{20}Cu_2(MnFe)_3$, and 99.999% Cu in 0.1 M Na_2SO_4 + 0.005 M NaCl after 2 h at pH 6 compared with those of their counterparts at (a) pH 3 and (b) pH 10

Reproduced with permission from G. O. Ilevbare, O. Schneider, R. G. Kelly, and J. R. Scully, J. Elec. Soc., 151(8). (2004) p. B453

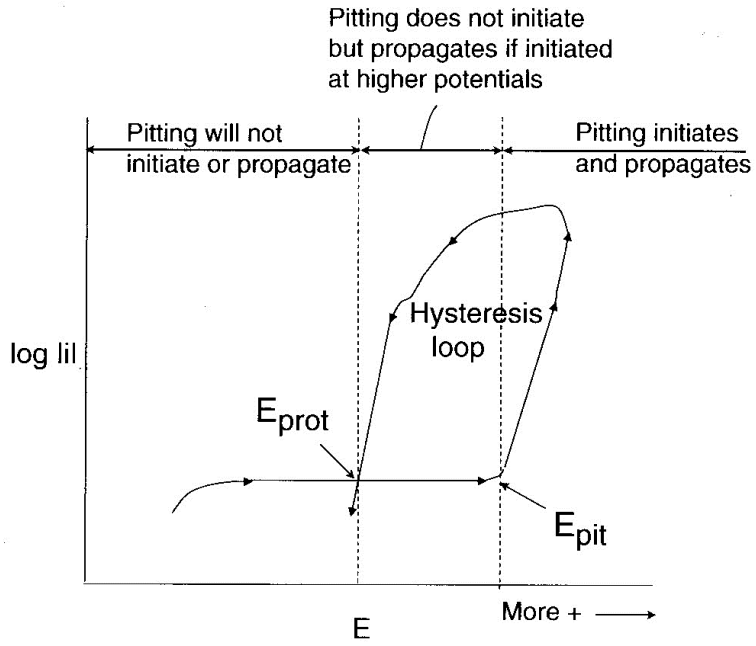

Figure 1.4. Schematic illustration of the pitting potential E_{pit} and the protection potential E_{prot}.
The arrows show the direction of polarization.
E. McCafferty, *Introduction to Corrosion Science*. Springer, (2010) p. 288

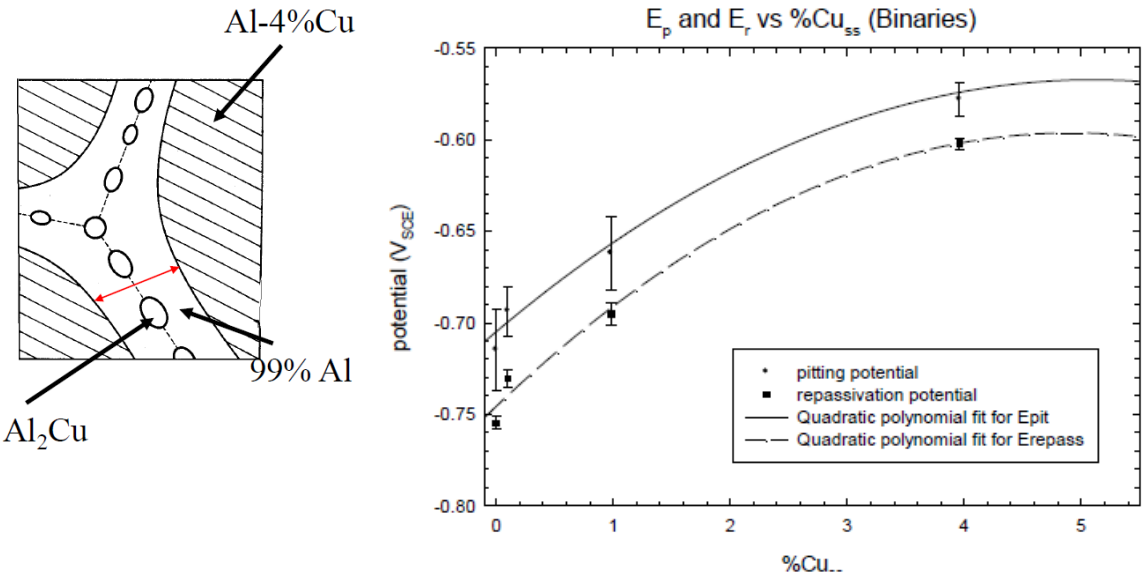

(a) (b)

Figure 1.5. Schematic of Cu depletion zones along grain boundaries in Al-Cu-X alloys (a) and repassivation and pitting potentials of binary Al-Cu alloys (b).
Reproduced with permission from J. R. Galvele and S. M. de De Micheli, Mechanism of Intergranular Corrosion of Al-Cu Alloys, Corros Sci, 10, (1970), pp. 795-807.

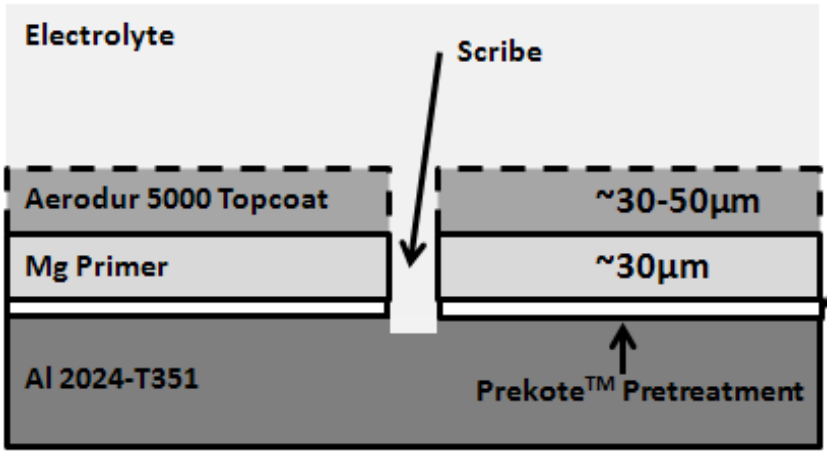

Figure 1.6. Schematic of MgRP coating system stack-up.
System consisted of AA2024-T351 substrate, pretreatment, ~30 µm thick layer of Mg-Rich Primer and a 30-50 µm layer of topcoat. A finite pretreatment layer is not assumed.

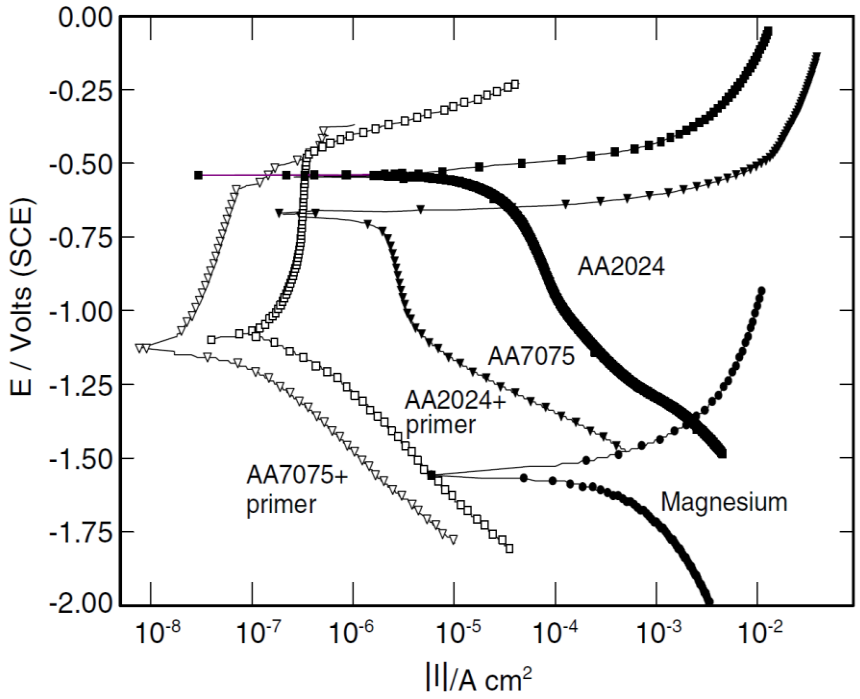

Figure 1.7. E-log(i) characteristics of bare AA2024, bare AA7075, bare Mg, MgRP-coated AA7075, and MgRP-coated AA2024 in 0.1% NaCl solution
Reproduced with permission from D. Battochi, A. M. Simoes, D. E. Tallman, G. P Bierwagen, Corrosion Science 48 (2006) 1292 - 1306

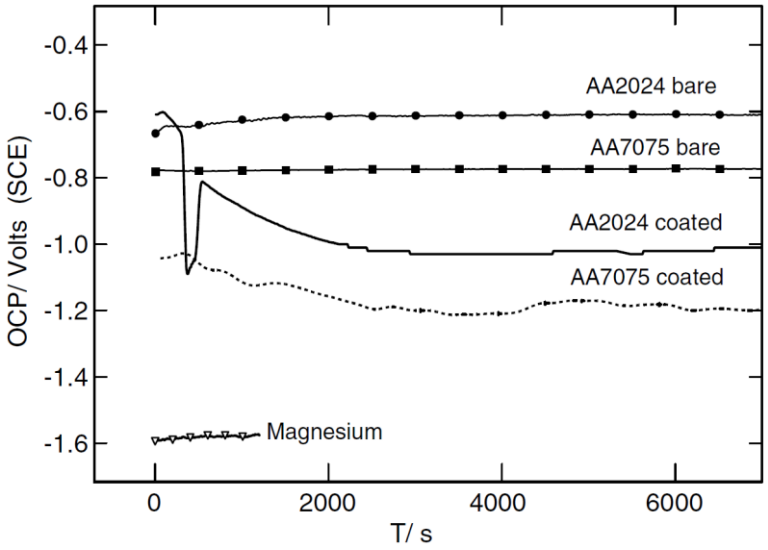

Figure 1.8. Open circuit potential of bare AA2024, bare AA7075, bare Mg, MgRP-coated AA7075, and MgRP-coated AA2024 in 0.1% NaCl solution
Reproduced with permission from D. Battochi, A. M. Simoes, D. E. Tallman, G. P Bierwagen, Corrosion Science 48 (2006) 1292 - 1306

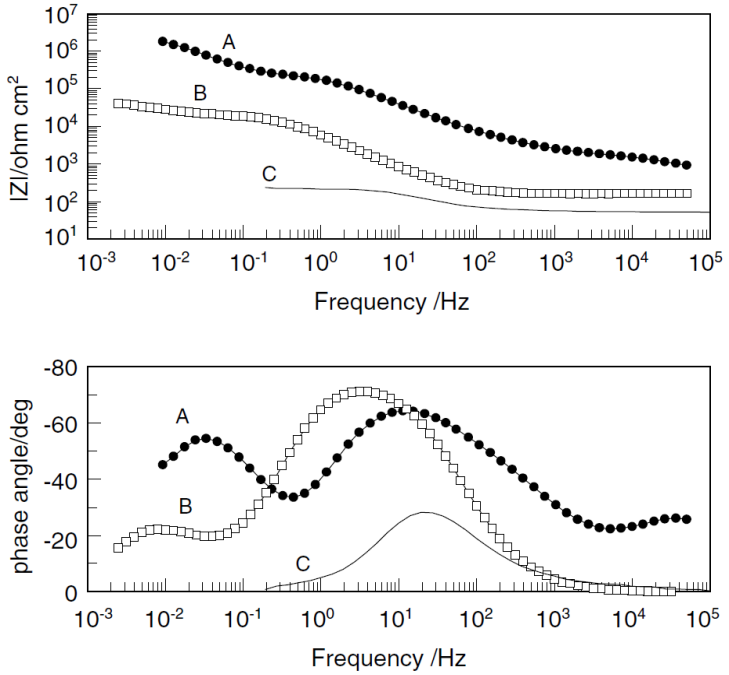

Figure 1.9. Electrochemical Impedance of (a) MgRP-coated AA2024, (b) bare AA2024-T3, and (c) bare Mg in 0.1% NaCl solution
Reproduced with permission from D. Battochi, A. M. Simoes, D. E. Tallman, G. P Bierwagen, Corrosion Science 48 (2006) 1292 - 1306

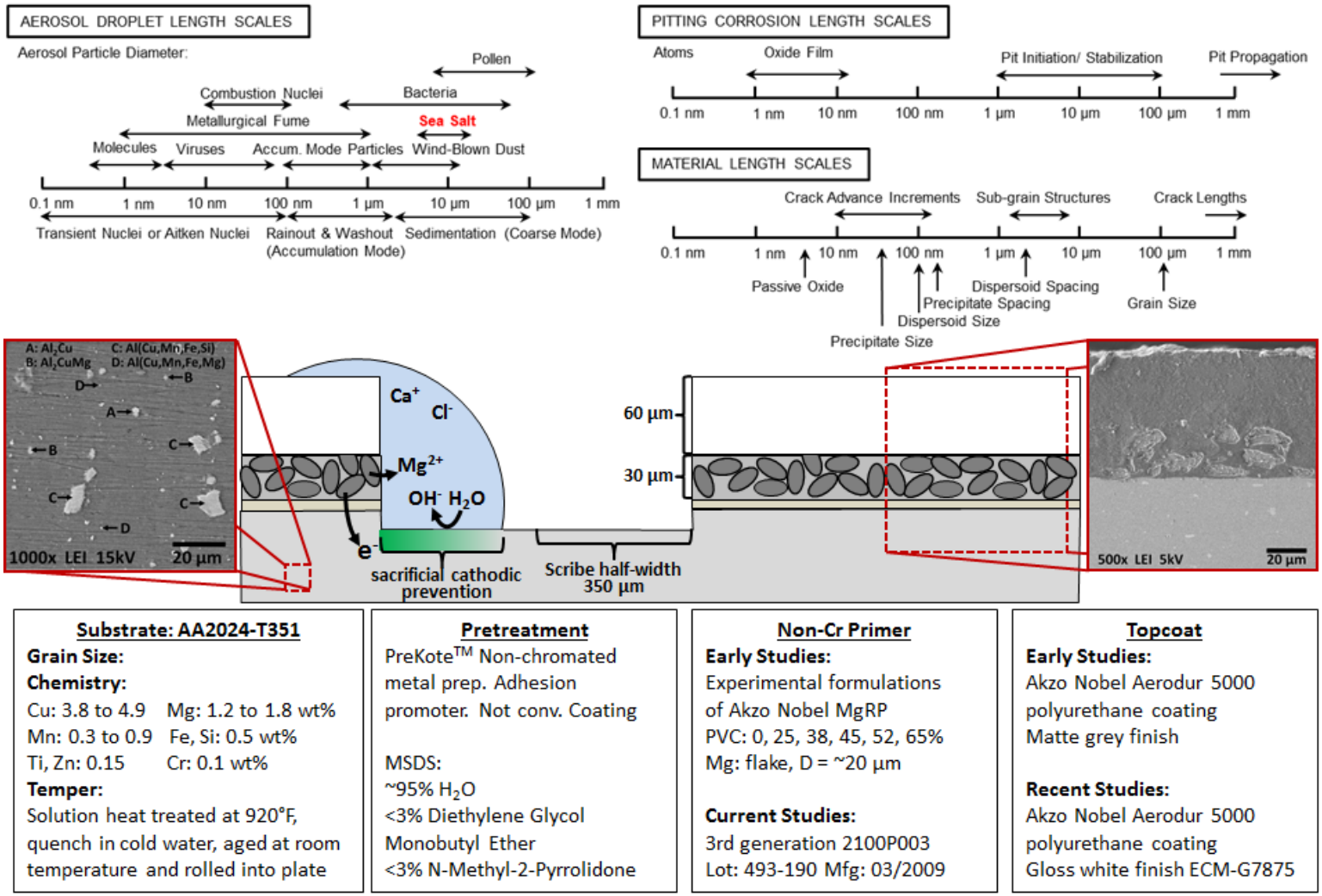

Substrate: AA2024-T351	Pretreatment	Non-Cr Primer	Topcoat
Grain Size: **Chemistry:** Cu: 3.8 to 4.9 Mg: 1.2 to 1.8 wt% Mn: 0.3 to 0.9 Fe, Si: 0.5 wt% Ti, Zn: 0.15 Cr: 0.1 wt% **Temper:** Solution heat treated at 920°F, quench in cold water, aged at room temperature and rolled into plate	PreKote™ Non-chromated metal prep. Adhesion promoter. Not conv. Coating MSDS: ~95% H_2O <3% Diethylene Glycol Monobutyl Ether <3% N-Methyl-2-Pyrrolidone	**Early Studies:** Experimental formulations of Akzo Nobel MgRP PVC: 0, 25, 38, 45, 52, 65% Mg: flake, D = ~20 µm **Current Studies:** 3rd generation 2100P003 Lot: 493-190 Mfg: 03/2009	**Early Studies:** Akzo Nobel Aerodur 5000 polyurethane coating Matte grey finish **Recent Studies:** Akzo Nobel Aerodur 5000 polyurethane coating Gloss white finish ECM-G7875

Figure 1.10. Schematic of length scales pertinent to understanding MgRP and atmospheric corrosion

Sources: (1) I. S. Cole, N. S. Azmat, A. Kanta and M. Venkatraman, Int Mater Rev, 54, 3 (2009), pp. 117-133. (2) C. Leygraf and T. E. Graedel, Atmospheric Corrosion, The Electrochemical Society Series, (2000), p. xii, 354 p. (3)N. R. C. Research Opportunities in Corrosion Science and Engineering. Washington D.C., 2011,(4) A. D. King and J. R. Scully, , Corrosion, 67, 5 (2011), pp. 05500401-05500422.(5) S. B. Madden and J. R. Scully, , J Electrochem Soc, 161, 3 (2014), pp. C162-C175.

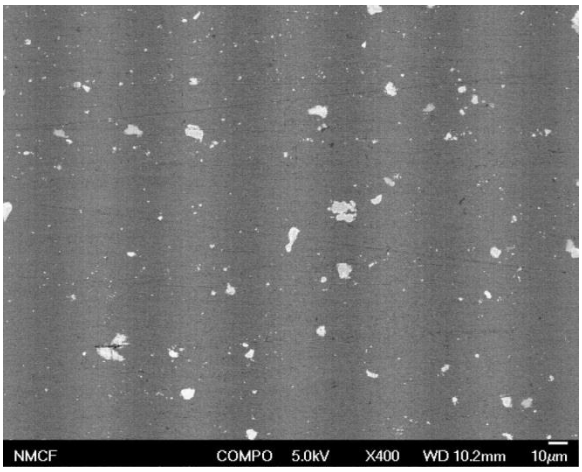

	Mean Nearest Neighbor Distance (um)	Area percent (%)	Average Radius (um)
Mean	5.021	1.995	0.661
Std. Dev.	3.625		0.649

Figure 1.11. SEM micrograph of AA2024-T351 LT surface and statistical analysis of constituent particle sizes.

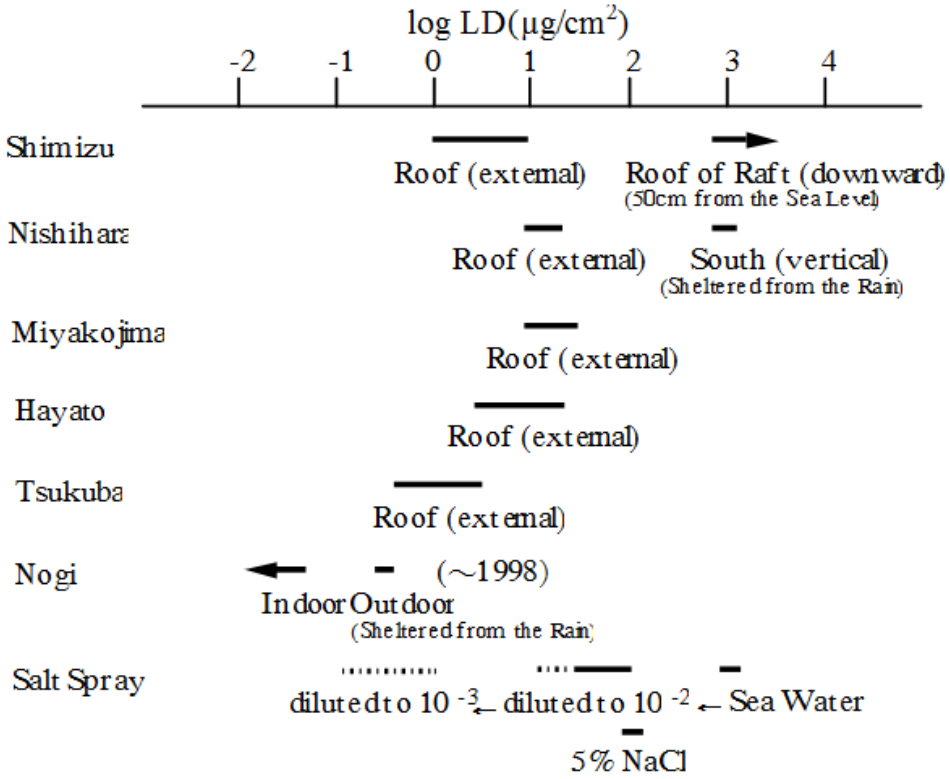

Figure 1.12. Literature values for salt loading density in field and lab environments. Data courtesy of Shinohara, Tahara, Hosoya, National Institute for Materials Science, Japan

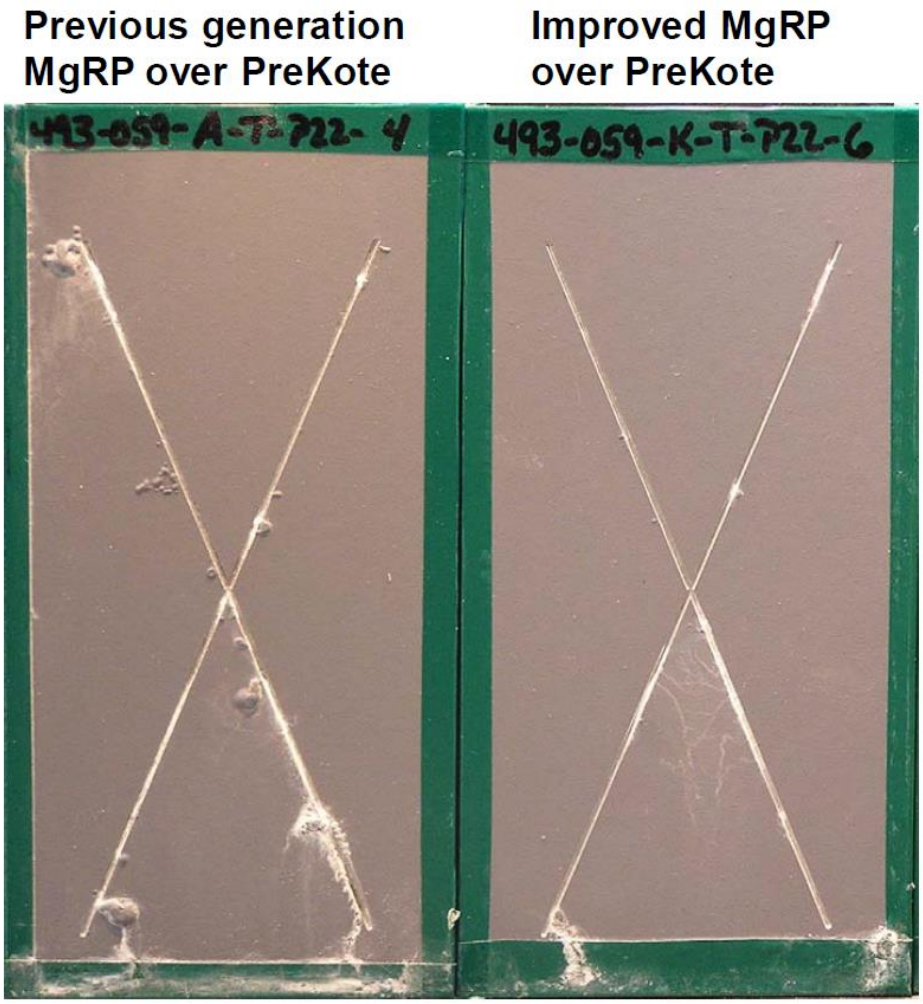

Figure 1.13. Improved, 3rd generation MgRP formulation versus previous, 2nd generation MgRP, 2000 hours ASTM B-117 Neutral Salt Spray, AA2024-T351 over non-chromate Prekote pretreatment
Reproduced with permission from G. P Bierwagen, R. Brown, D. Battocchi, and S. Hayes, 2009 DoD Corrosion Conference Proceedings (2009)

2 Sacrificial Anode-Based Galvanic and Barrier Corrosion Protection of 2024-T351 by a Mg-Rich Primer and Development of Test Methods for Remaining Life Assessment

Reference: *A. D. King and J. R. Scully, Sacrificial Anode-Based Galvanic and Barrier Corrosion Protection of 2024-T351 by a Mg-Rich Primer and Development of Test Methods for Remaining Life Assessment, Corrosion, 67, 5 (2011), pp. 05500401-05500422. DOI: http://dx.doi.org/10.5006/1.3590330*

Awarded the 2013 NACE A. B. Campbell Award for most outstanding manuscript published by a young author (< 35 yo) in a NACE publication.

Presented as part of the NACE CORROSION 2010 Research Topical Symposium; "Advanced Protection Concepts in Coatings," Mar. 2010, San Antonio, TX

Guest Editors: Dr. Rudolph Buchheit and Geraint Williams

2.1 Abstract

The sacrificial and barrier mechanisms of protection afforded to the AA2024-T351 substrate by a magnesium rich primer (MgRP) were investigated. Test methods were developed to estimate the total residual stored Mg anode capacity and electrically "well connected" Mg in the primer, as sensed electrochemically, after various environmental exposures. The residual barrier properties after depletion of the Mg primer were also assessed. In order to determine the quantity of magnesium that was electrically and ionically well connected to the AA2024-T351 substrate, as sensed electrochemically, and

to monitor coating barrier characteristics after partial MgRP utilization, a full immersion testing protocol was designed. The testing regimen included an open circuit hold to assess galvanic coupled potentials between the MgRP and 2024-T351, electrochemical impedance spectroscopy to assess coating barrier properties, potentiostatic holds to asses Mg anodic dissolution charge and X-ray diffraction to assess the total elemental Mg remaining in the MgRP. Changes in these parameters are reported after full immersion in 50 mM NaCl solution as a function of MgRP pigment volume fraction (PVC) with or without a topcoat. X-ray diffraction was used to estimate the total amount of Mg in the MgRP before and after full immersion. Preliminary findings suggest two possible modes of protection; long range protection of remote defects and local or short range Mg pigment-based protection of local and buried defects. Both modes of protection are mediated by the high ionic and electrical resistance of the coating system as a function of MgRP PVC, primer polymer and topcoat properties. A method for estimating the remaining capacity of the coating for each mode of protection is developed. Future testing will extend these methods to both field and accelerated test environments.

2.2 Introduction and Background

Recent field studies have shown very promising corrosion mitigation results for an organic coating system containing a Mg-pigmented organic primer (MgRP) on precipitation age hardened 2024-T351[1-6]. This system is a candidate coating system to replace chromate type surface pretreatments as well as chromate pigmented primers [1, 7, 8]. One of the likely corrosion inhibition mechanisms is sacrificial anode based cathodic protection of the aluminum alloy afforded by the MgRP. The MgRP is designed to

galvanically couple the Mg pigment in the primer to the substrate and provide sacrificial anode based cathodic protection to the aluminum alloy (AA2024-T351). This concept is well established in the design of zinc-rich primers for use on various steels and has been well documented [9-24]. Protection by these primers is afforded primarily by sacrificial anode based cathodic protection and secondarily by precipitation of $Zn(OH)_2$ at bare sites after migration of Zn^{+2} [18, 19]. Zinc also has a low self-corrosion rate. In this case, magnesium is also less noble than all of the precipitation age hardened aluminum alloys it might be used to protect and is readily available and actively corrodes in most electrolytes [4, 5, 25]. Alclad™ also protects by sacrificial cathodic protection but pits and thus is an inefficient anode [26-34]. When coupled to the AA2024-T351 substrate, the Mg pigment becomes an electron donor, and mixed potential theory can be used to explain the open circuit of the system when exposed to full immersion.

Results support the notion of mixed potential theory describing the galvanic coupling behavior between the primer and substrate [2-6, 25, 35, 36]. Potentiodynamic scans show a bare Mg electrode having an open circuit potential, in 0.1 wt. % NaCl solution, of about -1.55 V vs. SCE while bare AA2024-T351 has an open circuit potential of about -0.6 V vs. SCE. These potentiodynamic scans also show that the anodic reaction rate on Mg is relatively fast and that the cathodic reaction rate on AA2024-T351 is relatively slow [4]. The combination of a fast anodic reaction rate on Mg and a slow cathodic reaction rate on AA2024-T351 results in a polarizable cathode that enables a negative galvanic couple potential of as low as -1.5 V vs. SCE in 0.1 wt. % NaCl solution [4]. Unintended cathodic corrosion of Al could be an issue at such negative potentials. [37-43]

The galvanic couple potential between will depend on the surface area ratio between the two electrodes exposed to immersion as well as other factors. Hence, when the sacrificial Mg is placed in an organic polymer, the galvanic couple potential between the Mg pigment and AA2024-T351 substrate becomes a function of the wetted surface area ratio of the two materials actually exposed to an aqueous environment (e.g Mg pigment volume concentration that is wetted; AA2024-T351 that is wetted such as at scratch site), the kinetic properties of the anode and cathode, the electrolyte each is exposed to, the resistive path length and geometry as well as the electrical and ionic conductivities of the system. The PVC will affect both the resistive paths through the organic coating between the Mg pigment and the underlying AA2024-T351 substrate as well as the path through the organic coating and the electrolyte to any exposed AA2024-T351. All of these factors will mediate the galvanic couple potential existing at each metal surface. Additionally, the resistivity of the polymer used in the MgRP also affects the total resistivity of the MgRP. Changing the resistivity of the polymer, via water uptake or other characteristics, will also affect the galvanic coupling potential of the system. The resistivity of the system will also change if the organic polymer degrades as a result of an environmental exposure due to effects of UV radiation, temperature, chemical damage, or other environmental effects. The resistivities of the organic polymers may be an overlooked aspect of the factors governing the galvanic couple potential ultimately achieved in this system which is likely mediated by these resistances. Lastly, any resistive layer between the 2024-T351 and MgRP brought about by anodizing or adding a conversion coating could also serve to mediate the galvanic coupling potential of the system.

Work in the past has predicted and shown a direct dependence of a coating's conductance on the PVC of conducting pigment [44-52]. These studies have shown that there exists a critical pigment volume concentration (CPVC) that marks a composite coating's sharp transition from non-conductive to conductive behavior [44, 45, 51, 53]. The CPVC has been estimated by other groups to be about 50-60% [4, 25]. For this reason, it is predicted that samples with a Mg PVC of 45%, will have a pronounced drop in conductivity through the primer layer. This modest conductivity along the electrical pathway between the anode and cathode will limit the cathodic polarization afforded to the substrate by the Mg pigment at exposed areas in addition to the presence of a resistive ionic path through the electrolyte.

It has also been shown that, if aluminum or aluminum alloys are polarized to potentials as low as -1.5 V vs. SCE, significant cathodic corrosion can occur. By moderating the potential existing at the AA2024-T351 that is either exposed or buried underneath the coating [54], significant cathodic corrosion can be prevented. A PVC of 45% Mg pigment is slightly lower than the critical pigment volume concentration, estimated to be 50-60%. This may prevent excessive galvanic dissolution of the highly active Mg and may prevent cathodic corrosion of the AA2024-T351 due to severe negative polarization. It is speculated that mediation of cathodic polarization can, therefore, be brought about by raising the ionic resistance by lowering the PVC, adding an organic topcoat, as well as by limitations in the time of wetness on atmospheric exposure.

In an effort to predict the lifetime for this coating system in terms of ability to afford protection, accelerated laboratory cabinet testing has been conducted [35, 36, 55, 56]. Interestingly, there are often differences in corrosion behavior between field and laboratory exposures. Scribes in topcoated MgRP systems are not well protected. Moreover, blistering of topcoats due to localized corrosion of MgRP and underlying Al substrates is sometimes seen in ASTM B-117 laboratory tests but is not seen in field exposures such as at Daytona Beach with lower time of wetness [57]. Scribes in topcoated field exposed systems are free of corrosion and blisters are not often seen.

The first step in understanding differences between lab and field is to understand operative protection mechanisms. Determining the primary protection mechanisms during and after pigment depletion of the MgRP serves as motivation for this research.

Therefore, the objectives of this research are to further understand the sacrificial cathodic protection function afforded by the primer, define the role that the topcoat plays to limit self-corrosion and galvanic corrosion of the Mg pigment, elucidate primary and secondary modes of protection of the AA2024-T351, as well as provide a method for estimating the total and electrically “well connected” residual stored anode capacity in the primer, as sensed electrochemically, after environmental exposure.

This paper reports on progress involving laboratory full immersion exposures, pre- and post-mortem coating characterization of remaining sacrificial anode capacity and barrier properties after MgRP depletion. Initial tests in this study are conducted under full

immersion in aerated 50 mM NaCl solution to establish a foundation for behavior. This electrolyte is not necessarily recommended for lifetime assessment. Related important factors in the function of such a coating are its operating couple potential, its theoretical anode capacity, its "available" or useable anode capacity and Mg's self-corrosion rate. The remaining, usable anode capacity provides one measure of the remaining functional capability of the coating for both local and remote cathodic protection. This parameter should aid in forecasting the lifetime of the Mg-rich primer in various environments in terms of the ability to perform its main corrosion function of protecting remote and local coating defects.

2.3 Experimental Procedures

2.3.1 Materials

AA2024-T351, 99.8% pure magnesium ribbon, 99.9% pure magnesium rod, Mg powder as well as coated 1.6 mm thick AA2024-T351 panels were studied in these investigations. The Mg ribbon was 3.0 mm wide and 0.30 mm thick. The Mg rod was 8.0 mm in diameter and about 2.50 cm long. The Mg powder was flake geometry with 20 μm average diameter.

Table 2.1 and Table 2.2 show the chemical analysis of the AA2024-T351 and the three magnesium samples used in this work. Chemical analysis shows the Mg powder in the MgRP (Table 2.2a) to be roughly 99.89% pure with primary contaminants being Si and Al. The Mg rod and ribbon (Table 2.2b and Table 2.2c) were used as bare electrodes in

full immersion electrochemical tests and both had measured purities of over 99.9% and were substantially similar to the powder used in the MgRP.

Samples were mounted in EpoThin epoxy resin manufactured by Buehler, when necessary, in order to make clamping the sample to an electrochemical flat cell easier. The bare electrodes were used in electrochemical analysis and were prepared by alternating polishing with silicon-carbide paper and rinsing with 18.2 MΩ deionized water to a final polishing grit of 1200. The samples were then dried with lab tissue before use. The panels studied comprised of a 1.6 mm thick AA2024-T351 sheet with a 30 μm primer layer of magnesium rich primer of various pigment volume concentrations and a 50 μm thick topcoat of a high performance advanced polymer coating (Figure 2.1). The 2024 panels were pretreated with a non-toxic, non-corrosive, non-flammable, CFC free, ODS free, and chromate free surface pretreatment. The pretreatment does not contain any corrosion inhibitors and is not a conversion coating; but promotes adhesion between the primer and substrate. The high performance advanced polymer topcoat is a two-component polyurethane topcoat developed for military applications in a variety of exposure environments. The magnesium rich primer consists of a 1-part epoxy matrix with Mg metal flake pigment mixed in at various volume concentrations (PVC). The Mg pigment itself has flake geometry with an average diameter of 20 μm. All of our coated panels were provided and painted by the coating manufacturer. Panels had various volume concentrations of Mg (PVC) 0%, 25%, 38%, 45%, 52%, and 65% all in both topcoated and non-topcoated variations (Table 2.3).

2.3.2 Full Immersion Electrochemical Analysis

All full immersion tests reported in this paper were conducted in 50 mM NaCl solution with ambient aeration. Potential control during electrochemical experiments was maintained using a potentiostat with computer interface software. Saturated Calomel reference electrodes (SCE) were used in full immersion testing. These models were selected because they enable electrochemical impedance spectroscopy (EIS) measurements along with traditional electrochemical measurements.

2.3.3 Anodic Potentiodynamic Scans of Bare and Coated Electrodes

Anodic potentiodynamic scans were conducted on 99.9% pure, 8.0 mm diameter bare Mg electrodes as well as the manufacturer prepared Mg-rich primer coated AA2024-T351 panels with Mg PVC $\geq$ 25%. Both topcoated and non-topcoated panels were tested. The tests were run in 50 mM sodium chloride solution with ambient aeration and used a saturated calomel reference electrode. The bare Mg electrodes were polished to 1200 grit silicon carbide paper until a mirror finish was obtained. The potentiodynamic scans were conducted after a 10 minute OCP. A typical anodic scan started at -0.2 V vs OCP up to +0.7 V vs. OCP and scanned at 0.1667 mV per second for bare electrodes and 2.0 mV per second for the coated panels.

2.3.4 Cathodic Potentiodynamic Scans of Bare and Coated Electrodes

Cathodic potentiodynamic scans were conducted on bare AA2024-T351 electrodes as well as Mg-rich primer coated AA2024-T351 panels with Mg PVC = 0%. Both topcoated and non-topcoated panels were tested. The tests were run in 50 mM sodium chloride

solution with ambient aeration using a saturated calomel reference electrode. The bare AA2024-T351 electrodes were ground to 1200 grit silicon carbide paper until a mirror finish was obtained. The potentiodynamic scans were conducted after a 10 minute OCP. A typical cathodic scan started at +0.2 V vs OCP and scanned down to -1.0 V vs. OCP at 0.1667 mV per second.

2.3.5 Electrochemical Impedance Spectroscopy (EIS) of Bare and Coated Electrodes

EIS was conducted on bare Mg and AA2024-T351 electrodes as well as the manufacturer prepared Mg-rich primer coated AA2024-T351 panels. A typical EIS scan was acquired in sine sweep mode from 100 kHz to 0.01 Hz with 6 points per decade. Bare electrodes were scanned with an AC amplitude of 20 mV while coated panels were scanned with an AC amplitude of 60 or 80 mV to reduce noise. The tests were run in 50 mM sodium chloride solution with ambient aeration and used a saturated calomel reference electrode. The bare Mg and AA2024-T351 electrodes were polished to 1200 grit silicon carbide paper until a mirror finish was obtained.

2.3.6 Full Immersion, Electrochemical Testing Protocol (Cycle Test)

A full immersion, electrochemical testing regimen was designed to monitor selected coating characteristics over time. This test included a 10 minute OCP followed by an EIS measurement to assess, nondestructively, the galvanic couple potential of the primer coated AA2024-T351 substrate in order to later interpret cathodic protection and the residual barrier properties of the coating. These were followed by a potentiostatic hold at

-0.8 V vs. SCE to accelerate the Mg dissolution rate and measure the anodic charge supplied by the MgRP. The test always started and ended with a 10 minute OCP measurement followed by EIS. The cycle test was run under full immersion in 50 mM sodium chloride solution with ambient aeration and used a saturated calomel reference electrode. These three steps were repeated for a specified number of cycles. The cycles of exposure in full immersion cannot as yet be related to hours of exposure in natural environments.

2.3.7 X-Ray Diffraction of Bare and Coated Electrodes

X-Ray diffraction was conducted on a powder diffractometer utilizing a Cu-Kα source. The samples investigated included bare AA2024-T351, Mg powder and the manufacturer prepared, Mg-rich primer coated AA2024-T351 panels of all PVC's. All samples were scanned continuously from 10 to 120 degrees. Scans were run at a scan rate of 1.0 degrees per minute on bare electrodes and non-topcoated coatings and 2.0 degrees per minute on topcoated coatings. Both fresh Mg-rich coated panels and panels exposed in full immersion were examined with XRD. XRD Spectra obtained from bare AA2024-T351 and AA2024-T351 coated with MgRP were normalized against the fcc Al <200> $2\theta=44.7384^{o}$ peak. Samples of bare Mg electrodes were normalized against the Mg <101> $2\theta=36.6190^{o}$ peak.

2.3.8 Scanning Electron Microscopy and Energy Dispersive Spectroscopy

Scanning electron microscopy and energy dispersive spectroscopy were used for coating characterization and post-mortem analysis. A field emission SEM with EDS analytical

software was used to conduct these investigations. Various accelerating voltages and working distances were used depending on the samples and information being investigated. In general, for EDS, a working distance of 15 mm and an accelerating voltage of at least 3 times the energy of the maximum characteristic peak of interest were used. Signals for Mg and Al K_α energies were obtained.

2.4 Results

2.4.1 Initial Assessment of Sacrificial Anode Material Stored in Mg-Rich Primer

Figure 2.2 shows an SEM micrograph of cross sectioned magnesium rich primer on AA2024-T351 before the sample has been exposed to any weathering environment. The thickness of the primer layer was about 30 μm. For topcoated samples, the topcoat was about 50 μm thick. The total coating system thickness was about 80 μm. EDS spot scans conducted on magnesium pigment particles in the primer indicated low O levels which suggest the magnesium was largely unoxidized prior to weathering.

X-ray diffraction spectra were acquired on bare AA2024-T351 and magnesium powder (Figure 2.3) and compared to spectra obtained from AA2024-T351 coated with MgRP PVC = 45%, (Figure 2.3). Elemental Mg HCP <001>, <002> and <101> peaks were observed in the XRD spectra of both the Mg powder and AA2024-T351 coated with MgRP. This indicates that elemental Mg, with an HCP crystal structure, can be detected.

X-ray diffraction spectra were then obtained from AA2024-T351 panels coated with MgRP of PVC = 0%, 25%, 38%, 45%, 52%, and 65% and similar thickness. Three

prominent magnesium peaks were normalized against the Al <200> peak which appeared in each spectrum due to the underlying AA2024-T351 substrate. The relative intensities of the Mg peaks increased with increasing PVC (Figure 2.4). The intensities were plotted versus PVC and a trend line was fitted to each set of peak data (Figure 2.5). This fit provided three relationships relating peak intensities to PVC associated with elemental Mg in the MgRP. It is regarded that the peak intensities reflect the total Mg in the MgRP regardless of whether or not it is electrically connected or disconnected.

2.4.2 Initial Assessment of Electrochemical Behavior of Non-Topcoated Mg-Rich Primer

Electrochemical impedance measurements were taken after 10 min full immersion in 50 mM NaCl solution of bare Mg, bare AA2024-T351 and coated AA2024-T351 for comparison (Figure 2.6 and Figure 2.7). Bare AA2024-T351 and bare magnesium demonstrated low impedances at all frequencies with limited barrier attributes. The bare Mg electrode exhibited low corrosion resistance of 100 Ω-cm^2 and a solution resistance (high frequency impedance at 100 kHz) of about 10 Ω-cm^2. Bare AA2024-T341 showed intermediate corrosion resistance. AA2024-T351 coated with an organic polymer (MgRP PVC = 0%) possessed a very high impedance at all frequencies typical of an insulating polymer organic coating with high resistance, low capacitance and limited interfacial electrochemical reactions [58-60]. AA2024-T351 coated with MgRP (PVC = 45%) also exhibited high impedance at all frequencies similar to the impedance behavior of AA2024-T351 coated with MgRP PVC = 0%. This behavior strongly suggests that the Mg powder pigment in the polymer matrix is encapsulated by polymer and isolated (e.g. does not form a large connected network) from the substrate. AA2024-T351 coated with a MgRP (PVC = 65%) exhibited intermediate impedance behavior with respect to bare

AA2024-T351 and coated AA2024-T351. This suggests that with increasing PVC, the impedance through the MgRP coating decreases. However AA2024-T351 coated with MgRP with a PVC = 65% still has a larger impedance than a bare Mg electrode, even if a reduced surface area of bare Mg electrode is assumed given a finite pigment density and area coverage. These effects are interpreted to be due to the polymer encapsulation of the Mg pigment by the primer organic polymer. The area of Mg in the MgRP at a PVC of 65% (approx. 5-10 cm^2 depending on pigment geometry), if fully connected electrically, would produce similar EIS as seen for bare Mg. The Mg particles in the primer must still be partially isolated in the polymer matrix resulting in a finite Ohmic resistance between particles.

Potentiodynamic scans on bare electrodes and AA2024-T351 coated with MgRP in aerated 50 mM NaCl solution were compared (Figure 2.8). The exposure time at measurement is very important and recorded in the caption. The OCP of AA2024-T351 was approximately -0.55 V vs. SCE. Bare, high purity Mg (99.9%) had an OCP of -1.55 V vs SCE and an extremely fast anodic reaction rate with a low anodic Tafel slope yielding a high corrosion rate at OCP. This behavior suggests that Mg can effectively polarize AA2024-T351 and provide galvanic sacrificial protection of the AA2024-T351 substrate subject to the details of the electrical resistance in the conductors and ionic resistance in electrolytes between them. Also the possibility of cathodic corrosion of Al exists due to OH^- production and an alkaline pH shift. This is because OH^- is a product of both the oxygen reduction (ORR) and the hydrogen evolution reactions (HER). AA2024-T351 coated with organic polymer (MgRP PVC = 0%) displayed a slightly lower open

circuit potential (approximately -0.65 V vs. SCE) than that of bare AA2024-T351 with cathodic current densities approximately two to three orders of magnitude lower than bare AA2024-T351 owing to reduced or nil bare interfacial area and reduced reaction rates at the buried interface. This can be attributed to the significant reduction in exposed surface area of the coated electrode that can support the ORR and HER and high O_2 transport impedance through the polymer phase. The low cathodic current density on coated AA2024-T351 of about 10^{-7} amps/cm^2 confirms low background ORR rates on polymer coated Al 2024-T351. As MgRP PVC increased from 25% to 65%, the OCP of the AA2024-T351/MgRP system decreased until it approached bare Mg. The increase in magnitude of the uncorrected apparent anodic Tafel slopes on AA2024-T351 coated with MgRP can be attributed to an increase in the resistance of the ionic pathway and corresponding high Ohmic resistance. The reduction in conducting surface area on the Mg anode due to only partially connected Mg particle matrix accounts for low current densities. In addition a higher apparent open circuit potential (galvanic couple potential) is seen with decreasing MgRP PVC.

2.4.3 Behavior of Mg-Rich Primer Under Full Immersion Accelerated Testing

In order for magnesium to be available for remote sacrificial cathodic protection of the AA2024-T351 substrate it must be both electrically and ionically "well connected" to the AA2024-T351 substrate. Electrical conduction is required between metallic phases comprising anodes and cathodes while ionic conduction through the electrolyte phase is required between anodes and cathodes. To assess the amount of magnesium that was both electrically and ionically connected to the AA2024-T351 substrate as sensed

electrochemically and to monitor coating characteristics over time, a full immersion, electrochemical testing regimen was designed (Figure 2.9). This test included OCP and EIS measurements to assess, nondestructively, the galvanic corrosion (cathodic protection) potential and the residual barrier properties of the coating, respectively. These tests were followed by a potentiostatic hold at -0.8 V vs. SCE to simulate the Mg dissolution rate when coupled to AA2024-T351 and to measure the anodic charge consumed when cathodically protecting AA2024-T351. -0.8 V vs. SCE is regarded as a possible galvanic couple potential and also represents a potential where limited anodic or cathodic reactions are sensed on AA2024-T351 coated with a 0% PVC polymer (Figure 2.8). [2] An example timeline of the testing procedure used is shown in Table 2.4.

AA2024-T351 panels coated with MgRP of varying PVC were exposed to the full immersion, electrochemical testing regimen described in Figure 2.9. An AA2024-T351 panel coated with an organic polymer (MgRP PVC = 0%) exhibited a relatively constant OCP of approximately -0.65 V vs. SCE (Figure 2.10). In contrast, an AA2024-T351 panel coated with a MgRP of PVC = 45% exhibited an initial OCP approaching that of pure Mg (-1.6 V vs. SCE). After 5 to 8 cycles of the testing regimen the OCP of this system gradually increased to that of AA2024-T351 coated with an organic polymer free of Mg (Figure 2.10). This process was completed for samples of varying Mg PVC. All the samples coated with MgRP exhibited OCP's which slowly increased with time. However, it was observed that samples with higher Mg PVC retained and open circuit

[2] However, this accelerated full immersion test does not assess the lifetime in atmospheric exposures with lower time of wetness and possibly, a more benign electrolyte. -0.8 V would be equivalent to a potential sensed by a remote electrode and simulates what a remote AA2024-T351 scratch senses.

potential lower than -0.8 V vs. SCE for a longer period of time (Figure 2.10). Again, it is worth noting that these times are not equivalent to the protection time during atmospheric exposure.

In order to assess whether Mg was preserved in the MgRP after the OCP of the system had risen above -0.8 V vs. SCE a simple abrasion test was conducted. A sample of AA2024-T351 coated with MgRP (PVC = 45%) was exposed under full immersion in aerated 50 mM NaCl solution. The OCP of the system was measured continuously (Figure 2.11). Once the OCP of the system rose above -0.8V vs. SCE, the surface of the sample was lightly abraded in-situ. After abrasion of the surface, the OCP of the system decreased to -1.3V vs. SCE and again rose slowly over time. This result supplies evidence of Mg buried in the polymer matrix electrically connected to the AA2024-T351 substrate that was then exposed to electrolyte by the abrasion process and utilized for sacrificial protection of the substrate. It is reasonable to assume that along with abrasion, other chemical events such as an acid, oxidizer, or properly selected complexing agent or environmental effect such as UV or temperature that would dissolve or damage the organic polymer might also expose unoxidized, buried Mg, which was once preserved in the polymer matrix. This Mg could then be utilized for sacrificial protection of the substrate.

The net anodic charge from each potentiostatic hold of the full immersion testing regimen is plotted in Figure 2.12. An AA2024-T351 panel coated with an organic polymer (MgRP PVC = 0%) always exhibited a cathodic current density when held at -0.8 V vs. SCE

(Figure 2.12a). This net cathodic charge was consistent with ORR and HER as the predominant electrochemical reactions at this potential on bare or coated AA2024-T351. This charge is associated with ORR on coated AA2024-T351 as predicted from Figure 2.8. An AA2024-T351 panel coated with MgRP PVC = 45% initially exhibited a net anodic charge and as the test continued, eventually exhibited a net cathodic charge (Figure 2.12b). This shift from anodic to cathodic behavior is interpreted to signal that all of the Mg in the MgRP that had both exposure to 50 mM NaCl electrolyte and electrical continuity with the substrate through the primer and AA2024-T351 had been dissolved in solution.[3] This does not necessarily mean that the total Mg quantity in the Mg-rich primer has been consumed as will be shown below.

Electrochemical impedance measurements were taken at various stages during the full immersion testing regimen described in Figure 2.9 and Table 2.4 and are shown in Figure 2.13 and Figure 2.14. An AA2024-T351 panel coated with an organic polymer (MgRP PVC = 0%) exhibited relatively constant Bode magnitude and phase angle curves suggesting little barrier degradation of the coating throughout the entire test regimen. This indicates that neither the time of exposure in 50 mM NaCl solution nor the cycle test

[3] Clusters of buried magnesium pigment that lacked either electrical connection to the substrate and intermediate ionic resistance would not dissolve at -0.8 V vs. SCE and a large anodic charge would not be sensed by this method. It can be rationalized that to provide a remote location of AA2024-T351 with cathodic protection via sacrificial anodic dissolution at -0.8 V vs. SCE, a large anodic charge should not have been detected from electrically isolated Mg by electrochemical measurements with a remote counter electrode and reference electrode during this testing regimen. These isolated clusters, however, still contribute along with the polymer to barrier protection as they existed as part of the coating unless they dissolved into solution after immersion.

degraded the polymer or the polymer/metal interface. An AA2024-T351 panel coated with MgRP PVC = 45% exhibited an overall lower coating impedance and decrease in impedance of one to two orders of magnitude at 0.01 Hz over the life of the test and displayed a Bode phase angle shifting towards high frequencies. Both phenomena suggest a degradation of barrier properties of the organic coating or the development of porous pathways. This behavior is consistent with an increase in ionic conductivity likely associated with porosity development at sites of Mg pigment dissolution inside the polymer matrix of the MgRP.[58, 59, 61-65]

Figure 2.15 shows the total impedance magnitude at 0.01 Hz of AA2024-T351 panels coated with MgRP of varying PVC over the lifetime of the full immersion, electrochemical testing regimen. The highest impedance is seen for AA2024-T351 panels coated with MgRP PVC = 0% which exhibits no degradation after the 1200 min accelerated test. AA2024-T351 panels coated with MgRP with a PVC of 25% and 45% exhibited initial impedances of at least two orders of magnitude higher than that of a AA2024-T351 panel coated with MgRP of PVC = 65%. The Mg-rich primer with a Mg PVC of 65% apparently develops more substantial low ionic resistance pathways.

2.4.4 Characterization of Mg-Rich Primer After Accelerated Testing

After the full immersion, electrochemical testing regimen was completed the samples were removed from full immersion and cross-sectioned for post-exposure characterization. An SEM micrograph of a cross sectioned AA2024-T351 panel coated with MgRP PVC = 45% post-exposure (Figure 2.16) shows some Mg pigment still

preserved in the primer layer despite the shift from anodic to cathodic behavior displayed in the charge measurements (Figure 2.12b). EDS spot scans of the pigment particles present have a very low O_2 peak confirming the remaining undissolved pigment was largely unoxidized.

XRD spectra of each sample were also taken after the full immersion, electrochemical testing regimen was completed. The XRD spectrum measured from an AA2024-T351 panel coated with MgRP PVC = 45% after exposure clearly showed elemental magnesium still present in primer despite the shift from anodic to cathodic behavior displayed in the charge measurements shown in Figure 2.12b. This means that a reservoir of unoxidized MgRP remains in the coating even though electrochemically well connected Mg has dissolved during the potentiostatic test in full immersion. The remaining Mg will be discussed below.

The normalized intensities of the three Mg peaks observed after exposure were fit on the trend lines obtained in Figure 2.5 by solving for the PVC estimated by each trend line, given each respective peak's normalized intensity. The three resulting PVC estimations were then averaged. Using this technique it is estimated that during exposure, the PVC of the MgRP decreased from 45% to approximately 41%. Figure 2.17 shows the result of this estimation. The remaining Mg pigment would remain available for local protection of the AA2024-T351 substrate should new defects occur in the coating proximate to this buried Mg pigment.

2.4.5 Initial Stored Sacrificial Anode Material in Topcoated Mg-Rich Primer

X-ray diffraction spectra were also obtained from unexposed AA2024-T351 panels coated with MgRP of varying PVC and a high performance advanced polymer topcoat (Figure 2.18). Three prominent elemental magnesium peaks were normalized against the Al <200> peak which appeared in each spectrum from the AA2024-T351 substrate. Similar results were observed as with non-topcoated samples described earlier. The relative intensities of the Mg peaks were observed to increase with increasing PVC. The intensities were plotted versus PVC and a trend line was fitted to each set of peak data (Figure 2.19). These results indicate that Mg within the MgRP can be detected through topcoated systems.

2.4.6 Initial Electrochemical Behavior of Topcoated Mg-Rich Primer

Electrochemical impedance spectroscopy measurements were taken in full immersion of various bare and topcoated electrodes for comparison (Figure 2.20 and Figure 2.21). Recall that bare AA2024-T351 and bare magnesium rod demonstrated low impedances indicative of bare electrodes. AA2024-T351 coated with an organic polymer (MgRP PVC = 0%) and a high performance advanced polymer topcoat possessed a very high impedance. AA2024-T351 coated with MgRP of all PVC ranging from 0 to 65% also demonstrated a very high impedance that was independent of PVC and dominated by the influence of the polymer topcoat. As a result it was observed that the topcoat adds a resistive polymer layer that buries the Mg pigment under a polymer layer and raises the overall ionic resistance through the coating regardless of the PVC of the primer.

Potentiodynamic scans of bare electrodes and AA2024-T351 coated with MgRP and a high performance advanced polymer topcoat were plotted and compared (Figure 2.22) after 10 min full immersion exposure to aerated 50 mM NaCl solution. It is observed that the samples with a high performance advanced polymer topcoat have a high initial open circuit potential, similar to that of bare AA2024-T351, regardless of Mg PVC of the primer. Anodic E-log(i) kinetics are also suppressed as compared to the bare Mg electrodes or MgRP with no topcoat (Figure 2.22 & Figure 2.8). This implies less wetting of the Mg in the primer and high ionic resistance through the topcoat, at least initially, mediating Mg dissolution.

2.4.7 Behavior of Topcoated Mg-Rich Primer Under Full Immersion Accelerated Testing

AA2024-T351 panels coated with MgRP of various PVC levels ranging from 0-65% and a high performance advanced polymer topcoat were exposed to the full immersion, electrochemical testing regimen described in Figure 2.9 and summarized in Table 2.4. The results were compared to the results received when testing the non-topcoated specimen from Figures 10 - 16. The AA2024-T351 sample coated with MgRP and a high performance advanced polymer topcoat was observed to have an initial OCP of about -1.2 V vs. SCE as compared to -1.65 V vs. SCE of the non-topcoated sample (Figure 2.23b). The OCP of each sample was observed to initially decrease then gradually rise throughout the duration of the test to a final potential of about -0.8V vs SCE for the non-topcoated sample and -0.6V vs. SCE for the topcoated sample.

The trend in OCP is summarized as a function of PVC in Figure 2.23a for topcoated samples. All AA2024-T351 panels coated with a MgRP of PVC > 0% and a high performance advanced polymer topcoat had a similar initial OCP of about -1.0 to -1.2 V vs. SCE which all gradually rose to about -0.6 V vs. SCE over the test period (Figure 2.23a). The OCP of topcoated samples was observed to increase at a faster rate compared to non-topcoated samples (Figure 2.23b). The drop in OCP is attributed to initial water uptake and wetting of Mg in the MgRP and the subsequent rise in OCP is attributed to depletion of connected Mg by corrosion. An AA2024-T351 panel coated with an organic polymer (MgRP PVC = 0%) and a high performance advanced polymer topcoat initially exhibited a positive OCP of above 0.0 V that quickly declined to a consistent -0.5V vs. SCE.

Electrochemical impedance measurements of a topcoated sample taken during the full immersion, electrochemical testing regimen described in Figure 2.9 are shown in Figure 2.24 and Figure 2.25. The sample represented in Figure 2.24 and Figure 2.25 is coated with MgRP (PVC = 45%) and a high performance advanced polymer topcoat. AA2024-T351 coated with MgRP PVC = 45% and no topcoat exhibited a coating impedance at 0.01 Hz of about 10^7 ohms-cm^2 which quickly decreased to about 10^6 ohms-cm^2 over the lifetime of the cycle test and depletion of electrically connected Mg (Figure 2.13b). The non-topcoated samples also displayed a shifting Bode phase angle breakpoint frequency (Figure 2.14b). The breakpoint frequency is defined as the point on a Bode-Phase plot where following the curve from higher to lower frequency the phase shift first drops below 45 degrees. Scully and Hack have shown this breakpoint frequency to be directly

related to the defect area percentage [58]. As the defect area percentage (porosity) increases so does the breakpoint frequency. Both, decreasing low frequency impedance and a shifting phase angle breakpoint frequencies, suggest a degradation of barrier properties of the organic primer and the development of lower resistance paths. In contrast, an AA2024-T351 panel coated with MgRP PVC = 45% and a high performance advanced polymer topcoat exhibited a coating impedance at 0.01 Hz of about 10^8 ohms-cm^2 which gradually decreased to about 10^7 ohms-cm^2 over the lifetime of the test (Figure 2.24). The topcoated sample also exhibited fairly consistent Bode phase angle characteristics throughout the lifetime of the test regimen (Figure 2.25). These results are much higher than for primer only systems and indicate an improved barrier and improved residual barrier after MgRP utilization.

Figure 2.26a shows the magnitude of the complex impedance at 0.01 Hz of AA2024 - T351 panels coated with MgRP of varying PVC and a high performance advanced polymer topcoat over the lifetime of the full immersion, electrochemical testing regimen. It was observed that increasing PVC in the primer acts to decrease the complex impedance at 0.01 Hz of the entire coating system. However, the topcoat was observed to raise the impedance of all of the coating systems regardless of PVC relative to Mg-rich primer only systems (Figure 2.26b).

The net charge from each potentiostatic hold of the full immersion, electrochemical testing regimen is plotted in Figure 2.27. An AA2024-T351 panel coated with MgRP PVC = 45% initially exhibited a net anodic charge and as the test continued, eventually

exhibited a net cathodic charge (Figure 2.12b). This shift from anodic to cathodic behavior is presumably because all of the Mg in the MgRP that had both a low resistance path to electrolyte and possessed electrical continuity with the substrate had been dissolved in solution. The same behavior was observed for an AA2024-T351 panel coated with MgRP PVC = 45% and a high performance advanced polymer topcoat (Figure 2.27). However, the transition from anodic to cathodic behavior occurred much more rapidly and after lower anodic charge. This suggests that less Mg was electrochemically connected through the top of the outer layer of the coating in the presence of the topcoated system. This substantiates the claim that increased ionic resistance of the topcoat lowers the sacrificial anode function and mediates the cathodic protection potential.

2.4.8 Characterization of Topcoated Mg-Rich Primer After Accelerated Testing

Post-exposure characterization was also performed on an AA2024-T351 panel coated with MgRP PVC = 45% and a high performance advanced polymer topcoat. An SEM micrograph of a cross sectioned AA2024-T351 panel coated with MgRP PVC = 45% and a high performance advanced polymer topcoat post-exposure (Figure 2.28) shows considerable Mg pigment still preserved in the primer layer despite the shift from anodic to cathodic behavior displayed in the charge measurements. EDS spot scans of the pigment particles present showed that the remaining undissolved pigment was largely unoxidized by virtue of the absence of an oxygen peak.

The XRD spectrum measured from an AA2024-T351 panel coated with MgRP PVC = 45% and a high performance advanced polymer topcoat after exposure clearly showed elemental magnesium present in primer despite the shift from anodic to cathodic behavior displayed in the charge measurements.

The remaining Mg content in the primer was also assessed. The normalized intensities of the three Mg peaks observed after exposure were fit on the trend lines obtained in Figure 2.19 by solving for the PVC estimated by each trend line just as in Figure 2.17. Given each respective peak's normalized intensity, three resulting PVC estimations were obtained and then averaged. Using this technique it is estimated that during exposure, the PVC of the primer did not significantly decrease (Figure 2.29). In contrast, PVC of the MgRP decreased from 45% to 41% in the case studies involving the primer without the topcoat (Figure 2.17).

2.5 Discussion

2.5.1 Role of PVC in Determining the Protection Capacity of Mg-Rich Primer Systems

The PVC of the Mg-rich primer plays an important role in determining the sacrificial cathodic protection capabilities of the coating. The PVC not only determines the total supply of Mg sacrificial anode material available in the primer but also is a determining factor controlling the effective conductance of the primer layer. Primer formulations with high PVC (65%) not only have a larger total supply of Mg (Figure 2.5) but also have a higher conductance (lower resistance) through the coating (Figure 2.6), allowing a larger

percent of the distributed Mg pigment to be utilized to protect remote defects. Primer formulations with moderate PVC (45%) have a lower conductance (higher resistance) through the coating. This is a result of a smaller amount of electrically connected Mg throughout the polymer. For this reason, a smaller amount of Mg is electrochemically sensed by a remote counter electrode and available for protection of remote defects in the coating. For example, the net anodic charge consumed during potentiostatic hold of the full immersion, electrochemical testing regimen from a 1 cm^2 area of an AA2024-T351 panel coated with MgRP with a PVC of 45% and a thickness of 30 μm (Figure 2.12b) was measured to be 0.0026 C. However, a 1 cm^2 area of MgRP with a PVC of 45% and a thickness of 30 μm contains a theoretical total of 18.63 C of available sacrificial anode material.

Moreover, the remaining Mg pigment, insulated in the polymer from either the A2024-T351 substrate or the electrolyte, would be available to protect local defects as they occur throughout the coatings lifetime (Figure 2.30b). This is shown schematically in Figure 2.31. This will be the case as long as this buried Mg is not corroded under a topcoat and as long as the conductive path length is shortened by the formation of the defect. Otherwise, the Mg pigment would remain buried and insulated. Scratching of a MgRP after the accelerated test proves this point as shown in Figure 2.11. Moreover, as the Mg corrodes in the primer, pores develop in the primer coating. These pores, as well as new defects such as scratches, act to reduce the ionic resistance between remaining buried Mg and the electrolytic environment, enhancing the availability of remaining Mg for sacrificial protection. Moreover, a physical scratch may uncover nearby retained Mg or

create a lower resistance path. This accounts for the drop in potential upon creation of a new scratch (Figure 2.11).

2.5.2 The Role of a Topcoat in Determining the Protection Capacity of Mg-Rich Primer Systems

The topcoat serves multiple purposes in the protection afforded by the coating system. The organic polymer topcoat not only serves to add barrier protection to the substrate (Figure 2.20 and Figure 2.22) but acts to moderate or control the exposure of the Mg pigment in the primer to environmental conditions through the addition of an ionic resistance, in turn moderating the galvanic potential (Figure 2.22 and Figure 2.23). This helps to prevent the self-corrosion of much of the Mg pigment in the primer before it is utilized for protection of the AA2024-T351 substrate. This is shown schematically in Figure 2.32. This serves two functions, to preserve Mg pigment so that it is used solely for protection of the substrate when there are proximate defects or buried defects and is not consumed by self-corrosion, and to prevent the barrier properties of the coating system from degrading during environmental exposure due to the formation of pores in the primer coating after Mg is utilized. However the topcoat also limits protection of remote scratches by adding additional ionic resistance into the galvanic couple relationship when the ionic current path is through the coating. This aspect is discussed further below. Additionally, the presence of a topcoat may affect the nature of the under-coating environment and change the polarization characteristics of both Al and Mg, effecting the overall galvanic interaction between the Mg pigment and AA2024-T351 substrate. This possibility will be studied in future work.

2.5.3 Mixed Potential Theory and Implications to Cathodic Corrosion

It is important for the MgRP coating system to provide sacrificial cathodic corrosion protection or prevention[4]. It is also important for the coating system to avoid the detrimental effects of cathodic corrosion of the AA2024-T351 substrate that is caused by severe cathodic polarization [38-43]. A moderate PVC formulation (45%) resulted in a more moderate polarization of the AA2024-T351, sensed remotely, than did higher PVC (65%) (Figure 2.10). This is due to a series of Ohmic resistances through the polymer which result in the low conductance observed through the coating (Figure 2.6). When galvanic current flows, several Ohmic voltage drops exist between the Mg pigment and the electrolyte (ionic) as well as between the Mg pigment and the substrate (electrical) (Figure 2.30). The application of a topcoat to the coating system will also increase the Ohmic resistance between the buried Mg pigment and the electrolyte. This additional resistance acts to limit the amount of Mg available for protection of remote defects; effectively decreasing the surface area and the galvanic couple current density of the sacrificial Mg anode. These series of Ohmic voltage drops also moderate the galvanic couple potential between the substrate and sacrificial Mg pigment so that AA2024-T351 is not as severely polarized (Figure 2.10 and Figure 2.23).

This can be demonstrated by mixed potential theory. Polarization scans of bare Mg rod (similar purity –Table 2.2b) and bare AA2024-T351 (Table 2.1) were used to create a mixed potential model of the galvanic coupling between Mg and AA2024-T351. Below

[4] Prevention involves a shift in the galvanic couple potential below the pitting potential of AA2024-T351.

are the current–potential relationships used in the mixed potential theory modeling depicted in Figure 2.33. The following kinetic expressions were used to construct the model. Equation 1 describes the potential associated with an Mg anode corroding under charge transfer control

$$E_{Mg}^{Mg/Mg^{2*}} = E_{Mg}^{corr} + b_{Mg}^{a} \ln\left(\frac{I}{i_{corr}^{Mg^{2+}/Mg} A_{Mg}}\right) \quad \text{Equation 1}$$

Where E_{Mg}^{corr} is the corrosion potential of Mg in aerated 50 mM NaCl solution (-1.54 V vs SCE), b_{Mg}^{a} is the Tafel slope of the anodic dissolution reaction occurring at the Mg electrode (0.0267 V/decade), I is the galvanic current in the system, $i_{corr}^{Mg^{2+}/Mg}$ is the corrosion current density of the anodic dissolution reaction occurring at the Mg electrode at its OCP (10^{-5} A/cm^2) and A_{Mg} is the area of the Mg electrode.

For AA2024-T351 (cathode) Equation 2:

$$E_{Al}^{ORR} = E_{Al}^{corr} - b_{Al}^{ORR} \ln\left(\frac{I}{i_{corr}^{ORR,Al} A_{Al}}\right) + \frac{RT}{nF} \ln\left(1 - \frac{I}{i_{L}^{ORR,Al} A_{Al}}\right) \quad \text{Equation 2}$$

and Equation 3

$$E_{Al}^{HER} = E_{Al}^{corr} - b_{Al}^{HER} \ln\left(\frac{I}{i_{corr}^{HER,Al} A_{Al}}\right) \quad \text{Equation 3}$$

Where E_{Al}^{corr} is the corrosion potential of Al in aerated 50 mM NaCl (-0.55 V vs. SCE), b_{Al}^{ORR} and b_{Al}^{HER} are the cathodic Tafel slopes of the ORR and HER cathodic reactions (-

0.160 V/decade and -0.127 V/decade respectively) occurring at the AA2024-T351 electrode, I is the galvanic current of the system, $i_{corr}^{ORR,Al}$ and $i_{corr}^{HER,Al}$ are the current densities of the cathodic reactions occurring at the AA2024-T351 electrode (7 x 10^{-7} A/cm^2 and 10^{-10} A/cm^2, respectively) selected here at the OCP of 2024-T351, $i_L^{ORR,Al}$ is the limiting current density of the ORR cathodic reaction at the AA2024-T351 electrode (3.5 x 10^{-6} A/cm^2) and A_{Al} is the area of the AA2024-T351 electrode exposed to full immersion.

The galvanic coupling potential difference can be described by Equation 4:

$$E_{OCP}^{2024} - E_{OCP}^{Mg} = \sum \eta_{cathode} + \sum \eta_{anode} + IR_{\Omega}^{solution} + IR_{\Omega}^{primer} + IR_{\Omega}^{topcoat} \qquad \text{Equation 4}$$

Where E_{OCP}^{2024} and E_{OCP}^{Mg} are the open circuit potentials of Mg and Al electrodes in aerated 50 mM NaCl solution[5], $R_{\Omega}^{solution}$ is the solution resistance along the ionic path length between Mg and AA2024-T351, R_{Ω}^{primer} is the added electrical and ionic resistances of the primer polymer and $R_{\Omega}^{topcoat}$ is the added ionic resistance of the topcoat polymer (Figure 2.30b), $\sum \eta_{cathode}$ and $\sum \eta_{anode}$ are the resulting absolute values of the magnitudes of polarization overpotentials of the anode (Mg) and the cathode (AA2024-T351).

Figure 2.33b depicts the theoretical galvanic coupling behavior of bare Mg and AA2024-T351 electrodes and the effect of changing the surface area of Mg exposed to solution. As can be seen, increasing the area of Mg incorporated in the galvanic couple system decreases the resulting galvanic couple potential (in the presence of IR drop) that the bare

[5] These could differ from the values in 50 mM NaCl if the underpaint electrolyte is different.

AA2024-T351 is polarized to (E_{Al}^{Bare} in Figure 2.33c). Figure 2.33c hypothetically depicts the galvanic coupling of Mg pigment in the MgRP and the AA2024-T351 substrate, incorporating the potential drop due to ionic resistances through the primer polymer to the electrolyte and Ohmic resistances through the primer polymer to the AA2024-T351 substrate. These resistances within the primer with a PVC of 45% have been estimated by automated circuit fitting analysis of impedance data (Figure 2.34) to be approximately 10^6 (Ω-cm^2). The areas of each electrode have been reduced in the model to account for the reduction in electrode area due to the polymer. The area of the AA2024-T351 electrode has been reduced to 0.1 cm^2 which is an estimate of the surface area of AA2024-T351 exposed in a scratch 1 mm wide and 1 cm long. The area of the Mg electrode has been reduced to 0.01 cm^2 in the model in an effort to mimic the area of MgRP electrochemically "sensed." This small area is consistent with the small amount of anodic charge measured by the full immersion electrochemical testing regimen relative to the theoretical amount of sacrificial anode material present in the 1 cm^2 exposure area. The Ohmic resistances in the primer acts to reduce the severity of cathodic polarization (galvanic protection potential) experienced by the AA2024-T351 (E_{Al}^{Primer} in Figure 2.33c). 1). The galvanic current that satisfies Equation 4 under these conditions, found at point E_{Al}^{Primer} in Figure 2.33c, is approximately 4.0 x 10^{-7} amps. Figure 2.33d hypothetically depicts the galvanic coupling of Mg pigment in the MgRP and the AA2024-T351 substrate, incorporating the potential drop due to ionic resistances through both the primer and topcoat polymers to the electrolyte and electrical resistances through the primer polymer to the AA2024-T351 substrate (Figure 2.30b). These resistances within the topcoated systems have been estimated by circuit fitting analysis of impedance

data (Figure 2.34) to be approximately 10^7 Ω-cm^2. The galvanic current that satisfies Equation 4 under these conditions, found at point $E_{Al}^{Primer+Topcoat}$ in Figure 2.33d, is approximately 1.2 x 10^{-7} amps. Therefore, the addition of the topcoat may further reduce the severity of cathodic polarization (galvanic protection potential) of the AA2024-T351 ($E_{Al}^{Primer+Topcoat}$ in Figure 2.33d).

2.5.4 Accelerated Testing via Full Immersion, Electrochemical Testing Protocol (Cycle Test)

These tests shed light on MgRP utilization with and without a topcoat and as a function of PVC. Two modes of sacrificial anode based cathodic protection are elucidated; long range Mg pigment-based protection of remote defects and local or short range Mg pigment-based protection of local and buried defects where the resistive path length is lower. The total reservoir of Mg available for protection can be utilized if the intrinsic ionic resistance is reduced by anion/cation ingress into the intact polymer or by the creation of new defects such as delaminations, blisters, or scratches that lower the ionic resistive path between Mg particles in the MgRP and the AA2024-T351. Meanwhile there is no evidence of the blocking of Mg based corrosion protection due to the formation of corrosion products at defect sites, at least in 50 mM NaCl solution at bulk pH of 5.7. No significant Mg corrosion product was observed optically or in the SEM. It is presumed the Mg corrosion product in the current test was soluble. The low frequency impedance of each system was not observed to fall and then increase, which would be expected if corrosion product blocking or passivation of Mg were to occur. However, it possible that some other environment might lead to passivation of the Mg pigment. Also,

it should be noted that coating lifetimes and MgRP reservoir availability in atmospheric exposures are not predicted in this solution and the information obtained is mechanistic.

Future work will incorporate the test methods established above to estimate the total residual stored Mg anode capacity and the electrically “well connected” Mg in the primer, as sensed electrochemically, in samples obtained from field exposures and samples exposed to laboratory accelerated weathering tests such as ASTM B-117.

Discrepancies between results of field and laboratory exposures will be examined as well as the effects of CO_2 and other environmental chemistry and time of wetness (TOW) effects.

2.6 Conclusion

The primary sacrificial and barrier mechanisms of protection afforded to the AA2024-T351 substrate by the magnesium rich primer (MgRP) were investigated. Test methods to estimate the total residual stored Mg anode capacity and electrically “well connected” Mg in the primer, as sensed electrochemically, after various environmental exposures were developed. The residual barrier properties after depletion of the primer were also assessed. A full immersion testing protocol was designed to assess the amount of magnesium that was electrically and ionically well connected to the AA2024-T351 substrate, as sensed electrochemically, and to monitor coating barrier characteristics after partial MgRP utilization. The testing regimen included an open circuit hold to assess

galvanic protection potentials, electrochemical impedance spectroscopy to assess coating barrier properties, potentiostatic holds to asses anodic dissolution charge and X-ray diffraction to assess total elemental Mg remaining in the MgRP. Changes in these parameters were reported after full immersion in aerated 50 mM NaCl solution as a function of MgRP PVC and with and without a topcoat. X-ray diffraction was used to estimate the total amount of Mg in the MgRP before and after full immersion. Preliminary findings suggest two possible modes of protection; long range protection of remote defects and local or short range Mg pigment-based protection of local and buried defects. Both modes of protection are mediated by the high ionic and electrical resistance of the coating system as a function of MgRP PVC and topcoat properties. A method for estimating the remaining capacity of the coating for each mode of protection was developed.

2.7 Acknowledgements

This work was supported by the Office of the Undersecretary of Defense Corrosion University Pilot Program under the direction of Mr. Daniel Dunmire. Akzo-Nobel™ Corporation is gratefully acknowledged for helpful suggestions and the supply of Mg-rich primers specifically: Pat Adams, Scott Hayes, Michael Chapman, and Roger Brown. Mr. William Abbott of Battelle and Mr. Craig Matzdorf of NAVAIR are acknowledged for correspondence and supply of primer and primer/topcoat specimens. Dr. Marta Jakob of Southwest Research Institute is acknowledged for the supply of bare AA2024-T351 panels.

2.8 References

1. G. P. Bierwagen, D. E. Tallman, M. Nanna, D. Battocchi, A. Stamness and V. J. Gelling, New developments in Cr-free primers for aerospace alloys., Abstr Pap Am Chem S, 228, (2004), pp. U360-U360.
2. A. Simoes, D. Battocchi, D. Tallman and G. Bierwagen, Assessment of the corrosion protection of aluminium substrates by a Mg-rich primer: EIS, SVET and SECM study, Prog Org Coat, 63, 3 (2008), pp. 260-266.
3. D. Battocchi, A. M. Simoes, D. E. Tallman and G. P. Bierwagen, Comparison of testing solutions on the protection of Al-alloys using a Mg-rich primer, Corros Sci, 48, 8 (2006), pp. 2226-2240.
4. D. Battocchi, A. M. Simoes, D. E. Tallman and G. P. Bierwagen, Electrochemical behaviour of a Mg-rich primer in the protection of Al alloys, Corros Sci, 48, 5 (2006), pp. 1292-1306.
5. H. Xu, D. Battocchi, D. E. Tallman and G. P. Bierwagen, Use of Magnesium Alloys as Pigments in Magnesium-Rich Primers for Protecting Aluminum Alloys, Corrosion, 65, 5 (2009), pp. 318-325.
6. G. Bierwagen, D. Battocchi, A. Simoes, A. Stamness and D. Tallman, The use of multiple electrochemical techniques to characterize Mg-rich primers for A1 alloys, Prog Org Coat, 59, 3 (2007), pp. 172-178.
7. U.S. Department of Health and Human Services., Report on Carcinogens, 12th Edition, U.S. Department of Health and Human Services, Public Health Services, National Toxicology Program, 2011.
8. R. G. Buchheit, Chromate and Chromate-Free Conversion Coatings, vol. 13A, ASM Handbook Volume 13A, Corrosion: Fundamentals, Testing, and Protection (ASM International) (Materials Park, Ohio, ASM International, 2003).
9. S. Feliu, R. Barajas, J. M. Bastidas and M. Morcillo, Ac Impedance Study About the Protection Mechanisms of Zinc-Rich Primers, Abstr Pap Am Chem S, 195, (1988), pp. 58-Pmse.
10. D. Pereira, J. D. Scantlebury, M. G. S. Ferreira and M. E. Almeida, The Application of Electrochemical Measurements to the Study and Behavior of Zinc-Rich Coatings, Corros Sci, 30, 11 (1990), pp. 1135-1147.
11. S. Feliu, M. Morcillo and S. Feliu, Deterioration of cathodic protection action of zinc-rich paint coatings in atmospheric exposure, Corrosion, 57, 7 (2001), pp. 591-597.
12. V. M. Rudoi, O. V. Yaroslavtseva, T. N. Ostanina, L. P. Yurkina and O. Y. Subbotina, Electrochemical behavior of protective anodic primers, Protection of Metals, 35, 3 (1999), pp. 277-281.
13. H. Marchebois, C. Savall, J. Bernard and S. Touzain, Electrochemical behavior of zinc-rich powder coatings in artificial sea water, Electrochim Acta, 49, 17-18 (2004), pp. 2945-2954.
14. C. M. Abreu, M. Izquierdo, M. Keddam, X. R. Novoa and H. Takenouti, Electrochemical behaviour of zinc-rich epoxy paints in 3% NaCl solution, Electrochim Acta, 41, 15 (1996), pp. 2405-2415.

15. S. G. Real, A. C. Elias, J. R. Vilche, C. A. Gervasi and A. Disarli, An Electrochemical Impedance Spectroscopy Study of Zinc Rich Paints on Steels in Artificial Sea-Water by a Transmission-Line Model, Electrochim Acta, 38, 14 (1993), pp. 2029-2035.
16. C. M. Abreu, M. Izquierdo, X. R. Novoa, C. Perez and A. Sanchez, Influence of different aggressive media on the protective behaviour of zinc rich paints, Rev Metal Madrid, 35, 3 (1999), pp. 182-189.
17. N. V. Kondrashova, S. A. Nesterenko, O. V. Naumenko and L. I. Antropov, Influence of Zinc and Magnesium Cations on the Electrochemical-Behavior of Steel with a Polymer Primer, Protection of Metals, 25, 1 (1989), pp. 73-75.
18. S. Feliu, R. Barajas, J. M. Bastidas and M. Morcillo, Mechanism of Cathodic Protection of Zinc-Rich Paints by Electrochemical Impedance Spectroscopy .1. Galvanic Stage, J Coating Technol, 61, 775 (1989), pp. 63-69.
19. S. Feliu, R. Barajas, J. M. Bastidas and M. Morcillo, Mechanism of Cathodic Protection of Zinc-Rich Paints by Electrochemical Impedance Spectroscopy .2. Barrier Stage, J Coating Technol, 61, 775 (1989), pp. 71-76.
20. C. M. Abreu, M. Izquierdo, P. Merino, X. R. Novoa and C. Perez, A new approach to the determination of the cathodic protection period in zinc-rich paints, Corrosion, 55, 12 (1999), pp. 1173-1181.
21. M. Morcillo, R. Barajas, S. Feliu and J. M. Bastidas, A-Sem Study on the Galvanic Protection of Zinc-Rich Paints, J Mater Sci, 25, 5 (1990), pp. 2441-2446.
22. R. A. Armas, C. A. Gervasi, A. Disarli, S. G. Real and J. R. Vilche, Zinc-Rich Paints on Steels in Artificial Seawater by Electrochemical Impedance Spectroscopy, Corrosion, 48, 5 (1992), pp. 379-383.
23. H. Marchebois, M. Keddam, C. Savall, J. Bernard and S. Touzain, Zinc-rich powder coatings characterisation in artificial sea water - EIS analysis of the galvanic action, Electrochim Acta, 49, 11 (2004), pp. 1719-1729.
24. O. O. Knudsen, U. Steinsmo and M. Bjordal, Zinc-rich primers - Test performance and electrochemical properties, Prog Org Coat, 54, 3 (2005), pp. 224-229.
25. M. E. Nanna and G. P. Bierwagen, Mg-rich coatings: A new paradigm for Cr-free corrosion protection of al aerospace alloys, Jct Research, 1, 2 (2004), pp. 69-80.
26. E. H. Hollingsworth and H. Y. Hunsicker, Corrosion of Aluminum and Aluminum Alloys, J. R. Davis, (Ed.), vol. 13b, Metals Handbook (Materials Park, OH, ASM International, 1987).
27. R. Baboian, Corrosion of Clad Metals, vol. 13b, ASM Handbook (Materials Park, OH, ASM International, 2005, p. 442-446).
28. J. R. Scully, F. Presuel-Moreno, M. Goldman, R. G. Kelly and N. Tailleart, User-selectable barrier, sacrificial anode, and active corrosion inhibiting properties of Al-Co-Ce alloys for coating applications, Corrosion, 64, 3 (2008), pp. 210-229.
29. F. J. Presuel-Moreno, M. E. Goldman, R. G. Kelly and J. R. Scully, Electrochemical sacrificial cathodic prevention provided by an Al-Co-Ce metal coating coupled to AA2024-T3, J Electrochem Soc, 152, 8 (2005), pp. B302-B310.

30. F. J. Presuel-Moreno, H. Wang, M. A. Jakab, R. G. Kelly and J. R. Scully, Computational modeling of active corrosion inhibitor release from an Al-Co-Ce metallic coating - Protection of exposed AA2024-T3, J Electrochem Soc, 153, 11 (2006), pp. B486-B498.
31. F. Presuel-Moreno, M. A. Jakab, N. Tailleart, M. Goldman and J. R. Scully, Corrosion-resistant metallic coatings, Mater Today, 11, 10 (2008), pp. 14-23.
32. J. R. Davis, Corrosion of aluminum and aluminum alloys, vol. (Materials Park, OH: ASM International, 1999), p. vii, 313 p.
33. R. H. Brown, Alclad and Clad Aluminum Alloy Products, A. G. H. Dietz, (Ed.), Engineering Laminates (Cambridge, MA, MIT Press, 1969, p. 227-239).
34. C. M. Reddy, Q. S. Yu, C. E. Moffitt, D. M. Wieliczka, W. Johnson, J. E. Deffeyes and H. K. Yasuda, Improved corrosion protection of aluminum alloys by system approach interface engineering: Part 1 - Alclad 2024-T3, Corrosion, 56, 8 (2000), pp. 819-831.
35. D. H. Wang, D. Battocchi, K. N. Allahar, S. Balbyshev and G. P. Bierwagen, In situ monitoring of a Mg-rich primer beneath a topcoat exposed to Prohesion conditions, Corros Sci, 52, 2 (2010), pp. 441-448.
36. S. S. Pathak, M. D. Blanton, S. K. Mendon and J. W. Rawlins, Investigation on dual corrosion performance of magnesium-rich primer for aluminum alloys under salt spray test (ASTM B117) and natural exposure, Corros Sci, 52, 4 (2010), pp. 1453-1463.
37. G. S. Frankel and Y. Baek, Electrochemical quartz crystal microbalance study of corrosion of phases in AA2024, J Electrochem Soc, 150, 1 (2003), pp. B1-B9.
38. S. I. Pyun and S. M. Moon, Corrosion mechanism of pure aluminium in aqueous alkaline solution, J Solid State Electr, 4, 5 (2000), pp. 267-272.
39. M. Mokaddem, P. Volovitch, F. Rechou, R. Oltra and K. Ogle, The anodic and cathodic dissolution of Al and Al-Cu-Mg alloy, Electrochim Acta, 55, 11 (2010), pp. 3779-3786.
40. H. Kaesche, Studies on the Corrosion of Aluminum, Zeitschrift für physikalische Chemie, 14, 7 (1963), pp. 557-566.
41. H. Kaesche, Zeitschrift für physikalische Chemie, 34, (1962), pp. 87-108.
42. S. M. Moon and S. I. Pyun, The corrosion of pure aluminium during cathodic polarization in aqueous solutions, Corros Sci, 39, 2 (1997), pp. 399-408.
43. R. D. Armstrong and V. J. Braham, The mechanism of aluminium corrosion in alkaline solutions, Corros Sci, 38, 9 (1996), pp. 1463-1471.
44. B. J. Last and D. J. Thouless, Percolation Theory and Electrical Conductivity, Phys Rev Lett, 27, 25 (1971), p. 1719.
45. G. R. Ruschau, S. Yoshikawa and R. E. Newnham, Resistivities of Conductive Composites, J Appl Phys, 72, 3 (1992), pp. 953-959.
46. M. T. Rodriguez, J. J. Gracenea, A. H. Kudama and J. J. Suay, The influence of pigment volume concentration (PVC) on the properties of an epoxy coating - Part I. Thermal and mechanical properties, Prog Org Coat, 50, 1 (2004), pp. 62-67.
47. M. T. Rodriguez, J. J. Gracenea, J. J. Saura and J. J. Suay, The influence of the critical pigment volume concentration (CPVC) on the properties of an epoxy coating - Part II. Anticorrosion and economic properties, Prog Org Coat, 50, 1 (2004), pp. 68-74.

48. G. R. Ruschau and R. E. Newnham, Critical Volume Fractions in Conductive Composites, J Compos Mater, 26, 18 (1992), pp. 2727-2735.
49. R. Y. Yang, R. P. Zou and A. B. Yu, Computer simulation of the packing of fine particles, Phys Rev E, 62, 3 (2000), pp. 3900-3908.
50. R. Y. Yang, R. P. Zou and A. B. Yu, Effect of material properties on the packing of fine particles, J Appl Phys, 94, 5 (2003), pp. 3025-3034.
51. G. P. Bierwagen, Cpvc Calculations, J Paint Technol, 44, 572 (1972), p. 28.
52. G. P. Bierwagen and T. E. Saunders, Studies of Effects of Particle-Size Distribution on Packing Efficiency of Particles, Powder Technol, 10, 3 (1974), pp. 111-119.
53. G. P. Bierwagen, Cpvc Calculations, J Paint Technol, 44, 574 (1972), p. 46.
54. K. N. Allahar, D. Battocchi, G. P. Bierwagen and D. E. Tallman, Transmission Line Modeling of EIS Data for a Mg-Rich Primer on AA 2024-T3, J Electrochem Soc, 157, 3 (2010), pp. C95-C101.
55. Astm, Standard Practice for Operating Salt Spray (Fog) Apparatus, ASTM B117 - 09, DOI: 10.1520/C0033-03, (2009).
56. G. P. Bierwagen, C. S. Jeffcoate, J. P. Li, S. Balbyshev, D. E. Tallman and D. J. Mills, The use of electrochemical noise methods (ENM) to study thick, high impedance coatings, Prog Org Coat, 29, 1-4 (1996), pp. 21-29.
57. W. H. Abbott, Personal correspondence with Mr. William Abbott of Battelle Memorial Institute, (2009).
58. H. P. Hack and J. R. Scully, Defect Area Determination of Organic Coated Steels in Seawater Using the Breakpoint Frequency Method, J Electrochem Soc, 138, 1 (1991), pp. 33-40.
59. M. Kendig and J. Scully, Basic Aspects of Electrochemical Impedance Application for the Life Prediction of Organic Coatings on Metals, Corrosion, 46, 1 (1990), pp. 22-29.
60. J. R. Scully, Electrochemical Impedance of Organic-Coated Steel - Correlation of Impedance Parameters with Long-Term Coating Deterioration, J Electrochem Soc, 136, 4 (1989), pp. 979-990.
61. F. Mansfeld, Determination of the Reactive Area of Organic Coated Metals - Physical Meaning and Limits of the Break-Point Method - Discussion, Electrochim Acta, 39, 10 (1994), pp. 1451-1452.
62. F. Mansfeld, Electrochemical Impedance Spectroscopy (Eis) as a New Tool for Investigating Methods of Corrosion Protection, Electrochim Acta, 35, 10 (1990), pp. 1533-1544.
63. F. Mansfeld, L. T. Han, C. C. Lee and G. Zhang, Evaluation of corrosion protection by polymer coatings using electrochemical impedance spectroscopy and noise analysis, Electrochim Acta, 43, 19-20 (1998), pp. 2933-2945.
64. F. Mansfeld, Models for the Impedance Behavior of Protective Coatings and Cases of Localized Corrosion, Electrochim Acta, 38, 14 (1993), pp. 1891-1897.
65. C. H. Hsu and F. Mansfeld, Technical note: Concerning the conversion of the constant phase element parameter Y-0 into a capacitance, Corrosion, 57, 9 (2001), pp. 747-748.

2.9 Tables

Table 2.1 Composition of AA2024-T351 used as a bare electrode in these investigations.

AA2024-T351	Al	Cu	Mg	Mn	Fe	Zn	Si	Ti	Cr	V
	Balance	4.56	1.26	0.59	0.22	0.12	0.08	0.02	0.01	0.01

Table 2.2 Compositions of various Mg samples used in this investigation

(a) Mg powder used in Mg-Rich Primer (b) Mg Rod (99.9%) purchased from Alfa Aesar (c) Mg Ribbon (99.8%) purchased from Sigma Aldrich Chemical corp. All compositions reported in wt. %. (Mg: Balance). Compositions provided by QUANT Quality Analysis and Testing Corporation. NR: Not Reported

Mg Sample	Si	Al	Fe	Cu	Zn	Mn	Ni	Zr	Pb	Sn	C	S	O
(a)	0.033	0.032	0.015	0.012	0.0067	0.0064	<0.001	<0.005	<0.001	<0.001	0.002	0.004	0.0012
(b)	NR	0.02	0.008	0.003	0.03	<0.01	<0.001	<0.01	NR	NR	<0.001	<0.001	0.001
(c)	NR	0.02	0.023	0.003	0.01	0.04	0.001	<0.01	NR	NR	<0.001	<0.001	0.0014

Table 2.3 Sample matrix provided by Coating Manufacturer Indicating the PVC of MgRP and Other Conditions

Color Pigment in Primer?	**Mg PVC**	**Topcoated?**
YES	25	No
YES	38	No
YES	45	No
YES	52	No
YES	65	No
YES	25	Yes
YES	38	Yes
YES	45	Yes
YES	52	Yes
YES	65	Yes
NO	45	No
NO	45	Yes
NO	0	No
NO	0	Yes

Table 2.4 Example timeline for accelerated test to assess sacrificial anode based cathodic protection potential, charge capacity and barrier degradation of Mg-rich primer.
*$T_{elapsed}$ = Total time elapsed prior to starting specified step

Cycle	Test	Duration	$T_{elapsed}$*
A	**OCP**	10	0
	EIS	15	10
	Potentiostatic Hold	10	25
B	**OCP**	10	35
	EIS	15	45
	Potentiostatic Hold	20	60
C	**OCP**	10	80
	EIS	15	90
	Potentiostatic Hold	40	105
D	**OCP**	10	145
	EIS	15	155
	Potentiostatic Hold	60	170
E	**OCP**	10	230
	EIS	15	240
	Potentiostatic Hold	120	255
F	**OCP**	10	375
	EIS	15	385
	Potentiostatic Hold	300	400
G	**OCP**	10	700
	EIS	15	710
	Potentiostatic Hold	600	725
H	**OCP**	10	1325
	EIS	15	1335
	Potentiostatic Hold	600	1350

2.10 Figures

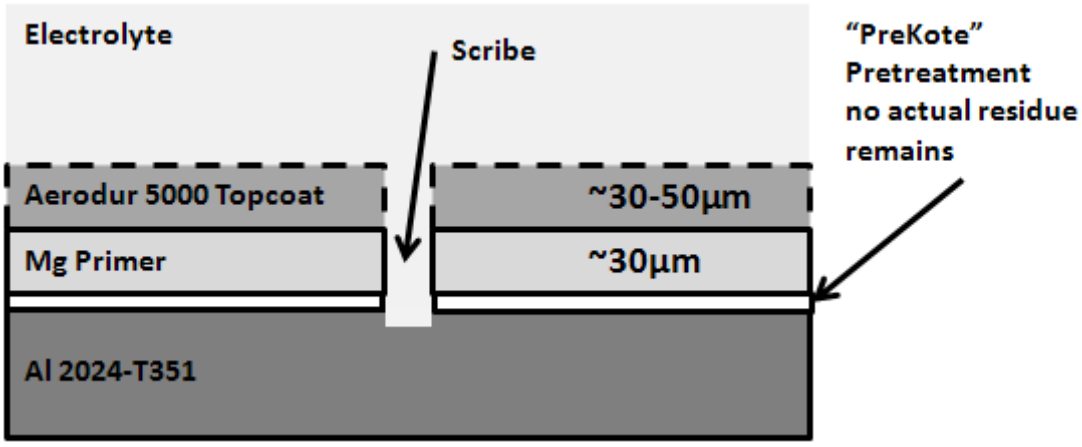

Figure 2.1. Schematic of coating system stack-up
System consisted of AA2024-T351 substrate, pretreatment, ~30 µm thick layer of Mg-Rich Primer and a 30-50 µm layer of topcoat. A finite pretreatment layer is not assumed.

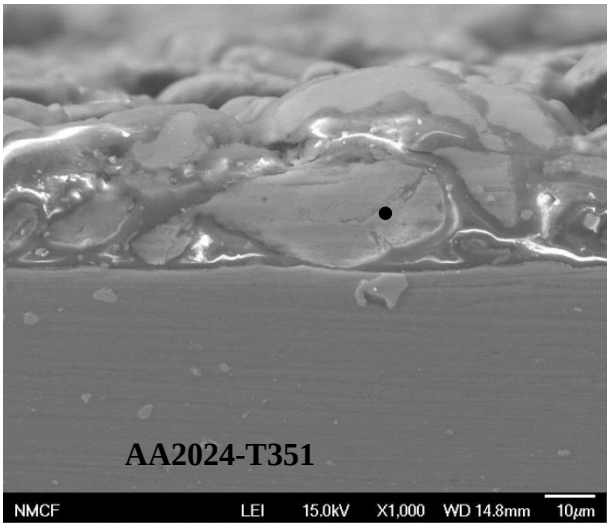

Figure 2.2. Scanning electron micrograph of cross sectioned sample, non-topcoated, PVC = 45%
Spot marker in Fig. 2 indicates approximate location of EDS analysis. Accelerating voltage = 15.0 KV, working distance = 15 mm.

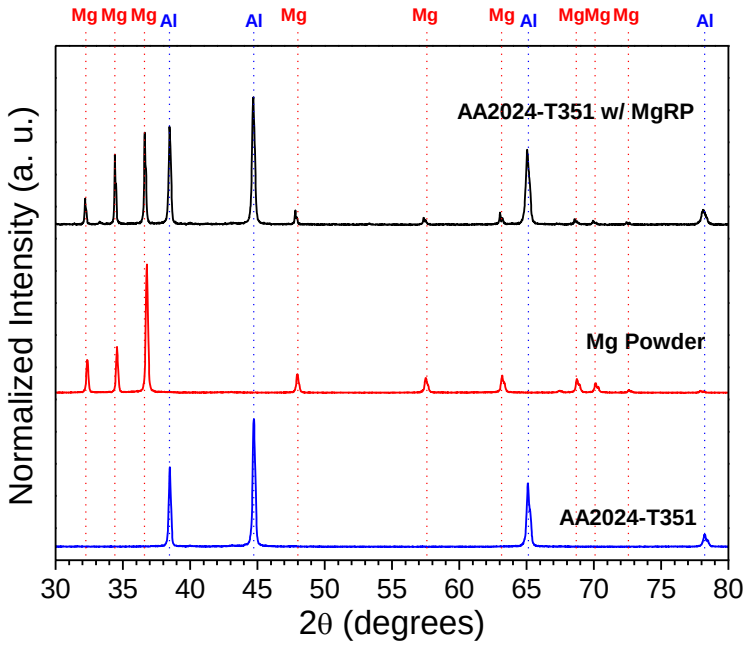

Figure 2.3. XRD spectra of bare AA2024-T351, bare Mg powder, and MgRP-coated AA2024-T351 (MgPVC = 45)

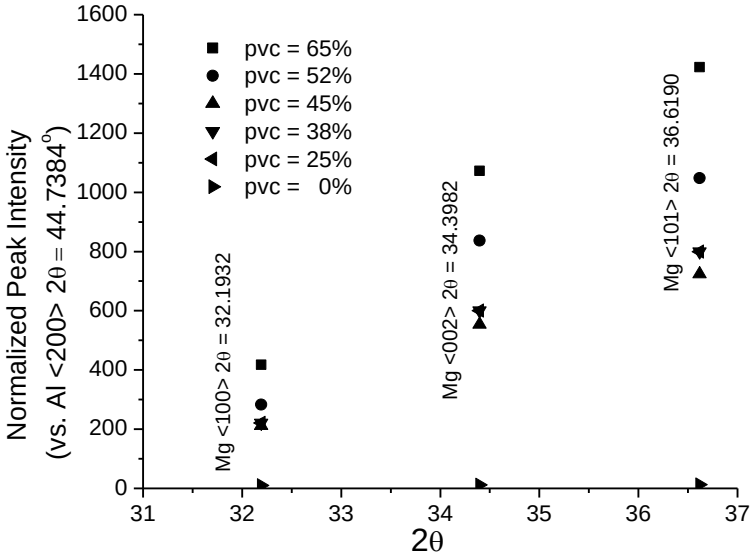

Figure 2.4. XRD normalized peak intensities of MgRP coated panels of various PVC and no topcoat.
Three prominent Mg peaks are shown. The relative intensities of these peaks decrease with decreasing PVC.

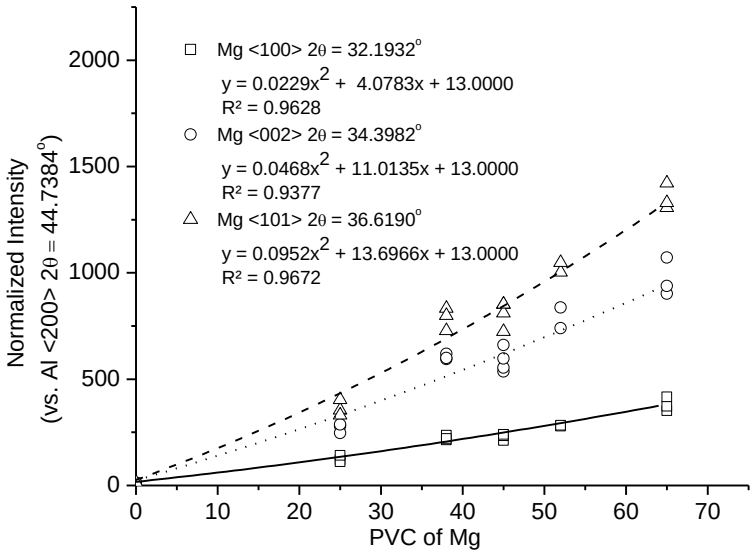

Figure 2.5. A plot of intensity of three prominent Mg peaks vs. MgRP PVC on samples with 30 μm thickness without a high performance advanced polymer topcoat.
Peaks were normalized to Al <200> 2θ = 44.7384° peak. Measurements were taken before electrochemical testing.

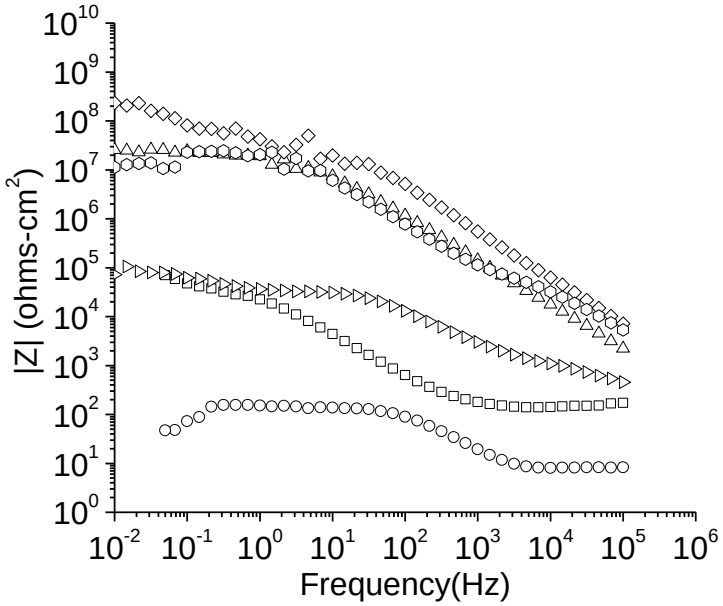

Figure 2.6. Initial Impedance profiles of bare electrodes and AA2024-T351 coated with MgRP exposed in 50 mM NaCl solution, ambient aeration after 10 min open circuit hold. □ = Bare 2024-T351, ○ = Bare Mg Ribbon 99.8% Pure, ◇ = Non-Topcoated MgRP PVC = 0% ⬡ = Non-Topcoated MgRP PVC = 25%, △= Non-Topcoated MgRP PVC = 45%, ▷ = NonTopcoated MgRP PVC = 65%.

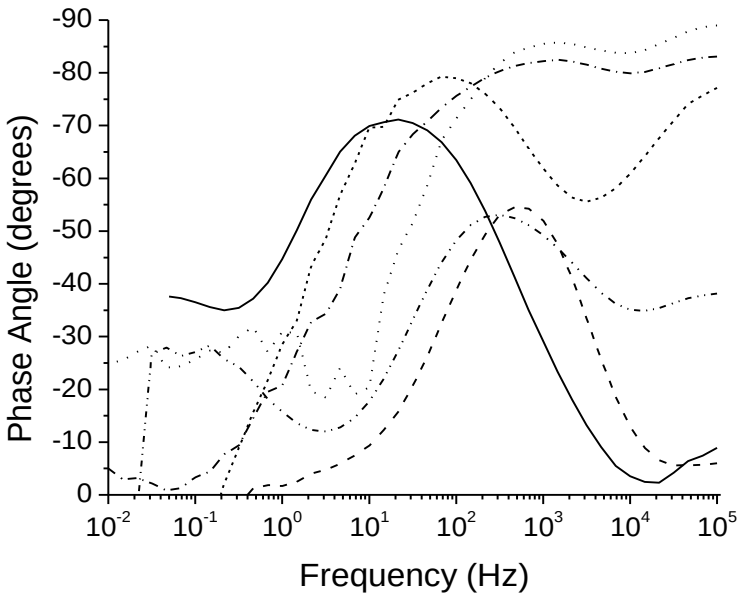

Figure 2.7. Phase angles of bare electrodes and AA2024-T351 coated with MgRP exposed in 50 mM NaCl solution, ambient aeration after 10 min open circuit hold
. ——— = Bare AA2024-T351, ━ ━ ━ = Bare Mg Ribbon 99.8% Pure, · · · · = Non-Topcoated MgRP PVC = 0%, ▪ ▪ ▪ ▪ = Non-Topcoated MgRP PVC = 25%, ━ · ━ = Non-Topcoated MgRP PVC = 45%, ━ · · ━ = Non-Topcoated MgRP PVC = 65%

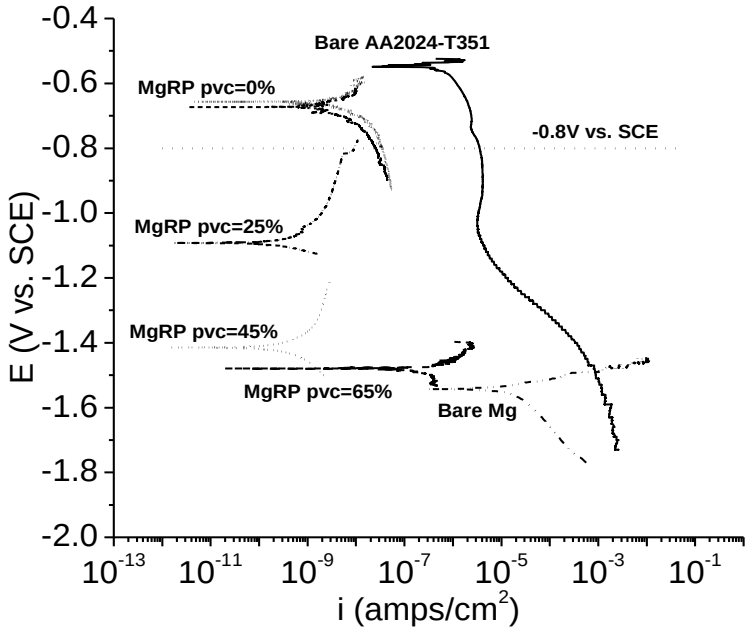

Figure 2.8. E-log(i) data for bare high purity Mg as well as AA2024-T351 sheet coated with MgRP exposed in 50 mM NaCl solution, ambient aeration after 10 min OCP. ——— = Bare AA2024-T351, ━ · · ━ = Bare Mg Rod 99.9% Pure, ····· = Non-Topcoated MgRP PVC = 0%, - - - - = Topcoated MgRP PVC = 0%, ━ · ━ = Non-Topcoated MgRP PVC = 25%, · · · · = Non-Topcoated MgRP PVC = 45% ━ ━ ━ = Non-Topcoated MgRP PVC = 65%.

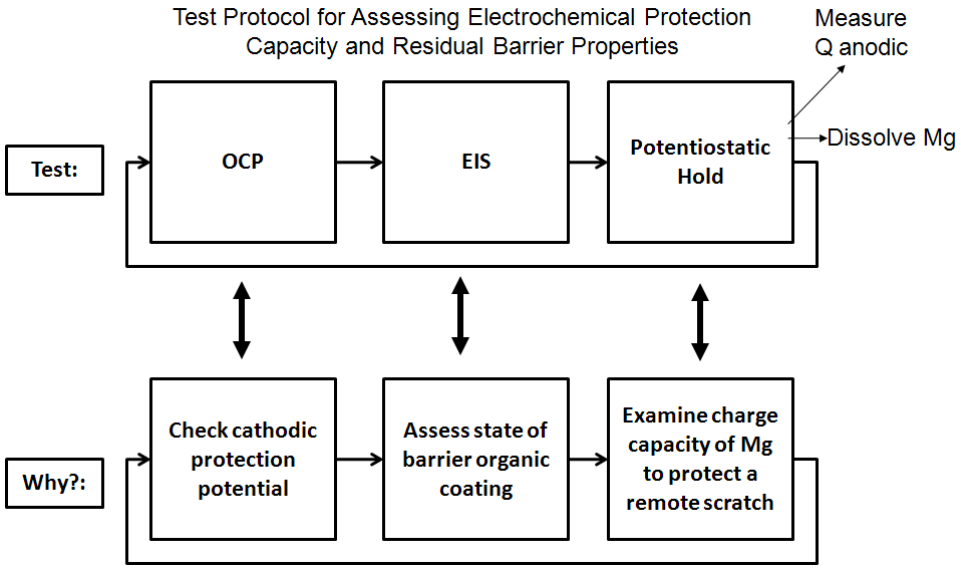

Figure 2.9. Block diagram illustrating protocol for accelerated test to assess sacrificial anode based cathodic protection potential, charge capacity and barrier degradation of Mg-rich primer.

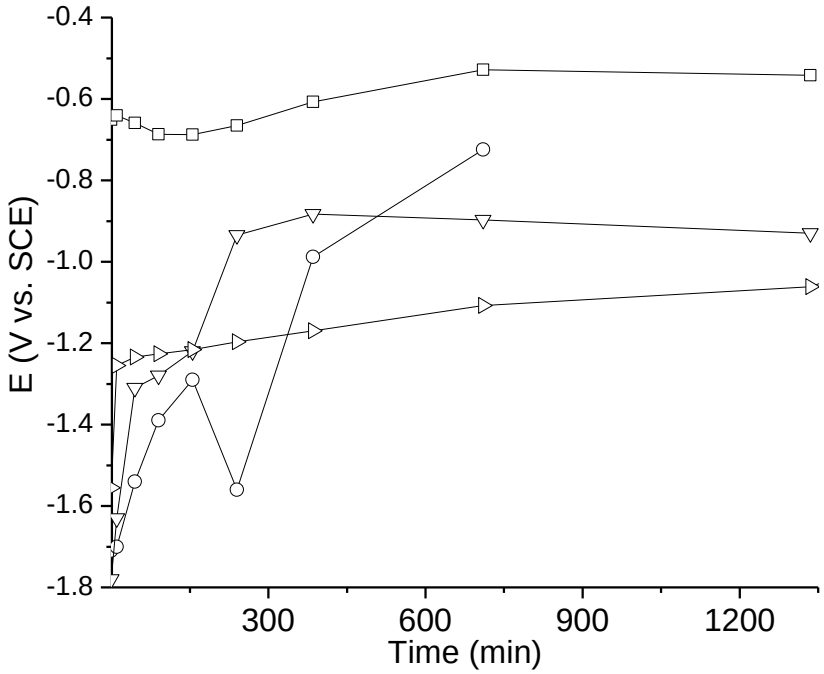

Figure 2.10. OCP vs. time of AA2024-T351 coated with Mg-rich primer of various PVC's during exposure in 50 mM NaCl solution, with ambient aeration during the accelerated test to asses charge capacity and barrier degradation.
□ = PVC = 0%, ○ = PVC = 25%, ▽ = PVC = 45%, ▷ = PVC = 65%.

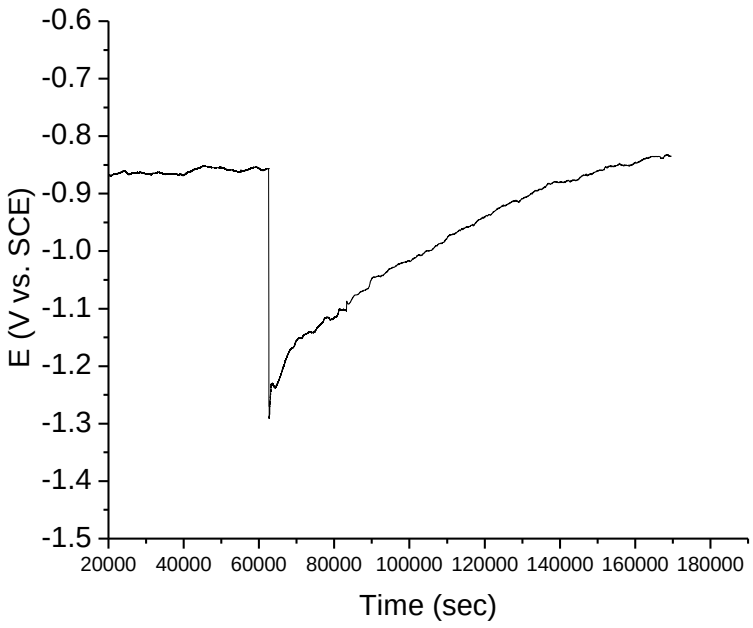

Figure 2.11. OCP vs. time of AA2024-T351 coated with Mg-rich primer PVC = 45% during exposure in 50 mM NaCl solution, with ambient aeration.
Sample was allowed to reach steady state OCP and then abraded in-situ in order to assess the presence of residual Mg in MgRP.

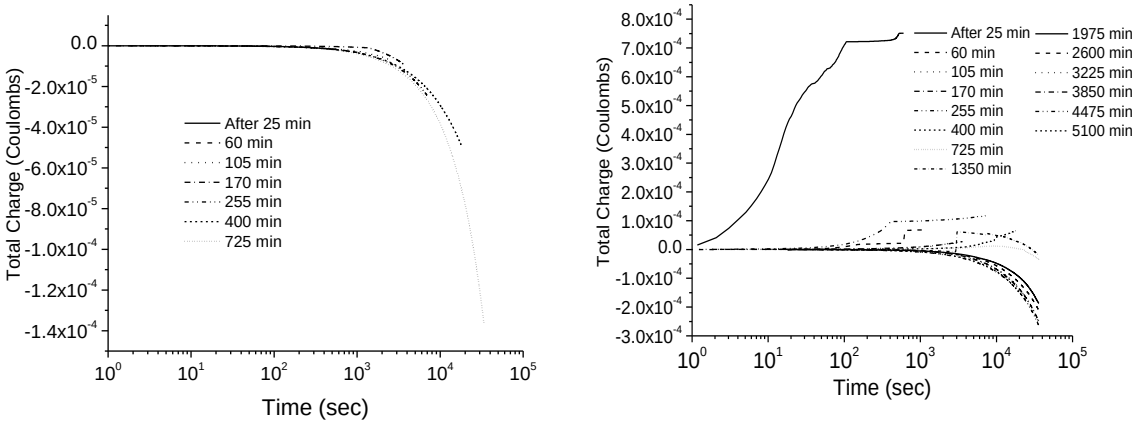

(a) (b)

Figure 2.12. Charge recorded during successive potentiostatic holds at -0.8 V vs. SCE of AA2024-T351 coated with Mg-rich primer exposed in 50 mM NaCl solution, ambient aeration during each cycle of the accelerated test to asses charge capacity with and without Mg pigment.
(a) Without Mg pigment. Sample non-topcoated PVC = 0% (b) With Mg pigment. PVC = 45% non-topcoated. The time indicated in the legend is the total elapsed time of the testing regimen prior to starting the potentiostatic hold. The time on the x-axis is the time of the potentiostatic hold period as indicated in Table 4.

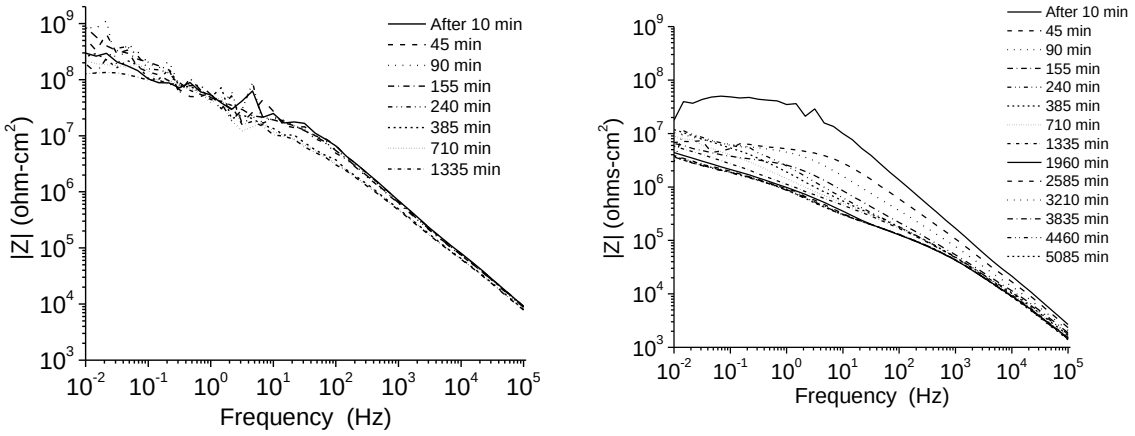

(a) (b)

Figure 2.13. Electrochemical impedance Bode magnitude and phase plots of AA2024-T351 coated with Mg-rich primer exposed in 50 mM NaCl solution, ambient aeration during each cycle of the accelerated test to asses charge capacity and barrier degradation with and without Mg pigment.
(a) Without Mg pigment. non-topcoated PVC = 0% (b) With Mg pigment. PVC = 45% non-topcoated. The time indicated in the legend is the total elapsed time of the testing regimen prior to starting the electrochemical impedance measurement.

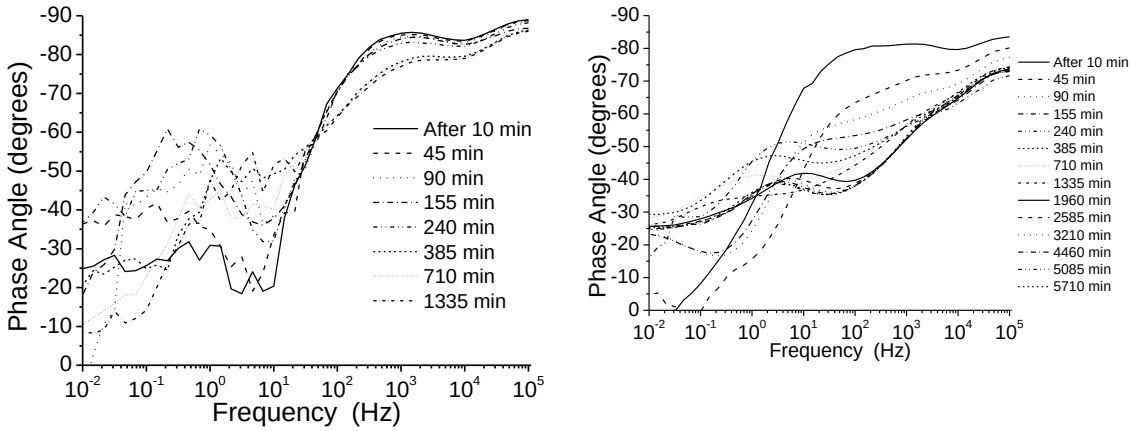

(a) (b)

Figure 2.14. Phase angle measurements of AA2024-T351 coated with Mg-rich primer exposed in 50 mM NaCl solution, ambient aeration during each cycle of the accelerated test to asses charge capacity and barrier degradation with and without Mg pigment.
(a) Without Mg pigment. non-topcoated PVC = 0% (b) With Mg pigment. PVC = 45% non-topcoated

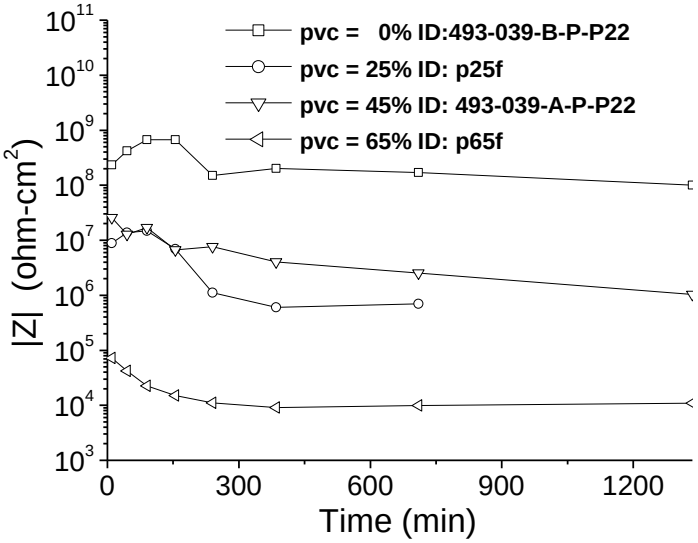

Figure 2.15. Impedance magnitude at 0.01 Hz vs. time of AA2024-T351 coated with varying PVC's of Mg-rich primer exposed in 50 mM NaCl solution, ambient aeration during each cycle of the accelerated test to asses charge capacity and barrier degradation.

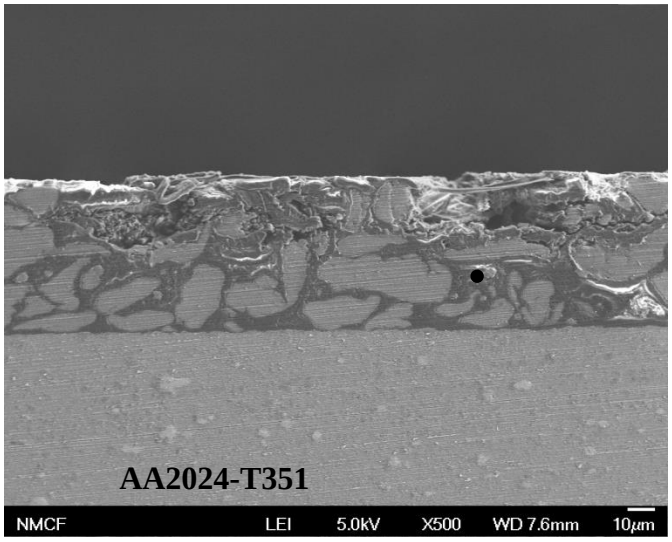

Figure 2.16. Scanning electron micrograph of AA2024-T351 coated with MgRP (PVC = 45%) after about 90 hours of potentiostatic hold at -0.8 V vs. SCE in 50 mM NaCl solution, ambient aeration during the accelerated test to asses charge capacity

EDS spectrum of Mg pigment taken approximately at spot marker in Figure 16. Accelerating voltage = 15.0 KeV, working distance = 15 mm.

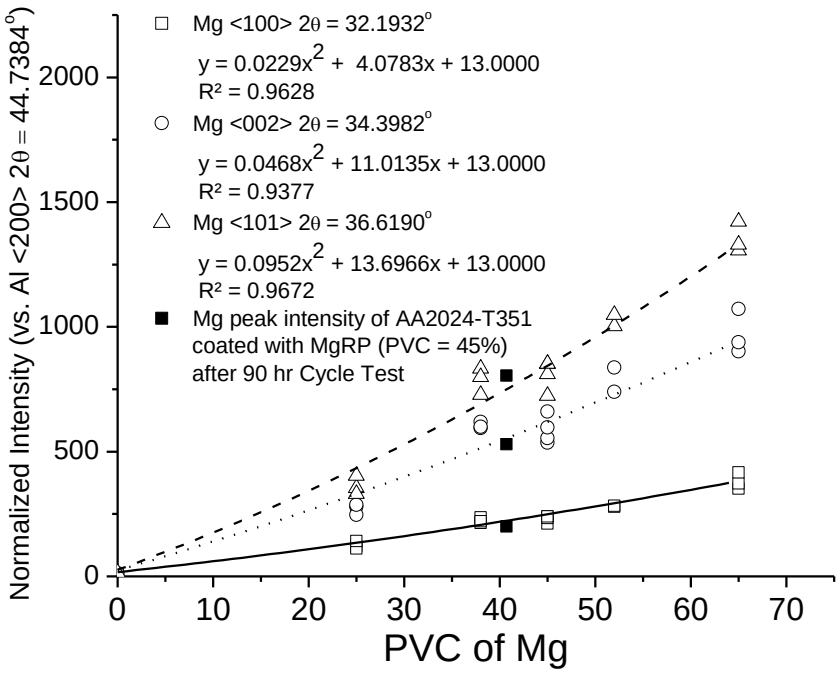

Figure 2.17. A plot of normalized intensity of three prominent Mg peaks vs. MgRP PVC on samples without a topcoat.
Mg peak intensity of AA2024-T351 coated with MgRP (PVC = 45%) have been fit onto the curves and averaged after being exposed to 50 mM NaCl solution, with ambient aeration for 90 hrs of the full immersion accelerated test to assess the charge capacity.

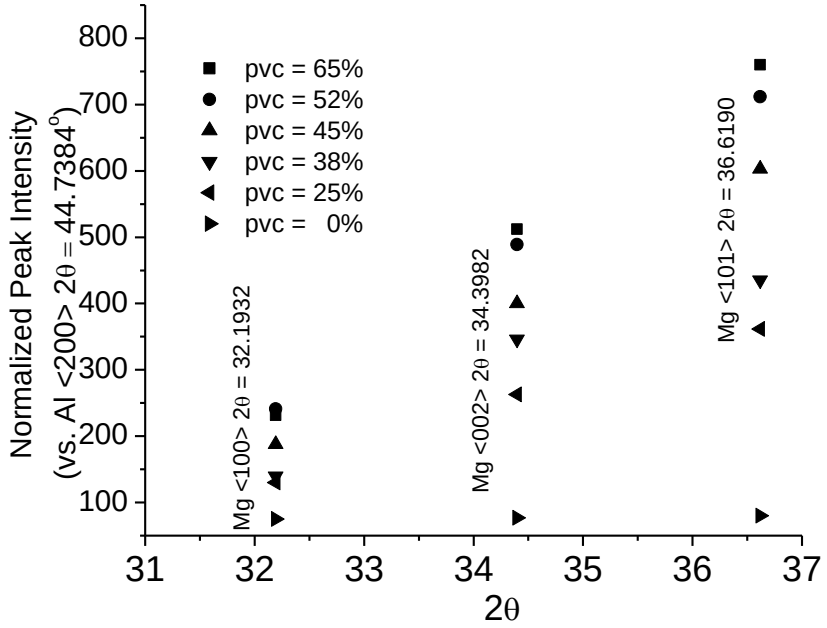

Figure 2.18. XRD normalized peak intensities of various PVC MgRP coated panels with a high performance advanced polymer topcoat.
Three known Mg peaks are shown. The relative intensities of these peaks decrease with decreasing PVC. The samples investigated are: 493-039-B-T-P22, T25F, T38F, T45F, T52F, and T65F

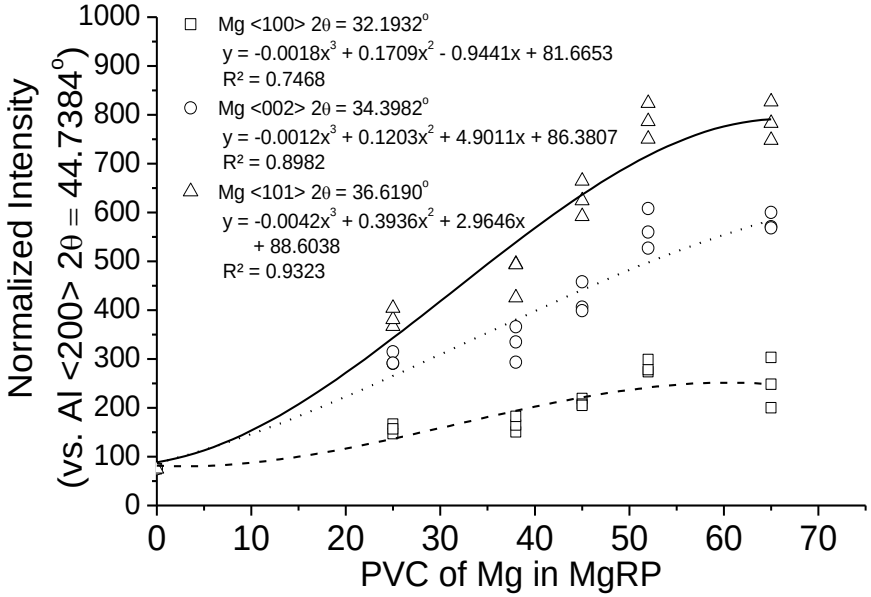

Figure 2.19. A plot of normalized intensity of three known Mg peaks vs. MgRP PVC on samples with a high performance advanced polymer topcoat.
Measurements were taken before electrochemical testing.

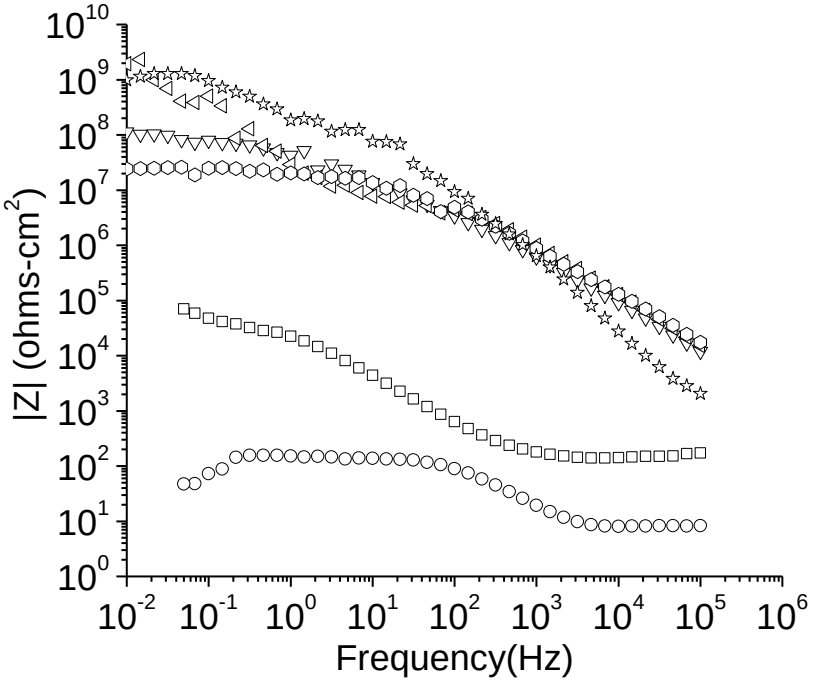

Figure 2.20. Initial Impedance spectra of bare electrodes and AA2024-T351 coated with MgRP + topcoat exposed in 50 mM NaCl solution, with ambient aeration after 10 min open circuit hold.
□ = Bare 2024-T351, ○ = Bare Mg Ribbon 99.8% Pure, ◁ = Topcoated MgRP PVC = 0%, ☆ = Topcoated MgRP PVC = 25%, ▽ = Topcoated MgRP PVC = 45%, ⬡ = Topcoated MgRP PVC = 65%.

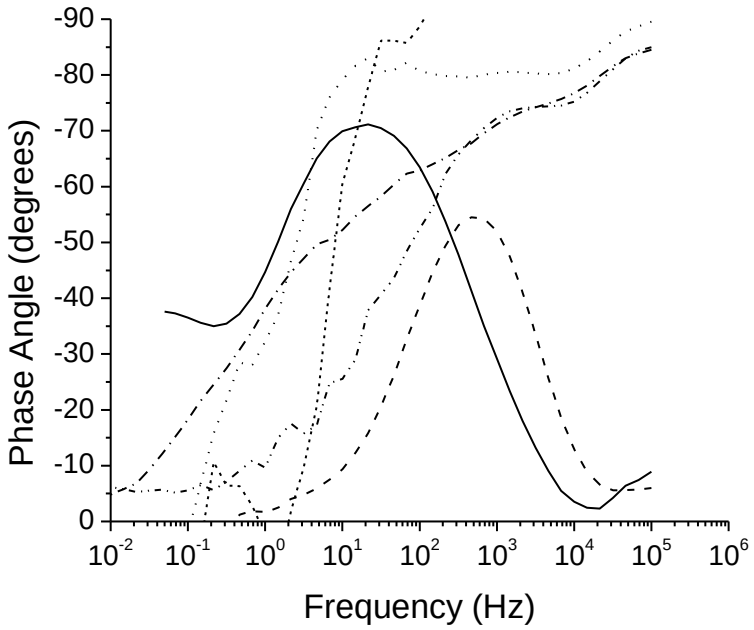

Figure 2.21. Electrochemical impedance spectroscopy phase angle spectra of bare electrodes and AA2024-T351 coated with MgRP + topcoat exposed in 50 mM NaCl solution, ambient aeration after 10 min open circuit hold.
——— = Bare AA2024-T351, ━ ━ ━ = Bare Mg Ribbon 99.8% Pure, · · · · = Topcoated MgRP PVC = 0%, - - - - = Topcoated MgRP PVC = 25%, ━ · ━ = Topcoated MgRP PVC = 45%, ━ · · ━ = Topcoated MgRP PVC = 65%

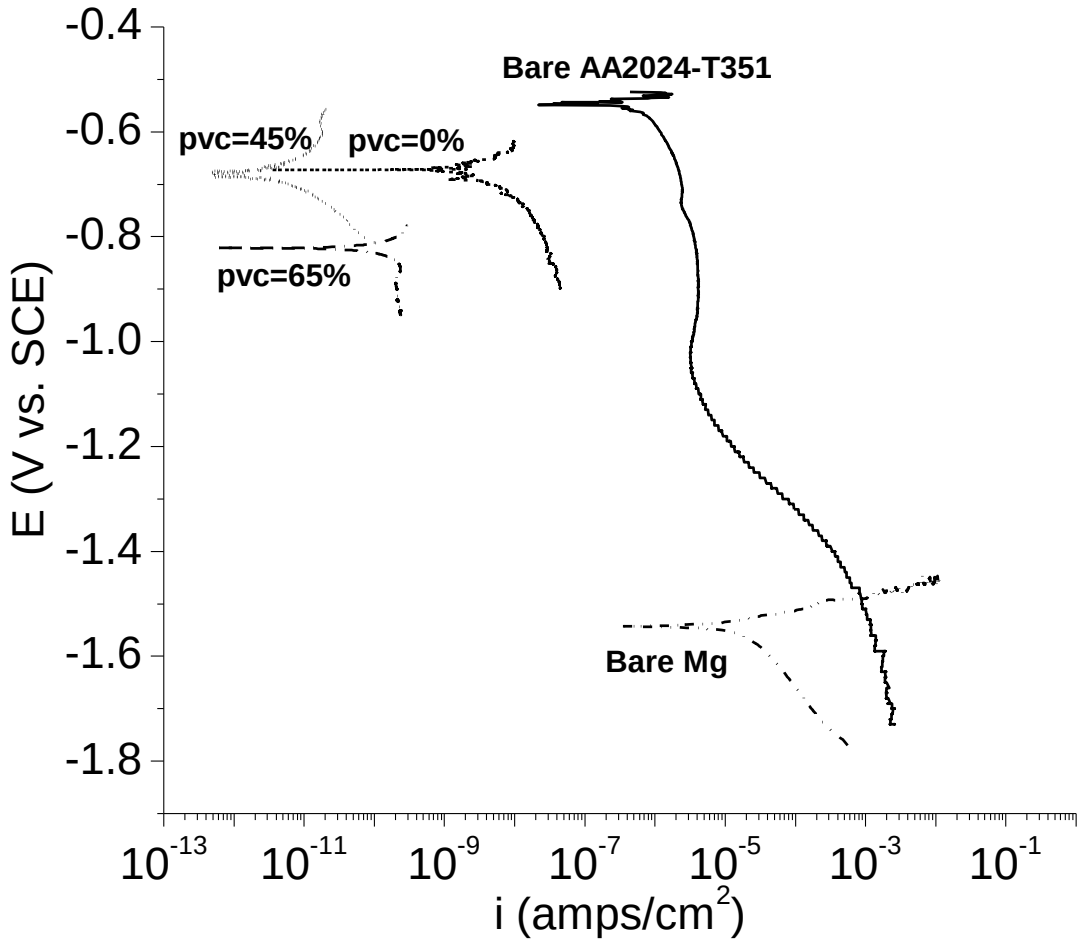

Figure 2.22. E-log(i) polarization behavior of bare electrodes and AA2024-T351 coated with MgRP + topcoat exposed in 50 mM NaCl solution for 10 min, ambient aeration . ——— = Bare AA2024-T351, – · · – = Bare Mg Rod 99.9% Pure, - - - - = Topcoated MgRP PVC = 0%, · · · · = Topcoated MgRP PVC = 45%, — · — = Topcoated MgRP PVC = 65%.

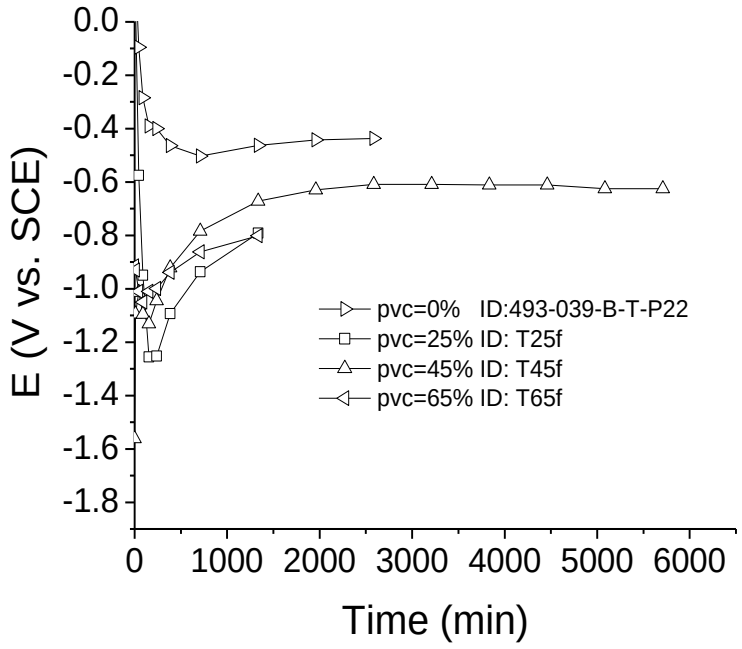

(a)

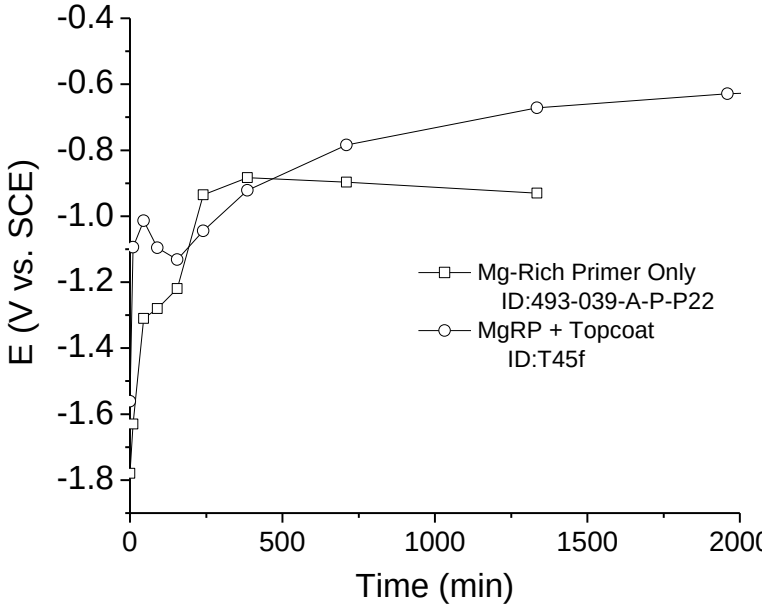

(b)

Figure 2.23. OCP vs. time of AA2024-T351 coated with Mg-rich primer exposed in 50 mM NaCl solution, ambient aeration during the accelerated test to asses charge capacity and barrier degradation.
(a) of varying PVC's and with a high performance advanced polymer topcoat (b) 45% PVC Mg-rich primer with and without a high performance advanced polymer topcoat

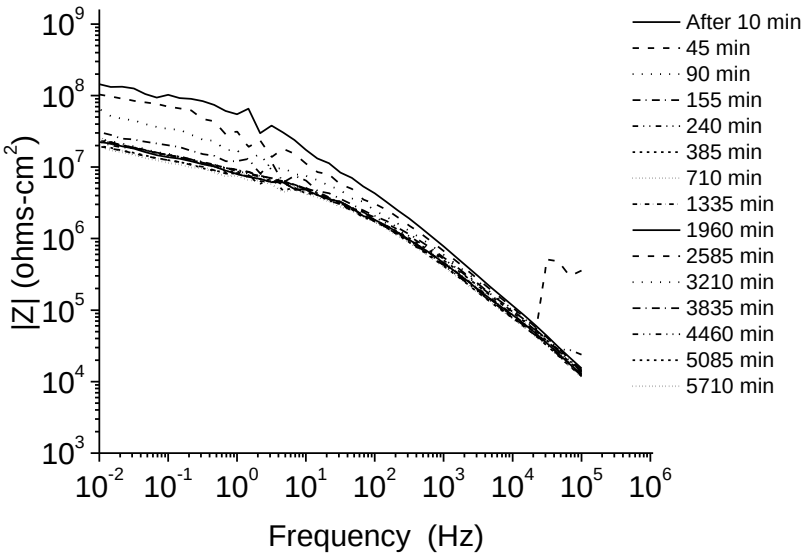

Figure 2.24. Electrochemical impedance Bode magnitude plots of AA2024-T351 coated with Mg-rich primer and a high performance advanced polymer topcoat exposed in 50 mM NaCl solution, ambient aeration during each cycle of the accelerated test to asses charge capacity and barrier degradation. PVC = 45%

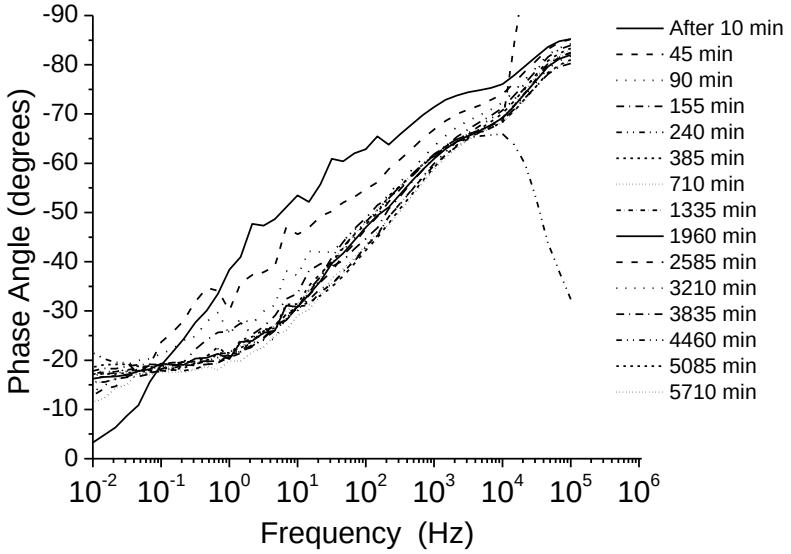

Figure 2.25. Phase angle plot of AA2024-T351 coated with MgRP and a high performance advanced polymer topcoat exposed in 50 mM NaCl solution, ambient aeration during each cycle of the accelerated test to asses charge capacity and barrier degradation. PVC = 45%

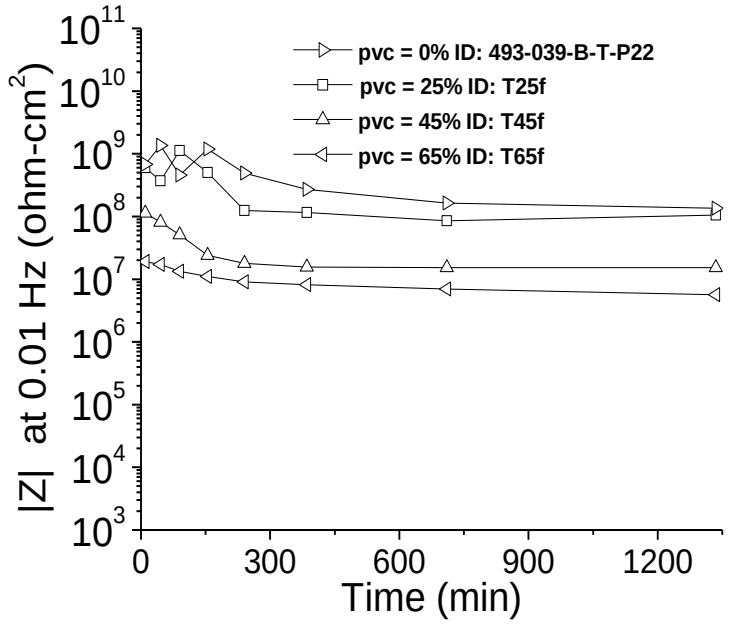

(a)

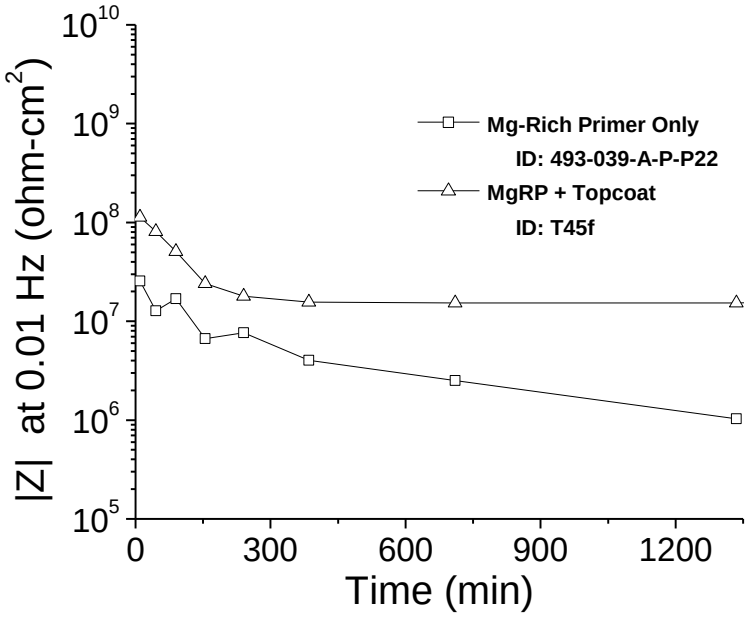

(b)

Figure 2.26. Impedance magnitude at 0.01 Hz vs. time from AA2024-T351 coated with Mg-rich primer exposed in 50 mM NaCl solution, ambient aeration during the accelerated test to asses charge capacity and barrier degradation.
(a) of varying PVC's and with a high performance advanced polymer topcoat (b) 45% PVC Mg-rich primer with and without a high performance advanced polymer topcoat

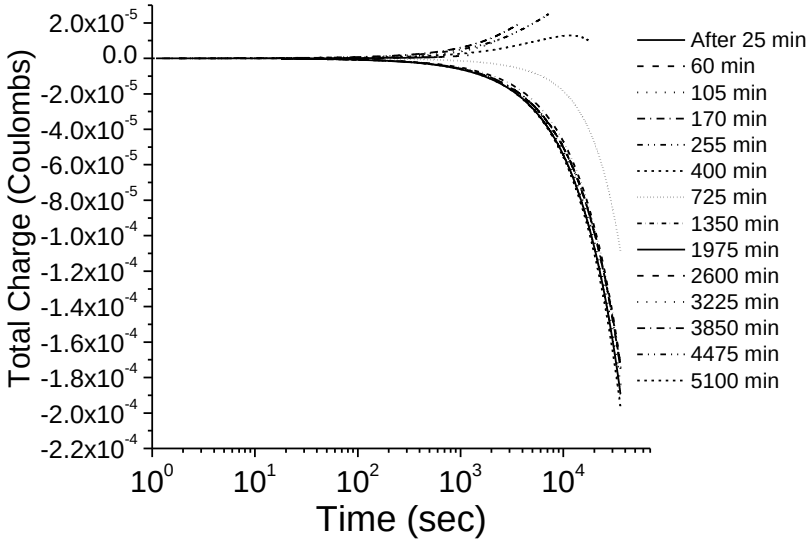

Figure 2.27. Charge during potentiostatic hold at -0.8V vs. SCE of AA2024-T351 coated with MgRP and high performance advanced polymer topcoat exposed in 50 mM NaCl solution, with ambient aeration during each cycle of the accelerated test to asses charge capacity. PVC = 45%.

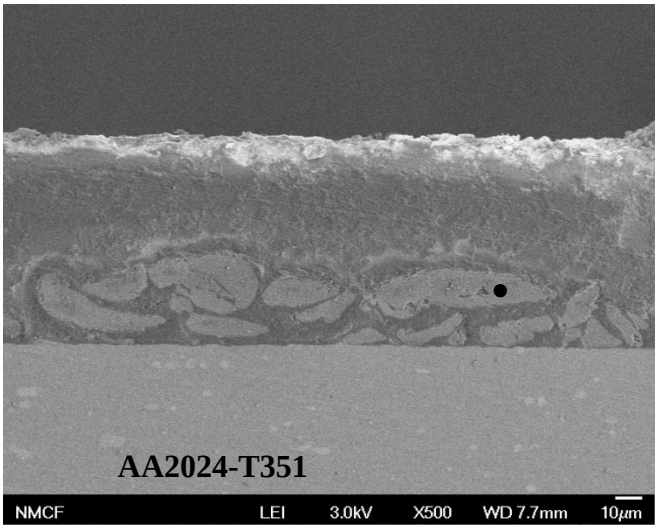

Figure 2.28. Scanning electron micrograph of AA2024-T351 coated with MgRP + topcoat, PVC = 45% after about 90 hours of potentiostatic hold at -0.8V vs. SCE in 50 mM NaCl solution, ambient aeration.
EDS spectrum of Mg pigment taken approximately at spot marker in figure 28 Accelerating voltage = 15.0 kV, working distance = 15 mm.

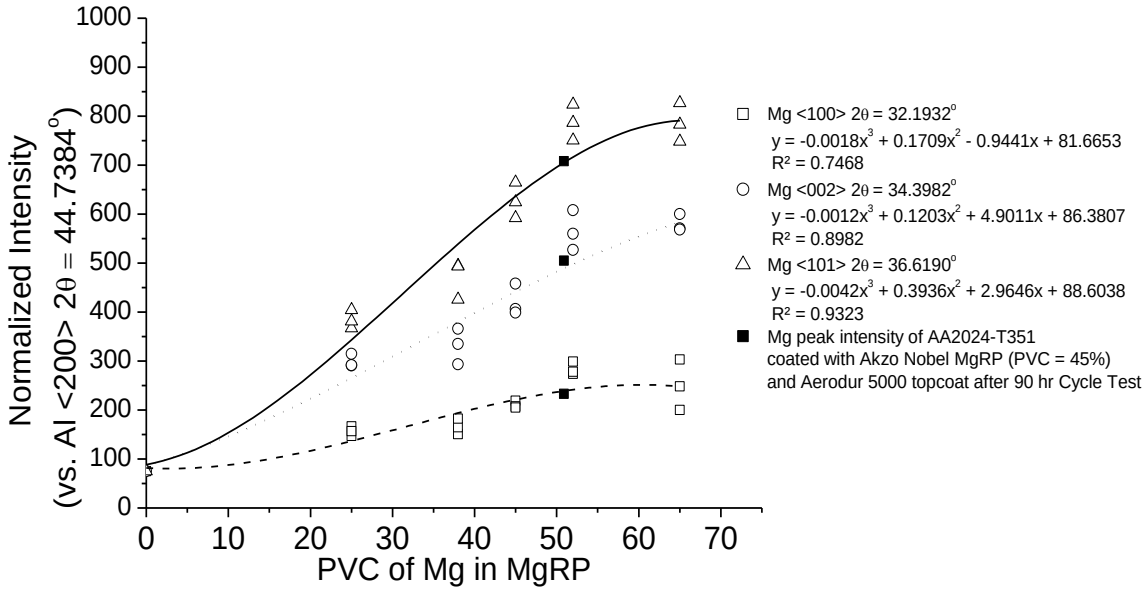

Figure 2.29. Normalized intensity of three known Mg peaks vs. MgRP PVC with a topcoat.

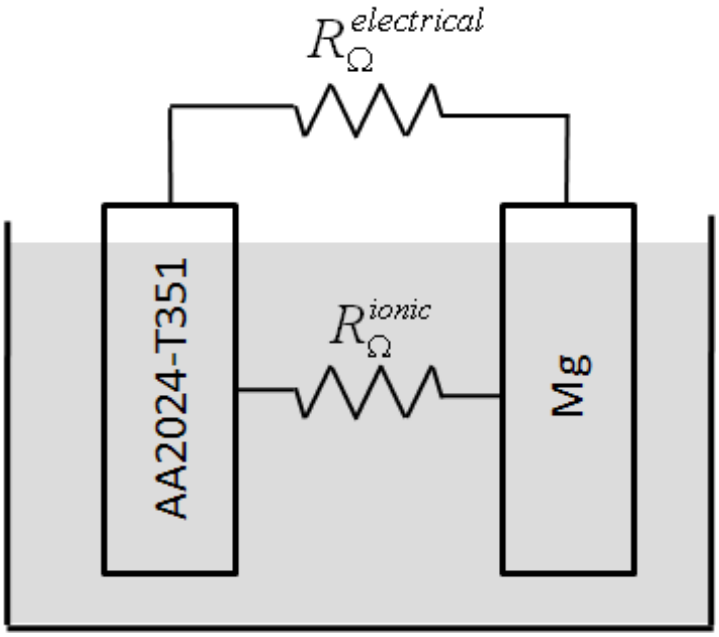

(a)

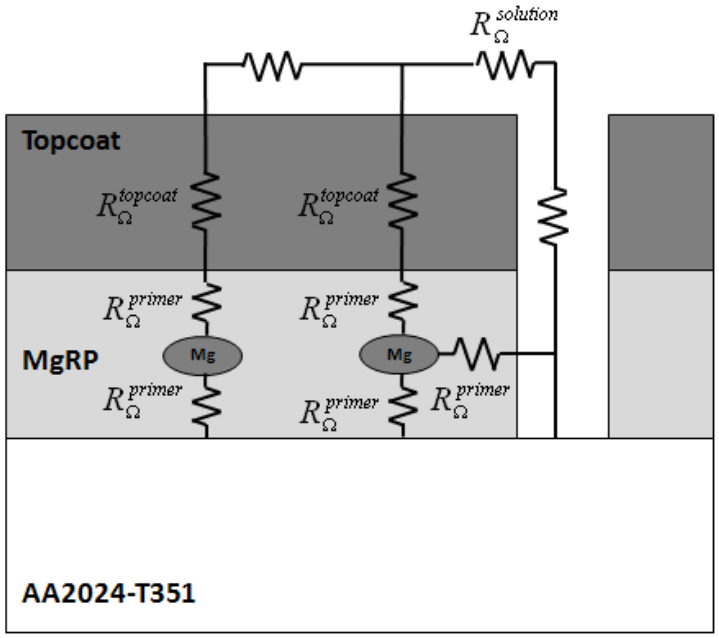

(b)

Figure 2.30. Schematic showing the Ohmic resistances that exist between the Mg pigment and the electrolyte (ionic) as well as between the Mg pigment and the substrate (electrical).
(Interfacial resistances are omitted) (a) simplified case (b) 2024/MgRP/Topcoat with a scratch.

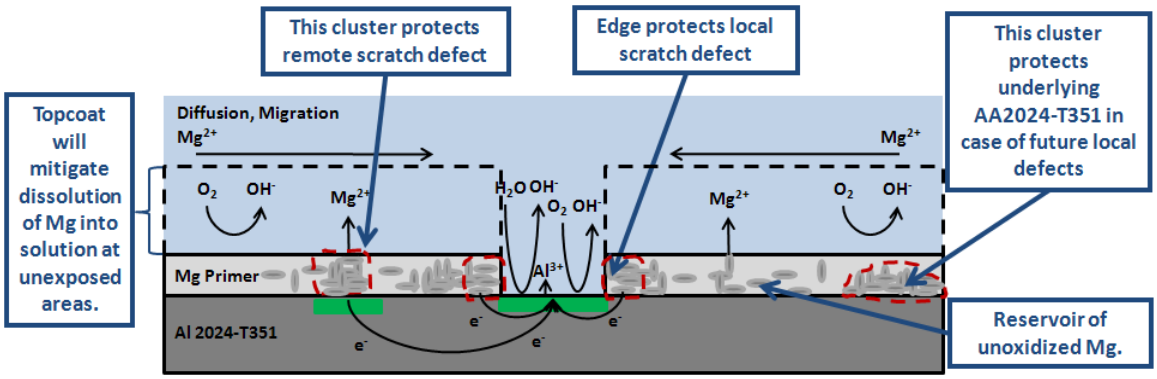

Figure 2.31. Schematic of AA2024-T351 coated with MgRP under full immersion.

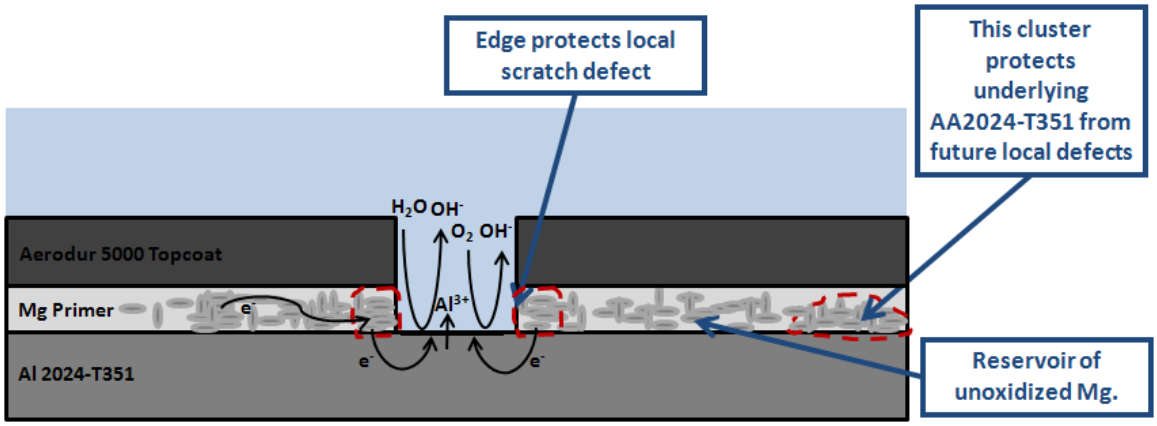

Figure 2.32. Schematic of AA2024-T351 coated with MgRP and a high performance advanced polymer topcoat under full immersion

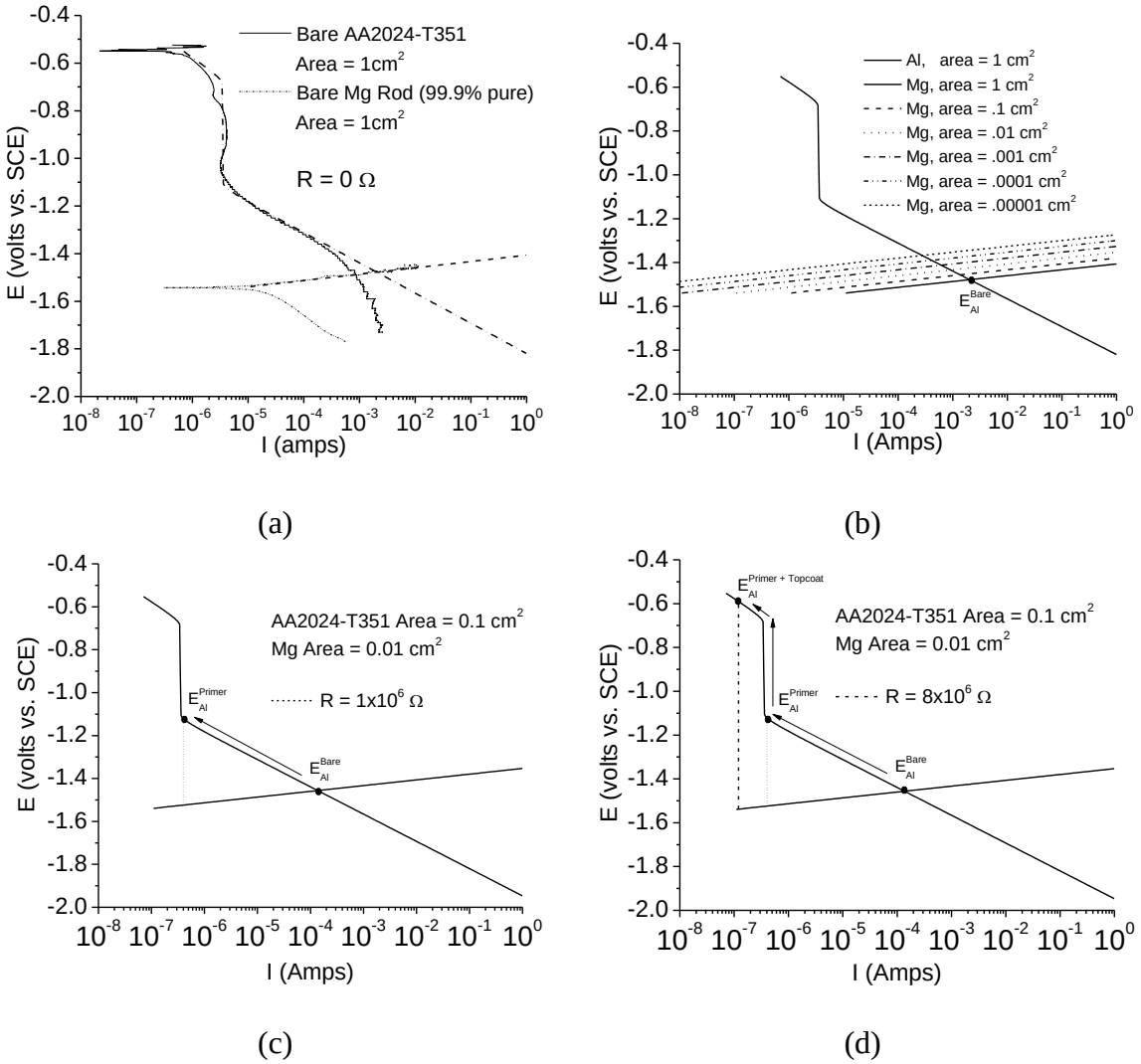

Figure 2.33. Mixed potential theory modeling based upon polarization scans of bare Mg and bare AA2024-T351.

(a) Polarization scans of bare AA2024-T351 and bare Mg with mixed potential model overlayed. (b) depicts the theoretical galvanic coupling behavior of bare Mg and AA2024-T351 electrodes. (c) hypothetically depicts the galvanic coupling of Mg pigment in the MgRP and the AA2024-T351 substrate, incorporating the potential drop due to ionic resistances through the primer polymer to the electrolyte and Ohmic resistances through the primer polymer to the AA2024-T351 substrate. (d) Hypothetically depicts the galvanic coupling of Mg pigment in the MgRP and the AA2024-T351 substrate, incorporating the potential drop due to ionic resistances through both the primer and topcoat polymers to the electrolyte and Ohmic resistances through the primer polymer to the AA2024-T351 substrate.

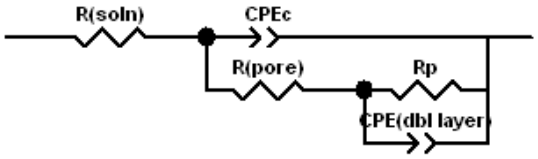

(a)

	PVC = 45% No Topcoat		PVC = 45% With Topcoat	
R(soln):	1.75E+02	Ω-cm²	1.75E+02	Ω-cm²
CPEc-Y°:	2.09E-09	F/cm²	1.98E+09	F/cm²
CPEc-n:	9.02E-01	-	7.60E-01	-
R(pore):	2.06E+07	Ω-cm²	9.62E+07	Ω-cm²
Rp:	9.13E+06	Ω-cm²	3.69E+07	Ω-cm²
CPE(dbl layer)-Y°:	uncertain	F/cm²	uncertain	F/cm²
CPE(dbl layer)-n:	uncertain	-	uncertain	-

(b)

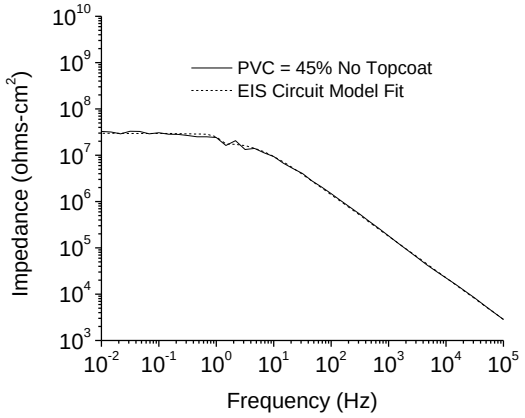

(c)

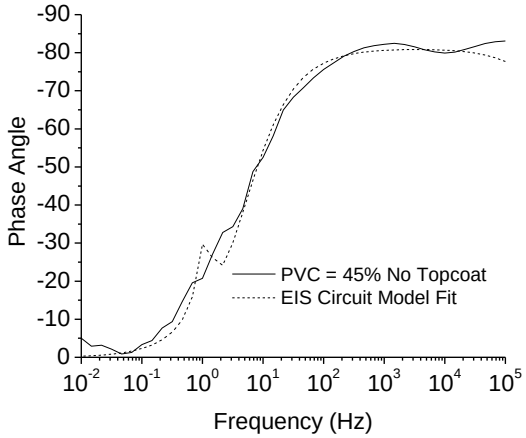

(d)

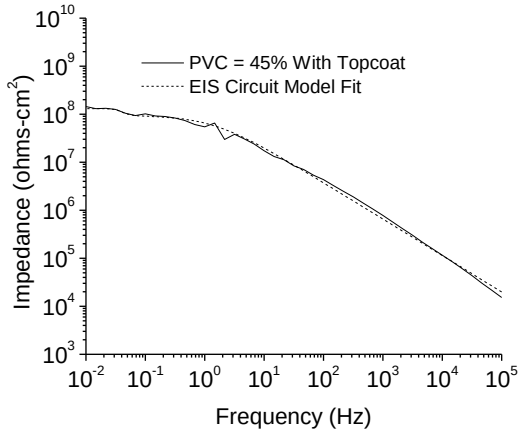

(e)

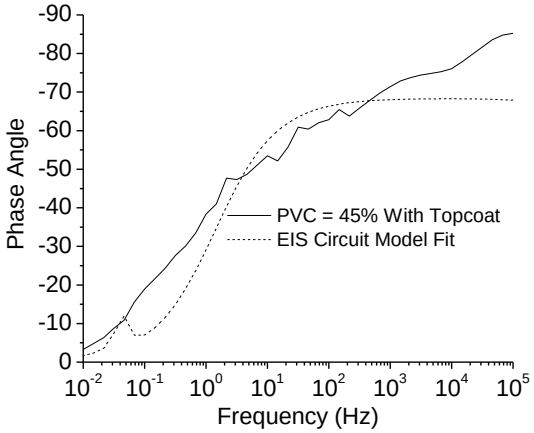

(f)

Figure 2.34. EIS circuit fitting of AA2024-T351 panels coated with Mg-rich primer exposed in aerated 50 mM NaCl solution.

(a) Electrical equivalent circuit used (b) Values of parameters estimated by fitting procedure (c,d,e,f) raw data vs. resulting circuit fit. $z_c = \frac{1}{j\omega C}$, $z_{CPE} = \frac{1}{Y_o (j\omega)^n}$, $Y_o = C$ if $n \to 1$

[J. R. Scully, Kelly, R. G., Asm Handbook: Corrosion: Fundamentals, Testing and Protection, vol. 13A, (Materials Park, Ohio: ASM Internat., 2003)]

3 Environmental Degradation of a Mg-Rich Primer in Selected Field and Laboratory Environments – Part I. Without a Topcoat

Reference: *A. D. King, B. Kannan and J. R. Scully, Environmental Degradation of a Mg-Rich Primer in Selected Field and Laboratory Environments – Part I. Without a Topcoat, Corrosion, 70, 5 (2014), DOI: http://dx.doi.org/10.5006/0988*

Presented as part of the NACE CORROSION 2013 Research Topical Symposium; "Functionalized Coatings for Durable Materials and Interfaces," Mar. 2013, Orlando, FL.

Guest Editor: Dr. Victoria Gelling

3.1 Abstract

Magnesium rich primer in a non-topcoated, scribed condition, was utilized for the corrosion protection of an AA2024-T351 substrate pretreated with PreKote™ surface pretreatment. Exposures were conducted in the field at a coastal marine site, Kennedy Space Center, FL (KSC); at an inland rural site, Birdwood Golf Course in Charlottesville, VA; in ASTM B-117 with 5% NaCl, and the same standard test modified with ASTM Artificial Seawater as well as in full immersion in ambiently aerated 5% NaCl solution. Mg pigment depletion rate, global galvanic protection potential and coating barrier properties were tracked throughout exposure periods in both field and laboratory environments. Analysis near and far from the scribe was performed. Post-mortem characterization with SEM/EDS was conducted to elucidate coating and scribe morphology, corrosion products present, corrosion of the AA2024-T351 substrate, as well as in an attempt to interrogate the throwing power of the coating system with respect

to scratches exposing bare AA2024-T351. Full immersion in ambiently aerated 5% NaCl solution, ASTM B-117 in 5% NaCl and ASTM B-117 in ASTM artificial sea water all depleted the MgRP of metallic Mg pigment far from the scribe at various rates, with significant depletion (less than 5% by volume as detectable by XRD) occurring after approximately 1000 h of exposure in all cases. Field exposures in Charlottesville, VA and Kennedy Space Center, FL resulted in depletion of metallic Mg pigment far from the scribe after 2000 and 4000 h of exposure, respectively. The acceleration factors, with respect to Mg depletion rate, observed for field exposure versus the full immersion and salt fog cabinet exposures were approximately 2:1 and 4:1 respectively. As a result of remote pigment depletion mainly by self-corrosion, the global galvanic protection potential of the coating system, with respect to remote scratches, became more positive with exposure time in each environment, from values approximately equal to that of bare Mg (-1.6 V vs. SCE) to those approximately equal to that of bare AA2024-T351 (-0.55 V vs. SCE). The acceleration factors, with respect to global galvanic protection potential, observed for field exposure versus the full immersion and salt fog cabinet exposures were approximately 3:1 for non-topcoated MgRP systems. Barrier properties of the MgRP primer coating also degraded with time in each environment but corrosion of the AA2024-T351 substrate under the coating was not observed. In general, for all environments a significant decrease in barrier properties of MgRP-coated AA2024-T351 is observed with increased environmental exposure time but acceleration factors are difficult to determine due to inherent scatter in the EIS data from near random occurrence of defects in the coating. Characterization after 1000 h of salt fog exposure indicated a throwing power that extended the entire half-width ($\approx$ 350 μm) of the AA2024-T351

scribe in both standard and modified ASTM B-117 exposures which developed thin-layer electrolyte geometries during continuous wetting. Characterization after 24 weeks of exposure at Kennedy Space Center, FL indicated a throwing power that extended approximately 200 - 300 μm in the scribe from the coating edge. Characterization after 24 weeks of exposure at Charlottesville, VA was inconclusive due to the high self-corrosion rate of the MgRP and subsequent chemical dissolution of Mg-based corrosion products by high TOW and low pH rain (pH ≈ 5). The differences in rate-of-change of Mg depletion from the coating upon environmental exposure are presumed to originate from differences in time-of-wetness and in rates of polymer degradation, specifically resistivity, due to UV exposure. Differences in throwing power in lab and field environments were theorized to be caused by differences in electrolyte geometries. A second part of this study examines the performance of a MgRP in a topcoated, scribed condition where MgRP self-corrosion is slow.

3.2 Introduction and Background

Very promising corrosion mitigation results have been reported for an organic coating system containing a metallic Mg-pigmented organic primer (MgRP) used for the corrosion protection of the precipitation age hardened aluminum alloy 2024-T351.[1-14] MgRP is a primary candidate coating system to replace chromate type surface pretreatments and chromate pigmented primers which are known for their toxicity and carcinogenic properties.[2, 15, 16] The full MgRP coating system, as intended for commercial use, consists of three individual components, the surface pretreatment, the primer coating (MgRP) and the topcoat coating; all of which are applied to AA2024-T351, an Al-Cu-Mg alloy commonly used in aerospace applications.[17] The manufacturers are clear that the

commercial MgRP coating is not intended to be used in a non-topcoated condition.[17] However, the fact remains that circumstances arise, either intentionally or un-intentionally, such that the coating may exist in service in a non-topcoated condition.[18, 19] Therefore, it is important and necessary to characterize the performance and evolution of the coating in a non-topcoated condition in addition to a topcoated condition. A scientific study requires the systematic evaluation of each component. It is necessary to study the evolution of the individual protection modes provided by the MgRP with exposure time to understand the ramifications of this evolution on the entire coating system. The analysis of a topcoated condition is presented in Part II of this study.[20] The protection mechanisms provided by the MgRP are distinctly different than those offered by chromate pigmented organic primers based on ionic inhibitor release. While barrier protection of the aluminum alloy is also afforded by the MgRP, the MgRP has been designed and shown to provide sacrificial anode based cathodic protection to the aluminum alloy by galvanically coupling the metallic Mg pigment in the MgRP to the AA2024-T351 substrate.[1, 5, 7-9]

Barrier protection is afforded to the AA2024-T351 substrate by the continuous physical barrier consisting of the organic epoxy polymer matrix of the MgRP, the Mg pigment particles, and any other insoluble pigments in the primer or corrosion products which may have formed within defects in the coating. Also, an organic polyurethane polymer topcoat is often applied to add additional barrier protection, decrease the coating system's susceptibility to UV degradation, and limit the coating's degradation by self-corrosion of the Mg pigment separate from the intended cathodic protection function.[8, 21, 22]

Secondarily, the coating can serve as a transport barrier to resist corrodant ingress such as Cl^-. Ingress is often controlled by pigmentation with insoluble species at an appropriate pigment volume fraction and/or by cross-linking and vulcanization in the polymer matrix that serves as the binder for the pigment.[23] These properties of the polymer coating system are degraded by a host of "stresses" including UV photonic radiation, chemical reaction of the coating with the environment whether by hydrolysis or saponification, or by mechanical forces which destroy adhesion.[23, 24] The latter can include osmotic blistering, corrosion product wedging, hydroxyl ion production, and reductive dissolution of oxides that destroy wet adhesion.

The MgRP is designed to galvanically couple the active, metallic Mg pigment in the primer to the more noble AA2024-T351 substrate and provide sacrificial anode based cathodic protection to the aluminum alloy. This approach is well established in the design of zinc-rich primers for use on various steels and has been well documented.[25-40] When coupled to the AA2024-T351 substrate, the galvanically coupled Mg pigment becomes an electron donor, and mixed potential theory can be used to explain the open circuit of the system when exposed to full immersion. This has been verified with open circuit and anodic polarization measurements of AA2024-T351 coated with experimental formulations of MgRP. [5, 6, 8, 9, 41] However, the throwing power of the cathodic protection into a scratch exposing bare AA2024-T351 is unknown.

For Mg to be available for sacrificial cathodic protection of the AA2024-T351 substrate it must be both electrically and ionically "well connected" to the substrate. Both electrical

and ionic conduction is required between metallic phases comprising anodes and cathodes. During environmental exposure, electrical conduction is obtained through the AA2024-T351 substrate's physical contact with the conductive Mg pigment matrix in the primer while ionic conduction is achieved between the substrate and Mg pigment through the electrolyte. When galvanic current flows, several ohmic voltage drops exist between the Mg pigment and the electrolyte (ionic) and also between the Mg pigment and the substrate (electrical) which result from resistive layers associated with substrate pretreatments, polymer matrix, and Mg pigment volume concentration (MgPVC).[8] The MgPVC of the Mg-rich primer plays an important role in determining the sacrificial cathodic protection capabilities of the coating and can be assessed nondestructively with XRD.[8] The MgPVC not only determines the total supply of Mg sacrificial anode material available in the primer, but also is a determining factor controlling the effective conductivity of the primer layer and resulting cathodic protection afforded to the AA2024-T351 by the Mg pigment in the primer.[42-48] The application of a topcoat to the coating system also significantly increases the ohmic ionic resistance between the buried Mg pigment and the electrolyte.

Past lab and field exposure studies were conducted in hopes of determining an optimal primer formulation with respect to Mg pigment volume concentration along with optimal coating system stack-ups.[18, 19, 21, 49-51] Most of these studies have pointed to an optimal Mg pigment volume concentration of approximately 45% which is at, or just below, the calculated theoretical critical pigment concentration.[1, 6, 11, 41-44, 52] This formulation is speculated to provide a balance of moderated sacrificial cathodic protection, good long-

term barrier protection, and the beneficial characteristic of preserved, isolated clusters of Mg pigment available for the protection of future defects as they occur throughout a coating's lifetime in a given exposure environment.[8, 10, 41] Thus, two possible modes of protection are described by King and Scully; long range protection of remote defects by the global galvanic protection potential afforded to the substrate and local or short range Mg pigment-based protection of local and buried defects.[8] Both modes of protection are mediated by the high ionic and electrical resistance of the coating system as a function of MgPVC, substrate pretreatments, primer polymer, and topcoat properties.[8, 10] The mediation of the cathodic protection abilities is important in the application of MgRP. It is important for the coating system to provide adequate cathodic protection to the AA2024-T351 substrate, but to also avoid the detrimental effects of cathodic corrosion of the amphoteric AA2024-T351 substrate, which is always a concern when cathodically polarizing Al-based alloys.[53-56] It has been hypothesized that cathodic corrosion of the AA2024-T351 substrate can be caused, in the case of MgRP, by increased localized pH due to severe cathodic polarization and/or excessive Mg pigment dissolution, but has yet to be definitively observed in field exposures of the MgRP coating system.[8, 10, 53-55, 57-60]

The period of protection provided by a coating system depends critically on the severity of the environment of exposure, the relevant alloy, surface finish, and electrochemical driving forces such as galvanic coupling. The outdoor corrosion of bare and coated metal alloys is controlled by several factors; including corrodant deposition rate, type of corrodant, time of wetness by rain or condensation, dew point, UV light, wet/dry cycling, relative humidity, temperature, and temperature cycling. Corrosivity of Al and steel in natural environments is typically a function of metrological parameters such as time of

wetness, time above a certain relative humidity (e.g., 35% RH), Cl^-, SO_x, and NO_x deposition rates.[61, 62] Polymer coating degradation likely depends on UV wavelength, the cumulative dosage of UV light, time of wetness and corrodant concentration. In the past, several empirical environmental severity indexes have been proposed that rank the corrosivity of various environments towards bare, finished, and/or coated metals.[61, 63, 64] A critical need resolved in this study is to understand MgRP's degradation rate and characteristics in various relevant exposure environments in hopes of identifying environmental factors that are significant to MgRP's degradation. The first step involves understanding the degradation characteristics without a topcoat.

Previous work attempting to determine detailed, long term performance characteristics of a representative MgRP coating system have utilized laboratory accelerated life testing (LALT), primarily ASTM B-117 salt fog cabinet testing.[1, 2, 18, 19, 41, 50, 52, 65, 66] However, this testing environment was designed to be used for qualification testing (MIL–A-8625F Military Specification for Anodic Coatings for Al and Al Alloys, MIL-C-5541E Military Specification for Chemical Conversion Coatings on Al and Al Alloys, MIL-PRF-23377 Military Specification for Epoxy, High Solids Primers, and MIL-PRF-32239 Military Performance Specification for Advanced Performance Coating Systems for Aerospace Applications), not lifetime assessment, and the qualification standards of which were determined utilizing completely different coating technologies. The validity of the ASTM B-117 exposure environment has largely been questioned, particularly because the ASTM B-117 exposure environment makes no effort to realistically reproduce field exposure environments with respect to many factors commonly accepted to be relevant to

environmental severity, such as electrolyte chemistry, atmosphere composition, time of wetness (TOW), relative humidity, cycling, or UV intensity. Additionally, unique macroscopic failure modes (i.e. blisters, scribe creep, etc.) of early generations of the MgRP coating system were observed in the ASTM B-117 environment that are not typically seen in the field.[1, 18, 19, 52] The discrepancies in MgRP degradation phenomena between the lab and field also eliminates the chance to estimate lab vs. field acceleration factors from standard laboratory lifetime tests. However, newer, optimized generations (in this case Akzo Nobel Aerodur 2100 Product #: 2100P003 Lot #: 493-190 MFG: 03/2009) of the coating system do not typically display unique failure modes in field or LALT environments when applied to AA2024-T351.[12, 14, 18, 19] Therefore, assuming a similarity of corrosion modes in the absence of any blistering phenomena in these accelerated environments, the determination of acceleration factors with respect to specific, measurable coating properties is also a worthy goal.

The objective of this study is to compare the degradation of a representative MgRP coating formulation throughout its lifetime in various lab versus field environments in the effort to observe any discrepancies and to gain further understanding of how the MgRP primer coating, itself, provides protection to the AA2024-T351 substrate and how these protection mechanisms evolve over exposure time in lab vs. field. The salt fog cabinet was not intended, in this study, to be used for coating qualification purposes. A working understanding of the coating system's degradation in relevant lab and field environments will be developed by measuring global Mg pigment depletion rate, galvanic protection potential and coating barrier properties throughout each exposure. The throwing power,

or protection distance, in a AA2024-T351 scratch is investigated. These measurements, in conjunction with post-mortem characterization, diagnostic electrochemical experiments, and mixed potential modeling, will provide insight into the significant factors controlling environmental severity in the context of the MgRP.

3.3 Experimental Procedures

3.3.1 Materials

The MgRP-coated AA2024-T351 samples studied were comprised of AA2024-T351 sheet, pretreated with Prekote surface pretreatment, and primed with a 30 ± 10 μm thick layer of magnesium-rich primer, "MgRP" (Akzo Nobel Aerodur 2100 Product# 2100P003 Lot# 493-190 MFG 03/2009). All tested panels were provided and painted by collaborators at NAVAIR.[18, 19] Coating thickness was measured via SEM cross-section. After curing for approximately 4 weeks in a dry box, a 50.8 mm (2") by 101.6 mm (4") "X" with a width of approximately 0.7 mm was machine scribed through the coating layers of the panel, exposing bare AA2024-T351, to simulate a scratch prior to environmental exposure. In general, the scribe penetrated 20 to 50 μm into the substrate. A schematic and optical micrograph of the MgRP coated AA2024-T351 panels investigated in this study are shown in Figure 3.1and Figure 3.2, respectively. Figure 3.3 shows cross-sectioned MgRP on AA2024-T351, before the sample has been exposed to any weathering environment near and far from the scribe. The thickness of the primer layer is approximately 30 μm and the scribe can be seen to penetrate into the substrate approximately 30-50 μm. Mg pigment particles have an approximate diameter of 20 μm.

EDS spot scans conducted on the Mg particles in the cross-sectioned MgRP also indicated low O levels (Figure 3.3c), which suggest the Mg is largely unoxidized prior to weathering. A planar SEM micrograph of a scribed MgRP-coated AA2024-T351 panel, before the sample has been exposed to any weathering environment, is shown in Figure 3.4. EDS spot scans were taken at points labeled 1 and 2 in Figure 3.4. EDS of the MgRP coating (Figure 3.4b) shows strong Mg and C intensities and low O levels, which suggests the as-applied MgRP to contain unoxodized Mg pigment encapsulated in the carbon-rich epoxy polymer matrix. EDS of the bare AA2024-T351 scribe show only the presence of Al.

3.3.2 ASTM B-117 and Modified ASTM B-117 Salt Fog Exposure

Mg-rich primer-coated AA2024-T351 panels were exposed to salt spray in a QFog Cyclic Corrosion Tester (QFog model CCT 1100) according to ASTM B-117 "Standard Practice for Operating Salt Spray (Fog) Apparatus" with neutral 5% NaCl solution (pH = 6.9 ± 0.4) as the electrolyte for at least 1000 hours.[65] During a second exposure, the standard ASTM B-117 salt fog environment was altered such that the standard 5% NaCl solution electrolyte was replaced with ASTM artificial seawater (pH = 8.2 ± 0.3).[67] In all salt fog exposures reported on in this report, ambient air was supplied to the chamber and to the atomizer for fog production. Ambient concentrations of CO_2 were measured in-situ to be approximately 425 ppm.[10] Other ambient gas concentrations were not measured. The QFog Cyclic Corrosion Test cabinet used for exposure of MgRP-coated AA2024-T351 to ASTM B-117 Salt Spray testing is shown in Figure 3.5a. The samples were mounted in the chamber according to ASTM B-117 (Figure 3.5b).[65] Panels were removed from

exposure at a front-weighted removal schedule for imaging, electrochemical interrogation and post-mortem characterization. Typical removal times for salt spray exposures were 24, 48, 96, 192, 408, 696, and 1008 hours. Pertinent environmental parameters for the ASTM B-117 environment such as mean temperature, mean relative humidity, mean dew point, mean precipitation rate, precipitation pH, and chloride deposition rate are shown in Table 3.1.

3.3.3 Field Exposures of AA2024-T351 coated with MgRP

Natural weathering exposures of Mg-rich primer-coated AA2024-T351 panels were conducted at a coastal marine site 30 m from the high tide line at Kennedy Space Center Corrosion Technology Lab in Titusville, FL (28.59406ºN, 80.58283ºW, elevation = 0 m, dates of exposure 11/7/2011 – 11/5/2012) and at a rural inland site at Birdwood Golf Course in Charlottesville, VA in Central Virginia's Albemarle County (38.0402ºN, 78.54.27ºW, elevation = 172 m, dates of exposure: 2/14/2012 – 2/12/2013). The sample test racks at Kennedy Space Center face the water and are shown in Figure 3.6. The sample test racks at Birdwood Gold Course face south and are shown in Figure 3.7. During exposure, panels were mounted on unsheltered atmospheric test racks with full exposure to natural elements according to ASTM G-4 and G-50.[68, 69] Panels were removed at a front-weighted removal schedule for imaging, XRD analysis, electrochemical interrogation and post-mortem characterization initially in two week intervals and, after 8 weeks of exposure, in 4 week intervals. Pertinent environmental parameters for Kennedy Space Center, FL 30 m lot and Birdwood Golf Course such as mean temperature, mean relative humidity, mean dew point, mean precipitation rate,

precipitation pH and chloride deposition rate are shown in Table 3.1. RH, temperature, dew point, and precipitation information was retrieved from the National Climate Data Center. Chloride deposition rates were estimated with chloride candle at KSC and the wet-deposition fluxes of major ions (including Cl^-) were directly recorded at Charlottesville, VA.

3.3.4 Full Immersion and Electrochemical Impedance Spectroscopy (EIS) Analysis

The electrolyte used for full-immersion exposure as well as post-mortem analysis after field and salt fog exposures was ambiently aerated 5% NaCl solution. Ambient concentrations of atmospheric gases, such as CO_2, are assumed. Full immersion measurements were made by clamping the environmentally exposed, MgRP-coated AA2024-T351 panel to a flat cell with a defined 1 cm^2 area circular window sealed around the edges by a Teflon knife-edge washer to prevent crevice corrosion (shown in Figure 3.8). The area tested is far away ($\geq$ 2 cm away) from any edge or scribe and the entire cell/sample assembly is placed in a Faraday cage to prevent interference from outside sources during measurement. A typical EIS scan was acquired in sine sweep mode from 100 kHz to 0.01 Hz with 6 points per decade. Coated panels were scanned with an AC amplitude of 50 - 80 mV to overcome the voltage drop though the polymer and to reduce noise. The measurement limits for the potentiostat/FRA instrumentation used for EIS measurements is shown in Figure 3.9. EIS and polarization measurements were repeated at least three consecutive times although, typically, one representative data set is presented in a figure. Painted panels were exposed in replicate sets of 6 or 10 and, at each removal interval, one panel was removed and put into dry storage for future

analysis. An equivalient circuit, automated fitting routine module built into Scribner Associate's ZView 3.1c was used for circuit fitting of raw EIS data. An equivalent circuit consisting of a nested Randle's circuit was used as the conceptual model for fitting.[70-73] It is important to note that breakpoint and saddle frequency analysis may not be valid for other systems with high MgPVC (approaching 65%[8]) where the coating is highly conductive with low electrochemical impedance and barrier properties.

3.3.5 X-Ray Diffraction and Scanning Electron Microscopy

X-Ray diffraction was conducted on a PANalytical X'pert powder X-Ray diffractometer utilizing a Cu-Kα source. The samples investigated included MgRP-coated AA2024-T351 panels before and after environmental exposure. XRD measurements of pristine and environmentally exposed samples were made at areas far away (≥ 2 cm away) from any edge or scribe, presumed to be representative of global coating degradation. All samples were scanned, continuously, from 10 to 120 degrees with a step size of 0.02 degrees. XRD Spectra obtained from bare AA2024-T351 and AA2024-T351 coated with MgRP were normalized against the fcc Al <111> $2\theta = 38.4721^{o}$ peak for comparison. Peak normalization and integration was performed with Origin Lab 7.5 software. First-order approximation of XRD penetration depth as a function of 2θ in pure Al and pure Mg are shown in Figure 3.10.[74-76] The penetration depths responsible for 99% of the diffracted intensity vary by material and with incident beam angle but range from 40 to 125 μm in the principle ranges of 2θ studied ($2\theta \approx 30^{o} - 50^{o}$) in pure Al and Mg and for this reason is commonly considered to be a bulk characterization technique. The detection limit of bulk Bragg-Brentano X-ray diffraction for mixed or composite materials containing

several crystalline phases is approximately 3 - 5% of the sample by volume.[76] Below these levels, it is unlikely that a crystalline phase will be detected in the XRD spectra. This estimate of the lower-bound of detection is supported by XRD measurements, shown in previous work[8], performed on pristine samples of MgRP-coated AA2024-T351 panels coated with MgRP of varying PVC.

Scanning electron microscopy and energy dispersive spectroscopy were used for coating characterization and post-mortem analysis. A JEOL 6700f field emission SEM with Spirit™ Energy dispersive X-ray spectroscopy (EDS) analytical software was used to conduct these investigations. An accelerating voltage of 2 – 5 kV was used for imaging to reduce charging of the polymer coating. For EDS, a working distance of 15 mm and an accelerating voltage of at least 3 times the energy of the maximum characteristic peak of interest were used (typically 15 kV). The first-order approximation of penetration depth[77] with respect to accelerating voltage in various materials of interest is plotted in Figure 3.11a. At an accelerating voltage of 15 kV and in materials investigated in this study, EDS has a penetration depth of roughly 2 to 5 μm, making the technique suitable to investigate the composition of surface products on the MgRP-coated AA2024-T351 before and after environmental exposure. Simulated EDS spectra for bulk samples of various materials relevant to the environmentally exposed MgRP-coated AA2024-T351 system are shown in Figure 3.11b. These simulations show the type of EDS fingerprint expected for each form of Mg possibly present and other species of interest. Figure 3.12 presents the simulated EDS spectra of a sphere of various diameter, D, of metallic Mg or $CaCO_3$ on a bulk substrate of Al. These simulations were produced to gain an idea of the

effect of particle size on EDS detection, in scenarios relevant to the MgRP coating system. The simulated EDS spectra in Figure 3.11 and Figure 3.12 were produced with NIST DTSA-II software. DTSA-II is a multiplatform software package for quantitative x-ray microanalysis.[78]

3.4 Results

3.4.1 Behavior During and After Exposure at Kennedy Space Center:

Optical micrographs of MgRP coated AA2024-T351 panels that have been exposed at Kennedy Space Center 30 m lot for 0, 12, and 24 weeks are shown in Figure 3.13 and Figure 3.14. The coating was observed to turn ivory white in color and have a chalky texture with increased exposure time, presumably due to the accumulation of corrosion products (such as $Mg(OH)_2$), deposited calcareous salts, and the degradation of the polymer matrix. At moderate exposure times (T > 20 weeks), small areas of the shiny Al substrate can begin to be seen beneath the MgRP coating layer. The scribe appears, at low magnification, to be relatively clean and without significant damage. It is important to note that no blistering or similar macroscopic coating failure phenomena are observed in the MgRP or along the scribe lines after exposure for 24 weeks at Kennedy Space Center, FL 30 m lot. Upon closer investigation with the SEM (Figure 3.15, Figure 3.16, and Figure 3.17a), after 12 and 24 weeks of exposure, two apparent regions or zones can be viewed in the scribe (outlined by dashed lines in Figure 3.17a) corrosion product deposits exist along the edge of the scribe whereas the center of the scribe is mostly free of deposits.

To further investigate the composition of the deposits in the scribe, and of the MgRP proximate to the scribe, 16 consecutive EDS spot scans were obtained across the width of the scribe and coating interface (labeled 1-16 in Figure 3.17). The spacing between scans was approximately 65 μm. The basic EDS spectra obtained across the scribe and coating interface show combinations of peaks indicative of C, O, Mg, Al, Si, and Ca. The EDS spot scans proximate to the edge of the scribe, labeled 1, 2, 3, 10, 11, and 12 show the presence of $Mg(OH)_2$ or MgO indicated by Mg and O peaks (compared with simulated EDS spectra in Figure 3.11b), as well as the presence of calcareous deposits. Calcareous deposits primarily consist of $CaCO_3$ and, along with Mg deposits, are indicative of regions of cathodic protection afforded to the AA2024-T351 by the MgRP.[79-86] The presence of these species 200 – 300 μm into the scribe, suggests a throwing power of the same dimensions can be observed upon environmental exposure at Kennedy Space Center, FL. The significant Al peaks present in the EDS spectra obtained at positions 13, 14, 15 and 16, in the once-MgRP coated region, further corroborate that most of the coating has been washed or dissolved away during exposure. The first-order approximation of the penetration depth of the EDS measurements at 15 keV (Figure 3.11) is estimated to be no more than 5 μm.[77] This indicates that the remaining coating layer and any residual corrosion products present are likely no more than 5 μm thick at the locations of the EDS measurements. If the remaining coating layer and any residual corrosion products were more than 5 μm thick at the locations of the EDS measurements, the Al peak would be suppressed similar to the EDS spectra of a pristine sample obtained in Figure 3.4 at spot 1.

Cross-sectioned MgRP on AA2024-T351 far away from the scribe after 12 weeks of exposure in the field at Kennedy Space Center, FL, 30 m lot, are shown in Figure 3.18a. Multiple EDS spot scans were obtained on the cross-sectioned coating layer after 12 and 24 weeks of exposure. Representative spectra are shown in Figure 3.18c. The EDS spectra indicate the presence of some metallic, unoxidized Mg in the coating after 12 weeks of exposure. Combined with the presence of a prominent O peak in the EDS spectrum obtained after 24 weeks of exposure, this suggests oxidation and depletion of a significant amount of the metallic Mg pigment. A SEM micrograph of cross-sectioned MgRP on AA2024-T351 proximate to the scribe after 12 weeks of exposure in the field at Kennedy Space Center, 30 m lot, is shown in Figure 3.18b for visual inspection. Overall, the edges and walls of the scribes appear relatively clean and without significant damage. An overall dissipation of the MgRP coating can be observed.

X-Ray Diffraction (XRD) spectra of MgRP coated AA2024-T351 (initial MgPVC = 45%) were acquired to track the depletion rate of the metallic Mg pigment in the MgRP throughout environmental exposure. XRD measurements of environmentally exposed samples were made over areas far away from the scribe, such that none of the interaction area of the incident X-rays included the scribed region of the samples. The areas far away from the scribe were presumed to be areas representative of global coating degradation. XRD spectra of MgRP coated AA2024-T351 after 0, 12 and 24 weeks of exposure in the field at Kennedy Space Center, FL, 30 m lot, are shown in Figure 3.19. Three prominent Mg hexagonal close packed peaks (<100>, <200>, and<101>) were normalized against the Al <101> peak which appeared in each spectrum as a result of the

underlying AA2024-T351 substrate. The relative intensities of the Mg peaks, shown in Figure 3.19, decrease with increasing exposure time in the field at Kennedy Space Center, FL, which indicates a depletion of metallic Mg pigment from the coating system to below the detection limit of bulk XRD (≤ 5% by volume[76]) after 24 weeks. Principle XRD peaks of relevant Mg or Al corrosion products are labeled a, b, c, and d in Figure 3.19. Detectable surface products were not present in the XRD spectra of MgRP coated AA2024-T351 after 12 and 24 weeks of exposure in the field at Kennedy Space Center, FL, 30 m lot.

Electrochemical impedance spectroscopy (EIS) measurements were also taken at each removal interval of environmental exposure. An automated fitting routine was used to fit the measured EIS spectra to a nested Randle's circuit, a schematic of which is shown in Figure 3.20, which is an accepted solid state representation of polymer coated metals.[72] EIS measurements of MgRP coated AA2024-T351 (initial MgPVC = 45%) taken after 0, 2, 6, 12, and 24 weeks of exposure in the field at Kennedy Space Center, FL (scatter plot), and the results of the automated fitting analysis (lines), are shown in Figure 3.21. The values of each representative circuit component produced by the automated fitting routine for selected exposure times at Kennedy Space Center, FL 30 m lot are tabulated in Table 3.2. The MgRP coated AA2024-T351 displayed a decrease of four orders of magnitude of the low frequency (at 0.01 Hz) impedance as well as a shift towards high frequencies, in both the break point and saddle frequency, throughout environmental exposure at Kennedy Space Center, FL. Both phenomena indicate a significant loss of barrier protection capability throughout the duration of the exposure.[70, 71]

3.4.2 Behavior During and After Exposure at Charlottesville, VA:

Optical micrographs of MgRP-coated AA2024-T351 panels that have been exposed at Birdwood Golf Course in Charlottesville, VA for 0, 12, and 24 weeks are shown in Figure 3.22 and Figure 3.23. The coating was observed to turn chalky and opaque taupe in color and eventually lose mass with increased exposure time, due to UV or acidic degradation of the epoxy polymer, dissolution of the Mg pigment and subsequent washing away by acidic rain precipitation (Table 3.1). Even at low exposure times (as low as 16 weeks), the shiny Al substrate can begin to be seen beneath the MgRP coating layer. The scribe appears, at low magnification, to be relatively clean and without significant damage. It is important to note that no blistering or similar macroscopic coating failure phenomena are observed in the MgRP or along the scribe lines after exposure for 24 weeks. Upon closer investigation with the SEM (Figure 3.24, Figure 3.25, and Figure 3.26), after 12 and 24 weeks of exposure the scribes appear extremely clean and largely damage free.

Sixteen consecutive EDS spot scans were acquired across the width of the scribe and coating interface (labeled 1-16 in Figure 3.26b) with 65 μm spacing. The basic EDS spectra obtained across the scribe and coating interface shows combinations of peaks indicative of O, Mg, Al, and Si. The EDS spot scans throughout the width of the scribe, labeled 1 - 12 show very little indication of Mg or Ca deposits. It does not appear that a throwing power can be observed with EDS upon environmental exposure at Birdwood

Golf Course in Charlottesville, VA after 24 weeks. The presence of the Al peak in the EDS spectra obtained at positions 13, 14, 15, and 16, in the once-MgRP coated region, indicate that most of the coating has been damaged during exposure based on the first-order approximation of the penetration depth of the EDS measurements at 15 keV (Figure 3.11) that is estimated to be no more than 5 μm.[77] If the remaining coating layer and any residual corrosion products were more than 5 μm thick at the locations of the EDS measurements, the Al peak would be suppressed as was observed in the EDS spectra of a pristine sample, obtained in Figure 3.4 at spot 1.

Cross-sectioned MgRP on AA2024-T351 far away from the scribe after 12 weeks of exposure in the field at Birdwood Golf Course in Charlottesville, VA is shown in Figure 3.27a. After only 12 weeks of exposure, the remaining MgRP coating layer is observed to be much thinner as compared to the as-applied 30 μm thickness (Figure 3.3). Multiple EDS spot scans were obtained on the coating layer after 12 and 24 weeks of exposure at Birdwood Golf Course in Charlottesville, VA. Representative spectra are shown in Figure 3.27c. The EDS spectra show the presence of primarily Al, which indicates the depletion of a large percentage of the polymer and metallic, unoxidized Mg pigment. A SEM micrograph of cross-sectioned MgRP on AA2024-T351 proximate to the scribe after 12 weeks of exposure in the field at Kennedy Space Center, 30 m lot, is shown in Figure 3.27b for visual inspection. Overall, the edges and walls of the scribes appear relatively clean and without significant damage. An overall dissipation of the MgRP coating can be observed such that a MgRP coating thickness of less than 5 μm is remaining.

XRD spectra of MgRP (initial MgPVC = 45%) coated AA2024-T351 after 0, 12, and 24 weeks of exposure in the field at Birdwood Golf Course in Charlottesville, VA are shown in Figure 3.28. The relative intensities of the Mg peaks, shown in Figure 3.28, decrease with increasing exposure time in the field at Birdwood Golf Course in Charlottesville, VA. This indicates a depletion of metallic Mg pigment from the coating system to below the detection limit of bulk XRD ($\leq$ 5% by volume[76]) after only 12 weeks of exposure. Principle XRD peaks of relevant Mg or Al corrosion products are labeled a, b, c, and d in Figure 3.28. Detectable surface products were not present in the XRD spectra of MgRP coated AA2024-T351 after 12 or 24 weeks of exposure at Birdwood Golf Course in Charlottesville, VA which, combined with a lack of significant corrosion product build-up on the sample as viewed in SEM, suggests the majority of such corrosion products were washed away by acidic precipitation during exposure.

EIS measurements of MgRP-coated AA2024-T351 (initial MgPVC = 45%) taken after 0, 2, 6, 12, and 24 weeks of exposure at Birdwood Golf Course in Charlottesville, VA (scatter plot) and the results of the automated fitting analysis (lines) are shown in Figure 3.29. The values of each representative circuit component produced by the automated fitting routine for selected exposure times at Birdwood Golf Course in Charlottesville, VA are tabulated in Table 3.3. The MgRP coated AA2024-T351 displayed a decrease of four orders of magnitude of the low frequency (at 0.01 Hz) impedance. Also, a shift towards high frequencies in the break point frequency of the Bode phase angle occurred in as little as 12 weeks of environmental exposure at Birdwood Golf Course in

Charlottesville, VA. Both phenomena indicate a significant loss of barrier protection capability throughout the duration of the exposure.[70, 71]

3.4.3 Behavior During and After Exposure in ASTM B-117 with 5% NaCl

Optical micrographs of MgRP coated AA2024-T351 panels that have been exposed in ASTM B-117 with 5% NaCl solution for 0, 384, and 984 hours are shown in Figure 3.30 and Figure 3.31. The coating was observed to turn bright white in color with increased exposure time, presumably due to conversion of the metallic Mg pigment to $Mg(OH)_2$ corrosion product which has limited solubility in solutions of pH $\geq$ 8. After 984 hours of exposure in ASTM B-117 with 5% NaCl solution the scribe appears, at low magnification, to be moderately clean and without significant damage. No blistering or similar macroscopic coating failure phenomena was observed in the MgRP or along the scribe lines after exposure for 984 hours in ASTM B-117 with 5% NaCl solution.

After 384 and 984 hours of exposure, the MgRP-coated region appears to be very rough in texture (Figure 3.32); and both the coating and scribe surfaces (Figure 3.33) appear to contain lamellar flowers typically associated with $Mg(OH)_2$.[52, 60] Metallic Mg is known to be readily converted to $Mg(OH)_2$ in most ambient aqueous environments. At higher magnification a moderate amount of $Mg(OH)_2$ precipitates are also present in the scribed region. Sixteen consecutive EDS spot scans were obtained across the width of the scribe and coating interface (labeled 1-16 in Figure 3.34b) with 65 μm spacing. EDS spectra acquired across the scribe and coating interface show combinations of peaks indicative of C, O, Mg, Al, Si, and Cl. The EDS spot scans obtained throughout the width of the

scribe, labeled 1 – 12, all show detectable amounts of Mg species present in the scribe, suggesting that the whole scribe was subjected to cathodic protection in the ASTM B-117 with 5% NaCl solution environment. Increased Mg intensities, along with significant amounts of Cl, are detected at locations more proximate to the scribe edges (positions 1, 2, 3, 11, and 12), possibly indicating increased cathodic protection in these regions compared with regions in the middle of the scribe (positions 4 – 10). Significant Mg, O and Cl peaks are present in the EDS spectra aquired over the MgRP coating at positions 13, 14, 15, and 16. The significant Mg, O, and Cl peaks present at positions 13, 14, 15, and 16 appear very similar to the modeled EDS spectra of $Mg(OH)_2$ and $MgCl_2$ in Figure 3.11b. This similarity suggests the surface of the coating consists of a layer of residual $Mg(OH)_2$ and $MgCl_2$. Based on first order approximations of EDS penetration depth (Figure 3.11a) the coating/product layer is at least 2 - 5 μm thick.[77]

A SEM micrograph of cross-sectioned MgRP on AA2024-T351 far away from the scribe, after 384 hours of exposure in ASTM B-117 with 5% NaCl solution, is shown in Figure 3.35a. After 384 and 984 hours of exposure, the remaining MgRP coating layer is observed to be approximately 20 - 40 μm thick. Multiple EDS spot scans were obtained in the coating layer after 384 and 984 hours of exposure in ASTM B-117 with 5% NaCl. Representative EDS spectra are shown in Figure 3.35c. EDS spot scans obtained on the coating layer after 384 hours of exposure in ASTM B-117 with 5% NaCl solution indicate the presence of a significant amount of metallic, unoxidized Mg in the coating. Similar EDS measurements obtained on the coating layer after 984 hours of exposure indicate the presence of Mg, O, and Cl in the coating. It is unclear from EDS analysis

whether all of the Mg present in the coating layer is oxidized after 984 hours of exposure in ASTM B-117 with 5% NaCl solution. A SEM micrograph of cross-sectioned MgRP on AA2024-T351 proximate to the scribe after 384 hours of exposure in ASTM B-117 with 5% NaCl solution is shown in Figure 3.35b for visual inspection. The MgRP coating layer is approximately 20 – 30 μm thick. Overall, the edges and walls of the scribes appear to have moderate amounts of corrosion product deposited on them.

XRD spectra of MgRP (initial MgPVC = 45%) coated AA2024-T351 after 0, 384 and 984 hours of exposure in ASTM B-117 with 5% NaCl solution are shown in Figure 3.36. The relative intensities of the Mg peaks shown in Figure 3.36 decrease to zero with increasing exposure time in ASTM B-117 with 5% NaCl solution. This decrease in Mg peaks indicates a depletion of metallic Mg pigment from the coating system to below the detection limit of bulk XRD (≤ 5% by volume[76]) after 984 hours of exposure. Principle XRD peaks of relevant Mg or Al corrosion products are labeled a, b, c, and d in Figure 3.36. No relevant Mg or Al corrosion products were observed with XRD after 384 or 984 hours of exposure in ASTM B-117 with 5% NaCl solution. It is likely that the corrosion products formed are either not voluminous enough to be detected by XRD, or are of an amorphous crystal structure rendering them undetectable by XRD. With increasing exposure time, NaCl became prevalent in the XRD spectra as a result of the high deposition rate and continuous wetting characteristics of the salt fog environment.

EIS measurements of MgRP-coated AA2024-T351 (initial MgPVC = 45%) taken after 0, 168, 384, 744, and 984 hours of exposure in ASTM B-117 with 5% NaCl solution

(scatter plot) and the results of the automated fitting analysis (lines) are shown in Figure 3.37. The values of each representative circuit component produced by the automated fitting routine for selected exposure times in ASTM B-117 with 5% NaCl solution are tabulated in Table 3.4. The MgRP coated AA2024-T351 displayed a decrease of three orders of magnitude of the low frequency (at 0.01 Hz) impedance as well as a shift towards high frequencies in the break point frequency of the Bode phase angle in as little as 168 hours of environmental exposure in ASTM B-117 with 5% NaCl solution. Both phenomena indicate a significant loss of barrier protection capability throughout the duration of the exposure.[70, 71]

3.4.4 Behavior During and After Exposure in ASTM B-117 Modified with ASTM Seawater:

Optical micrographs of MgRP coated AA2024-T351 panels that have been exposed in ASTM B-117 modified with ASTM artificial sea water solution for 0, 408, and 1000 hours are shown in Figure 3.38 and Figure 3.39. The coating developed a dense, ivory colored film covering the whole sample. When viewed in SEM (Figure 3.40, Figure 3.41, and Figure 3.42), the scribe is full of corrosion product or deposit after 408 and 1000 hours of exposure in the ASTM B-117 environment modified with ASTM artificial seawater. No blistering or similar macroscopic coating failure phenomena are observed in the MgRP or along the scribe lines after exposure for 1000 hours in the ASTM B-117 environment modified with ASTM artificial seawater. Upon closer investigation (Figure 3.40, Figure 3.41, and Figure 3.42), after 408 and 1000 hours of exposure the scribe and

MgRP-coated region appear to be very rough in texture and covered in spherical groupings of needle-like precipitates. Sixteen consecutive EDS spot scans were obtained across the width of the scribe and coating interface after 100 hrs of exposure (labeled 1-16 in Figure 3.42b) with spacing of 65 μm. Two basic EDS spectra, one consisting solely of Ca, and a second consisting of both Mg and Al, were observed across the scribe and coating interface. The EDS spot scans throughout almost the entire width of the scribe (positions labeled 1 – 11), as well as over the MgRP coating (positions labeled 14, 15, and 16), solely show significant amounts of Ca species present. Calcareous deposits primarily consist of $CaCO_3$ and are indicative of regions of cathodic protection afforded to the AA2024-T351 by the MgRP.[79-86] The deposition of Ca species throughout most of the scribe suggests that the whole scribe may have been subject to cathodic protection in the ASTM B-117 environment modified with ASTM artificial seawater. Based on first order approximations of EDS penetration depth (Figure 3.11a), the lack of Al peaks at positions 1 – 11 and 14-16, indicates that the layer of calcareous deposits is thicker than 3 μm. Positions 12 and 13, which are directly proximate to the edge of the MgRP coating on one side of the scribe, show Al and Mg peaks from the substrate and MgRP coating. This is likely the side of the scribe that is positioned towards the top of the panel during exposure, resulting in a thinner electrolyte layer at this position and subsequently less depositon of the Ca-containing precipitate.

Cross-sectioned MgRP far away from the scribe after 408 hours of exposure in ASTM B-117 environment modified with ASTM artificial seawater is shown in Figure 3.43a. After 408 and 1000 hours of exposure, the remaining MgRP coating layer is observed to be

approximately 20 - 30 μm thick. Multiple EDS spot scans were obtained in the coating layer after 408 and 1000 hours of exposure in ASTM B-117 with ASTM artificial seawater. Representative EDS spectra are shown in Figure 3.43c. EDS spot scans obtained on the coating layer after 408 and 1000 hours of exposure in the ASTM B-117 environment modified with ASTM artificial seawater indicate the presence of a significant amount of Mg in the coating as well as Cl and significant amounts of Ca. It is unclear from EDS analysis whether all of the Mg present in the coating layer is oxidized after 408 hours of exposure in ASTM B-117 environment modified with ASTM artificial seawater. Similar EDS measurements obtained on the coating layer after 1000 hours of exposure indicate the presence of Ca, C, and O, suggesting the Ca-rich deposit covering the sample is a calcareous deposit. A SEM micrograph of cross-sectioned MgRP on AA2024-T351 proximate to the scribe after 408 hours of exposure in the ASTM B-117 environment modified with ASTM artificial seawater is shown in Figure 3.43b for visual inspection. The MgRP coating layer is approximately 20 – 30 μm thick. Overall, the edges and walls of the scribes appear to have corrosion product deposited on them.

XRD spectra of MgRP (initial MgPVC = 45%) coated AA2024-T351 after 0, 408, and 1000 hours of exposure in the ASTM B-117 environment modified with ASTM artificial seawater are shown in Figure 3.44. The relative intensities of the Mg peaks shown in Figure 3.44 decrease with increasing exposure time in the ASTM B-117 environment modified with ASTM artificial seawater which indicates a depletion of metallic Mg pigment from the coating system to below the detection limit of bulk XRD (≤ 5% by volume[76]) after 1000 hours of exposure. Principle XRD peaks of relevant Mg or Al

corrosion products are labeled a, b, c, and d in Figure 3.36. No relevant Mg or Al corrosion products were observed with XRD after 408 or 1000 hours of exposure in the ASTM B-117 environment modified with ASTM artificial seawater. With increasing exposure time, $CaCO_3$ became prevalent in the XRD spectra, and is shown to be the predominant calcareous deposit covering the samples.

EIS measurements of MgRP-coated AA2024-T351 (initial MgPVC = 45%) taken after 0, 192, 408, 698, and 1000 hours of exposure in the ASTM B-117 environment modified with ASTM artificial seawater (scatter plot) and the results of the automated fitting analysis (lines) are shown in Figure 3.45. The values of each representative circuit component produced by the automated fitting routine for selected exposure times in ASTM B-117 modified with ASTM artificial sea water are tabulated in Table 3.5. The MgRP coated AA2024-T351 displayed a decrease of three orders of magnitude of the low frequency (at 0.01 Hz) impedance as well as a shift towards high frequencies in the break point frequency of the Bode phase angle in as little as 192 hours of environmental exposure at Birdwood Golf Course in Charlottesville, VA. Both phenomena indicate a significant loss of barrier protection capability throughout the duration of the exposure.[70, 71]

3.4.5 Tracking MgRP Degradation throughout Environmental Exposure:

The integrated normalized XRD Mg <101 2θ = 36.6170> peak intensity is plotted versus exposure time in each environment in Figure 3.46. The integrated normalized intensity of metallic Mg was observed to decrease with increased exposure time in each exposure

environment. It was found that full immersion in ambiently aerated 5% NaCl solution, ASTM B-117 in 5% NaCl, and ASTM B-117 in ASTM artificial seawater deplete the MgRP of metallic Mg pigment at approximately equal rates, with depletion (less than 5% by volume as detectable by XRD[76]) occurring after approximately 1000 h of exposure. Field exposures in Charlottesville, VA and Kennedy Space Center, FL resulted in depletion of metallic Mg pigment after 2000 and 4000 h of exposure, respectively. The acceleration factors, with respect to Mg depletion rate, observed for field exposure versus the full immersion and salt fog cabinet exposures were approximately 2:1 and 4:1 respectively. It is important to note that even though metallic Mg pigment is not detectable after extended exposure times in each environment, it is likely that there still exists a small amount (less than 5% PVC) of encapsulated metallic Mg pigment dispersed through any residual polymer coating that remains. This is particularly likely in samples that were not exposed to environments without significant UV, such as in ASTM B-117 salt spray testing, as the polymer does not degrade as readily in these environments.

The global[6] galvanic protection potential of the coating system (as measured in ambiently aerated 5% NaCl solution) became more positive with exposure in each environment, from values approximately equal to that of bare Mg (-1.6 V vs. SCE) to those approximately equal to that of bare AA2024-T351 (-0.55 V vs. SCE). In an attempt to develop acceleration factors with respect to galvanic protection potential in each exposure environment the open circuit potential of the MgRP-coated AA2024-T351

[6] "Global" refers to the capability to protect a remote, bare area of AA2024-T351 as long as it is electrically and ionically connected to the coating.

panel in ambiently aerated 5% NaCl solution is plotted versus exposure time in each environment in Figure 3.47. It was found that global galvanic protection potential became more positive, comparative to that of bare AA2024-T351 (-0.6 V vs. SCE) at similar rates (after ~300 hours of exposure) in full immersion in ambiently aerated 5% NaCl solution, ASTM B-117 in 5% NaCl and in ASTM B-117 with ASTM artificial seawater. Field exposures in Charlottesville, VA and Kennedy Space Center, FL both resulted in a more positive global galvanic protection potential comparative to that of bare AA2024-T351 (-0.6 V vs. SCE) after approximately 1000 hours of exposure. The acceleration factors, with respect to global galvanic protection potential, observed for field exposure versus the full immersion and salt fog cabinet exposures were approximately 3:1 for non-topcoated MgRP systems. The correlation between global galvanic protection potential afforded to the AA2024-T351 substrate and metallic Mg pigment remaining in the coating is presented in Figure 3.48. In general, in all environments studied, the galvanic protection potential of the coating system (as measured in ambiently aerated 5% NaCl solution) increases with exposure in each environment, as a result of Mg pigment depletion.

The low frequency impedance (at 0.01 Hz), the breakpoint frequency[70, 87], the saddle frequency[88] and R_{coat}[89] of the MgRP-coated AA2024-T351 panel in ambiently aerated 5% NaCl solution are plotted versus exposure time in each environment in Figure 3.49, Figure 3.50, Figure 3.51, and Figure 3.52, respectively. In general, for all environments a significant decrease in barrier properties of MgRP-coated AA2024-T351 is observed with increased environmental exposure time but acceleration factors are difficult to determine

due to inherent scatter in the EIS data from near random occurrence of defects in the coating.

3.5 Discussion

3.5.1 Effects of Chemical Environment on E-i characteristics of Mg and AA2024-T351

Table 3.6 summarizes observations with regard to blistering, underpaint corrosion, cathodic corrosion and throwing power on AA2024-T351 panels coated with MgRP after environmental exposure in the field and lab. A large source of variation between performance of the coating in the salt fog and field exposure environments, with regards to throwing power and pigment depletion rate, is the electrolyte chemistry in each environment and its effect on the electrochemical behavior of the MgRP and AA2024-T351 substrate. Varying electrolyte chemistry changes the electrochemical characteristics of the anode and cathode in the galvanic couple between the Mg pigment and the AA2024-T351 substrate which is governed by mixed potential theory. Figure 3.53 depicts the E-log(i) characteristics of bare Mg and bare AA2024-T351 in some chemical environments deemed relevant to the environmental exposure of MgRP-coated AA2024-T351. Figure 3.53a and b show the E-log(i) characteristics of bare Mg and bare AA2024-T351 in varying concentrations of ambiently aerated NaCl and ASTM artificial seawater. During an episodic wetting or drying event the electrolyte concentration will subsequently decrease or increase, shifting the E-log(i) characteristics of both the anode and cathode as seen in the polarization measurements. Figure 3.53c depicts the E-log(i)

characteristics of bare Mg and bare AA2024-T351 in as-mixed, ambiently aerated 1.0 M NaCl and ASTM artificial seawater solutions before and after Mg shavings were allowed to dissolve in the solution. The dissolution of the Mg shavings in solution produces $Mg(OH)_2$, which increases the pH of the solutions (to 10.5 in 1.0 M NaCl and 9.6 in ASTM ASW). At high pH, Al's oxides are soluble[60], and not protective, which acts to shift the corrosion potential of the AA2024-T351 to lower potentials. Such a scenario might develop in environments with low precipitation or infrequent rinsing such that continuous Mg pigment dissolution locally increases the pH of the electrolyte layer or droplet. The ASTM B-117, laboratory salt fog, environment produces a constant, thin-layer electrolyte and does not experience variances in chloride concentration or pH effects (due to acid rain or Mg pigment dissolution) which are expected in the field. The cathodic current density on the AA2024-T351 did not vary with varying chloride concentration (Figure 3.53a and b) or pH (Figure 3.53c). However, the corrosion potential of AA2024-T351 was greatly affected by both chloride concentration and pH. An increase in either chloride concentration or pH resulted in a significant decrease in the corrosion potential of bare AA2024-T351. The anodic current density on bare Mg was observed to increase and the corrosion potential of bare Mg was observed to decrease with increased chloride concentration. The effect of chloride concentration and pH on the corrosion potential of bare Mg was much less than on that of bare AA2024-T351. Therefore, under high chloride or high pH conditions the difference between the corrosion potentials of Mg and AA2024-T351 (ΔE) will be decreased. ΔE is the driving force for cathodic protection.

3.5.2 Throwing Power

The “throwing power” of the MgRP primer coating on AA2024-T351 in various lab and field environments is of significant interest. The “throwing power” pertains to the distance over which the MgRP coating system can protect bare AA2024-T351 by sacrificial anode based cathodic protection. Predicting the throwing power is quite complicated because the scribe size, coating formulation, electrolyte composition, electrolyte geometry, interfacial electrochemical properties, and bare/coated area ratios can all be limiting factors when considering protection ability or throwing power of a coating that protects by sacrificial anode based galvanic protection.

A source of variation between performance of the coating in the salt fog and field exposure environments, with regards to throwing power, is the electrolyte geometry in each environment. A sacrificial coating can only protect defects, or bare substrate at scratches, which it is both electrically and ionically connected to. In an artificial environment like ASTM B-117 salt fog, in a rainstorm with large drops, or during a dewing event, the whole panel is wet with a continuous electrolyte layer and the "throwing power/ability" of the MgRP that is measured or observed will be limited electrochemically based on the secondary or tertiary current distribution associated with cathodic protection of AA2024-T351 from mixed potential theory (showed schematically in Figure 3.54a and b). In these cases the throwing power will spread across the scratch. However, if the environment is such that the electrolyte layer is tortuous, and individual droplets start to form, a limitation in throwing power brought about by the high resistivity

of a tortuous electrolyte (ionic path), occurs (showed schematically in Figure 3.54c).[7] Under these conditions of a tortuous electrolyte path an environmental limitation rather than an electrochemical limitation is placed on the throwing power of the coating system. The throwing power is observed with EDS in the field at Kennedy Space Center (Figure 3.17) to be approximately 200 – 300 μm and in the salt fog environment (Figure 3.34 and Figure 3.42) to cover the full half-width of the scribe (≥350 μm) because the tortuous and limited electrolyte increases the resistance of the ionic path between the anode and cathode. It should be noted that during a given episodic drying or wetting event, throwing power may be temporarily increased or diminished.

Additional factors which complicate the determination of a throwing power result from the chemical dissolution of chemical species used as markers indicative of zones of cathodic protection as well as difficulties in distinguishing between definitive regions of protection and of substrate corrosion in defect areas. Chemical dissolution of the precipitates that are common to zones of cathodic protection is likely in acidic and high TOW environments, like that of Birdwood Golf Course in Charlottesville, VA, which is subject to regular acidic precipitation (Table 3.1). EDS spot scans obtained throughout the width of the scribe after 24 weeks of exposure at Birdwood Golf Course in Charlottesville, VA, (Figure 3.26) showed very little indication of Mg or Ca deposits common to regions of cathodic protection, making evidence and observation for throwing power in this environment difficult. However, it is likely that the throwing power of the

[7] . If a droplet is not in contact with the MgRP and instead exists only above bare AA2024-T351 substrate, there can be no sacrificial protection due to a remote coating within the area covered by that droplet.

MgRP could be detected in EDS spot scans obtained throughout the width of the scribe after exposure at Kennedy Space Center, FL (Figure 3.17) due to the more alkaline exposure conditions. Not only is the rain precipitation at Kennedy Space Center, FL slightly alkaline as compared to Charlottesville, VA (Table 3.1), but the proximity of the test racks to the ocean make the samples susceptible to spray from the ocean surf which has a pH of roughly 8.2.[67] This alkaline pH suppresses the chemical dissolution of species used to identify zones of cathodic protection.

3.5.3 Residual Protection After Mg Pigment Depletion

Variations in MgRP polymer degradation were also observed between laboratory salt fog and field exposure environments. In the field, the polymer exhibited severe damage and dissolution as evidenced by EDS (Figure 3.17 and Figure 3.26) and SEM cross-section (Figure 3.18 and Figure 3.27). In the lab, a significant amount of the MgRP polymer was observed to remain after prolonged exposures in ASTM B-117 with 5% NaCl (Figure 3.34 and Figure 3.35) and with ASTM artificial seawater (Figure 3.42 and Figure 3.43). This variation in performance in the field is presumed to be due to UV degradation. Kennedy Space Center, FL is known to be a severe site of UV exposure.[90] UV radiation is known to severely degrade epoxy organic polymers that are used in the Mg-rich primer.[19, 21, 23, 24] The degradation process is referred to "chalking" due to the continuous breakdown of the polymeric backbone and subsequent formation of a chalky mixture of polymer and pigment fragments on the coating's surface.[23] This chalking behavior was observed on MgRP-coated AA2024-T351 panels exposed in the field at Kennedy Space Center, FL (Figure 3.13 and Figure 3.14) and at Birdwood Golf Course in Charlottesville,

VA (Figure 3.22and Figure 3.23), but not in laboratory ASTM B-117 exposures where UV exposure is extremely low. Polyurethane organic polymers undergo far less degradation as a result of UV exposure. For this reason Polyurethane polymers with UV absorbing pigments, like the one used in the Aerodur 5000 Topcoat, are primarily used as topcoat polymers.[21, 24] It is recognized that primer only systems may not be deployed in service and that exposing the primer in a non-topcoated condition allows for self-corrosion of any Mg pigment with little or no ionic resistance to the electrolyte. However, this is an initial step necessary to understand performance in this system.

It is apparent that modest corrosion protection is still afforded to the AA2024-T351 substrate by the MgRP polymer after the Mg pigment is largely depleted (to less than 5% by volume as evidenced by XRD in Figure 3.46), particularly after exposure in low UV environments where significant chalking is avoided. Evidence of residual barrier protection afforded to the AA2024-T351 substrate by the MgRP primer polymer after 1000 hours of exposure in ASTM B-117 with 5% NaCl and in ASTM B-117 with ASTM artificial seawater is provided by elevated low-frequency Bode electrochemical impedance (at 0.01 Hz) shown in Figure 3.49 as compared to that of bare abraded AA2024-T351. Moreover, interface corrosion under the MgRP is not seen in SEM cross-section (Figure 3.18, Figure 3.27, Figure 3.35, and Figure 3.43). Additionally, any unoxidized Mg pigment that remains in the MgRP after the MgRP has been largely depleted of Mg pigment and has lost most of its remote protection capability (as evidenced by XRD in Figure 3.46 and a more positive global galvanic protection

potential shown in Figure 3.47) is likely available for the protection of proximate localized defects

3.5.4 Anodic Undermining and Cathodic Corrosion

The MgRP coating system must provide adequate cathodic protection to the AA2024-T351 substrate, but also avoid the detrimental effects of cathodic corrosion of the amphoteric AA2024-T351 substrate and of anodic undermining (or scribe creep) of the coating polymer at coating defect sites. In the case of early generation MgRP-coated AA2024-T351 studied in the past[10], cathodic corrosion of the AA2024-T351 substrate was caused by increased localized pH due to severe cathodic polarization and/or excessive Mg pigment dissolution. [8, 10, 53-55, 57-60] Anodic undermining (scribe creep) of early generation MgRP-coated AA2024-T351 studied in the past was observed and proposed to be caused by a classical mechanism, often associated with organic polymer coatings, involving anodic disbondment of the organic polymer [91, 92]. The primary mechanism for this phenomenon on aluminum alloys, particularly those containing Cu such as AA2024, has been proposed to be anodic coating disbondment through anodic undermining aided in this case by H_2 production. In contrast to similar environmental exposures of earlier generation commercial products in the past[8, 10], no indications of cathodic corrosion, as evidenced by narrow pinholes, or underpaint corrosion or anodic undermining, as evidenced by large areas of coating delamination above regions of Al corrosion, are visible at the coating/metal interface when viewed in SEM cross-section after environmental exposure in these field and laboratory environments. These observations are summarized in Table 3.6.

3.6 Conclusions

- Full immersion in ambiently aerated 5% NaCl solution, ASTM B-117 in 5% NaCl and ASTM B-117 in ASTM artificial seawater deplete the MgRP of metallic Mg pigment at approximately equal rates, with significant depletion of Mg pigment occurring mainly by self-corrosion owing to the absence of a topcoat after approximately 1000 h of exposure. Field exposures in Charlottesville, VA and Kennedy Space Center, FL resulted in significant depletion of metallic Mg pigment after 2000 and 4000 h of exposure respectively indicating acceleration factors of about 2 and 4.

- The gobal galvanic protection potential of the coating system, with respect to remote scratches, became more positive with exposure time in each environment, from values approximately equal to that of bare Mg (-1.6 V vs. SCE) to those approximately equal to that of bare AA2024-T351 (-0.55 V vs. SCE). It was found that this rise took approximately 300 hours in full immersion in ambiently aerated 5% NaCl solution, ASTM B-117 in 5% NaCl, and in ASTM B-117 with ASTM artificial seawater and approximately 1000 h in the field at Charlottesville, VA and Kennedy Space Center, FL. The acceleration factors, with respect to global galvanic protection potential, observed for field exposure versus the full immersion and salt fog cabinet exposures were approximately 3:1.

- Residual barrier properties of the MgRP with an initial MgPVC of 45% coating system also degrade with time in each environment. However, similar to other investigations[12], corrosion under the residual coating polymer after Mg pigment depletion was not observed. Therefore the primer provides some residual barrier protection.

- SEM/EDS after 1000 h of salt fog exposure indicate a throwing power that extended the entire half-width (≈ 350 μm) of the scribe in both standard and modified ASTM B-117 exposures with thin-layer electrolyte geometries and continuous wetting. A significant thickness of primer polymer was shown to remain after 1000 hours in both environments.

- SEM/EDS after 24 weeks of exposure in the field at Kennedy Space Center, FL indicates a throwing power that extends approximately 200 - 300 μm in the scribe from the coating edge. A significant thickness of primer polymer was shown to be damaged after 24 weeks of exposure at Kennedy Space Center, FL.

- SEM/EDS after 24 weeks of exposure in the field at Charlottesville, VA was inconclusive due to the likely dissolution of the MgRP coating by self-corrosion and subsequent corrosion products by high TOW and low pH rain (pH ≈ 5,Table 3.1). A significant thickness of primer polymer was shown to be damaged after 24 weeks of exposure at Birdwood Golf Course in Charlottesville, VA.

- It is likely that there still exists a small amount (less than 5% PVC) of encapsulated metallic Mg pigment dispersed through any residual polymer coating that remains after environmental exposure. This is particularly likely in samples that are not exposed to environments without significant UV, such as in ASTM B-117 salt spray testing, where it was observed that the polymer does not degrade as readily.

- The differences in rate-of-change of Mg depletion from the coating are presumed to stem from differences in time-of-wetness and in rates of polymer degradation, specifically resistivity, due to UV exposure. Differences in throwing power in lab and field

environments are presumed to stem from differences in electrolyte geometries; continuous thin-layer in salt fog cabinet exposures and droplet geometries in field exposures.

- No indications of cathodic corrosion, as evidenced by narrow pinholes, or underpaint corrosion or anodic undermining, as evidenced by large areas of coating delamination above regions of Al corrosion, were visible at the coating/metal interface when viewed in SEM cross-section after environmental exposure in these field and laboratory environments.

3.7 Acknowledgements

This work was supported by the OUSD Corrosion University Pilot Program under the direction of Mr. Daniel Dunmire. Members of NAVAIR[1] and Battelle Memorial Institute[2] are acknowledged for graciously conducting field exposures at Kennedy Space Center, FL and for the generous supply and preparation of MgRP-coated AA2024-T351 panels specifically: Mr. Craig Matzdorf[1], Mr. Frank Pepe[1], Mr. Jerry Curran[1] and Mr. William Abbott[2]. Dr. Jason Lee of the US Naval Research Lab is acknowledged for helpful discussions regarding throwing power.

3.8 References

1. S. S. Pathak, M. D. Blanton, S. K. Mendon and J. W. Rawlins, Investigation on dual corrosion performance of magnesium-rich primer for aluminum alloys under salt spray test (ASTM B117) and natural exposure, Corros Sci, 52, 4 (2010), pp. 1453-1463.
2. G. P. Bierwagen, D. E. Tallman, M. Nanna, D. Battocchi, A. Stamness and V. J. Gelling, New developments in Cr-free primers for aerospace alloys., Abstr Pap Am Chem S, 228, (2004), pp. U360-U360.

3. A. Simoes, D. Battocchi, D. Tallman and G. Bierwagen, Assessment of the corrosion protection of aluminium substrates by a Mg-rich primer: EIS, SVET and SECM study, Prog Org Coat, 63, 3 (2008), pp. 260-266.
4. D. Battocchi, A. M. Simoes, D. E. Tallman and G. P. Bierwagen, Comparison of testing solutions on the protection of Al-alloys using a Mg-rich primer, Corros Sci, 48, 8 (2006), pp. 2226-2240.
5. D. Battocchi, A. M. Simoes, D. E. Tallman and G. P. Bierwagen, Electrochemical behaviour of a Mg-rich primer in the protection of Al alloys, Corros Sci, 48, 5 (2006), pp. 1292-1306.
6. H. Xu, D. Battocchi, D. E. Tallman and G. P. Bierwagen, Use of Magnesium Alloys as Pigments in Magnesium-Rich Primers for Protecting Aluminum Alloys, Corrosion, 65, 5 (2009), pp. 318-325.
7. G. Bierwagen, D. Battocchi, A. Simoes, A. Stamness and D. Tallman, The use of multiple electrochemical techniques to characterize Mg-rich primers for A1 alloys, Prog Org Coat, 59, 3 (2007), pp. 172-178.
8. A. D. King and J. R. Scully, Sacrificial Anode-Based Galvanic and Barrier Corrosion Protection of 2024-T351 by a Mg-Rich Primer and Development of Test Methods for Remaining Life Assessment, Corrosion, 67, 5 (2011), pp. 05500401-05500422.
9. B. Maier and G. S. Frankel, Behavior of Magnesium-Rich Primers on AA2024-T3, Corrosion, 67, 5 (2011), p. 055001.
10. A. D. King and J. R. Scully, Blistering Phenomena in Early Generation Mg-Rich Primer Coatings on AA2024-T351 and the Effects of CO_2, NACE DoD 2011 Conference Proceedings, (Palm Springs, CA, 2011).
11. J. Nie, M. C. Yan, J. Wang, D. E. Tallman, D. Battocchi and G. P. Bierwagen, Cathodic Corrosion Protection Performance of Mg-Rich Primers: Effect of Pigment Shape and Pigment Volume Concentration, ECS Transactions, 24, 1 (2010), pp. 261-275.
12. W. H. Abbott, Performance of Chrome-Free Paint Systems In Field and Lab Environments: Summary of 4+ Years of Flight and Ground Exposures, NACE DoD 2011 Conference Proceedings, (Palm Springs, CA, 2011).
13. W. H. Abbott, A Decade of Corrosion Monitoring in the World's Military Operating Environments - A Summary of Results, (2009).
14. W. H. Abbott, H. O. Pate and F. Fernandez, Acceleration Factors For Severe Outdoor Exposures vs. Flight on Military Aircraft, NACE DoD 2013 Cyber Conference Proceedings, 2013).
15. U.S. Department of Health and Human Services., Report on Carcinogens, 12th Edition, U.S. Department of Health and Human Services, Public Health Services, National Toxicology Program, 2011.
16. R. G. Buchheit, Chromate and Chromate-Free Conversion Coatings, vol. 13A, ASM Handbook Volume 13A, Corrosion: Fundamentals, Testing, and Protection (ASM International) (Materials Park, Ohio, ASM International, 2003).
17. G. Bierwagen, R. Brown, D. Battocchi and S. Hayes, Active metal-based corrosion protective coating systems for aircraft requiring no-chromate pretreatment, Prog Org Coat, 67, 2 (2010), pp. 195-208.

18. W. H. Abbott, Personal correspondence with Mr. William Abbott of Battelle Memorial Institute, (2009).
19. C. Matzdorf, Personal correspondence with Mr. Craig Matzdorf of NAVAIR, (2009).
20. A. D. King and J. R. Scully, Environmental Degradation of a Mg-Rich Primer in Selected Field and Laboratory Environments - Part II. Primer and Topcoat, Corrosion Journal, accepted, (2013).
21. P. J. Adams, Personal correspondence with Dr. Pat J. Adams of AkzoNobel Aerospace Coatings Inc., (2011).
22. W. Funke, Mechanisms of Protecting Metals by Organic Coatings against Corrosion, J Electrochem Soc, 133, 8 (1986), pp. C304-C304.
23. Z. W. Wicks, Organic coatings : science and technology, 3rd, vol. (Hoboken, N.J.: Wiley-Interscience, 2007), p. xxiii, 722 p.
24. A. Forsgren, Corrosion control through organic coatings, Corrosion technology, vol. (Boca Raton, FL: CRC/Taylor & Francis, 2006), p. 161 p.
25. S. Feliu, R. Barajas, J. M. Bastidas and M. Morcillo, Ac Impedance Study About the Protection Mechanisms of Zinc-Rich Primers, Abstr Pap Am Chem S, 195, (1988), pp. 58-Pmse.
26. D. Pereira, J. D. Scantlebury, M. G. S. Ferreira and M. E. Almeida, The Application of Electrochemical Measurements to the Study and Behavior of Zinc-Rich Coatings, Corros Sci, 30, 11 (1990), pp. 1135-1147.
27. S. Feliu, M. Morcillo and S. Feliu, Deterioration of cathodic protection action of zinc-rich paint coatings in atmospheric exposure, Corrosion, 57, 7 (2001), pp. 591-597.
28. V. M. Rudoi, O. V. Yaroslavtseva, T. N. Ostanina, L. P. Yurkina and O. Y. Subbotina, Electrochemical behavior of protective anodic primers, Protection of Metals, 35, 3 (1999), pp. 277-281.
29. H. Marchebois, C. Savall, J. Bernard and S. Touzain, Electrochemical behavior of zinc-rich powder coatings in artificial sea water, Electrochim Acta, 49, 17-18 (2004), pp. 2945-2954.
30. C. M. Abreu, M. Izquierdo, M. Keddam, X. R. Novoa and H. Takenouti, Electrochemical behaviour of zinc-rich epoxy paints in 3% NaCl solution, Electrochim Acta, 41, 15 (1996), pp. 2405-2415.
31. S. G. Real, A. C. Elias, J. R. Vilche, C. A. Gervasi and A. Disarli, An Electrochemical Impedance Spectroscopy Study of Zinc Rich Paints on Steels in Artificial Sea-Water by a Transmission-Line Model, Electrochim Acta, 38, 14 (1993), pp. 2029-2035.
32. C. M. Abreu, M. Izquierdo, X. R. Novoa, C. Perez and A. Sanchez, Influence of different aggressive media on the protective behaviour of zinc rich paints, Rev Metal Madrid, 35, 3 (1999), pp. 182-189.
33. N. V. Kondrashova, S. A. Nesterenko, O. V. Naumenko and L. I. Antropov, Influence of Zinc and Magnesium Cations on the Electrochemical-Behavior of Steel with a Polymer Primer, Protection of Metals, 25, 1 (1989), pp. 73-75.

34. S. Feliu, R. Barajas, J. M. Bastidas and M. Morcillo, Mechanism of Cathodic Protection of Zinc-Rich Paints by Electrochemical Impedance Spectroscopy .1. Galvanic Stage, J Coating Technol, 61, 775 (1989), pp. 63-69.
35. S. Feliu, R. Barajas, J. M. Bastidas and M. Morcillo, Mechanism of Cathodic Protection of Zinc-Rich Paints by Electrochemical Impedance Spectroscopy .2. Barrier Stage, J Coating Technol, 61, 775 (1989), pp. 71-76.
36. C. M. Abreu, M. Izquierdo, P. Merino, X. R. Novoa and C. Perez, A new approach to the determination of the cathodic protection period in zinc-rich paints, Corrosion, 55, 12 (1999), pp. 1173-1181.
37. M. Morcillo, R. Barajas, S. Feliu and J. M. Bastidas, A-Sem Study on the Galvanic Protection of Zinc-Rich Paints, J Mater Sci, 25, 5 (1990), pp. 2441-2446.
38. R. A. Armas, C. A. Gervasi, A. Disarli, S. G. Real and J. R. Vilche, Zinc-Rich Paints on Steels in Artificial Seawater by Electrochemical Impedance Spectroscopy, Corrosion, 48, 5 (1992), pp. 379-383.
39. H. Marchebois, M. Keddam, C. Savall, J. Bernard and S. Touzain, Zinc-rich powder coatings characterisation in artificial sea water - EIS analysis of the galvanic action, Electrochim Acta, 49, 11 (2004), pp. 1719-1729.
40. O. O. Knudsen, U. Steinsmo and M. Bjordal, Zinc-rich primers - Test performance and electrochemical properties, Prog Org Coat, 54, 3 (2005), pp. 224-229.
41. M. E. Nanna and G. P. Bierwagen, Mg-rich coatings: A new paradigm for Cr-free corrosion protection of al aerospace alloys, Jct Research, 1, 2 (2004), pp. 69-80.
42. G. Bierwagen, R. Fishman, T. Storsved and J. Johnson, Recent studies of particle packing in organic coatings, Prog Org Coat, 35, 1-4 (1999), pp. 1-9.
43. G. P. Bierwagen, A Reexamination of Cpvc as a Transition Point in Coatings Properties, Abstr Pap Am Chem S, 200, (1990), pp. 41-Pmse.
44. G. P. Bierwagen, Critical Pigment Volume Concentration (Cpvc) as a Transition Point in the Properties of Coatings, J Coating Technol, 64, 806 (1992), pp. 71-75.
45. G. P. Bierwagen, Cpvc Calculations, J Paint Technol, 44, 572 (1972), p. 28.
46. G. P. Bierwagen, Cpvc Calculations, J Paint Technol, 44, 574 (1972), p. 46.
47. G. P. Bierwagen and R. G. Mallinger, Comparison of Prediction and Experiment for the Critical Pigment Volume Concentration in Thermoplastic Coatings, J Coating Technol, 54, 690 (1982), pp. 73-73.
48. G. P. Bierwagen and D. C. Rich, The Critical Pigment Volume Concentration in Latex Coatings, Prog Org Coat, 11, 4 (1983), pp. 339-352.
49. K. N. Allahar, D. Battocchi, G. P. Bierwagen and D. E. Tallman, Transmission Line Modeling of EIS Data for a Mg-Rich Primer on AA 2024-T3, J Electrochem Soc, 157, 3 (2010), pp. C95-C101.
50. K. N. Allahar, D. Wang, D. Battocchi, G. P. Bierwagen and S. Balbyshev, Real-Time Monitoring of a United States Air Force Topcoat/Mg-Rich Primer System in ASTM B117 Exposure by Embedded Electrodes, Corrosion, 66, 7 (2010).
51. D. H. Wang, D. Battocchi, K. N. Allahar, S. Balbyshev and G. P. Bierwagen, In situ monitoring of a Mg-rich primer beneath a topcoat exposed to Prohesion conditions, Corros Sci, 52, 2 (2010), pp. 441-448.

52. S. S. Pathak, M. D. Blanton, S. K. Mendon and J. W. Rawlins, Carbonation of Mg powder to enhance the corrosion resistance of Mg-rich primers, Corros Sci, 52, 11 (2010), pp. 3782-3792.
53. H. Kaesche, Studies on the Corrosion of Aluminum, Zeitschrift für physikalische Chemie, 14, 7 (1963), pp. 557-566.
54. H. Kaesche, Zeitschrift für physikalische Chemie, 34, (1962), pp. 87-108.
55. M. Mokaddem, P. Volovitch, F. Rechou, R. Oltra and K. Ogle, The anodic and cathodic dissolution of Al and Al-Cu-Mg alloy, Electrochim Acta, 55, 11 (2010), pp. 3779-3786.
56. G. S. Frankel and Y. Baek, Electrochemical quartz crystal microbalance study of corrosion of phases in AA2024, J Electrochem Soc, 150, 1 (2003), pp. B1-B9.
57. S. M. Moon and S. I. Pyun, The corrosion of pure aluminium during cathodic polarization in aqueous solutions, Corros Sci, 39, 2 (1997), pp. 399-408.
58. S. I. Pyun and S. M. Moon, Corrosion mechanism of pure aluminium in aqueous alkaline solution, J Solid State Electr, 4, 5 (2000), pp. 267-272.
59. R. D. Armstrong and V. J. Braham, The mechanism of aluminium corrosion in alkaline solutions, Corros Sci, 38, 9 (1996), pp. 1463-1471.
60. M. Pourbaix, Atlas of electrochemical equilibria in aqueous solutions, 2d English, vol. (Houston, Tex.: National Association of Corrosion Engineers, 1974), p. 644.
61. D. Knotkova and K. Barton, Effects of Acid Deposition on Corrosion of Metals, Atmos Environ a-Gen, 26, 17 (1992), pp. 3169-3177.
62. W. W. Kirk, H. H. Lawson and American Society for Testing and Materials., Atmospheric corrosion, Stp, vol. (Philadelphia, PA: ASTM, 1995), p. vii, 280 p.
63. S. Feliu, M. Morcillo and S. Feliu, The Prediction of Atmospheric Corrosion from Meteorological and Pollution Parameters .1. Annual Corrosion, Corros Sci, 34, 3 (1993), pp. 403-414.
64. S. Feliu, M. Morcillo and S. Feliu, The Prediction of Atmospheric Corrosion from Meteorological and Pollution Parameters .2. Long-Term Forecasts, Corros Sci, 34, 3 (1993), pp. 415-422.
65. Astm, Standard Practice for Operating Salt Spray (Fog) Apparatus, ASTM B117 - 09, DOI: 10.1520/C0033-03, (2009).
66. J. Li, J. He, B. J. Chisholm, M. Stafslien, D. Battocchi and G. P. Bierwagen, An investigation of the effects of polymer binder compositional variables on the corrosion control of aluminum alloys using magnesium-rich primers, J Coat Technol Res, 7, 6 (2010), pp. 757-764.
67. Astm, Standard Practice for the Preparation of Substitute Ocean Water, ASTM D1141 - 98, DOI: 10.1520/D1141-98R08 (1998).
68. Astm, Standard Practice for Conducting Atmospheric Corrosion Tests on Metals, ASTM G50 - 76, DOI: 10.1520/D1141-98R08 (2003).
69. Astm, Standard Guide for Conducting Corrosion Tests in Field Applications, ASTM G4 - 01, DOI: 10.1520/G0004-01R08, (2001).
70. H. P. Hack and J. R. Scully, Defect Area Determination of Organic Coated Steels in Seawater Using the Breakpoint Frequency Method, J Electrochem Soc, 138, 1 (1991), pp. 33-40.

71. F. Mansfeld, Determination of the Reactive Area of Organic Coated Metals - Physical Meaning and Limits of the Break-Point Method - Discussion, Electrochim Acta, 39, 10 (1994), pp. 1451-1452.
72. A. Amirudin and D. Thierry, Application of electrochemical impedance spectroscopy to study the degradation of polymer-coated metals, Prog Org Coat, 26, 1 (1995), pp. 1-28.
73. J. E. B. Randles, Kinetics of rapid electrode reactions, Discussions of the Faraday Society, 1, (1947), pp. 11-19.
74. B. D. Cullity, Elements of x-ray diffraction, Addison-Wesley series in metallurgy and materials, 2d, vol. (Reading, Mass.: Addison-Wesley Pub. Co., 1978), p. xii, 555 p.
75. J. H. Hubbell and S. M. Seltzer, Tables of X-Ray Mass Attenuation Coefficients and Mass Energy-Absorption Coefficients from 1 keV to 20 MeV for Elements Z = 1 to 92 and 48 Additional Substances of Dosimetric Interest, NIST Standard Reference Database 126, vol. NIST Chemistry WebBook, 2004),
76. V. K. Pecharsky and P. Y. Zavalij, Fundamentals of powder diffraction and structural characterization of materials, 2nd, vol. (New York: Springer, 2009), p. xxiii, 741 p.
77. R. Castaing, Electron Probe Microanalysis, L. Marton and M. Claire, Eds., vol. Volume 13, Advances in Electronics and Electron Physics, Academic Press, 1960, p. 317-386).
78. N. W. M. Ritchie, DTSA-II Desktop Spectrum Analyzer Quantitative X-ray Microanalysis Software, vol. National Institute of Standards and Technology, 2012),
79. C. Deslouis, A. Doncescu, D. Festy, O. Gil, V. Maillot, S. Touzain and B. Tribollet, Kinetics and characterisation of calcareous deposits under cathodic protection in natural sea water, Electrochemical Methods in Corrosion Research Vi, Pts 1 and 2, 289-2, (1998), pp. 1163-1180.
80. C. Deslouis, D. Festy, O. Gil, G. Rius, S. Touzain and B. Tribollet, Characterization of calcareous deposits in artificial sea water by impedance techniques - I. Deposit of CaCO3 without Mg(OH)(2), Electrochim Acta, 43, 12-13 (1998), pp. 1891-1901.
81. R. A. Humble, Cathodic protection of steel in seawater with magnesium anodes, Corrosion, 4, (1948), pp. 358-370.
82. R. U. Lee and J. R. Ambrose, Influence of Cathodic Protection Parameters on Calcareous Deposit Formation, Corrosion, 44, 12 (1988), pp. 887-891.
83. F. G. Liu, S. R. Wu and C. S. Lu, Characterisation of calcareous deposits on freely corroding low carbon steel in artificial sea water, Corros Eng Sci Techn, 46, 5 (2011), pp. 611-617.
84. C. Rousseau, F. Baraud, L. Leleyter, M. Jeannin and O. Gil, Calcareous deposit formed under cathodic protection in the presence of natural marine sediments: A 12 month experiment, Corros Sci, 52, 6 (2010), pp. 2206-2218.
85. C. Barchiche, C. Deslouis, D. Festy, O. Gil, P. Refait, S. Touzain and B. Tribollet, Characterization of calcareous deposits in artificial seawater by impedance

techniques 3 - Deposit of CaCO3 in the presence of Mg(II), Electrochim Acta, 48, 12 (2003), pp. 1645-1654.

86. C. Deslouis, D. Festy, O. Gil, V. Maillot, S. Touzain and B. Tribollet, Characterization of calcareous deposits in artificial sea water by impedances techniques: 2-deposit of Mg(OH)(2) without CaCO3, Electrochim Acta, 45, 11 (2000), pp. 1837-1845.
87. F. Deflorian, L. Fedrizzi and P. L. Bonora, Determination of the Reactive Area of Organic Coated Metals Using the Breakpoint Method, Corrosion, 50, 2 (1994), pp. 113-119.
88. M. Kendig and J. Scully, Basic Aspects of Electrochemical Impedance Application for the Life Prediction of Organic Coatings on Metals, Corrosion, 46, 1 (1990), pp. 22-29.
89. J. R. Scully and S. T. Hensley, Lifetime Prediction for Organic Coatings on Steel and a Magnesium Alloy Using Electrochemical Impedance Methods, Corrosion, 50, 9 (1994), pp. 705-716.
90. J. D. Morrison, Report on Relative Corrosivity of Atmospheres at Various Distances from the Seacoast, 1980.
91. D. A. Little, M. A. Jakab and J. R. Scully, Effect of surface pretreatment on the underpaint corrosion of AA2024-T3 at various temperatures, Corrosion, 62, 4 (2006), pp. 300-315.
92. E. L. Koehler, U. R. Evans, B. F. Brown, J. Kruger, R. W. Staehle and National Association of Corrosion Engineers. Research Committee., Corrosion Under Organic Coatings, Localized Corrosion (Houston, Tex., National Association of Corrosion Engineers, 1974, p. 117-133).

3.9 Tables

Table 3.1.Exposure conditions in field and lab accelerated life testing environments.

Environment	Mean Temp (°C)				Mean RH (%)				Mean Dew Point (°C)			
	Win.	Spr.	Sum.	Fall	Win.	Spr.	Sum.	Fall	Win.	Spr.	Sum.	Fall
KSC	18.7	23.3	28.2	24.2	71.7	69.7	74	72.7	13.5	17.4	23.1	19
Birdwood	8.1	19.9	24	10.2	59.3	58.3	75.2	65.5	0.6	11	19.3	4
B-117	35				95				34			
B-117 w/ ASW	35				95				34			

Environment	Mean Precipitation (mm/hr)				Precip. pH	Mean Cl^- ($\mu g/cm^2/hr$)
	Win.	Spr.	Sum.	Fall		
KSC	0.066	0.154	0.245	0.184	5.4 ± 0.4	0.8
Birdwood	0.102	0.102	0.135	0.139	4.9 ± 0.3	0.002
B-117	0.190				6.9 ± 0.4	600
B-117 w/ ASW	0.190				8.2 ± 0.3	390

Table 3.2. Fitting results of EIS measured on AA2024-T351 panels coated with MgRP (MgPVC = 45%) after field exposure at Kennedy Space Center 30 m lot for 0, 2, 6, 12, and 24 weeks. Tested in ambiently aerated 5% NaCl Solution.

	units	0 wk	2 wk	6 wk	12 wk	24 wk
R_s	(Ω-cm^2)	10.000	10.000	10.000	10.000	10.000
C_{coat}-Y^o	($\mu F/cm^2$)	0.007	0.172	0.037	0.168	2.200
C_{coat}-n	-	0.357	0.703	0.790	0.723	0.774
R_{coat}	($k\Omega$-cm^2)	0.003	44.250	869.900	0.992	0.918
C_{dl}-Y^o	($\mu F/cm^2$)	0.005	0.969	0.167	7.790	14.820
C_{dl}-n	-	0.863	0.524	0.435	0.407	0.726
R_{corr}	($G\Omega$-cm^2)	10.000	10.000	10.000	10.000	10.000
F_{45}	(Hz)	0.04	21.31	0.68	10078.13	676.08
F_{saddle}	(Hz)	0.01	4.68	0.02	2159.93	≥100000

Table 3.3. Fitting results of EIS measured on AA2024-T351 panels coated with MgRP (MgPVC = 45%) after field exposure at Charlottesville, VA for 0, 2, 6, 12, and 24 weeks. Tested in ambiently aerated 5% NaCl Solution.

	units	0 wk	2 wk	6 wk	12 wk	24 wk
R_s	(Ω-cm^2)	10.000	10.000	10.000	10.000	10.000
C_{coat}-Y^o	(μF/cm^2)	0.007	0.257	1.328	4.361	7.932
C_{coat}-n	-	0.357	0.689	0.708	0.870	0.888
R_{coat}	(kΩ-cm^2)	0.003	8.917	0.450	0.017	0.033
C_{dl}-Y^o	(μF/cm^2)	0.005	3.272	1.321	28.020	63.440
C_{dl}-n	-	0.863	0.521	0.725	0.166	0.113
R_{corr}	(GΩ-cm^2)	10.000	0.002	0.001	0.065	0.083
F_{45}	(Hz)	0.04	2159.93	≥100000	≥100000	≥100000
F_{saddle}	(Hz)	0.01	158.49	≥100000	≥100000	≥100000

Table 3.4. Fitting results of EIS measured on AA2024-T351 panels coated with MgRP (MgPVC = 45%) after LALT in ASTM B-117 for 0, 168, 384, 744, and 984 hours. Tested in ambiently aerated 5% NaCl Solution.

	units	0 hrs	168 hrs	384 hrs	744 hrs	984 hrs
R_s	(Ω-cm^2)	10.000	10.000	10.000	10.000	16.920
C_{coat}-Y^o	(μF/cm^2)	0.007	0.318	0.451	1.087	6.856
C_{coat}-n	-	0.357	0.680	0.638	0.617	0.531
R_{coat}	(kΩ-cm^2)	0.003	67.070	26.460	17.280	4.038
C_{dl}-Y^o	(μF/cm^2)	0.005	1.971	5.700	4.162	44.390
C_{dl}-n	-	0.863	0.638	0.614	0.698	0.817
R_{corr}	(GΩ-cm^2)	10.000	10.000	10.000	10.000	0.000
F_{45}	(Hz)	0.04	217.01	1459.32	1459.32	21609.38
F_{saddle}	(Hz)	0.01	9.93	21.31	31.62	21.31

Table 3.5. Fitting results of EIS measured on AA2024-T351 panels coated with MgRP (MgPVC = 45%) after LALT in ASTM B-117 modified with artificial sea water for 0, 192, 408, 698 and 1000 hours. Tested in ambiently aerated 5% NaCl Solution.

	units	0 hrs	192 hrs	408 hrs	698 hrs	1000 hrs
R_s	(Ω-cm^2)	10.000	10.000	10.000	10.000	10.000
C_{coat}-Y^o	(μF/cm^2)	0.007	0.198	0.617	0.608	2.848
C_{coat}-n	-	0.357	0.696	0.630	0.629	0.572
R_{coat}	(kΩ-cm^2)	0.003	122.000	63.400	23.070	5.517
C_{dl}-Y^o	(μF/cm^2)	0.005	1.730	2.691	6.294	42.560
C_{dl}-n	-	0.863	0.570	0.783	0.674	0.540
R_{corr}	(GΩ-cm^2)	10.000	10.000	10.000	10.000	10.000
F_{45}	(Hz)	0.04	100.45	315.50	3170.96	4641.54
F_{saddle}	(Hz)	0.01	2.15	10.00	14.74	14.74

Table 3.6. Summary of observations made after environmental exposure in various environments.

Environment	UV?	Macroscopic Blistering	Underpaint Corrosion	Cathodic Corrosion	Throwing Power
Kennedy Space Center, FL – 24 wks	YES	NO	NO	NO	200 - 300 µm
Charlottesville, VA – 24 wks	YES	NO	NO	NO	n/a
ASTM B-117 w/ 5% NaCl – 1000 h	NO	NO	NO	NO	≥ 350 µm
ASTM B-117 w/ ASW – 1000 h	NO	NO	NO	NO	≥ 350 µm
Full Immersion in ambiently aerated 5% NaCl – 170 h	NO	NO	NO	NO	No scribe*

*a non-scribed area of MgRP-coated AA2024-T351 was exposed in a flat cell to 5% NaCl to study the representative global degradation of the coating. Follow up experiments include the same exposure and include variations in the area of bare AA2024-T351.

3.10 Figures

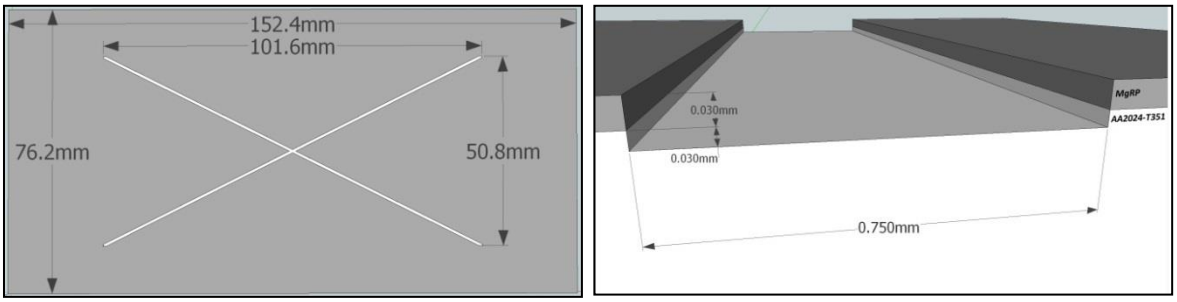

(a) (b)

Figure 3.1. Schematic of AA2024-T351 panels coated with Mg-rich primer coating.

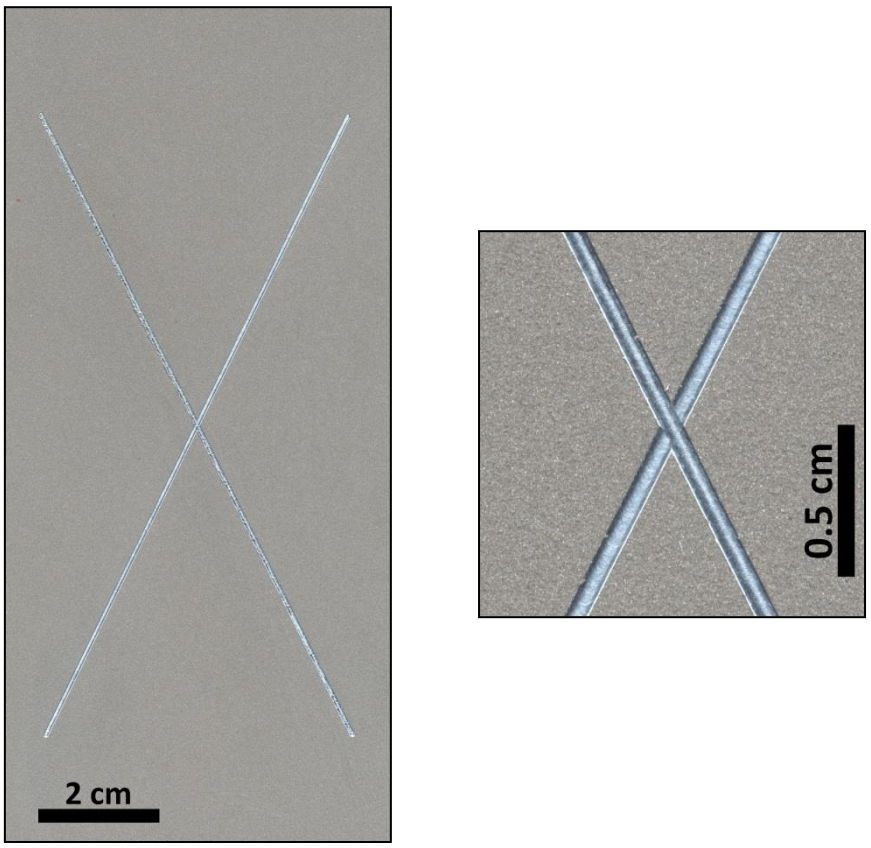

(a) (b)

Figure 3.2. Optical micrograph of AA2024-T351 panels coated with MgRP that have not been environmentally exposed.

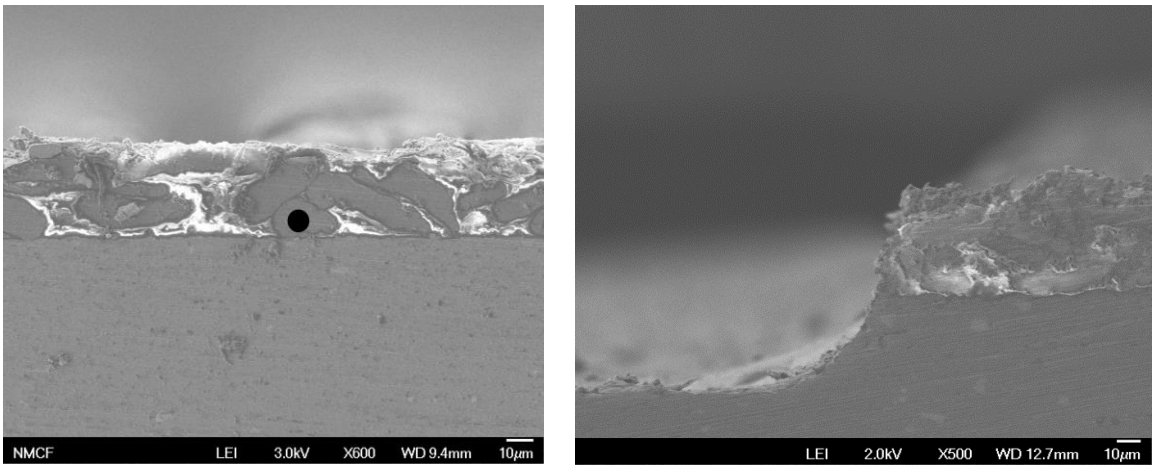

(a) (b)

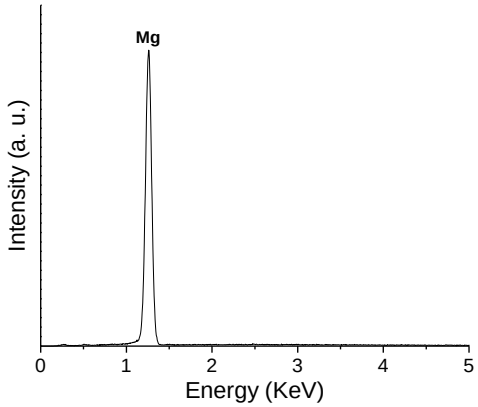

Figure 3.3. Cross-section SEM micrograph (a) far away from and (b) near the scribe and (c) EDS of MgRP (initial MgPVC = 45%) on AA2024-T351 pretreated with Prekote. Spot markers indicate approximate location of EDS analysis in (a).

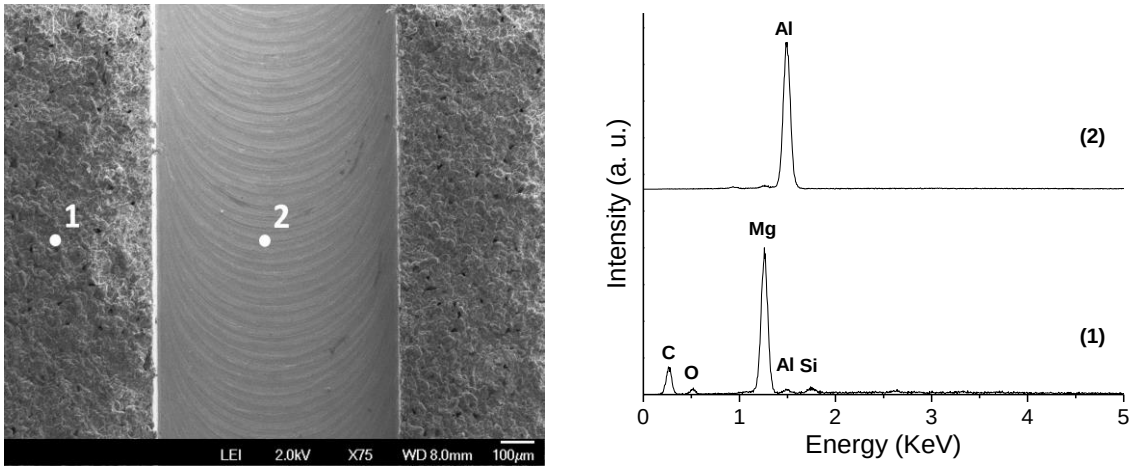

(a) (b)

Figure 3.4. Scanning electron micrograph (a) and EDS (b) of AA2024-T351 pretreated with Prekote and coated with MgRP (MgPVC = 45%) as applied before environmental exposure. Spot markers indicate approximate location of EDS analysis.

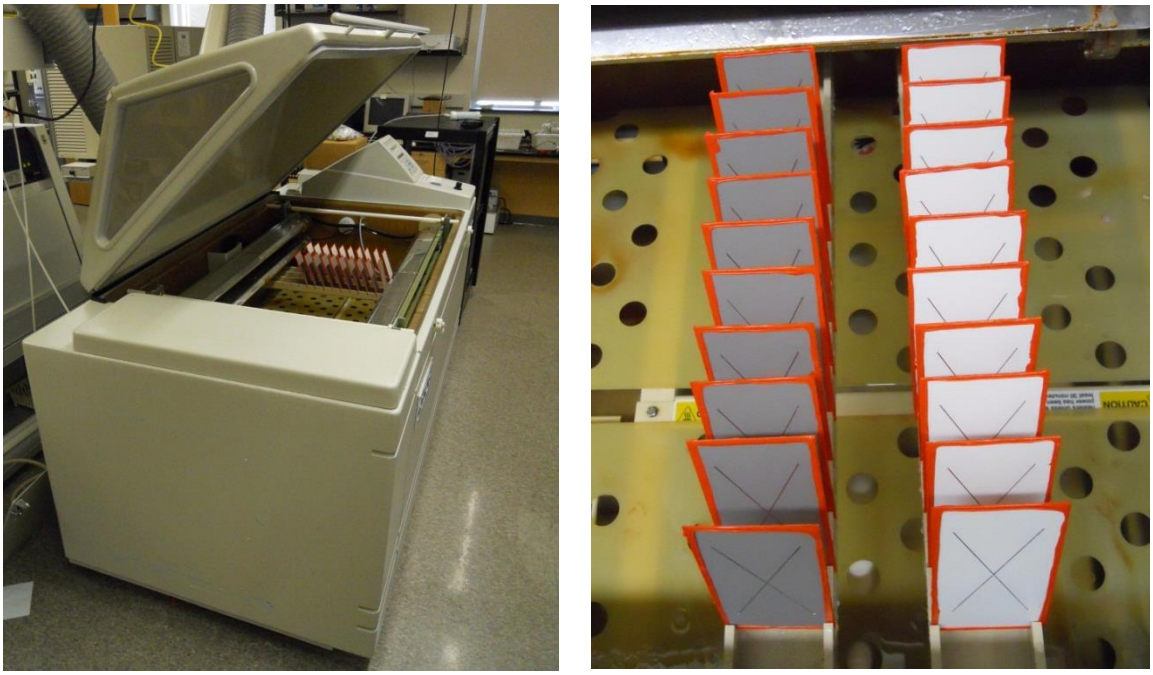

(a) (b)

Figure 3.5. Picture of (a) QFog Cyclic Corrosion Tester Model: CCT 1100 (b) MgRP-coated AA2024-T351 samples mounted for exposure in the QFog Cyclic Corrosion Tester at t = 0 hrs.

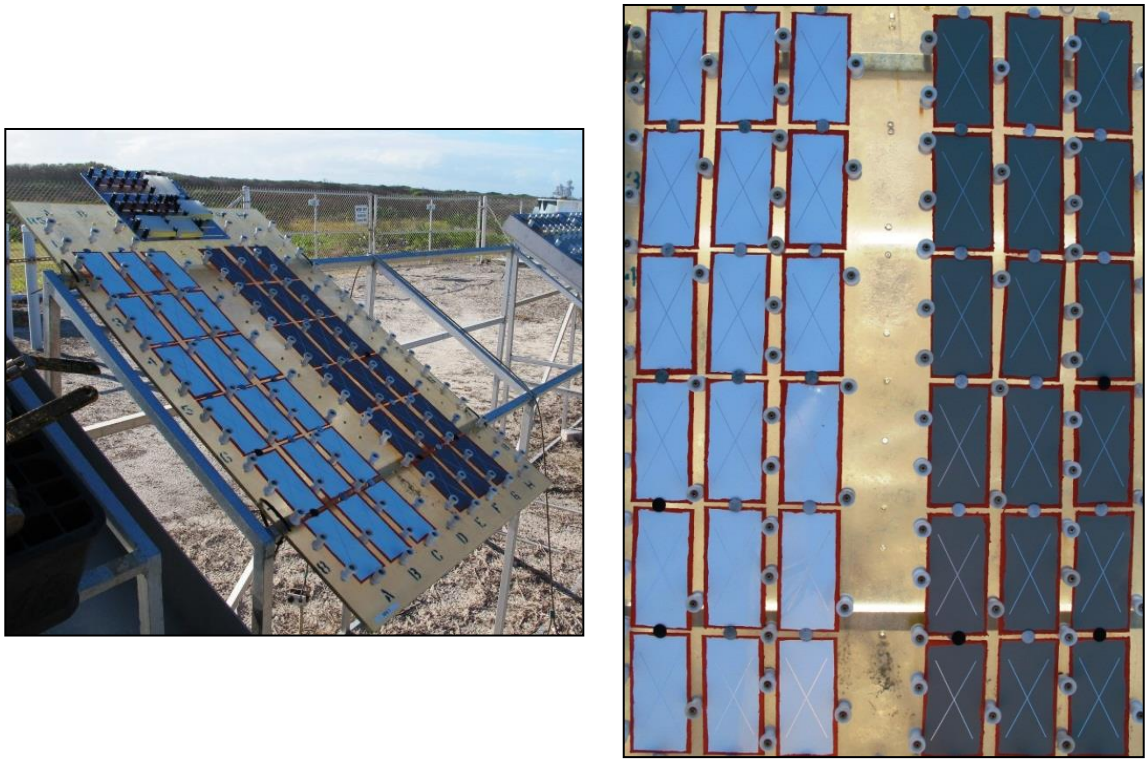

(a) (b)

Figure 3.6. Picture of (a) test rack and (b) MgRP-coated AA2024-T351 samples on exposure at Kennedy Space Center, FL 30 m site at t = 0 hrs. (28.59406ºN, 80.58283ºW, elevation = 0 m)

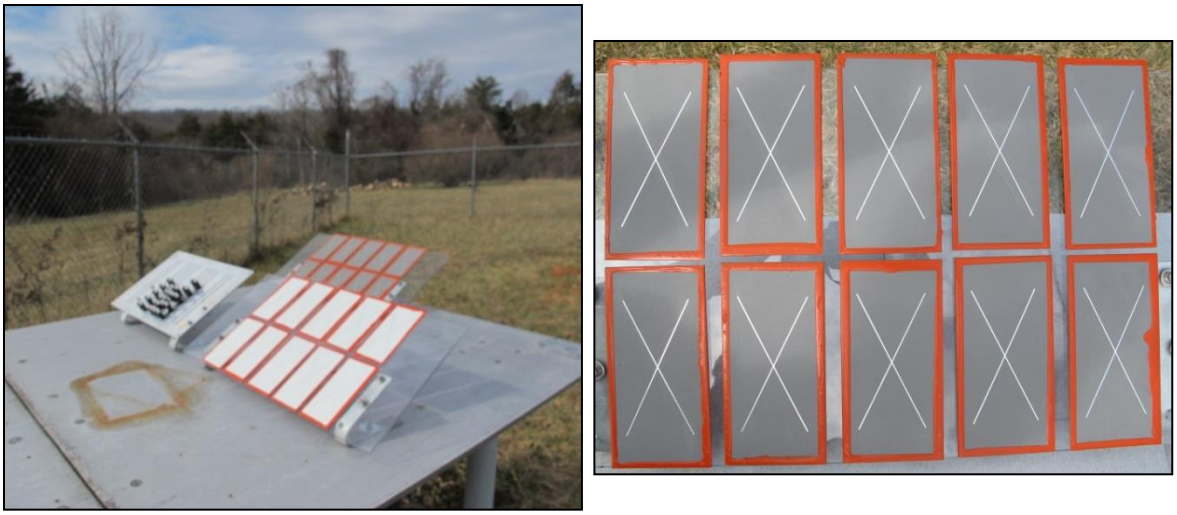

(a) (b)

Figure 3.7. Picture of (a) test rack and (b) MgRP-coated AA2024-T351 samples on exposure at Birdwood GC in Charlottesville, VA at t = 0 hrs. (38.0402ºN, 78.54.27ºW, elevation = 172 m)

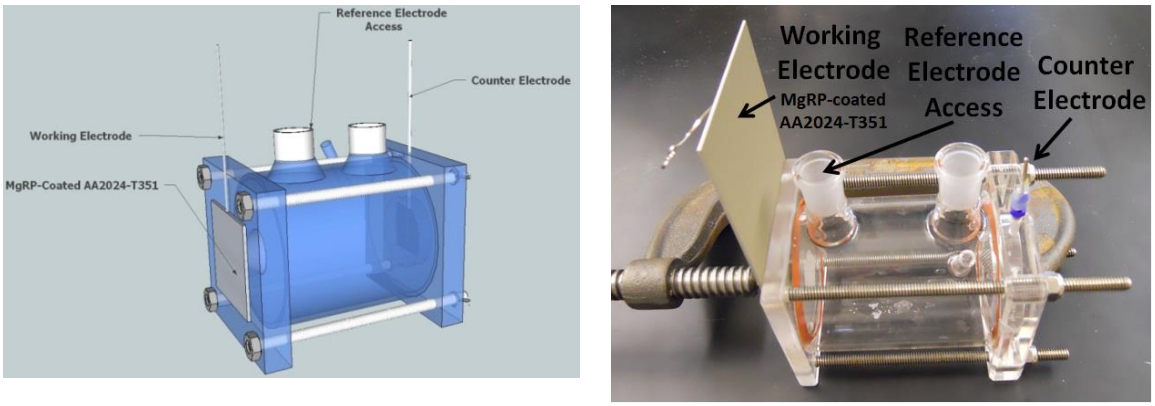

(a) (b)

Figure 3.8. Labeled (a) schematic and (b) picture of electrochemical flat cell with 1 cm^2 window used for full immersion exposure and post-mortem characterization.

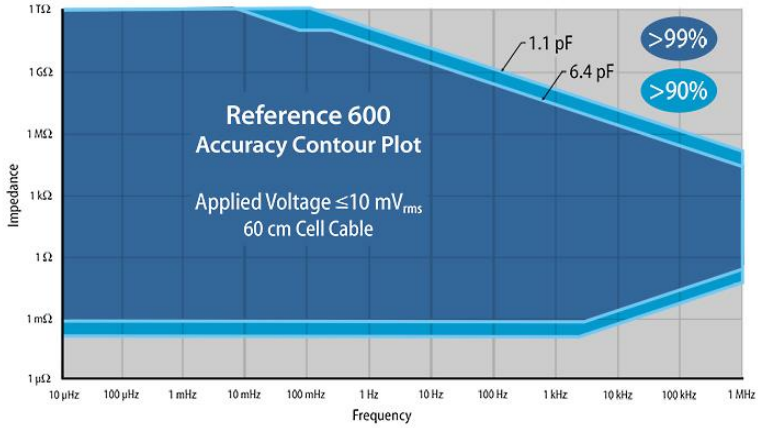

Figure 3.9. Measurement limits for the Gamry Reference 600 potentiostat/FRA instrumentation used for EIS measurements.

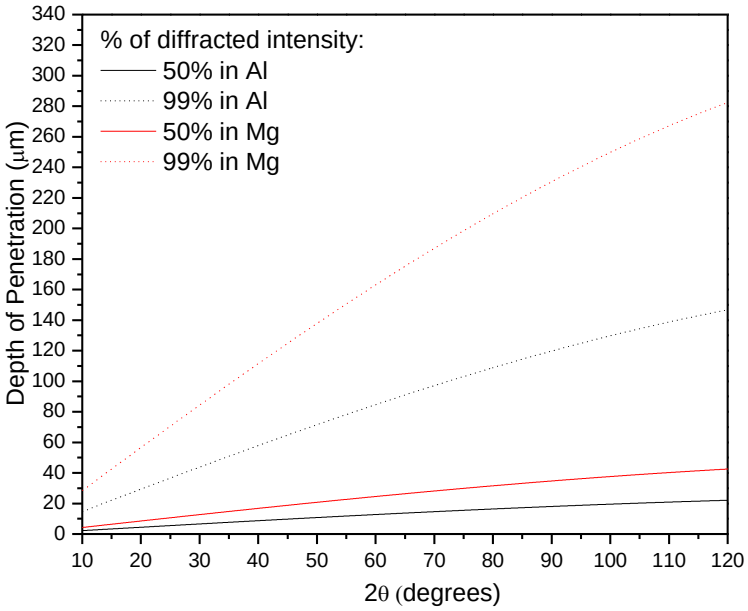

Figure 3.10. First-order approximation of XRD penetration depth as a function of 2θ in pure Al and pure Mg. The penetration depths responsible for 50% and 99% of the diffracted intensity are shown.

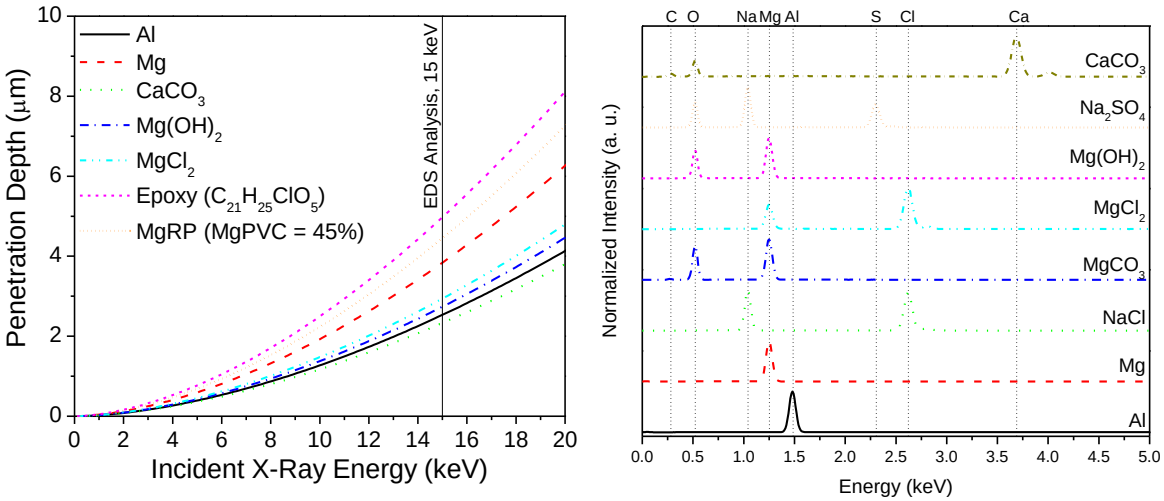

(a) (b)

Figure 3.11. (a) plot of first-order approximation[77] of EDS penetration depth in various materials (b). Simulated Energy dispersive X-ray (EDS) spectra for various bulk materials relevant to the MgRP/AA2024-T351 system and environmental exposure.[78]

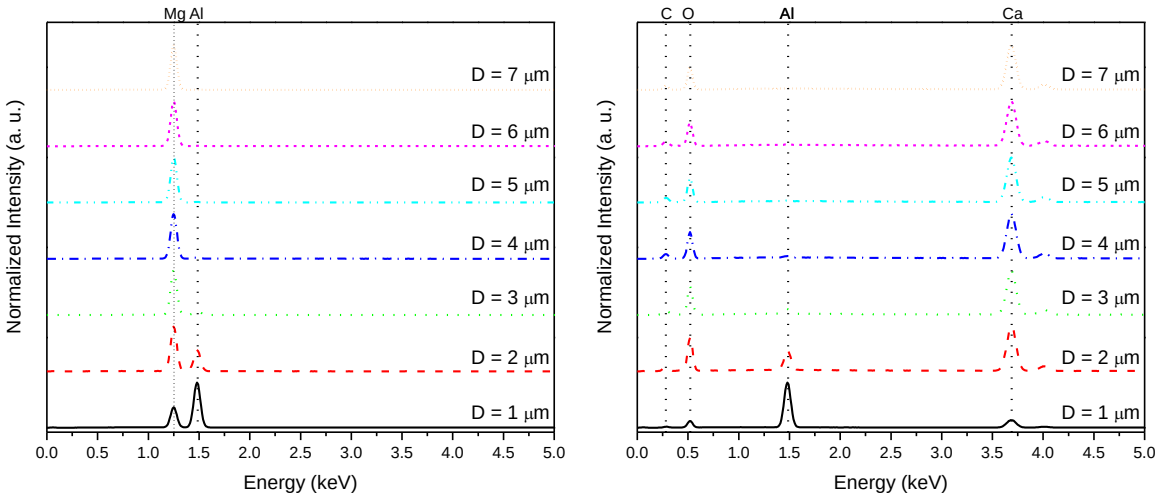

(a) (b)

Figure 3.12. Simulated Energy dispersive X-ray (EDS) spectra for a sphere of (a) metallic Mg and (b) $CaCO_3$ with various diameter, D, on top of a bulk substrate of Al.[78]

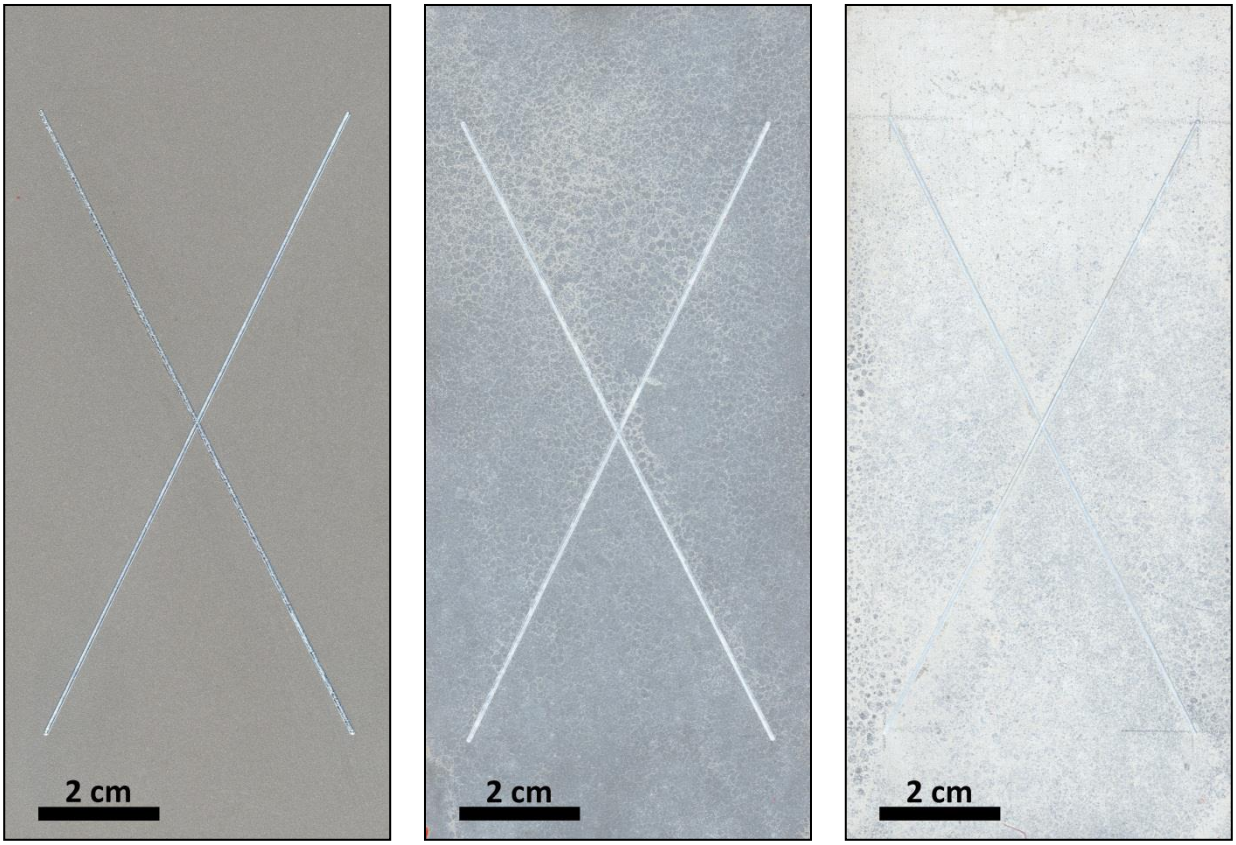

a) (b) (c)

Figure 3.13. Optical micrograph of AA2024-T351 panels coated with MgRP (initial MgPVC = 45%) that have been exposed at Kennedy Space Center at 30 m lot for (a) 0 weeks (b) 12 weeks (c) 24 weeks

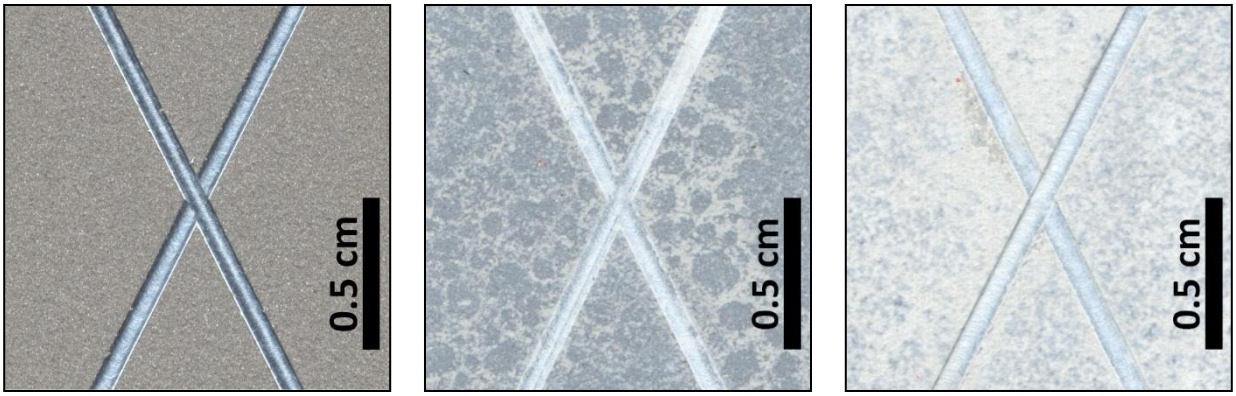

(a) T = 0 weeks in field at KSC

(b) T = 12 weeks in field at KSC

(c) T = 24 weeks in field at KSC

Figure 3.14. Optical micrograph of AA2024-T351 panels coated with MgRP (initial MgPVC = 45%) that have been exposed at Kennedy Space Center at 30 m lot for (a) 0 weeks (b) 12 weeks (c) 24 weeks

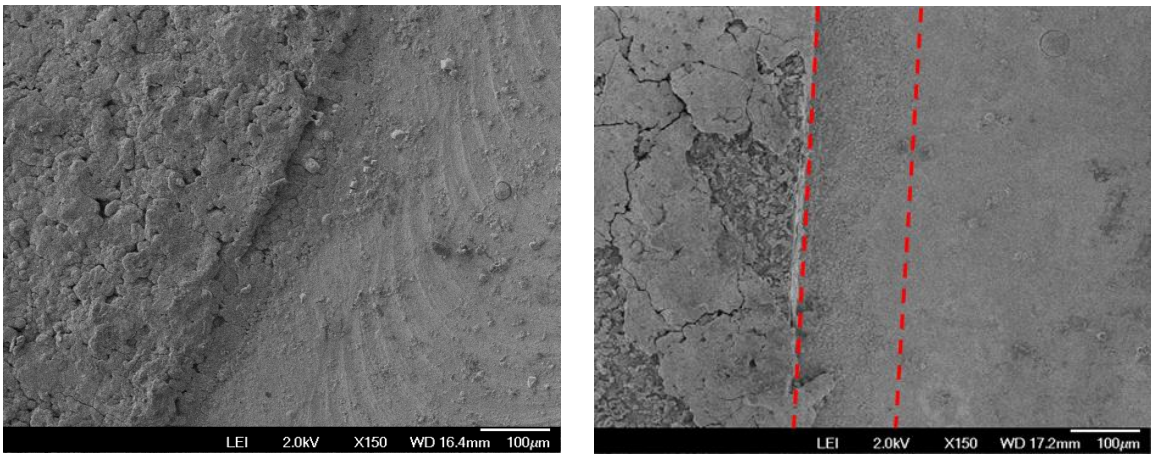

(a) (b)

Figure 3.15. Scanning electron micrograph of AA2024-T351 pretreated with Prekote and coated with MgRP (initial MgPVC = 45%) after environmental exposure in the field at KSC for (a) 12 weeks and (b) 24 weeks.

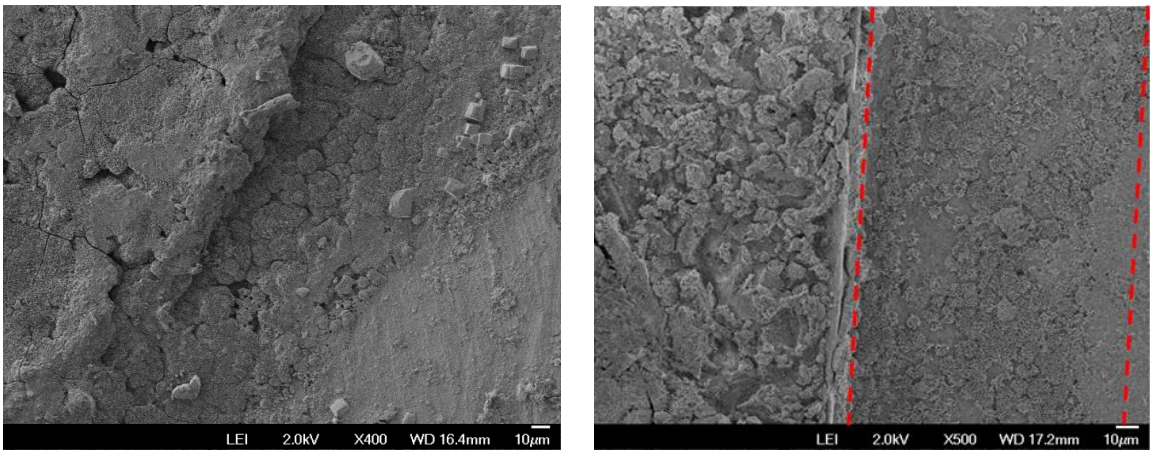

(a) (b)

Figure 3.16. Higher magnification scanning electron micrograph (planar view) of scribed AA2024-T351 pretreated with Prekote and coated with MgRP (initial MgPVC = 45%) after field exposure at Kennedy Space Center 30 m lot for (a) 12 weeks and (b) 24 weeks.

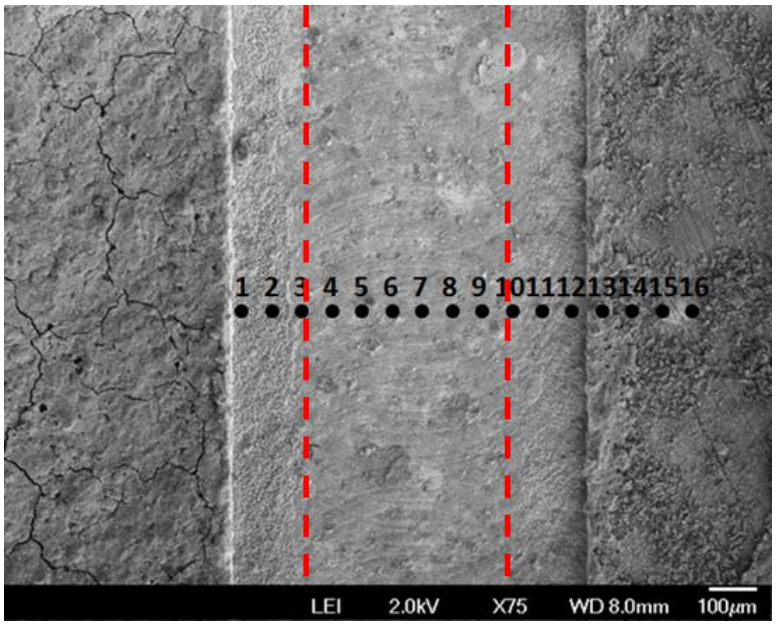

(a)

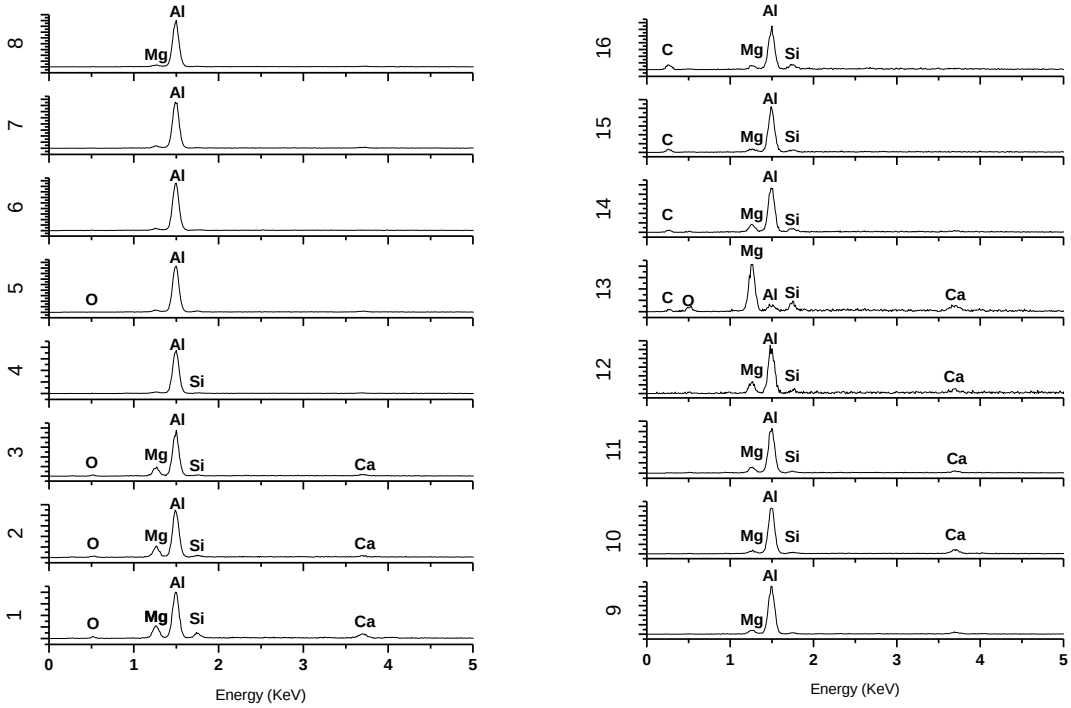

(b)

Figure 3.17. Planar-view SEM micrograph (a) of scribed AA2024-T351 pretreated with Prekote and coated with MgRP (initial MgPVC = 45%) after field exposure in the field at Kennedy Space Center, FL 30 m lot for 24 weeks. Spot markers indicate approximate location of EDS analysis shown in (b).

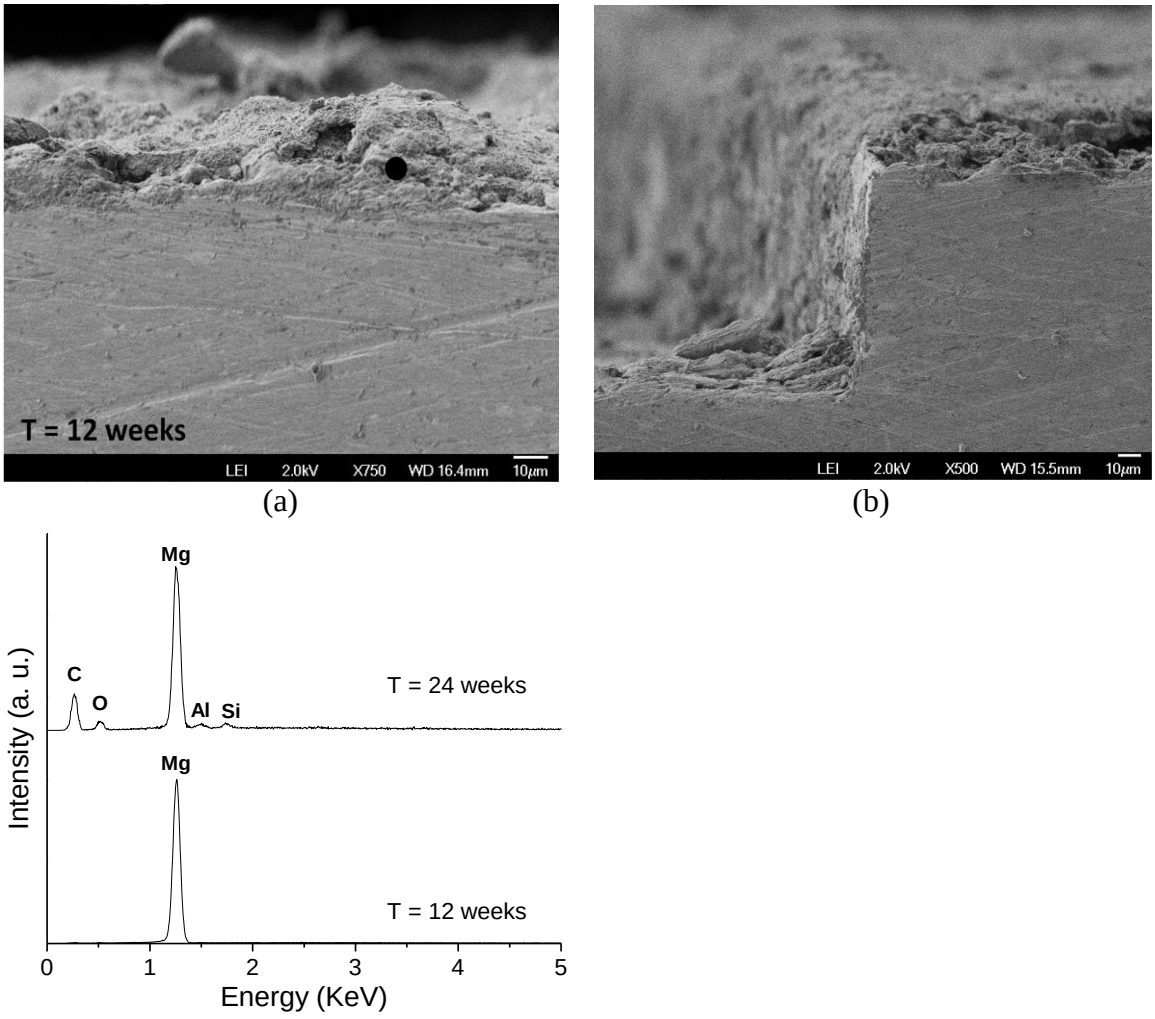

Figure 3.18. SEM micrograph (a) far away from and (b) near the scribe and (c) EDS of cross-sectioned MgRP (initial MgPVC = 45%) on AA2024-T351 pretreated with Prekote after field exposure at Kennedy Space Center, FL 30 m lot for 12 weeks. Spot markers in (a) indicate approximate location of EDS analysis shown in (c).

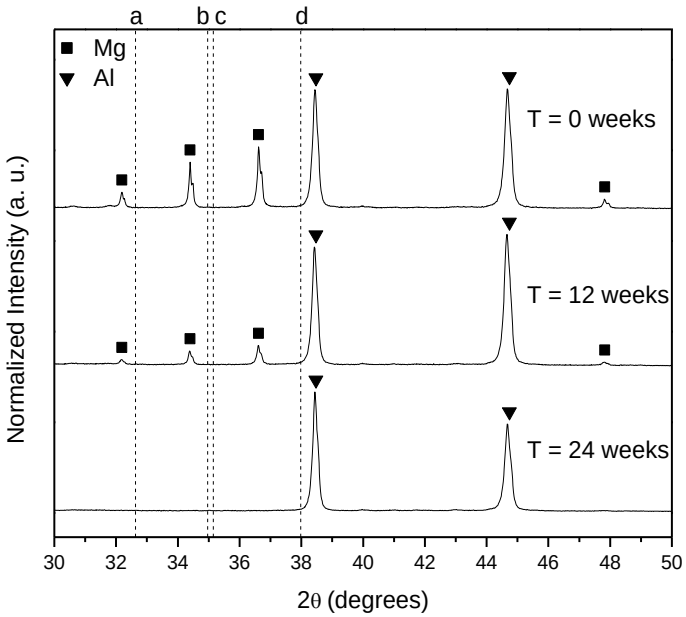

Figure 3.19. X-Ray diffraction spectra of AA2024-T351 panels coated with MgRP (initial MgPVC = 45%) after field exposure at Kennedy Space Center, FL 30 m lot for 0, 12, and 24 weeks. Dotted lines indicate the position of the most intense diffraction peak for (a) $MgCO_3$ (b) $MgCl_2$(c) Al_2O_3 and (d) $Mg(OH)_2$.

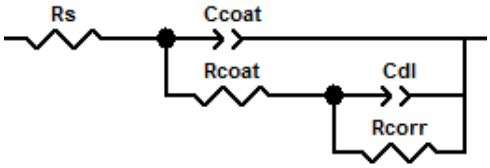

Figure 3.20. EIS equivalent circuit for a polymer coated metal used for fitting analysis.

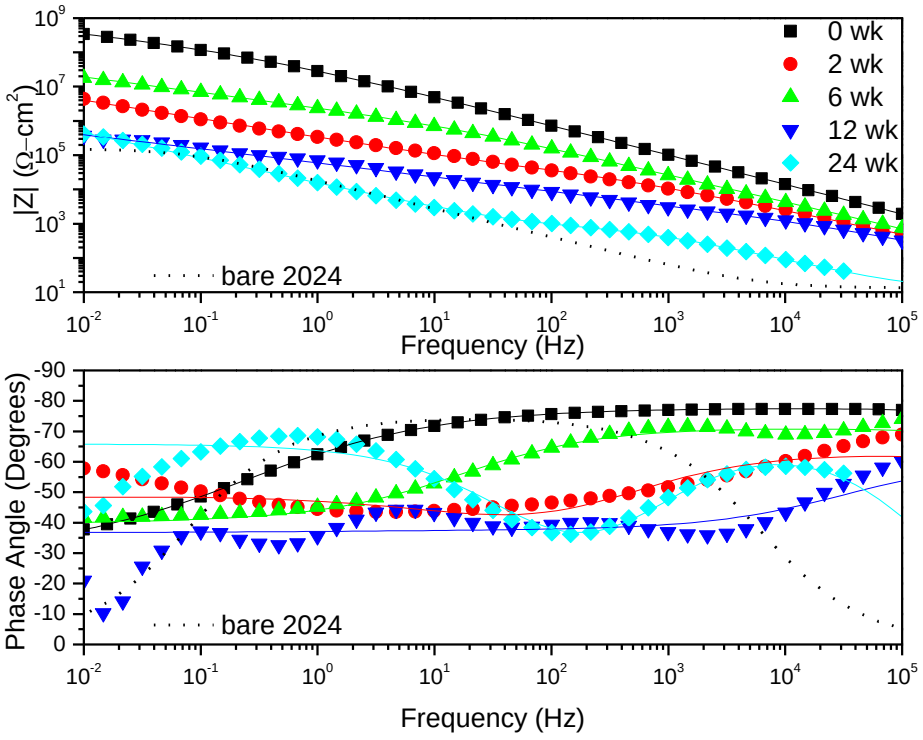

(a)

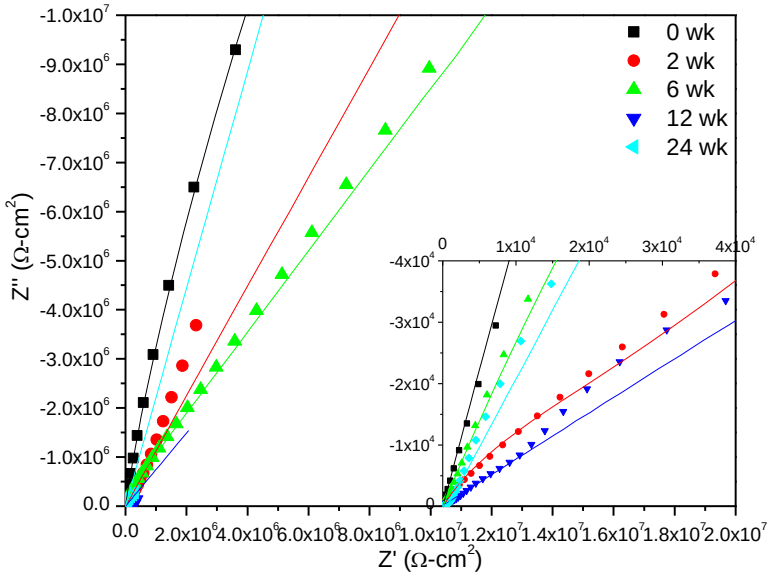

(b)

Figure 3.21. (a) Bode and (b) Nyquist plots of EIS of AA2024-T351 panels coated with MgRP (initial MgPVC = 45%) after field exposure at Kennedy Space Center, FL 30 m lot for 0, 2, 6, 12, and 24 weeks. Tested in ambiently aerated 5% NaCl solution. Fit results tabulated in Table 3.2.

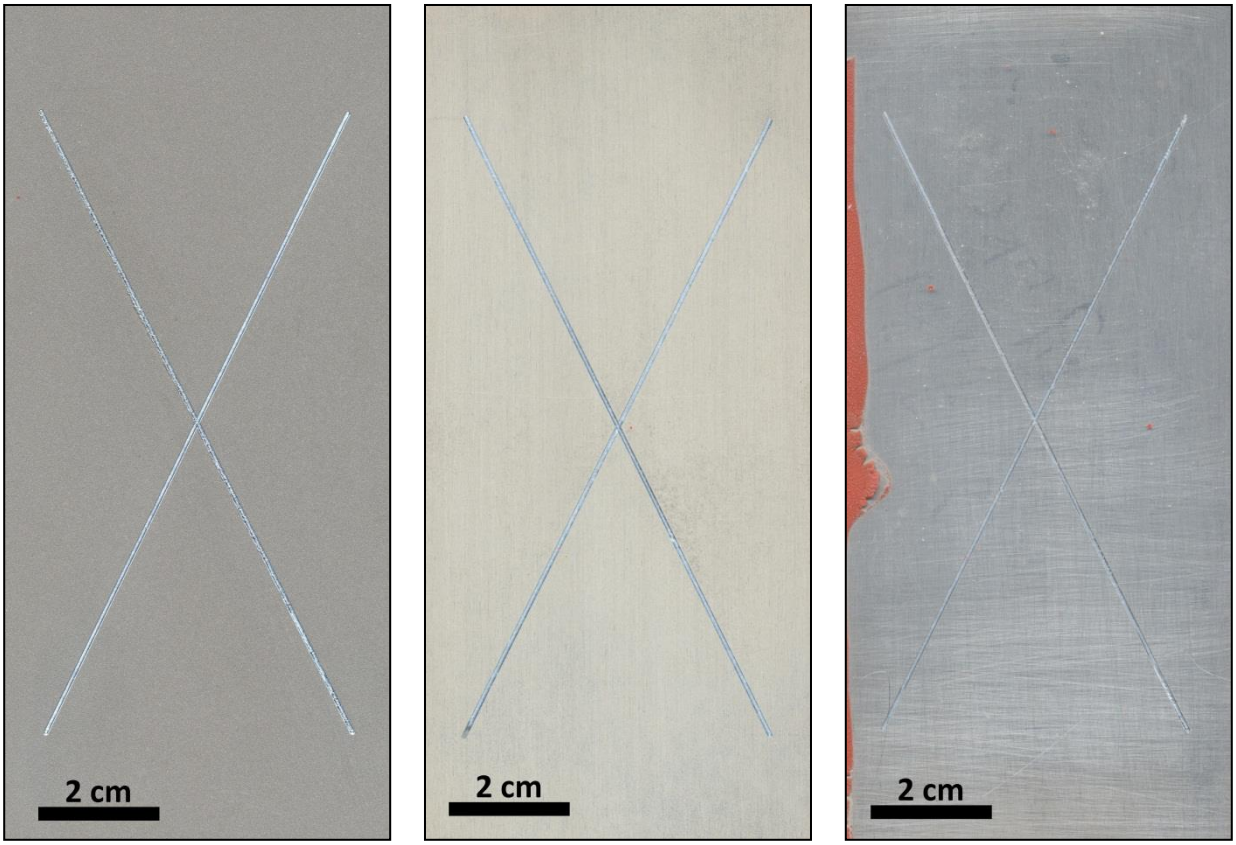

(a) (b) (c)

Figure 3.22. Optical micrograph of AA2024-T351 panels coated with MgRP (initial MgPVC = 45%) that have been exposed at Charlottesville, VA for (a) 0 weeks (b) 12 weeks and (c) 24 weeks.

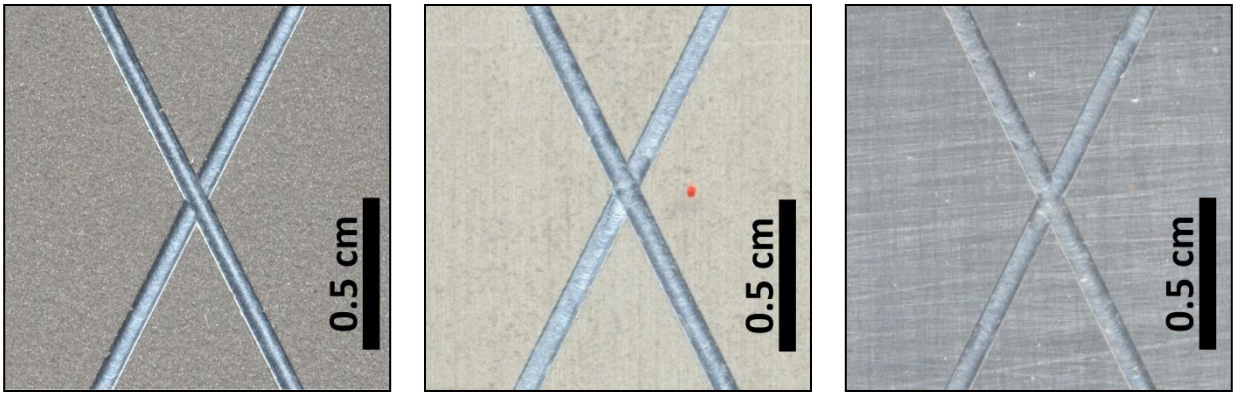

(a) T = 0 weeks in field at KSC

(b) T = 12 weeks in field at KSC

(c) T = 24 weeks in field at KSC

Figure 3.23. Optical micrograph of AA2024-T351 panels coated with MgRP (initial MgPVC = 45%) that have been exposed at Charlottesville, VA for (a) 0 weeks (b) 12 weeks and (c) 24 weeks.

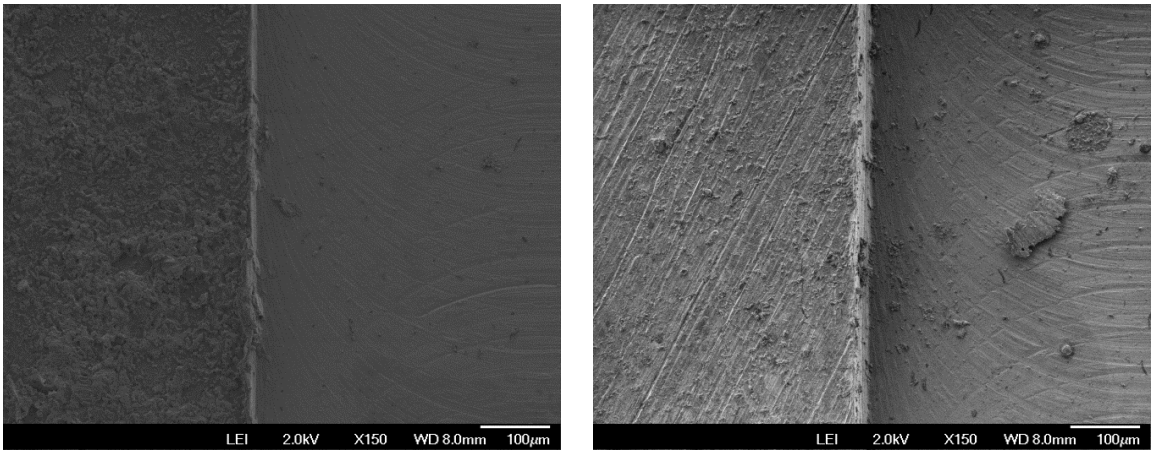

(a) (b)

Figure 3.24. Scanning electron micrograph of AA2024-T351 pretreated with Prekote and coated with MgRP (initial MgPVC = 45%) after environmental exposure in the field at Charlottesville, VA for (a) 12 weeks and (b) 24 weeks.

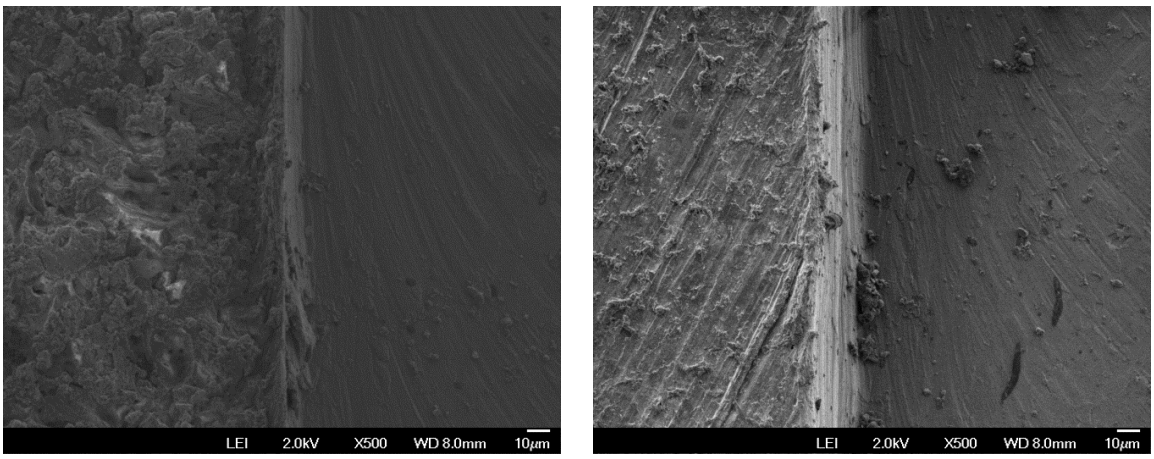

(a) (b)

Figure 3.25. Higher magnification scanning electron micrograph (planar view) of scribed AA2024-T351 pretreated with Prekote and coated with MgRP (initial MgPVC = 45%) after field exposure at Charlottesville, VA for (a) 12 weeks and (b) 24 weeks.

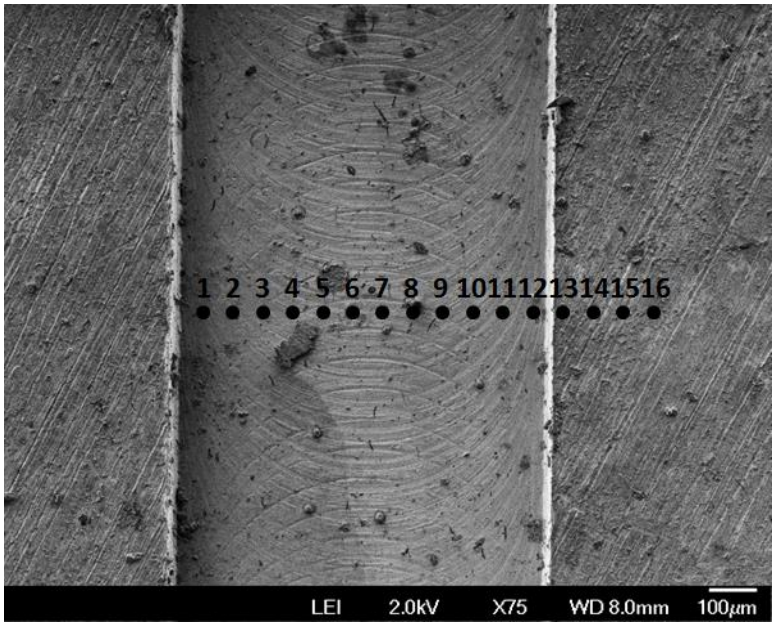

(a)

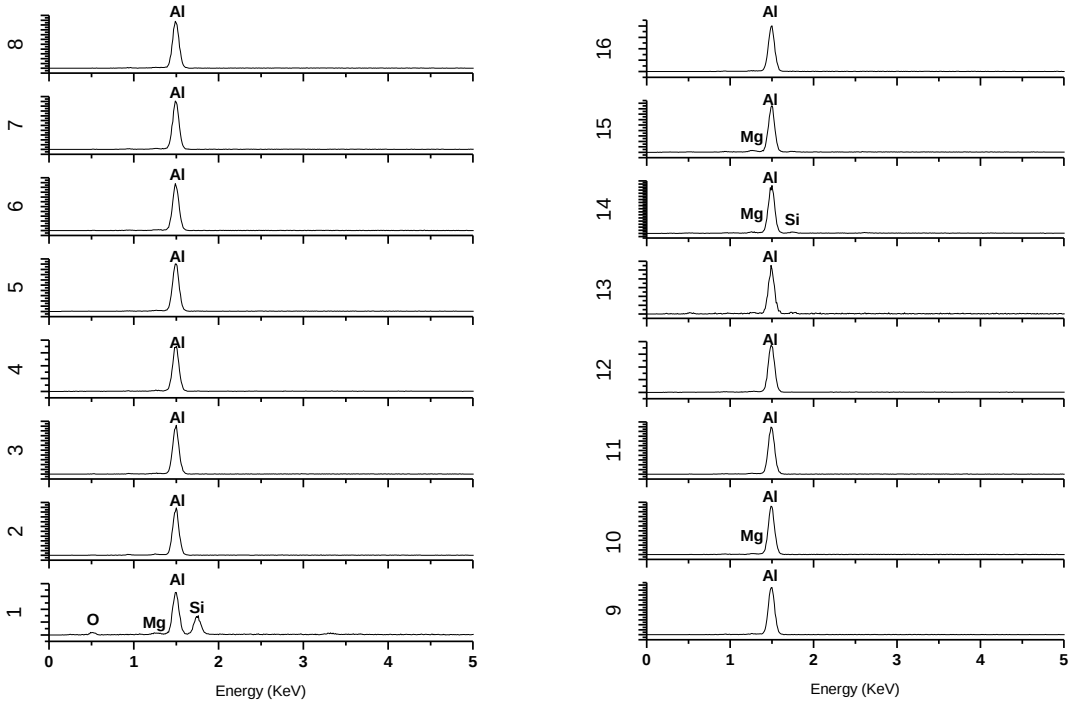

(b)

Figure 3.26. Planar-view SEM micrograph (a) of scribed AA2024-T351 pretreated with Prekote and coated with MgRP (initial MgPVC = 45%) after field exposure at Charlottesville, VA for 24 weeks. Spot markers indicate approximate location of EDS analysis shown in (b).

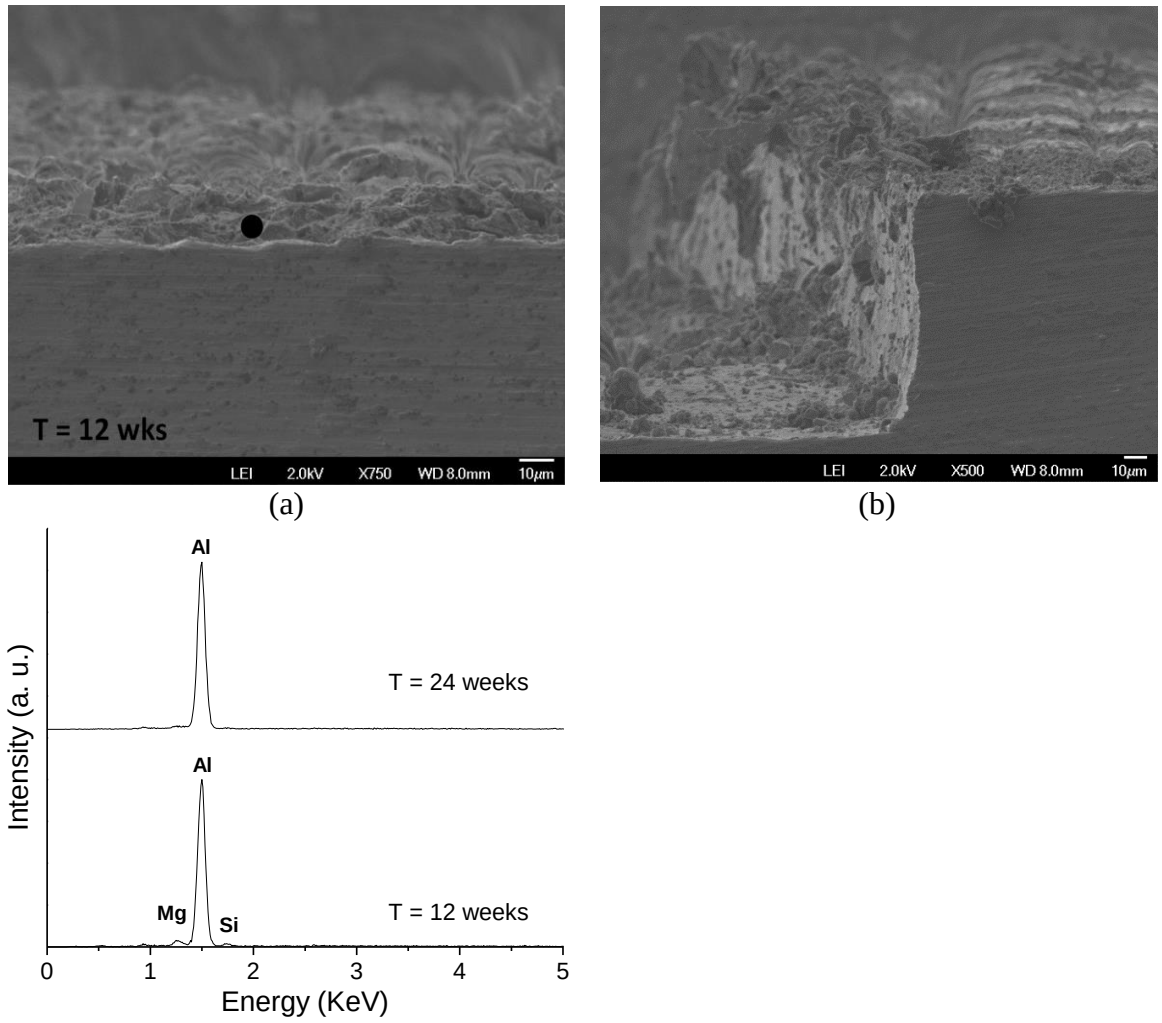

Figure 3.27. SEM micrograph (a) far away from and (b) near the scribe and (c) EDS of cross-sectioned MgRP (initial MgPVC = 45%) on AA2024-T351 pretreated with Prekote after field exposure at Charlottesville, VA for 12 weeks. Spot markers in (a) indicate approximate location of EDS analysis shown in (c).

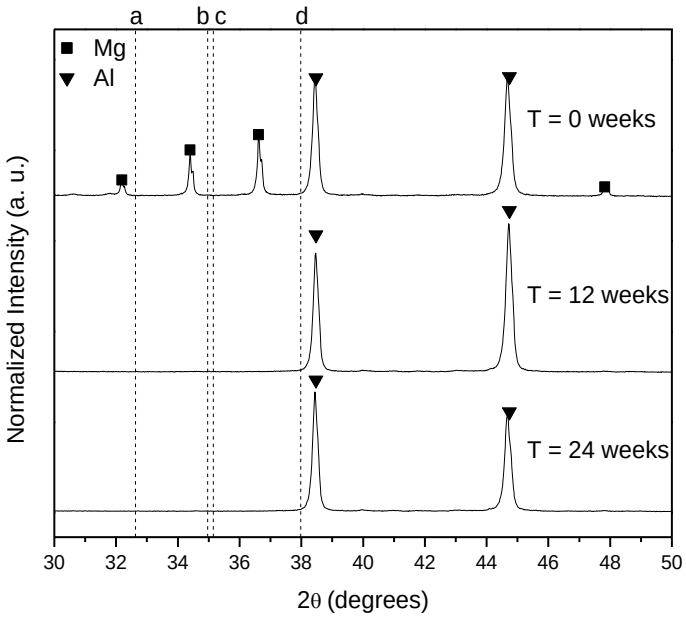

Figure 3.28. X-Ray diffraction spectra of AA2024-T351 panels coated with MgRP (initial MgPVC = 45%) after field exposure at Charlottesville, VA for 0, 12, and 24 weeks. Dotted lines indicate the position of the most intense diffraction peak for (a) $MgCO_3$ (b) $MgCl_2$ (c) Al_2O_3 and (d) $Mg(OH)_2$.

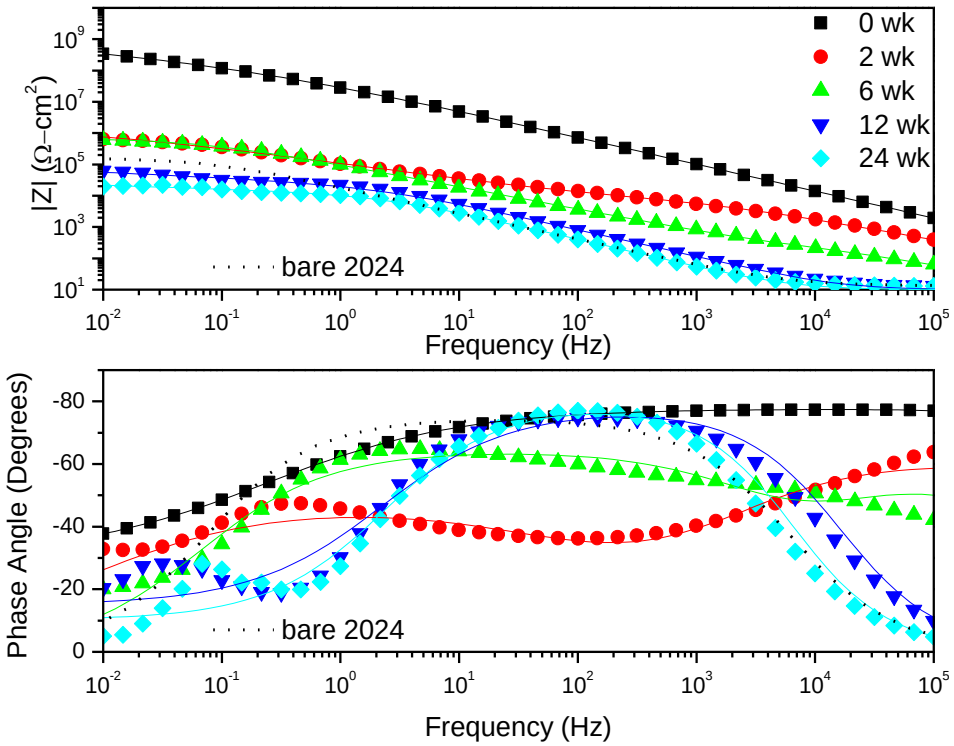

(a)

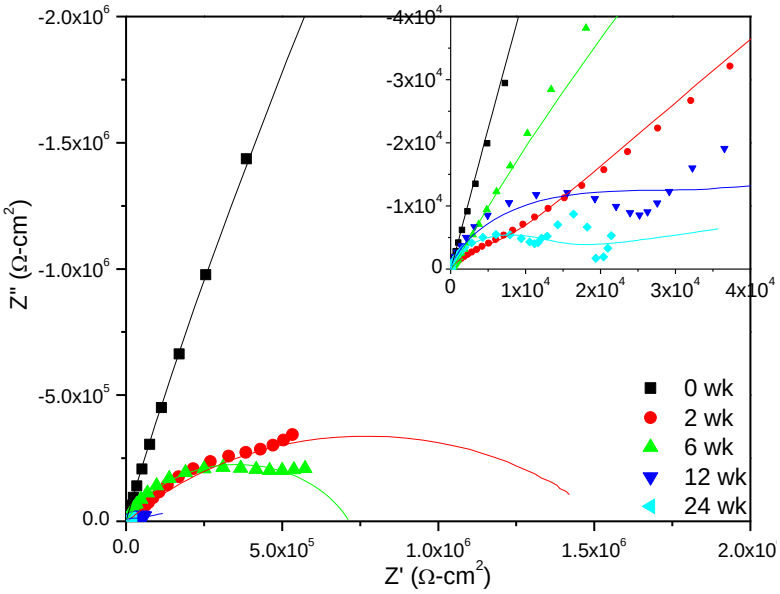

(b)

Figure 3.29. (a) Bode and (b) Nyquist plots of EIS of AA2024-T351 panels coated with MgRP (initial MgPVC = 45%) after field exposure at Charlottesville, VA for 0, 2, 6, 12, and 24 wk. Tested in ambiently aerated 5% NaCl solution. Fit results tabulated in Table 3.3.

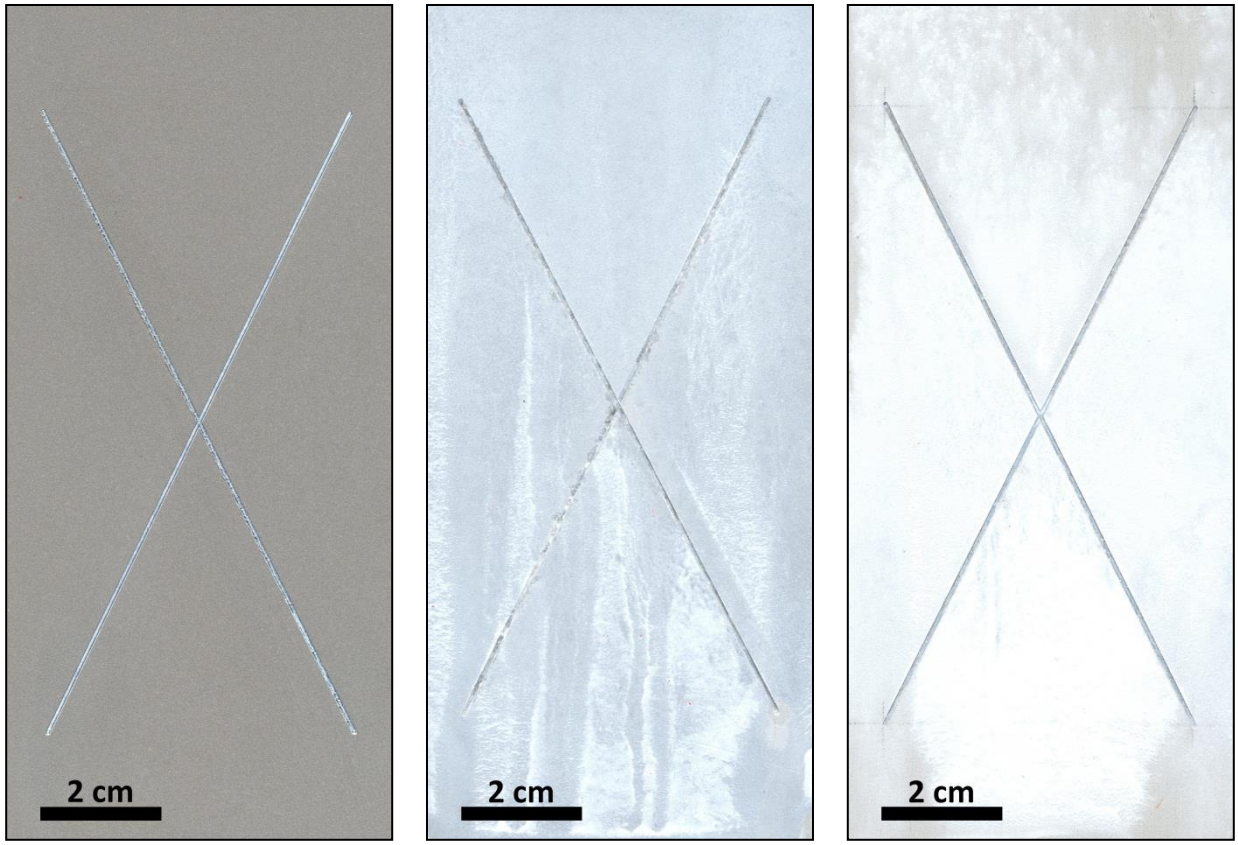

(a) (b) (c)

Figure 3.30. Optical micrograph of AA2024-T351 panels coated with MgRP (initial MgPVC = 45%) after lab accelerated life testing in ASTM B-117 for (a) T = 0 hrs (b) T = 384 hrs (c) T = 984 hrs

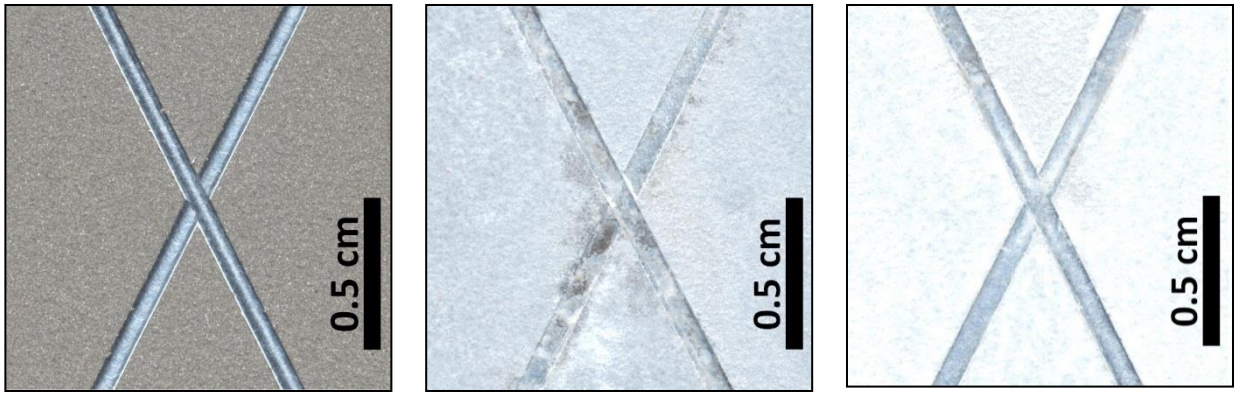

(a) T = 0 hrs in ASTM B-117 (b) T = 384 hrs in ASTM B-117 (c) T = 984 hrs in ASTM B-117

Figure 3.31. Optical micrograph of AA2024-T351 panels coated with MgRP (initial MgPVC = 45%) after lab accelerated life testing in ASTM B-117 for (a) T = 0 hrs (b) T = 384 hrs (c) T = 984 hrs

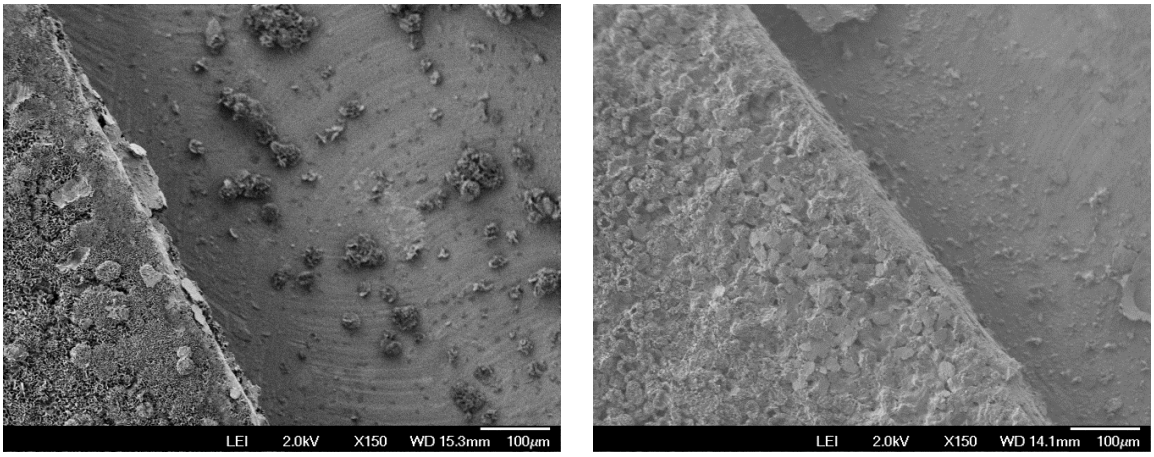

(a) (b)

Figure 3.32. Scanning electron micrograph (planar view) of scribed AA2024-T351 pretreated with Prekote and coated with MgRP (initial MgPVC = 45%) after lab accelerated life testing in ASTM B-117 for (a) 384 hrs and (b) 984 hrs.

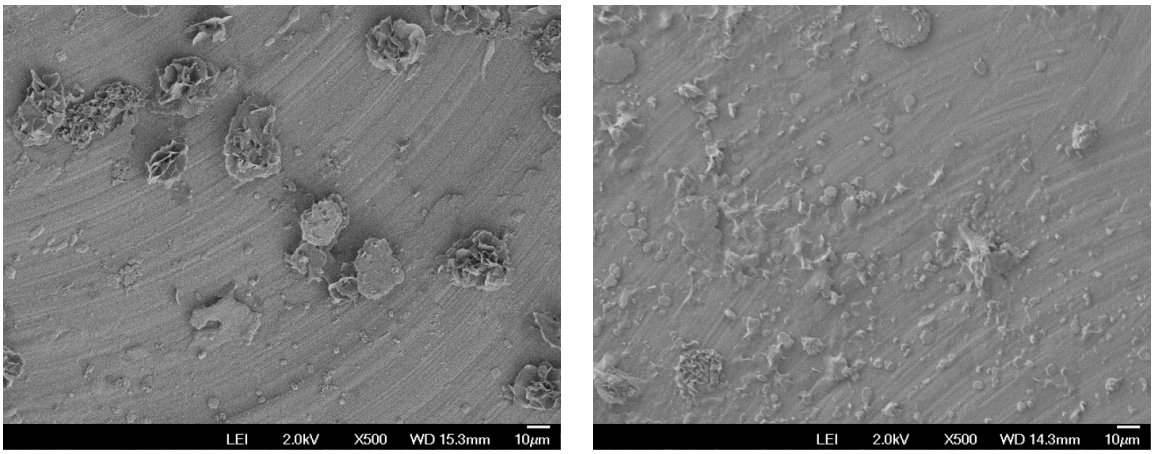

(a) (b)

Figure 3.33. Scanning electron micrograph (planar view) inside bare scribe area of scribed AA2024-T351 pretreated with Prekote and coated with MgRP (initial MgPVC = 45%) after lab accelerated life testing in ASTM B-117 for (a) 384 hrs and (b) 984 hrs.

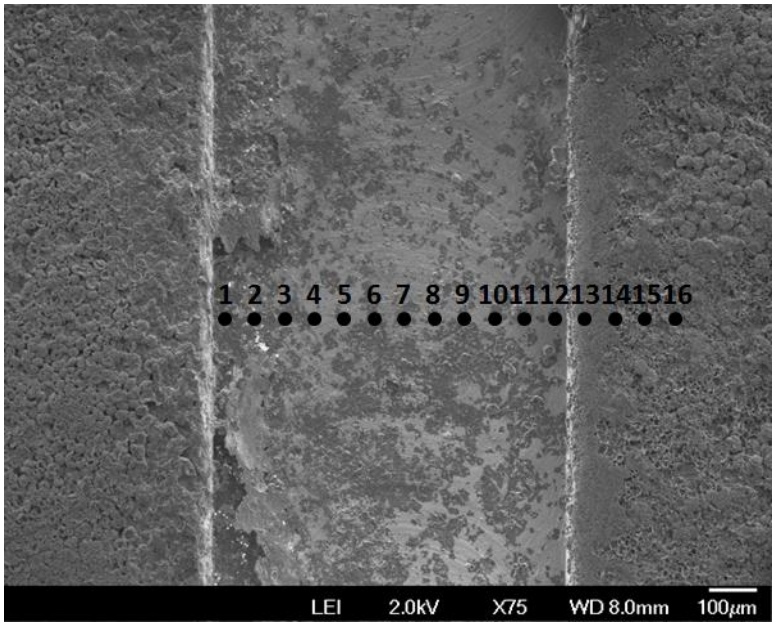

(a)

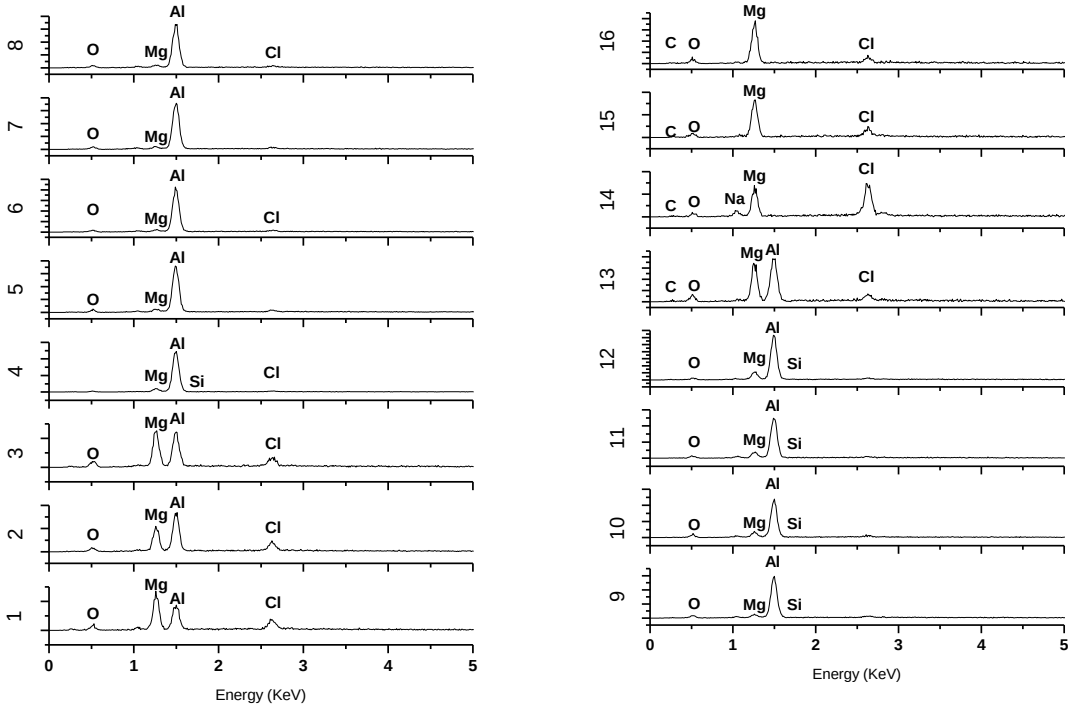

(b)

Figure 3.34. Planar-view SEM micrograph (a) of scribed AA2024-T351 pretreated with Prekote and coated with MgRP (initial MgPVC = 45%) after lab accelerated life testing in ASTM B-117 for 984 h. Spot markers indicate approximate location of EDS analysis shown in (b).

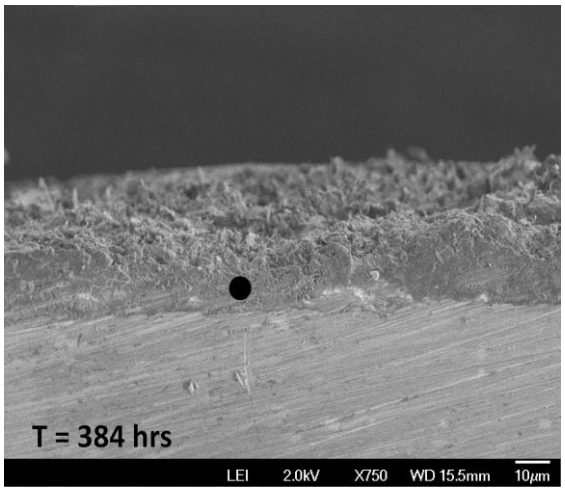

(a)

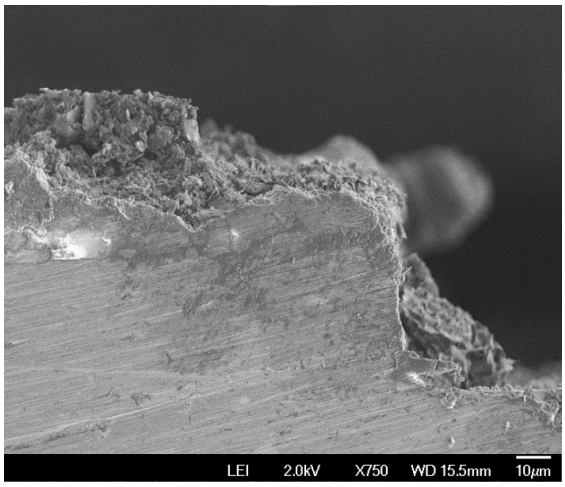

(b)

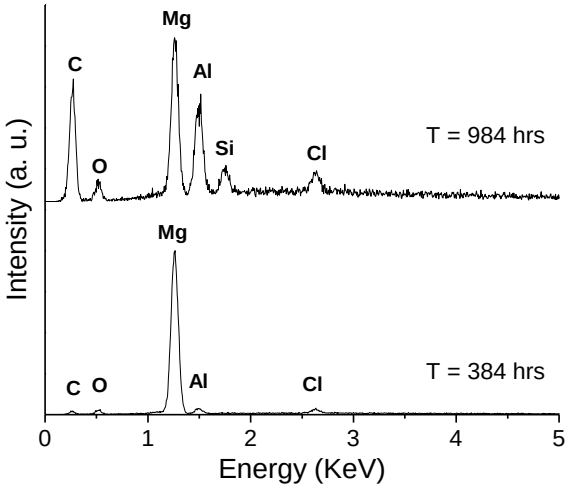

(c)

Figure 3.35. SEM micrograph (a) far away from and (b) near the scribe and (c) EDS of cross-sectioned MgRP (initial MgPVC = 45%) on AA2024-T351 pretreated with Prekote after lab accelerated life testing in ASTM B-117 with 5% NaCl for 384 h. Spot markers in (a) indicate approximate location of EDS analysis shown in (c).

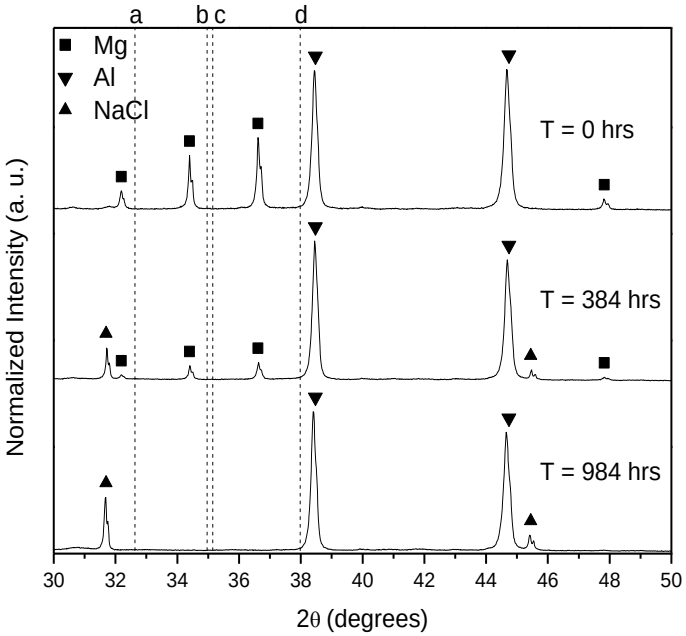

Figure 3.36. X-Ray diffraction spectra of AA2024-T351 panels coated with MgRP (initial MgPVC = 45%) that have been environmentally exposed in ASTM B-117 with 5% NaCl for 0, 384 and 984 hours. Dotted lines indicate the position of the most intense diffraction peak for (a) $MgCO_3$ (b) $MgCl_2$(c) Al_2O_3 and (d) $Mg(OH)_2$.

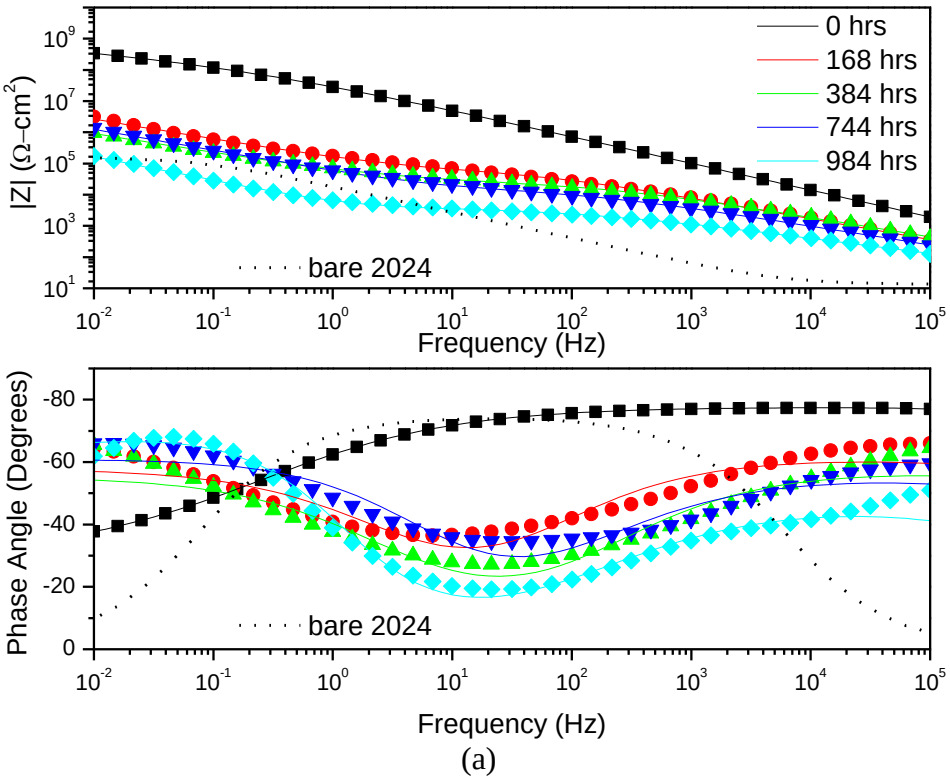

(a)

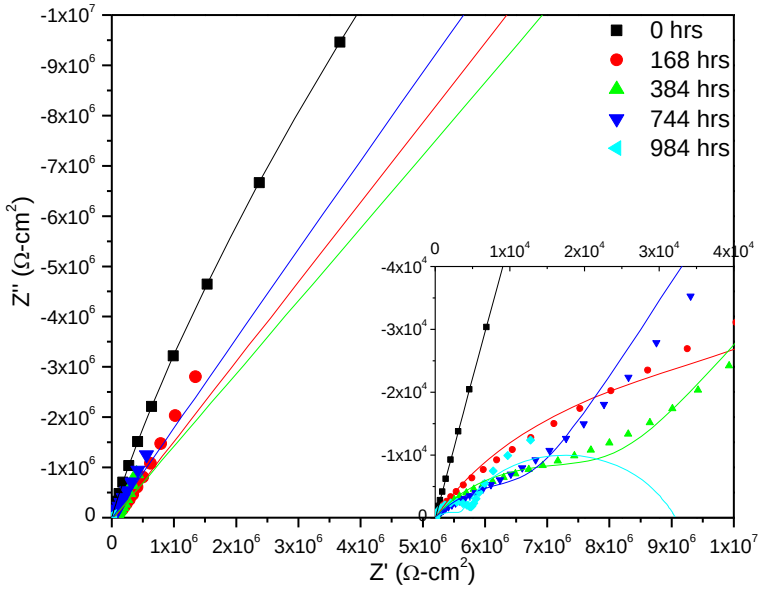

(b)

Figure 3.37. (a) Bode and (b) Nyquist plots of EIS of AA2024-T351 panels coated with MgRP (initial MgPVC = 45%) that have been environmentally exposed in ASTM B-117 with 5% NaCl for 0, 168, 384, 744, and 984 hours. Tested in ambiently aerated 5% NaCl solution. Fit results tabulated in Table 3.4.

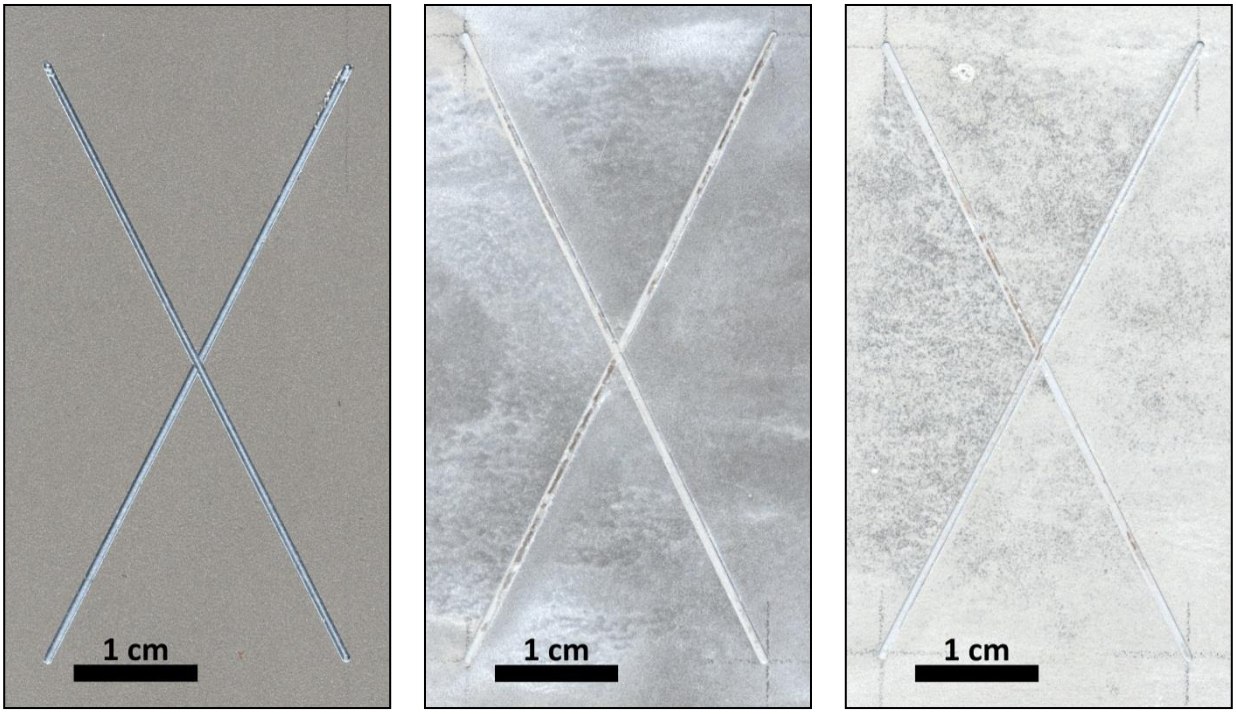

(a) (b) (c)

Figure 3.38. Optical micrograph of AA2024-T351 panels coated with MgRP (initial MgPVC = 45%) after lab accelerated life testing in ASTM B-117 modified with artificial sea water. (a) T = 0 hrs (b) T = 408 hrs (c) T = 1000 hrs

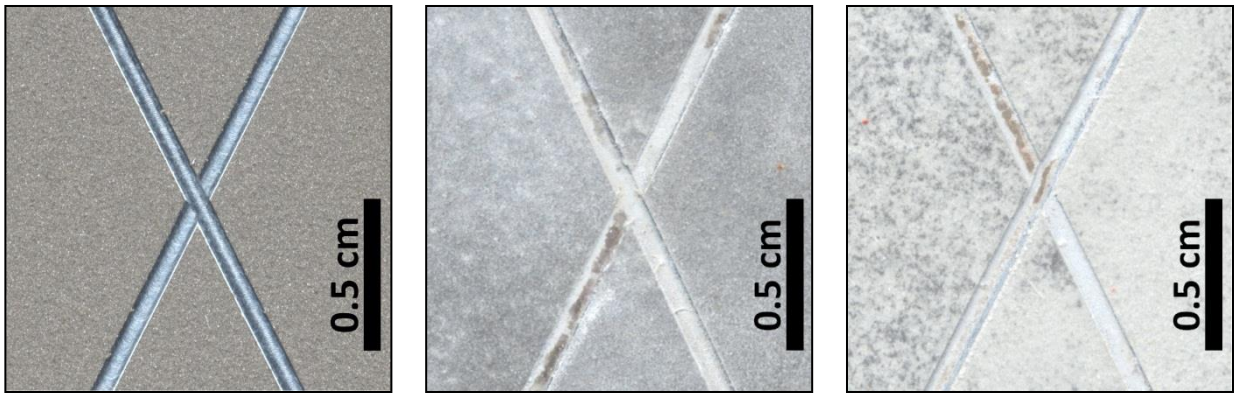

(a) T = 0 hrs in ASTM B-117 w/ ASW

(b) T = 408 hrs in ASTM B-117 w/ ASW

(c) T = 1000 hrs in ASTM B-117 w/ ASW

Figure 3.39. Optical micrograph of AA2024-T351 panels coated with MgRP (initial MgPVC = 45%) after lab accelerated life testing in ASTM B-117 modified with artificial sea water. (a) T = 0 hrs (b) T = 408 hrs (c) T = 1000 hrs

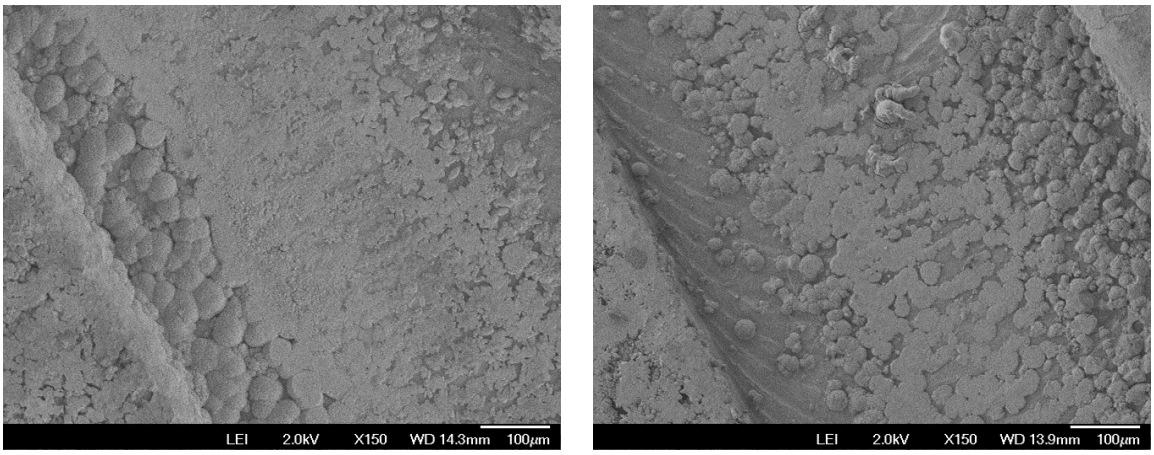

(a) (b)

Figure 3.40. Scanning electron micrograph (planar view) of scribed AA2024-T351 pretreated with Prekote and coated with MgRP (initial MgPVC = 45%) after lab accelerated life testing in ASTM B-117 modified with artificial sea water for (a) 408 hrs and (b) 1000 hrs.

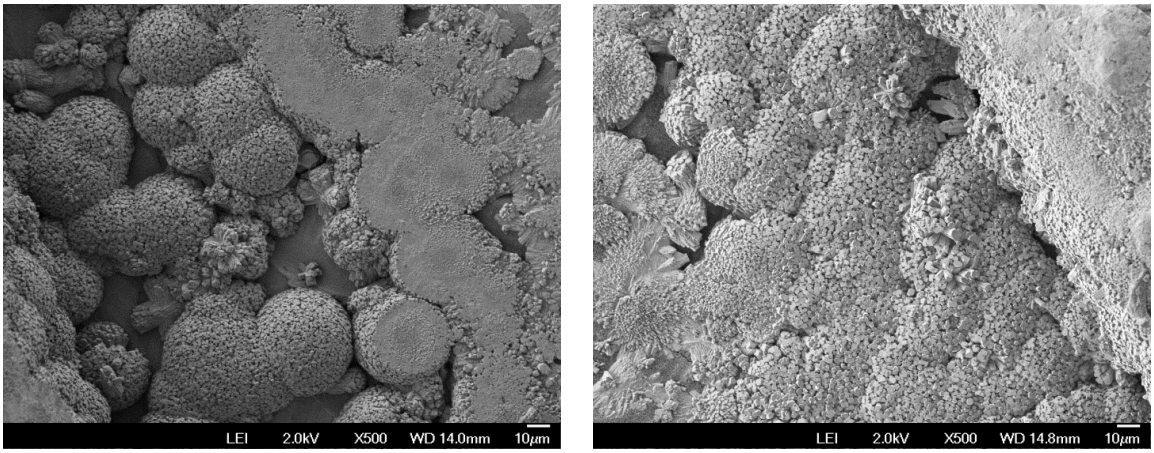

(a) (b)

Figure 3.41. Higher magnification scanning electron micrograph (planar view) of scribed AA2024-T351 pretreated with Prekote and coated with MgRP (initial MgPVC = 45%) after lab accelerated life testing in ASTM B-117 modified with artificial sea water for (a) 408 hrs and (b) 1000 hrs.

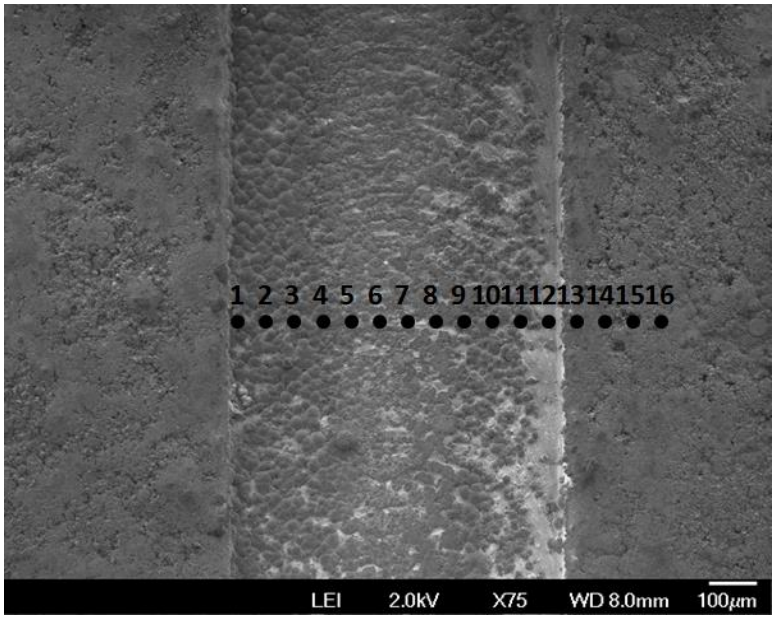

(a)

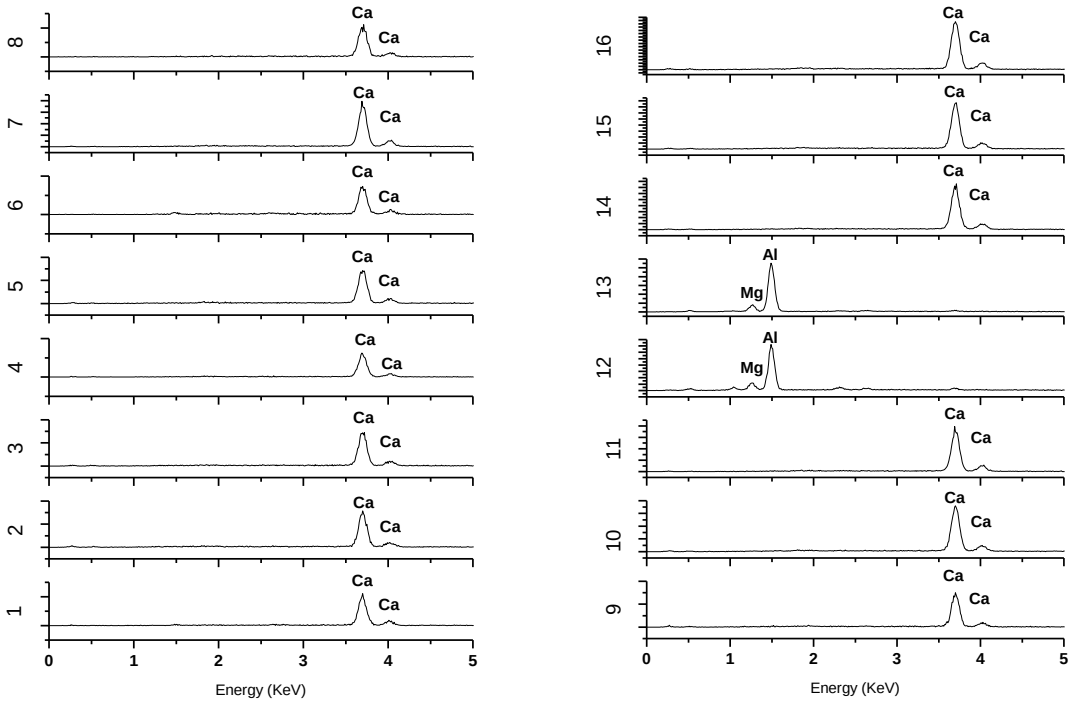

(b)

Figure 3.42. Planar-view SEM micrograph (a) of scribed AA2024-T351 pretreated with Prekote and coated with MgRP (initial MgPVC = 45%) after after lab accelerated life testing in ASTM B-117 modified with ASTM artificial sea water for 1000 h. Spot markers indicate approximate location of EDS analysis shown in (b).

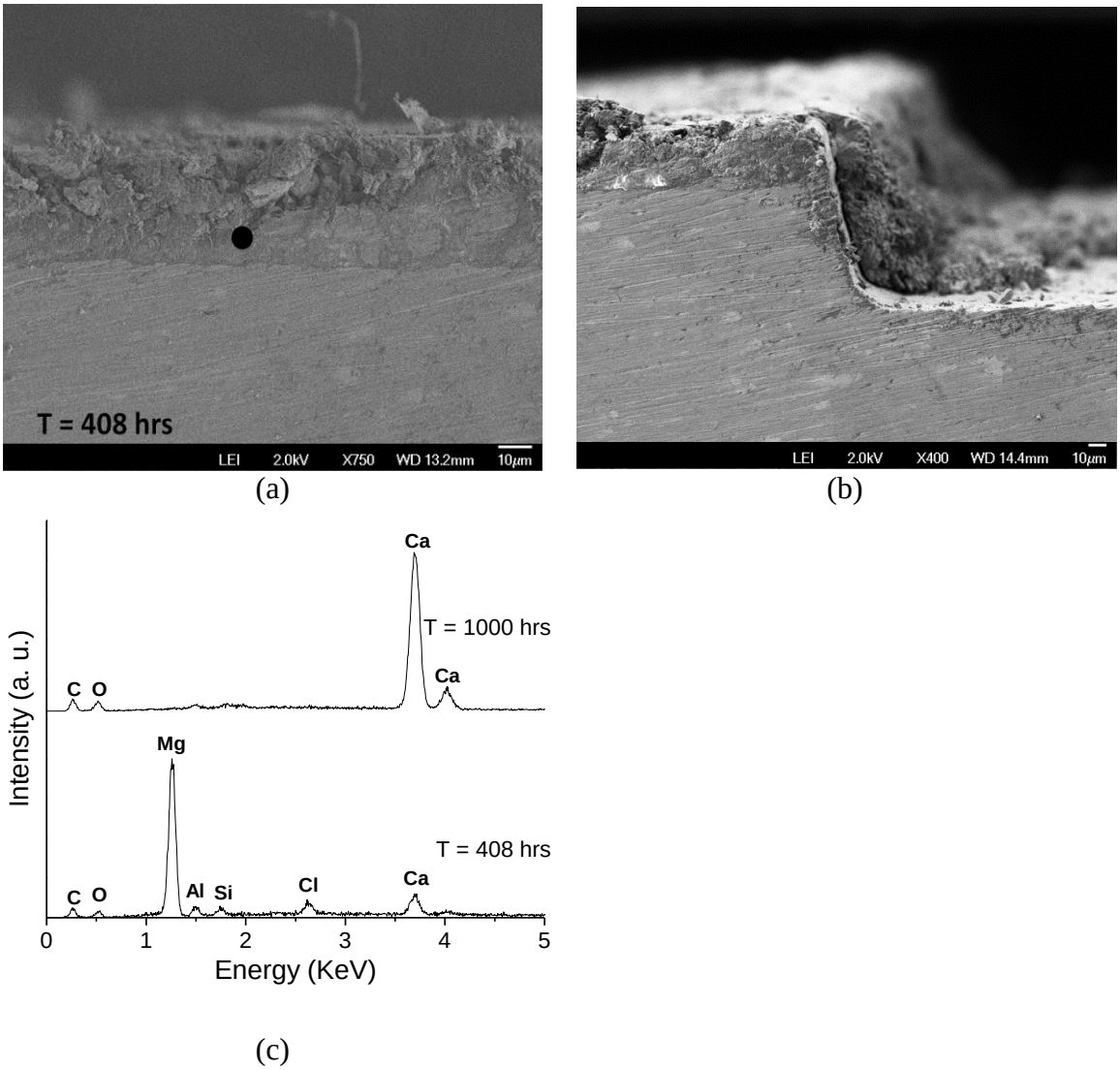

Figure 3.43. SEM micrograph (a) far away from and (b) near the scribe and (c) EDS of cross-sectioned MgRP (initial MgPVC = 45%) on AA2024-T351 pretreated with Prekote after lab accelerated life testing in ASTM B-117 modified with ASTM artificial sea water for 408 h. Spot markers in (a) indicate approximate location of EDS analysis shown in (c).

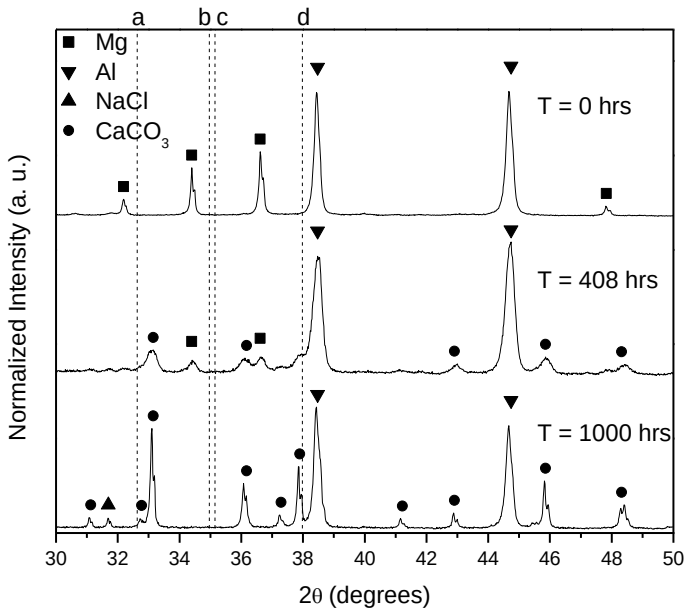

Figure 3.44. X-Ray diffraction spectra of AA2024-T351 panels coated with MgRP (initial MgPVC = 45%) after lab accelerated life testing in ASTM B-117 modified with ASTM artificial sea water for 0, 408 and 1000 hours. Dotted lines indicate the position of the most intense diffraction peak for (a) $MgCO_3$ (b) $MgCl_2$(c) Al_2O_3 and (d) $Mg(OH)_2$.

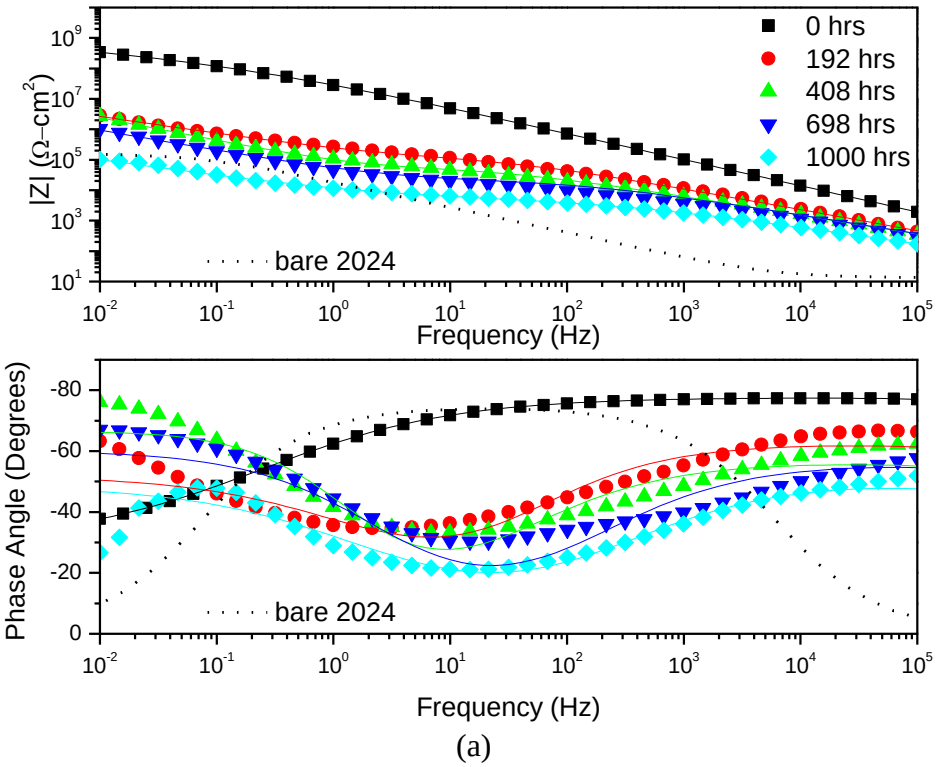

(a)

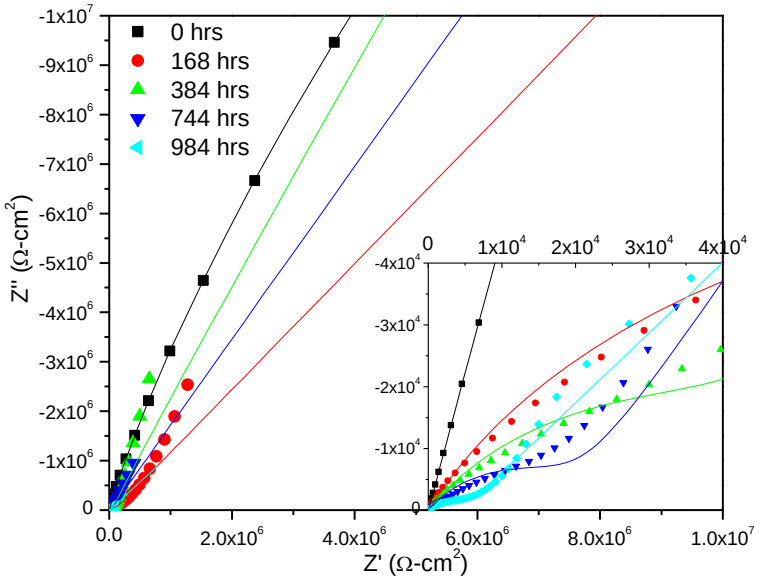

(b)

Figure 3.45. (a) Bode and (b) Nyquist plots of EIS of AA2024-T351 panels coated with MgRP (initial MgPVC = 45%) after lab accelerated life testing in ASTM B-117 modified with ASTM artificial sea water for 0, 192, 408, 698, and 1000 hours. Tested in ambiently aerated 5% NaCl solution. Fit results tabulated in Table 3.5.

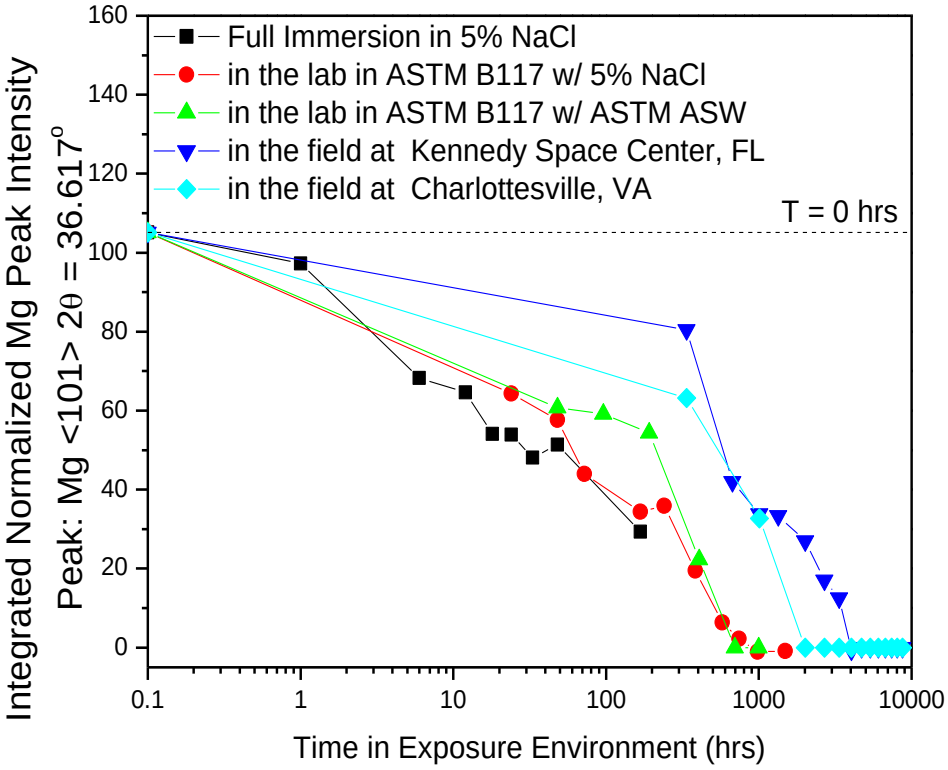

Figure 3.46. Integrated Mg peak (Mg <200> 2θ = 36.6170°) intensity vs. environmental exposure time in various lab and field exposure environments for panels of AA2024-T351 coated with MgRP (initial MgPVC = 45%). Dotted line indicates initial integrated Mg peak intensity of an unexposed panel. XRD Detection limit is estimated to be 3 – 5% of samples by volume.[76]

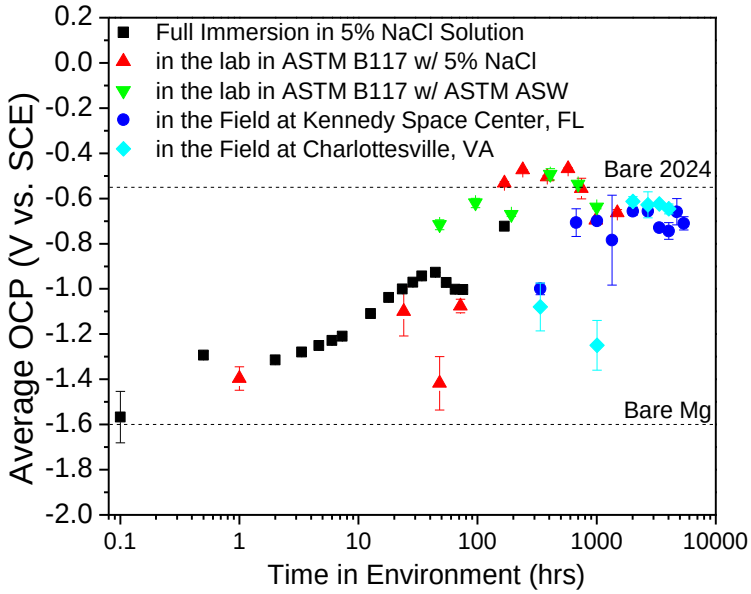

Figure 3.47. Galvanic protection potential of AA2024-T351 coated with MgRP (initial MgPVC = 45%) in ambiently aerated 5% NaCl solution vs. environmental exposure time in various lab and field exposure environments.

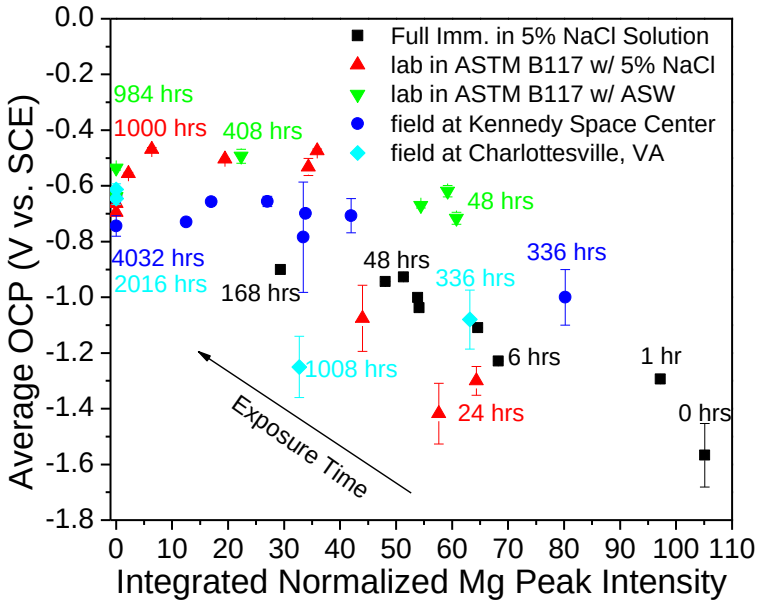

Figure 3.48. Correlation between integrated Mg peak (Mg <200> 2θ = 36.6170°) intensity vs. galvanic protection potential of AA2024-T351 coated with MgRP (initial MgPVC = 45%) in ambiently aerated 5% NaCl solution after exposure in various environments.

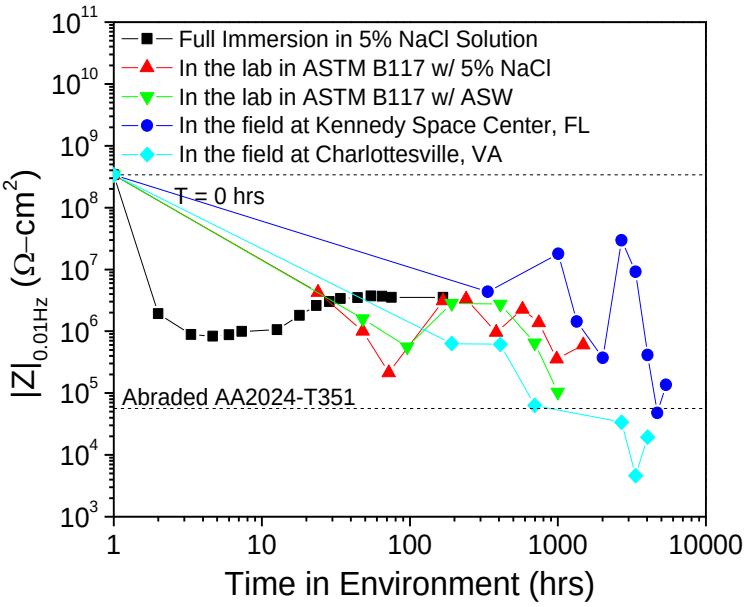

Figure 3.49. Magnitude of electrochemical impedance at 0.01 Hz in ambiently aerated 5% NaCl solution vs. environmental exposure time in various exposure environments for panels of AA2024-T351 coated with MgRP (initial MgPVC = 45%).

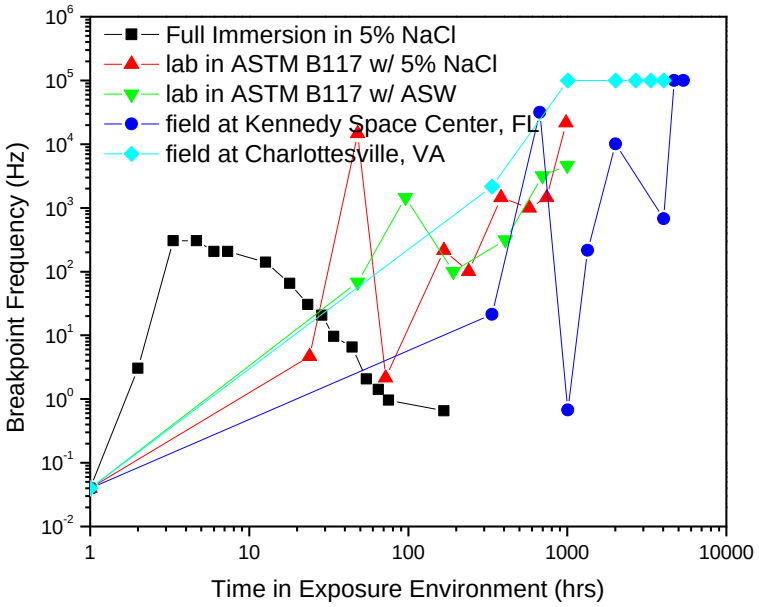

Figure 3.50. Breakpoint frequency in ambiently aerated 5% NaCl solution vs. environmental exposure time in various exposure environments for panels of AA2024-T351 coated with MgRP (initial MgPVC = 45%).

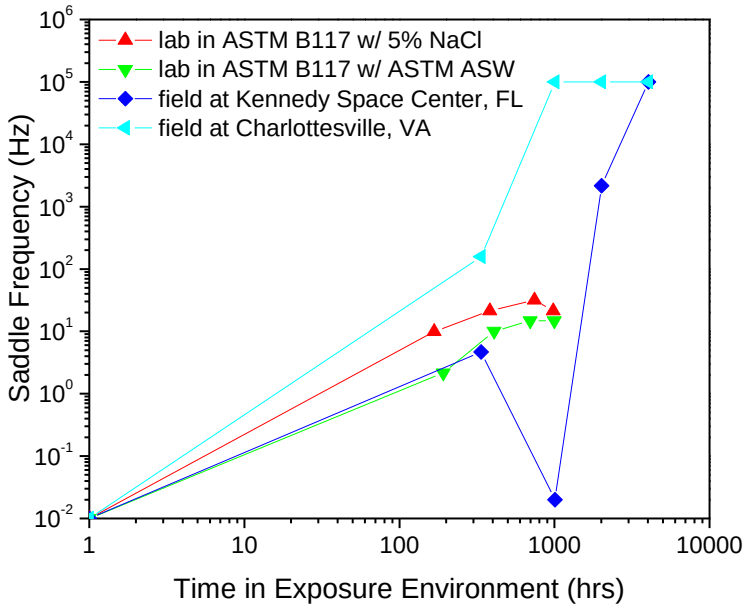

Figure 3.51. Saddle Frequency in ambiently aerated 5% NaCl solution vs. environmental exposure time in various exposure environments for panels of AA2024-T351 coated with MgRP (initial MgPVC = 45%).

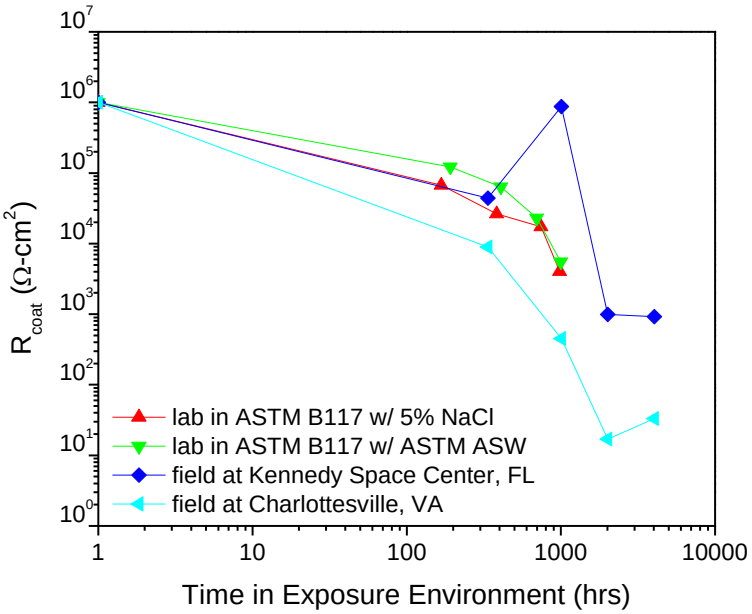

Figure 3.52. R_{coat} in ambiently aerated 5% NaCl solution vs. environmental exposure time in various exposure environments for panels of AA2024-T351 coated with MgRP (initial MgPVC = 45%).

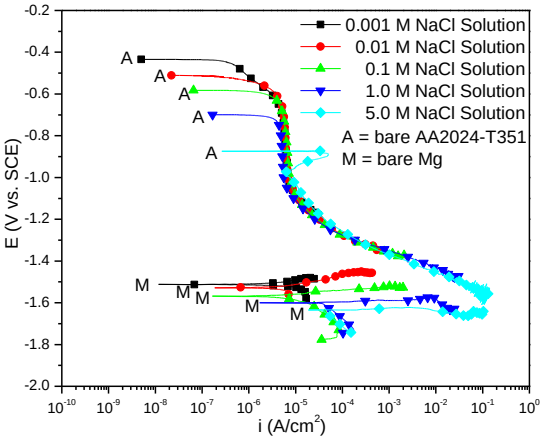

(a)

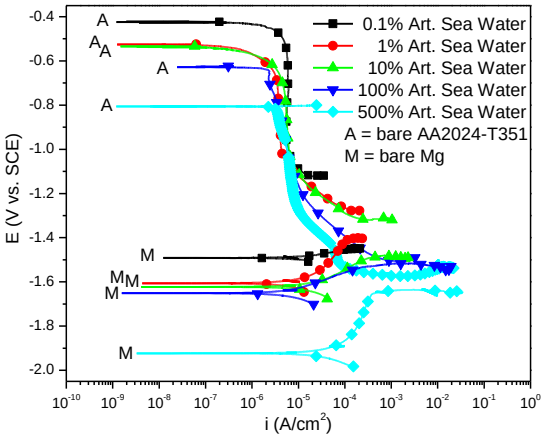

(b)

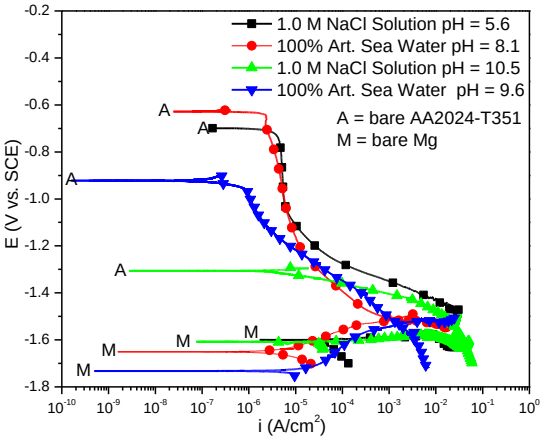

(c)

Figure 3.53. E-log(i) data for bare high purity Mg and bare AA2024-T351 sheet in (a) various concentrations of ambiently aerated NaCl solution (b) various concentrations of ambiently aerated ASTM artificial sea water and (c) in ambiently aerated NaCl solution and ambiently aerated ASTM artificial sea water in which bare Mg flake has been allowed to dissolve.

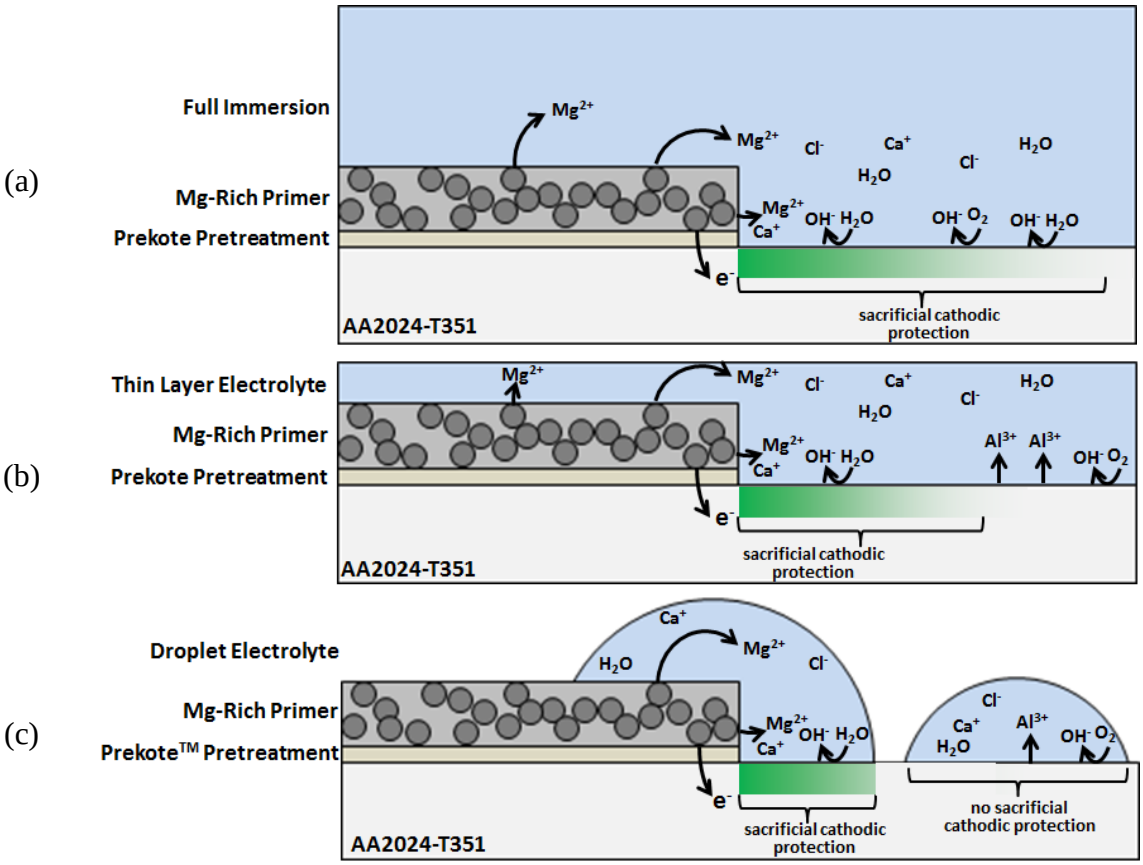

Figure 3.54. Hypothetical schematic of AA2024-T351 coated with MgRP depicting MgRP sacrificial cathodic protection function under (a) full immersion (b) thin-layer electrolyte and (c) droplet electrolyte conditions

4 Environmental Degradation of a Mg-Rich Primer in Selected Field and Laboratory Environments – Part II. Primer and Topcoat

Reference: *A. D. King, B. Kannan and J. R. Scully, Environmental Degradation of a Mg-Rich Primer in Selected Field and Laboratory Environments – Part II. Primer and Topcoat, Corrosion, 70, 5 (2014), DOI: http://dx.doi.org/10.5006/0989*

Presented as part of the NACE CORROSION 2013 Research Topical Symposium; "Functionalized Coatings for Durable Materials and Interfaces," Mar. 2013, Orlando, FL.

Guest Editor: Dr. Victoria Gelling

4.1 Abstract

Magnesium-rich primer (Akzo Nobel Aerodur 2100 Product #: 2100P003 Lot #: 493-190 MFG: 03/2009), in a topcoated (Akzo Nobel Aerodur 5000 Product #: ECM-G7875 Lot #: RC548-25A MFG: 08/2010), scribed condition, was utilized for the corrosion protection of an AA2024-T351 substrate pretreated with PreKote™ surface pretreatment. Exposures were conducted in the field at a coastal marine site; Kennedy Space Center, FL (KSC), at a inland rural site; at Birdwood Golf Course in Charlottesville, VA, in ASTM B-117 with 5% NaCl, and the same standard test modified with ASTM Seawater as well as in full immersion in ambiently aerated 5% NaCl solution. Mg pigment depletion rate, global galvanic protection potential, and coating barrier properties were tracked throughout exposure periods in both field and laboratory environments. Analysis near and far from the scribe was performed. Characterization with SEM/EDS was

conducted to elucidate coating and scribe morphology, corrosion products present, corrosion of the AA2024-T351 substrate, as well as in an attempt to interrogate the throwing power of the coating system. The topcoat was observed to strongly mediate the depletion of Mg pigment from the MgRP, due to self-corrosion, in all exposure environments studied as compared to identical environmental exposures of non-topcoated samples. Full immersion in ambiently aerated 5% NaCl solution, ASTM B-117 in 5% NaCl, and ASTM B-117 in ASTM artificial seawater all resulted in only partial depletion of metallic Mg pigment in the MgRP far from the scribe after 1000 hours. Field exposures in Charlottesville, VA and Kennedy Space Center, FL also resulted in similar low levels of Mg pigment depletion far from the scribe after 1 year of exposure. As a result of partial depletion of remote Mg pigment particles, the global galvanic protection potential of the coating system, with respect to remote scratches only, increased slightly with exposure time in each environment, from initial values of approximately -1.0 V vs. SCE to -0.7 V vs. SCE after extensive environmental exposure. These values fall between the open circuit potentials of bare AA2024-T351 (-0.6 V vs. SCE) and bare Mg (-1.6 V vs. SCE) and are predicted by mixed potential theory. Barrier properties of the Mg-rich primer coating, as assessed by electrochemical impedance, also slightly degrade with time in each environment but, overall, remain very high ($\geq 10^9$ Ω-cm^2 at 0.01 Hz) throughout exposure indicating significant barrier protection remains after all environmental exposures studied. Characterization after 1000 h of salt fog exposure in ASTM B-117 modified with ASTM artificial seawater indicates a throwing power that extended the entire half-width of the scribe and a throwing power that extends approximately 200 μm into the scribe after environmental exposure in the field at

Kennedy Space Center, FL. Characterization after 1 year of exposure in the field at Charlottesville, VA and after 1000 hours of exposure in ASTM B-117 with 5% NaCl was inconclusive. The uniformity in performance in the lab and field is presumed to be due to the polyurethane topcoat polymer's excellent resistance to UV degradation and electrolyte ingress, negating the presence of UV in the field and high TOW in the lab and results in no clear determination of acceleration factors between field vs. lab exposures with respect to pigment depletion, galvanic protection potential, or barrier properties of the coating system. No chalking, or any other phenomena signifying significant UV degradation was observed in lab and field exposures of AA2024-T351 panels coated with MgRP (initial MgPVC = 45%) and Aerodur 5000 topcoat reported on in this study.

4.2 Introduction and Background

Very promising corrosion mitigation results have been reported for an organic coating system containing a metallic Mg-pigmented organic primer (MgRP) used for the corrosion protection of the precipitation age hardened aluminum alloy 2024-T351.[1-12] MgRP is a primary candidate coating system to replace chromate type surface pretreatments and chromate pigmented primers which are known for their toxicity and carcinogenic properties.[2, 13, 14] While barrier protection of the aluminum alloy is also afforded by the MgRP, the MgRP has been designed and shown to provide sacrificial anode based cathodic protection to the aluminum alloy by galvanically coupling the metallic Mg pigment in the MgRP to the AA2024-T351 substrate.[1, 5, 7-9]

Barrier protection is afforded to the AA2024-T351 substrate by the continuous physical barrier consisting of the organic epoxy polymer matrix of the MgRP, the Mg pigment

particles, and any other insoluble pigments in the primer or corrosion products which may have formed within defects in the coating. Also, the organic polyurethane polymer topcoat adds additional barrier protection and greatly decreases the coating system's susceptibility to UV degradation.[15, 16] Secondarily, the coating can serve as a transport barrier to resist corrodant ingress such as Cl^-. These properties of the polymer coating system are degraded by a host of "stresses" including UV photonic radiation, chemical reaction of the coating with the environment, whether by hydrolysis or saponification, or by mechanical forces which destroy adhesion.[17, 18]

For Mg to be available for sacrificial cathodic protection of the AA2024-T351 substrate both electrical and ionic conduction is required between metallic phases comprising anodes and cathodes. Ionic conduction is achieved between the substrate and Mg pigment through the electrolyte. The effect of several ohmic voltage drops that exist between the Mg pigment and the electrolyte (ionic) and also between the Mg pigment and the substrate (electrical) were discussed in part I of this study.[19] The application of a topcoat to the coating system, as studied in this investigation, also significantly increases the ohmic ionic resistance between the buried Mg pigment and the electrolyte.

Two possible modes of protection are described by King and Scully; long range protection of remote defects by the global galvanic protection potential afforded to the substrate and local or short range Mg pigment-based protection of local and buried defects. Both modes of protection are mediated by the high ionic and electrical resistance of the coating system as a function of MgPVC, substrate pretreatments, primer polymer,

and topcoat properties.[8, 10] The mediation of the cathodic protection abilities is important in the application of MgRP. It is important for the coating system to provide adequate cathodic protection to the AA2024-T351 substrate, but to also avoid the detrimental effects of cathodic corrosion of the amphoteric AA2024-T351 substrate which can be caused by increased localized pH due to severe cathodic polarization and/or excessive Mg pigment dissolution. [8, 10, 20-26]

A critical need resolved in this study is to understand MgRP's degradation rate and characteristics in various relevant exposure environments in hopes of identifying environmental factors that are significant to MgRP's degradation. In part I of this study[12], magnesium-rich primer (Akzo Nobel Aerodur 2100 Product #: 2100P003 Lot #: 493-190 MFG: 03/2009), in a non-topcoated, scribed condition, was utilized for the corrosion protection of an AA2024-T351 substrate pretreated with PreKote™ surface pretreatment. Exposures were conducted in the field at a coastal marine site; Kennedy Space Center, FL (KSC), at an inland rural site; Birdwood Golf Course in Charlottesville, VA, in ASTM B-117 with 5% NaCl, and the same standard test modified with ASTM Artificial Seawater as well as in full immersion in ambiently aerated 5% NaCl solution. Mg pigment depletion rate, global galvanic protection potential, and coating barrier properties were tracked throughout exposure periods in both field and laboratory environments. Analysis near and far from the scribe was performed. Post-mortem characterization with SEM/EDS was conducted to elucidate coating and scribe morphology, corrosion products present, corrosion of the AA2024-T351 substrate, as well as in an attempt to interrogate the throwing power of the coating system. Full immersion in ambiently aerated 5% NaCl

solution, ASTM B-117 in 5% NaCl and ASTM B-117 in ASTM artificial seawater all depleted the MgRP of metallic Mg pigment far from the scribe at various rates, with significant depletion (less than 5% by volume as detectable by XRD) occurring after approximately 1000 h of exposure in all cases. Field exposures in Charlottesville, VA and Kennedy Space Center, FL resulted in depletion of metallic Mg pigment far from the scribe after 2000 and 4000 h of exposure, respectively. As a result of remote pigment depletion, the global galvanic protection potential of the coating system, with respect to remote scratches, increased with exposure time in each environment, from values approximately equal to that of bare Mg (-1.6 V vs. SCE) to those approximately equal to that of bare AA2024-T351 (-0.55 V vs. SCE). Barrier properties of the MgRP primer coating also degraded with time in each environment, but corrosion of the AA2024-T351 substrate under the coating was not observed. Characterization after 1000 h of salt fog exposure indicated a throwing power that extended the entire half-width (≈ 350 μm) of the scribe, in both standard and modified ASTM B-117 exposures which developed thin-layer electrolyte geometries during continuous wetting. Characterization after 24 weeks of exposure at Kennedy Space Center, FL indicated a throwing power that extended approximately 200 - 300 μm in the scribe from the coating edge. Characterization after 24 weeks of exposure at Charlottesville, VA was inconclusive due to the high self-corrosion rate of the MgRP and subsequent chemical dissolution of Mg-based corrosion products by high TOW and low pH rain (pH ≈ 5). The differences in rate-of-change of Mg depletion from the coating upon environmental exposure are presumed to originate from differences in time-of-wetness and in rates of polymer degradation, specifically resistivity, due to UV exposure. Differences in throwing power in lab and field

environments were theorized to be caused by differences in electrolyte geometries. A second part of this study examines the performance of a MgRP in a topcoated, scribed condition where MgRP self-corrosion is slow.

The objective of this study is to track the degradation of a representative MgRP coating formulation (Akzo Nobel Aerodur 2100 Lot# 493-190 MFG 03/2009) and topcoat (Akzo Nobel Aerodur 5000 Product #: ECM-G7875 Lot #: RC548-25A MFG: 08/2010) coating system stack-up throughout its lifetime in various environments. A working understanding of the coating system's degradation in relevant lab and field environments will be developed by measuring Mg pigment depletion rate far away from, and proximate to, a scribe (as measured by XRD and SEM/EDS), galvanic protection potential, and coating barrier properties throughout each exposure. These measurements, in conjunction with post-mortem characterization, diagnostic electrochemical experiments, and mixed potential modeling, will provide insight into the significant factors controlling environmental severity in the context of the MgRP.

4.3 Experimental Procedure

4.3.1 Materials

The MgRP-coated AA2024-T351 samples studied were comprised of AA2024-T351 sheet, pretreated with Prekote surface pretreatment, and primed with a 30 ± 10 μm thick layer of magnesium rich primer, "MgRP" (Akzo Nobel Aerodur 2100 Product# 2100P003 Lot# 493-190 MFG 03/2009) and topcoated with a 60 ± 10 μm thick layer of high performance organic polyurethane polymer (Akzo Nobel Aerodur 5000 Product #:

ECM-G7875 Lot #: RC548-25A MFG: 08/2010). The MgRP is described further in part I of this study.[12] The high performance advanced polymer topcoat is a two-component polyurethane topcoat developed for military and defense applications. All tested panels were provided and painted by collaborators at NAVAIR.[27, 28] After curing for approximately 4 weeks in a dry box, the panels were scribed identically to those described in Part I of this study. A schematic and optical micrograph of the MgRP coated AA2024-T351 panels investigated in this study are shown in Figure 4.1 and Figure 4.2, respectively. A cross-section schematic of the scribed region is shown in Figure 4.1b. A planar SEM micrograph of a scribed AA2024-T351 panel coated with Mg-rich primer and polyurethane topcoat, before the sample has been exposed to any weathering environment, is shown in Figure 4.3. EDS spot scans were taken at points labeled 1 and 2 in Figure 4.3. EDS of the coating (spot 2) shows strong C, O, Al, Si, and Ti intensities which suggests the as-applied topcoat contains aluminum hydroxide, silica, and rutile pigments encapsulated in the carbon-rich polyurethane topcoat matrix, which are all listed on the coating's material safety and data sheet (MSDS). Figure 3.3 shows a SEM micrograph of a cross-sectioned AA2024-T351 panel coated with Mg-rich primer and polyurethane topcoat, before the sample has been exposed to any weathering environment, far away from the scribe. The thickness of the primer layer is approximately 30 μm and the thickness of the topcoat layer is approximately 50 – 70 μm. EDS analysis of the Mg pigment shows that the pigment is not significantly oxidized.

4.3.2 Lab and Field Exposures of AA2024-T351 coated with MgRP and Topcoat

AA2024-T351 panels coated with MgRP and polyurethane topcoat were exposed in full immersion, in ASTM B-117 salt spray, in modified ASTM B-117 salt spray, in the field at Kennedy Space Center, FL, and in the field at Birdwood Golf Course in Charlottesville, VA, as described in Part I of this study.[12] Pertinent environmental parameters for each environment are described in Table 4.1. The electrolyte used for full-immersion exposure as well as post-mortem analysis after field and salt fog exposures was ambiently aerated 5% NaCl solution.

4.3.3 X-Ray Diffraction and Scanning Electron Microscopy

X-Ray diffraction of pristine and environmentally exposed AA2024-T351 panels coated with MgRP and polyurethane topcoat was conducted on a PANalytical X'pert powder X-Ray diffractometer as described in Part I of this study.[19] The detection limit of bulk Bragg-Brentano X-ray diffraction for mixed or composite materials containing several crystalline phases is approximately 3 - 5% of the sample by volume.[29] Below these levels, it is unlikely that a crystalline phase will be detected in the XRD spectra. This estimate of the lower-bound of detection is supported by XRD measurements, shown in a previous work[8], performed on pristine samples of MgRP-coated AA2024-T351 panels coated with MgRP of varying pigment volume concentration (PVC).

Scanning electron microscopy and energy dispersive spectroscopy were used for coating characterization and post-mortem analysis. Typical operating parameters are described in Part I of this study.[19] Simulated EDS spectra for bulk samples of various materials

relevant to the environmentally exposed MgRP-coated AA2024-T351 system presented in part I of this study show the type of EDS fingerprint expected for various Mg products that may be present after environmental exposure.

4.4 Results

4.4.1 Behavior During and After Exposure at Kennedy Space Center:

Optical micrographs of AA2024-T351 panels coated with Mg-rich primer and polyurethane topcoat that have been exposed at Kennedy Space Center 30 m lot for 0, 24, and 52 weeks are shown in Figure 4.5 and Figure 4.6. In general, the coating was observed to change color from bright white to ivory with increased exposure time. The scribe appears, at low magnification, to be relatively clean and without significant damage. It is important to note that no blistering or similar macroscopic coating failure phenomena are observed in the coating or along the scribe lines after exposure for 52 weeks at Kennedy Space Center, FL, 30 m lot. In SEM, after 12 and 24 weeks of exposure (Figure 4.7, Figure 3.24 and Figure 3.25), the entire scribe appears to be mostly bare, with small deposits of corrosion product or salts and a few pitting sites.

To further investigate the composition of the products and deposits in the scribe region, and of the coating proximate to the scribe, 16 consecutive EDS spot scans were obtained across the width of the scribe and coating interface (labeled 1-16 in Figure 4.10). The spacing between scans was approximately 65 μm. The typical EDS spectra obtained across the scribe and coating interface show combinations of peaks indicative of C, O, Mg, Al, and Si. The EDS spot scans across the entire width of the scribe, labeled 1

through 12, show the presence of $Mg(OH)_2$ or MgO indicated by Mg and O peaks. Hydrotalcite deposits throughout the entire width of the scribe are indicative of regions of cathodic protection afforded to the AA2024-T351 by the MgRP. Hydrotalcites[30] and calcareous[30-38] deposits are known to readily precipitate in the alkaline environment present at cathodic sites in cathodic protection schemes. The presence of these species throughout the scribe suggest a throwing power of at least the half width of the scribe (≥ 350 μm) upon environmental exposure at Kennedy Space Center, FL. The significant Al and Si peaks present in the EDS spectra obtained at positions 13, 14, 15, and 16, in the coated region, are a result of aluminum hydroxide and silica pigments present in the topcoat. The first-order approximation of the penetration depth of the EDS measurements at 15 keV is estimated to be no more than 5 μm[19] suggesting that the C, O, Al, Mg, and Si peaks are a result of surface products and/or pigmentation in the carbon-rich polymer matrix of the topcoat, not detection of Al in the substrate or Mg in the primer layer.[39]

A SEM micrograph of cross-sectioned MgRP on AA2024-T351 far away from the scribe after 24 weeks of exposure in the field at Kennedy Space Center, FL, 30 m lot, is shown in Figure 4.11a. After 24 weeks of exposure, the remaining total coating layer thickness is observed to be approximately 50 - 70 μm thick. Multiple EDS spot scans were obtained on the coating layer after 12 and 24 weeks of exposure at Kennedy Space Center, FL. Representative spectra are shown in Figure 4.11b. The EDS spectra indicate the presence of metallic, unoxidized Mg in the primer coating after both 12 and 24 weeks of exposure. A SEM micrograph of cross-sectioned MgRP on AA2024-T351 proximate to the scribe after 24 weeks of exposure in the field at Kennedy Space Center, 30 m lot, is

shown in Figure 4.11c for visual inspection. Overall, no significant dissipation of the MgRP coating, as evidenced by a decrease in coating thickness, can be observed.

X-Ray Diffraction (XRD) spectra of AA2024-T351 panels coated with Mg-rich primer (initial MgPVC = 45%) and polyurethane topcoat were obtained at each removal interval of environmental exposure in an attempt to track the depletion rate of the metallic Mg pigment in the MgRP throughout environmental exposure. XRD measurements of environmentally exposed samples were made over areas far away from the scribe, such that none of the interaction area of the incident X-rays interacted with the scribed region of the samples. The areas far away from the scribe were presumed to be areas representative of global coating degradation. XRD spectra of MgRP coated AA2024-T351 and polyurethane topcoat after 0, 24, and 52 weeks of exposure in the field at Kennedy Space Center, FL, 30 m lot, are shown in Figure 4.12. Three prominent Mg hexagonal close packed peaks (<100>, <200>, and <101>) were normalized against the Al <101> peak which appeared in each spectrum as a result of the underlying AA2024-T351 substrate. The relative integrated peak areas of the Mg peaks shown in Figure 4.12 do not significantly decrease with increasing exposure time in the field at Kennedy Space Center, FL, which indicates no significant depletion of metallic Mg pigment from the coating system after 52 weeks. Rutile (TiO_2) was identified in the XRD spectra of AA2024-T351 panels coated with MgRP and polyurethane topcoat as a result of the significant amount of rutile pigment in the topcoat. Principle XRD peaks of relevant Mg or Al corrosion products are labeled a, b, c, and d in Figure 4.12. Detectable surface products were not present in the XRD spectra of AA2024-T351 coated with MgRP and

polyurethane topcoat after 24 and 52 weeks of exposure in the field at the Kennedy Space Center, FL, 30 m lot.

OCP measurements of AA2024-T351 panels coated with Mg-rich primer (initial MgPVC = 45%) and polyurethane topcoat were taken after 0, 6, 12, 24, and 52 weeks of exposure in the field at Kennedy Space Center, FL. Due to the long wetting and capacitive discharge period of the high performance polyurethane topcoat, a stable OCP could not be measured on environmentally exposed, topcoated samples until approximately 6 hours of immersion in 5% NaCl solution. These values fall between the open circuit potentials of bare AA2024-T351 (-0.6 V vs. SCE) and bare Mg (-1.6 V vs. SCE) in ambiently aerated 5% NaCl solution which suggest that Mg pigment remains in the MgRP coating and is available for sacrificial galvanic protection of the AA2024-T351 substrate after environmental exposure in the field at Kennedy Space Center, FL.

Electrochemical impedance spectroscopy (EIS) measurements of MgRP coated AA2024-T351 (initial MgPVC = 45%) were also taken at each removal interval of environmental exposure in an attempt to track the evolution of the coating barrier properties of the MgRP throughout environmental exposure. An automated fitting routine was used to fit the measured EIS spectra to a nested Randle's circuit, a schematic of which is shown in Figure 4.13. The nested Randle's circuit is an accepted solid state representation of polymer coated metals.[40] EIS measurements of AA2024-T351 panels coated with Mg-rich primer (initial MgPVC = 45%) and polyurethane topcoat taken after 0, 6, 12, 24, and 52 weeks of exposure in the field at Kennedy Space Center, FL (scatter plot) and the

results of the automated fitting analysis (lines) are shown in Figure 4.14. The values of each representative circuit component produced by the automated fitting routine for selected exposure times at Kennedy Space Center, FL 30 m lot are tabulated in Table 4.2. AA2024-T351 coated with MgRP and polyurethane topcoat displayed a decrease of less than one order of magnitude of the low frequency (at 0.01 Hz) impedance as well as little shift in the break point frequency of the Bode phase angle throughout environmental exposure at Kennedy Space Center, FL. Both phenomena indicate very little loss of barrier protection capability throughout the duration of the exposure.[41, 42]

4.4.2 Behavior During and After Exposure at Charlottesville, VA:

Optical micrographs of AA2024-T351 panels coated with Mg-rich primer and polyurethane topcoat that have been exposed at Birdwood Golf Course in Charlottesville, VA for 0, 24, and 52 weeks are shown in Figure 4.15 and Figure 4.16. In general, the coating was observed to change color from bright white to ivory or gray with increased exposure time. The scribe appears, at low magnification, to be relatively clean and without significant damage. It is important to note that no blistering or similar macroscopic coating failure phenomena are observed in the MgRP or along the scribe lines after exposure for 52 weeks at Birdwood Golf Course in Charlottesville, VA.

Upon closer inspection with the SEM, after 12 and 24 weeks of exposure (Figure 4.17, Figure 4.18, and Figure 4.19) of the scribe appears extremely clean and largely damage free. To further investigate the composition of any deposits in the scribe, and of the

MgRP proximate to the scribe, 16 consecutive EDS spot scans were obtained across the width of the scribe and coating interface (labeled 1-16 in Figure 4.20). The spacing between scans was approximately 65 μm. The basic EDS spectra obtained across the scribe and coating interface shows combinations of peaks indicative of C, O, Mg, Al, Si, and Ti. The EDS spot scans throughout the width of the scribe, labeled 1 – 12, show very little indication of Mg or Ca deposits which may be due to chemical dissolution and subsequent washing away by acidic rain precipitation (Table 4.1). A throwing power cannot be detected using EDS upon environmental exposure at Birdwood Golf Course in Charlottesville, VA after 24 weeks. The significant Al, Si, and Ti peaks present in the EDS spectra obtained at positions 13, 14, 15, and 16, in the coated region are a result of aluminum hydroxide, silica, and rutile pigments present in the topcoat. The first-order approximation of the penetration depth of the EDS measurements at 15 keV are estimated to be no more than 5 μm[12], suggesting that the C, O, Al, Si, and Ti peaks are a result of surface products and/or pigmentation in the carbon-rich polymer matrix of the topcoat and not detection of Al in the substrate or Mg in the primer layer.[39]

A SEM micrograph of cross-sectioned MgRP on AA2024-T351 far away from the scribe after 24 weeks of exposure in the field at Birdwood Golf Course in Charlottesville, VA is shown in Figure 4.21. After 24 weeks of exposure, the remaining total coating layer thickness is observed to be approximately 50 - 70 μm thick. Multiple EDS spot scans were obtained on the coating layer after 12 and 24 weeks of exposure at Birdwood Golf Course in Charlottesville, VA. A representative spectra is shown in Figure 4.21b. EDS indicates the presence of metallic, unoxidized Mg in the primer coating after both 12 and

24 weeks of exposure. A SEM micrograph of cross-sectioned MgRP on AA2024-T351 proximate to the scribe after 24 weeks of exposure in the field at Birdwood Golf Course in Charlottesville, VA is shown in Figure 4.21c for visual inspection. Overall, no significant dissipation of the MgRP coating, as evidenced by a decrease in coating thickeness, can be observed.

XRD spectra of AA2024-T351 panels coated with Mg-rich primer (initial MgPVC = 45%) and polyurethane topcoat after 0, 24, and 52 weeks of exposure in the field at Birdwood Golf Course in Charlottesville, VA are shown in Figure 4.22. The relative integrated peak intensities of the Mg peaks shown in Figure 4.22 do not significantly decrease with increasing exposure time in the field at Birdwood Golf Course in Charlottesville, VA, which indicates no significant depletion of metallic Mg pigment from the coating system after 52 weeks. Rutile (TiO_2) was identified in the XRD spectra of AA2024-T351 panels coated with MgRP and polyurethane topcoat as a result of the significant amount of rutile pigment in the topcoat. Principle XRD peaks of relevant Mg or Al corrosion products are labeled a, b, c, and d in Figure 4.22. Detectable surface products were not present in the XRD spectra of MgRP coated AA2024-T351 and polyurethane topcoat after 24 or 52 weeks of exposure at Birdwood Golf Course in Charlottesville, VA.

OCP measurements of AA2024-T351 panels coated with Mg-rich primer (initial MgPVC = 45%) and polyurethane topcoat were taken after 0, 6, 12, 24, and 52 weeks of exposure in the field at Birdwood Golf Course in Charlottesville, VA. Due to the long wetting and

capacitive discharge period of the high performance polyurethane topcoat, a stable OCP could not be measured on environmentally exposed, topcoated samples until approximately 6 hours of immersion in 5% NaCl solution. These values fall between the open circuit potentials of bare AA2024-T351 (-0.6 V vs. SCE) and bare Mg (-1.6 V vs. SCE) in ambiently aerated 5% NaCl solution, which suggest that Mg pigment remains in the MgRP coating and is available for sacrificial galvanic protection of the AA2024-T351 substrate after environmental exposure in the field at Birdwood Golf Course in Charlottesville, VA

EIS measurements of AA2024-T351 panels coated with Mg-rich primer (initial MgPVC = 45%) and polyurethane topcoat taken after 0, 6, 12, 24, and 52 weeks of exposure in the field at Birdwood Golf Course in Charlottesville, VA (scatter plot) and the results of the automated fitting analysis (lines) are shown in Figure 4.23. The values of each representative circuit component produced by the automated fitting routine for selected exposure times at Birdwood Golf Course in Charlottesville, VA are tabulated in Table 3.3. The AA2024-T351 coated with MgRP and polyurethane topcoat did not display a decrease of the low frequency (at 0.01 Hz) impedance or a shift in the break point frequency of the Bode phase angle throughout environmental exposure at Birdwood Golf Course in Charlottesville, VA. Both phenomena indicate very little or no loss of barrier protection capability throughout the duration of the exposure.[41, 42]

4.4.3 Behavior During and After Exposure in ASTM B-117 with 5% NaCl

Optical micrographs of MgRP coated AA2024-T351 panels that have been exposed in ASTM B-117 with 5% NaCl solution for 0, 384, and 984 hours are shown in Figure 4.24 and Figure 4.25. In general, the coating was observed to remain bright white in color throughout the exposure period. After 984 hours of exposure in ASTM B-117 with 5% NaCl solution, the scribe appears, at low magnification, to contain some salt or corrosion product. It is important to note that no blistering or similar macroscopic coating failure phenomena are observed in the MgRP or along the scribe lines after exposure for 984 hours in ASTM B-117 with 5% NaCl solution. Upon closer investigation with the SEM (Figure 4.26, Figure 4.27, and Figure 4.28), after 384 and 984 hours of exposure, the scribed region appears to contain areas of AA2024-T351 substrate corrosion.

To further investigate the composition of any corrosion products or deposits in the scribe, and of the MgRP proximate to the scribe, 16 consecutive EDS spot scans were obtained across the width of the scribe and coating interface (labeled 1-16 in Figure 4.29). The spacing between scans was approximately 65 μm. The basic EDS spectra obtained across the scribe and coating interface shows combinations of peaks indicative of C, O, Na, Mg, Al, Si, and Cl. The EDS spot scans obtained throughout the width of the scribe, labeled 1 – 12, all show detectable amounts of Al, O, Na, and Cl species present in the scribe, suggesting that the bare AA2024-T351 in the scribe was subject to some corrosion. Positions 12 and 13, which are directly proximate to the edge of the MgRP coating on one side of the scribe, show significant Na and Mg peaks. This is likely the side of the scribe that is positioned towards the bottom of the panel during exposure, resulting in a

thicker electrolyte layer at this position and subsequently greater deposition of NaCl and Mg corrosion product. A throwing power cannot be observed with EDS upon environmental in ASTM B-117 with 5% NaCl solution after 984 hours of exposure. The significant C and O peaks present in the EDS spectra obtained at positions 13, 14, 15, and 16, in the coated region, are a result of the carbon rich polymer matrix of the topcoat. The first-order approximation of the penetration depth of the EDS measurements at 15 keV is estimated to be no more than 5 μm[19] suggesting that the C, O, and Cl intensities from this region are a result of surface products and/or the carbon-rich polymer matrix of the topcoat and not from the substrate or primer layer.[39]

A SEM micrograph of cross-sectioned MgRP on AA2024-T351 far away from the scribe, after 984 hours of exposure in ASTM B-117 with 5% NaCl solution is shown in Figure 4.30a. After 984 hours of exposure, the remaining total coating layer thickness is observed to be approximately 50 - 70 μm thick. Multiple EDS spot scans were obtained in the coating layer after 384 and 984 hours of exposure in ASTM B-117 with 5% NaCl. A representative EDS spectrum is shown in Figure 4.30b. EDS spot scans obtained on the coating layer after 984 hours of exposure in ASTM B-117 with 5% NaCl solution indicate the presence of metallic, unoxidized Mg in the coating. Similar EDS measurements obtained on the coating layer after 984 hours of exposure indicate the presence of a significant amount of metallic, unoxidized Mg, but also trace amounts of O and Cl in the coating. It is unclear from EDS analysis how much of the buried Mg pigment is oxidized after 984 hours of exposure in ASTM B-117 with 5% NaCl solution. SEM micrographs of cross-sectioned MgRP on AA2024-T351 proximate to the scribe

after 984 hours of exposure in ASTM B-117 with 5% NaCl solution are shown in Figure 4.30c for visual inspection. The coating layer is approximately 50 – 70 µm thick. Overall, the edges and walls of the scribes appear to have moderate amounts of corrosion product deposited on them.

XRD spectra of AA2024-T351 panels coated with Mg-rich primer (initial MgPVC = 45%) and polyurethane topcoat after 0, 384, and 984 hours of exposure in ASTM B-117 with 5% NaCl solution are shown in Figure 4.31. The relative integrated peak intensities of the Mg peaks shown in Figure 4.31 do not significantly decrease with increasing exposure time in ASTM B-117 with 5% NaCl solution which indicates no significant depletion of metallic Mg pigment from the coating system after 984 h. Rutile (TiO_2) was identified in the XRD spectra of AA2024-T351 panels coated with MgRP and polyurethane topcoat as a result of the significant amount of rutile pigment in the topcoat. Principle XRD peaks of relevant Mg or Al corrosion products are labeled a, b, c, and d in Figure 4.31. With increasing exposure time, NaCl became prevalent in the XRD spectra as a result of the high deposition rate and continuous wetting characteristics of the salt fog environment.

OCP measuremnts of AA2024-T351 panels coated with Mg-rich primer (initial MgPVC = 45%) and polyurethane topcoat were taken after 0, 168, 384, 744, and 984 hours of exposure in ASTM B-117 with 5% NaCl solution. Due to the long wetting and capacitive discharge period of the high performance polyurethane topcoat, a stable OCP could not be measured on environmentally exposed, topcoated samples until approximately 6 hours

of immersion in 5% NaCl solution. These values fall between the open circuit potentials of bare AA2024-T351 (-0.6 V vs. SCE) and bare Mg (-1.6 V vs. SCE) in ambiently aerated 5% NaCl solution which suggest that Mg pigment remains in the MgRP coating and is available for sacrificial galvanic protection of the AA2024-T351 substrate after environmental exposure in ASTM B-117 with 5% NaCl solution.

EIS measurements of MgRP-coated AA2024-T351 (initial MgPVC = 45%) taken after 0, 168, 384, 744, and 984 hours of exposure in ASTM B-117 with 5% NaCl solution (scatter plot) and the results of the automated fitting analysis (lines) are shown in Figure 4.32. The values of each representative circuit component produced by the automated fitting routine for selected exposure times in ASTM B-117 with 5% NaCl solution are tabulated in Table 3.4. The AA2024-T351 panels coated with Mg-rich primer (initial MgPVC = 45%) and polyurethane topcoat displayed a decrease of less than one order of magnitude of the low frequency (at 0.01 Hz) impedance as well as little shift in the break point frequency of the Bode phase angle throughout environmental exposure in ASTM B-117 with 5% NaCl solution. Both phenomena indicate very little loss of barrier protection capability throughout the duration of the exposure.[41, 42]

4.4.4 Behavior During and After Exposure in ASTM B-117 Modified with ASTM Seawater:

Optical micrographs of AA2024-T351 panels coated with Mg-rich primer (initial MgPVC = 45%) and polyurethane topcoat that have been exposed in ASTM B-117

modified with ASTM artificial sea water solution for 0, 408, and 1000 hours are shown in Figure 4.33 and Figure 4.34. In general, the coating was observed to remain bright white in color throughout the exposure period. After 1000 hours of exposure in the ASTM B-117 environment modified with ASTM artificial seawater the scribe appears, at low magnification, to be full of tan or ivory colored deposits. No blistering or similar macroscopic coating failure phenomena are observed in the MgRP or along the scribe lines after exposure for 1000 hours in the ASTM B-117 environment modified with ASTM artificial seawater. After 408 and 984 hours of exposure, the scribed region appears to be very rough in texture and covered in lamellar structures typically associated with $Mg(OH)_2$[26, 30, 43] as well as spherical groupings of needle-like precipitates typically associated with calcareous deposits (Figure 4.35, Figure 4.36, Figure 4.37).[31-38] Metallic Mg is known to be readily converted to $Mg(OH)_2$ in most ambient aqueous environments.[44] The precipitates appear to condense closer to the edges of the scribe, proximate to the coating, and dissipate towards the center of the scribe.

To further investigate the composition of the coating and the deposits in the scribe 16 consecutive EDS spot scans were obtained across the width of the scribe and coating interface (labeled 1-16 in Figure 4.38). The spacing between scans was approximately 65 μm. EDS spot scans acquired throughout the entire width of the scribe (positions labeled 1 – 11) contained O, Mg, Al, S, Ca, and Cl and each obtained over the coating consisting of C, O, and Al. Hydrotalcite[30] and calcareous[31-38] deposits are indicative of regions of cathodic protection afforded to the AA2024-T351 by the MgRP. The deposition of Mg and Ca species throughout most of the scribe suggests that the entire scribe width may

have been subject to cathodic protection in the ASTM B-117 environment modified with ASTM artificial seawater. The significant C and O peaks present in the EDS spectra were obtained in the coated region at positions 14, 15, and 16. The first-order approximation of the penetration depth of the EDS measurements at 15 keV are estimated to be no more than 5 μm[19] suggesting that the C, O, and Al intensities from this region are a result of surface products and/or the carbon-rich polymer matrix of the topcoat and not from the substrate or primer layer.[39]

A SEM micrograph of a cross-sectioned AA2024-T351 panel coated with Mg-rich primer (initial MgPVC = 45%) and polyurethane topcoat far away from the scribe after 1000 hours of exposure in the ASTM B-117 environment modified with ASTM artificial seawater is shown in Figure 4.39a. After 1000 hours of exposure, the remaining total coating layer is observed to be approximately 50 - 70 μm thick. Multiple EDS spot scans were obtained in the coating layer after 408 and 1000 hours of exposure in ASTM B-117 with ASTM artificial seawater. A Representative EDS spectrum is shown in Figure 4.39b. EDS obtained on the coating layer after 1000 hours of exposure indicate the presence of C, O, Mg, Al, Si, and Ti which, besides Mg, all result from pigments in the topcoat. A SEM micrograph of cross-sectioned MgRP on AA2024-T351 proximate to the scribe after 1000 hours of exposure in the ASTM B-117 environment modified with ASTM artificial seawater is shown in Figure 4.39c for visual inspection. The total coating layer is approximately 50 – 70 μm thick. Overall, the edges and walls of the scribes appear to have corrosion product deposited on them.

XRD spectra of AA2024-T351 panels coated with Mg-rich primer (initial MgPVC = 45%) and polyurethane topcoat after 0, 408, and 1000 hours of exposure in the ASTM B-117 environment modified with ASTM artificial seawater are shown in Figure 4.40. The relative integrated intensities of the Mg peaks shown in Figure 4.40 do not significantly decrease with increasing exposure time in the ASTM B-117 environment modified with ASTM artificial seawater which indicates no significant depletion of metallic Mg pigment from the coating system after 1000 hours of exposure. Rutile (TiO_2) was identified in the XRD spectra of AA2024-T351 panels coated with MgRP and polyurethane topcoat as a result of the significant amount of rutile pigment in the topcoat. Principle XRD peaks of relevant Mg or Al corrosion products are labeled a, b, c, and d in Figure 4.40. Mg or Al corrosion products were not observed with XRD after 408 or 1000 hours of exposure in ASTM B-117 modified with ASTM artificial seawater. With increasing exposure time, NaCl became prevalent in the XRD spectra as a result of the high deposition rate and continuous wetting characteristics of the salt fog environment. After 1000 hours of exposure in ASTM B-117 modified with ASTM artificial seawater, $CaCO_3$ became prevalent in the XRD spectra and is shown to be the predominant crystalline calcareous deposit covering the samples which indicates a high pH existed over the coating during environmental exposure.

OCP measuremnts of AA2024-T351 panels coated with Mg-rich primer (initial MgPVC = 45%) and polyurethane topcoat were taken after 0, 192, 408, 698, and 1000 hours of exposure in the ASTM B-117 environment modified with ASTM artificial seawater. Due to the long wetting and capacitive discharge period of the high performance polyurethane

topcoat, a stable OCP could not be measured on environmentally exposed, topcoated samples until approximately 6 hours of immersion in 5% NaCl had been accrued. These values fall between the open circuit potentials of bare AA2024-T351 (-0.6 V vs. SCE) and bare Mg (-1.6 V vs. SCE) in ambiently aerated 5% NaCl solution which suggest that Mg pigment remains in the MgRP coating and is available for sacrificial galvanic protection of the AA2024-T351 substrate after environmental exposure in the ASTM B-117 environment modified with ASTM artificial seawater

EIS measurements of AA2024-T351 panels coated with Mg-rich primer (initial MgPVC = 45%) and polyurethane topcoat taken after 0, 192, 408, 698, and 1000 hours of exposure in the ASTM B-117 environment modified with ASTM artificial seawater (scatter plot) and the results of the automated fitting analysis (lines) are shown in Figure 4.41. The values of each representative circuit component produced by the automated fitting routine for selected exposure times in ASTM B-117 modified with ASTM artificial sea water are tabulated in Table 3.5. The AA2024-T351 panels coated with Mg-rich primer (initial MgPVC = 45%) and polyurethane topcoat displayed a decrease of less than one order of magnitude of the low frequency (at 0.01 Hz) impedance as well as a slight shift towards lower frequencies in the break point frequency of the Bode phase angle after 192, 696, and 1000 hours of environmental exposure in ASTM B-117 modified with ASTM artificial seawater. Both phenomena indicate very little loss of barrier protection capability throughout the duration of the exposure.[41, 42] However, the electrochemical impedance measured after 408 hours of exposure was one or two orders of magnitude lower (at 0.01 Hz) than the measurements taken after all other exposure

times. A large shift in the break point frequency of the Bode phase angle was observed, as well, in the measurement taken after 408 hours of exposure. The lower barrier properties measured after 408 hours of exposure are presumed to be the result of a coating defect at the site of the measurement and not representative of the global condition of the coating.

4.4.5 Tracking MgRP Degradation throughout Environmental Exposure:

The integrated, normalized XRD Mg <200> peak ($2\theta = 34.3982^{o}$) intensity is plotted versus exposure time in each environment in Figure 4.42 for comparison. Multiple XRD measurements were obtained from areas of the coating far from the scratch and the results were averaged to reduce scatter caused by the polyurethane topcoat. In each exposure environment investigated in this study, the integrated normalized intensity of metallic Mg was observed to, on average, slightly decrease with increased exposure time. None of the environmental exposures reported on in this study resulted in full depletion (less than 5% by volume as detectable by XRD[29]) of Mg pigment from the MgRP under a high performance polyurethane topcoat. The topcoat was observed to severely mediate the depletion of Mg pigment from the MgRP in all exposure environments studied as compared to identical environmental exposures of non-topcoated variations.[19] Full immersion in ambiently aerated 5% NaCl solution, salt fog cabinet exposure in ASTM B-117 with 5% NaCl, and salt fog cabinet exposure in ASTM B-117 with ASTM artificial seawater all resulted in partial depletion of metallic Mg pigment in the MgRP far from the scribe after 1,000 hours. Field exposures in Charlottesville, VA and Kennedy Space

Center, FL also resulted in similar levels of Mg pigment depletion far from the scribe after 1 year of exposure. Hence, the general qualitative aspects of Mg pigment depletion were similar in all environments studied.

The global galvanic protection potential (open circuit potential) of the AA2024-T351 panels coated with Mg-rich primer (initial MgPVC = 45%) and polyurethane topcoat, as measured after 6 hours of immersion in ambiently aerated 5% NaCl solution, is plotted versus exposure time in each environment in Figure 4.43 for comparison. As a result of partial depletion of remote Mg pigment particles, the global galvanic protection potential of the coating system, with respect to remote scratches, increased slightly with exposure time in each environment. The global galvanic protection potential increased from initial values of approximately -1.0 V vs. SCE to -0.7 V vs. SCE after extensive environmental exposure. These values fall between the open circuit potentials of bare AA2024-T351 (-0.6 V vs. SCE) and bare Mg (-1.6 V vs. SCE) in ambiently aerated 5% NaCl solution and are predicted by mixed potential theory.[8] These mixed potentials suggest that Mg pigment that is available for sacrificial galvanic protection of the AA2024-T351 substrate remains in the MgRP coating after the environmental exposures studied.

The correlation between global galvanic protection potential afforded to the AA2024-T351 substrate and metallic Mg pigment remaining in the coating is presented in Figure 3.48. Due to the combined scatter of both the XRD and the full immersion measurements of OCP caused by the thick, polyurethane topcoat layer, there exists a large amount of scatter in the correlation between the global galvanic protection potential and metallic Mg

pigment remaining in the coating. However, in general, in all environments studied, the galvanic protection potential of the coating system (as measured in ambiently aerated 5% NaCl solution) increases with exposure in each environment, as a result of Mg pigment depletion.

Initial electrochemical impedance measurements of bare AA2024-T351 pretreated with Prekote, AA2024-T351 panels coated with Mg-rich primer (initial MgPVC = 45%), and of AA2024-T351 panels coated with Mg-rich primer (initial MgPVC = 45%) and polyurethane topcoat are shown in Figure 4.45. Adding both the MgRP (MgPVC = 45%) and the polyurethane topcoat layer significantly increases the electrochemical impedance of the sample with respect to bare AA2024-T351. This is particularly true at very low frequencies, which correlates directly to the barrier properties of the sample in question.[41, 42, 45-51] In general, for all environments, very little degradation in barrier properties of the coating system is observed with increased environmental exposure time. The low frequency impedance at 0.01 Hz (Figure 4.46) in ambiently aerated 5% NaCl solution remains very high ($>10^9$ Ω-cm^2) over the course of all exposures studied. The breakpoint frequency[42, 52] and the saddle frequency[51] primarily occur at frequencies below the lower limit of the frequency range interrogated. As well, there is inherent scatter in the data at longer exposure times due to the near random occurrence of, and random interrogation of, defects in the coating. However, in all environments studied, the electrochemical impedance at 0.01 Hz never fell below 10^9 Ω–cm^2, which is two to four orders of magnitude higher than measurements of non-topcoated variations that were exposed to identical environments.

4.5 Discussion

Table 4.6 summarizes observations with regard to blistering, underpaint corrosion, cathodic corrosion, and throwing power on AA2024-T351 panels coated with MgRP and polyurethane topcoat after environmental exposure in the field and lab.

4.5.1 Throwing Power

One purpose of this study was to determine the "throwing power" of the MgRP primer coating on AA2024-T351 in a topcoated condition in various lab and field environments.[8] Predicting the throwing power is quite complicated because the scribe size, coating formulation, electrolyte composition, electrolyte geometry, and bare/coated area ratios can all be limiting factors when considering protection ability or throwing power of a coating that protects by sacrificial anode based galvanic protection. A large source of variation between performance of the coating in the salt fog and field exposure environments, with regards to throwing power, is the electrolyte geometry in each environment. A sacrificial coating can only protect defects (or bare substrate at scratches) which it is both electrically and ionically connected to. Also, the addition of a topcoat in full immersion (Figure 4.47a), thin-layer electrolyte (Figure 4.47b), or droplet electrolyte (Figure 4.47c) scenarios serves to limit the distance over which Mg pigment in the coating can protect remote scratches by adding additional ionic resistance into the galvanic couple relationship of Mg pigment particles whose ionic current path is through the coating layer. The result of this is that scratches can only be protected by Mg pigment that is directly proximate to the scribe unless sufficient continuous time-of-wetness is

[8] The "throwing power" pertains to the distance over which the MgRP coating system can protect bare AA2024-T351 by sacrificial anode based cathodic protection.

accrued for the topcoat and primer polymers to wet and allow for Mg pigment further away from the scratch to provide protection. For these reasons it is understandable why there exists a larger deposition of Mg species proximate to the coating edge compared to the center of the scribe after exposure in the field at Kennedy Space Center (Figure 4.10) as the electrolyte layer was subject to cyclic wetting and drying (shown schematically in Figure 4.47b and c). During a given episodic wetting or drying event, throwing power is likely cyclically increased or diminished. In the ASTM seawater salt fog environment (Figure 4.38) the electrolyte layer is subject to continuous wetting (shown schematically in Figure 4.47b) enabling a large throwing power such that Mg deposits cover the scribe relatively uniformly. These effects are still expected to operate with a topcoat.

One factor which complicates the determination of a throwing power in environments, such as in the field at Birdwood Golf Course in Charlottesville, VA (Figure 4.20) and in the lab in ASTM B-117 with 5% NaCl (Figure 4.29), is the limited availability of Mg and Ca species which precipitate at sites of cathodic protection and which are used as markers to identify zones of cathodic protection as discussed in Part I of this study. A second factor that complicates the determination of a throwing power in such environments is the mediation of the galvanic protection potential afforded to remote defects (Figure 4.43). This mediation of galvanic protection potential by the increased ionic resistance of the polyurethane topcoat (Figure 4.45) at sites of cathodic protection acts to limit the increase in pH at such sites, increasing the solubility of Mg and Ca species, which prevents their precipitation.

A third factor that complicates the determination of a throwing power after environmental exposure is the chemical dissolution of the marker precipitates in acidic, high TOW environments, like that of Birdwood Golf Course in Charlottesville, VA, which is subject to regular acidic precipitation (Table 4.1). EDS spot scans obtained throughout the width of the scribe after 1 year of exposure at Birdwood Golf Course in Charlottesville, VA, (Figure 4.20) showed very little indication of Mg or Ca deposits common to regions of cathodic protection, making evidence and observation for throwing power in this environment difficult.

It is likely that the throwing power of the MgRP could be detected in EDS spot scans obtained throughout the width of the scribe after exposure at Kennedy Space Center, FL (Figure 4.10) and after ASTM B-117 with ASTM seawater (Figure 4.38) due to the more alkaline exposure conditions (Table 4.1) and the increased availability of Mg and Ca species in the ambient electrolyte.[53] Not only is the rain precipitation at Kennedy Space Center, FL slightly alkaline as compared to Charlottesville, VA (Table 4.1), but the proximity of the test racks to the ocean make the samples susceptible to spray from the ocean surf which has a pH of roughly 8.2 and contains high concentrations of Mg and Ca species.[53, 54] This alkaline pH suppresses the chemical dissolution of species used to identify zones of cathodic protection. Additionally, in most exposure environments and moderate pH ranges, aluminum is well known to form a barrier oxide film that reforms quickly when damaged, leaving the primary form of attack observed after exposure in most service environments to be non-uniform pitting corrosion.[55] For this reason, in all

environments studied in this report, definitive zones of significant Al corrosion in the scribes could not be identified due to low pit densities.

4.5.2 Primary Effects of the Topcoat and the Residual Protection Available After Prolonged Environmental Exposure

No significant variations in global topcoat or MgRP polymer degradation were observed between laboratory salt fog and field exposure environments as assessed by SEM cross section and electrochemical impedance. After prolonged exposure in both laboratory salt fog and field environments it is clear that both significant barrier and sacrificial galvanic protection mechanisms remain active and are available to protect the AA2024-T351 substrate.

In all environments, no significant decrease in thickness of the MgRP and topcoat polymers was observed after prolonged exposures in laboratory salt fog and field exposures (Figure 4.11, Figure 4.21, Figure 4.30, and Figure 4.39). As well, the low frequency (at 0.01 H) electrochemical impedance of AA2024-T351 panels coated with MgRP (initial MgPVC = 45%) and Aerodur 5000 topcoat (Figure 4.46) remained very high ($\geq 10^9$ Ω–cm^2) throughout all lab and field exposures reported on in this study indicating high barrier protection afforded to the substrate. The galvanic protection potential, as measured in ambiently aerated 5% NaCl solution increased from initial values of approximately -1.0 V vs. SCE to -0.7 V vs. SCE after extensive environmental exposure. These values fall between the open circuit potentials of bare AA2024-T351 (-

0.6 V vs. SCE) and bare Mg (-1.6 V vs. SCE) in ambiently aerated 5% NaCl solution which suggests that Mg pigment that is both electrically and ionically connected to the AA2024-T351 can provide sacrificial galvanic protection of the AA2024-T351 substrate in extended time-of-wetness events.

The uniformity in performance in the lab and field is presumed to be due to the polyurethane topcoat polymer's resistance to UV degradation. Polyurethane organic polymers undergo far less degradation as a result of UV exposure. For this reason Polyurethane polymers with UV absorbing pigments, like the one used in the Aerodur 5000 Topcoat, are primarily used as topcoat polymers.[15, 17] Kennedy Space Center, FL is known to be a severe site of UV exposure.[56] UV radiation is known to severely degrade epoxy organic polymers that are used in the Mg-rich primer.[15, 17, 18, 27] No chalking, or any other phenomena signifying significant UV degradation was observed in lab and field exposures of AA2024-T351 panels coated with MgRP (initial MgPVC = 45%) and Aerodur 5000 topcoat reported on in this study.

4.5.3 Potential Limitations in Extrapolating Laboratory Exposure Results

It is important to note that NaCl and ASW are generally not considered direct proxies for ambient marine aerosol however are commonly used as standard lab environments in corrosion coating system qualification studies.[57-60] Natural seawater is alkaline and contains low concentrations of organic matter and oxidants.[58] In contrast, in most marine

regions, marine aerosols are acidic, highly enriched in organic matter, and contain high concentrations of oxidants that vary as a function of solar radiation. Given that photochemistry produces acidic reaction products in the atmosphere while corrosion produces alkalinity, there is a possibility of variability in acid-base chemistry on corroding surfaces over diel cycles with associated impacts on the corrosion processes/rates that are not captured in these salt fog lab exposures. These factors may have also played a role in the interpretation of field results reported in this study; however organic aerosol chemistry was not characterized during either field exposure and can not be commented on. However, it is the view of the authors that once corrosion is initiated on the surface of the MgRP coated panel in such field scenarios, the dissolution of Mg pigment from the primer in combination with the alkanization at cathodic sites on the AA2024-T351 substrate would ultimately dominate the evolution of pH and electrolyte chemistry on the surface of the sample. However, it would be useful and prudent, in future lab studies, to include relevant concentrations of organic matter commonly found in marine aerosols and to include the effects UV radiation as well as diligently characterize aerosol chemistry during future field exposures.

4.5.4 Future Work

In light of the findings in Part I[19] and II of this study and possible limitations highlighted in section 4.5.3, additional modifications to the ASTM environment will be studied including an acidified electrolyte and the inclusion of UV light in the test chamber (see Appendix B for Figures). Future studies will also include diagnostic full immersion and

droplet experiments aimed at studying the effects of environmental factors pertinent to environmental severity such as electrolyte chemistry, atmospheric chemistry, and UV exposure. To further understand and predict the throwing power of the MgRP, finite element analysis needs to be conducted.

4.6 Conclusions

- The Aerodur 5000 topcoat was observed to severely mediate the depletion of Mg pigment from the MgRP in all exposure environments studied as compared to identical environmental exposures of non-topcoated samples as measured by XRD.

- Full immersion in ambiently aerated 5% NaCl solution, ASTM B-117 in 5% NaCl, and ASTM B-117 in ASTM artificial seawater all resulted in partial depletion of metallic Mg pigment in the MgRP far from the scribe after 1000 hours.

- Field exposures in Charlottesville, VA and Kennedy Space Center, FL also resulted in similar levels of Mg pigment depletion far from the scribe after 1 year of exposure.

- The global galvanic protection potential of the coating system, with respect to remote scratches, increased slightly with exposure time in each environment, from initial values of approximately -1.0 V vs. SCE to -0.7 V vs. SCE after extensive environmental exposure. These values fall between the open circuit potentials of bare AA2024-T351 (-0.6 V vs. SCE) and bare Mg (-1.6 V vs. SCE) and are predicted by mixed potential theory. This suggests that Mg pigment that is both electrically and ionically connected to

the AA2024-T351 can provide sacrificial galvanic protection of the AA2024-T351 substrate in extended time-of-wetness events.

- Barrier properties of the MgRP primer coating, as assessed by electrochemical impedance, also slightly degrade with time in each environment but, overall, remain very high ($\geq 10^9$ Ω-cm^2 at 0.01 Hz) throughout exposure in each environment indicating significant barrier protection remains after all environmental exposures studied.

- SEM/EDS after 1000 h of salt fog exposure indicate a throwing power that extended the entire half-width of the scribe in ASTM B-117 exposure modified with ASTM artificial seawater with thin-layer electrolyte geometries, increased availability of Mg and Ca species, and continuous wetting.[53]

- SEM/EDS after 1 year of exposure indicates a throwing power that extends approximately 200 µm into the scribe in the field at Kennedy Space Center, FL with cyclic wetting and drying events, a more alkaline ambient electrolyte (close proximity to sea water spray, pH = 8.1), and increased availability of Mg and Ca species,

- SEM/EDS after 1 year of exposure in the field at Charlottesville, VA and after 1000 hours of exposure in ASTM B-117 with 5% NaCl was inconclusive due to:

  - the likely dissolution of the MgRP coating and subsequent corrosion products by high TOW and low pH rain (pH ≈ 5,Table 4.1).

- the limited availability of Mg and Ca species in these two environments which typically precipitate at sites of cathodic protection and which are used as markers to identify zones of cathodic protection.

- the mediation of the galvanic protection potential afforded to remote defects which acts to limit the increase in pH at such sites, increasing the solubility of Mg and Ca species, which prevents their precipitation.

- The uniformity in performance in the lab and field is presumed to be due to the polyurethane topcoat polymer's resistance to UV degradation and electrolyte ingress. No chalking, or any other phenomena signifying significant UV degradation was observed in lab and field exposures of AA2024-T351 panels coated with MgRP (initial MgPVC = 45%) and Aerodur 5000 topcoat reported on in this study.

4.7 Acknowledgements

This work was supported by the OUSD Corrosion University Pilot Program under the direction of Mr. Daniel Dunmire. Members of NAVAIR[1] and Battelle Memorial Institute[2] are acknowledged for graciously conducting field exposures at Kennedy Space Center, FL and for the generous supply and preparation of MgRP-coated AA2024-T351 panels specifically: Mr. Craig Matzdorf[1], Mr. Frank Pepe[1], Mr. Jerry Curran[1], and Mr. William Abbott[2]. Dr. Jason Lee of the US Naval Research Lab is acknowledged for helpful discussions regarding throwing power.

4.8 References

1. S. S. Pathak, M. D. Blanton, S. K. Mendon and J. W. Rawlins, Investigation on dual corrosion performance of magnesium-rich primer for aluminum alloys under salt spray test (ASTM B117) and natural exposure, Corros Sci, 52, 4 (2010), pp. 1453-1463.
2. G. P. Bierwagen, D. E. Tallman, M. Nanna, D. Battocchi, A. Stamness and V. J. Gelling, New developments in Cr-free primers for aerospace alloys., Abstr Pap Am Chem S, 228, (2004), pp. U360-U360.
3. A. Simoes, D. Battocchi, D. Tallman and G. Bierwagen, Assessment of the corrosion protection of aluminium substrates by a Mg-rich primer: EIS, SVET and SECM study, Prog Org Coat, 63, 3 (2008), pp. 260-266.
4. D. Battocchi, A. M. Simoes, D. E. Tallman and G. P. Bierwagen, Comparison of testing solutions on the protection of Al-alloys using a Mg-rich primer, Corros Sci, 48, 8 (2006), pp. 2226-2240.
5. D. Battocchi, A. M. Simoes, D. E. Tallman and G. P. Bierwagen, Electrochemical behaviour of a Mg-rich primer in the protection of Al alloys, Corros Sci, 48, 5 (2006), pp. 1292-1306.
6. H. Xu, D. Battocchi, D. E. Tallman and G. P. Bierwagen, Use of Magnesium Alloys as Pigments in Magnesium-Rich Primers for Protecting Aluminum Alloys, Corrosion, 65, 5 (2009), pp. 318-325.
7. G. Bierwagen, D. Battocchi, A. Simoes, A. Stamness and D. Tallman, The use of multiple electrochemical techniques to characterize Mg-rich primers for A1 alloys, Prog Org Coat, 59, 3 (2007), pp. 172-178.
8. A. D. King and J. R. Scully, Sacrificial Anode-Based Galvanic and Barrier Corrosion Protection of 2024-T351 by a Mg-Rich Primer and Development of Test Methods for Remaining Life Assessment, Corrosion, 67, 5 (2011), pp. 05500401-05500422.
9. B. Maier and G. S. Frankel, Behavior of Magnesium-Rich Primers on AA2024-T3, Corrosion, 67, 5 (2011), p. 055001.
10. A. D. King and J. R. Scully, Blistering Phenomena in Early Generation Mg-Rich Primer Coatings on AA2024-T351 and the Effects of CO_2, NACE DoD 2011 Conference Proceedings, (Palm Springs, CA, 2011).
11. J. Nie, M. C. Yan, J. Wang, D. E. Tallman, D. Battocchi and G. P. Bierwagen, Cathodic Corrosion Protection Performance of Mg-Rich Primers: Effect of Pigment Shape and Pigment Volume Concentration, ECS Transactions, 24, 1 (2010), pp. 261-275.
12. A. D. King, B. Kannan and J. R. Scully, Environmental Degradation of a Mg-Rich Primer in Selected Field and Laboratory Environments – Part I. Without a Topcoat, Corrosion, 70, 5 (2014).
13. U.S. Department of Health and Human Services., Report on Carcinogens, 12th Edition, U.S. Department of Health and Human Services, Public Health Services, National Toxicology Program, 2011.

14. R. G. Buchheit, Chromate and Chromate-Free Conversion Coatings, vol. 13A, ASM Handbook Volume 13A, Corrosion: Fundamentals, Testing, and Protection (ASM International) (Materials Park, Ohio, ASM International, 2003).
15. P. J. Adams, Personal correspondence with Dr. Pat J. Adams of AkzoNobel Aerospace Coatings Inc., (2011).
16. W. Funke, Mechanisms of Protecting Metals by Organic Coatings against Corrosion, J Electrochem Soc, 133, 8 (1986), pp. C304-C304.
17. A. Forsgren, Corrosion control through organic coatings, Corrosion technology, vol. (Boca Raton, FL: CRC/Taylor & Francis, 2006), p. 161 p.
18. Z. W. Wicks, Organic coatings : science and technology, 3rd, vol. (Hoboken, N.J.: Wiley-Interscience, 2007), p. xxiii, 722 p.
19. A. D. King and J. R. Scully, Environmental Degradation of a Mg-Rich Primer in Selected Field and Laboratory Environments - Part I. Without a Topcoat, In Progress For Submission to CORROSION, (2013).
20. M. Mokaddem, P. Volovitch, F. Rechou, R. Oltra and K. Ogle, The anodic and cathodic dissolution of Al and Al-Cu-Mg alloy, Electrochim Acta, 55, 11 (2010), pp. 3779-3786.
21. S. M. Moon and S. I. Pyun, The corrosion of pure aluminium during cathodic polarization in aqueous solutions, Corros Sci, 39, 2 (1997), pp. 399-408.
22. S. I. Pyun and S. M. Moon, Corrosion mechanism of pure aluminium in aqueous alkaline solution, J Solid State Electr, 4, 5 (2000), pp. 267-272.
23. H. Kaesche, Studies on the Corrosion of Aluminum, Zeitschrift für physikalische Chemie, 14, 7 (1963), pp. 557-566.
24. H. Kaesche, Zeitschrift für physikalische Chemie, 34, (1962), pp. 87-108.
25. R. D. Armstrong and V. J. Braham, The mechanism of aluminium corrosion in alkaline solutions, Corros Sci, 38, 9 (1996), pp. 1463-1471.
26. M. Pourbaix, Atlas of electrochemical equilibria in aqueous solutions, 2d English, vol. (Houston, Tex.: National Association of Corrosion Engineers, 1974), p. 644.
27. C. Matzdorf, Personal correspondence with Mr. Craig Matzdorf of NAVAIR, (2009).
28. W. H. Abbott, Personal correspondence with Mr. William Abbott of Battelle Memorial Institute, (2009).
29. V. K. Pecharsky and P. Y. Zavalij, Fundamentals of powder diffraction and structural characterization of materials, 2nd, vol. (New York: Springer, 2009), p. xxiii, 741 p.
30. R. G. Buchheit, M. D. Bode and G. E. Stoner, Corrosion-Resistant, Chromate-Free Talc Coatings for Aluminum, Corrosion, 50, 3 (1994), pp. 205-214.
31. C. Deslouis, A. Doncescu, D. Festy, O. Gil, V. Maillot, S. Touzain and B. Tribollet, Kinetics and characterisation of calcareous deposits under cathodic protection in natural sea water, Electrochemical Methods in Corrosion Research Vi, Pts 1 and 2, 289-2, (1998), pp. 1163-1180.
32. C. Deslouis, D. Festy, O. Gil, G. Rius, S. Touzain and B. Tribollet, Characterization of calcareous deposits in artificial sea water by impedance techniques - I. Deposit of CaCO3 without Mg(OH)(2), Electrochim Acta, 43, 12-13 (1998), pp. 1891-1901.

33. R. A. Humble, Cathodic protection of steel in seawater with magnesium anodes, Corrosion, 4, (1948), pp. 358-370.
34. R. U. Lee and J. R. Ambrose, Influence of Cathodic Protection Parameters on Calcareous Deposit Formation, Corrosion, 44, 12 (1988), pp. 887-891.
35. F. G. Liu, S. R. Wu and C. S. Lu, Characterisation of calcareous deposits on freely corroding low carbon steel in artificial sea water, Corros Eng Sci Techn, 46, 5 (2011), pp. 611-617.
36. C. Rousseau, F. Baraud, L. Leleyter, M. Jeannin and O. Gil, Calcareous deposit formed under cathodic protection in the presence of natural marine sediments: A 12 month experiment, Corros Sci, 52, 6 (2010), pp. 2206-2218.
37. C. Barchiche, C. Deslouis, D. Festy, O. Gil, P. Refait, S. Touzain and B. Tribollet, Characterization of calcareous deposits in artificial seawater by impedance techniques 3 - Deposit of CaCO3 in the presence of Mg(II), Electrochim Acta, 48, 12 (2003), pp. 1645-1654.
38. C. Deslouis, D. Festy, O. Gil, V. Maillot, S. Touzain and B. Tribollet, Characterization of calcareous deposits in artificial sea water by impedances techniques: 2-deposit of Mg(OH)(2) without CaCO3, Electrochim Acta, 45, 11 (2000), pp. 1837-1845.
39. R. Castaing, Electron Probe Microanalysis, L. Marton and M. Claire, Eds., vol. Volume 13, Advances in Electronics and Electron Physics, Academic Press, 1960, p. 317-386).
40. A. Amirudin and D. Thierry, Application of electrochemical impedance spectroscopy to study the degradation of polymer-coated metals, Prog Org Coat, 26, 1 (1995), pp. 1-28.
41. F. Mansfeld, Determination of the Reactive Area of Organic Coated Metals - Physical Meaning and Limits of the Break-Point Method - Discussion, Electrochim Acta, 39, 10 (1994), pp. 1451-1452.
42. H. P. Hack and J. R. Scully, Defect Area Determination of Organic Coated Steels in Seawater Using the Breakpoint Frequency Method, J Electrochem Soc, 138, 1 (1991), pp. 33-40.
43. S. S. Pathak, M. D. Blanton, S. K. Mendon and J. W. Rawlins, Carbonation of Mg powder to enhance the corrosion resistance of Mg-rich primers, Corros Sci, 52, 11 (2010), pp. 3782-3792.
44. M. M. Avedesian, H. Baker and Asm International. Handbook Committee., Magnesium and magnesium alloys, ASM specialty handbook, vol. (Materials Park, OH: ASM International, 1999), p. ix, 314 p.
45. F. Mansfeld, Models for the Impedance Behavior of Protective Coatings and Cases of Localized Corrosion, Electrochim Acta, 38, 14 (1993), pp. 1891-1897.
46. F. Mansfeld, Electrochemical Impedance Spectroscopy (Eis) as a New Tool for Investigating Methods of Corrosion Protection, Electrochim Acta, 35, 10 (1990), pp. 1533-1544.
47. F. Mansfeld, Corrosion Rate Measurements with the Ac Impedance Technique, J Electrochem Soc, 127, 8 (1980), pp. C365-C365.

48. F. Mansfeld, L. T. Han, C. C. Lee and G. Zhang, Evaluation of corrosion protection by polymer coatings using electrochemical impedance spectroscopy and noise analysis, Electrochim Acta, 43, 19-20 (1998), pp. 2933-2945.
49. F. Mansfeld, M. W. Kendig and S. Tsai, Evaluation of Corrosion Behavior of Coated Metals with Ac Impedance Measurements, Corrosion, 38, 9 (1982), pp. 478-485.
50. F. Mansfeld and C. H. Tsai, Determination of Coating Deterioration with Eis .1. Basic Relationships, Corrosion, 47, 12 (1991), pp. 958-963.
51. M. Kendig and J. Scully, Basic Aspects of Electrochemical Impedance Application for the Life Prediction of Organic Coatings on Metals, Corrosion, 46, 1 (1990), pp. 22-29.
52. F. Deflorian, L. Fedrizzi and P. L. Bonora, Determination of the Reactive Area of Organic Coated Metals Using the Breakpoint Method, Corrosion, 50, 2 (1994), pp. 113-119.
53. Astm, Standard Practice for the Preparation of Substitute Ocean Water, ASTM D1141 - 98, DOI: 10.1520/D1141-98R08 (1998).
54. A. Turnbull, S. Zhou, P. Nicholson and G. Hinds, Chemistry of concentrated salts formed by evaporation of Seawater on duplex stainless steel, Corrosion, 64, 4 (2008), pp. 325-333.
55. J. G. Kaufman, Corrosion of Aluminum and Aluminum Alloys, vol. 13B, ASM Handbook Volume 13B, Corrosion: Materials (ASM International) (Materials Park, Ohio, ASM International, 2003, p. 95-124).
56. J. D. Morrison, Report on Relative Corrosivity of Atmospheres at Various Distances from the Seacoast, 1980.
57. W. C. Keene, M. S. Long, A. a. P. Pszenny, R. Sander, J. R. Maben, A. J. Wall, T. L. O'halloran, A. Kerkweg, E. V. Fischer and O. Schrems, Latitudinal variation in the multiphase chemical processing of inorganic halogens and related species over the eastern North and South Atlantic Oceans, Atmos Chem Phys, 9, 19 (2009), pp. 7361-7385.
58. W. C. Keene, H. Maring, J. R. Maben, D. J. Kieber, A. a. P. Pszenny, E. E. Dahl, M. A. Izaguirre, A. J. Davis, M. S. Long, X. L. Zhou, L. Smoydzin and R. Sander, Chemical and physical characteristics of nascent aerosols produced by bursting bubbles at a model air-sea interface, J Geophys Res-Atmos, 112, D21 (2007).
59. W. C. Keene, R. Sander, A. a. P. Pszenny, R. Vogt, P. J. Crutzen and J. N. Galloway, Aerosol pH in the marine boundary layer: A review and model evaluation, Journal of Aerosol Science, 29, 3 (1998), pp. 339-356.
60. M. C. Facchini, M. Rinaldi, S. Decesari, C. Carbone, E. Finessi, M. Mircea, S. Fuzzi, D. Ceburnis, R. Flanagan, E. D. Nilsson, G. De Leeuw, M. Martino, J. Woeltjen and C. D. O'dowd, Primary submicron marine aerosol dominated by insoluble organic colloids and aggregates, Geophys Res Lett, 35, 17 (2008).

4.9 Tables

Table 4.1. Exposure conditions in field and lab accelerated life testing environments.

Environment	Mean Temp (ºC)				Mean RH (%)				Mean Dew Point (ºC)			
	Win.	Spr.	Sum.	Fall	Win.	Spr.	Sum.	Fall	Win.	Spr.	Sum.	Fall
KSC	18.7	23.3	28.2	24.2	71.7	69.7	74	72.7	13.5	17.4	23.1	19
Birdwood	8.1	19.9	24	10.2	59.3	58.3	75.2	65.5	0.6	11	19.3	4
B-117	35				95				34			
B-117 w/ ASW	35				95				34			

Environment	Mean Precipitation (mm/hr)				Precip. pH	Mean Cl^- ($\mu g/cm^2/hr$)
	Win.	Spr.	Sum.	Fall		
KSC	0.066	0.154	0.245	0.184	5.4 ± 0.4	0.8
Birdwood	0.102	0.102	0.135	0.139	4.9 ± 0.3	0.002
B-117	0.190				6.9 ± 0.4	600
B-117 w/ ASW	0.190				8.2 ± 0.3	390

Table 4.2. Fitting results of EIS measured on AA2024-T351 panels coated with MgRP (MgPVC = 45%) after field exposure at Kennedy Space Center 30 m lot for 0, 2, 6, 12, and 24 weeks. Tested in ambiently aerated 5% NaCl Solution. Circuit model shown in Figure 3.20.

	units	0 wk	6 wk	12 wk	24 wk	52 wk
R_s	(Ω-cm^2)	10.000	10.000	10.000	10.000	10.000
C_{coat}-Y^o	(nF/cm^2)	0.164	0.134	0.134	0.059	0.159
C_{coat}-n	-	0.966	0.965	0.962	1.000	0.956
R_{coat}	(MΩ-cm^2)	10.000	10.000	10.000	10.000	10.000
C_{dl}-Y^o	(nF/cm^2)	0.201	0.145	0.193	4.247	0.391
C_{dl}-n	-	0.607	0.665	0.588	0.626	0.646
R_{corr}	(GΩ-cm^2)	152.300	37.950	38.710	6.118	7.338

Table 4.3. Fitting results of EIS measured on AA2024-T351 panels coated with MgRP (MgPVC = 45%) after field exposure at Charlottesville, VA for 0, 2, 6, 12, and 24 weeks. Tested in ambiently aerated 5% NaCl Solution. Circuit model shown in Figure 3.20.

	units	0 wk	6 wk	12 wk	24 wk	52 wk
R_s	(Ω-cm^2)	10.000	10.000	10.000	10.000	10.000
C_{coat}-Y^o	(nF/cm^2)	0.164	0.245	0.111	0.180	0.156
C_{coat}-n	-	0.966	0.958	0.993	0.968	0.965
R_{coat}	(MΩ-cm^2)	10.000	10.000	10.000	10.000	10.000
C_{dl}-Y^o	(nF/cm^2)	0.201	0.547	0.240	0.203	0.218
C_{dl}-n	-	0.607	0.541	0.761	0.698	0.592
R_{corr}	(GΩ-cm^2)	152.300	13.300	18.700	13.180	9.139

Table 4.4. Fitting results of EIS measured on AA2024-T351 panels coated with MgRP (MgPVC = 45%) after LALT in ASTM B-117 for 0, 168, 384, 744, and 984 hours. Tested in ambiently aerated 5% NaCl Solution. Circuit model shown in Figure 3.20.

	units	0 hrs	168 hrs	384 hrs	744 hrs	984 hrs
R_s	(Ω-cm^2)	10.000	10.000	10.000	10.000	10.000
C_{coat}-Y^o	(nF/cm^2)	0.164	0.221	0.107	0.121	0.223
C_{coat}-n	-	0.966	0.938	0.975	0.963	0.943
R_{coat}	(MΩ-cm^2)	10.000	10.000	10.000	21.940	16.500
C_{dl}-Y^o	(nF/cm^2)	0.201	0.202	0.077	0.357	5.456
C_{dl}-n	-	0.607	0.530	0.658	0.429	0.789
R_{corr}	(GΩ-cm^2)	152.300	260.700	190.200	1000.000	10.870

Table 4.5. Fitting results of EIS measured on AA2024-T351 panels coated with MgRP (MgPVC = 45%) after LALT in ASTM B-117 modified with artificial sea water for 0, 192, 408, 698 and 1000 hours. Tested in ambiently aerated 5% NaCl Solution. Circuit model shown in Figure 3.20.

	units	0 hrs	192 hrs	408 hrs	698 hrs	1000 hrs
R_s	(Ω-cm^2)	10.000	10.000	10.000	10.000	10.000
C_{coat}-Y^o	(nF/cm^2)	0.164	0.096	0.178	0.206	0.292
C_{coat}-n	-	0.966	0.985	0.941	0.954	0.932
R_{coat}	(MΩ-cm^2)	10.000	10.000	114.700	10.000	10.000
C_{dl}-Y^o	(nF/cm^2)	0.201	0.110	8.981	0.399	0.062
C_{dl}-n	-	0.607	0.714	0.596	0.451	0.567
R_{corr}	(GΩ-cm^2)	152.300	199.600	1000.000	8.008	202.600

Table 4.6. Summary of observations made after environmental exposure in various environments.

Environment	UV?	Macroscopic Blistering	Underpaint Corrosion	Cathodic Corrosion	Throwing Power
Kennedy Space Center, FL – 52 wks	YES	NO	NO	NO	200 - 300 µm
Charlottesville, VA – 52 wks	YES	NO	NO	NO	n/a
ASTM B-117 w/ 5% NaCl – 1000 h	NO	NO	NO	NO	n/a
ASTM B-117 w/ ASW – 1000 h	NO	NO	NO	NO	≥ 350 µm
Full Immersion in ambiently aerated 5% NaCl – 840 h	NO	NO	NO	NO	No scribe*

*a non-scribed area of MgRP-coated AA2024-T351 was exposed in a flat cell to 5% NaCl solution to study the representative global degradation of the coating. Follow up experiments include the same exposure and include variations in the area of bare AA2024-T351.

4.10 Figures

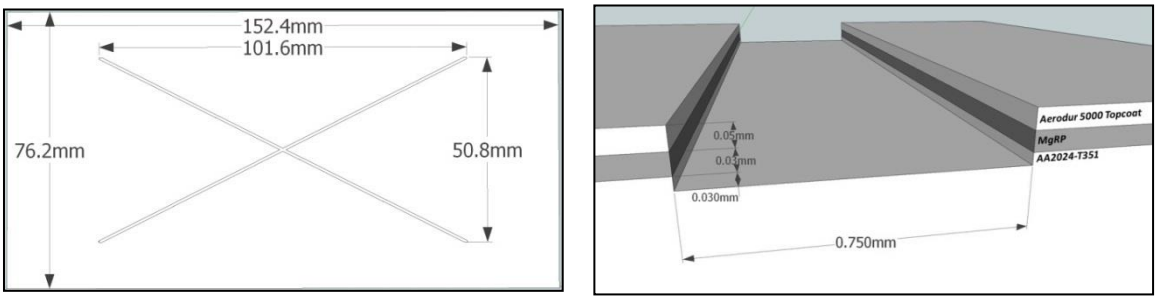

(a) (b)

Figure 4.1.Schematic of AA2024-T351 panels coated with Mg-rich primer and Aerodur 5000 advanced life polyurethane topcoat.

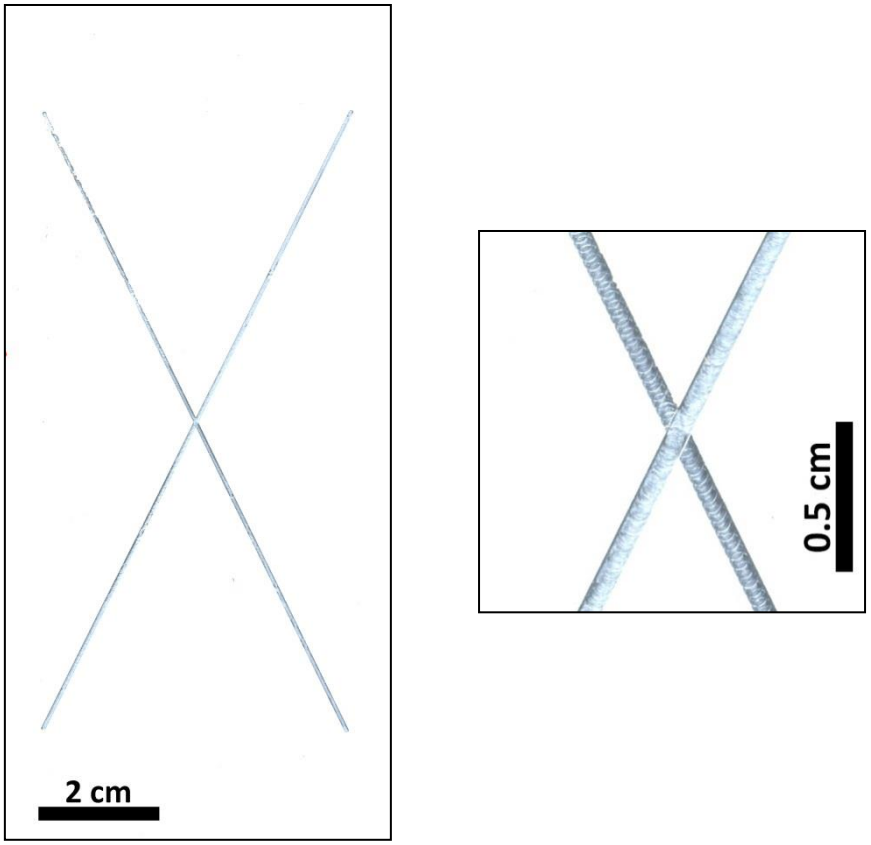

(a) (b)

Figure 4.2. Optical micrograph of AA2024-T351 panels coated with MgRP and Aerodur 5000 advanced life polyurethane topcoat that have not been environmentally exposed.

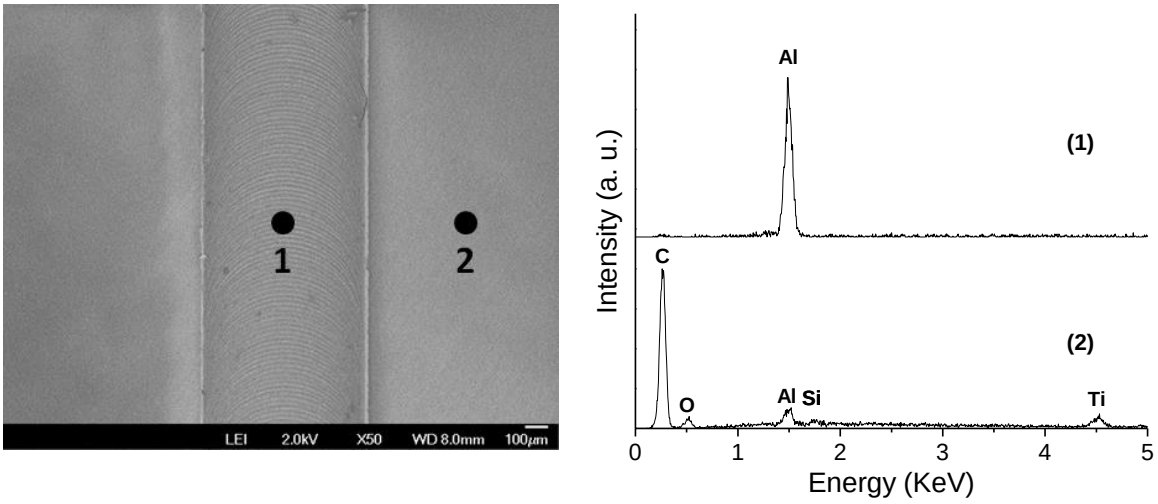

(a) (b)

Figure 4.3. Scanning electron micrograph (a) and EDS (b) of AA2024-T351 pretreated with Prekote and coated with MgRP (MgPVC = 45%) as applied before environmental exposure. Spot markers indicate approximate location of EDS analysis.

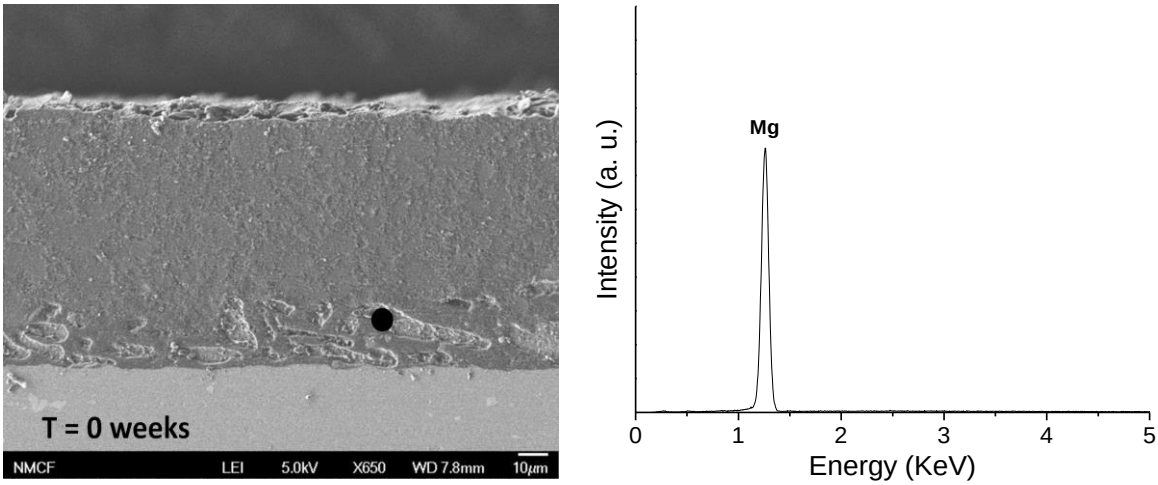

(a) (b)

Figure 4.4. SEM micrograph (a) far away from and (b) near the scribe and (c) EDS of cross-sectioned MgRP (initial MgPVC = 45%) on AA2024-T351 pretreated with Prekote. Spot markers indicate approximate location of EDS analysis in (a).

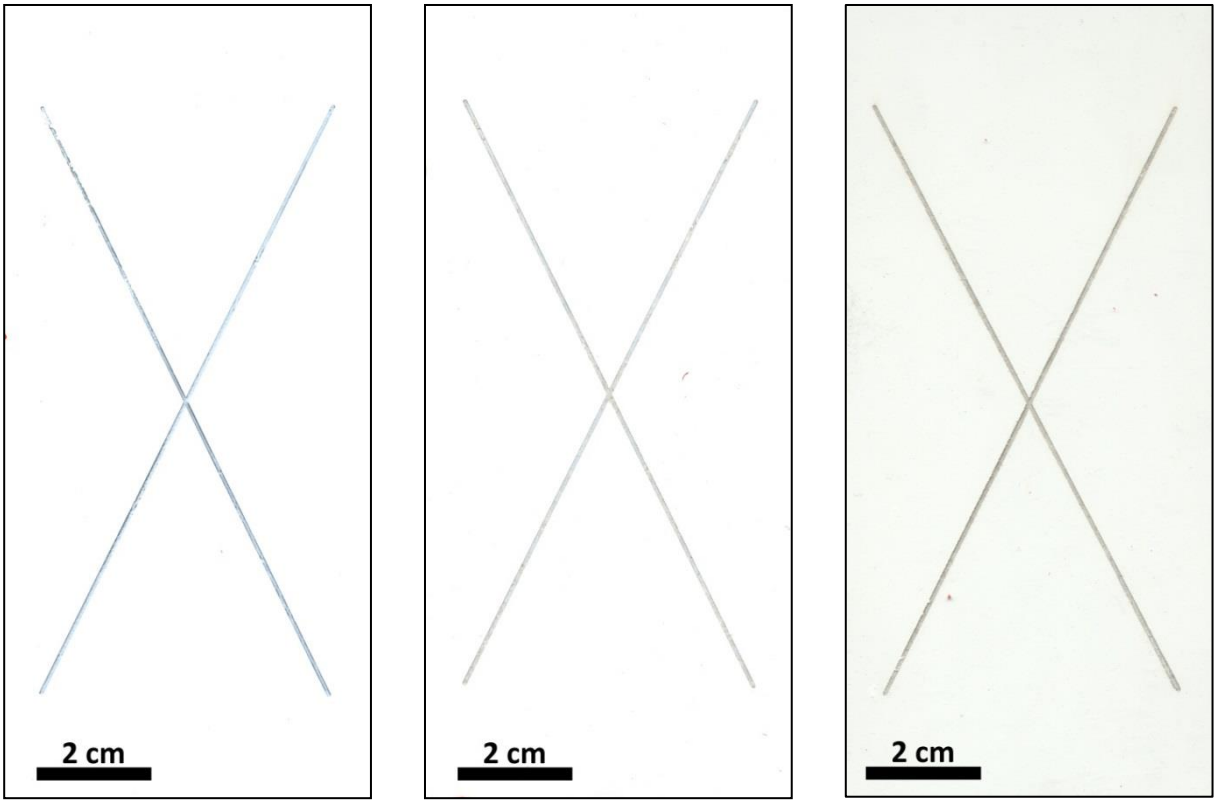

(a) (b) (c)

Figure 4.5. Optical micrograph of AA2024-T351 panels coated with Mg-rich primer (initial MgPVC = 45%) and polyurethane topcoat that have been environmentally exposed in the field at KSC. (a) T = 0 weeks (b) T = 24 weeks (c) T = 52 weeks

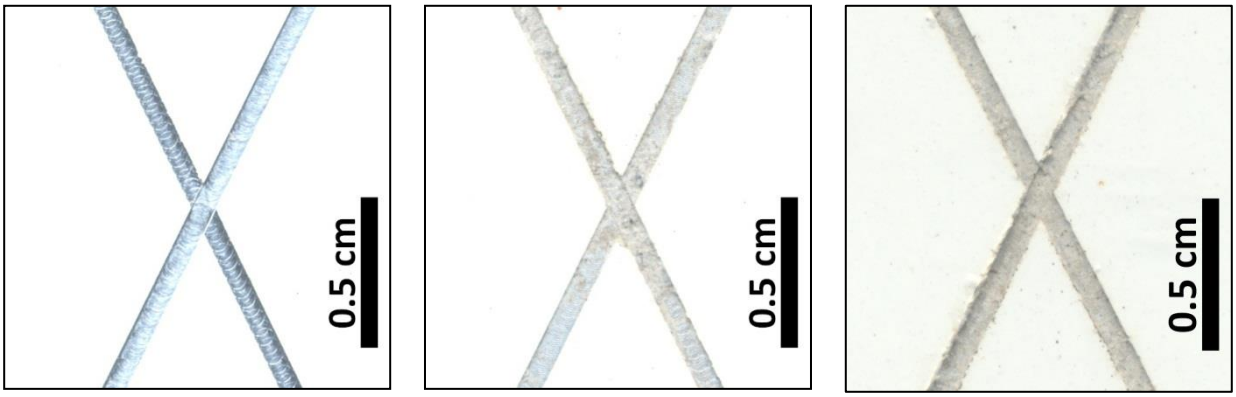

(a) T = 0 weeks in field at KSC

(b) T = 24 weeks in field at KSC

(c) T = 52 weeks in field at KSC

Figure 4.6. Optical micrograph of AA2024-T351 panels coated with Mg-rich primer (initial MgPVC = 45%) and polyurethane topcoat that have been environmentally exposed in the field at KSC. (a) T = 0 weeks (b) T = 24 weeks (c) T = 52 weeks

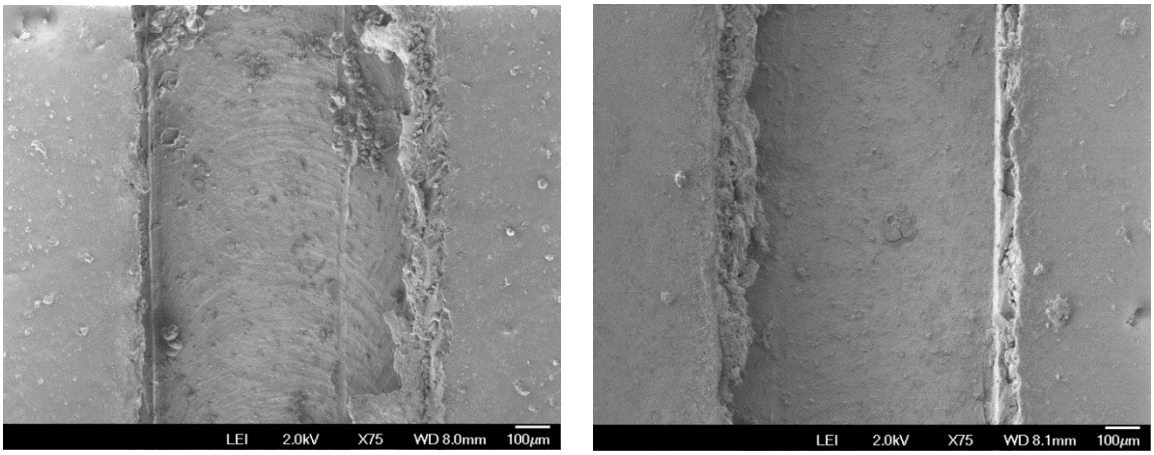

(a) (b)

Figure 4.7. Scanning electron micrograph of AA2024-T351 pretreated with Prekote and coated with MgRP (initial MgPVC = 45%) and Aerodur 5000 topcoat after environmental exposure in the field at KSC for (a) 12 weeks and (b) 24 weeks.

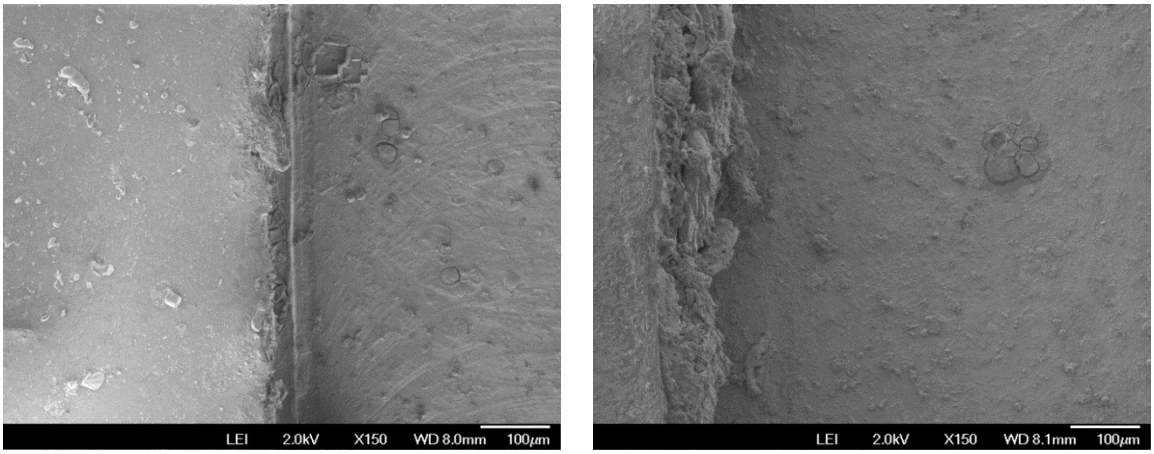

(a) (b)

Figure 4.8. Scanning electron micrograph of AA2024-T351 panels coated with Mg-rich primer (initial MgPVC = 45%) and polyurethane topcoat after environmental exposure in the field at KSC for (a) 12 weeks and (b) 24 weeks.

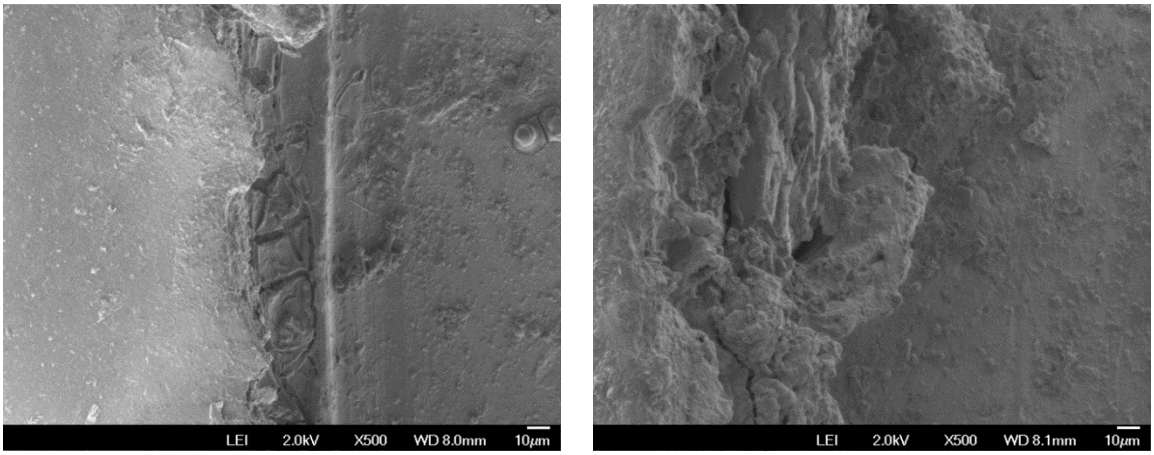

(a) (b)

Figure 4.9. Higher magnification scanning electron micrograph of AA2024-T351 panels coated with Mg-rich primer (initial MgPVC = 45%) and polyurethane topcoat after environmental exposure in the field at KSC for (a) 12 weeks and (b) 24 weeks.

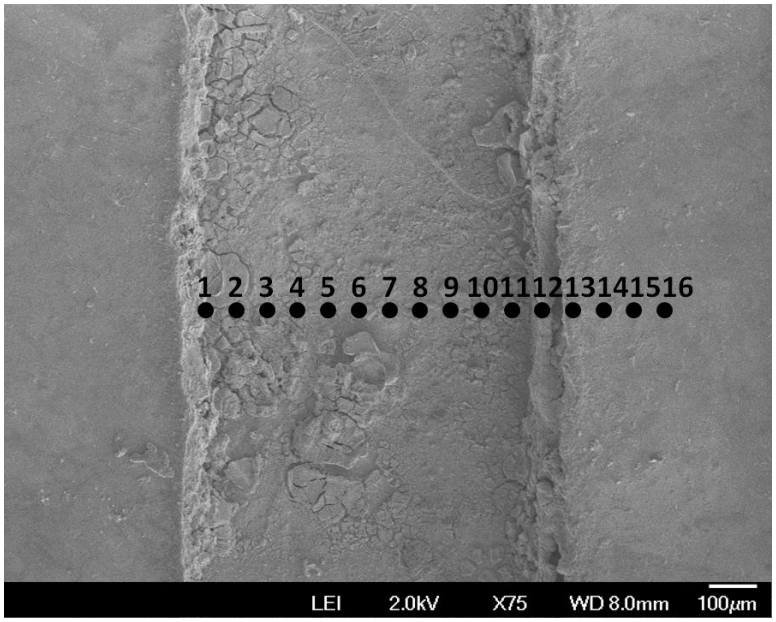

(a)

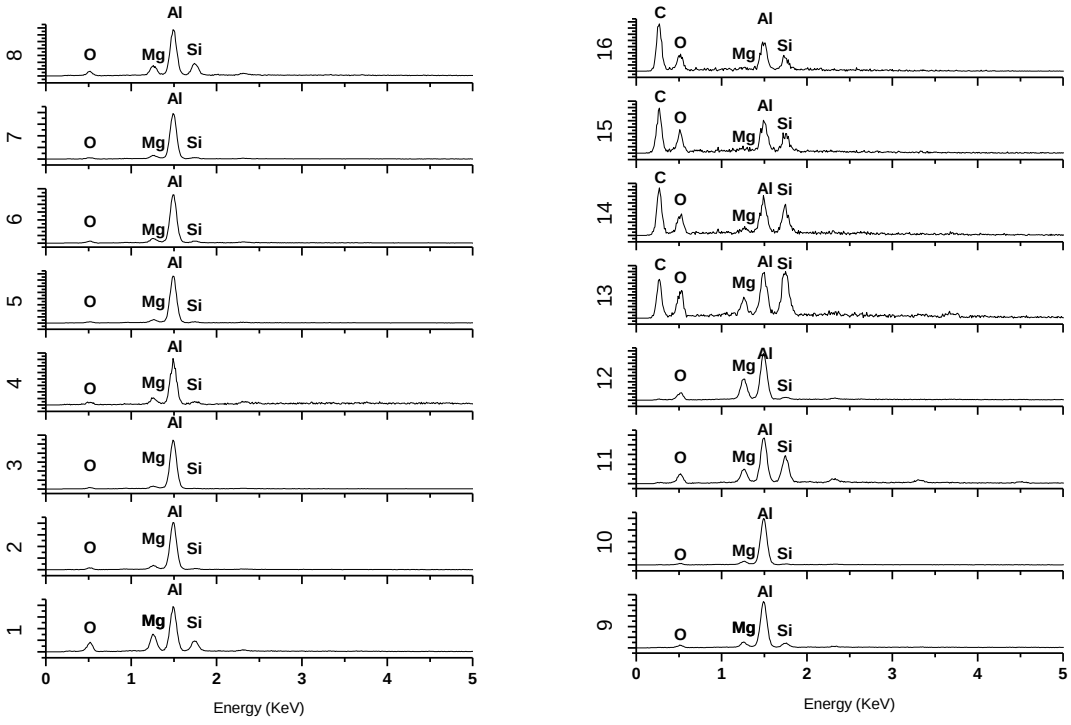

(b)

Figure 4.10. Planar-view SEM micrograph (a) of scribed AA2024-T351 panels coated with Mg-rich primer (initial MgPVC = 45%) and polyurethane topcoat after field exposure in the field at KSC for 24 weeks. Spot markers indicate approximate location of EDS analysis shown in (b).

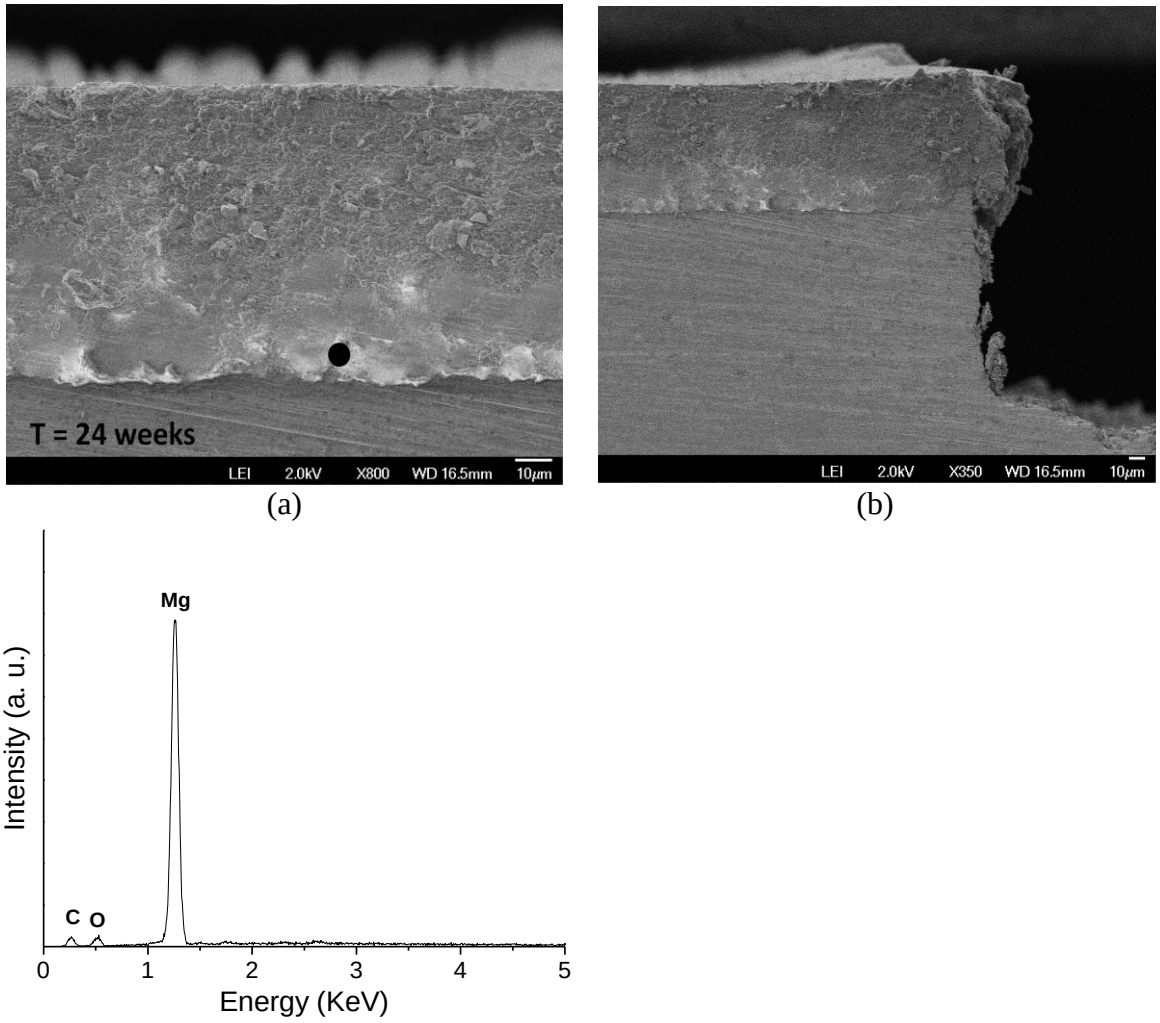

Figure 4.11. SEM micrograph (a) far away from and (b) near the scribe and (c) EDS of cross-sectioned AA2024-T351 panels coated with Mg-rich primer (initial MgPVC = 45%) and polyurethane topcoat after environmental exposure at KSC for 24 weeks. Spot markers in (a) indicate approximate location of EDS analysis shown in (c).

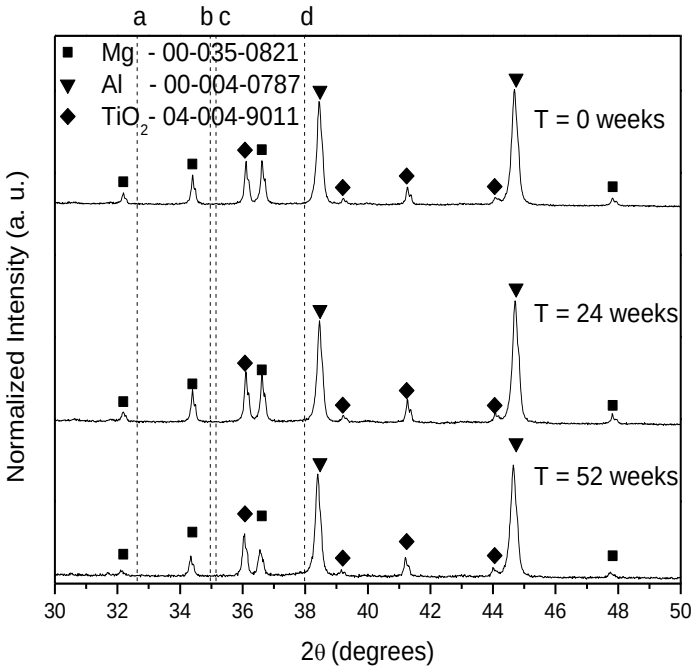

Figure 4.12. X-Ray diffraction spectra of AA2024-T351 panels coated with Mg-rich primer (initial MgPVC = 45%) and polyurethane topcoat that have been environmentally exposed in the field at KSC for 0, 12, and 24 weeks. Dotted lines indicate the position of the most intense diffraction peak for (a) $MgCO_3$, (b) $MgCl_2$, (c) Al_2O_3, and (d) $Mg(OH)_2$.

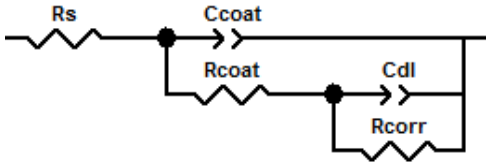

Figure 4.13. EIS equivalent circuit for a polymer coated metal used for fitting analysis.

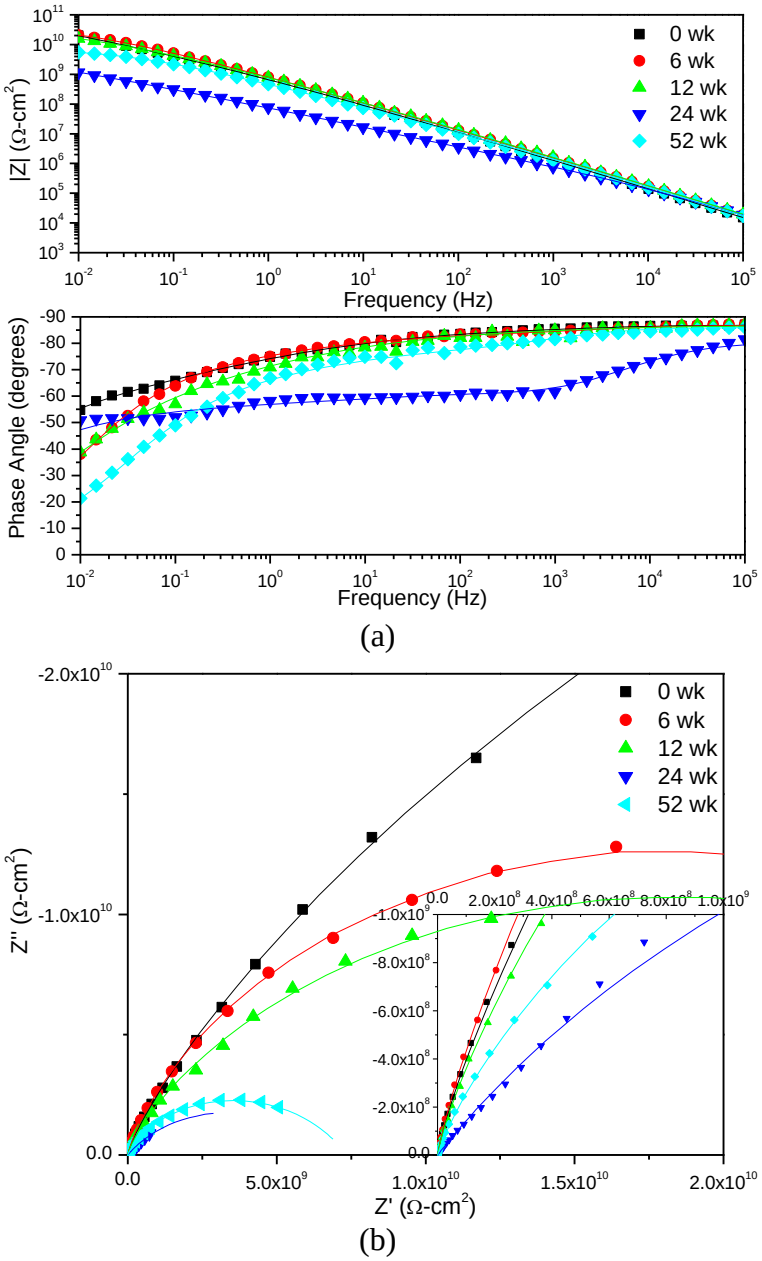

Figure 4.14. (a) Bode and (b) Nyquist plots of EIS of AA2024-T351 panels coated with Mg-rich primer (initial MgPVC = 45%) and polyurethane topcoat after field exposure at Kennedy Space Center 30 m lot for 0, 6, 12, 24, and 52 weeks. Tested in ambiently aerated 5% NaCl Solution.

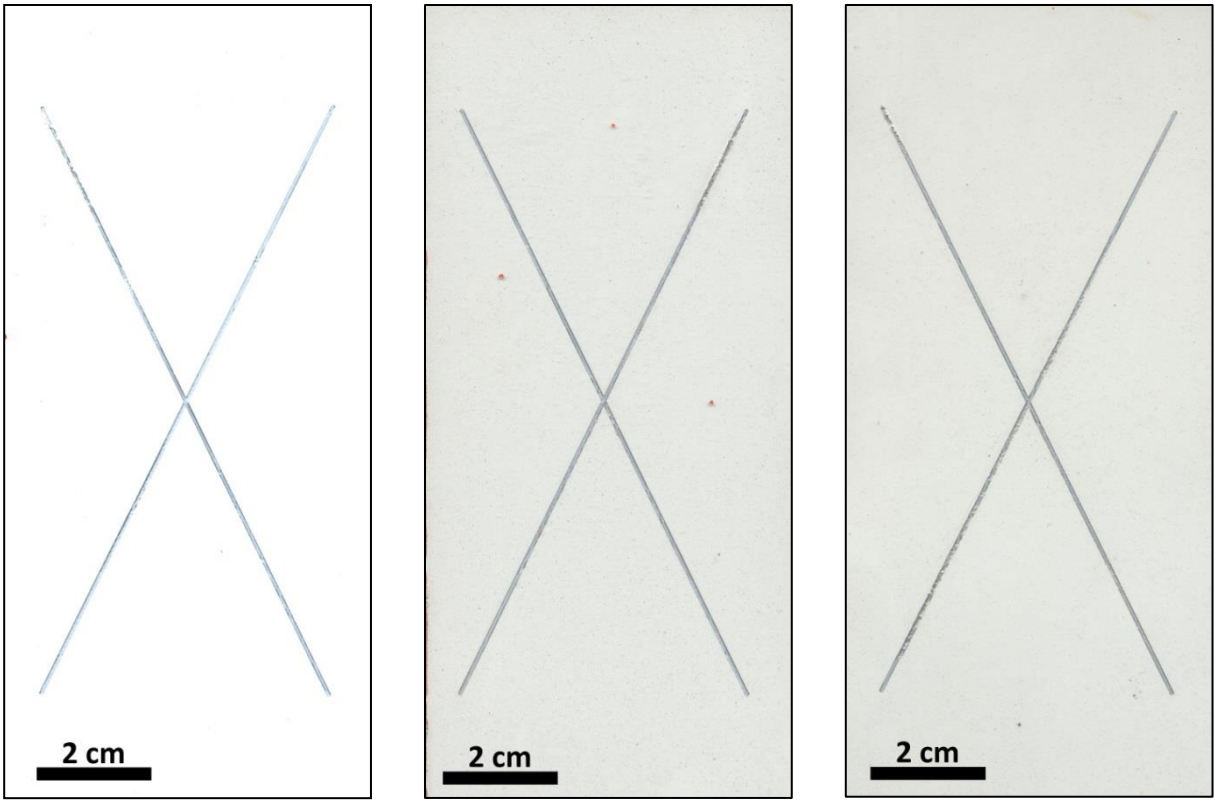

(a) (b) (c)

Figure 4.15. Optical micrograph of AA2024-T351 panels coated with MgRP (initial MgPVC = 45%) and polyurethane topcoat that have been environmentally exposed in the field at Birdwood Golf Course in Charlottesville, VA for (a) T = 0 (b) T = 24 weeks (c) T = 52 weeks

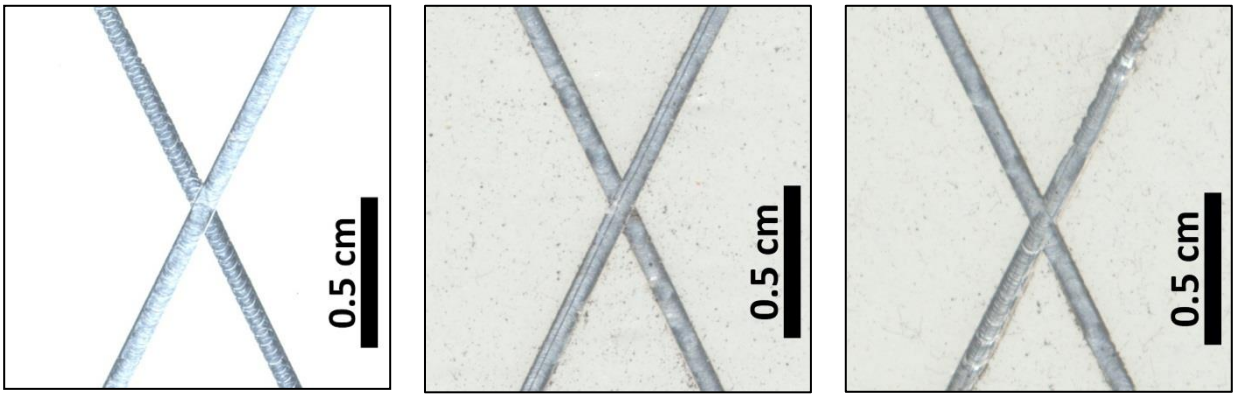

(a) T = 0 wks in Charlottesville, VA

(b) T = 24 wks in Charlottesville, VA

(c) T = 52 wks in Charlottesville, VA

Figure 4.16. Optical micrograph of AA2024-T351 panels coated with MgRP (initial MgPVC = 45%) and polyurethane topcoat that have been environmentally exposed in the field at Birdwood Golf Course in Charlottesville, VA for (a) T = 0 (b) T = 24 weeks (c) T = 52 weeks

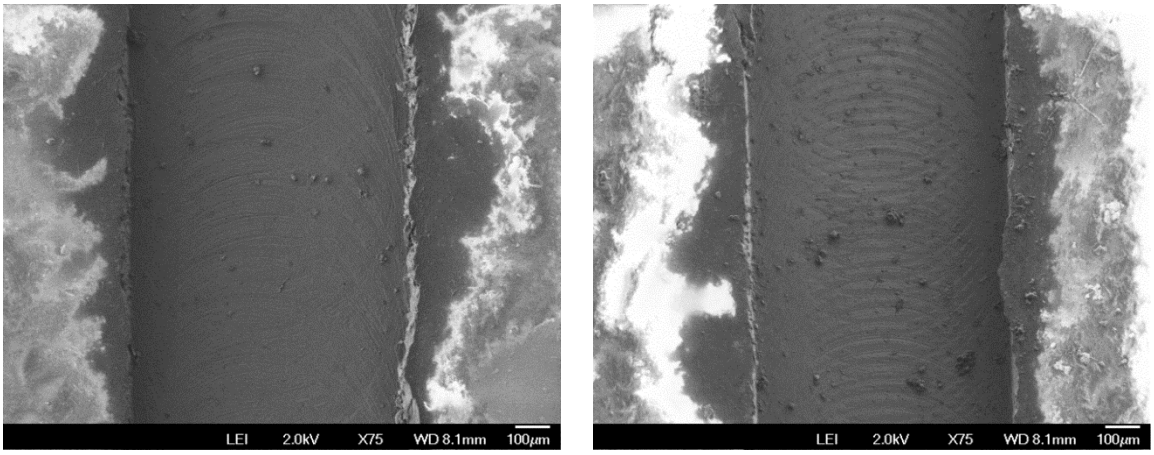

(a) (b)

Figure 4.17. Scanning electron micrograph of AA2024-T351 pretreated with Prekote and coated with MgRP (initial MgPVC = 45%) and Aerodur 5000 topcoat after environmental exposure in the field at Birdwood Golf Course in Charlottesville, VA for (a) 12 weeks and (b) 24 weeks.

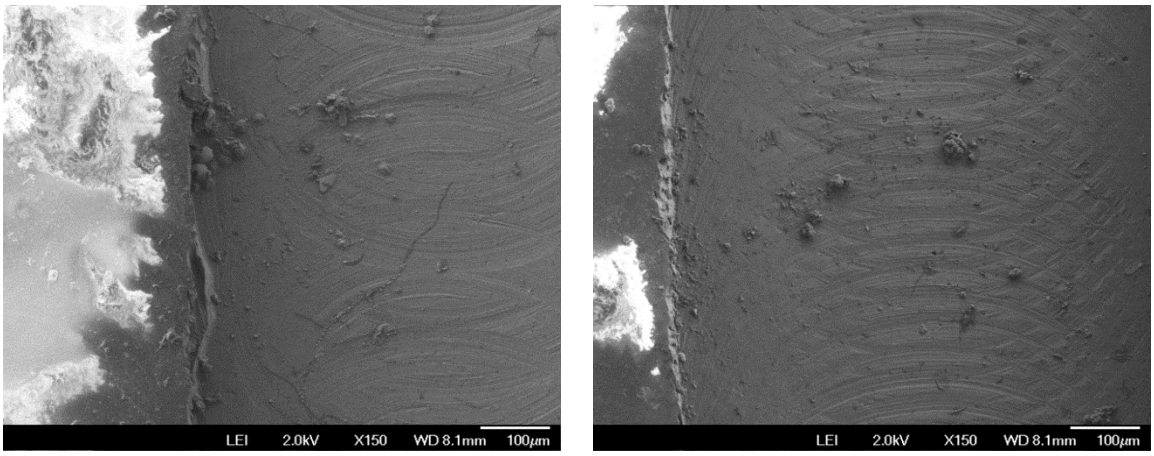

(a) (b)

Figure 4.18. Scanning electron micrograph of AA2024-T351 pretreated with Prekote and coated with MgRP (initial MgPVC = 45%) and Aerodur 5000 topcoat after environmental exposure in the field at Birdwood Golf Course in Charlottesville, VA for (a) 12 weeks and (b) 24 weeks.

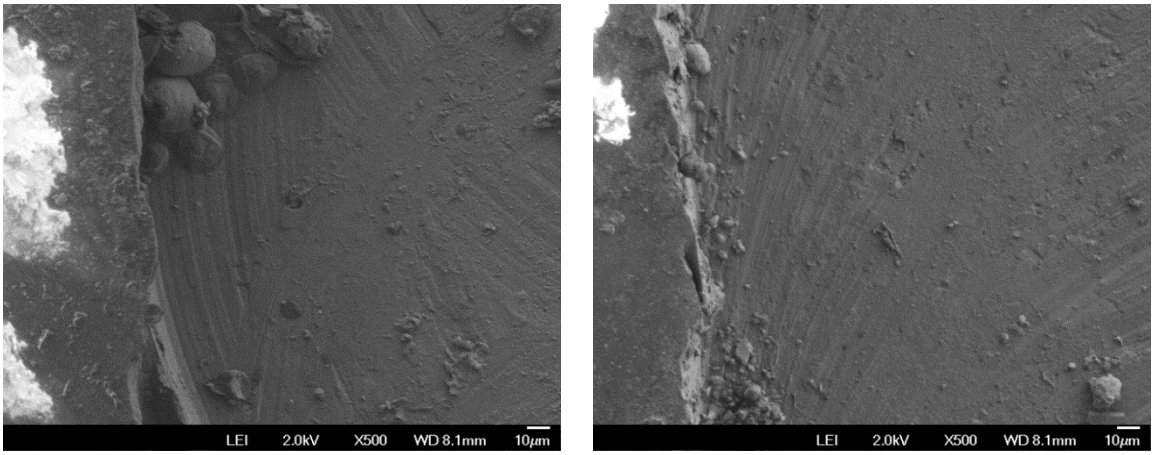

(a) (b)

Figure 4.19. Higher magnification scanning electron micrograph of AA2024-T351 panels coated with Mg-rich primer (initial MgPVC = 45%) and polyurethane topcoat after environmental exposure in the field at Birdwood Golf Course in Charlottesville, VA for (a) 12 weeks and (b) 24 weeks.

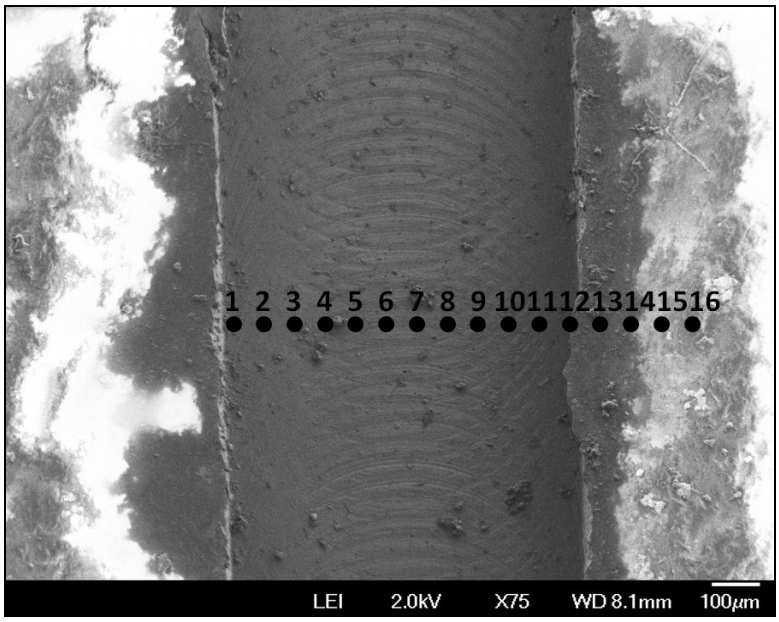

(a)

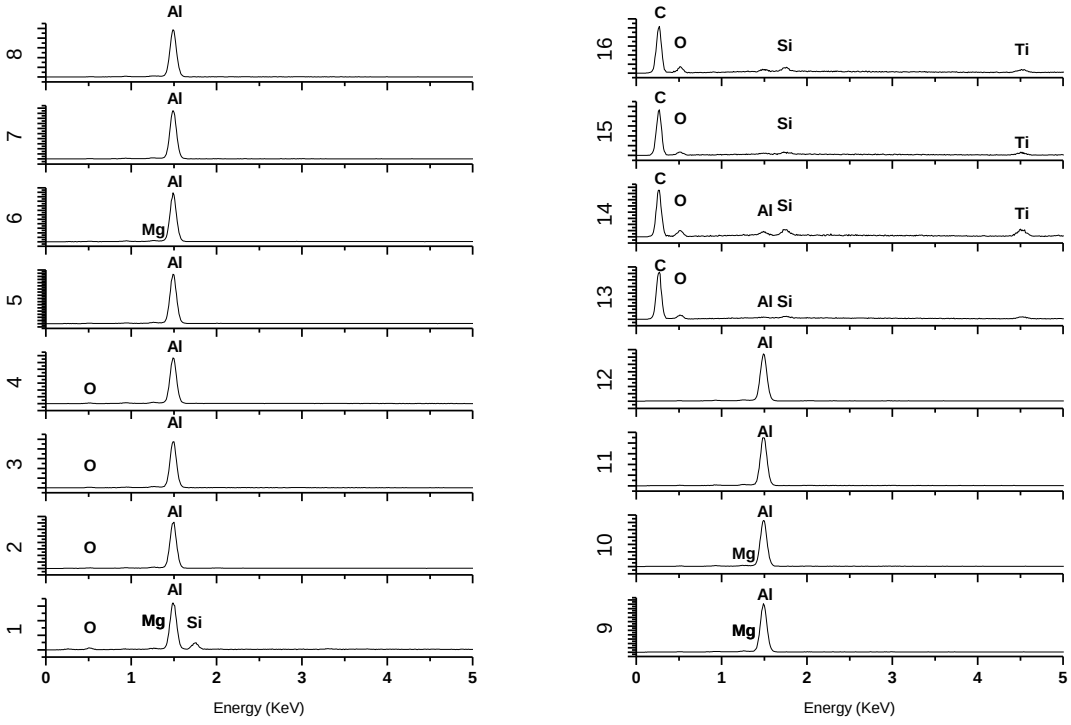

(b)

Figure 4.20. Planar-view SEM micrograph (a) of scribed AA2024-T351 panels coated with Mg-rich primer (initial MgPVC = 45%) and polyurethane topcoat after field exposure at Birdwood Golf Course in Charlottesville, VA for 24 weeks. Spot markers indicate approximate location of EDS analysis shown in (b).

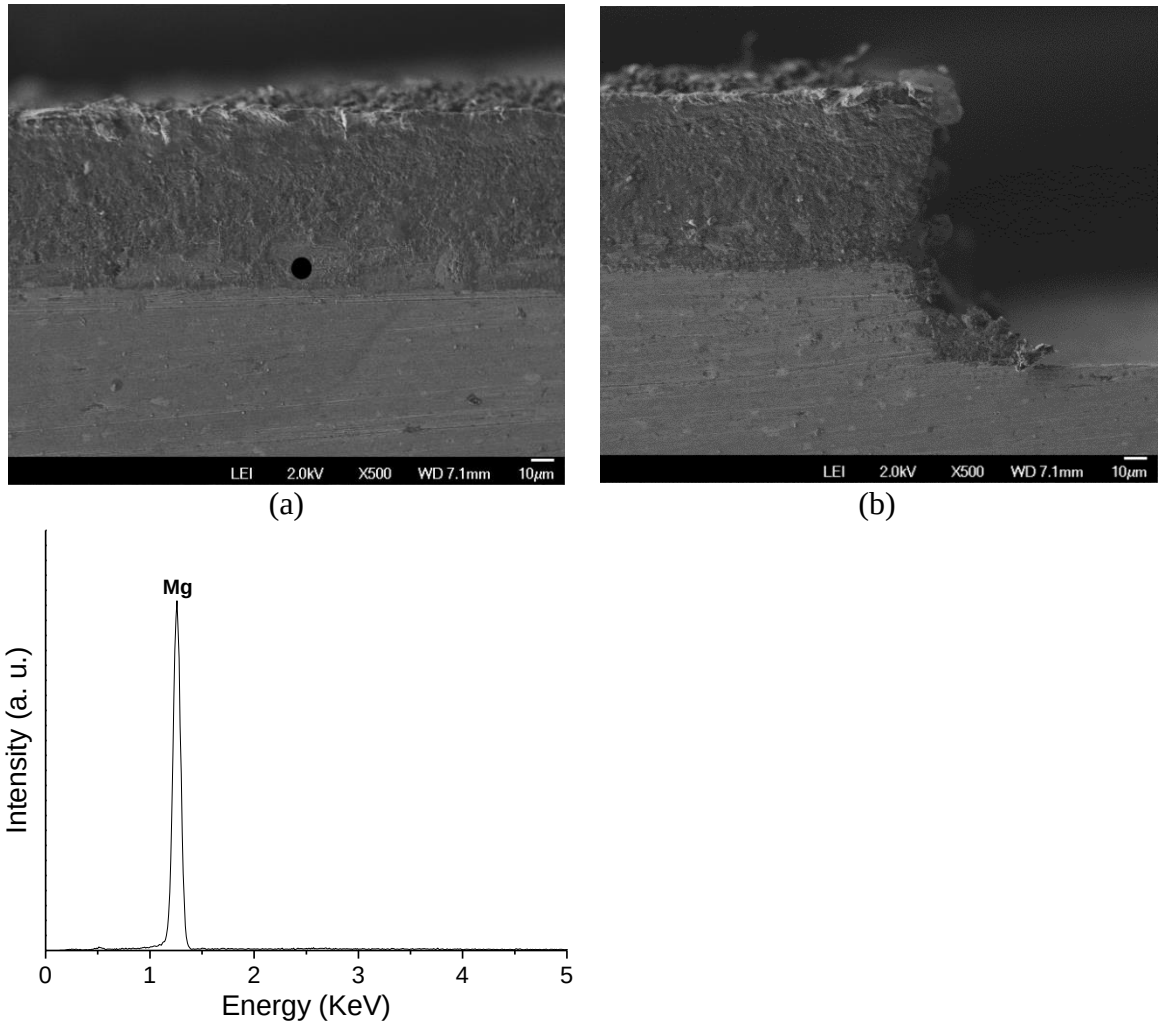

Figure 4.21. SEM micrograph (a) far away from and (b) near the scribe and (c) EDS of cross-sectioned AA2024-T351 panels coated with Mg-rich primer (initial MgPVC = 45%) and polyurethane topcoat after environmental exposure at Birdwood Golf Course in Charlottesville, VA for 24 weeks. Spot markers in (a) indicate approximate location of EDS analysis shown in (c).

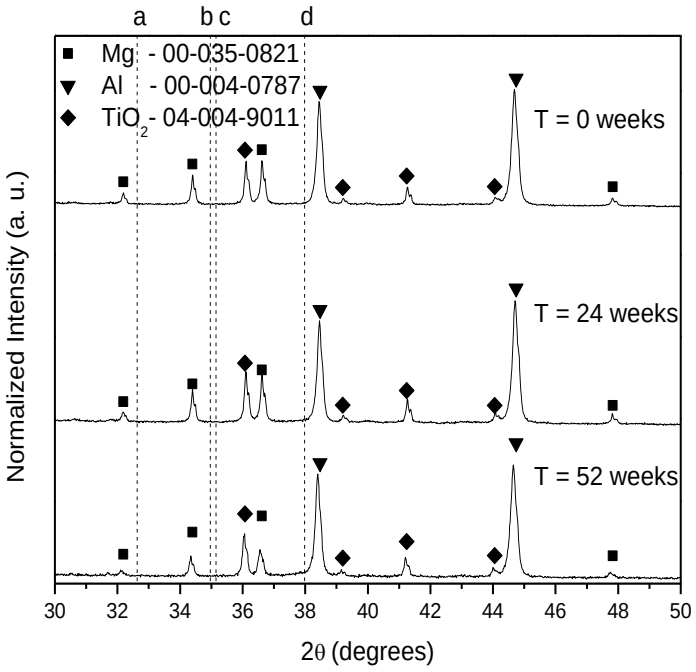

Figure 4.22. X-Ray diffraction spectra of AA2024-T351 panels coated with Mg-rich primer (initial MgPVC = 45%) and polyurethane topcoat that have been environmentally exposed in the field at Birdwood Golf Course in Charlottesville, VA for 0, 12, and 24 weeks. Dotted lines indicate the position of the most intense diffraction peak for (a) $MgCO_3$, (b) $MgCl_2$, (c) Al_2O_3, and (d) $Mg(OH)_2$.

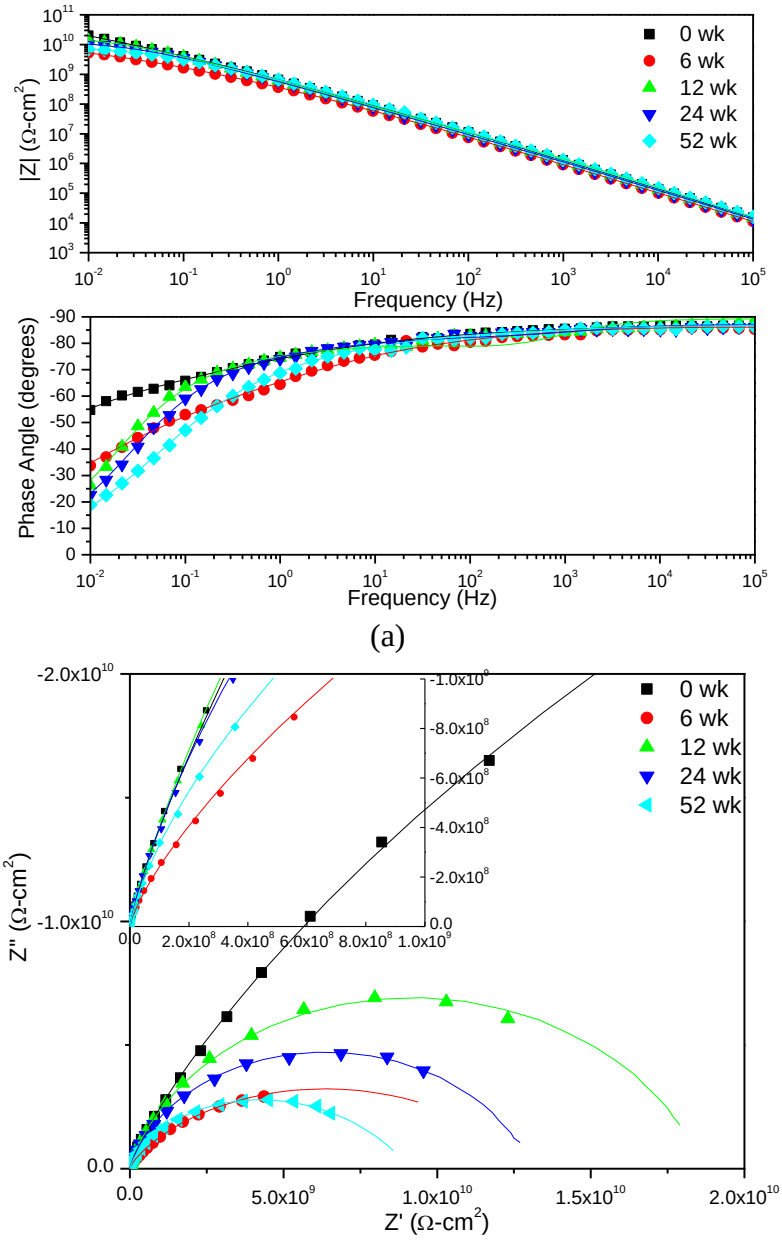

Figure 4.23. (a) Bode and (b) Nyquist plots of EIS of AA2024-T351 panels coated with Mg-rich primer (initial MgPVC = 45%) and polyurethane topcoat after field exposure at Birdwood Golf Course in Charlottesville, VA for 0, 6, 12, 24, and 52 weeks. Tested in ambiently aerated 5% NaCl Solution.

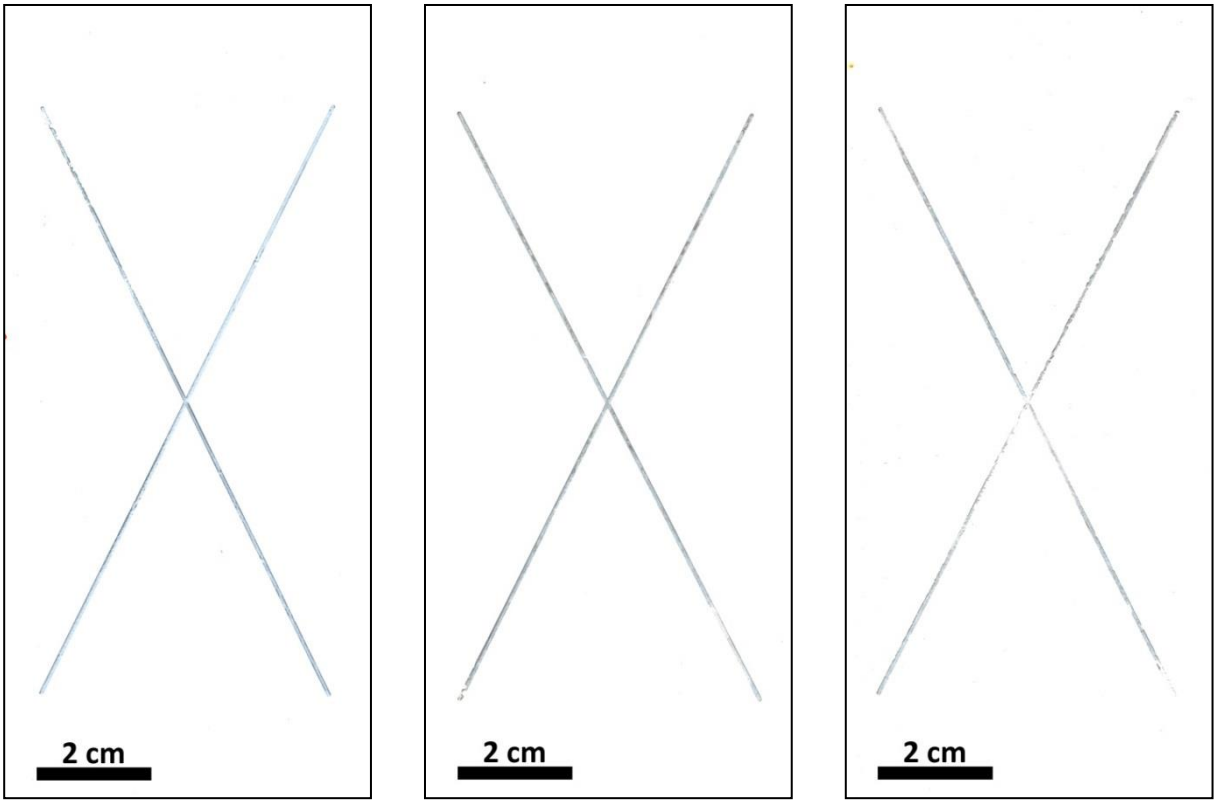

(a) (b) (c)

Figure 4.24. Optical micrograph of AA2024-T351 panels coated with Mg-rich primer (initial MgPVC = 45%) and polyurethane topcoat that have been environmentally exposed in ASTM B-117 for (a) T = 0 hrs (b) T = 384 hrs (c) T = 984 hrs

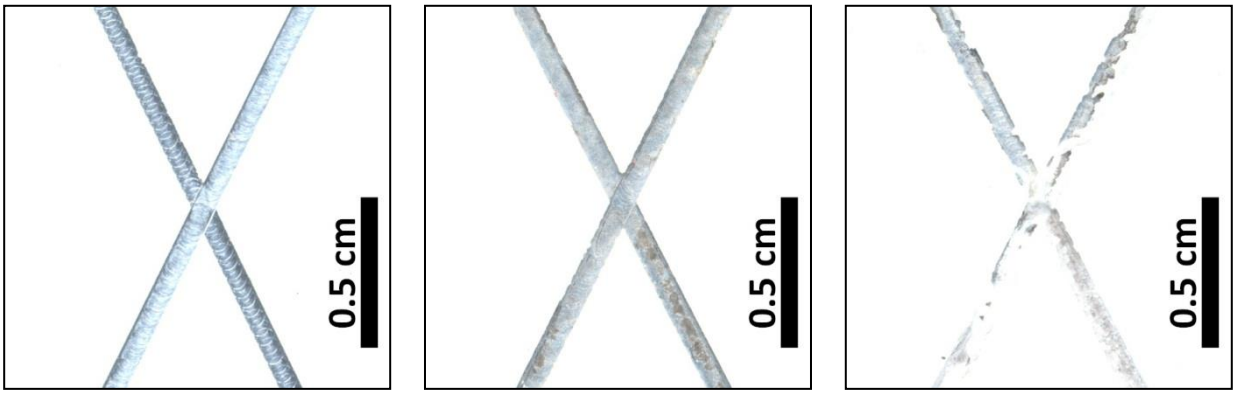

(a)
T = 0 hrs
in ASTM B-117

(b)
T = 384 hrs
in ASTM B-117

(c)
T = 984 hrs
in ASTM B-117

Figure 4.25. Optical micrograph of AA2024-T351 panels coated with Mg-rich primer (initial MgPVC = 45%) and polyurethane topcoat that have been environmentally exposed in ASTM B-117 for (a) T = 0 hrs (b) T = 384 hrs (c) T = 984 hrs

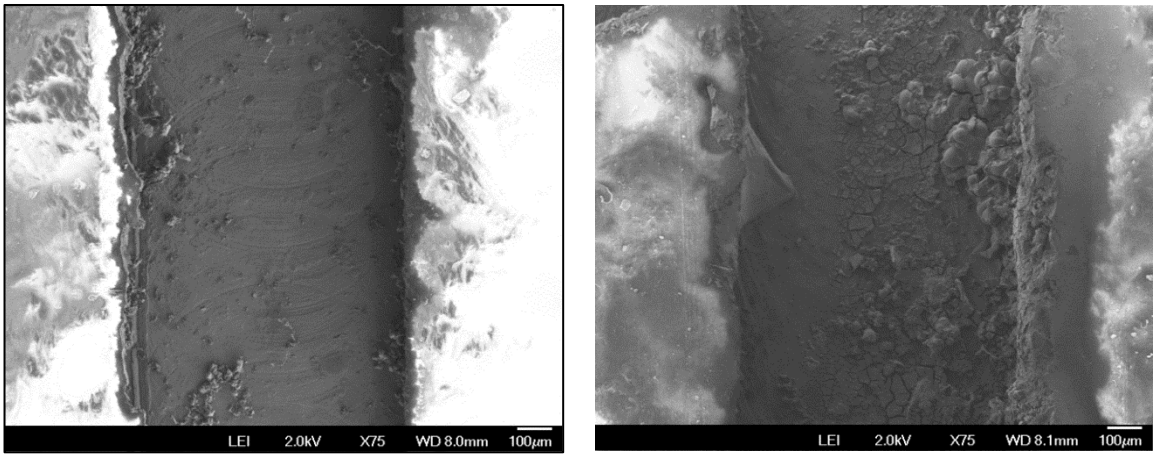

(a) (b)

Figure 4.26. Scanning electron micrograph of AA2024-T351 panels coated with Mg-rich primer (initial MgPVC = 45%) and polyurethane topcoat after environmental exposure in ASTM B-117 for (a) 384 hrs and (b) 984 hrs.

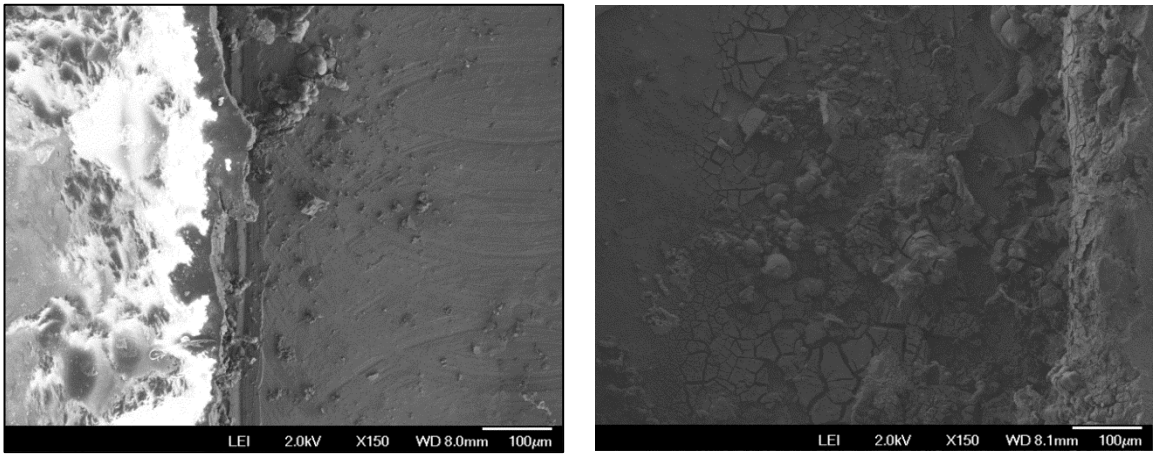

(a) (b)

Figure 4.27. Scanning electron micrograph of AA2024-T351 panels coated with Mg-rich primer (initial MgPVC = 45%) and polyurethane topcoat after environmental exposure in ASTM B-117 for (a) 384 hrs and (b) 984 hrs.

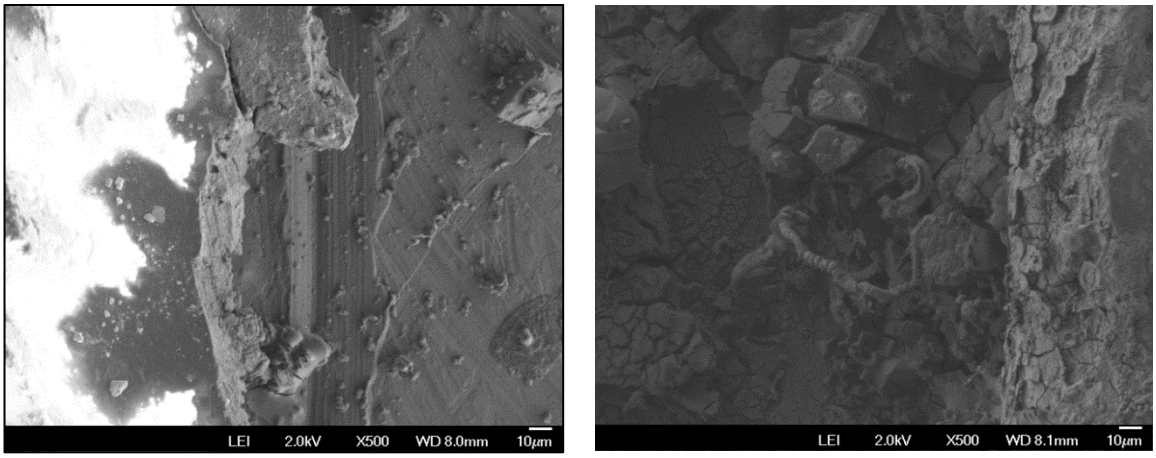

(a) (b)

Figure 4.28. Higher magnification scanning electron micrograph of AA2024-T351 panels coated with Mg-rich primer (initial MgPVC = 45%) and polyurethane topcoat after environmental exposure in ASTM B-117 for (a) 384 hrs and (b) 984 hrs.

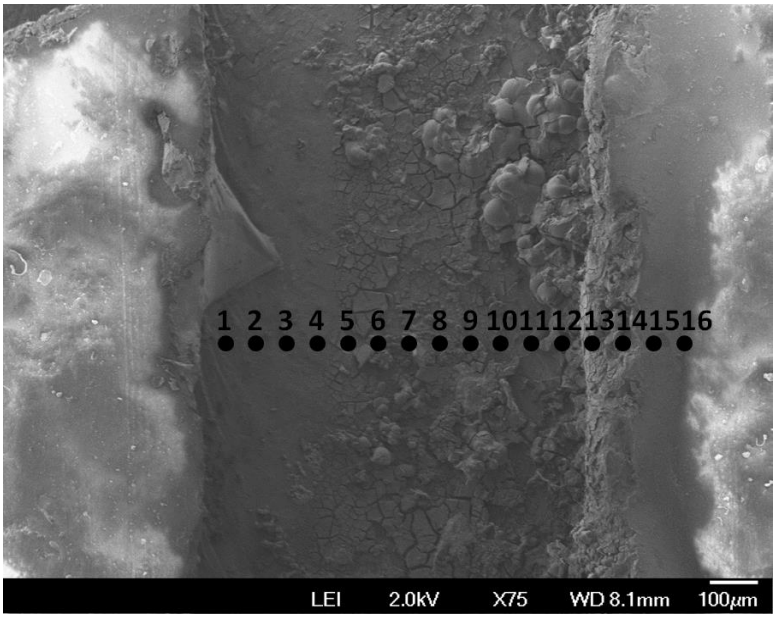

(a)

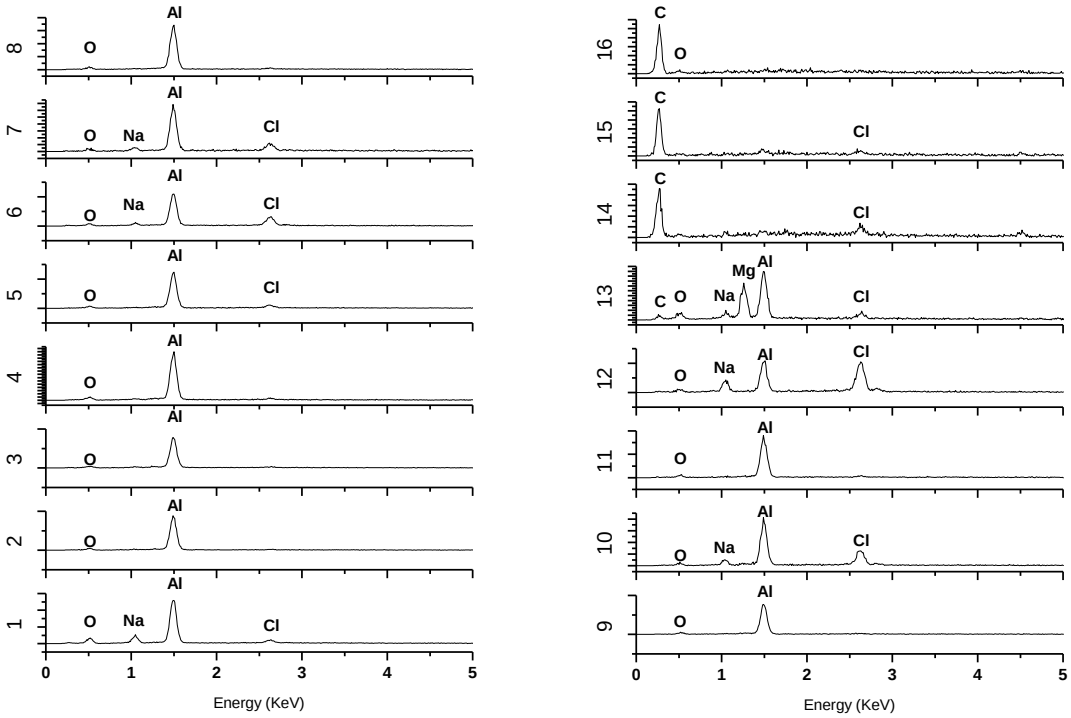

(b)

Figure 4.29. Planar-view SEM micrograph (a) of scribed AA2024-T351 panels coated with Mg-rich primer (initial MgPVC = 45%) and polyurethane topcoat after exposure in ASTM B-117 for 984 h. Spot markers indicate approximate location of EDS analysis shown in (b).

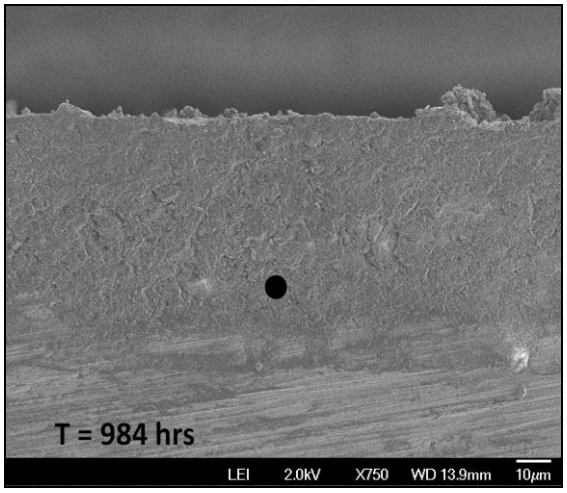

(a)

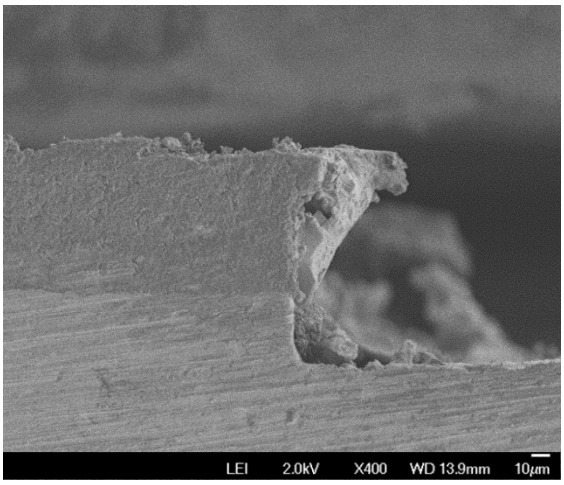

(b)

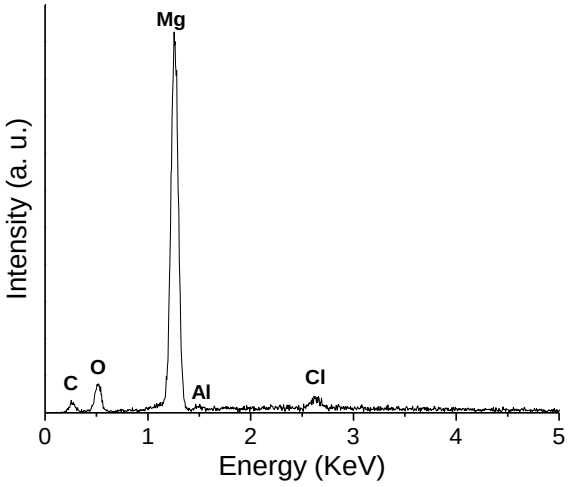

(c)

Figure 4.30. SEM micrograph (a) far away from and (b) near the scribe and (c) EDS of cross-sectioned AA2024-T351 panels coated with Mg-rich primer (initial MgPVC = 45%) and polyurethane topcoat after environmental exposure in ASTM B-117 for 984 h. Spot markers in (a) indicate approximate location of EDS analysis shown in (c).

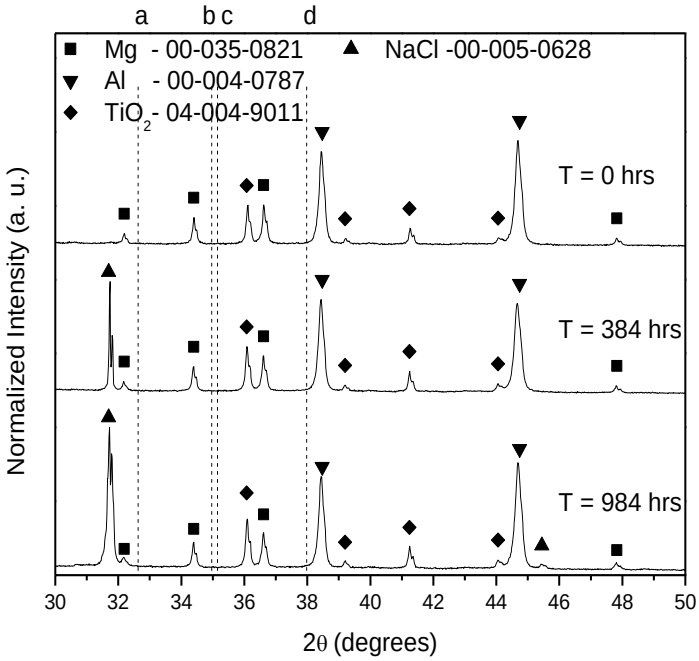

Figure 4.31. X-Ray diffraction spectra of AA2024-T351 panels coated with Mg-rich primer (initial MgPVC = 45%) and polyurethane topcoat that have been environmentally exposed in ASTM B-117 for 0, 384, and 984 hours. Dotted lines indicate the position of the most intense diffraction peak for (a) $MgCO_3$, (b) $MgCl_2$, (c) Al_2O_3, and (d) $Mg(OH)_2$.

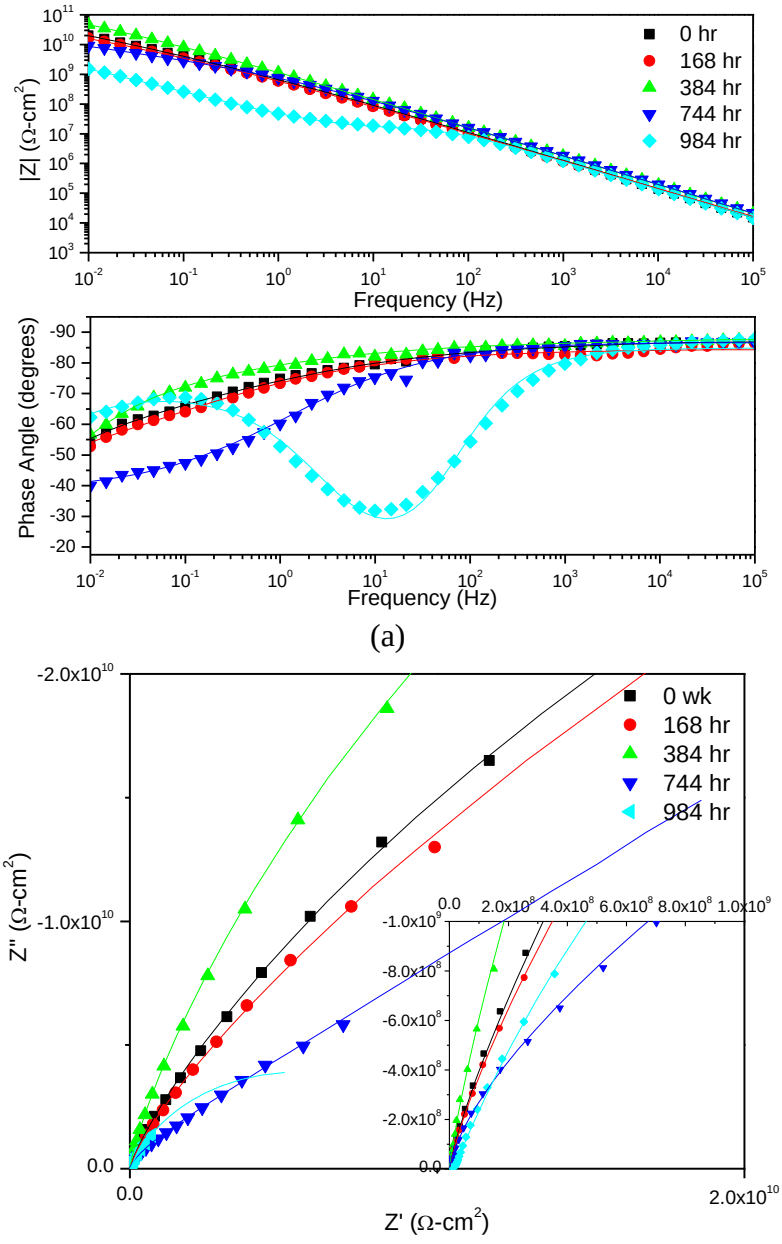

Figure 4.32. (a) Bode and (b) Nyquist plots of EIS of AA2024-T351 panels coated with Mg-rich primer (initial MgPVC = 45%) and polyurethane topcoat after exposure in ASTM B-117 for 0, 168, 384, 744, and 984 hours. Tested in ambiently aerated 5% NaCl solution.

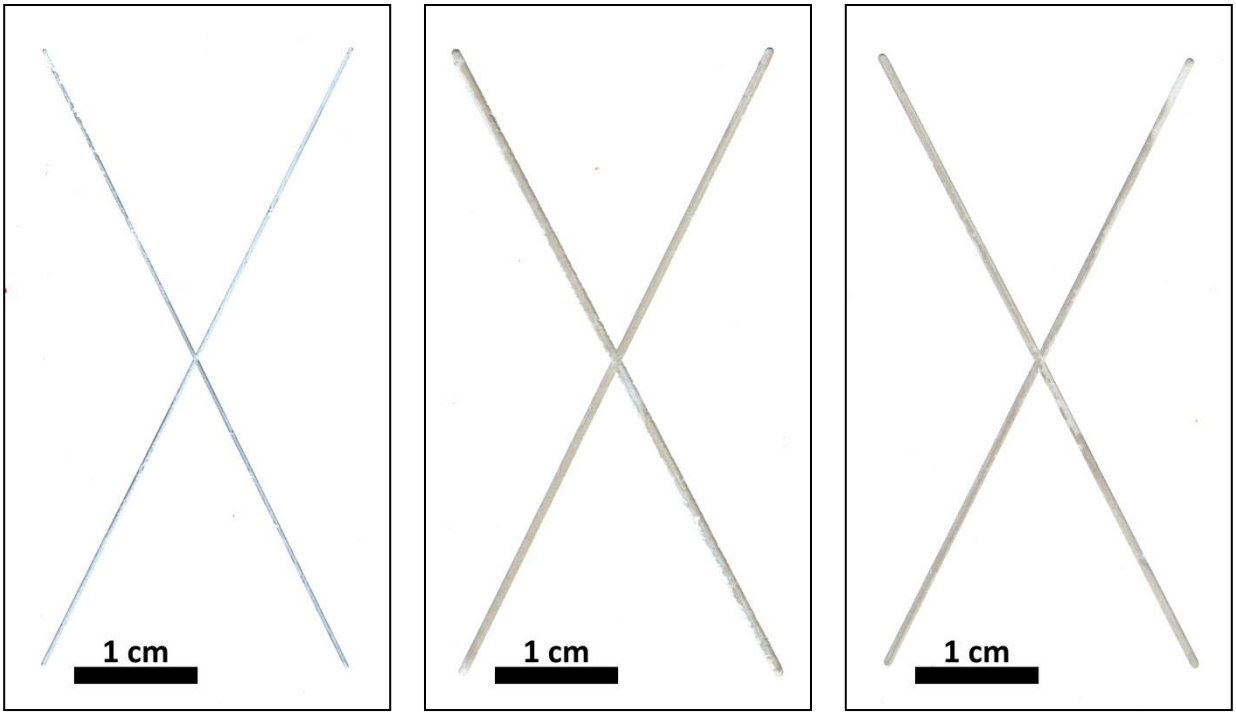

(a) T = 0 hrs in ASTM B-117 w/ ASW (b) T = 408 hrs in ASTM B-117 w/ ASW (c) T = 1000 hrs in ASTM B-117 w/ ASW

Figure 4.33. Optical micrograph of AA2024-T351 panels coated with Mg-rich primer (initial MgPVC = 45%) and polyurethane topcoat that have been environmentally exposed in ASTM B-117 modified with artificial sea water. (a) T = 0 hrs (b) T = 408 hrs (c) T = 1000 hrs

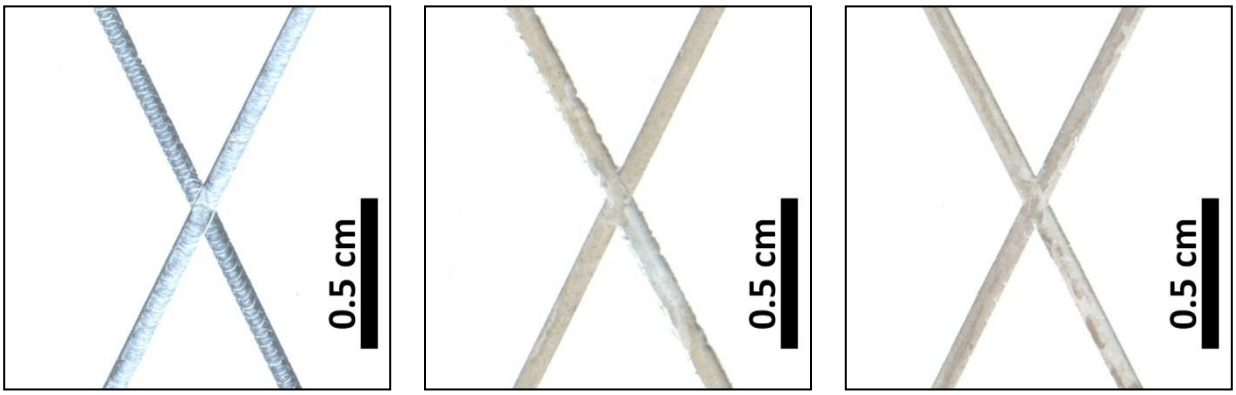

(a) T = 0 hrs in ASTM B-117 w/ ASW (b) T = 408 hrs in ASTM B-117 w/ ASW (c) T = 1000 hrs in ASTM B-117 w/ ASW

Figure 4.34. Optical micrograph of AA2024-T351 panels coated with Mg-rich primer (initial MgPVC = 45%) and polyurethane topcoat that have been environmentally exposed in ASTM B-117 modified with artificial sea water. (a) T = 0 hrs (b) T = 408 hrs (c) T = 1000 hrs

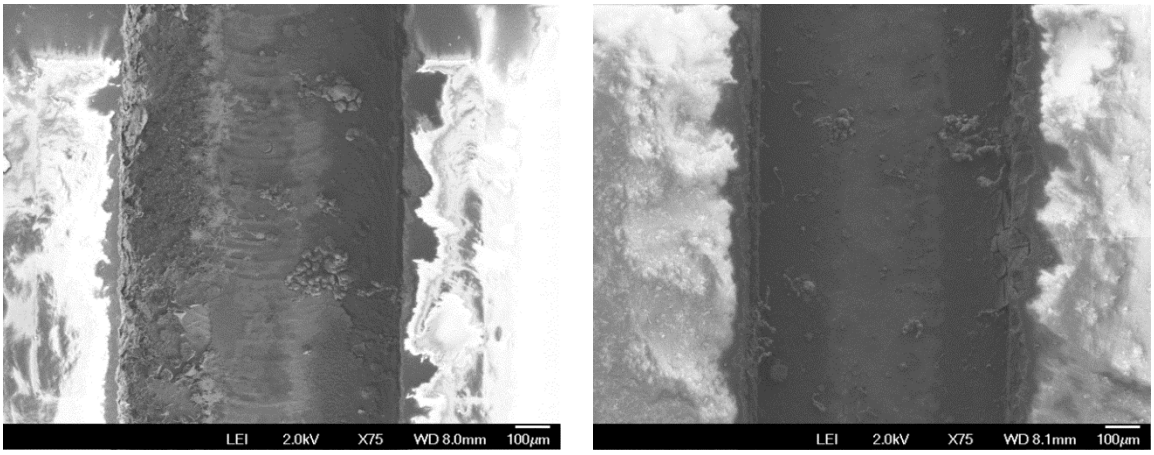

(a) (b)

Figure 4.35. Scanning electron micrograph of AA2024-T351 panels coated with Mg-rich primer (initial MgPVC = 45%) and polyurethane topcoat after environmental exposure in ASTM B-117 modified with artificial sea water for (a) 408 hrs (c) 1000 hrs.

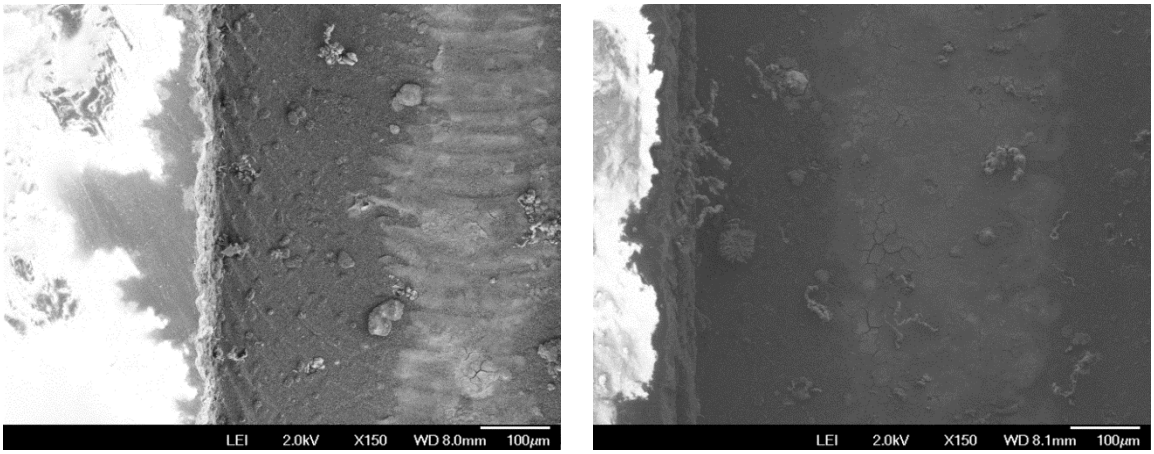

(a) (b)

Figure 4.36. Scanning electron micrograph of AA2024-T351 panels coated with Mg-rich primer (initial MgPVC = 45%) and polyurethane topcoat after environmental exposure in ASTM B-117 modified with artificial sea water for (a) 408 hrs (c) 1000 hrs.

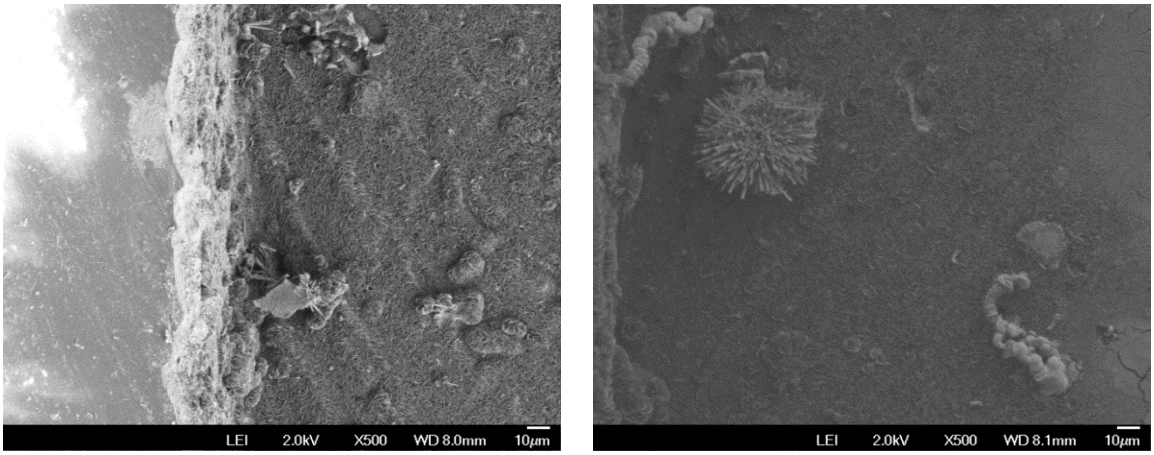

(a) (b)

Figure 4.37. Higher magnification scanning electron micrograph of AA2024-T351 panels coated with Mg-rich primer (initial MgPVC = 45%) and polyurethane topcoat after environmental exposure in ASTM B-117 modified with artificial sea water for (a) 408 hrs (c) 1000 hrs.

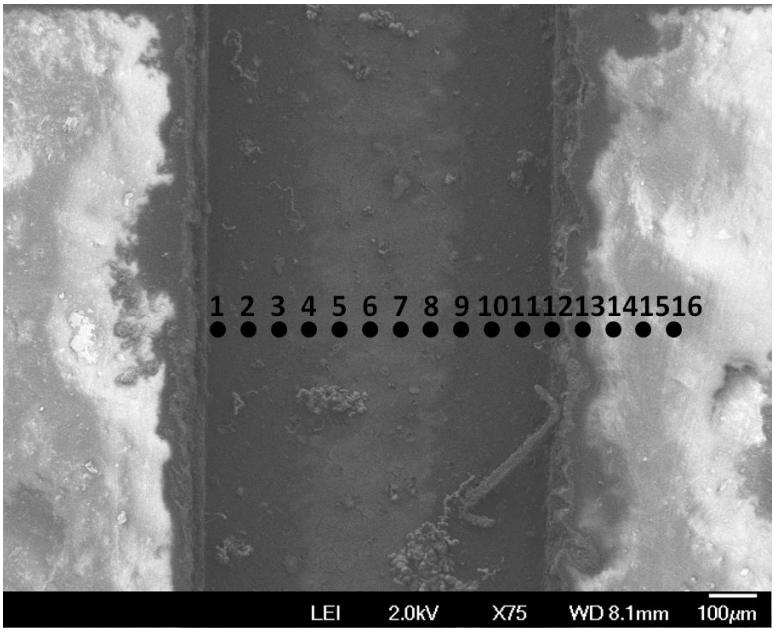

(a)

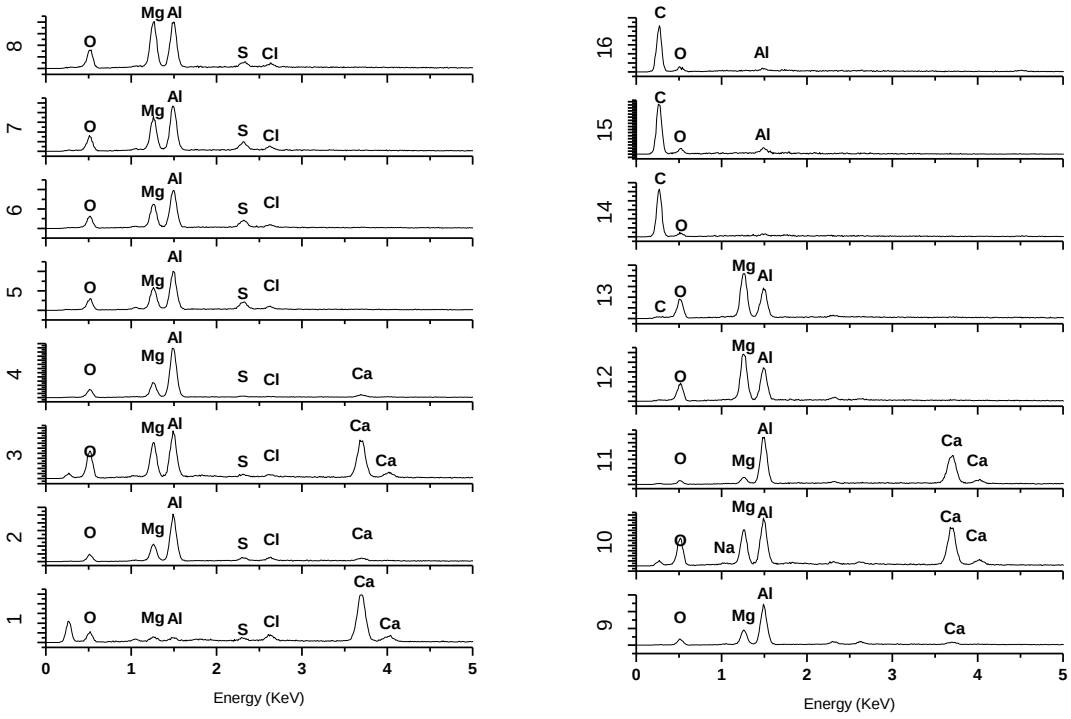

(b)

Figure 4.38. Planar-view SEM micrograph (a) of scribed AA2024-T351 panels coated with Mg-rich primer (initial MgPVC = 45%) and polyurethane topcoat after exposure in ASTM B-117 modified with ASTM Seawater for 1000 h. Spot markers indicate approximate location of EDS analysis shown in (b).

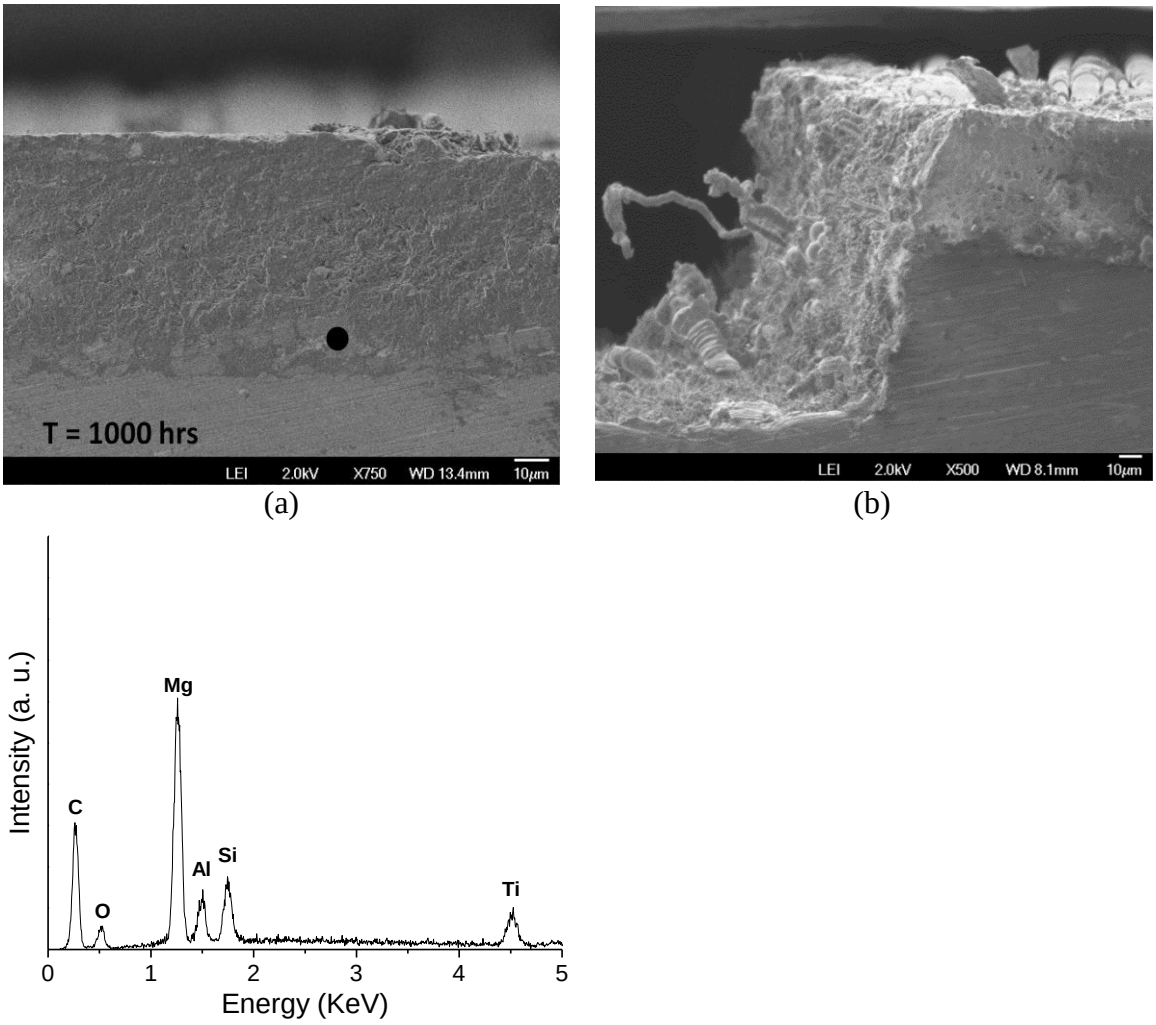

Figure 4.39. SEM micrograph (a) far away from and (b) near the scribe and (c) EDS of cross-sectioned AA2024-T351 panels coated with Mg-rich primer (initial MgPVC = 45%) and polyurethane topcoat after environmental exposure in ASTM B-117 modified with artificial seawater for 1000 h. Spot markers in (a) indicate approximate location of EDS analysis shown in (c).

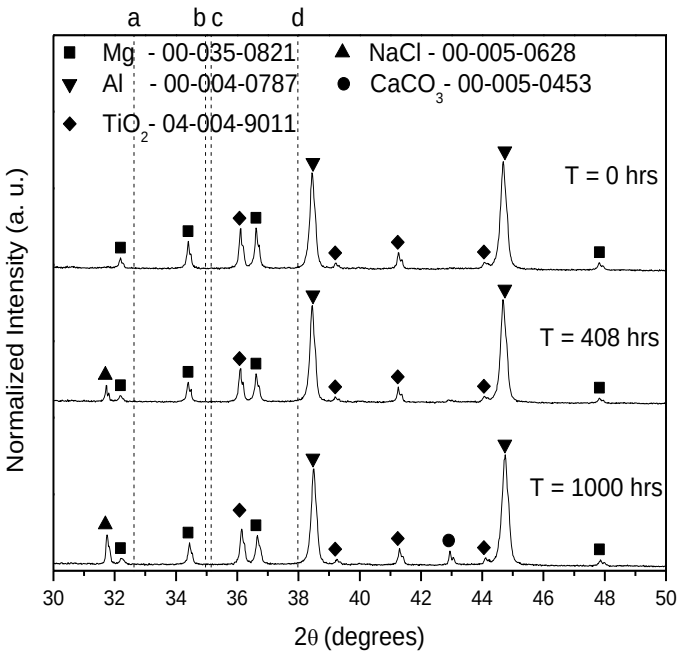

Figure 4.40. X-Ray diffraction spectra of AA2024-T351 panels coated with Mg-rich primer (initial MgPVC = 45%) and polyurethane topcoat that have been environmentally exposed in ASTM B-117 modified with artificial seawater for 0, 408, and 1000 hours. Dotted lines indicate the position of the most intense diffraction peak for (a) $MgCO_3$, (b) $MgCl_2$, (c) Al_2O_3, and (d) $Mg(OH)_2$.

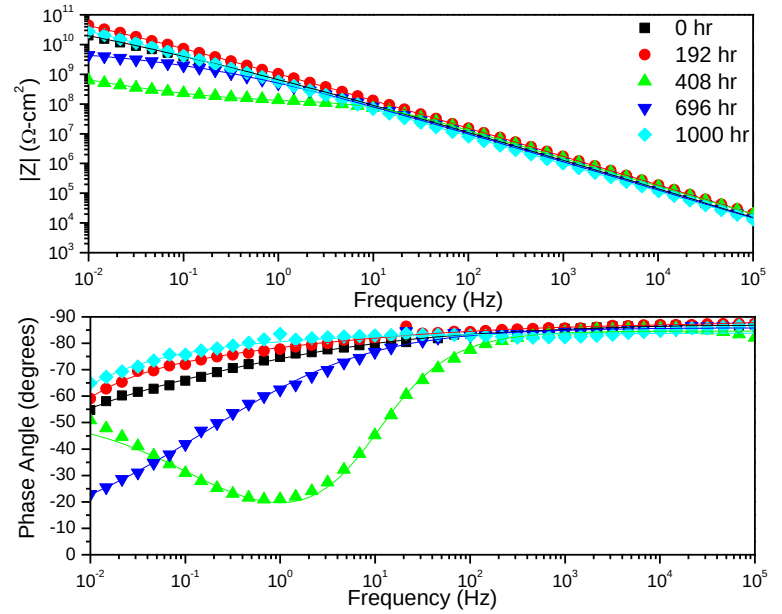

(a)

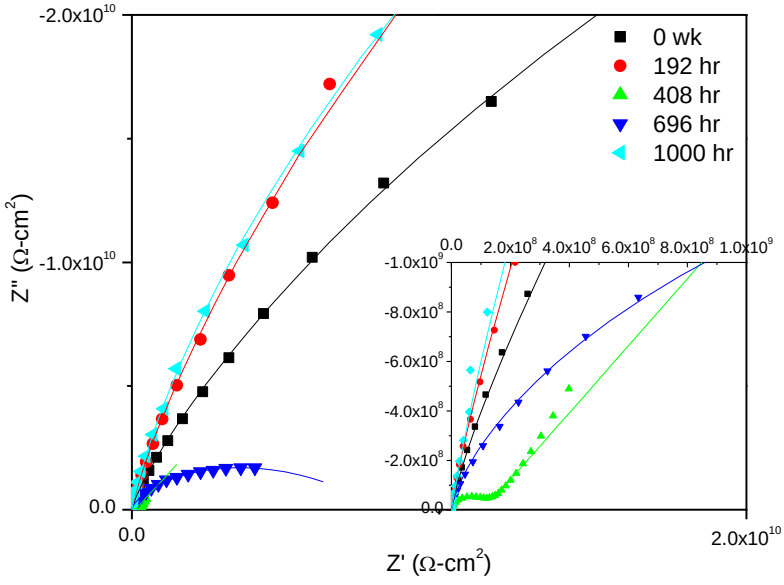

(b)

Figure 4.41. (a) Bode and (b) Nyquist plots of EIS AA2024-T351 panels coated with Mg-rich primer (initial MgPVC = 45%) and polyurethane topcoat after exposure in ASTM B-117 modified with ASTM Seawater for 0, 192, 408, 698, and 1000 hours. Tested in ambiently aerated 5% NaCl Solution..

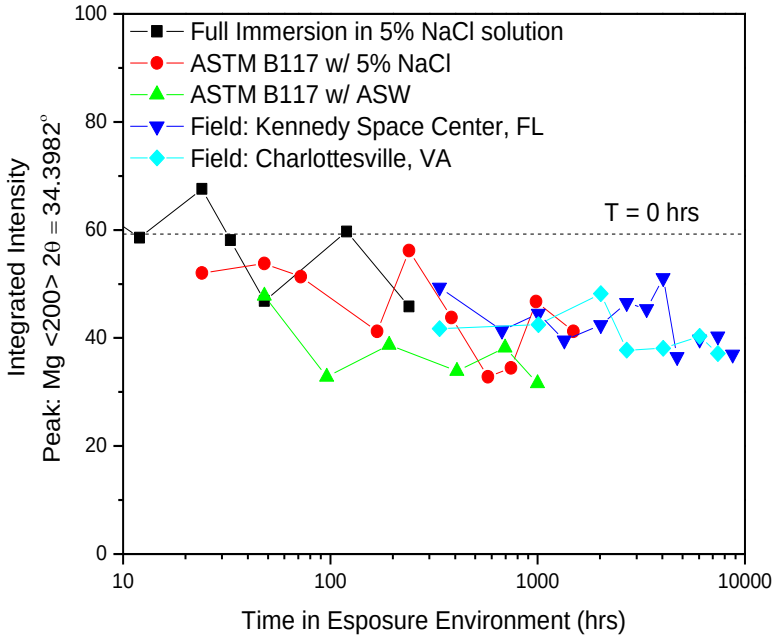

Figure 4.42. Integrated peak intensity vs. environmental exposure time in various exposure environments for AA2024-T351 panels coated with Mg-rich primer (initial MgPVC = 45%) and polyurethane topcoat.

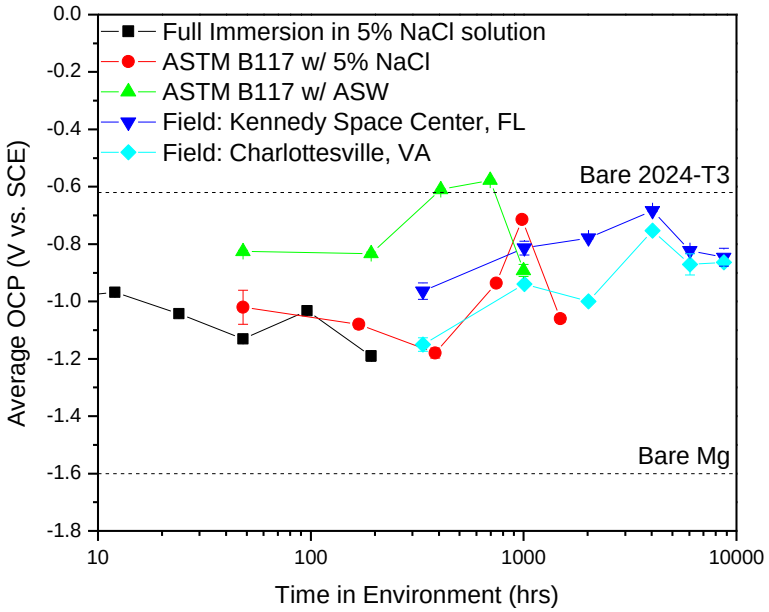

Figure 4.43. Galvanic protection potential in ambiently aerated 5% NaCl vs. environmental exposure time in various exposure environments for AA2024-T351 panels coated with Mg-rich primer (initial MgPVC = 45%) and polyurethane topcoat.

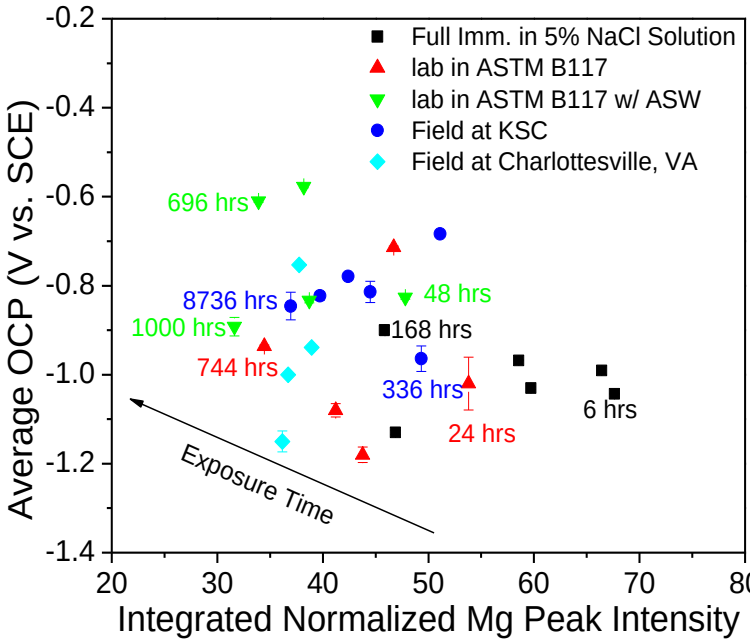

Figure 4.44. Correlation between integrated Mg peak (Mg <200> 2θ = 36.6170°) intensity vs. galvanic protection potential of AA2024-T351 panels coated with Mg-rich primer (initial MgPVC = 45%) and polyurethane topcoat in ambiently aerated 5% NaCl solution after exposure in various environments.

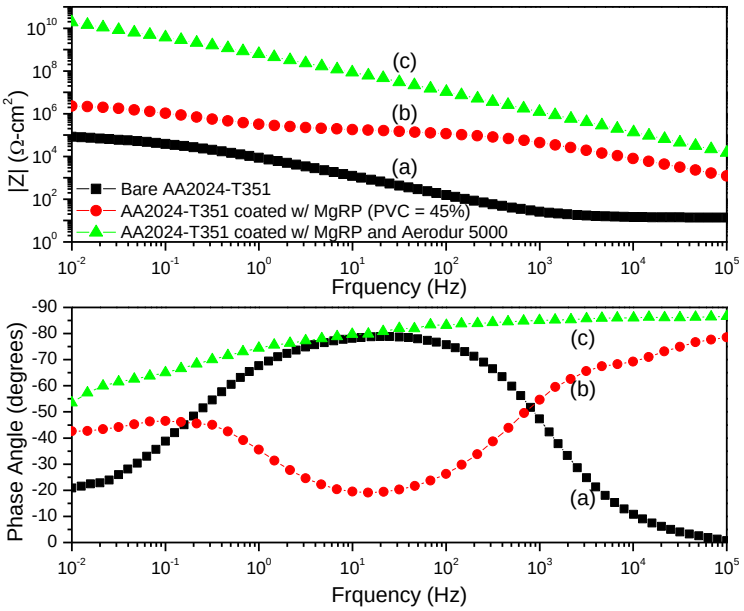

Figure 4.45. EIS Bode Magnitude and Phase Angle of (a) bare AA2024-T351 pretreated with Prekote after 10 min OCP (b) AA2024-T351 panels coated with Mg-rich primer (initial MgPVC = 45%) after 10 min OCP (c) AA2024-T351 panels coated with Mg-rich primer (initial MgPVC = 45%) and polyurethane topcoat after 6 hour OCP.

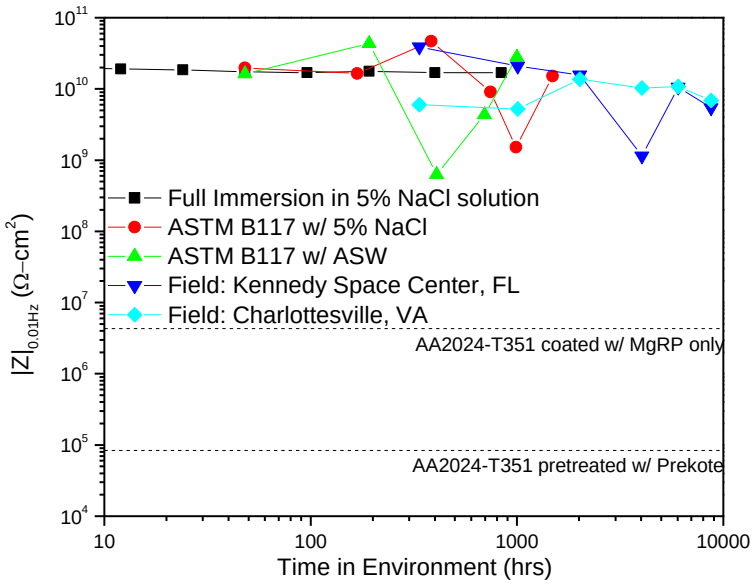

Figure 4.46. Magnitude of electrochemical impedance at 0.01 Hz in ambiently aerated 5% NaCl vs. environmental exposure time in various exposure environments for AA2024-T351 panels coated with Mg-rich primer (initial MgPVC = 45%) and polyurethane topcoat.

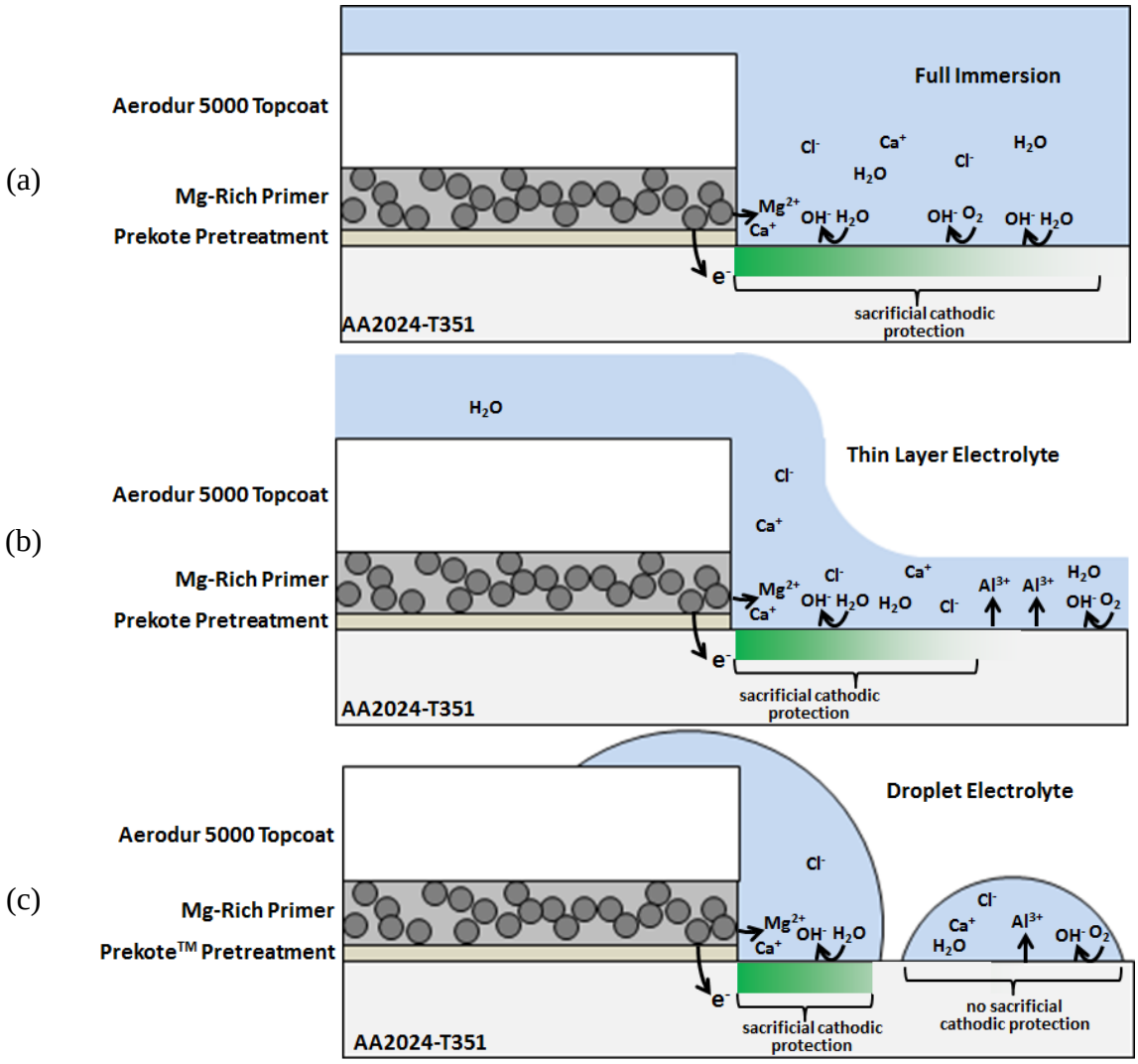

Figure 4.47. Schematic of AA2024-T351 panels coated with Mg-rich primer and polyurethane topcoat depicting MgRP sacrificial cathodic protection function under (a) full immersion, (b) thin-layer electrolyte, and (c) droplet electrolyte conditions.

5 Full Immersion Electrochemistry of Mg and AA2024-T351

Reference: *A. D. King, N. Birbilis and J. R. Scully, Accurate Electrochemical Measurement of Magnesium Corrosion Rates; a Combined Impedance, Mass-Loss and Hydrogen Collection Study, Electrochim Acta, 121, 0 (2014), pp. 394-406.*

DOI: http://dx.doi.org/10.1016/j.electacta.2013.12.124

5.1 Abstract

Chapter 5 focuses on the foundational electrochemistry of AA2024-T351 and high purity Mg. The purpose of Chapter 5 is to study the effects of electrolyte chemistry on the E-i electrochemical boundary conditions of both bare Mg and bare AA2024-T351. Information is sought to understand a galvanic couple between the two materials such as in the case of a MgRP on AA2024-T351. In this work, diagnostic full immersion potentiodynamic polarization tests were utilized in an effort to determine E-i electrochemical boundary conditions of both bare, commercially pure Mg and bare AA2024-T351 in various electrolyte chemistries that are relevant to realistic atmospheric MgRP deployment scenarios. It was found that the HER cathodic current density on the AA2024-T351 does not vary with varying chloride concentration however the diffusion limiting current density for ORR was decreased as salt concentration was increased to near solubility limits. Additionally, an increase in chloride concentration resulted in a significant decrease in the free corrosion potential of bare AA2024-T351. The anodic

current density on bare Mg was observed to increase and the free corrosion potential of bare Mg was observed to decrease with increased chloride concentration. The effect of chloride concentration on the corrosion potential of bare Mg was much less than on that of bare AA2024-T351. Therefore, under high chloride conditions the difference between the corrosion potentials of Mg and AA2024-T351 (ΔE) will be decreased. ΔE is the driving force for cathodic prevention and protection.

Moreover, an important consideration in understanding the inefficiencies of Mg as an anode is whether there is a Mg^{+1} intermediate step when Mg oxidizes to Mg^{+2} and whether all e^- produced in the oxidation from Mg to Mg^{+2} are available for supply to the cathode. As such, the anodic inefficiencies of Mg as an anode are discussed, characterized, and quantified. In an effort to circumvent the negative difference effect (NDE), in-situ EIS and H_2 collection and post-mortem mass-loss and ion concentration techniques were utilized to characterize the anodic dissolution rates of high purity Mg in NaCl solutions, providing three or four unique measures of magnesium corrosion for the same specimen. It was determined that analysis of impedance data, while accounting for a physically justified inductive response at low frequencies, enabled the determination of the polarization resistance, R_P, of freely corroding magnesium at the zero frequency limit. At OCP, the determination of R_P with EIS provided excellent correlation to the mass loss and volume of hydrogen collected. This finding is elaborated in a broader discussion that critically addresses previous studies which have utilized the impedance behavior of freely corroding magnesium and which claim electrochemical tests may underestimate Mg corrosion when attempting to use a charge transfer resistance at intermediate frequencies.

When the Mg was anodically polarized, the increased H_2 evolution and extremely fast anodic reaction rate made the EIS spectra extremely noisy and difficult to analyze. However, under anodic polarization, the sum of H_2 gas collected above the surface of the Mg specimen and the $I_{applied}$ correlated well with the gravimetric mass loss of magnesium as well as with the resulting concentration of Mg^{2+} in solution as measured by ICP-OES, giving some insight into the origins of the NDE. These findings support the notion that Mg oxidizes from $Mg \rightarrow Mg^{+2}$ with all e^- released eligible for supply to the cathode.

5.2 Introduction and Background

The full MgRP coating system, as intended for commercial use, consists of three individual components, the surface pretreatment, the primer coating (MgRP) and the topcoat coating (Aerodur 5000); all of which are applied to AA2024-T351, an Al-Cu-Mg, solution heat treated alloy commonly used in aerospace applications. The ability of the MgRP coating system to provide sacrificial anode based galvanic and barrier corrosion protection to the substrate is a result, not only of the contributions and interplay of each individual component, but also the environmental severity characteristics associated with the particular service environment in which the MgRP coating system is utilized. Much work has been done to study the characteristics and roles of each component of the MgRP coating system, with respect to long term corrosion protection, in standard lab and field environments.[1-16] As a result, conceptual understandings of the sacrificial galvanic and barrier protection strategies that are designed into the full-up MgRP coating system are widely held.[1-16] However, there exists a need for a more robust understanding of the

sacrificial anode based galvanic corrosion protection mechanism afforded by the full-up Mg-rich primer (MgRP) coating system in the context of mixed potential theory beyond empirical, qualitative assessments. This foundation may be essential to understand the difference in performance between field and lab environmental exposures.

Much is known about the corrosion of bare, precipitation-age-hardened Al alloys containing Cu and Fe such as AA2024-T351. As discussed more thoroughly in Chapter 1 of this thesis, aluminum-based precipitation-age-hardened alloys containing Cu and Fe (such as AA2024-T351), when left to corrode freely in an aerated aqueous electrolyte, are prone to active phase dissolution, localized corrosion such as pitting induced by galvanic interactions between Cu-rich intermetallic compounds and the Al-alloy matrix.[17-40] These local galvanic cells, formed by Cu- and Fe- containing intermetallics or replated Cu, induce acid pitting and alkaline attack.[17, 22-40] One strategy to protect this and similar Al alloys is cathodic polarization via sacrificial galvanic protection by a primer coating made of, or containing, a more active material such as Mg.[41-43]

Bare AA2024-T351 and similar alloys have typical OCP's of -0.4 to -0.8 V vs. SCE in aerated, aqueous chloride-containing electrolytes typical to a marine service environment they may be exposed in. High purity Mg, with a typical OCP of -1.5 to -1.9 V vs. SCE in similar environments, is more active than the Al matrix and all of the intermetallic phases that exist in AA2024-T351[17, 44, 45] and can provide sacrificial galvanic corrosion prevention to the AA2024-T351 substrate. In the literature, potentiodynamic polarization scans of bare AA2024-T351 and bare, commercially pure Mg, show that the anodic

reaction rate on Mg is relatively fast and that the cathodic reaction rate on AA2024-T351 is relatively slow.[5] The combination of a fast anodic reaction rate on Mg and a slow cathodic reaction rate on AA2024-T351 results in a polarizable cathode (AA2024-T351 substrate) that enables a galvanic couple potential of as low as -1.5 V vs. SCE in 0.1 wt. % NaCl solution to be achieved between equal areas of bare AA2024-T351 and bare, commercially pure Mg.[5]

Realistic MgRP deployment scenarios can include a wide range of electrolyte chemistries and concentrations due to variations in precipitation chemistry, time-of-wetness (TOW), rinsing frequency, salt deposition rate, UV exposure and relative humidity. The electrolyte that exists on the surface of the coating in service can be created by any combination of rainfall, aerosol deposition, ocean spray, immersion, or deliquescence of deposited salts. It is also known that the equilibrium concentration of an electrolyte decreases with increasing ambient relative humidity which will play a role in environmental exposures where the electrolyte layer is small such as a thin layer or in a droplet formed by deliquescence of deposited salts.[46] Under such environmental conditions the concentration of salts in the electrolyte will vary as the sample wets, dries or equilibrates with a changing relative humidity. These variations in electrolyte chemistry will affect the E-i electrochemical boundary conditions of both the AA2024-T351 and the Mg electrode and consequentially, the mixed-potential-governed, galvanic couple behavior between them.

It is the purpose of this chapter to study the effects of electrolyte chemistry on the anodic E-i electrochemical boundary conditions of bare Mg and the cathodic E-i electrochemical boundary conditions of bare AA2024-T351 in the context of a galvanic couple between the two materials. In this work, diagnostic full immersion polarization tests were utilized in an effort to determine E-i electrochemical boundary conditions of both bare, commercially pure Mg and bare AA2024-T351 in various electrolyte chemistries that are relevant to realistic MgRP deployment scenarios. These E-i electrochemical boundary conditions will be inputs into mixed potential modeling similar to the modeling used in Chapter 2 as well as in finite element modeling of the throwing power of the MgRP system under thin layer electrolytes, presented in Chapter 7. The mixed potential modeling will give insight into the electrochemical mechanisms and characteristics of sacrificial galvanic corrosion prevention afforded by the MgRP in each chemical environment. It was also the goal of this study to develop a robust set of E-i data relevant to the MgRP/AA2024-T351 system and to possibly illuminate feasible chemical environments that would result in detrimental ramifications for the MgRP with respect to its ability to provide sacrificial anode based galvanic corrosion protection. Currently, to cover a wide range of chemistries and to get a general idea of the effects of each common salt and their concentration, polarization test are being conducted in a wide range of concentrations of ambiently aerated NaCl, $MgCl_2$, $CaCl_2$, $AlCl_3$, Na_2SO_4, and ASTM Artifical Sea Water. These individual components constitute some of the compounds with the largest concentration in sea water.[47, 48] These experimental environments can be roughly correlated to environmental phenomena such as immersion, rinsing, wetting, drying, and a range of ambient relative humidity.

In an effort to circumvent the little-understood negative difference effect (NDE), in-situ EIS and H_2 collection and post-mortem mass loss techniques were utilized. The so-called negative difference effect is well known to cause discrepancies in the estimated anodic dissolution of bare, pure Mg determined from traditional electrochemical measurements. In the case of bare, pure Mg, an increase in anodic polarization of the material in aqueous electrolytes results in increased mass lass that does not quantitatively agree with applied current measurements and also results in an increase in H_2 gas production.[49-52] In contrast, on a typical metal, an increase in anodic polarization results in a suppression of the corresponding cathodic reactions such as hydrogen evolution.[50] This atypical behavior of apparent increase of cathodic activity (hydrogen production) on Mg under anodic polarization, in conjunction with mass loss that is under-estimated by applied anodic current density, is known as the negative difference effect (NDE) and has been a source of scientific debate for many years.[53-59] It is important to clarify that the applied current measured on the Mg anode by traditional electrochemical techniques accurately accounts for the current available for protection of the AA2024-T351 cathode. However, in order to accurately predict the physical depletion of the Mg anode material from the MgRP coating, the actual anodic dissolution must be characterized. For this reason, in addition to full immersion polarization tests, it is important to corroborate independent measurements of the dissolution of bare, commercially pure Mg at open circuit as well as under anodic polarization utilizing multiple techniques such as EIS, mass loss, and H_2 collection.

5.2.1 Accurately Determining the Corrosion Rate of Mg at OCP Electrochemically

There are many reports of the determination of corrosion rate of Mg and most commercial Mg-alloys.[60-69] Tests can be classified as short term (such as potentiodynamic polarization or one-time electrochemical impedance spectroscopy, EIS), or as longer term (such as mass loss or hydrogen gas collection). Such methods have been applied to many metal systems for several decades, and the relative merits and demerits of the methods are well-established.[70] Perhaps the most obvious issue is that short-term experiments may not be indicative of long-term corrosion, and that long-term corrosion tests may require untenable test durations with respect to maintenance of constant test conditions. As such, there is a paucity of reports with correlation between short and long term testing – even for full immersion conditions. However in the case of Mg corrosion, the rapid corrosion rates nominally realized, allow for mass loss testing to occur within relatively short time frames (often hours to days). Moreover, the fact that the electrode corrosion potential is very electronegative (<< -1V vs. SHE) with respect to the hydrogen evolution reaction also permits the collection of hydrogen for the assessment of the primary cathodic partial reaction.

There are further considerations that have been identified as important for the accurate determination of corrosion rate for Mg, and these factors vary from test to test, as noted by Kirkland.[70] Rather than review all the information in the relevant papers, the key points are mentioned here for context as to why the present study was executed. There can be no doubt that potentiodynamic polarization offers significant kinetic information, and is the only method which can reveal the relative anodic and cathodic contributions

(and how these may vary from alloy to alloy) that lead to an instantaneous corrosion rate. The method however is short-term and destructive in nature. As such, whilst potentiodynamic polarization is indispensable in understanding the mechanistic origins of corrosion rate, it may not serve as a good index to long-term corrosion rates. This latter point is not surprising, however, in spite of works claiming that potentiodynamic polarization is unsuited to Mg[68, 71], on the basis that the near surface electrolyte and corroding surface itself is (very) dynamic in the case of Mg. During dissolution, the near surface pH can rise to alkaline levels (pH >10) for Mg, and the surface of Mg also displays enhanced catalytic activity (i.e. ability to support the cathodic reaction) as shown by independent works.[72, 73] Therefore comparing an instant test to a long-term test is not valid as the electrolyte and relative rates of reaction have altered with time.

Many Mg corrosion studies employ the collection of gaseous hydrogen (H_2) on the basis that that the primary cathodic reaction ($2H_2O + 2e^- \rightarrow 2OH^- + H_2$) is an index to the rate of anodic dissolution (where at open circuit, $I_{anodic} = I_{cathodic}$). As a standalone method, however, the method is not without its shortcomings, given that (i) hydrogen collection may be inefficient in cases where experiment design is not ideal, (ii) the solubility of hydrogen in water varies significantly relative to sea level and temperature, and (iii) studies rarely pre-saturate the electrolyte with hydrogen. This latter point is imposed on essentially all the Mg corrosion studies reporting hydrogen collection to date.[68, 71 (and refs therein)]

Hydrogen collection alone has also been shown to be problematic on the basis that Mg dissolution also occurs in the 'cathodic regime' of Mg (below open circuit), and that hydrogen evolution persists in the 'anodic regime' of Mg (above open circuit). The latter effect has often been termed the negative difference effect (NDE), where an increase in anodic polarization of the metal results in an increase in H_2 gas production [49-52]. Despite a commonly postulated theory for this based on the purported existence of Mg^+, recent data eliminates the mechanism [49, 72-75]. Specifically, the role of EIS used as a means for rationalizing the existence of Mg^+ is further critiqued below.

EIS in itself does not directly provide a corrosion current density, so the means to such a value is determined from the value of the polarization resistance, R_P[76]. The corrosion rate of freely corroding metal in absence of coverage effects is inversely proportional to polarization resistance as described by the Stern-Geary relationship [76, 77]:

$$i_{corr} = \frac{B}{R_P} = \frac{\beta_a \beta_c}{2.303 R_P (\beta_a + \beta_c)} \qquad \text{Equation 1}$$

Where β_a and β_c are the anodic and cathodic tafel slopes (listed in Table 5.5 and Table 5.7), respectfully.[51, 57, 78] It should be recognized that the form of the Stern-Geary equation expressed in Equation 1 is not strictly correct in the case of voltage dependent coverage effects which affect the values of the term B in Equation 1, represented by the added terms in Equation 2 [76, 79, 80]. However, i_{corr} depends strongly on R_p^{-1} and weakly on B (in brackets in Equation 2). R_p does incorporate effects of coverage as expressed in Equation 2 at low frequency where coverage near E_{corr} can adjust to potential.

$$\frac{1}{R_P} = \frac{\partial I_{app}}{\partial E} = 2.303 I_{corr}\left[\left(\frac{1}{\beta_{a\theta(a)corr}} + \frac{1}{\beta_{c\theta(c)corr}}\right) + \left(\frac{1}{\theta_a}\frac{\partial \theta_a}{\partial E} - \frac{1}{\theta_c}\frac{\partial \theta_c}{\partial E}\right)\right] \quad \text{Equation 2}$$

where θ_a and θ_c are the coverage of anodic and cathodic intermediates, respectively and $\beta_{a\theta(a)corr}$ is the Tafel slope at the coverage present at E_{corr}. R_P can be replaced by R_t when the coverage is frozen and the second term on the right of Equation 2 is zero. The anodic charge consumed can then be estimated by integrating the EIS-estimated corrosion rate over the time of exposure, with knowledge of appropriate Tafel slopes with Equation 3 assuming the second term on the right of Equation 2 is negligible and β is evaluated near E_{corr}:

$$Q_a^{EIS} = \int i_{corr} \cdot A \cdot dt = \int \frac{\beta_a \beta_c A}{2.303 R_p (\beta_a + \beta_c)} dt \quad \text{Equation 3}$$

The effective use of Equation 1, Equation 2, and Equation 3 implies that appropriate Tafel slopes of Mg are used, with the values for β_a for Mg nominally within a rather well defined window on the basis that Mg is non-polarizable (anodically) resulting in low values (≤150 mV/decade), and that reports of β_c for Mg are nominally in the vicinity of 200-300mV/decade. [49, 68, 71, 73, 81]

In determining R_P, the use of an equivalent circuit to represent the impedance response is required. A survey of reported EIS data for Mg indicates that the electrochemical response displays inductive behavior with decreasing frequency. [57, 71, 81-89] The extraction of a meaningful R_P from EIS data which includes an inductive response mandates the

inclusion of an inductor in any equivalent circuit as a prerequisite. The determination of R_P from systems displaying inductive behavior was previously given considerable attention in the Fe in acid system, which also indicated some of the foundations for the assessment of impedance data.[90-93] Of those works, the corresponding mass loss was determined using either atomic adsorption or gravimetric methods to unequivocally relate the actual corrosion with the EIS determined corrosion rate.[90-93] It can be summarized that in these studies, accurate determination of corrosion rate was possible when the EIS-determined R_P parameter at the zero frequency limit was properly defined and electrochemically assessed. Whilst many studies use the terms R_P, R_t, and R_{CT} (or similar R_X terms) somewhat interchangeably, herein it is important to qualify their meaning. R_t is defined as the value corresponding to Z' when $-Z''= 0$, usually obtained at intermediate frequencies, whilst R_P is defined as the zero frequency impedance at $-Z'' = 0$ often assessed at $f\rightarrow 0$ but not under DC conditions.[76] In spite of a now appreciated understanding that the polarization resistance at zero frequency is related to corrosion rate, there are works which have not reported this, as such, placing an even greater emphasis to elucidate the correlations in the case of Mg [79, 80]. This is seen graphically for an inductive system in Figure 5.5 where the frequency range for determination of R_P versus R_t are indicated.

Inspection of Figure 5.5 reveals that if using (what is defined here as) R_t in place of R_P in Equation 1, then i_{corr} will be (rather grossly) underestimated. This has been noted to occur in the literature, when reviewing quoted R_P values [71, 81], which correspond to what we

defined as Z' when Z"= 0 (in point of fact, R_t in Fig. 1), in spite of an obvious inductive component that is neglected.

Under freely corroding conditions (open circuit), all of the H_2 gas evolved on the surface of the Mg electrode is assumed to be produced by the HER cathodic reaction and occur at an equal rate to anodic dissolution of the Mg. The volume of H_2 gas evolved can be converted to a corresponding cathodic charge (Q_c) via a combination of the ideal gas law and Faraday's Law:[94, 95]

$$Q_c^{H_2} = Q_a = znF = \frac{zPVF}{RT} \qquad \text{Equation 4}$$

Where z is equivalent moles of electrons per mole of H_2 (in this case assumed to be 2), *n* is the number of moles of H_2 produced, F is Faraday's constant, *a* is the molar mass, P is the pressure inside the buret (≈ 1 atm), V is the volume of H_2 gas collected, R is the ideal gas constant and T is the temperature.

The mass loss of Mg (Δm), as measured gravimetrically, can be converted to consumed anodic charge (Q_a) via Faraday's law:[94, 95]

$$Q_a^{\Delta m} = znF = \frac{z\Delta mF}{a} \qquad \text{Equation 5}$$

Where z is equivalent moles of electrons per mole of Mg (in this case assumed to be 2), *n* is the number of moles of Mg consumed, F is Faraday's constant and *a* is the molar mass.

A combined experiment was designed to permit in-situ EIS and H_2 collection, along with subsequent post-mortem mass loss. Whilst it is recognized that Mg displays the so-called negative difference effect (NDE) which is purported to result in discrepancies in the estimated anodic dissolution of Mg determined from electrochemical measurements, the combined assessment of electrochemical response, H_2 gas collection, and mass loss unequivocally shows good agreement with conventional theories. The purpose of the present study is to corroborate three independent measurements, whilst also subsequently validating the use of EIS as a means for serving as an expedient method for corrosion rate assessment of freely corroding Mg based on the protocol described here using R_P determined at the zero frequency limit.

5.2.1 Accurately Determining the Corrosion Rate of Anodically Polarized Mg

When Mg is anodically polarized, the increased H_2 evolution and extremely fast anodic reaction rate made the EIS spectra, especially at low frequency, extremely noisy and difficult to analyze. For this reason a reliable R_P could not be determined from potentiostatic EIS measurements at anodic polarizations of +150 mV and + 300 mV vs. OCP. However, under anodic polarization, the sum of H_2 gas collected above the surface of the Mg specimen and the net $I_{applied}$ correlated well with the gravimetric mass loss of magnesium as well as with the resulting concentration of Mg^{2+} in solution as measured by ICP-OES, giving some insight into the origins of the NDE.

5.3 Experimental Procedures

5.3.1 Materials

99.9% pure magnesium rod and 1.6 mm thick AA2024-T351 sheet were studied in these investigations. The 99.9% pure Mg rod was 8.0 mm in diameter and 2.50 cm long. Table 5.1 and Table 5.2 show the chemical analysis of both the AA2024-T351 and the magnesium rod used in this work. Chemical analysis shows the Mg rod had a measured purity of over 99.9% and is substantially similar to the powder used in commercial Mg-Rich Primer (MgRP) Products.[2]

The Mg rod was mounted in EpoThin epoxy resin manufactured by Buehler in order to make clamping the sample to an electrochemical flat cell easier. The bare electrodes were prepared by alternating polishing with silicon-carbide paper and rinsing with 18.2 MΩ deionized water to a final polishing grit of 1200. The samples were then dried with lab tissue before use.

5.3.2 Full Immersion Electrochemical Analysis

Potential control during electrochemical experiments was maintained using a potentiostat with computer interface software. Solartron 1287A/1255B and Gamry Reference 600 potentiostats were selected because they enable electrochemical impedance spectroscopy (EIS) measurements along with traditional electrochemical measurements. Saturated Calomel reference electrodes (SCE) were used in full immersion testing.

5.3.3 Anodic E-log(i) behavior of Mg

Anodic potentiodynamic scans were conducted on 99.9% pure, 8.0 mm diameter bare Mg electrodes The tests were run in various solutions with ambient aeration and used a saturated calomel reference electrode. The bare Mg electrodes were polished to 1200 grit silicon carbide paper. The potentiodynamic scans were conducted after a 10 minute OCP. A typical anodic scan started at -0.2 V vs OCP up to +0.7 V vs. OCP and scanned at 1.0 mV per second.

5.3.4 Cathodic E-log(i) behavior of AA2024-T351

Cathodic potentiodynamic scans were conducted on bare AA2024-T351 sheet. The tests were run in various solutions with ambient aeration using a saturated calomel reference electrode. The bare AA2024-T351 electrodes were ground to 1200 grit silicon carbide paper and then clamped to an electrochemical flat cell with a 1 cm^2 window. The potentiodynamic scans were conducted after a 10 minute OCP. A typical cathodic scan started at +0.2 V vs OCP and scanned down to -1.0 V vs. OCP at 0.1667 mV per second.

5.3.5 Electrochemical Impedance Spectroscopy (EIS)

EIS was conducted on bare Mg electrodes. A typical EIS scan was acquired in sine sweep mode from 100 kHz to 0.005 Hz with 6 points per decade. Electrodes were scanned with an AC amplitude of 20 mV. The bare Mg electrodes were polished to 1200 grit silicon carbide paper.

5.3.6 Test to Measure Simultaneous Mass Loss, H_2 Evolution and EIS of bare Mg

A full immersion, electrochemical testing regimen was designed to simultaneously measure, mass loss, electrochemical impedance, and the volume of H_2 gas evolved on a bare Mg electrode. This test regimen was comprised of either an open circuit measurement or a potentiostatic hold at a constant anodic overpotential; with intermittent EIS measurement. These two steps were then repeated for a specified number of cycles. The experimental setup was comprised of a vertical flat cell with a 1 cm^2 sample window attached to a vertically mounted, inverted, volumetric buret (see Appendix C for further details). The inverted buret was centered above the sample window and a glass funnel was attached to the end of the buret to aid with the collection of H_2 bubbles. A large piece of Pt mesh was used as the counter electrode and a saturated calomel electrode was used as the reference electrode. A schematic of the setup is shown in Figure 5.2. It is important to note that it is necessary to saturate the electrolyte with H_2 gas prior to exposing the working electrode of interest, as H_2 gas is significantly soluble in most aqueous environments (~14 mL H_2 gas per 1.0 L H_2O via Crozier, et. al.).[96] The electrolyte was saturated with H_2 gas by cathodically polarizing a second Pt mesh electrode to – 1.5 V vs. SCE for 1.5 h. The test electrolytes used include quiescent 0.1, 1.0 and 5.0 M NaCl solutions at ambient aeration, which established pH values of 5.4, 5.2, and 5.1 respectively. Following testing, specimens were cleaned with ASTM G1 standard chromic acid solution (200g/L CrO3) and dried in a dry box for at least 24 hrs. Negligible mass loss from the bulk Mg resulted from this cleaning procedure.

5.4 Results

5.4.1 Cathodic E-log(i) Characteristics of Bare AA2024-T351 and Anodic E-log(i) Characteristics of Bare Commercially Pure Mg

Figure 5.3 and Figure 5.4 depict the E-log(i) characteristics of bare Mg and bare AA2024-T351 in some chemical environments deemed relevant to the environmental exposure of MgRP-coated AA2024-T351. During an episodic wetting or drying event the electrolyte concentration will subsequently decrease or increase to equilibrate with the ambient RH, shifting the E-log(i) characteristics of both the anode and cathode. Figure 5.3(a-f) show the cathodic E-log(i) characteristics of bare AA2024-T351 and the anodic E-log(i) characteristics of bare, commercially pure Mg in varying concentrations of ambiently aerated NaCl, $MgCl_2$, $AlCl_3$. $CaCl_2$, Na_2SO_4, and ASTM artificial seawater. Figure 5.4 depicts the E-log(i) characteristics of bare Mg and bare AA2024-T351 in as-mixed, ambiently aerated 1.0 M NaCl and ASTM artificial seawater solutions before and after Mg shavings were allowed to dissolve in the solution. The dissolution of the Mg shavings in solution produces $Mg(OH)_2$, which increases the pH of the solutions (to 10.5 in 1.0 M NaCl and 9.6 in ASTM ASW). At high pH, Al's oxides are soluble[97] (Figure 5.1b), and not protective, which acts to shift the corrosion potential of the AA2024-T351 to lower potentials. Such a scenario might develop on the surface of MgRP coated AA2024-T351 in environments with low precipitation or infrequent rinsing such that continuous Mg pigment dissolution locally increases the pH of the electrolyte layer or droplet. The ASTM B-117, laboratory salt fog environment produces a constant, thin-

layer electrolyte and does not experience variances in chloride concentration or pH effects (due to acid rain or Mg pigment dissolution) which are expected in the field.

The cathodic current density on the AA2024-T351 did not vary significantly with varying chloride concentration (Figure 5.3) or pH (Figure 5.4). However, the corrosion potential of AA2024-T351 was greatly affected by both chloride concentration and pH. An increase in either chloride concentration or pH resulted in a significant decrease in the corrosion potential of bare AA2024-T351. The anodic current density on bare Mg was observed to increase and the corrosion potential of bare Mg was observed to decrease with increased chloride concentration. In most environments studied, the effect of chloride concentration and pH on the corrosion potential of bare Mg appears to be less than on that of bare AA2024-T351. Therefore, under high chloride or high pH conditions the difference between the corrosion potentials of Mg and AA2024-T351 (ΔE) will be decreased where ΔE is the driving force for sacrificial anode based cathodic protection.

5.4.2 EIS of Mg in chloride containing environments and equivalent circuit model

The EIS spectrum of pure Mg (at open circuit) in quiescent 0.1 M NaCl (Figure 5.5(a-c)) characteristically displays two capacitive loops and an inductive loop. An inductive loop was indicated in the Nyquist plot (Figure 5.5 (a)) by a positive imaginary component (Z”) and decreasing real component (Z’) with decreasing frequency. Additionally, the inductive behavior was also observed in the Bode magnitude plot (Figure 5.5(b)) by the decreasing impedance magnitude at low frequencies ($f < 0.1$ Hz), along with the hallmark

trait of positive phase angles (indicating the current response is leading applied potential). This behavior is noted in several independent works.[57, 71, 81-89] A system can be considered to be reasonably stationary through the direct integration of the Kramers-Kronig (K-K) transformations of the real and imaginary components.[98] Herein, we applied the K-K transform and present the results for Mg after 0 and 24 hours in 0.1 M NaCl (Figure 5.6) which displays good correlation and low residual noise (<<1% of calculated) indicating that the data is consistent and causal, and this was also found for the K-K transformations in 1.0 and 5.0 M NaCl. Consistency of impedance data for Mg, inspite of its activity and inductive response, has also been confirmed by the works of Baril[82-85] who stated the presented impedance diagrams were consistent with the K-K relations.

The frequency dependent impedance response of the entire equivalent circuits shown in Figure 6a and 6b can be determined by simple circuit analysis and are described by Equation 6 and Equation 7, respectively:

In 0.1 and 1.0 M NaCl:

$$|Z| = \left(\frac{1}{Z_{C1}} + \frac{1}{\left(\frac{1}{Z_{C2}} + \frac{1}{Z_{R2}} \right)^{-1} + Z_{R1}} + \frac{1}{Z_L + Z_{R3}} \right)^{-1} + Z_{Rs} \qquad \text{Equation 6}$$

In 5.0 M NaCl:

$$|Z| = \left(\frac{1}{Z_{C1}} + \frac{1}{\left(\frac{1}{Z_{C2}} + \frac{1}{Z_{R2} + \left(\frac{1}{Z_{R4}} + \frac{1}{Z_{C4}} \right)^{-1}} \right)^{-1} + Z_{R1}} + \frac{1}{Z_L + Z_{R3}} \right)^{-1} + Z_{Rs} \qquad \text{Equation 7}$$

At intermediate frequencies where $-Z'' = 0$ (f_{Rt} in Figure 5.5(c)) the impedance of the entire circuit (Equation 6), less the solution resistance, is a charge transfer resistance, R_t, and is a complex function of R_1, C_1, R_2, and C_2 but is approximately equal to (but not exactly) $R_1 + R_2$. The polarization resistance of pure Mg under freely corroding conditions was defined as the difference in impedance between the solution resistance ($|Z|$ when $f \rightarrow \infty$) and low frequency asymptote ($|Z|$ when $f \rightarrow 0$).[76, 92, 99-102] The impedance relationships of various solid state equivalent electrical circuit elements commonly used in equivalent circuits For EIS are shown in Table 5.3 As frequency trends to zero ($f \rightarrow 0$), capacitive components of a system approach infinite impedance ($Z_c = \infty$) and inductive components approach zero impedance ($Z_L = 0$), shown in Figure 5.5(d). As a result, and as shown schematically in Figure 5.7, this enables circuit simplification and the subsequent calculation of the polarization resistance, R_P, to be estimated by Equation 8 and Equation 9:

In 0.1 and 1.0 M NaCl:

$$\frac{1}{R_p} = \frac{1}{R_1 + R_2} + \frac{1}{R_3} \qquad \text{Equation 8}$$

In 5.0 M NaCl:

$$\frac{1}{R_p} = \frac{1}{R_1 + R_2 + R_4} + \frac{1}{R_3} \qquad \text{Equation 9}$$

Simulated EIS spectra produced from regression fit analysis are shown as solid lines in Figure 5.5(a-c) and exhibit good agreement with the model. The typical frequencies where R_s, R_t, and R_P are determined are shown in Figure 5.5(c).

5.4.3 EIS of Mg as a function of time and chloride concentration.

The impedance of pure Mg in 0.1, 1.0, and 5.0 M NaCl was periodically recorded over 24 h and was regression fit against the relevant equivalent circuits shown in Figure 5.7. The '0 hrs' data was collected following a 10 min period at open circuit and serves as a start-point for presenting the subsequent time dependent response. In all environments studied, the electrochemical impedance spectra contained two (in 0.1 and 1.0 M NaCl) or three (in 5.0 M NaCl) capacitive loops at high or moderate frequencies in combination with an inductive loop at low frequencies. The low frequency |Z| was observed to steadily increase and the breakpoint frequency was observed to shift towards lower frequencies over the 24 h exposure period (Figure 5.8, Figure 5.9, and Figure 5.10). This is corroborated by a decline in the rate of H_2 collected with exposure time (Figure 5.11). Spectra produced from regression fits using the equivalent circuits shown in Figure 5.7 (solid lines in Figure 5.8, Figure 5.9, and Figure 5.10) showed excellent correlation with the experimental data. It is important to clarify that the simulated data, plotted as solid lines in Figure 5.8, Figure 5.9, and Figure 5.10 are simply for visual comparison and are a result of simulating the frequency response of the representative solid state circuit (which was determined by regression fitting of only the measured data over a frequency range where these circuit parameters dominate the faradaic impedance) extended to the zero

frequency limit. It is also important to note that R_P, for use in corrosion rate estimation, is calculated with Equation 8 and Equation 9, not from graphical analysis involving extrapolation of Figure 5.8, Figure 5.9, and Figure 5.10. Different equivalent circuits are used for 0.1, 1.0, and 5.0 M NaCl solutions because, at very high NaCl concentrations of 5.0 M, a third capacitive loop becomes significant at high frequencies, visible in the Nyquist Plot (Figure 5.10). This third loop, upon close investigation, is also present in low chloride concentration conditions as well, but is so low in magnitude, that it becomes insignificant and makes it difficult for a regression fit routine to converge to rational results.

In this work, we did not need to use a constant phase element for the representation of the capactive elements, and hence the reported values represent a capacitance in the units of $\mu F/cm^2$. Rather than report a large amount of tabulated data for the many tests reported here, one set of typical values for equivalent circuit components are reported in Table 5.4. Note that this set of data (Table 5.4) is just one set from replicates of the same test condition, but is given such that the actual values determined can be rationalized in terms of their magnitude and comparison with reported literature values from other works.

The impedance, and subsequent polarization resistance, of pure Mg was observed to decrease with increasing NaCl concentration (Figure 5.12) indicating a higher corrosion rate in concentrated environments (Equation 3). K-K transformations of the real and imaginary components of the impedance of pure Mg after 0 and 24 hours in 0.1 M NaCl

(Figure 5.6), 1.0 M NaCl, and 5.0 M NaCl show good correlation and low residual noise (<<1% of calculated) indicating that the data is consistent and causal.[101]

5.4.4 Corroborating Mass Loss, H_2 Collection and EIS of pure Mg at OCP

The polarization resistance of commercially pure Mg, and subsequently the corrosion current density according to Equation 3, was calculated from the periodic measurement of EIS throughout exposure in quiescent 0.1, 1.0, and 5.0 NaCl and is shown in Figure 5.13. It is seen that a decrease in the corrosion rate (i_{corr}) in 0.1 and 1.0M NaCl occurs with increasing exposure time, while the i_{corr} in 5.0 M NaCl is both consistent and comparatively higher. The decrease in corrosion rate with time is rationalized on the basis of alkalization of the near surface electrolyte, and is discussed further below. Integration of the corrosion current density over the exposure period via Equation 3, conversion of the mass loss via Faraday's Law (Equation 5), and conversion of the accumulated H_2 gas via the ideal gas law and Faraday's Law (Equation 4) all resulted in anodic charge estimations that are similar in value for each environment (Table 5.5, Figure 5.14).

To provide some illumination into the inductive response pertinent to Mg, additional tests were carried out and reported in Figure 5.15, where the impedance was determined during an anodic and cathodic potential bias. In this case the bias was either +300 or -300mV from OCP. When the sample is cathodically polarized (negative DC bias), such that the dominant feature in the EIS response is HER, there is no inductive response. However, there are at least two time constants consistent with presence of a $Mg(OH)_2$

layer. Further, if the sample is anodically polarized (positive DC bias), such that the dominant reaction in the EIS is the oxidation of Mg, likely occurring in several stages, there is a larger contribution from the inductive response (i.e. greater difference between R_P and R_t). This suggests that an adsorbed intermediate does play a role in Mg corrosion.

5.4.1 Corroborating Mass Loss, H_2 Collection, $I_{applied}$, and ICP-OES of pure Mg under anodic polarization

The net applied current (Figure 5.16 and Figure 5.17) and the electrochemical impedance of anodically polarized, pure Mg in 1.0 M NaCl was periodically recorded over 2.5 h and a best effort attempt was made to regression fit the data against the relevant equivalent circuits shown in Figure 5.7. In ambiently aerated 1.0 M NaCl solution, the electrochemical impedance spectra of anodically polarized (+0.150 V and +0.300 V vs. OCP), commercially pure Mg contained two capacitive loops at high or moderate frequencies in combination with an inductive loop at low frequencies. An inductive loop was indicated in the Nyquist plot (Figure 5.18a and Figure 5.19a) by a positive imaginary component (Z") and decreasing real component (Z') with decreasing frequency. Additionally, the inductive behavior was also observed in the Bode magnitude plot (Figure 5.18b and Figure 5.19b) by the decreasing impedance magnitude at low frequencies ($f < 0.1$ Hz), along with the hallmark trait of positive phase angles. Spectra produced from regression fits using the equivalent circuits shown in Figure 5.7 (solid lines in Figure 5.18 and Figure 5.19) showed good correlation with the experimental data at high frequency. However the increased H_2 evolution and extremely fast anodic

reaction rate made the EIS spectra extremely noisy and difficult to analyze at low frequencies. For this reason, reliable determination of R_P during anodic polarizations via potentiostatic EIS was not possible. However, under anodic polarization, the sum of cathodic charge consumed (as estimated by the H_2 gas collected above the surface of the Mg specimen and analyzed by Equation 4) and the partial anodic charge consumed (as estimated by integration of the net $I_{applied}$ in Figure 5.17 assuming z = 2), shown in Figure 5.20, correlated well with total anodic charge estimations determined from gravimetric mass loss of magnesium (according to Equation 5) as well as with the resulting concentration of Mg^{2+} in solution as measured by ICP-OES (converted to mass loss, assuming z = 2 and assessed with Equation 5), giving some insight into the origins of the NDE as being equal and opposite to an increase in HER cathodic reaction rate. The close agreement of these results is significant because the concurrence of estimates of anodic charge consumed is achieved when it is assumed that z = 2 in all assessment techniques (Equation 4 and 5). As a result, an assumed valance of +2 for Mg endures anodic polarization of up to +300 mV vs. OCP in 1.0 M NaCl and supports the hypothesis that Mg is ultimately oxidized to Mg^{2+} and, whether or not it occurs with an intermediate step, almost all of the e^- produced by the oxidation of Mg during dissolution are available for supply to a cathode. In the context of utilizing Mg as a sacrificial anode in a MgRP for protection of AA2024-T351, the anode efficiency of Mg pigment is roughly 50 – 60% in all environments studied in this work, not including any losses of Mg pigment that may occur purely due to self-corrosion of the coating.

5.5 Discussion

This work presents a simple approach for the combined and accurate assessment of the corrosion rate determination of Mg. In isolation, all such methods herein are routinely applied. However, when applied in concert, important mechanistic information can be obtained. One key aspect to this investigation, which differentiates it from other Mg EIS studies, is the presentation of an alternate approach to the assessment of EIS data for Mg. As described in the introduction, the impedance response for Mg includes an inductive component that is evident with decreasing frequency. This feature of the data cannot be ignored. A review of the literature indicates that the inductance has, however, been ignored in the prior works which report that EIS determined i_{corr} underestimates corrosion rate [82-85, 102, 103]. In that regard, the visual inspection of Figure 5.8, Figure 5.9, and Figure 5.10 reveal just how different the values of R_P and R_t are. In most cases, it is a factor of 2 (and often larger). Consequently the following can be asserted; (i) the use of an equivalent circuit without the inclusion of an inductor, (ii) the use of visual inspection for determination of R_P by use of R_t at intermediate frequency from the intersection of the EIS data with the Z" axis at Z" = 0, or (iii) tests which do not terminate at sufficiently low frequency; will all result in gross overestimation of R_P (Figure 5.5), hence underestimation of i_{corr}.

The application of the circuit model presented in this work accounts for the inductance, and the circuit itself merits some comment. Whilst the multi-component nested Randle's type circuits given in Figure 5.7 appear complicated, the circuits are rationalized on the basis that they include the minimum number of capacitive time-constants and the

necessary inductance to faithfully represent the data. The circuit models shown in Figure 5.7 not only faithfully reproduce the experimental data but are physically justified. The physical situation during Mg corrosion involves coupled electrochemical reactions and intermediate surface coverage dependent on potential [98]. This was verified in this work through EIS at ± 300 mV vs. E_{corr}. C_1 (Figure 5.7) is likely a double layer capacitance which is reasonable given the values indicated in Table 3. Values in the range of 10-150 $\mu F/cm^2$ are consistent with a double layer capacitance on a roughened electrode [90, 98, 99]. This double layer capacitance shorts the entire interface at high frequency as seen in Figure 5.8, Figure 5.9, and Figure 5.10. The next feature is a set of series and parallel resistors and capacitors [i.e., $R_1/(R_2//C_2)$], (where "/" indicates series and "//" indicates parallel) and a series resistor inductor combination (i.e., R_3/L). This arrangement is also reasonable and physically justified for Mg. It is known that Mg corrodes non-uniformly even in conditions such as NaCl solution at near neutral pH values [54]. It is likely that patches of weakly passivated (e,g. $Mg(OH)_2$ covered) and actively corroding surfaces exist simultaneously in addition to cathodic sites where water reduction occurs. The weakly passivated (inactive) patches and actively dissolving areas are represented by the parallel circuit paths shown in Figure 5.7. Each of these processes likely includes adsorption pseudo capacitances (C_2, C_4) which are capacitances arising as a consequence of the faradaic reaction producing the potential dependent coverages of the adsorbed intermediates [76]. The equivalent circuit for the adsorption of an intermediate followed by charge transfer can be represented by a resistor and capacitor in series [76, 104]. The adsorbed intermediate coverage responds to AC and DC potential and, once a high surface coverage is established, the reaction is slowed [$R_1/(R_2//C_2)$] when a pseudo

capacitance appears in the circuit. Thus, the impedance of capacitors C_2 and C_4 tends towards infinity at the DC limit (Table 2 and Figure 5.5(d)) as indicated in Figure 5.7(c) and (d), and hence justified as the origin of R_P in Equations 8 and 9. At intermediate and high frequency the coverage is "frozen in" as the potential is changing back and forth so fast that the coverage cannot follow [76, 104]. This gives rise to R_t (indicated in Figure 5.5), which, in this instance, is greater than R_P, for reasons discussed below, involving an inductor (Figure 5.4). Thus C_2 and C_4 differ from true capacitors which are governed strictly by physical charge separation since charge is transferred to create them. Hence, the high pseudo capacitance values given in Table 3 are justified as discussed by Gileadi and Murray in the case of a pseudo capacitance [105]. C_4 with its high values may even represent a finite diffusional impedance mimicked by a large capacitor as rationalized by Gileadi and Taylor [104] and explained elsewhere [76].

The significance of the inductor (L) in electrochemistry is reasonable, however a short-coming of the corrosion field has been a failure to broadly acknowledge the physical significance of the inductor, despite much discussion [99]. It is inappropriate to ignore this important factor. Just as the adsorption pseudo capacitance represents an adsorbed intermediate that may slow the reaction at fully adjusted potential dependent coverage; the inductor suitably represents just the opposite in an electrochemical system as discussed by Orazem and Tribollet [99]. If a parallel electrochemical process during the corrosion of Mg involves another adsorbed intermediate involved in the coupled corrosion reaction (in fact, it may even be unreasonable to claim a corrosion reaction at OCP does not involve at least two adsorbed intermediates), the physical process related to

the inductor can be explained. Once the second coverage, governed by applied potential, is attained, a faster electrochemical reaction rate is enabled such as Mg^{2+} dissolution via fast intermediate steps. If this is the case, then an inductor physically explains the observation. This physical process, in electrochemistry, is appropriately represented by the series circuit parameters R_3/L. At intermediate and high frequencies Z_L approaches high values (Table 2) because the reaction enabling coverage cannot adjust to the quickly changing AC potential. This represents the situation where R_t is measured and is given by R_1/R_2. At low frequency, Z_L approaches zero and the series circuit R_3/L approaches R_3 because the coverage has time to adjust to the potential and the reaction can thus occur at a high rate. The overall impedance, |Z|, for circuit in Figure 5.7(a) at very low frequency is given by Equation 6. R_P is given by Equation 8. R_t is given by R_1/R_2 at intermediate frequencies because L/R_3 is too large at the frozen coverage. Note that this is the exact opposite behavior from the pseudo capacitance associated with an intermediate coverage that inhibits reactions, in contrast with a second coverage which enables them; which is described by the inductor. For DC corrosion, both must be taken into account, obviously. Thus, R_P represents the combination of R_1-R_4 as shown in Figure 5.7 and Equation 8 and 9 at the DC limit. $R_P < R_t$ in this particular two coverage situation where one type of intermediate coverage is best described by an adsorption pseudo capacitance and one by an inductor. This is the correct treatment for DC corrosion where the coverage obviously has time to adjust to the prevailing conditions and affects R_P. These issues are discussed extensively in works by Scully [76], Orazem [99], Taylor [104], and Murray [105]; and there is no need to reproduce the mathematical descriptions shown there. In summary, the circuit model shown in Figure 5.7 and the data in Table 3 both faithfully reproduce the data and

are physically justified. Regarding the chemical species responsible for the inductive response, this is an issue that has not been given the attention it deserves, and will require future work given the increasing demand for Mg and its accurate corrosion rate determination. Future work in Mg corrosion should seek to elucidate further these intermediate coverage effects and identify the species responsible. However, clearly one is associated with the anodic process as it disappears at cathodic polarization when the dominant AC reaction response is the hydrogen evolution reaction (HER).

Of the works in the literature, Baril [82-85] proposed a model based on adsorbed monovalent Mg in unfilmed areas of the Mg surface, which can now be challenged in light of more recent research [49, 54, 72, 74, 75, 106]. That study was accompanied with text that suggested the inductive loop was attributed to diffusion through a porous, metastable $Mg(OH)_2$ layer. However there was no experimental validation. Similarly, in this work we do not pursue the detailed characterization of the interface as that will be future work which is emerging in the literature for Mg alloys [107-111], but in that regard, what can be asserted from recent works is that there are several important processes which must be taken into consideration. These are:

a) Cathode growth during open circuit corrosion of Mg, such that the anode to cathode ratio is evolving with time which affects the balance of current being maintained by alteration in local current density. The cathode intensity also changes with immersion time, such that previously anodic sites become cathodically activated and may become strong

cathodes as a result of prior corrosion [73]. This has the implication that sites that were previously anodes can 'flip' to become cathodes [54].

b) Corrosion of Mg is associated with film growth, such that Mg ions released during corrosion participate in reactions with OH^- from cathode sites, forming an $Mg(OH)_2$ film. Such films can actually grow to be several hundreds of nm thick, and also form during anodic polarization [74, 107-109, 111].

This study was intended to focus on the validation of EIS as a means for serving as an expedient method for corrosion rate assessment of Mg using the protocol described herein. This was somewhat of a gap in the literature, with conflicting (or no) equivalent electrical circuits presented, and lack of clarity in regards to the use of what we define as R_t, as opposed to what we define as R_P (Figure 5.5). The corrosion rate of Mg as determined by electrochemical techniques (in this case, EIS) and non-electrochemical techniques (in this case hydrogen collection and mass loss) are entirely consistent with each other. The intercept of the inductive loop with the Z" axis as $f \rightarrow 0$ is considered. After all, R_P applies to the case of $f \rightarrow 0$ and R_t applies to the case of a frozen coverage as discussed elsewhere [76, 99]. Moreover, of most relevance to this study, is the simplification that can be implemented as depicted in Figure 5.7(c) and Figure 5.7(d), as $f \rightarrow 0$, resulting in the expressions given in Equations 8 and 9. Such expressions are noted for their simplicity and their applicability to the analysis at hand – permitting a reproducible and straightforward manner for assessment of EIS data that has excellent correlation with both hydrogen and mass loss. Such a method is advocated more widely, and whilst we

have not imposed it on other published data, it is evident that it could be applied for a more faithful determination of EIS derived i_{corr} (since it accounts for the obvious inductance which cannot be rationally neglected) providing a stronger correlation with mass loss in such works.

The implications of accurate determination of Mg corrosion rates using on-line EIS are obvious in the context of understanding the corrosion of Mg and its alloys for use as a sacrificial pigment in a polymer coating system or more generally as a structural element. The variation in corrosion rate of Mg with time as a result of rapid alteration of surface pH also necessitates non-destructive real time methods to gain a longer term appraisal of material corrosion. Furthermore, accurate corrosion rate assessment will also avoid issues associated with the common underestimation of corrosion rate.

Even though reliable determination of R_P during anodic polarizations ($E_{Applied} > E_{OCP}$) via potentiostatic EIS was not possible, accurate estimations of corrosion rate were successfully obtained with mass-loss, H_2 gas collection plus applied current, and ICP-OES. Under anodic polarization, the sum of cathodic charge consumed (as estimated by the H_2 gas collected above the surface of the Mg specimen and analyzed by Equation 4) and the partial anodic charge consumed (as estimated by integration of the net $I_{applied}$ in Figure 5.17 assuming z = 2), shown in Figure 5.20, correlated well with total anodic charge estimations determined from gravimetric mass loss of magnesium (according to Equation 5) as well as with the resulting concentration of Mg^{2+} in solution as measured by ICP-OES (converted to mass loss and assessed with Equation 5), giving some insight

into the origins of the negative difference effect as being equal and opposite to an increase in HER cathodic reaction rate. The close agreement of these results is significant because the concurrence of estimates of anodic charge consumed is achieved when it is assumed that z = 2 in all assessment techniques. As a result, an assumed valance of +2 for Mg endures anodic polarization of up to +300 mV vs. OCP in 1.0 M NaCl and supports the hypothesis that Mg is ultimately oxidized to Mg^{2+} and, whether or not it occurs with an intermediate step, almost all of the $2e^-$ produced by the oxidation of a Mg atom during dissolution are available for supply to a cathode. In the case of commercially pure Mg, the cathode can take the form of a local cathodic reaction (HER) or in the case of a MgRP coating on AA2024-T351, the cathode can also be galvanically coupled AA2024-T351 substrate. It is important to clarify that the applied current measured on the Mg anode by traditional electrochemical techniques accurately accounts for the percentage of anodic charge available for protection of a remote AA2024-T351 cathode, with roughly 50 – 60% of the e^- produced by oxidation of Mg to Mg^{2+} being consumed locally by an increased HER on the Mg itself and not available for cathode protection. In the context of utilizing Mg as a sacrificial anode in a MgRP for protection of AA2024-T351, the anode efficiency of Mg pigment is roughly 50 – 60% in all environments studied in this work, not including any losses of Mg pigment purely due to self-corrosion of the coating.

5.6 Conclusions

1. The work herein presents a simple approach for the combined, accurate, instantaneous and capable long-term determination of the corrosion rate of high purity Mg via mass loss, H_2 gas collection, and EIS-estimated polarization resistance.

2. The impedance response for Mg under conditions dominated by an anodic reaction is shown to include an inductive component that is evident with decreasing frequency which cannot be ignored. An equivalent circuit which accounts for the inductive behavior of Mg and which includes the minimum number of capacitive time-constants to faithfully represent the data, is presented. It was determined that analysis of impedance data, while accounting for a physically justified inductive response at low frequencies, enabled the determination of the polarization resistance, R_P, of freely corroding magnesium at the zero frequency limit. At OCP, the determination of R_P with EIS provided excellent correlation to the mass loss and volume of hydrogen collected.

3. In the literature, EIS determined j_{corr} values derived from $R_{t,}$ which do not account for the electrochemically justified inductive behavior, underestimate the corrosion rate of Mg; in most cases by a factor of 2 or larger. Consequently it can be asserted that for Mg:
    a. the use of an equivalent circuit without the inclusion of an inductor,
    b. the use of visual inspection for determination of R_P from the intersection of the data with the Z" axis at Z" = 0, at intermediate frequency.
    c. tests which do not terminate at sufficiently low frequency

    will all result in overestimation of R_P, hence underestimation of j_{corr}.

4. To provide some illumination into the inductive response, the impedance was determined during an anodic and cathode potential bias. It was observed that if Mg is cathodically polarized (negative DC bias), there is no inductive response. Further, if Mg is anodically polarized (positive DC bias) such that the Mg/Mg^{2+} overall reaction dominates the EIS current response, there is a larger inductive contribution (i.e., greater difference between R_P and R_t) as compared to the open circuit condition. The increase in the difference between R_P and R_t with increasing potential suggests that there is a potential dependency of the inductance, and that this is associated with the acceleration of anodic dissolution.

5. In ambiently aerated 1.0 M NaCl solution, the electrochemical impedance spectra of anodically polarized (+0.150 V and +0.300 V vs. OCP), commercially pure Mg contained two capacitive loops at high or moderate frequencies in combination with an inductive loop at low frequencies which showed good correlation with the experimental data at high frequency. However, the increased H_2 evolution and extremely fast anodic reaction rate on anodically polarized Mg made the EIS spectra extremely noisy and difficult to analyze at low frequencies. For this reason, reliable determination of Rp at during anodic polarizations via potentiostatic EIS was not possible.

6. Even though reliable determination of R_P during anodic polarizations ($E_{Applied} > E_{OCP}$) via potentiostatic EIS was not possible, accurate estimations of corrosion rate were successfully obtained with mass-loss, H_2 gas collection, and ICP-OES. Under anodic polarization, the sum of cathodic charge consumed (as estimated by the H_2 gas collected

above the surface of the Mg specimen) and the partial anodic charge consumed (as estimated by integration of the net $I_{applied}$ assuming z = 2) correlated well with total anodic charge estimations determined from gravimetric mass loss of magnesium as well as with the resulting concentration assuming Mg^{2+} in solution as measured by ICP-OES. The close agreement of these results is significant because the concurrence of estimates of anodic charge consumed is achieved when it is assumed that z = 2 in all assessment techniques. As a result, an assumed valance of +2 for Mg endures during anodic polarization of up to +300 mV vs. OCP in 1.0 M NaCl and supports the hypothesis that Mg is ultimately oxidized to Mg^{2+} and, whether or not the overall reaction occurs involving an intermediate step, is a detail beyond the scope of this work. As a result, almost all of the e^- produced by the oxidation of Mg during dissolution are available for supply to a cathode, whether the cathode is a local cathodic site on the surface of the Mg, a remote piece of AA2024-T351, or a potentiostat.

7. It is important to clarify that the applied current measured on the Mg anode by traditional electrochemical techniques accurately accounts for the percentage of anodic charge available for protection of a remote AA2024-T351 cathode, with roughly 50 – 60% of the e^- produced by oxidation of Mg to Mg^{2+} being consumed locally by an increased HER. In the context of utilizing Mg as a sacrificial anode in a MgRP for protection of AA2024-T351, the anode efficiency of Mg pigment is roughly 50 – 60% in all environments studied in this work, not including any losses of Mg pigment purely due to self-corrosion of the coating. This is consistent with the literature on Mg anode behavior.

5.7 Acknowledgements

This work was supported by the US DoD OUSD Corrosion University Pilot Program under the direction of Mr. Daniel Dunmire and by the National Science Foundation under NSF DMR #0906663. This material is based on research sponsored by the US Air Force Academy under agreement number FA7000-13-2-0020. The U.S. Government is authorized to reproduce and distribute reprints for Governmental purposes notwithstanding any copyright notation thereon. The views and conclusions contained herein are those of the authors and should not be interpreted as necessarily representing the US Air Force Academy or the U.S. Government. Dr. Nick Birbilis acknowledges the Australian Research Council.

5.8 References

1. A. D. King and J. R. Scully, Blistering Phenomena in Early Generation Mg-Rich Primer Coatings on AA2024-T351 and the Effects of CO_2, NACE DoD 2011 Conference Proceedings, (Palm Springs, CA, 2011).
2. A. D. King and J. R. Scully, Sacrificial Anode-Based Galvanic and Barrier Corrosion Protection of 2024-T351 by a Mg-Rich Primer and Development of Test Methods for Remaining Life Assessment, Corrosion, 67, 5 (2011), pp. 05500401-05500422.
3. B. Maier and G. S. Frankel, Behavior of Magnesium-Rich Primers on AA2024-T3, Corrosion, 67, 5 (2011), p. 055001.
4. D. Battocchi, A. M. Simoes, D. E. Tallman and G. P. Bierwagen, Comparison of testing solutions on the protection of Al-alloys using a Mg-rich primer, Corros Sci, 48, 8 (2006), pp. 2226-2240.
5. D. Battocchi, A. M. Simoes, D. E. Tallman and G. P. Bierwagen, Electrochemical behaviour of a Mg-rich primer in the protection of Al alloys, Corros Sci, 48, 5 (2006), pp. 1292-1306.
6. G. Bierwagen, D. Battocchi, A. Simoes, A. Stamness and D. Tallman, The use of multiple electrochemical techniques to characterize Mg-rich primers for A1 alloys, Prog Org Coat, 59, 3 (2007), pp. 172-178.
7. G. P. Bierwagen, D. E. Tallman, M. Nanna, D. Battocchi, A. Stamness and V. J. Gelling, New developments in Cr-free primers for aerospace alloys., Abstr Pap Am Chem S, 228, (2004), pp. U360-U360.
8. M. E. Nanna and G. P. Bierwagen, Mg-rich coatings: A new paradigm for Cr-free corrosion protection of al aerospace alloys, Jct Research, 1, 2 (2004), pp. 69-80.
9. A. Simoes, D. Battocchi, D. Tallman and G. Bierwagen, Assessment of the corrosion protection of aluminium substrates by a Mg-rich primer: EIS, SVET and SECM study, Prog Org Coat, 63, 3 (2008), pp. 260-266.
10. R. L. Twite and G. P. Bierwagen, Review of alternatives to chromate for corrosion protection of aluminum aerospace alloys, Prog Org Coat, 33, 2 (1998), pp. 91-100.
11. D. H. Wang, D. Battocchi, K. N. Allahar, S. Balbyshev and G. P. Bierwagen, In situ monitoring of a Mg-rich primer beneath a topcoat exposed to Prohesion conditions, Corros Sci, 52, 2 (2010), pp. 441-448.
12. H. Xu, D. Battocchi, D. E. Tallman and G. P. Bierwagen, Use of Magnesium Alloys as Pigments in Magnesium-Rich Primers for Protecting Aluminum Alloys, Corrosion, 65, 5 (2009), pp. 318-325.
13. K. N. Allahar, D. Battocchi, G. P. Bierwagen and D. E. Tallman, Transmission Line Modeling of EIS Data for a Mg-Rich Primer on AA 2024-T3, J Electrochem Soc, 157, 3 (2010), pp. C95-C101.
14. K. N. Allahar, D. Battocchi, M. E. Orazem, G. P. Bierwagen and D. E. Tallman, Modeling of electrochemical impedance data of a magnesium-rich primer, J Electrochem Soc, 155, 10 (2008), pp. E143-E149.

15. K. N. Allahar, B. R. Hinderliter, G. P. Bierwagen and D. E. Tallman, Army Vehicle Primer Properties During Wet-Dry Cycling, Corrosion, 65, 2 (2009), pp. 126-135.
16. K. N. Allahar, D. Wang, D. Battocchi, G. P. Bierwagen and S. Balbyshev, Real-Time Monitoring of a United States Air Force Topcoat/Mg-Rich Primer System in ASTM B117 Exposure by Embedded Electrodes, Corrosion, 66, 7 (2010).
17. R. G. Buchheit, R. K. Boger, M. C. Carroll, R. M. Leard, C. Paglia and J. L. Searles, The electrochemistry of intermetallic particles and localized corrosion in Al alloys, Jom-J Min Met Mat S, 53, 7 (2001), p. 29.
18. R. G. Buchheit, R. P. Grant, P. F. Hlava, B. Mckenzie and G. L. Zender, Local dissolution phenomena associated with S phase (Al2CuMg) particles in aluminum alloy 2024-T3, J Electrochem Soc, 144, 8 (1997), pp. 2621-2628.
19. N. Birbilis and R. G. Buchheit, Electrochemical characteristics of intermetallic phases in aluminum alloys - An experimental survey and discussion, J Electrochem Soc, 152, 4 (2005), pp. B140-B151.
20. G. O. Ilevbare, O. Schneider, R. G. Kelly and J. R. Scully, In situ confocal laser scanning microscopy of AA 2024-T3 corrosion metrology - I. Localized corrosion of particles, J Electrochem Soc, 151, 8 (2004), pp. B453-B464.
21. O. Schneider, G. O. Ilevbare, J. R. Scully and R. G. Kelly, In situ confocal laser scanning microscopy of AA 2024-T3 corrosion metrology - II. Trench formation around particles, J Electrochem Soc, 151, 8 (2004), pp. B465-B472.
22. G. S. Chen, M. Gao and R. P. Wei, Microconstituent-Induced Pitting Corrosion in Aluminum Alloy 2024-T3, Corrosion, 52, 1 (1996), pp. 8-15.
23. R. R. Leard and R. G. Buchheit, Electrochemical Characterization of Copper-bearing Intermetallic Compounds and Localized Corrosion of Al-Cu-Mg-Mn Alloy 2024, Material Science Forum, 396-402, (2002), pp. 1491-1496.
24. R. G. Buchheit, Journal of Electrochemical Society, 142, (1995), p. 3994.
25. R. G. Buchheit, R. P. Grant, P. F. Hlava, B. Mckenzie and G. L. Zender, Local Dissolution Phenomena Associated with S Phase (Al_2CuMg) Particles in Aluminum Alloy 2024-T3, Journal of Electrochemical Society, 144, 8 (1997), pp. 2621-2628.
26. G. S. Chen, C.-M. Liao, K.-C. Wan, M. Gao and R. P. Wei, ASTM STP 1298, ASTM, p. 18, 1997).
27. M. A. Alodan and W. H. Smyrl, Detection of Localized Corrosion Using Fluorescence Microscopy, Journal of Electrochemical Society, 144, 10 (1997), pp. L282-L284.
28. M. A. Alodan and W. H. Smyrl, Journal of Electrochemical Society, 145, (1998), p. 1571.
29. M. Büchler, J. Kerimo, F. Guillaume and W. H. Smyrl, Journal of Electrochemical Society, 147, (2000), p. 3691.
30. M. J. Pryor and D. S. Keir, Journal of Electrochemical Society, 102, (1955), p. 605.
31. J. R. Scully, T. O. Knight, R. G. Buchheit and D. E. Peebles, Electrochemical Characteristics of the Al_2Cu, Al_3Ta and Al_3Zr Intermetallic Phases and Their

Relevancy to the Localized Corrosion of Al Alloys, Corros Sci, 35, 1-4 (1993), pp. 185-195.
32. P. Schmutz and G. S. Frankel, Journal of Electrochemical Society, 145, (1998), p. 2295.
33. R. G. Buchheit, L. P. Montez, M. A. Martinez, J. Michael and J. Hlava, Journal of Electrochemical Society, 146, (1999), p. 4426.
34. V. Guillaumin and G. Mankowski, Localized Corrosion of 2024 T351 Aluminum Alloy in Chloride Media, Corros Sci, 41, (1999), pp. 421-438.
35. G. O. Ilevbare and J. R. Scully, Mass-Transport-Limited Oxygen Reduction Reaction on AA2024-T3 and Selected Intermetallic Compounds in Chromate-Containing Solutions, Corrosion, 57, 2 (2001), pp. 134-152.
36. G. O. Ilevbare, J. R. Scully, J. Yuan and R. G. Kelly, Inhibition of Pitting Corrosion on Aluminum Alloy 2024-T3: Effect of Soluble Chromate Additions vs. Chromate Conversion Coating, Corrosion, 56, 3 (2000), pp. 227-242.
37. D. A. Little, "Role(s) of Pretreatment, Inhibitors, and Other Process Steps That Effect Surface Composition On the Under-Paint Corrosion of An Al-Cu-Mg Alloy 2024-T3" University of Virginia, 2006),
38. D. A. Little, "An Electrochemical Framework to Explain the Intergranular Stress Corrosion Path in Two Al-Cu-Mg-Ag Alloys, C415 and C416" (MS Thesis, University of Virginia, 2001),
39. D. A. Little, M. A. Jakab and J. R. Scully, Effect of surface pretreatment on the underpaint corrosion of AA2024-T3 at various temperatures, Corrosion, 62, 4 (2006), pp. 300-315.
40. D. A. Little, J. R. Scully and J. R. Ferrell, The Effect of Pretreatment and Temper on the Under-paint Corrosion of AA2024, NACE CORROSION 2004, (New Orleans, LA, 2004).
41. F. Presuel-Moreno, M. A. Jakab, N. Tailleart, M. Goldman and J. R. Scully, Corrosion-resistant metallic coatings, Mater Today, 11, 10 (2008), pp. 14-23.
42. J. R. Scully, F. Presuel-Moreno, M. Goldman, R. G. Kelly and N. Tailleart, User-selectable barrier, sacrificial anode, and active corrosion inhibiting properties of Al-Co-Ce alloys for coating applications, Corrosion, 64, 3 (2008), pp. 210-229.
43. N. R. Tailleart, B. Gauthier, S. Eidelman and J. R. Scully, Metallurgical and Physical Factors Controlling the Multi-Functional Corrosion Properties of Pulsed Thermal-Sprayed Al-Co-Ce Coatings, Corrosion, 68, 3 (2012).
44. J. R. Davis, Corrosion of aluminum and aluminum alloys, vol. (Materials Park, OH: ASM International, 1999), p. vii, 313 p.
45. E. H. Hollingsworth and H. Y. Hunsicker, Corrosion of Aluminum and Aluminum Alloys, J. R. Davis, (Ed.), vol. 13b, Metals Handbook (Materials Park, OH, ASM International, 1987).
46. T. Prosek, A. Iversen, C. Taxen and D. Thierry, Low-Temperature Stress Corrosion Cracking of Stainless Steels in the Atmosphere in the Presence of Chloride Deposits, Corrosion, 65, 2 (2009), pp. 105-117.
47. Astm, Standard Practice for the Preparation of Substitute Ocean Water, ASTM D1141 - 98, DOI: 10.1520/D1141-98R08 (1998).

48. A. Turnbull, S. Zhou, P. Nicholson and G. Hinds, Chemistry of concentrated salts formed by evaporation of Seawater on duplex stainless steel, Corrosion, 64, 4 (2008), pp. 325-333.
49. G. S. Frankel, A. Samaniego and N. Birbilis, Evolution of hydrogen at dissolving magnesium surfaces, Corros Sci, 70, (2013), pp. 104-111.
50. M. M. Avedesian, H. Baker and Asm International. Handbook Committee., Magnesium and magnesium alloys, ASM specialty handbook, vol. (Materials Park, OH: ASM International, 1999), p. ix, 314 p.
51. G. L. Makar and J. Kruger, Corrosion of Magnesium, Int Mater Rev, 38, 3 (1993), pp. 138-153.
52. G. L. Makar and J. Kruger, Corrosion Studies of Rapidly Solidified Magnesium Alloys, J Electrochem Soc, 137, 2 (1990), pp. 414-421.
53. A. Atrens and W. Dietzel, The negative difference effect and unipositive Mg+, Advanced Engineering Materials, 9, 4 (2007), pp. 292-297.
54. G. Williams and H. N. Mcmurray, Localized corrosion of magnesium in chloride-containing electrolyte studied by a scanning vibrating electrode technique, J Electrochem Soc, 155, 7 (2008), pp. C340-C349.
55. N. T. Kirkland, G. Williams and N. Birbilis, Observations of the galvanostatic dissolution of pure magnesium, Corros Sci, 65, (2012), pp. 5-9.
56. S. Bender, J. Goellner, A. Heyn and S. Schmigalla, A new theory for the negative difference effect in magnesium corrosion, Mater Corros, 63, 8 (2012), pp. 707-712.
57. G. Song, A. Atrens, D. St John, X. Wu and J. Nairn, The anodic dissolution of magnesium in chloride and sulphate solutions, Corros Sci, 39, 10-11 (1997), pp. 1981-2004.
58. G. Song, A. Atrens, D. Stjohn, J. Nairn and Y. Li, The electrochemical corrosion of pure magnesium in 1 N NaCl, Corros Sci, 39, 5 (1997), pp. 855-875.
59. T. R. Thomaz, C. R. Weber, T. Pelegrini, L. F. P. Dick and G. Knornschild, The negative difference effect of magnesium and of the AZ91 alloy in chloride and stannate-containing solutions, Corros Sci, 52, 7 (2010), pp. 2235-2243.
60. G. L. Song and A. Atrens, Corrosion mechanisms of magnesium alloys, Advanced Engineering Materials, 1, 1 (1999), pp. 11-33.
61. P. Volovitch, M. Serdechnova and K. Ogle, Aqueous Corrosion of Mg-Al Binary Alloys: Roles of Al and Mg, Corrosion, 68, 6 (2012), pp. 557-570.
62. A. D. Sudholz, K. Gusieva, X. B. Chen, B. C. Muddle, M. A. Gibson and N. Birbilis, Electrochemical behaviour and corrosion of Mg-Y alloys, Corros Sci, 53, 6 (2011), pp. 2277-2282.
63. G. Song and D. St. John, The effect of zirconium grain refinement on the corrosion behaviour of magnesium-rare earth alloy MEZ, Journal of Light Metals, 2, 1 (2002), pp. 1-16.
64. A. D. Südholz, N. Birbilis, C. J. Bettles and M. A. Gibson, Corrosion behaviour of Mg-alloy AZ91E with atypical alloying additions, J Alloy Compd, 471, 1–2 (2009), pp. 109-115.
65. K. D. Ralston, G. Williams and N. Birbilis, Effect of pH on the Grain Size Dependence of Magnesium Corrosion, Corrosion, 68, 6 (2012), pp. 507-517.

66. G. Williams, K. Gusieva and N. Birbilis, Localized Corrosion of Binary Mg-Nd Alloys in Chloride-Containing Electrolyte Using a Scanning Vibrating Electrode Technique, Corrosion, 68, 6 (2012), pp. 489-498.
67. D. B. Huang, J. Y. Hu, G. L. Song and X. P. Guo, Self-corrosion, galvanic corrosion and inhibition of GW103 and AZ91D Mg alloys in ethylene glycol solution, Corros Eng Sci Techn, 48, 2 (2013), pp. 155-160.
68. F. Y. Cao, Z. M. Shi, J. Hofstetter, P. J. Uggowitzer, G. L. Song, M. Liu and A. Atrens, Corrosion of ultra-high-purity Mg in 3.5% NaCl solution saturated with Mg(OH)(2), Corros Sci, 75, (2013), pp. 78-99.
69. M. C. Turhan, D. Ruckle, M. S. Killian, H. Jha and S. Virtanen, Corrosion Behavior of Polypyrrole/AZ91D in Simulated Body Fluid Solutions and its Functionalization with Albumin Monolayers, Corrosion, 68, 6 (2012), pp. 536-547.
70. N. T. Kirkland, N. Birbilis and M. P. Staiger, Assessing the corrosion of biodegradable magnesium implants: A critical review of current methodologies and their limitations, Acta Biomater, 8, 3 (2012), pp. 925-936.
71. Z. X. Qiao, Z. M. Shi, N. Hort, N. I. Z. Abidin and A. Atrens, Corrosion behaviour of a nominally high purity Mg ingot produced by permanent mould direct chill casting, Corros Sci, 61, (2012), pp. 185-207.
72. G. Williams, N. Birbilis and H. N. Mcmurray, The source of hydrogen evolved from a magnesium anode, Electrochemistry Communications, 0 (2013).
73. J. Swiatowska, P. Volovitch and K. Ogle, The anodic dissolution of Mg in NaCl and Na2SO4 electrolytes by atomic emission spectroelectrochemistry, Corros Sci, 52, 7 (2010), pp. 2372-2378.
74. S. Lebouil, A. Duboin, F. Monti, P. Tabeling, P. Volovitch and K. Ogle, A novel approach to on-line measurement of gas evolution kinetics: Application to the negative difference effect of Mg in chloride solution, Electrochim Acta, 0 (2013).
75. R. M. Souto, A. Kiss, J. Izquierdo, L. Nagy, I. Bitter and G. Nagy, Spatially-resolved imaging of concentration distributions on corroding magnesium-based materials exposed to aqueous environments by SECM, Electrochemistry Communications, 26, (2013), pp. 25-28.
76. J. R. Scully, Polarization resistance method for determination of instantaneous corrosion rates, Corrosion, 56, 2 (2000), pp. 199-218.
77. M. Stern and A. L. Geary, Electrochemical Polarization: I . A Theoretical Analysis of the Shape of Polarization Curves, J Electrochem Soc, 104, 1 (1957), pp. 56-63.
78. N. Pebere, C. Riera and F. Dabosi, Investigation of Magnesium Corrosion in Aerated Sodium-Sulfate Solution by Electrochemical Impedance Spectroscopy, Electrochim Acta, 35, 2 (1990), pp. 555-561.
79. I. Epelboin, C. Gabrielli, M. Keddam and H. Takenouti, Alternating-Current Impedance Measurements Applied to Corrosion Studies and Corrosion-Rate Determination, ASTM STP 727, (1981), p. 150.
80. I. Epelboin, M. Keddam and H. Takenouti, Use of impedance measurements for the determination of the instant rate of metal corrosion, J Appl Electrochem, 2, 1 (1972), pp. 71-79.

81. A. Pardo, S. Feliu, M. C. Merino, R. Arrabal and E. Matykina, Electrochemical Estimation of the Corrosion Rate of Magnesium/Aluminium Alloys, International Journal of Corrosion, (2010).
82. G. Baril, C. Blanc, M. Keddam and N. Pebere, Local electrochemical impedance spectroscopy applied to the corrosion behavior of an AZ91 magnesium alloy, J Electrochem Soc, 150, 10 (2003), pp. B488-B493.
83. G. Baril, C. Blanc and N. Pebere, AC impedance spectroscopy in characterizing time-dependent corrosion of AZ91 and AM50 magnesium alloys - Characterization with respect to their microstructures, J Electrochem Soc, 148, 12 (2001), pp. B489-B496.
84. G. Baril, G. Galicia, C. Deslouis, N. Pebere, B. Tribollet and V. Vivier, An impedance investigation of the mechanism of pure magnesium corrosion in sodium sulfate solutions, J Electrochem Soc, 154, 2 (2007), pp. C108-C113.
85. G. Baril and N. Pebere, The corrosion of pure magnesium in aerated and deaerated sodium sulphate solutions, Corros Sci, 43, 3 (2001), pp. 471-484.
86. I. Nakatsugawa, R. Martin and E. J. Knystautas, Improving corrosion resistance of AZ91D magnesium alloy by nitrogen ion implantation, Corrosion, 52, 12 (1996), pp. 921-926.
87. Y. C. Xin, C. L. Liu, W. J. Zhang, J. Jiang, T. Y. Guoyi, X. B. Tian and P. K. Chua, Electrochemical behavior Al2O3/Al coated surgical AZ91 magnesium alloy in simulated body fluids, J Electrochem Soc, 155, 5 (2008), pp. C178-C182.
88. A. M. Fekry and M. A. Ameer, Electrochemistry and Impedance Studies on Titanium and Magnesium Alloys in Ringer's Solution, Int J Electrochem Sc, 6, 5 (2011), pp. 1342-1354.
89. S. Feliu, C. Maffiotte, A. Samaniego, J. C. Galvan and V. Barranco, Effect of the chemistry and structure of the native oxide surface film on the corrosion properties of commercial AZ31 and AZ61 alloys, Applied Surface Science, 257, 20 (2011), pp. 8558-8568.
90. I. Epelboin, Faradaic Impedances - Diffusion Impedance and Reaction Impedance, J Electrochem Soc, 117, 8 (1970), p. 1052.
91. W. J. Lorenz and F. Mansfeld, Determination of Corrosion Rates by Electrochemical Dc and Ac Methods, Corros Sci, 21, 9-10 (1981), pp. 647-672.
92. F. Mansfeld, M. W. Kendig and S. Tsai, Recording and Analysis of Ac Impedance Data for Corrosion Studies .2. Experimental Approach and Results, Corrosion, 38, 11 (1982), pp. 570-580.
93. D. C. Silverman, Corrosion Rate Estimation from Pseudo-Inductive Electrochemical Impedance Response, Corrosion, 45, 10 (1989), pp. 824-830.
94. D. A. Jones, Principles and prevention of corrosion, 2nd, vol. (Upper Saddle River, NJ: Prentice Hall, 1996), p. xvi, 572 p.
95. C. H. Hamann, A. Hamnett and W. Vielstich, Electrochemistry, vol. (Weinheim ; New York: Wiley-VCH, 1998), p. xvii, 423 p.
96. T. E. Crozier and S. Yamamoto, Solubility of Hydrogen in Water, Seawater, and Nacl Solutions, J Chem Eng Data, 19, 3 (1974), pp. 242-244.
97. M. Pourbaix, Atlas of electrochemical equilibria in aqueous solutions, 2d English, vol. (Houston, Tex.: National Association of Corrosion Engineers, 1974), p. 644.

98. P. Agarwal, M. E. Orazem and L. H. Garciarubio, Measurement Models for Electrochemical Impedance Spectroscopy .1. Demonstration of Applicability, J Electrochem Soc, 139, 7 (1992), pp. 1917-1927.
99. M. E. Orazem and B. Tribollet, Electrochemical impedance spectroscopy, The Electrochemical Society series, vol. (Hoboken, N.J.: Wiley, 2008), p. 523.
100. F. Mansfeld, Electrochemical Impedance Spectroscopy (Eis) as a New Tool for Investigating Methods of Corrosion Protection, Electrochim Acta, 35, 10 (1990), pp. 1533-1544.
101. F. Mansfeld, Corrosion Rate Measurements with the Ac Impedance Technique, J Electrochem Soc, 127, 8 (1980), pp. C365-C365.
102. F. Mansfeld, Recording and Analysis of Ac Impedance Data for Corrosion Studies .1. Background and Methods of Analysis, Corrosion, 37, 5 (1981), pp. 301-307.
103. M. E. Orazem, N. Pebere and B. Tribollet, Enhanced graphical representation of electrochemical impedance data, J Electrochem Soc, 153, 4 (2006), pp. B129-B136.
104. S. R. Taylor and E. Gileadi, Physical Interpretation of the Warburg Impedance, Corrosion, 51, 9 (1995), pp. 664-671.
105. J. N. Murray, P. J. Moran and E. Gileadi, Utilization of the Specific Pseudocapacitance for Determination of the Area of Corroding Steel Surfaces, Corrosion, 44, 8 (1988), pp. 533-538.
106. G. Lee and J. Park, Reaction of zero-valent magnesium with water: Potential applications in environmental remediation, Geochim Cosmochim Ac, 102, (2013), pp. 162-174.
107. J. R. Kish, Y. Hu, J. Li, W. Zheng and J. R. Mcdermid, Technical Note: Examination of Focused Ion Beam-Sectioned Surface Films Formed on AM60B Mg Alloy in an Aqueous Saline Solution, Corrosion, 68, 6 (2012), pp. 468-474.
108. R. C. Phillips and J. R. Kish, Nature of Surface Film on Matrix Phase of Mg Alloy AZ80 Formed in Water, Corrosion, 69, 8 (2013), pp. 813-820.
109. M. Taheri, R. C. Phillips, J. R. Kish and G. A. Botton, Analysis of the surface film formed on Mg by exposure to water using a FIB cross-section and STEM-EDS, Corros Sci, 59, (2012), pp. 222-228.
110. R. M. Asmussen, P. Jakupi, M. Danaie, G. A. Botton and D. W. Shoesmith, Tracking the corrosion of magnesium sand cast AM50 alloy in chloride environments, Corros Sci, 75, (2013), pp. 114-122.
111. M. Danaie, R. M. Asmussen, P. Jakupi, D. W. Shoesmith and G. A. Botton, The role of aluminum distribution on the local corrosion resistance of the microstructure in a sand-cast AM50 alloy, Corros Sci, 77, (2013), pp. 151-163.

5.9 Tables

Table 5.1. Composition of AA2024-T351 used as a bare electrode in these investigations. Compositions provided by QUANT Quality Analysis and Testing Corporation.

AA2024-T351	Al	Cu	Mg	Mn	Fe	Zn	Si	Ti	Cr	V
	Balance	4.56	1.26	0.59	0.22	0.12	0.08	0.02	0.01	0.01

Table 5.2. Compositions of Mg Rod (99.9%) purchased from Alfa Aesar. All compositions reported in wt. %. (Mg: Balance). Compositions provided by QUANT Quality Analysis and Testing Corporation. NR: Not Reported

element	Si	Al	Fe	Cu	Zn	Mn	Ni	Zr	Pb	Sn	C	S	O
wt. %	NR	0.02	0.008	0.003	0.03	<0.01	<0.001	<0.01	NR	NR	<0.001	<0.001	0.001

Table 5.3. Impedan0ce relationships and low frequency asymptote for solid state circuit elements typically used in the equivalent circuit model of a corroding metal.

Component	**Impedance**
resistor	$Z_r = R,\ f \to 0, Z_c = R$
capacitor	$Z_c = \frac{1}{2\pi fC},\ f \to 0, Z_c \to \infty$
inductor	$Z_L = 2\pi fL,\ f \to 0, Z_c \to 0$

Table 5.4. Typical results of fitting analysis of electrochemical impedance measurements made on bare Mg, 99.9% purity, exposed in ambiently aerated 0.1, 1.0, and 5.0 M NaCl solution at open circuit after 0, 8, 16, and 24 hrs of immersion.

		0.1 mol.dm^{-3} NaCl				1.0 mol.dm^{-3} NaCl				5.0 mol.dm^{-3} NaCl			
		0 hrs	8 hrs	16 hrs	24 hrs	0 hrs	8 hrs	16 hrs	24 hrs	0 hrs	8 hrs	16 hrs	24 hrs
R_s	($\Omega \cdot cm^2$)	54	46	53	55	7	6	7	7	4	3	3	3
C_1	($\mu F/cm^2$)	133	201	161	152	23	195	162	132	10	61	63	58
R_1	($\Omega \cdot cm^2$)	27	121	160	194	39	65	91	85	2	7	7	5
C_2	($\mu F/cm^2$)	3455	27102	31103	14742	15866	75201	53512	59206	99	170	165	161
R_2	($\Omega \cdot cm^2$)	5	16	26	26	8	12	17	15	11	16	18	19
L	($\Omega \cdot s \cdot cm^2$)	77	5697	8056	16831	53	2360	3355	2470	40	818	876	959
R_3	($\Omega \cdot cm^2$)	51	181	220	152	46	41	43	50	5	5	5	2
R_p	($\Omega \cdot cm^2$)	20	78	101	90	23	27	31	33	4	4	4	2
C_4	($\mu F/cm^2$)	NA	NA	NA	NA	NA	NA	NA	NA	119229	444679	478917	422934
R_4	($\Omega \cdot cm^2$)	NA	NA	NA	NA	NA	NA	NA	NA	3	7	8	7

Table 5.5. Anodic Mg charge consumed as calculated by mass loss, hydrogen accumulation and integration of i_{corr} derived from EIS-estimated polarization resistance after exposure in ambiently aerated 0.1, 1.0, and 5.0 M NaCl solution at open for 24 hrs.

	0.1 mol.dm^{-3} NaCl	1.0 mol.dm^{-3} NaCl	5.0 mol.dm^{-3} NaCl
Δm	10 ± 1 mg/cm^2	11 mg/cm^2	32 ± 3 mg/cm^2
$\sum Q_{\Delta m}$	82 ± 6 C/cm^2	90 C/cm^2	256 ± 25 C/cm^2
ΔV_{H2}	11 ± 1 mL/cm^2	16 mL/cm^2	35 ± 6 mL/cm^2
$\sum Q_{H2}$	83 ± 13 C/cm^2	122 C/cm^2	280 ± 44 C/cm^2
β_c	315 mV/dec	315 mV/dec	315 mV/dec
β_a	150 mV/dec	90 mV/dec	30 mV/dec
$\sum Q_{EIS}$	80 ± 13 C/cm^2	101 C/cm^2	265 ± 36 C/cm^2

Table 5.6. Test protocol for potentiostatic, anodic polarizations of Mg.

Cycle	Time Elapsed (min)	Step
A	0	Potentiostatic EIS
	15	Potentiostatic Hold
B	25	Potentiostatic EIS
	40	Potentiostatic Hold
C	50	Potentiostatic EIS
	65	Potentiostatic Hold
D	75	Potentiostatic EIS
	90	Potentiostatic Hold
E	100	Potentiostatic EIS
	115	Potentiostatic Hold
F	125	Potentiostatic EIS
	140	Potentiostatic Hold
-	150	END

Table 5.7. Anodic Mg charge consumed as calculated by mass loss, hydrogen accumulation, integration of measured i_{net}, and integration of i_{corr} derived from EIS-estimated polarization resistance after exposure in ambiently aerated 1.0 M NaCl solution at various anodic polarizations after 2.5 hrs.

	0 mV vs. OCP		100 mV vs. OCP		300 mV vs. OCP	
Δm	0.6	mg	13.6	mg	33.1	mg
$\sum Q_{\Delta m}$	4.8	C	108.0	C	262.8	C
ΔV_{H2}	0.8	cm^3	8.2	cm^3	18.2	cm^3
$\sum Q_{H2}$	6.3	C	64.7	C	143.6	C
β_c	315.0	mV/dec	315.0	mV/dec	315.0	mV/dec
β_a	90.0	mV/dec	90.0	mV/dec	90.0	mV/dec
$\sum Q_{EIS}$	5.1	C	105.2	C	196.9	C
$\sum Q_i$	0.0	C	43.8	C	115.6	C

5.10 Figures

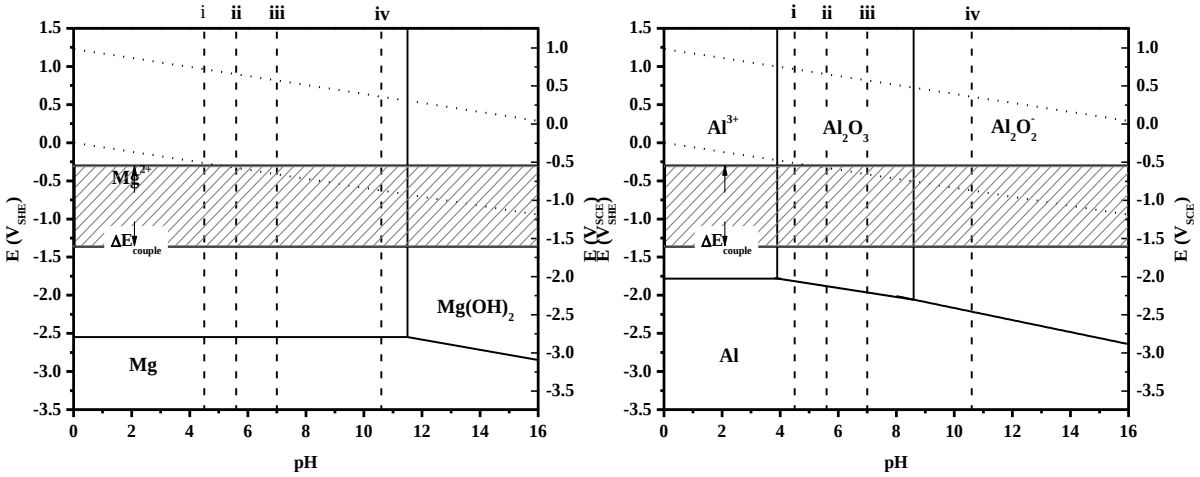

(a) (b)

Figure 5.1.Potential-pH equilibrium diagram for the (a) Mg-H_2O system and (b) the Al-H_2O system at 25°C assuming an ion concentration of 10^{-6}.
pH indications: (i) pH = 4.5 Aerated 1.0 M NaCl with CO_2 sparge (ii) pH = 5.6 Aerated 1.0 M NaCl (iii) pH = 7.0 Aerated 1.0 M NaCl with dissolved Mg shavings and CO_2 sparge (iv) pH = 10.5 Aerated 1.0 M NaCl with dissolved Mg shavings

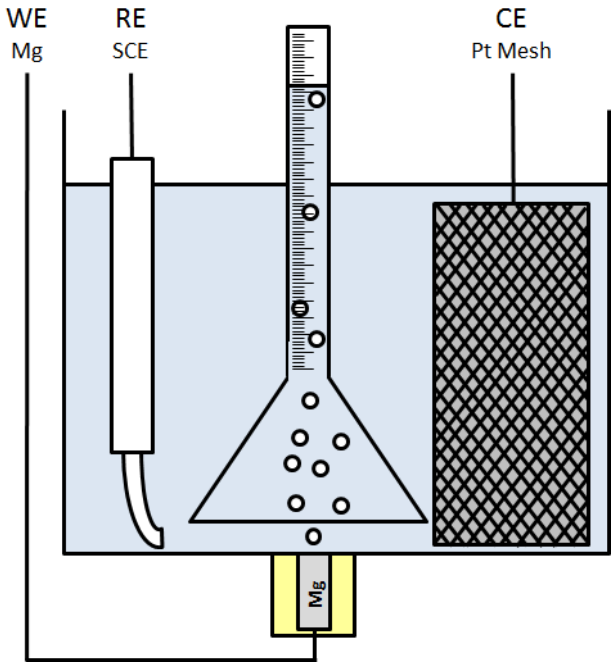

Figure 5.2. Schematic of 3-electrode experimental setup to collect evolved H_2 and measure EIS. See Appendix C for more details.

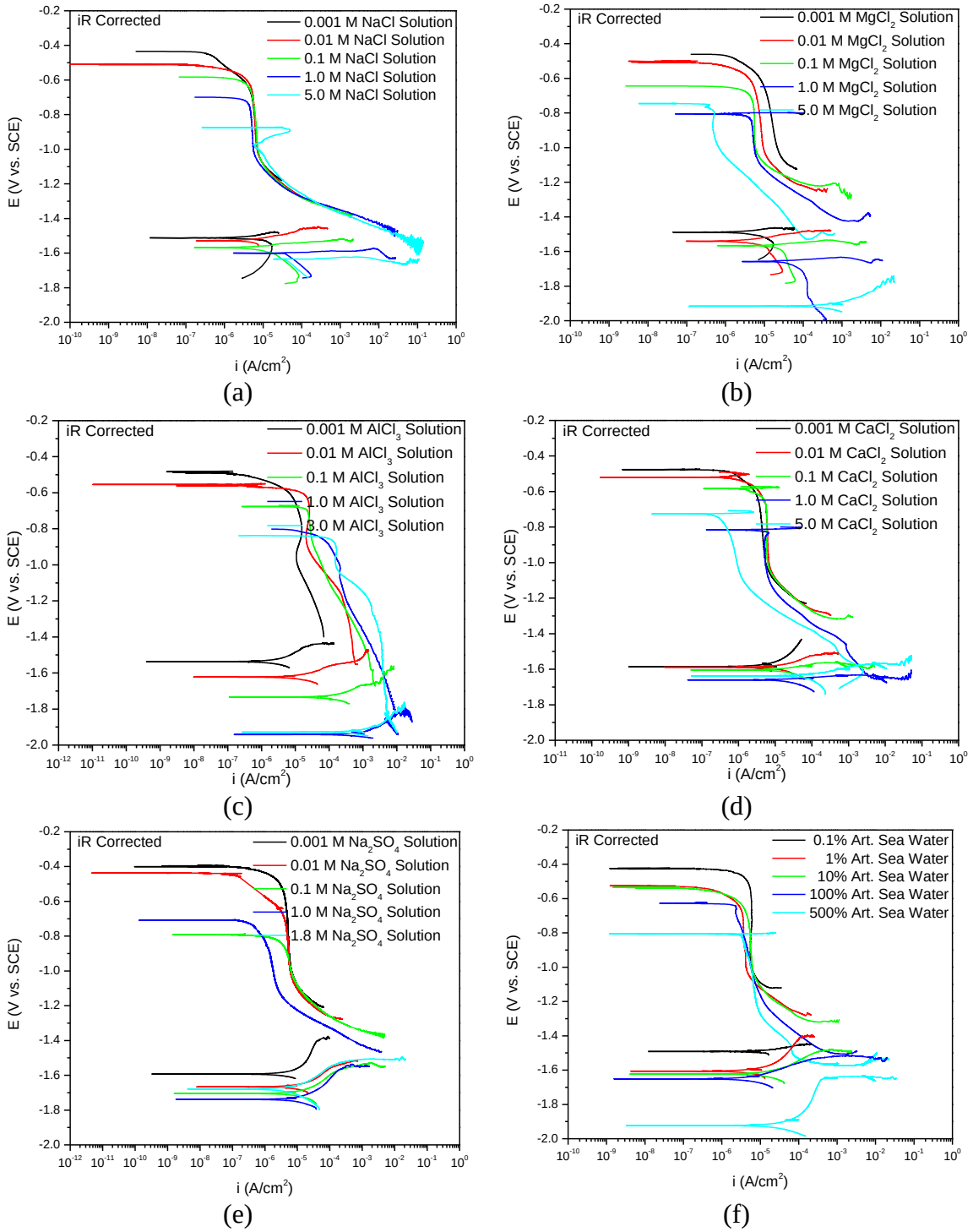

Figure 5.3. I-R Corrected E vs. log(i) polarization behavior of bare AA2024-T351 and bare 99.9% pure Mg in various concentrations of ambiently aerated (a) NaCl, (b) $MgCl_2$, (c) $AlCl_3$, (d) $CaCl_2$, (e) Na_2SO_4, and (f) ASTM Artificial Sea Water.

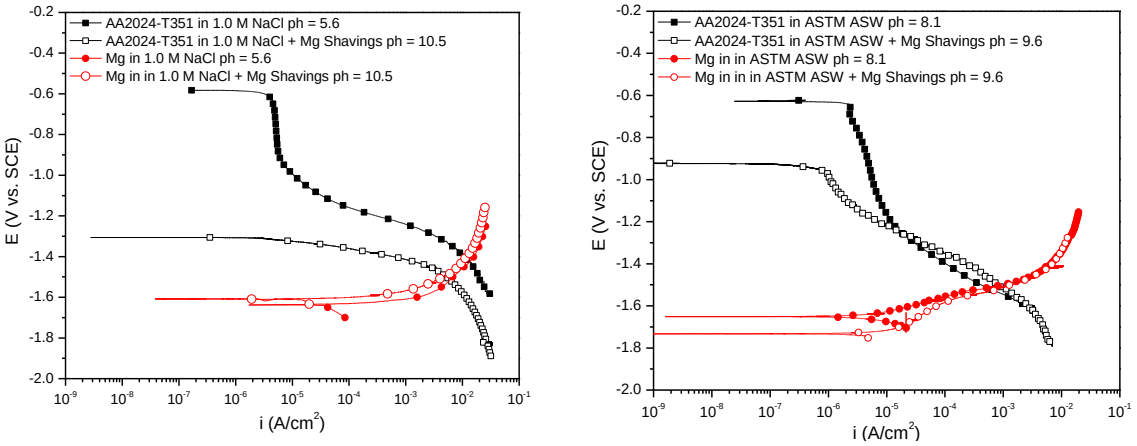

(a) (b)

Figure 5.4. Non i-R Corrected E vs. log(i) polarization behavior of bare AA2024-T351 and bare 99.9% pure Mg in ambiently aerated (a) 1.0 M NaCl and (b) ASTM ASW before and after Mg shavings were allowed to dissolve into solution.

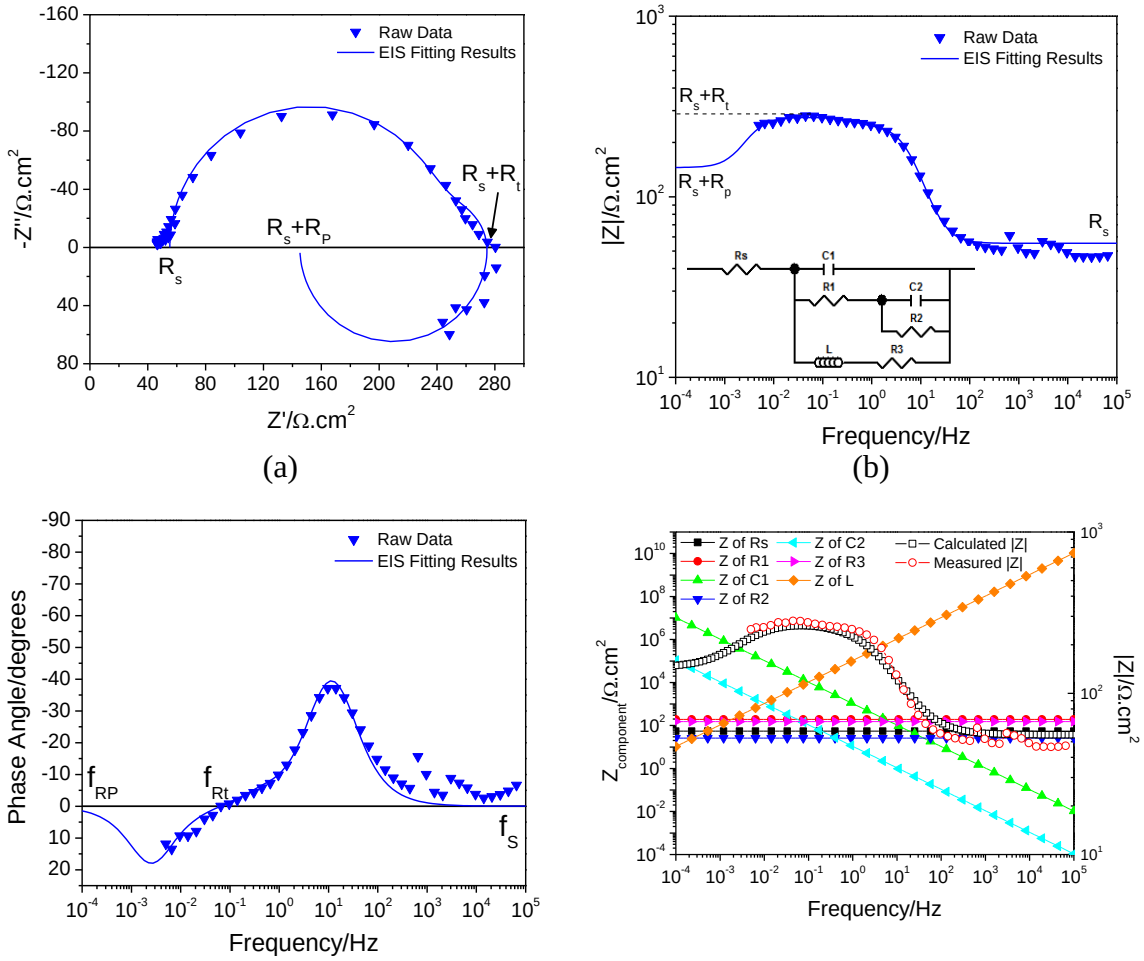

Figure 5.5. EIS measurement (scatter plot) and model fit (solid lines) of high purity Mg after 24 hrs of immersion at open circuit in quiescent 0.1 M NaCl. (a) Nyquist Plot (b) Bode Magnitude (c) Bode Phase Angle and (d) frequency dependent impedance response of each component in the equivalent circuit per equations in Table 2. Fitting Results: $R_S = 55\Omega\cdot cm^2, C_1 = 152\mu F/cm^2$ $R_1 = 193\Omega\cdot cm^2$, $C_2 = 14{,}750\mu F/cm^2$, $R_2 = 26\Omega\cdot cm^2$, $L = 16800\Omega\cdot s\cdot cm^2$, $R_3 = 152\Omega\cdot cm^2$, $R_P = 90\Omega\cdot cm^2$, $\beta_a \approx 0.150, \beta_c \approx 0.315$, $i_{corr} = 491\mu A/cm^2$.

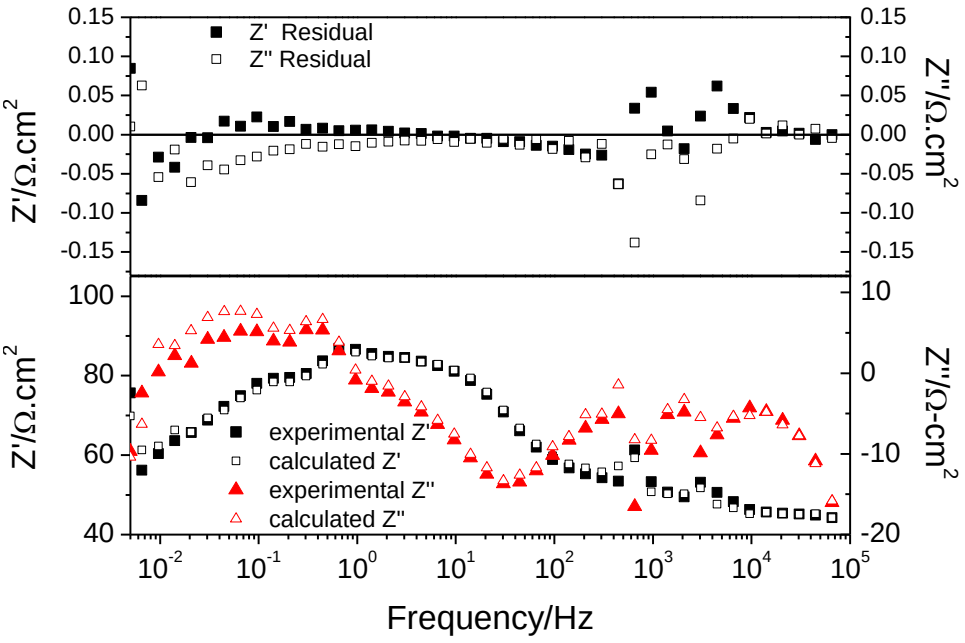

(a)

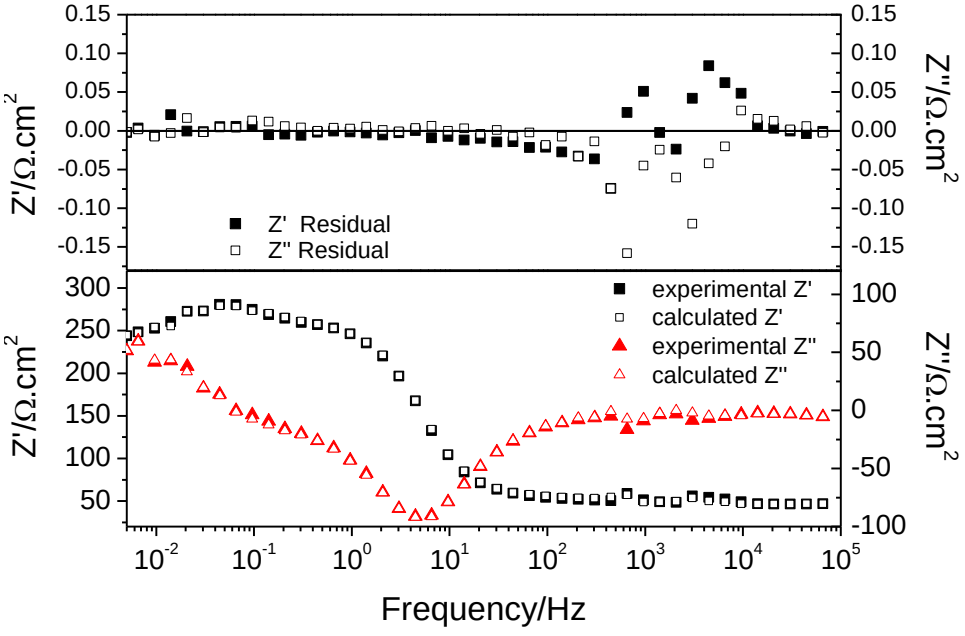

(b)

Figure 5.6. Typical Kramers-Kronig transforms of the real and imaginary components of the impedance of high purity Mg after (a) 0 h and (b) 24 h immersion in 0.1 M NaCl

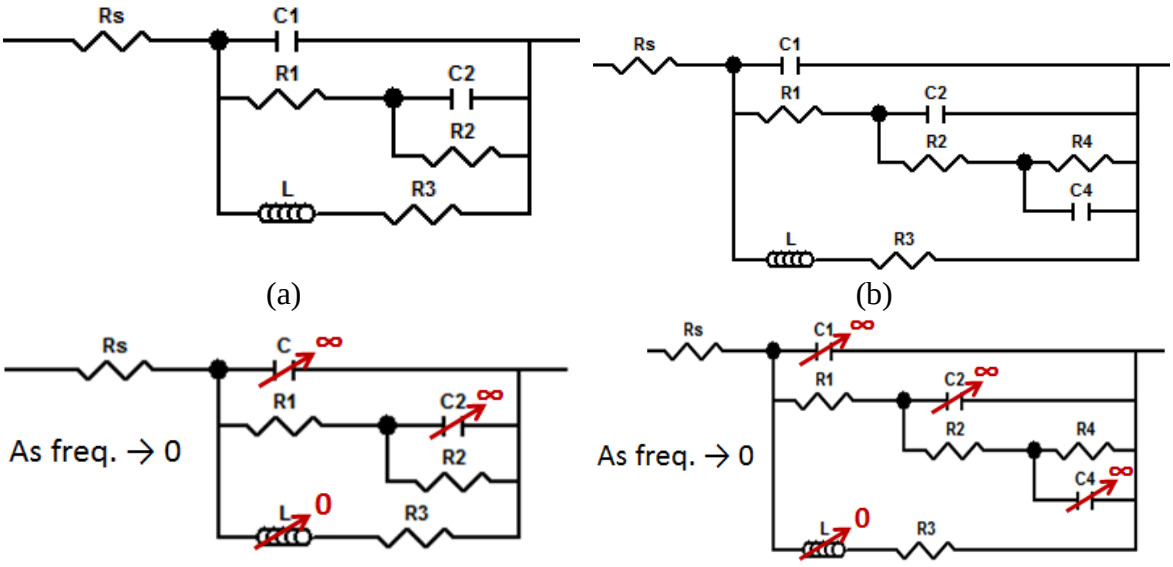

$$\frac{1}{R_p} = \frac{1}{R_1 + R_2} + \frac{1}{R_3}$$

$$\frac{1}{R_p} = \frac{1}{R_1 + R_2 + R_4} + \frac{1}{R_3}$$

Figure 5.7. Circuit diagram used to model pseudo-inductive electrochemical impedance response in ambiently aerated (a) 0.1 and 1.0 M NaCl solution and (b) 5.0 M NaCl solution.

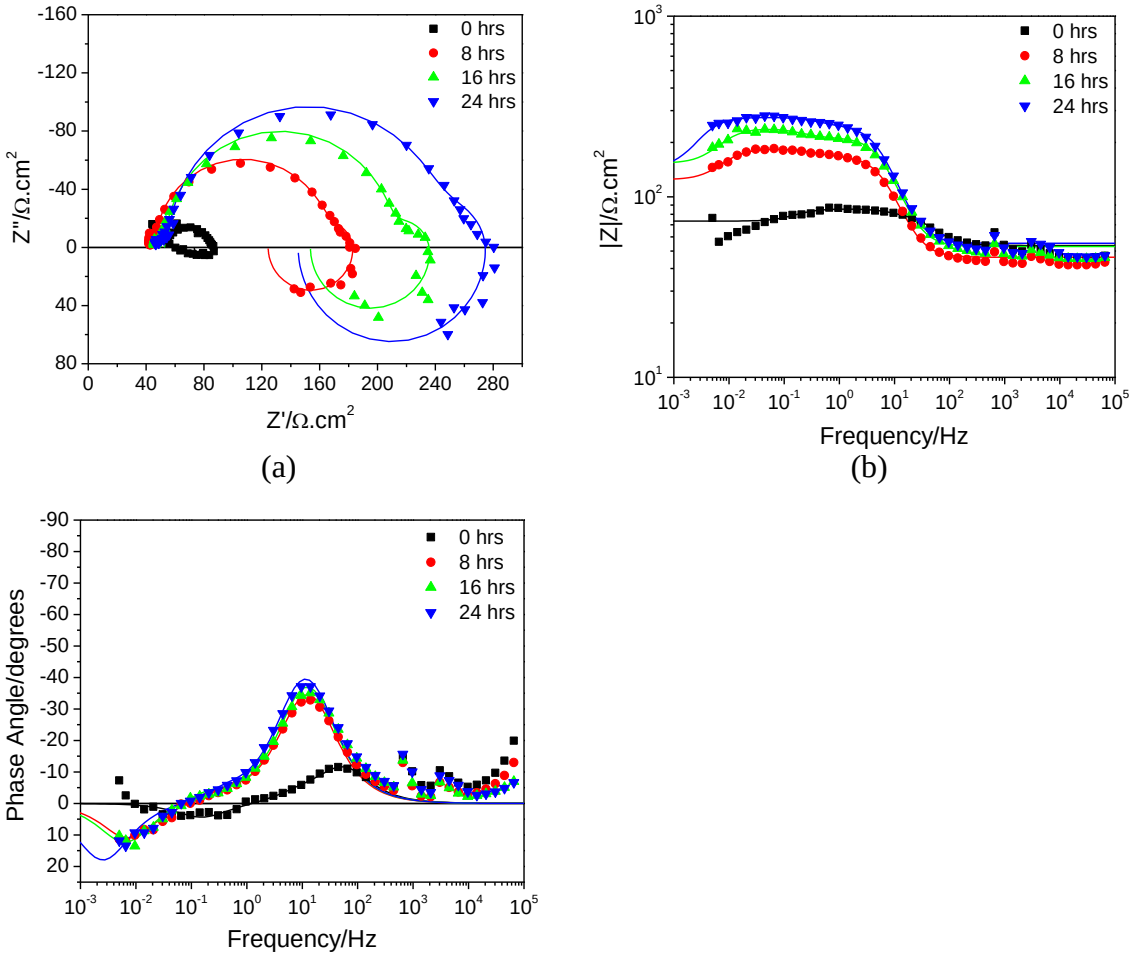

Figure 5.8. EIS measurements (scatter plot) and regression fits (solid lines) of bare Mg, 99.9% purity, after 0, 8, 16, and 24 hrs of immersion at open circuit in ambiently aerated 0.1 M NaCl solution.

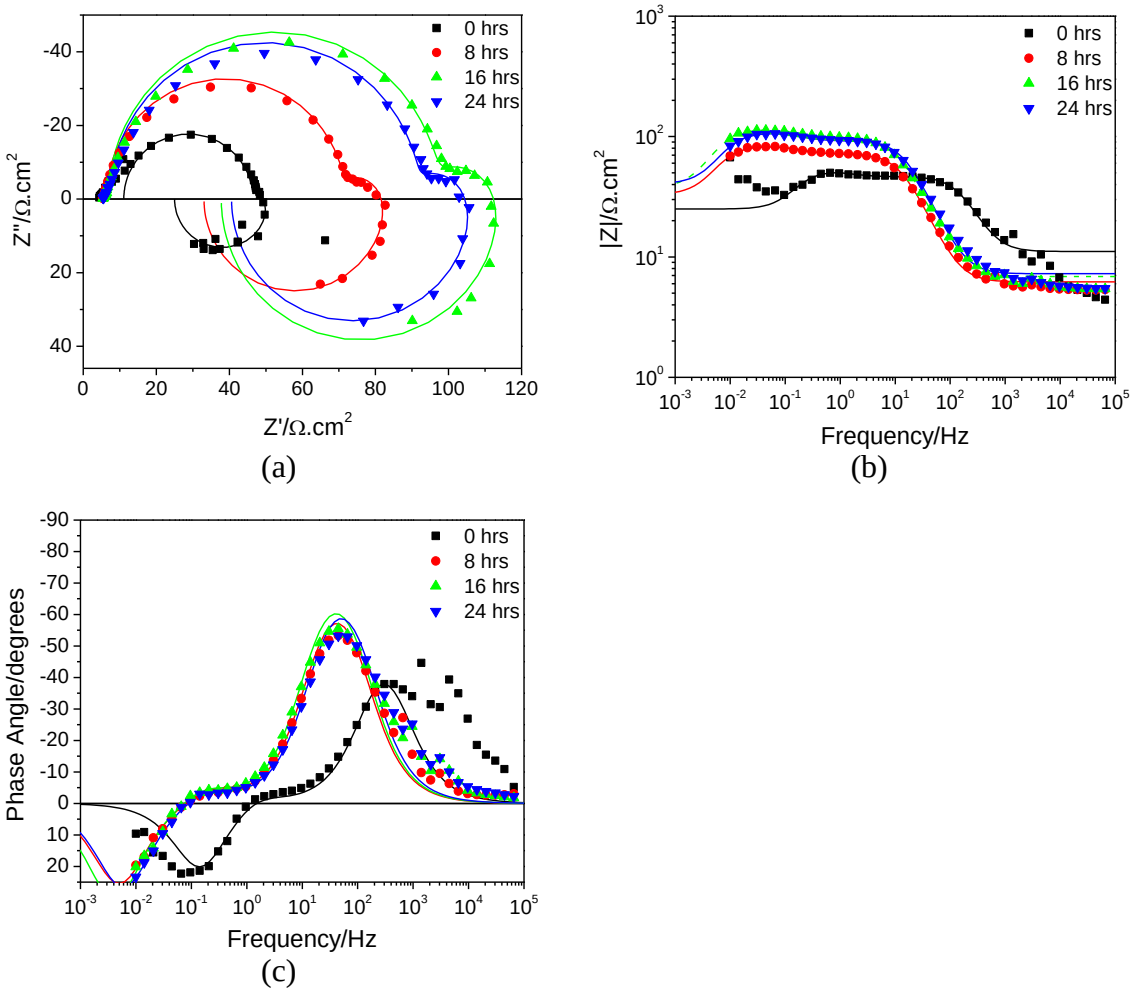

Figure 5.9. EIS measurements (scatter plot) and regression fits (solid lines) of bare Mg, 99.9% purity, after 0, 8, 16, and 24 hrs of immersion at open circuit in ambiently aerated 1.0 M NaCl solution.

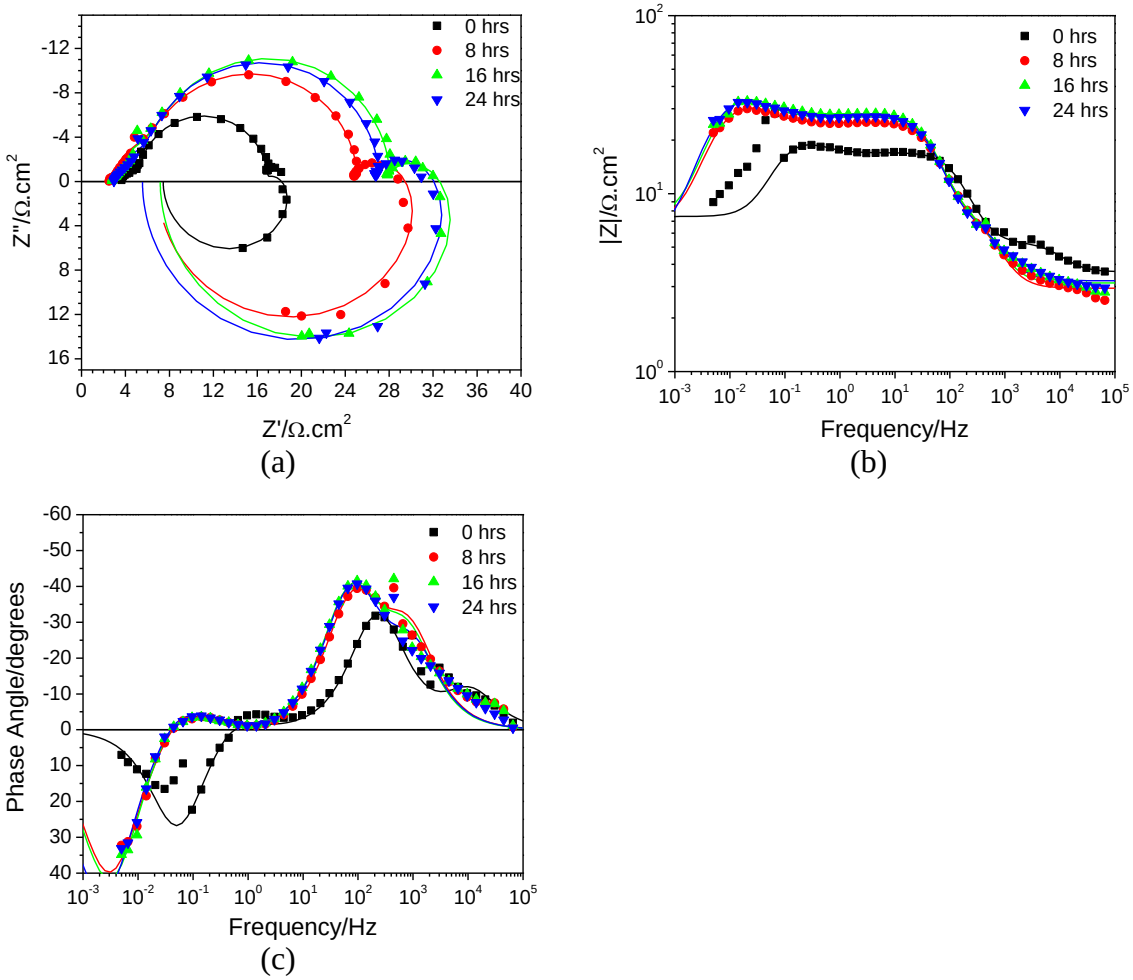

Figure 5.10. EIS measurements (scatter plot) and regression fits (solid lines) of bare Mg, 99.9% purity, after 0, 8, 16, and 24 hrs of immersion at open circuit in ambiently aerated 5.0 M NaCl solution.

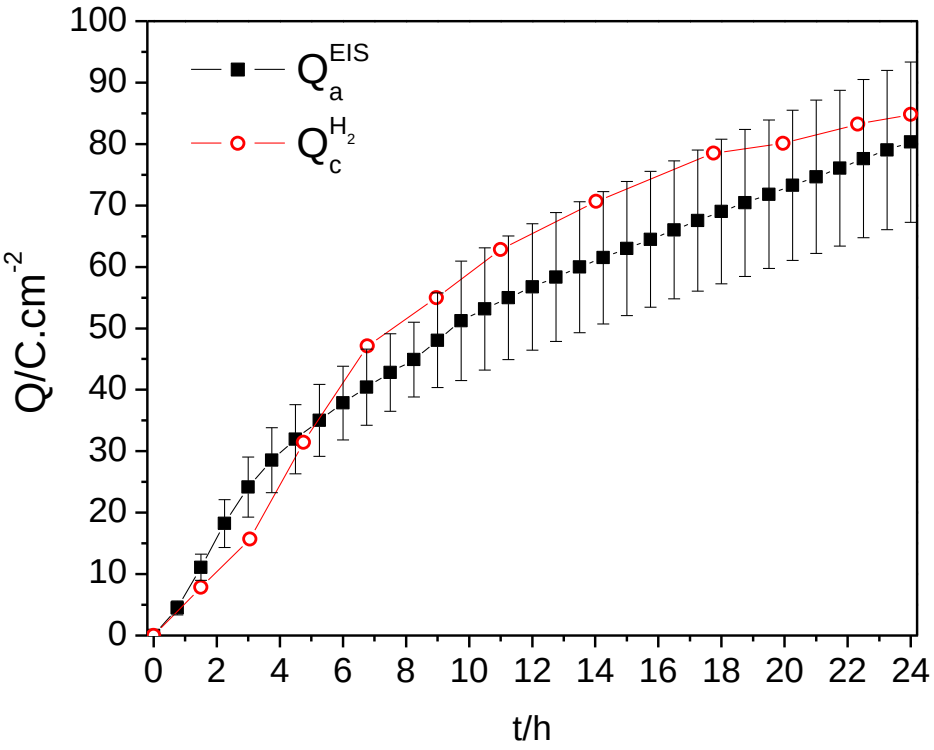

Figure 5.11. $Q_c^{H_2}$ determined from the volume of H_2 gas (Eq. 3) collected above the surface of high purity Mg compared to Q_a^{EIS} determined from Eq. 2 while the Mg was immersed in 0.1 M NaCl for 24 h. See Appendix C for more procedural details.

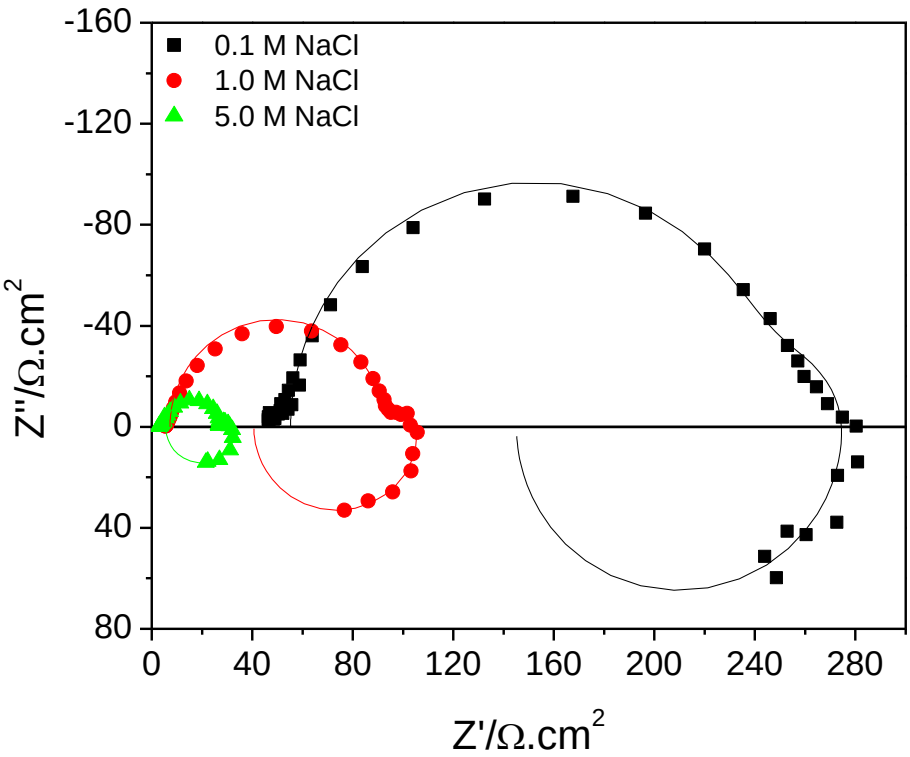

(a)

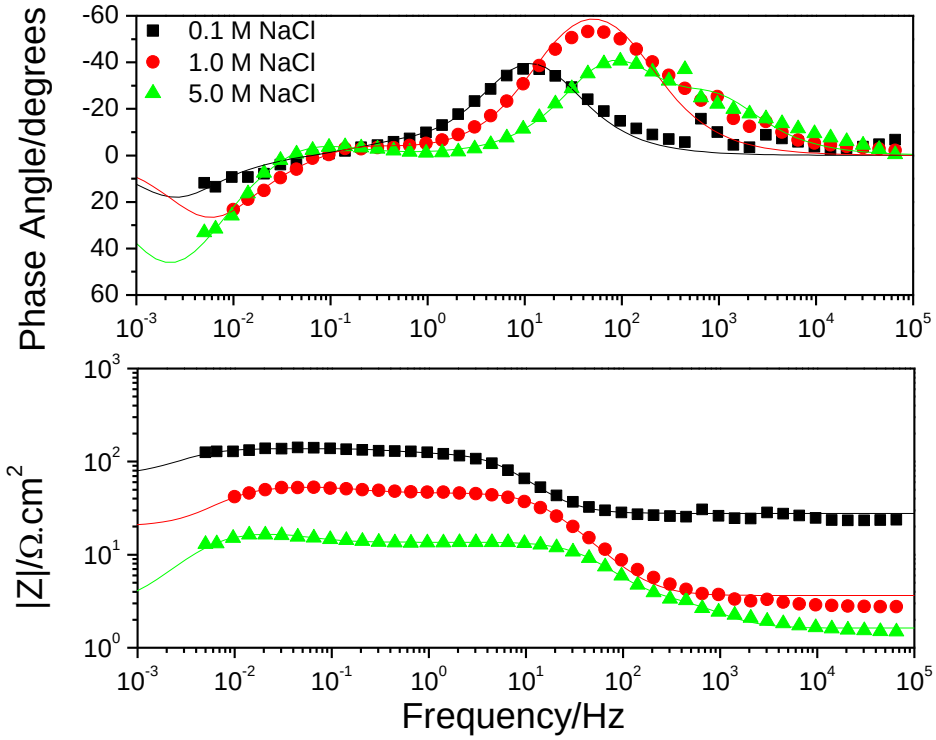

(b)

Figure 5.12. Nyquist and Bode plots of EIS after 24 hrs in ambiently aerated 0.1 M NaCl, 1.0 M NaCl and 5.0 M NaCl solution at open circuit. Raw data is symbols, line is fit.

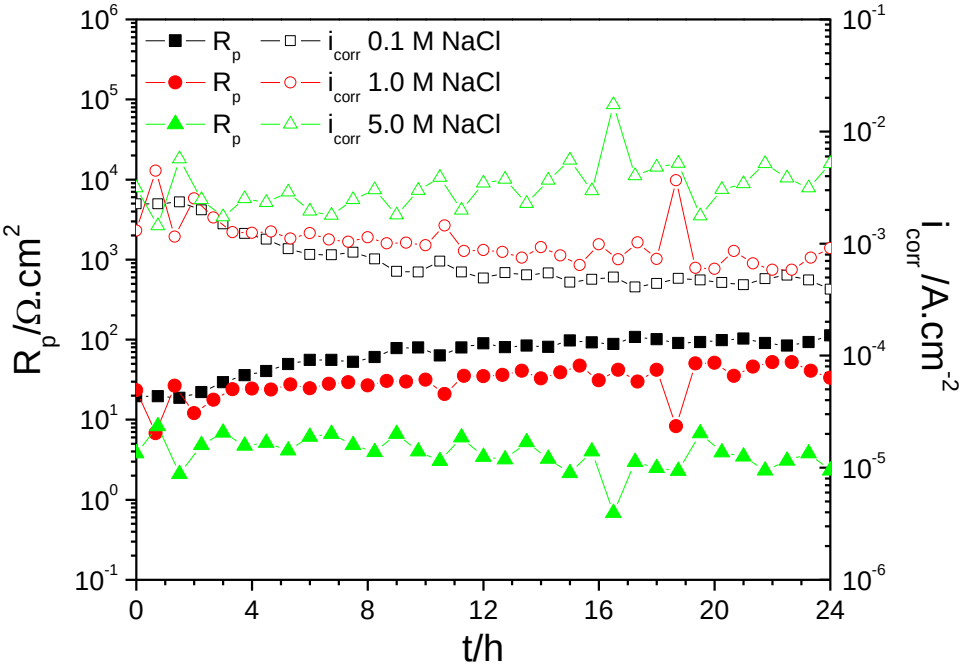

Figure 5.13. Typical EIS-estimated polarization resistance and corresponding corrosion current density vs. time of exposure in ambiently aerated (a) 0.1 M NaCl (b) 1.0 M NaCl and (c) 5.0 M NaCl solution at open circuit

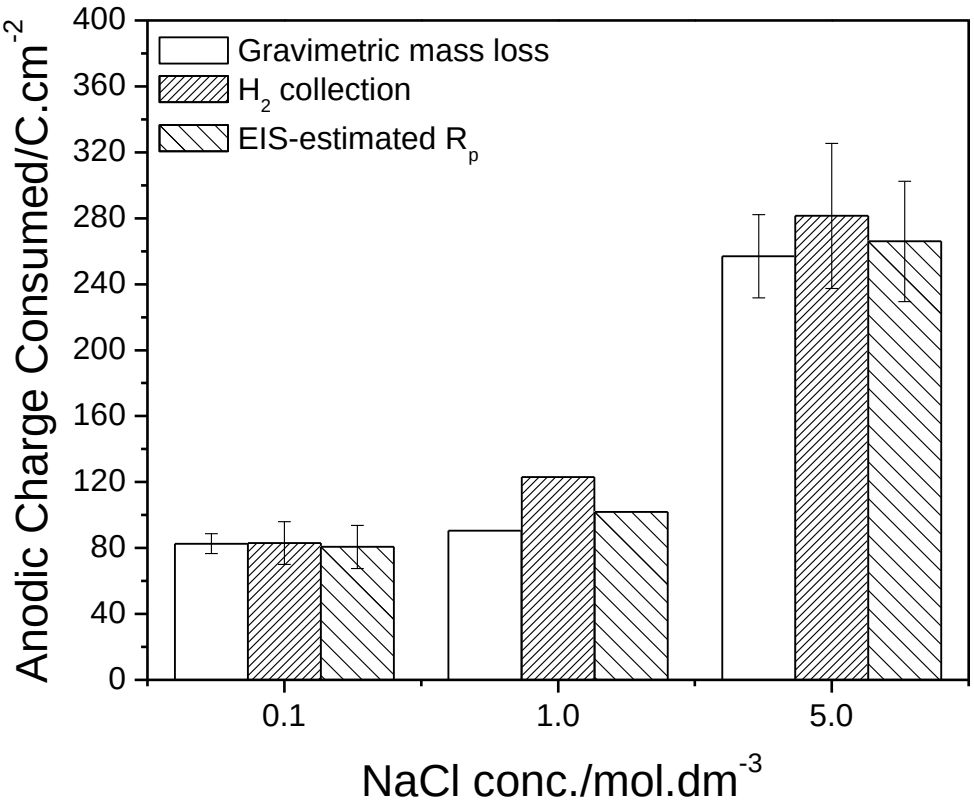

Figure 5.14. Anodic Mg charge consumed in ambiently aerated 0.1, 1.0, and 5.0 M NaCl solution at open circuit after 24 hrs immersion as estimated by gravimetric mass loss, H_2 collection, and EIS-estimated R_p.

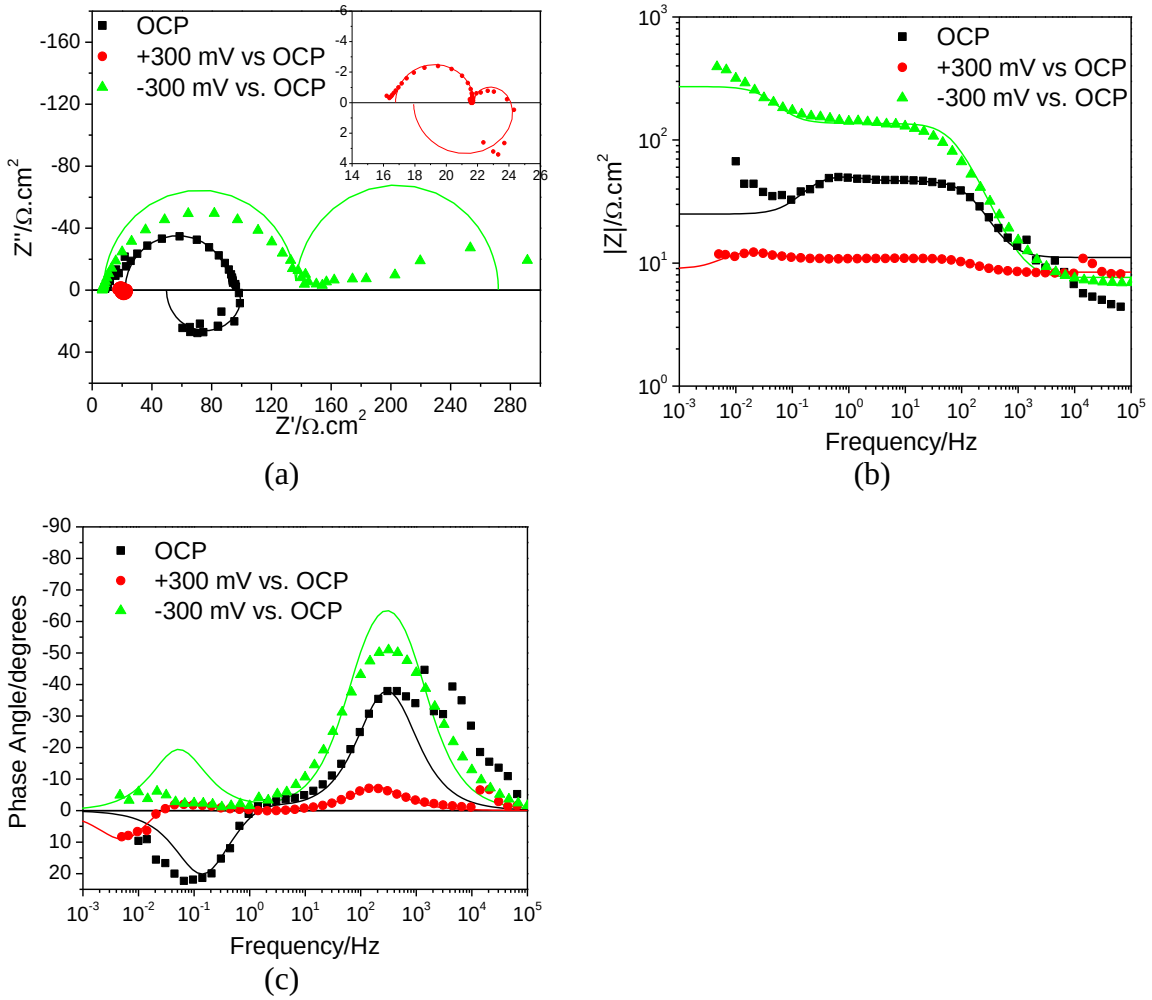

Figure 5.15. EIS measurements (scatter plot) and model fits (solid lines) of high purity Mg after 10 min of immersion in 1.0 M NaCl potentiostatically held at -300 mV vs. OCP, OCP, and +300 mV vs. OCP.

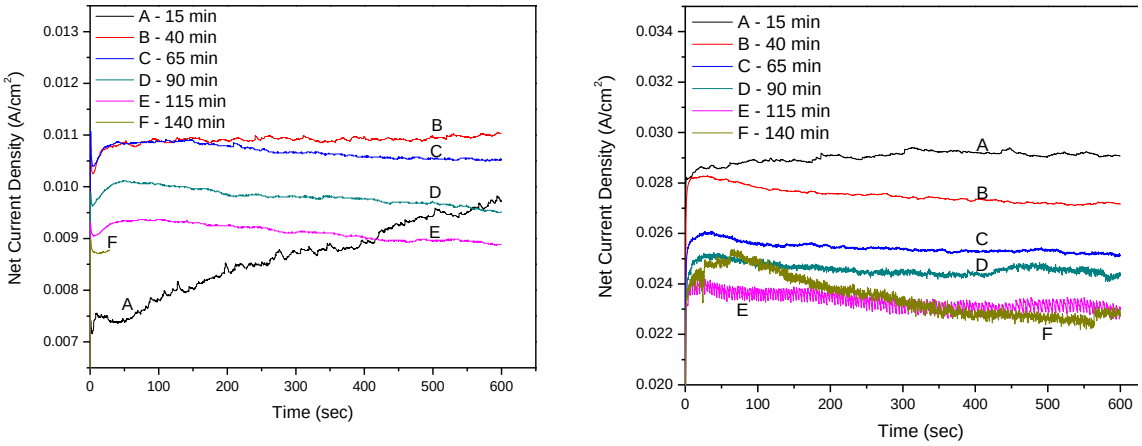

(a) (b)

Figure 5.16. Applied current density of bare, pure Mg immersed in ambiently aerated 1.0 M NaCl solution potentiostatically polarized to (a) +150 and (b) +300 mV vs. OCP.

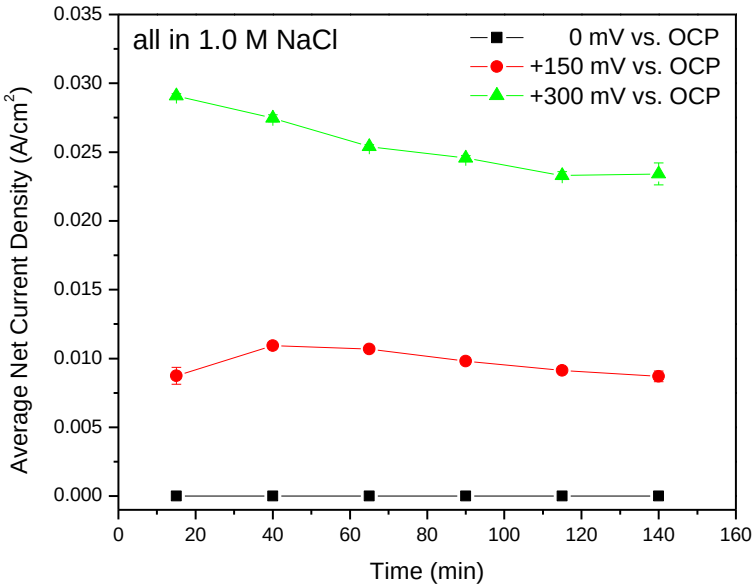

Figure 5.17. Average applied current density of bare, pure Mg immersed in ambiently aerated 1.0 M NaCl solution at 0, +150, and +300 mV vs. OCP.

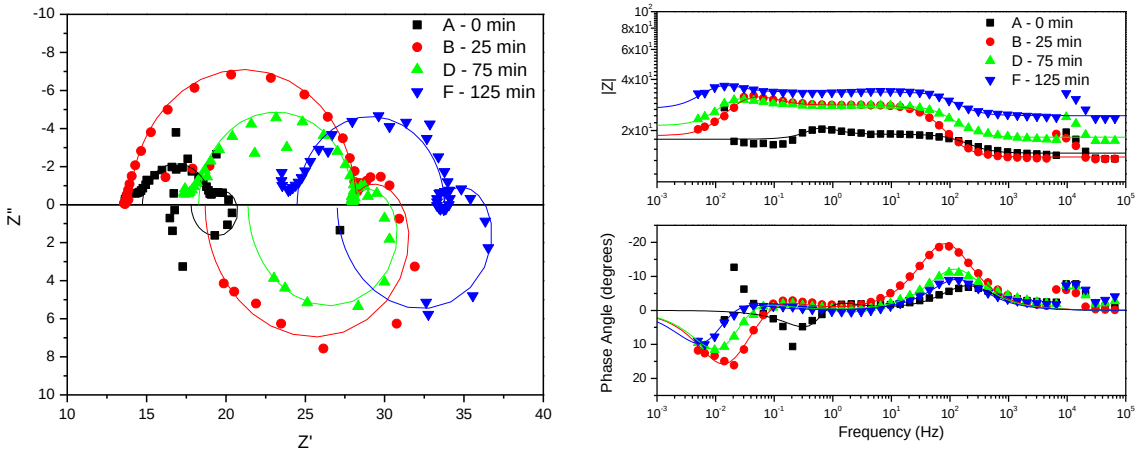

(a) (b)

Figure 5.18. Nyquist (a) and Bode (b) |Z| and phase angle measurements (scatter plot) vs. fit (lines) in ambiently aerated 1.0 M NaCl solution potentiostatically polarized to +150 mV vs. OCP.

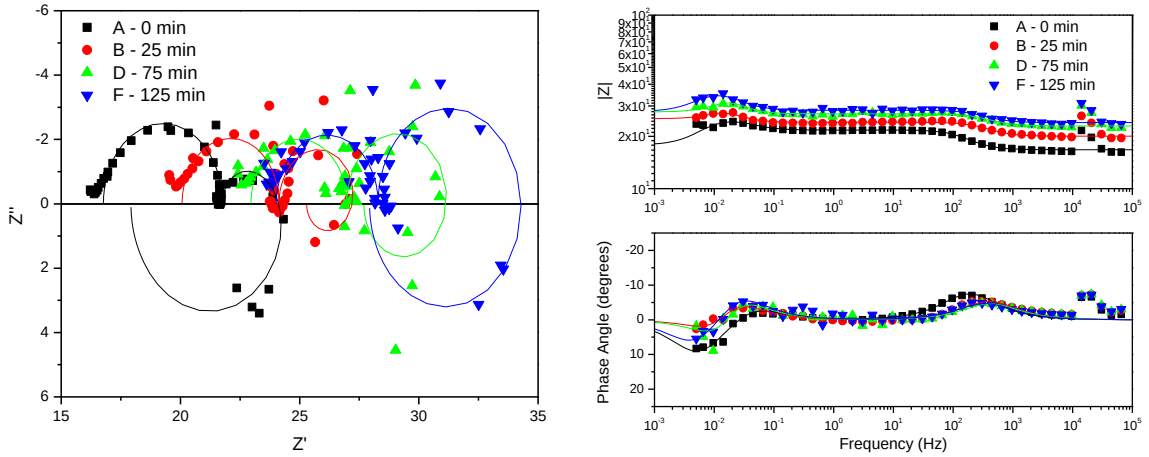

(a) (b)

Figure 5.19. Nyquist (a) and Bode (b) |Z| and phase angle measurements (scatter plot) vs. fit (lines) in ambiently aerated 1.0 M NaCl solution potentiostatically polarized to +300 mV vs. OCP.

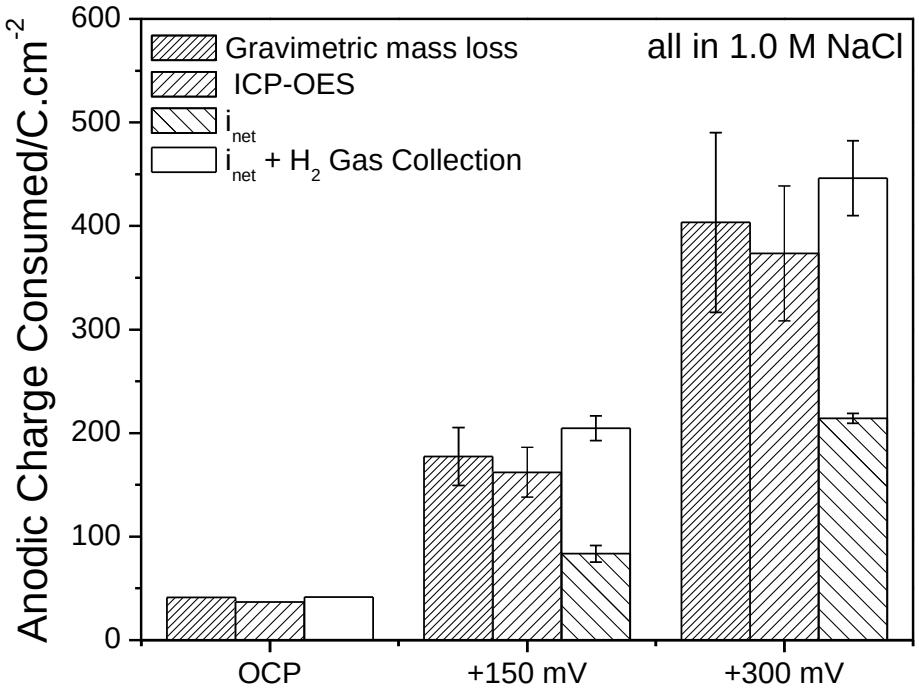

Figure 5.20. Anodic Mg charge consumed in ambiently aerated 1.0 M NaCl solution at 0, 150, and 300 mV vs. OCP after 2.5 hrs immersion as estimated by gravimetric mass loss, ICP-OES, and the sum of applied current and H_2 collection.

6 Assessment of Galvanic Throwing Power of a MgRP and AA2024-T351 Scribe via Experimental Microelectrode Arrays and Finite Element Analysis of Current and Potential Distributions

6.1 Abstract

The “galvanic throwing power” (TP) of the MgRP coating system pertains to the distance extending perpendicularly away from the edge of a scribe in the MgRP coating exposing bare AA2024-T351 over which the MgRP coating system can protect exposed AA2024-T351 by sacrificial anode based cathodic protection. In past field studies of the MgRP coating system, it was found that during a given episodic drying or wetting event, throwing power was temporarily increased or diminished, making a definitive determination of throwing power by post-mortem sample evaluation difficult. As such, in this work, the galvanic throwing power of the MgRP was studied directly via finite element analysis modeling in conjunction with diagnostic multi-electrode arrays (MEAs), which enable the spatial distribution of cathodic protection to be elucidated. The galvanic protection capabilities of the coating in various full immersion, thin layer, and droplet electrolyte geometries relevant to field service helps eo explain long misunderstood field behavior. Current and potential distributions extended across simulated defects when electrolyte layer was thick, continuous and more conductive (higher concentration) and in the absence of a polymer coating. Current and potential distributions did not extend across simulated defects when the electrolyte became discontinuous or the ionic path became tortuous due to drying or the addition of a polymer coating. Additionally, galvanic protection is shown to intensify during drying and re-wetting over short

distances rationalized to be caused by changing solution conductivity, E-i behavior, and electrode area effects. The drying characteristics of individual salts was also shown to have an effect on the evolution of throwing power as $MgCl_2$ (due to its low deliquescence point of ~35% RH at STP) was shown to be less susceptible to drying at low RH, thus extending the time of which the galvanic couple was active compared to pure NaCl or ASTM Artifical Sea Water.

6.2 Introduction and Background

Over the past few years, a commercial organic coating system containing a Mg-pigmented polymer primer (Mg-rich primer, MgRP) has been developed for the corrosion protection of aluminum alloys, such as precipitation age hardened 2024-T351, and has performed well in field studies.[1-13] The MgRP is designed to be applied to an aluminum alloy substrate as a primer layer, above any pretreatments, but below any topcoats which may be used (shown schematically in Figure 6.1). The MgRP is designed to galvanically couple the Mg pigment in the primer to the substrate and provide sacrificial anode based cathodic protection to the aluminum alloy (AA2024-T351). When coupled to the AA2024-T351 (or similar alloy) substrate, the Mg pigment becomes an electron donor, and mixed potential theory can be used to explain the open circuit of the MgRP/AA2024-T351 system when exposed to full immersion. Results in the literature support the notion of mixed potential theory describing the galvanic coupling behavior between the primer and substrate.[1, 3-7, 14, 15]

The galvanic couple potential sensed at a given location on an anode (Mg pigment) or cathode (AA2024-T351 substrate) will depend on the geometric arrangement of the anode and cathode, the surface area ratio between the two electrodes exposed to immersion as well as other factors such as any electrical and ionic resistances that may exist between the anode and cathode.[8] When the sacrificial Mg is placed in an organic polymer, the galvanic couple potential between the Mg pigment and AA2024-T351 substrate (and subsequent cathodic protection) becomes a function of the electrochemical driving force (ΔE_{OCP}) between anodes and cathodes, the wetted surface area ratio of the two materials actually exposed to an aqueous environment (e.g., Mg pigment volume concentration that is wetted / AA2024-T351 that is wetted such as at scratch site), the kinetic boundary conditions of the anode and cathode in the electrolyte that each is exposed to, the resistive path length and geometry as well as the electrical and ionic conductivities of the system. The Mg pigment volume concentration (PVC) will affect both the resistive paths through the organic coating between the Mg pigment and the underlying AA2024-T351 substrate as well as the path through the organic coating and the electrolyte above to any exposed AA2024-T351.[8] All of these factors will mediate the galvanic couple potential existing along each metal surface.

A critical issue with regards to predicting MgRP's protection capabilities in the field is developing a means for predicting the throwing power or spatial current-potential distribution of the physical MgRP/AA2024-T351 system. The distance over which the MgRP coating system can protect a scratch or defect exposing bare AA2024-T351 by sacrificial anode based cathodic protection, is termed the "galvanic throwing power" and

is depicted with green shading in Figure 6.1. Conversely, the “inverse galvanic throwing power” is the distance into the MgRP coating in which Mg pigment is anodically polarized while actively galvanically coupled to the AA2024-T351 scribe, scratch, or defect (depicted with red shading in Figure 6.1). A question remains in the literature as to whether a discernable region of increased Mg pigment depletion exists along the edges of a defect due to such an inverse throwing power. Understanding and predicting the throwing power and inverse throwing power of a sacrificial coating such as MgRP is quite complicated because the scribe size, coating formulation, electrolyte composition, electrolyte geometry, and bare/coated area ratios can all be limiting factors when considering protection ability or throwing power of a coating that protects by sacrificial anode based galvanic protection.

A large source of variation between performance of the coating in the salt fog and field exposure environments, with regards to throwing power, is the electrolyte geometry in each environment. A sacrificial coating can only protect defects (or bare substrate at scratches) which it is both electrically and ionically connected to. In an artificial environment like ASTM B-117 salt fog, in a rainstorm with large drops, or during a dewing event, the whole panel might be wet with a continuous electrolyte layer and the galvanic throwing power of the MgRP that is measured or observed will be limited electrochemically based in the secondary or tertiary current distribution based on mixed potential theory. In these cases the throwing power will spread across the scratch. However if the environment is such that the electrolyte layer is tortuous and individual droplets start to form due to the drying of a thin electrolyte layer or the deliquescence

(wetting) of deposited salts due to increasing ambient RH, a limitation in throwing power brought about by a tortuous electrolyte (ionic path), will be observed.

The cathodic current distribution that is spread across a scribe or coating defect exposing bare AA2024-T351 will be controlled by various factors and can be relatively summarized qualitatively by examining the Wagner number or Wagner polarization factor pertaining to various geometric and chemical exposure scenarios. [16, 17]The Wagner number can be used to evaluate the relative degree of uniformity of the galvanic current distribution. The Wagner number (W) is described by the ratio of the electrochemical polarization resistance of the anode and cathode (K) to the resistance to ionic conduction in the electrolyte path separating the anode and cathode (L).[17] If for any reason, the ionic pathway becomes tortuous (L is large) the Wagner number becomes small ($W \rightarrow 0$) and the current distribution over the scribe is expected to be more non-uniform. Conversely, when the interfacial resistance is large and ohmic resistance and path difficulty is small then $W \rightarrow \infty$ and the current and potential distributions are more uniform.

Finite element analysis, or similar spatially resolved computational methods, of potential and current distribution in galvanic systems has long been studied in the literature.[16-22] Such studies are often carried out to investigate fundamental effects of electrolyte geometry[21, 23], electrode kinetics[20, 24, 25], unique part geometries[17], crevice corrosion[19, 26], and sacrificial anode based, cathodic protection schemes[27]. However, these studies do not involve the addition of resistive polymer layers or study the effects of volume concentration of pigment electrode material in a semi-permeable matrix.

The deliquescence point and subsequent thermodynamic equilibrium concentrations with respect to ambient RH of various salts relevant to sea water are shown in Figure 6.2. As a given deposited salt deliquesces on a surface it will, over time, equilibrate to the ambient RH to form an electrolyte layer or droplet of equilibrium concentration. Figure 6.3 presents the resulting equilibrium electrolyte layer thickness with respect to initial deposition density and ambient RH for NaCl assuming a uniform, infinitely long, continuous electrolyte layer at 25 °C. A hypothetical RH cycle which could be observed in an environmental exposure is depicted in Figure 6.4a. As the RH in an exposure environment changes with time, so does the equilibrium salt concentration and geometry of the electrolyte layer (Figure 6.4b), playing an important part in dictating the galvanic throwing power and subsequent cathodic protection vs. scratch distance afforded by the MgRP coating system.

If a droplet is not in contact with the MgRP and instead exists only above bare AA2024-T351 substrate, there can be no sacrificial protection due to a remote coating within the area covered by that droplet (shown schematically in Figures 3.53 and 4.47). Under these conditions of a tortuous electrolyte path, an environmental limitation, rather than an electrochemical limitation, is placed on the throwing power of the coating system.

In the past couple years, in an attempt to characterize the throwing power of MgRP, post-mortem characterization has been conducted on scribes of environmentally exposed test panels (Chapters 3 and 4 of this thesis). Calcareous deposits, primarily consisting of

$CaCO_3$, along with Mg deposits, are indicative of regions of cathodic protection afforded to the AA2024-T351 by the MgRP.[28-35] An attempt was made to examine the throwing power after exposure in the lab and field by obtaining EDS of the bare scribe. In the field at Kennedy Space Center the throwing power was estimated with post-mortem EDS characterization to be approximately 200 – 300 μm and in the salt fog environment to cover the full half-width of the scribe (≥350 μm).[12, 13] It should be noted that during a given episodic drying or wetting event, throwing power may be temporarily increased or diminished, making a definitive determination of throwing power difficult. At the end of the exposure, the definitive throwing power and inverse throwing power is complicated by corrosion during drying or isolated drop formation. Additional factors which complicate the determination of a throwing power via post mortem characterization of environmentally exposed panels result from the chemical dissolution of chemical species used as markers indicative of zones of cathodic protection (such as $Mg(OH)_2$ and $CaCO_3$) as well as difficulties in distinguishing between definitive regions of protection and of substrate corrosion in defect areas. Chemical dissolution of the precipitates that are common to zones of cathodic protection is likely in acidic, high TOW environments, like that of Birdwood Golf Course in Charlottesville, VA, which is subject to regular acidic precipitation. EDS spot scans obtained throughout the width of the scribe after 24 weeks of exposure at Birdwood Golf Course in Charlottesville, VA, showed very little indication of Mg or calcareous deposits common to regions of cathodic protection, making evidence and observation for throwing power in this environment difficult. At the end of exposure, the definitive throwing power is complicated by corrosion during drying or isolated droplet formation. Moreover, it is likely that the throwing power of the MgRP

could be detected in EDS spot scans obtained throughout the width of the scribe after exposure at Kennedy Space Center, FL presumably due to the more alkaline exposure conditions. Not only is the rain precipitation at Kennedy Space Center, FL slightly alkaline as compared to Charlottesville, VA, but the proximity of the test racks to the ocean make the samples susceptible to spray from the ocean surf which has a pH of roughly 8.2.[36] This alkaline pH suppresses the chemical dissolution of species (such as $Mg(OH)_2$ and $CaCO_3$) used to identify zones of cathodic protection. Additionally, in most exposure environments and moderate pH ranges, aluminum is well known to form a barrier oxide film that reforms quickly when damaged, leaving the primary form of attack in the scribe observed after exposure in most service environments to be non-uniform pitting corrosion.[37] For this reason, in all environments studied in previous chapters, definitive zones of significant Al corrosion in the scribes could not be identified due to low pit densities.

For these reasons, there exists a critical need in the literature to directly assess and measure the throwing power of the MgRP system. The objective of this study to utilize instrumented electrode arrays to quantitatively observe the spatial distribution of throwing power over a model Mg/AA2024-T351 galvanic couple under various environmental conditions and to gain a better understanding of the evolution of the galvanic throwing power as a function of variables described above. Moreover, a secondary goal is to define the attributes that promote uniform current and potential distribution across the scribe.

It is also the objective of this study to utilize finite element computational modeling software (COMSOL), in conjunction with previously obtained electrochemical boundary conditions of Mg, AA2024-T351 (outlined in Chapter 5) under relevant chemical conditions, and the MgRP coating system, to develop a fully functional, physically representative model, to accurately predict the galvanic throwing power of the MgRP coating system as a function of coating parameters, physical conditions, as well as environment.

6.3 Experimental Procedure

6.3.1 Materials

99.9% pure magnesium rod (8.0 mm diam.), 500 μm diameter 99.9% magnesium wire, 1.6 mm thick AA2024-T351 sheet, and 254 μm diameter AA2024-T4 wire were studied in these investigations. Table 5.1 and Table 5.2 show the chemical analysis of both the AA2024 and the Mg used in this work. Chemical analysis shows the Mg rod and wire had a measured purity of over 99.9% and is substantially similar to the powder used in commercial Mg-Rich Primer (MgRP) Products.[8] The AA2024-T4 wire was insulated with a 25 μm thick polyimide coating making the total wire diameter approximately 300 μm.

The Mg rod was mounted in EpoThin epoxy resin manufactured by Buehler in order to make clamping the sample to an electrochemical flat cell easier. The bare electrodes were

prepared by alternating polishing with silicon-carbide paper and rinsing with 18.2 MΩ deionized water to a final polishing grit of 1200. The samples were then dried with lab tissue before use.

6.3.2 Full Immersion Electrochemical Analysis to Establish Boundary Conditions

Potential control during electrochemical experiments was maintained using a potentiostat with computer interface software. Solartron 1287A/1255B and Gamry Reference 600 potentiostats were selected because they enable electrochemical impedance spectroscopy (EIS) measurements along with traditional electrochemical measurements. Saturated Calomel reference electrodes (SCE) were used in full immersion testing.

Anodic potentiodynamic scans were conducted on 99.9% pure, 8.0 mm diameter bare Mg electrodes. The tests were run in various concentrations of ambiently aerated NaCl as well as NaCl pre-saturated with $Mg(OH)_2$. A commercial saturated calomel electrode was used as a reference electrode. The bare Mg electrodes were polished to 1200 grit silicon carbide paper. The potentiodynamic scans were conducted after a 10 minute OCP. A typical anodic scan started at -0.2 V vs OCP up to +0.7 V vs. OCP and scanned at 1.0 mV per second.

Cathodic potentiodynamic scans were conducted on bare AA2024-T351 sheet. The tests were run in various solutions with ambient aeration using a saturated calomel reference electrode. The bare AA2024-T351 electrodes were ground to 1200 grit silicon carbide

paper and then clamped to an electrochemical flat cell with a 1 cm^2 window. The potentiodynamic scans were conducted after a 10 minute OCP. A typical cathodic scan started at +0.2 V vs OCP and scanned down to -1.0 V vs. OCP at 0.1667 mV per second.

6.3.3 One-dimensional Multichannel Microelectrode Galvanic Array

A microelectrode array consisting of one 500 µm diameter, flush mounted 99.9% Mg electrode and twenty isolated, 254 µm diameter, flush mounted AA2024-T4 electrodes (300 µm total diameter including polyimide insulation) arranged in a single ribbon was mounted in EpoThin epoxy resin to diagnostically represent the MgRP/AA2024 galvanic couple system next to a scribe or scratch. The array simulates the bare AA2024-T351 perpindicular to the scribe length and parallel to the scratch width. A cross-section schematic of the array is shown in Figure 6.5 and an optical micrograph is shown in Figure 6.6. The spacing between electrodes was approximately 30 – 50 µm (Figure 6.6). A Scribner model MMA910B was used to provide a graphical interface and data acquisition of each microelectrode current. The MMA 910B is capable of galvanically coupling together and measuring up to 100 working electrode current channels and contains an individual zero resistance ammeter (ZRA) on each current channel with a measureable current range of 3.3 nA to 100 uA per channel. The electrode connections to the MMA910B are shown schematically in Figure 6.7. It is important to note that neither a counter electrode or reference electrode were used in this study as only localized galvanic currents were obtained. In the results reported in this work, the throwing power of the Mg across the AA2024-T4 array is often depicted spatially by a blue/red color map

at various times of interest. In each color map, dark red indicates an anodic current ≥ 1 x 10^{-7} A and dark blue indicates a cathodic current of ≤ -1 x 10^{-7} A. Microelectrodes which are freely corroding pass a net current of zero and are color coded white.

In three separate experiments, approximately 40 µL of 1) 0.9 M NaCl solution, 2) 0.6 M $MgCl_2$ solution, and 3) ASTM Artificial Sea Water solution were each applied in a thin layer to the top of the microelectrode galvanic array such that the electrolyte covered every electrode in the array. The height of the as-applied, thin layer electrolyte film was measured with a digital multimeter and vertical digital caliper setup to be approximately 500 ± 100 µm at the center for each experiment. The array was then placed in the relative humidity controlled cabinet and electrically connected to the MMA. Over the course of 6 hours, the relative humidity in the cabinet was cycled from ambient RH to low RH (< 20%), up to high RH (> 90%) and back to low RH (< 20%) in order to observe the effect of a wet/dry cycle on the throwing power of the single Mg electrode over the AA2024 microelectrodes under 0.9 M NaCl solution, 0.6 M $MgCl_2$ solution, and ASTM Artificial Sea Water solution.

In a fourth set of experiments, a clear, quick-drying acrylic polymer was applied to the surface of the Mg electrode in the Mg/AA2024-T4 microelectrode array in order to mimic the ionic resistance of the primer polymer in the MgRP coating system. This polymer was chosen for its ease of application (brush), brief drying time, and clear color. Electrochemical impedance measurements through the clear, quick-drying acrylic polymer were obtained (Figure 6.8) and compared to that of MgRP coated (with PVC_{Mg}

= 45%) AA2024-T351. The EIS measurements were obtained utilizing a traditional full immersion, three electrode cell and FRA/potentiostat setup in 0.9 M NaCl, utilizing the Mg wire in the microelectrode array as the working electrode, a commercial SCE reference electrode, and a Pt mesh counter electrode. The low frequency impedance (~ 4 x 10^6 $\Omega \cdot cm^2$), saddle frequency ($\leq$ 0.01 Hz), and breakpoint frequency (~ 3 Hz) for the quick drying acrylic polymer were similar to that of the MgRP coating over AA2024-T351 (Figure 6.8) making it a suitable analogue to simulate the ionic resistance added by the MgRP polymer to the MgRP/AA2024-T351 galvanic couple system for the purpose of studying throwing power.

In additional experiments, 10, 100, 250, and 1000 $\mu g/cm^2$ of both NaCl and ASTM Artificial Sea Water salts were applied to the surface of the bare Mg/bare AA2024-T4 microelectrode array. The salts were applied using a spray bottle application method in which a known concentration of electrolyte was sprayed from a spray bottle at a constant distance from the samples surface in an enclosed chamber. The average deposition volume per spray using this specific setup was characterized and calibrated by both rinsed-solution conductivity measurements and weight gain measurements. Using the known deposition volume per spray and the known electrolyte concentration in the spray bottle, a desired salt deposition density was applied to the array's surface. The size of the electrolyte droplets applied by the spray bottle method were characterized by optical analysis with computational image analysis software (ImageJ) and had a mean diameter of approximately 160 µm ± 60 µm. The mean diameter of the applied droplets, within

one standard deviation, was larger than the microelectrode array inter-electrode spacing of 50 µm (spacing shown in Figure 6.6).

To validate that charge was conserved during the microeletrode array experiments in accordance with mixed potential theory, the net current of the array (the sum of the total anodic and total cathodic current from each electrode) during one exposure, the details of which are discussed more thoroughly later, is plotted vs. time in Figure 6.9 along with the residual noise of the instrument. The total of the net cathodic current passing through each and every AA2024-T4 microelectrode was found to be equal in magnitude and opposite in sign to the total anodic current passing through the galvanically coupled Mg microelectode. The residual noise of the entire microelectrode array remained 0 ± 200 nA throughout the length of the experiment, which is within the accuracy range of the instrument, confirming that the galvanic interaction between the Mg and AA2024-T351 microelectrodes was in accordance with mixed potential theory.

6.3.4 Instrumented Relative Humidity Controlled Cabinet

The microelectrode array was housed in an instrumented, relative humidity controlled cabinet. The ribbon cable connections were made to the MMA900B via a feed through in the wall of the cabinet. The RH controlled cabinet was produced from a Plas-Labs desiccator cabinet (PN: 861-CG) and is shown schematically in Figure 6.10. The cabinet was instrumented with an OMEGA OM-EL-USB-2-LCD-PLUS RH and temperature data logger and a DINO-LITE AD7013MT USB microscope utilized for time lapse

imaging. RH was controlled via the flow of dry or humid air into the chamber. Humid air was produced by passing house compressed air through a series of four 2 L H_2O diffuser bubblers, achieving an ambient RH of up to 95%. Dry air was produced by passing house air through Drierite gas drying jars, achieving an ambient RH of as low as 10%. Pictures of the cabinet with the microelectrode array positioned under the microscope camera are shown in Figure 6.11.

6.3.5 Two-Dimensional Finite Element Computational Modeling (COMSOL)

COMSOL Multiphysics^{TM} finite element analysis, solver and simulation software was used to develop a physically representative, simplified 2-dimensional model of a AA2024-T351 panel coated with MgRP. The model geometry is shown schematically in Figure 6.12. The model geometry consists of a 10 mm wide section of bare AA2024-T351 directly next to a 10 mm wide piece of 99.9% pure Mg coated with a zero-dimensional, resistive polymer film layer. The model is designed to simulate the bare AA2024-T351 perpindicular to the scribe length and parallel to the scribe width on a typical MgRP-coated AA2024-T351 panel often used in environmental studies of coating performance. The Mg and AA2024-T351 are side by side along the x-direction, the electrolyte layer is above both the AA2024-T351 and Mg in the y-direction, and the model's depth (defined as 1 m in this case of simplicity of units) is in the z-direction extending out of the page. The Mg is a fixed height 30 μm taller than the AA2024-T351 surface to mimic the geometry of the coating layer. The resistive polymer film layer covers both the horizontal and vertical surfaces of the Mg electrode and current is

distributed along both regions. Parametric studies were conducted to observe the effect of varying the NaCl electrolyte concentration (from 0.001 M NaCl to 5.0 M NaCl), the electrolyte layer thickness (from 1 μm to 1000 μm), and the polymer layer resistance (from 0 to 1,000 $\Omega \cdot m^2$). The values of these parameters were chosen based on real-life estimates of possible chloride concentrations found in field and lab environments (discussed in Ch. 1, 3, and 4), electrolyte layer thicknesses (Figure 6.3) and barrier properties of relevant pretreatment layers, commercial MgRP polymers, and commercial topcoat polymers (Ch's 3 and 4).

The electrochemical boundary conditions utilized for the AA2024-T351 and Mg materials were based on best fit approximations of experimentally obtained, full immersion polarization data shown in Figure 6.13a. The electrochemical boundary conditions were input into the COMSOL software as E,i pairs. The specific electrochemical boundary conditions used in the model for various concentrations of NaCl are plotted in Figure 6.13b (Figure 6.13b depicts the group of boundary conditions used for computational modeling as fitted from Figure 6.13a). Intermediate E,i positions that are not listed in the boundary condition data set are interpolated as needed via a piece wise fitting algorithm built into COMSOL. The electrolyte conductivites (listed in Table 6.3) utilized in the finite element computational model developed in COMSOL were calculated with OLI simulation software for electrolyte chemistry.

The typical products of the model include potential and current profiles mapped along the surface of the galvanic couple. Potential profiles are provided from just above the

polymer film surface (termed "$E_{Surface}$" and depicted schematically as the red line in Figure 6.12 and the potential labeled $E_{Surface}$ in Figure 6.14) which takes into account the potential drop through the polymer film above the Mg but where solution resistance is otherwise zero. The model also directly outputs the localized galvanic couple potential along the surface of each metal in the galvanic couple, underneath the polymer film on the Mg (termed "E_{couple}" and depicted schematically as the blue line in Figure 6.12 and the potential labeled E_{couple} Figure 6.14). It is important to note, due to a lack of polymer over the AA2024-T351 surface, $E_{Surface} = E_{couple}$ over the AA2024-T351. The model also produces the net current along the surface of each metal in the galvanic couple, underneath the polymer film on the Mg.

To validate that charge was conserved in the finite element computational modeling in accordance with mixed potential theory, the net cathodic and anodic current in various scenarios (under 100 μm of 1.0 M NaCl with no polymer covering the Mg, under 100 μm of 0.01 M NaCl with no polymer covering the Mg, and under 100 μm of 1.0 M NaCl with 10 $\Omega \cdot m^2$ polymer covering the Mg) is plotted in Figure 6.15. The net current of the entire microelectrode array remained 0 ± 10 nA, confirming that the finite element computational modeling of the galvanic interaction between the bare AA2024-T351 and the bare or polymer coated Mg was in accordance with mixed potential theory.

Additionally, to validate that the results of the finite element computational modeling were consistent with the E-i boundary conditions, the resulting potential and current values for various positions on the surface of the galvanic couple between bare AA2024-

T351 and polymer coated Mg, as predicted by finite element computational modeling, were plotted on a mixed potential model (points labeled A, B, C_1, C_2, D, and E in Figure 6.16). The predictions made by the finite element computational model were found to be consistent with values from the E-i boundary conditions shown in Figure 6.13b.

6.4 Results

6.4.1 Multichannel Microelectrode Galvanic Couple Array

6.4.1.1 Throwing Power (TP) Predicted by a Coupled Electrode Multichannel Microelectrode Array Under Continuous Thin Layer Electrolytes During Wetting and Drying

Under both a thin layer of 0.9 M NaCl (Figure 6.17) and a thin layer of ASTM Artificial Sea Water (Figure 6.18) covering the entire microelectrode array, the cathodic polarization provided by the Mg electrode was initially observed to spread across the entire width of the array indicating a TP greater than or equal to 5750 μm. This is indicated by blue color coded electrodes in the t_1 color map in Figure 6.17b and Figure 6.18b, respectively, extending to last electrode in the array. H_2 bubbles produced by increased hydrogen evolution were observed to actively form on each cathodically polarized AA2024-T351 electrode in the array. Upon lowering the cabinet RH to less than 20%, the electrolyte layer was visually observed to decrease in thickness and area (optical micrograph t_2 in Figure 6.17b) and salt was continuously deposited at the edge of the inward shrinking electrolyte layer until the array was completely dry (t_3 in Figure

6.17b). As the electrolyte layer decreased in thickness and radius, the throwing power of the Mg electrode decreased from the full width of the array (t_1 color map in Figure 6.17b) to zero (t_3 color map in Figure 6.17b and Figure 6.18b) indicating cessation in sacrificial galvanic protection of the AA2024-T4 electrodes by the Mg electrode. During drying, the net cathodic current density on the individual AA2024-T4 electrodes closest to the Mg electrode was observed to increase to a peak (at time t_2 in Figure 6.17b and Figure 6.18b) presumably due to the combined effects of the increasing electrolyte concentration and the decreasing area of the active cathode. At time t_2 during drying under NaCl (t_2 in Figure 6.17a), AA2024-T4 electrode #1 had cathodic current density of -1.2×10^{-1} A/cm^2 corresponding to a local interfacial potential of approximately -1.5 V_{SCE} (determined from Figure 6.13b), a distant AA2024-T4 electrode #10 had a cathodic current density of -1.6×10^{-4} A/cm^2 corresponding to a local interfacial potential of -1.3 V_{SCE}, and AA2024-T4 electrode #20 had a steady net current density of zero indicating the electrode was not coupled to Mg and either freely corroding (at OCP) or dry. After t_2, the net cathodic current density on the AA2024-T4 electrodes closest to the Mg electrode were then observed to decrease in magnitude to zero as the effect of the increasingly thin and tortuous electrolyte geometry reduced the ionically conductive path despite the increase in concentration of NaCl.

Upon increasing the RH in the cabinet to approximately 93% the electrolyte layer (t_4 in Figure 6.17b and Figure 6.18b, respectively) was observed to re-wet with time and spread back across the entirety of the array. Upon re-wetting of the electrolyte layer, a similar trend was observed in the net cathodic current density on the individual AA2024-T4

electrodes closest to the Mg to what was observed during drying but in reverse. The net cathodic current density on the AA2024-T4 electrodes closest to the Mg electrode was observed to increase in magnitude from zero as the electrolyte layer re-wet and grew until a peak current density was observed (around t = 4500 s in Figure 6.17a and t = 9400 s in Figure 6.18b) spread back across the AA2024-T4 array. As the electrolyte layer grew further, wetting more AA2024-T4 electrodes, the cathodic current density on the AA2024-T4 electrodes closest to the Mg electrode decreased slightly and stabilized at an intermediate magnitude (5000 s < t < 7000 s in Figure 6.17a and 10,000 s < t < 13,000 s in Figure 6.18a). Upon lowering the RH of the cabinet back down to below 40% once again, a peak in cathodic current density on the individual AA2024-T4 electrodes closest to the Mg electrode was again observed (around t = 7300 s in Figure 6.17a and t = 14,000 s in Figure 6.18a) before the throwing power again decreased to zero.

Under a thin layer of 0.6 M $MgCl_2$ (Figure 6.19) covering the entire microelectrode array, the cathodic polarization provided by the Mg electrode was initially observed to spread across the entire width of the array indicating a TP greater than or equal to 5750 μm (indicated by blue color code at t_1 color map in Figure 6.19b). Upon lowering the cabinet RH to less than 20% for more than 2 h, the electrolyte layer was visually observed to slightly decrease in thickness and a semi-solid salt cap was observed to form over the liquid electrolyte layer (t_3 in Figure 6.19b). H_2 bubbles could be seen to form and move under the salt cap and the magnitude of the cathodic current density on each AA2024-T4 electrode in the array was reduced but did not reach zero (t_3 in Figure 6.19a) and held steady at approximately 5.0 x 10^{-4} A/cm^2 corresponding to a couple potential of -1.5 V_{SCE}

(assuming 5.0 M $MgCl_2$ curve in Figure 6.13c). This is a marked difference between the behavior under NaCl and ASTM ASW where the cathodic current density on each AA2024-T4 electrode in the array was reduced to zero upon "drying". Under the salt cap, the throwing power as measured by the cathodic polarization of the AA2024-T4 electrodes spanned across the entire array. After 2 h at an RH less than 20%, the RH of the cabinet was increased to roughly 93%. The salt cap was observed to dissolve and the magnitude of cathodic current density on the AA2024-T4 electrodes increased.

6.4.1.2 Throwing Power Predicted by a Coupled Electrode Multichannel Microelectrode Array With the Addition of a Polymer Layer Over the Mg

In a fourth experiment, approximately 40 µL of 0.9 M NaCl solution was applied in a thin layer to the top of the polymer coated Mg/bare AA2024-T4 microelectrode galvanic array such that the electrolyte covered every electrode in the array. The height of the as-applied, thin layer electrolyte film was measured with a digital multimeter and vertical digital caliper setup to be approximately 500 ± 100 µm. The array was then placed in the relative humidity controlled cabinet and electrically connected to the MMA. Over the course of 3 hours, the relative humidity in the cabinet was held constant at approximately 94% (Figure 6.20a).

The added resistance of the clear acrylic polymer (with DC impedance of $10^2 – 10^3\ \Omega{\cdot}m^2$) initially mediated the sacrificial galvanic protection afforded by the Mg electrode to the

AA2024-T4 electrodes in the microelectrode array (t_1 in Figure 6.20a and Figure 6.20b) shown by net current densities of zero on the Mg and AA2024-T4 electrodes (at t_1 TP = 0 μm). During this time the AA2024-T4 electrodes were freely corroding at open circuit under the 0.9 M NaCl droplet. After approximately 3000 s (t_2 in Figure 6.20), a defect formed in the clear acrylic coating, which shorted the ionic resistance of the polymer coating. As soon as the coating defect formed, the Mg electrode and AA2024-T4 electrodes in the microelectrode array became galvanically coupled and the throwing power extended across the entire width of the array (at t_2 and t_3 TP = 5750 μm) for an electrolyte thickness of 500 ± 100 μm.

6.4.1.3 Maximum Throwing Power Predicted by a Coupled Electrode Multichannel Microelectrode Array Under Various Salt Deposition Densities

After depositing the electrolyte of interest onto the array, the array was placed into an RH controlled cabinet which had been purged with dry air (RH ≈ 10%) to quickly dry the electrolyte droplets. Optical micrographs of the dry array with NaCl applied at various deposition densities are shown in Figure 6.21. The array was then connected to the MMA and the galvanic current between the microelectrodes was recorded. The RH in the cabinet was quickly increased to 94% to deliquesce the deposited salts (which primarily have deliquescence points below 75%, Figure 6.2). Over the course of 3 additional hours, the relative humidity in the cabinet was held constant at approximately 94% in an attempt to equilibrate the electrolyte layer concentration with ambient temperature and humidity.

Optical micrographs of the re-wet array with NaCl applied at various deposition densities are shown in Figure 6.21.

The recorded galvanic current profiles between the microelectrodes under various salt deposition densities at 94% RH were used to estimate the throwing power of Mg over the array. The AA2024-T4 electrode furthest away from the Mg electrode which was cathodically polarized to a cathodic current density greater than 2.5×10^{-8} A (5.0×10^{-5} A/cm^2) in magnitude was used as the indicator of throwing power distance. Triplicate exposures were conducted with each of 10, 100, 250, and 1000 µg/cm^2 of both NaCl and ASTM Artificial Sea Water salts.

The throwing power, as estimated by the bare Mg/bare AA2024-T4 microelectrode array, for each exposure is reported in Table 6.4 and the mean values are reported in Table 6.5 and Figure 6.22. A detectable throwing power could not be observed under salt deposition densities less than 250 µg/cm^2. This is presumably due to the relatively large 50 µm spacing between electrodes, and small sample size. The throwing power under NaCl and ASTM ASW was observed to increase with salt deposition density (Figure 6.22). For example, throwing power was estimated to be < 50 µm under 100 µg/cm^2 of ASTM ASW to ≥ 2000 µm under 1000 µg/cm^2 of ASTM ASW. Due to variation in the particular location of deposited salt crystals and the variation in the location of individual droplets, there are significant variability of these estimations between runs (error bars in Figure 6.22). Additionally, the throwing power under ASTM Artificial Sea Water was observed to be greater than under pure NaCl. This is possibly due to the presence of

$MgCl_2$ and $CaCl_2$ in the ASTM ASW which equilibrate to lower concentrations (larger droplet volume) than pure NaCl at a given RH causing larger droplets to form and coalesce. Additionally, it was noticed that the dry ASW (after wet application and subsequent drying) appeared to have a greater dispersion of salt crystals across the surface of the array possibly due to different salt species segregation upon drying of the ASW solution.

The recorded galvanic current between the microelectrodes under 1000 μg/cm^2 of NaCl (run #2 in Table 6.4) is shown in Figure 6.23a and a corresponding optical micrograph and color coded diagram taken at the time of maximum throwing power during this exposure are shown in Figure 6.23b. The color coded array diagram in Figure 6.23b indicates that the second AA2024-T4 electrode away from the Mg electrode was the farthest AA2024-T4 electrode cathodically polarized by being galvanically coupled to the Mg electrode. This resulted in an estimation of throwing power to be 350 μm. 350 μm was the shortest distance from the closest edge of the Mg electrode to the closest edge of the furthest away, catholically polarized AA2024-T4 electrode.

The recorded galvanic current between the microelectrodes under 1000 μg/cm^2 of ASTM Artificial Sea Water salt (run #1 in Table 6.4) is shown in Figure 6.24a and a corresponding optical micrograph and color coded diagram taken at the time of maximum throwing power during this exposure are shown in Figure 6.24b. The color coded array diagram in Figure 6.24b indicates that the 14th AA2024-T4 electrode away from the Mg electrode was the farthest AA2024-T4 electrode cathodically polarized by the Mg

electrode. This results in an estimation of throwing power to be 3950 μm. 3950 μm is the shortest distance from the closest edge of the Mg electrode to the closest edge of the furthest away catholically polarized AA2024-T4 electrode. In the optical micrograph in Figure 6.24 it can be seen that separate droplets coalesced into a larger droplet which was "C" shaped such that it covered the Mg electrode, AA2024-T351 electrodes #1 – 6 (labels described in Figure 6.5), and also electrodes 11 – 14 but not #'s 7 – 10.

6.4.2 Finite Element Computational Modeling (COMSOL) of Throwing Power of MgRP on AA2024-T351

6.4.2.1 Effects of Electrolyte Layer Thickness

Figure 6.25 presents the modeled potential ($E_{Surface}$ and E_{couple}) and current over a galvanic couple between AA2024-T351 and polymer coated 99.9% Mg as predicted by finite element computational modeling (COMSOL) under 1.0 M NaCl electrolyte layers of various thickness with polymer layer resistances of 0 $\Omega \cdot m^2$ (left column) and 10 $\Omega \cdot m^2$ (right column). Given the same electrolyte chemistry (1.0 M NaCl) and in the absence of a polymer layer (Figure 6.25a), the galvanic couple potential, in all electrolyte layer thicknesses studied, that is sensed by the AA2024-T351 and the Mg at the interface between the AA2024 and Mg is equal (-1.52 V_{SCE}) and agrees with estimates from Figure 6.13b. However, a thicker electrolyte layer results in less ohmic drop through the electrolyte and enables the Mg to cathodically polarize the AA2024-T351 to a lower E_{couple} at the far geometrical limit of the AA2024-T351 (10 mm from couple interface), as low as -1.37 V_{SCE} (η^{AA2024} with respect to $E_{corr} \approx$ -680 mV). This is an indication of

increased throwing power under thicker electrolyte layers, all else equal. When the polymer resistance is zero (Figure 6.25a, c, and e) the model predicts that, in 1.0 M NaCl, the Mg anode material is largely non-polarizable (a result of fast Mg anodic kinetics, observed in Figure 6.13a and b) and as a consequence experiences a maximum anodic overpotential (η^{Mg} with respect to E_{corr} of Mg), proximate to the couple interface, of +100 mV vs. OCP or less. When the electrolyte layer is less than 100 μm an inverse throwing power (distance away from galvanic couple interface the Mg is anodically polarized above its OCP) of no more than 6 mm. As larger polymer resistances are added in to the model over the Mg anode (Figure 6.25b and d), the maximum anodic overpotential (η^{Mg}), proximate to the couple interface is less than 5 mV. Additionally, when larger polymer resistances (i.e, 10 to 10,000 $\Omega \cdot m^2$) are included in the model over the Mg anode (Figure 6.25b, d and f), the effect of the ohmic drop through the electrolyte becomes overshadowed by the mediation of the galvanic current by the resistance of the polymer layer. In such a case, the effect of electrolyte layer thickness, over the range studied here, is minimal. However, at thickness > 1 μm, the couple potential over the AA2024 drops to $-0.9V_{SCE}$. In all specific scenarios studied by the model where the galvanic couple is operative, a thicker electrolyte layer results in increased cathodic polarization of the AA2024-T351and subsequently increased throwing power of Mg.

6.4.2.2 Effect of Electrolyte Concentration

Figure 6.26 presents potential ($E_{Surface}$ and E_{couple}) and current profiles over a galvanic couple between AA2024-T351 and polymer coated 99.9% Mg as predicted by finite element computational modeling (COMSOL) under a 100 μm thick NaCl electrolyte layer of varying concentration with polymer resistance of 0 $\Omega \cdot m^2$. In the absence of a polymer layer (Figure 6.26), the galvanic couple potential, in all electrolyte layer thicknesses studied, that is sensed by the AA2024-T351 and the Mg at the interface between the AA2024 and Mg become more negative and the and galvanic current increases with increasing NaCl concentration and agree with the mixed potential model Figure 6.14. The NaCl electrolyte concentration plays a role in governing both the E-i boundary condition characteristics of the Mg and AA2024-T351 but also the ohmic drop through the electrolyte layer on the surface of the modeled couple.

As the concentration of the NaCl solution is increased from 0.001 M to 5.0 M, the boundary conditions of Mg become more active (Figure 6.13) presumably as a result of increased solution conductivity and chloride attack. The characteristics of the ORR and HER cathodic kinetics on the AA2024-T351 are largely unaffected by an increase in NaCl solution concentration, with the largest affect being a decrease in the free corrosion potential of the AA2024 (Figure 6.13). Due to the similarity of E-i boundary conditions of both the Mg and AA204-T351, in all NaCl electrolyte concentrations studied, the maximum anodic overpotential (η^{Mg}), proximate to the couple interface sensed by the Mg anode material is a relatively constant value of +100 mV vs. OCP. The model also

predicts that increasing the NaCl solution concentration by an order of magnitude results in an increase in the galvanic current by roughly one order of magnitude (Figure 6.26c) which also agrees with the mixed potential model shown in Figure 6.14. The inverse throwing power is roughly 4 mm except for the condition of 0.1 M NaCl. Interestingly, in the NaCl concentrations studied here, ΔE_{couple} (potential difference between freely corroding Mg and AA2024-T351) is at a maximum in 0.1 M NaCl (Figure 6.13). The moderate solution conductivity, in conjunction with a large ΔE_{couple}, results in the maximum η^{AA2024} sensed by the AA2024-T351 as well as the largest inverse throwing power over the Mg, extending the full distance of the Mg electrode compared to 4 mm for 0.001 M NaCl and 5.0 M NaCl respectively. In the case of very concentrated solutions ΔE_{couple} is not at a maximum, in fact approaches a minimum (Figure 6.13b). Even though the ohmic drop through the electrolyte layer is minimized due to high solution conductivity, the electrochemical driving force for sacrificial protection is lower in 5.0 M NaCl than in moderate electrolyte concentrations of 0.1 M NaCl (Figure 6.13) but the current density is still the greatest in magnitude and the local couple potential on the AA2024 is still the lowest. Conversely, under very dilute electrolyte layers (0.001 M NaCl in Figure 6.26) the decreased solution conductivity becomes significant, and reduces the throwing power over the AA2024-T351 and the inverse throwing power over the Mg, significantly due to the ohmic drop through the electrolyte layer.

6.4.2.3 Effect of Polymer Resistance

Figure 6.27 presents the modeled potential ($E_{Surface}$ and E_{couple}) and current profiles over a galvanic couple between AA2024-T351 and polymer coated 99.9% Mg as predicted by

finite element computational modeling (COMSOL) with various polymer layer resistances under 1.0 M NaCl electrolyte layers of thickness of 1 μm and 100 μm. When the electrolyte layer is thick (100 μm in Figure 6.27b, d, and f), the ohmic drop through the electrolyte layer over the horizontal length of the model (10 mm) is minimal and the pure effect of the polymer resistance on the galvanic couple potential sensed at the interface between the AA2024-T31 and the Mg can be observed more clearly. The ionic resistance of the added polymer layer over the Mg electrode acts to strongly mediate the galvanic current passing between anodes and cathodes (Figure 6.27e and f) and, when large enough, completely prevents the galvanic coupling of the electrodes altogether (when $R_{polymer}$ = 1000 $\Omega \cdot m^2$ in Figure 6.27). The combination of a very thin electrolyte layer and moderate to high polymer resistance (when $R_{polymer} \geq 0.1$ $\Omega \cdot m^2$ in Figure 6.27a, c, and e) results in further mediation of the galvanic couple potential sensed at the interface between the AA2024 and Mg as well as the galvanic throwing power over both materials.

It is important to note that even a modest polymer coating resistance of 0.1 $\Omega \cdot m^2$ between the Mg anode and AA2024-T351 cathode significantly moderates the sacrificial galvanic protection function afforded by the Mg to the AA2024-T351 (Figure 6.27b). For this reason, in the MgRP system the electrical and ionic resistances of any pretreatment layers, primer formulations, or topcoat systems appear to be the most important factor governing the galvanic protection function of the MgRP pertaining to throwing power and self-corrosion of the Mg pigment.

6.4.2.4 The Effect of Mg Pigment Depletion ($Area^{Mg}/Area^{AA2024}$)

In service, the MgRP contains a pigment volume concentration of roughly 45% and a pigment geometry of irregularly shaped flake with a mean width of 20 μm and thickness of 10 μm. The primer coating is applied in a 30 - 60 μm thick layer over the AA2024-T351 substrate. Such a configuration results in a maximum possible area ratio of Mg to AA2024-T351 (assuming all pigment is wetted) of roughly 10:1 (Table 6.6).

The effective area ratio between the Mg pigment and the AA2024-T351 substrate will evolve with time in service as the polymer wets or dries, as the electrolyte layer grows or shrinks in size, as pigment is depleted from the coating, or as new scratches or defects are formed in the coating exposing bare AA2024-T351. As such, it is important to study the effect of a wide range of area ratios between the Mg pigment and the AA2024-T351 substrate. Since the polymer layer in the finite element computational model is dimensionless, and since the depletion of Mg from the MgRP coating would not change the horizontal dimension of the couple scenario with an array or model perpendicular to a scribe, it was decided that the appropriate way to accommodate an increase or decrease in PVC_{Mg} by shifting the anodic Mg kinetics in 1.0 M NaCl by multipliers of 0.001, 0.01, 0.1, 10, 100, and 1000 (plotted in Figure 6.28) rather than change the length of the Mg anode in the model. It is interesting to note, over the entire range of area ratios studied here, the mixed potential model in Figure 6.28 predicts a change in E_{couple} at the Mg/AA2024-T351 of only ± 50 mV compared to an Mg/AA2024-T351 area ratio of 1:1.

This is because the Mg is so active and non-polarizable in salt solutions (all cases in Figure 6.13b)

Figure 6.30 presents potential ($E_{Surface}$ and E_{couple}) profiles over a galvanic couple between AA2024-T351 and various area ratios of polymer coated 99.9% Mg as predicted by finite element computational modeling (COMSOL) under a 100 μm thick, 1.0 M NaCl electrolyte layer with polymer layer resistance of 0 $\Omega \cdot m^2$ and 0.1 $\Omega \cdot m^2$. The area ratio of Mg to AA2024-T351 ("A^{Mg}/A^{2024}") specifically pertaining to the depletion of Mg pigment from the MgRP in service are estimated in Table 6.6 shown in Figure 6.29 and are estimated to be between 0.1 and 10. Using this range of area ratios in Figure 6.30, it can be seen that a lower PVC coating will develop a larger anodic overpotential and subsequently exhibit a larger inverse throwing power (anodic polarization and subsequent pigment depletion further from the edge of the coating when $R_{polymer}$ = 0 to 10 $\Omega \cdot m^2$). It is important to note that Figure 6.30 portray a hypothetical situation in which a continuous electrical and ionic path exists between all pigment particles and the AA2024-T351 substrate such that they are not isolated in polymer. If after moderate pigment depletion, the remaining pigment particles exist isolated in the primer polymer or under a topcoat with greater polymer resistance, it is likely that the sacrificial galvanic function would be severely mediated or altogether not operative (similar to when $R_{polymer}$ = 10 or 1000 $\Omega \cdot m^2$ in Figure 6.27b, d, and f). Increasing the polymer resistance still alters the current distribution such that it spreads more uniformly across the Mg but is lower when the polymer resistance is high. Current density is always non-uniform and lower at positions

further away on the AA2024 but is lower when the polymer resistance is high at all Mg_{PVC}.

6.4.3 Comparing the Throwing Power Predictions during and Episodic Wet/Dry Cycle by Microelectrode Array and Finite Element Computational Modeling

In order to assess the consistency of the findings gained from both the microelectrode galvanic array and the finite element computational modeling their results were compared with each other. Specific current profiles produced by the finite element computational model were selected in order to best represent various times during the exposure depicted in Figure 6.17. In this exposure 40 µL of 0.9 M NaCl solution was applied in a thin layer to the top of the microelectrode galvanic array (described in Figure 6.5 and shown in Figure 6.6) such that the electrolyte covered every electrode in the array. The height of the as-applied, thin layer electrolyte film was measured with a digital multimeter and vertical digital caliper setup to be approximately 500 ± 100 µm at the center for each experiment. The array was then placed in the relative humidity controlled cabinet and electrically connected to the MMA. The relative humidity in the cabinet was cycled from ambient RH (~62%) to low RH (< 20%). Specific current profiles produced by the parametric studies of the finite element computational model were selected in best effort to closely match the thermodynamically predicted equilibrium electrolyte layer thickness and concentration assuming the same initial electrolyte layer thickness and concentration on the array. Those conditions correspond to an initial condition of a 500 µm thick

electrolyte layer of 1.0 M NaCl that upon drying concentrated to 5.0 M and 5 μm thick, then 6.2 M and 0 μm thick. The predicted spatially distributed current profiles produced by a galvanic couple between similarly sized pieces of bare AA2024-T351 and bare Mg during a drying cycle depicted in Figure 6.31a, produced by both a microelectrode galvanic array and finite element computational modeling are presented for comparison in Figure 6.31b and c. In general, the magnitude and distribution of cathodic current densities predicted by the model are a fair match to the current measured by the microelectrode array on the coupled electrodes. Specifically at t_1 (under the as-applied electrolyte layer) the current distribution spreads across the AA2024. At t_2 (< 40% RH) the current distribution on the AA2024 falls after 3 – 4 mm away from the interface of the galvanic couple with Mg. After 3 – 4 mm in the finite element analysis prediction the current distribution is still finite but below 10^{-3} A/cm^2. However, the finite element model assumes an infinitely long, thin electrolyte layer and does not take into account the shrinking geometric boundaries of the electrolyte layer as it dries. As the electrolyte layer dries over the microelectrode array, the geometric boundaries of the electrolyte layer shrink as the surface tension of the electrolyte draw the edges of the shrinking droplet inwards. There are also H_2 bubbles that form above the cathodically polarized AA2024 microelectrodes. This change in geometric boundaries causes the ionic pathway between the outermost microelectrodes to be cut off and the observed throwing power to be limited to within the geometric boundaries of the droplet. This effect can be observed at t_2 and t_3 in Figure 6.31b. At t_4 (<30% RH) the current density is below 10^{-7} A/cm^2 which is near the free corrosion current on AA2024 (Figure 6.13).

6.5 Discussion

6.5.1 Important Parameters Governing Galvanic Throwing Power of MgRP over Bare AA2024-T351

The experiments conducted in this work on a galvanic couple multichannel microelectrode array in addition to finite element computational modeling, shed light on how various aspects of MgRP coating formulation and properties of the exposure environment combine to produce the resulting galvanic throwing power for protection of the AA2024-T351 across a scribe or scratch. In both cases the current density was greater near the scratch/coating interface and could be leveled only by a large polymer resistance and thick electrolyte layer.

6.5.1.1 Effect of Electrolyte Layer on the Galvanic Throwing Power in the MgRP/AA2024-T351 System

The chemistry, thickness, and geometric area of coverage of the electrolyte layer were all shown, with both an instrumented galvanic microelectrode array and finite element modeling, to play an important role in governing the galvanic throwing power of Mg across a simulated defect or scratch of bare AA2024-T351. The chemistry (chemical species present and concentration) of the electrolyte layer (whether deposited by precipitation, immersion, or deliquescence of deposited salts) was shown with the

microelectrode array to accurately govern the electrochemical E-i boundary conditions (Figure 6.13) of the anode and cathode when the polymer resistance is zero. As evidence of this, the galvanic current on each anode and cathode in the microelectrode array (Figures 6.17, 6.18, and 6.19) was in agreement with estimations gleamed from a mixed potential model (Figure 6.14). Finite element computational modeling successfully predicted that increasing the NaCl solution concentration by an order of magnitude results in an increase in the galvanic current by almost one order of magnitude (Figure 6.26) which also agrees with the mixed potential model shown in Figure 6.14 and microelectrode array measurements in Figures 6.17, 6.18, and 6.19 in which the electrolyte is assumed to saturate just before drying. Interestingly, in the NaCl concentrations studied here, the finite element computational modeling highlighted that the ΔE_{couple} (potential difference between the corrosion potential of freely corroding Mg and AA2024-T351) is at a maximum in 0.1 M NaCl (Figure 6.13). The moderate solution conductivity, in conjunction with a large ΔE_{couple}, results in the maximum local cathodic overpotentials sensed by the AA2024-T351 proximate to the couple interface as well as the largest inverse throwing power over the Mg, compared to under 0.001 M NaCl or 5.0 NaCl (Figure 6.26).

The chemical species in the electrolyte also dictate the deliquescence and equilibrium behavior of the electrolyte layer exposed to various ambient RH (Figure 6.3). For example, when the microelectrode array was exposed under continuous, thin electrolyte layers of pure $MgCl_2$, rather than NaCl or ASTM Artificial Sea Water, the electrolyte

layer did not completely dry at low RH (Figure 6.19). In turn the galvanic interaction does not cease because full drying does not occur at low RH.

In conjunction with electrolyte chemistry, the thickness and geometric area of coverage of the electrolyte layer (which are all influenced by deposition density, immersion condition, or RH and deliquescence of deposited salts shown in Figures 6.2 , 6.3 , 6.4 , and 6.21) controls the amount of area of both the anode and the cathode that can be galvanically coupled together. A sacrificial anode (or sacrificial coating such as an MgRP) can only protect the area of a cathode (scratch or scribe exposing bare AA2024-T351 substrate) of which it is both electrically and ionically connected to. In exposures of the microelectrode array under continuous, thin electrolyte layers (t_1 in Figures 6.17, 6.18, and 6.19) the throwing power extended across the entire array. However, whenever the electrolyte became tortuous, either due to drying (t_3 in Figures 6.17, 6.18, and 6.19 and shown schematically in Figure 6.32b) or due to the formation of isolated droplets due to low initial salt deposition density at a given RH (Figures 6.21, 6.22, 6.23, and 6.24 and shown schematically in Figure 6.32c) the throwing power was limited by an increasingly tortuous electrolyte geometry which reduced the ionically conductive path length (Figures 6.31b and 6.32b and c). When electrolyte layer thickness was studied with finite element computational modeling it was found that a thicker electrolyte layer results in less ohmic drop through the electrolyte and allows for the Mg to cathodically polarize the AA2024-T351 to a more negative E_{couple} at the far geometrical limit of the AA2024-T351 in the model (Figure 6.25). This is an indication of increased throwing power under thicker electrolyte layers, all else equal.

6.5.1.2 Effect of Organic Polymers on the Galvanic Throwing Power in the MgRP/AA2024-T351 System

The role of the polymer layers in the MgRP/AA2024-T351 system is twofold. The primer and topcoat polymers both act to (1) act as a barrier to protect the Mg pigment from rapid self-corrosion and (2) to mediate the cathodic protection provided to the AA2024-T351 substrate by the Mg pigment to avoid detrimental cathodic corrosion of the AA2024-T351 substrate and subsequent blistering by rapid H_2 evolution at cathodic sites.[10]. When a quick-drying, acrylic polymer with similar barrier properties to that of a commercial MgRP (Figure 6.8) was applied to the surface of the Mg electrode in the Mg/AA2024-T4 microelectrode array, the added resistance of the polymer mediated the sacrificial galvanic protection afforded by the Mg electrode to the AA2024-T4 electrodes in the microelectrode array (t_1 in Figure 6.20a and Figure 6.20b) shown by net current densities of zero on the Mg and AA2024-T4 electrodes (at t_1 TP = 0 μm) due to the large ohmic resistance of the intact polymer. Similarly, when the effect of polymer resistance was studied with finite element computational modeling it was found that the ionic resistance of the added polymer layer over the Mg electrode acts to significantly mediate the galvanic current passing between anodes and cathodes (Figure 6.27e and f) and, when large enough, completely prevents the galvanic coupling of the electrodes altogether (when $R_{polymer}$ = 1000 $\Omega \cdot m^2$ in Figure 6.27).

It is important to note that even a modest polymer coating resistance of 0.1 $\Omega \cdot m^2$ between the Mg anode and AA2024-T351 cathode significantly moderates the sacrificial galvanic protection function afforded by the Mg to the AA2024-T351 (Figure 6.27). For this reason, in the MgRP system, besides any geometric limitations brought about by a discontinuous ionic pathway, the electrical and ionic resistances of any pretreatment layers, primer formulations, or topcoat systems appears to be the most important tunable factor at the disposal of the user governing the galvanic protection function of the MgRP pertaining to throwing power and self-corrosion of the Mg pigment. However, the polymer resistance levels the potential distribution and current distribution at the expense of the galvanic current which is lowered. The primer and topcoat polymers are shown to severely mediate the throwing power of the Mg over the AA2024 scribe. In the real-life coating scenario this is presumed to be the case except for locations very proximate to the edge of the coating where, different from the model, there exists a small area of bare Mg exposed to solution and where $R_{polymer}$ is zero or small.

6.5.2 Important Limitations of the Microelectrode Galvanic Array and the Finite Element Computational Model and Suggestions for Improvement and Future Work

The microelectrode galvanic array and finite element computational modeling both proved to be extremely useful tools in helping to examine the galvanic throwing power of

a simulated MgRP / AA2024-T351 system. These tools allowed for the study of how specific variables, such as electrolyte layer thickness, chemistry, or polymer layers play a role in dictating the galvanic throwing power of Mg over AA2024-T351 in a geometric scenario designed to simulate the bare AA2024-T351 perpendicular to the scribe length on a typical MgRP-coated AA2024-T351 test panel. However, there are many improvements which could be made to both the microelectrode array and the finite element computational model that would improve the correlation to real environmental exposure.

The microelectrode array could be designed to be more analogous to the real MgRP/AA2024-T351 system if the microelectrodes were embedded in AA2024-T351 sheet instead of mounted in epoxy polymer or an MgRP coating could be utilized in place of the Mg electrode. Similar modifications such as these were attempted in this work but fabrication proved unsuccessful. It is well known that the wettability of the surface of aluminum and its oxides is high compared to that of polished organic epoxy polymers. This difference would surely lead to larger throwing powers being observed on an array embedded in an AA2024-T351 panel as compared to those observed on the epoxy embedded array used in this work. Additionally, it would be useful to quantitatively simultaneously track the real-time electrolyte concentration over the microelectrode galvanic array throughout an environmental exposure. This could be accomplished by monitoring the electrochemical impedance between two close spaced electrodes added to the array.

The finite element computational model could be made more robust by including the consideration of evolving electrolyte chemistry and electrolyte geometry as a function of position and time. For example, in the MgRP/AA2024-T351 system, when Mg pigment corrodes, the the electrolyte becomes saturated with $Mg(OH)_2$. When this occurs the pH rises locally and can reach values as high as 10.5. This will have a dramatic effect on the electrochemical boundary conditions of the AA2024-T351 and Mg electrodes (Figure 6.33 compared to Figure 6.13). Additionally, the increased hydrogen evolution at sites of cathodic polarization can produce hydrogen bubbles. These hydrogen bubbles are a source of IR drop through the electrolyte layer. Such affects were not accounted for in this work and would prove valuable in furthering the predictive capabilities of the model. Additionally, the lack of ability of the model geometry to account for the shrinking of the geometric boundary of a droplet as it dries or the formation of H_2 bubbles is highlighted in Figure 6.31. As an electrolyte layer dries during an atmospheric exposure, not only does the layer thin but the geometric boundaries of the electrolyte layer shrink as the surface tension of the electrolyte draw the edges of the shrinking droplet inwards. This change in geometric boundaries causes the ionic pathway between the outermost microelectrodes to be cut off and the observed throwing power to be limited to within the geometric boundaries of the droplet. Similar geometric boundary effects occur when isolated droplets are deposited or form from deliquesced salts on the surface of the coating during environmental exposure. A valuable addition to the model would be the ability to predict and account for this changing electrolyte geometry. During drying, the net cathodic current density on the individual AA2024-T4 electrodes closest to the Mg electrode was observed to increase to a peak (at time t_2 in Figure 6.17b and Figure 6.18b)

presumably due to the combined effects of the increasing electrolyte concentration and the decreasing area of the active cathode. Upon further drying, the net cathodic current density on the AA2024-T4 electrodes closest to the Mg electrode were then observed to decrease in magnitude to zero as the effect of the increasingly thin and tortuous electrolyte geometry reduced the ionically conductive path despite the increase in concentration of NaCl.

6.6 Conclusions

- Both a microelectrode galvanic array and a finite element computational model were successfully developed to study the effects of electrolyte chemistry, electrolyte layer thickness, environmental wet/dry cycling, polymer layer resistance, and Mg pigment depletion on the galvanic throwing power in a simulated MgRP / AA2024-T351 system.
- The chemistry, thickness, and geometric area of coverage of the electrolyte layer were all shown, with both an instrumented galvanic microelectrode array and finite element modeling, to play an important role in governing the galvanic throwing power of Mg across a simulated defect or scratch of bare AA2024-T351.
    - The chemistry (chemical species present and concentration) of the electrolyte layer (whether deposited by precipitation, immersion, or deliquescence of deposited salts) was shown with the microelectrode array to accurately govern the electrochemical E-i boundary conditions of the anode and cathode.

- Finite element computational modeling successfully predicted that increasing the NaCl solution concentration by an order of magnitude results in an increase in the galvanic current by almost one order of magnitude.
- During drying, the net cathodic current density on the AA2024-T4 electrodes closest to the Mg electrode was observed to increase to a peak, presumably due to the combined effects of the increasing electrolyte concentration and the decreasing area of the active cathode. Upon further drying, the net cathodic current density on the AA2024-T4 electrodes closest to the Mg electrode were then observed to decrease in magnitude to zero as the effect of the increasingly thin and tortuous electrolyte geometry reduced the ionically conductive path despite the increase in concentration of NaCl
- The chemical species in the electrolyte also dictate the deliquescence and equilibrium behavior of the electrolyte layer exposed to various ambient RH and temperature. When the microelectrode array was exposed under continuous, thin electrolyte layers of pure $MgCl_2$, contrary to NaCl or ASTM Artificial Sea Water, the electrolyte layer did not completely dry at low RH.
- In exposures of the microelectrode array under continuous, thin electrolyte layers the throwing power extended across the entire array. However, whenever the electrolyte became tortuous, either due to drying or due to the formation of isolated droplets due to low initial salt deposition density

the throwing power was limited by an increasingly tortuous electrolyte geometry which reduced the ionically conductive path length.

  - When electrolyte layer thickness was studied with finite element computational modeling it was found that a thicker electrolyte layer results in less ohmic drop through the electrolyte and allows for the Mg to cathodically polarize the AA2024-T351 to a lower E_{couple} at the far geometrical limit of the AA2024-T351 in the model. This is an indication of increased throwing power under thicker electrolyte layers, all else equal.

- When a polymer with similar barrier properties to that of a commercial MgRP was applied to the surface of the Mg electrode in the Mg/AA2024-T4 microelectrode array, the added resistance of the polymer significantly mediated the sacrificial galvanic protection afforded by the Mg electrode to the AA2024-T4 electrodes in the microelectrode array Similarly, when the effect of polymer resistance was studied with finite element computational modeling it was found that the ionic resistance of the added polymer layer over the Mg electrode acts to strongly mediate the galvanic current passing between anodes and cathodes and, when large enough, completely prevents the galvanic coupling of the electrodes altogether. The most uniform current distribution was observed under high polymer resistances with a penalty of low galvanic current.
- In general, the magnitude and distribution of cathodic and anodic current densities predicted by the finite element computational model throughout a wet/dry cycle are a fair match to the current densities measured by the microelectrode galvanic

array on the coupled electrodes. However, the finite element model assumes an infinitely long, thin electrolyte layer and does not take into account the shrinking geometric boundaries of the electrolyte layer or variable electrolyte height as it dries.

6.7 Acknowledgements

This work was supported by the US DoD OUSD Corrosion University Pilot Program under the direction of Mr. Daniel Dunmire and by the National Science Foundation under NSF DMR #0906663. This material is based on research sponsored by the US Air Force Academy under agreement number FA7000-13-2-0020. The U.S. Government is authorized to reproduce and distribute reprints for Governmental purposes notwithstanding any copyright notation thereon. The views and conclusions contained herein are those of the authors and should not be interpreted as necessarily representing the US Air Force Academy or the U.S. Government.

6.8 References

1. S. S. Pathak, M. D. Blanton, S. K. Mendon and J. W. Rawlins, Investigation on dual corrosion performance of magnesium-rich primer for aluminum alloys under salt spray test (ASTM B117) and natural exposure, Corros Sci, 52, 4 (2010), pp. 1453-1463.
2. G. P. Bierwagen, D. E. Tallman, M. Nanna, D. Battocchi, A. Stamness and V. J. Gelling, New developments in Cr-free primers for aerospace alloys., Abstr Pap Am Chem S, 228, (2004), pp. U360-U360.
3. A. Simoes, D. Battocchi, D. Tallman and G. Bierwagen, Assessment of the corrosion protection of aluminium substrates by a Mg-rich primer: EIS, SVET and SECM study, Prog Org Coat, 63, 3 (2008), pp. 260-266.
4. D. Battocchi, A. M. Simoes, D. E. Tallman and G. P. Bierwagen, Comparison of testing solutions on the protection of Al-alloys using a Mg-rich primer, Corros Sci, 48, 8 (2006), pp. 2226-2240.

5. D. Battocchi, A. M. Simoes, D. E. Tallman and G. P. Bierwagen, Electrochemical behaviour of a Mg-rich primer in the protection of Al alloys, Corros Sci, 48, 5 (2006), pp. 1292-1306.
6. H. Xu, D. Battocchi, D. E. Tallman and G. P. Bierwagen, Use of Magnesium Alloys as Pigments in Magnesium-Rich Primers for Protecting Aluminum Alloys, Corrosion, 65, 5 (2009), pp. 318-325.
7. G. Bierwagen, D. Battocchi, A. Simoes, A. Stamness and D. Tallman, The use of multiple electrochemical techniques to characterize Mg-rich primers for A1 alloys, Prog Org Coat, 59, 3 (2007), pp. 172-178.
8. A. D. King and J. R. Scully, Sacrificial Anode-Based Galvanic and Barrier Corrosion Protection of 2024-T351 by a Mg-Rich Primer and Development of Test Methods for Remaining Life Assessment, Corrosion, 67, 5 (2011), pp. 05500401-05500422.
9. B. Maier and G. S. Frankel, Behavior of Magnesium-Rich Primers on AA2024-T3, Corrosion, 67, 5 (2011), p. 055001.
10. A. D. King and J. R. Scully, Blistering Phenomena in Early Generation Mg-Rich Primer Coatings on AA2024-T351 and the Effects of CO_2, NACE DoD 2011 Conference Proceedings, (Palm Springs, CA, 2011).
11. J. Nie, M. C. Yan, J. Wang, D. E. Tallman, D. Battocchi and G. P. Bierwagen, Cathodic Corrosion Protection Performance of Mg-Rich Primers: Effect of Pigment Shape and Pigment Volume Concentration, ECS Transactions, 24, 1 (2010), pp. 261-275.
12. A. D. King, B. Kannan and J. R. Scully, Environmental Degradation of a Mg-Rich Primer in Selected Field and Laboratory Environments – Part I. Without a Topcoat, Corrosion, 70, 5 (2014).
13. A. D. King, B. Kannan and J. R. Scully, Environmental Degradation of a Mg-Rich Primer in Selected Field and Laboratory Environments – Part II. Primer and Topcoat, Corrosion, 70, 5 (2014).
14. D. H. Wang, D. Battocchi, K. N. Allahar, S. Balbyshev and G. P. Bierwagen, In situ monitoring of a Mg-rich primer beneath a topcoat exposed to Prohesion conditions, Corros Sci, 52, 2 (2010), pp. 441-448.
15. M. E. Nanna and G. P. Bierwagen, Mg-rich coatings: A new paradigm for Cr-free corrosion protection of al aerospace alloys, Jct Research, 1, 2 (2004), pp. 69-80.
16. C. Wagner, Theoretical Analysis of the Current Density Distribution in Electrolytic Cells, J Electrochem Soc, 98, 3 (1951), pp. 116-128.
17. J. Scully and H. P. Hack, Prediction of tube-tubesheet galvanic corrosion using finite element and Wagner number analyses, ASTM STP 978 Galvanic Corrosion, (1988), p. 136.
18. F. J. Presuel-Moreno, H. Wang, M. A. Jakab, R. G. Kelly and J. R. Scully, Computational modeling of active corrosion inhibitor release from an Al-Co-Ce metallic coating - Protection of exposed AA2024-T3, J Electrochem Soc, 153, 11 (2006), pp. B486-B498.
19. J. S. Lee, M. L. Reed and R. G. Kelly, Combining rigorously controlled crevice geometry and computational modeling for study of crevice corrosion scaling factors, J Electrochem Soc, 151, 7 (2004), pp. B423-B433.

20. E. Kennard and J. T. Waber, Mathematical Study of Galvanic Corrosion - Equal Coplanar Anode and Cathode with Unequal Polarization Parameters, J Electrochem Soc, 117, 7 (1970), pp. 880-&.
21. J. T. Waber and B. Fagan, Mathematical Studies on Galvanic Corrosion: IV . Influence of Electrolyte Thickness on the Potential and Current Distributions over Coplanar Electrodes Using Polarization Parameters, J Electrochem Soc, 103, 1 (1956), pp. 64-72.
22. J. W. Fu, A Finite-Element Analysis of Corrosion Cells, Corrosion, 38, 5 (1982), pp. 295-296.
23. J. T. Waber, Mathematical Studies of Galvanic Corrosion: VI. . Limiting Case of Very Thin Films, J Electrochem Soc, 103, 10 (1956), pp. 567-570.
24. J. T. Waber, Mathematical Studies of Galvanic Corrosion: III . Semi-infinite Coplanar Electrodes with Equal Constant Polarization Parameters, J Electrochem Soc, 102, 7 (1955), pp. 420-429.
25. J. T. Waber and M. Rosenbluth, Mathematical Studies of Galvanic Corrosion: II . Coplanar Electrodes with One Electrode Infinitely Large and with Equal Polarization Parameters, J Electrochem Soc, 102, 6 (1955), pp. 344-353.
26. S. M. Sharland, C. P. Jackson and A. J. Diver, A finite-element model of the propagation of corrosion crevices and pits, Corros Sci, 29, 9 (1989), pp. 1149-1166.
27. F. J. Presuel-Moreno, M. E. Goldman, R. G. Kelly and J. R. Scully, Electrochemical sacrificial cathodic prevention provided by an Al-Co-Ce metal coating coupled to AA2024-T3, J Electrochem Soc, 152, 8 (2005), pp. B302-B310.
28. C. Deslouis, A. Doncescu, D. Festy, O. Gil, V. Maillot, S. Touzain and B. Tribollet, Kinetics and characterisation of calcareous deposits under cathodic protection in natural sea water, Electrochemical Methods in Corrosion Research Vi, Pts 1 and 2, 289-2, (1998), pp. 1163-1180.
29. C. Deslouis, D. Festy, O. Gil, G. Rius, S. Touzain and B. Tribollet, Characterization of calcareous deposits in artificial sea water by impedance techniques - I. Deposit of CaCO3 without Mg(OH)(2), Electrochim Acta, 43, 12-13 (1998), pp. 1891-1901.
30. R. A. Humble, Cathodic protection of steel in seawater with magnesium anodes, Corrosion, 4, (1948), pp. 358-370.
31. R. U. Lee and J. R. Ambrose, Influence of Cathodic Protection Parameters on Calcareous Deposit Formation, Corrosion, 44, 12 (1988), pp. 887-891.
32. F. G. Liu, S. R. Wu and C. S. Lu, Characterisation of calcareous deposits on freely corroding low carbon steel in artificial sea water, Corros Eng Sci Techn, 46, 5 (2011), pp. 611-617.
33. C. Rousseau, F. Baraud, L. Leleyter, M. Jeannin and O. Gil, Calcareous deposit formed under cathodic protection in the presence of natural marine sediments: A 12 month experiment, Corros Sci, 52, 6 (2010), pp. 2206-2218.
34. C. Barchiche, C. Deslouis, D. Festy, O. Gil, P. Refait, S. Touzain and B. Tribollet, Characterization of calcareous deposits in artificial seawater by impedance

techniques 3 - Deposit of CaCO3 in the presence of Mg(II), Electrochim Acta, 48, 12 (2003), pp. 1645-1654.

35. C. Deslouis, D. Festy, O. Gil, V. Maillot, S. Touzain and B. Tribollet, Characterization of calcareous deposits in artificial sea water by impedances techniques: 2-deposit of Mg(OH)(2) without CaCO3, Electrochim Acta, 45, 11 (2000), pp. 1837-1845.
36. Astm, Standard Practice for the Preparation of Substitute Ocean Water, ASTM D1141 - 98, DOI: 10.1520/D1141-98R08 (1998).
37. J. G. Kaufman, Corrosion of Aluminum and Aluminum Alloys, vol. 13B, ASM Handbook Volume 13B, Corrosion: Materials (ASM International) (Materials Park, Ohio, ASM International, 2003, p. 95-124).

6.9 Tables

Table 6.1. Composition of AA2024-T351 used as a bare electrode in these investigations. Compositions provided by QUANT Quality Analysis and Testing Corporation in wt. %

AA2024	Al	Cu	Mg	Mn	Fe	Zn	Si	Ti	Cr	V
T351 Sheet	Balance	4.56	1.26	0.59	0.22	0.12	0.08	0.02	0.01	0.01
T4 Wire	Balance	4.35	1.36	0.62	0.5	0.25	0.5	0.15	0.1	NR

Table 6.2. Compositions of Mg Rod (99.9%) purchased from Alfa Aesar. All compositions reported in wt. %. (Mg: Balance). Compositions provided by QUANT Quality Analysis and Testing Corporation. NR: Not Reported

element	Si	Al	Fe	Cu	Zn	Mn	Ni	Zr	Pb	Sn	C	S	O
rod/wire	NR	0.02	0.008	0.003	0.03	<0.01	<0.001	<0.01	NR	NR	<0.001	<0.001	0.001

Table 6.3. Conductivity (σ_{NaCl}) of NaCl electrolyte layer utilized in finite element computation modeling. Conductivities calculated by OLI^{TM}.

[NaCl] (mol/L)	σ_{NaCl} (S/m)
0.001	0.0013
0.010	0.1176
0.100	1.0607
1.000	8.4393
5.000	24.0164

Table 6.4. Galvanic throwing power distance for sacrificial anode based cathodic protection of bare AA2024-T351 by bare Mg as measured by a microelectrode array with various deposition densities of NaCl and ASTM ASW at 95% RH.

		TP (µm)	
		NaCl	ASW
10 µg/cm^2	Run 1	0	0
	Run 2	0	0
	Run 3	0	0
100 µg/cm^2	Run 1	0	0
	Run 2	0	0
	Run 3	0	0
250 µg/cm^2	Run 1	0	50
	Run 2	50	350
	Run 3	350	50
1000 µg/cm^2	Run 1	650	3950
	Run 2	350	650
	Run 3	50	1250

Table 6.5. Mean galvanic throwing power distance for sacrificial anode based cathodic protection of bare AA2024-T351 by bare Mg as measured by a microelectrode array with various deposition densities of NaCl and ASTM ASW at 95% RH.

	TP-NaCl (µm)		TP-ASW (µm)	
Dep. Density	Mean	Std. Dev.	Mean	Std. Dev.
10 µg/cm^2	0	0	0	0
100 µg/cm^2	0	0	0	0
250 µg/cm^2	133	155	133	141
1000 µg/cm^2	350	245	1950	1435

Table 6.6. Estimation of surface area ratio between Mg pigment and AA2024-T351 substrate of MgRP formulations of various pigment volume concentration (PVC) assuming a coating thickness of 30 μm and spherical pigment geometry with radius 10 μm or cylindrical pigment geometry with radius 10 μm and thickness 10 μm.

PVC_{Mg}	A_{Mg} / A_{2024}	
	sphere	**cylinder**
1	0.09	0.12
10	0.9	1.2
20	1.8	2.4
30	2.7	3.6
40	3.6	4.8
50	4.5	6
60	5.4	7.2
70	6.3	8.4
80	7.2	9.6

6.10 Figures

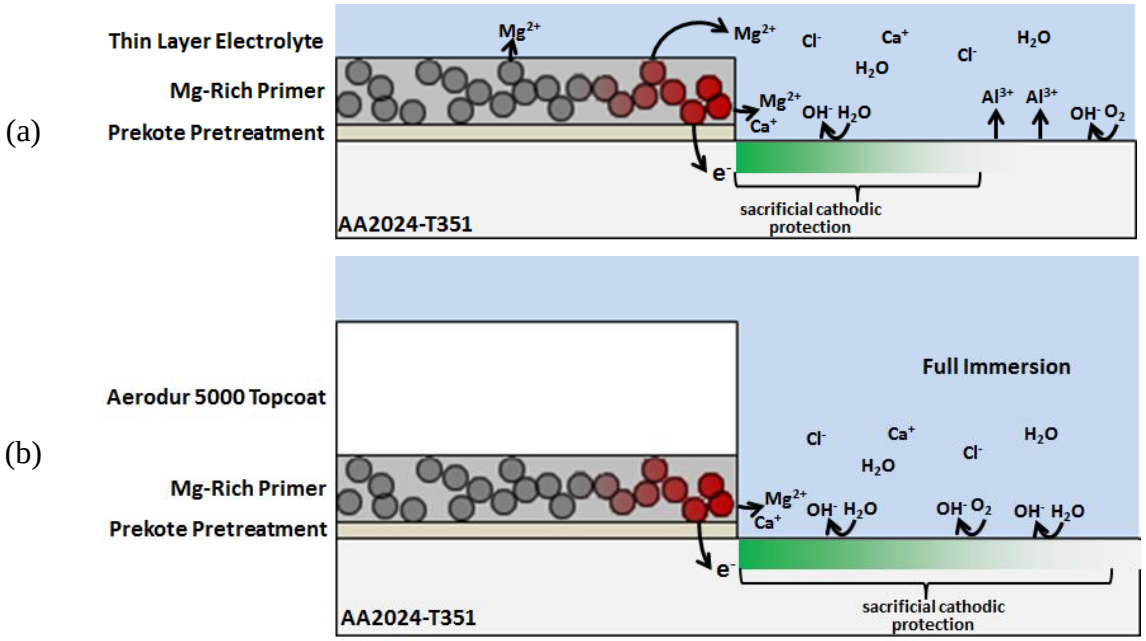

Figure 6.1. Hypothetical schematic of AA2024-T351 coated with (a) MgRP and (b) MgRP + Topcoat, depicting MgRP sacrificial cathodic protection function under an infinitely long, uniform electrolyte layer. Hypothetical galvanic throwing power extending away from the edge of the coating is indicated with green shading. Red shading indicates possible galvanic utilization of Mg or "inverse throwing power".

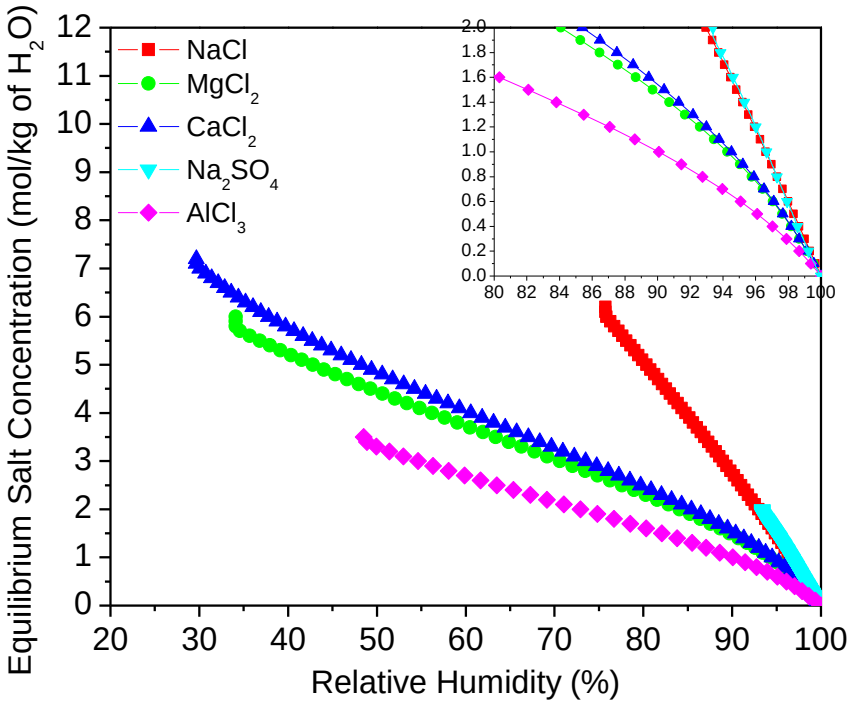

Figure 6.2. Thermodynamic equilibrium concentration of various saltwater solutions relative to the relative humidity in equilibrium. Calculated by OLI.

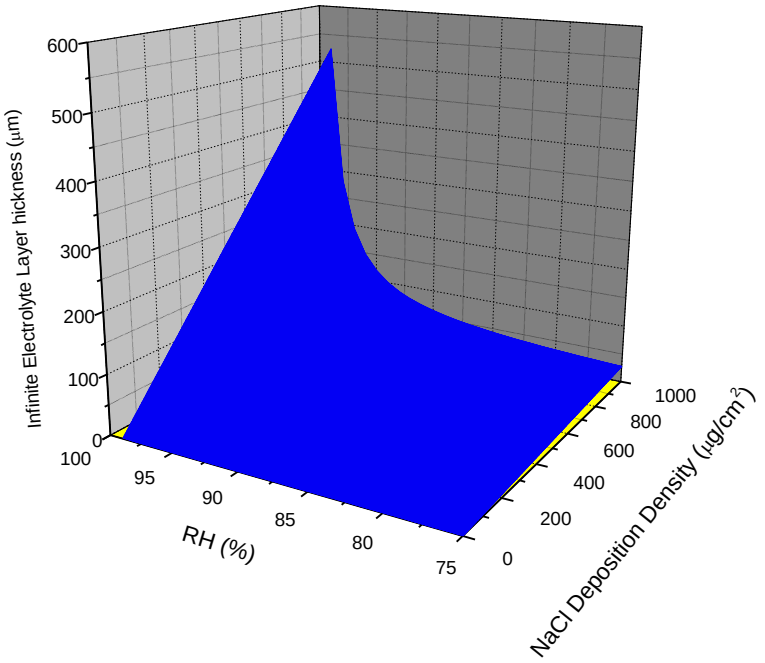

(a)

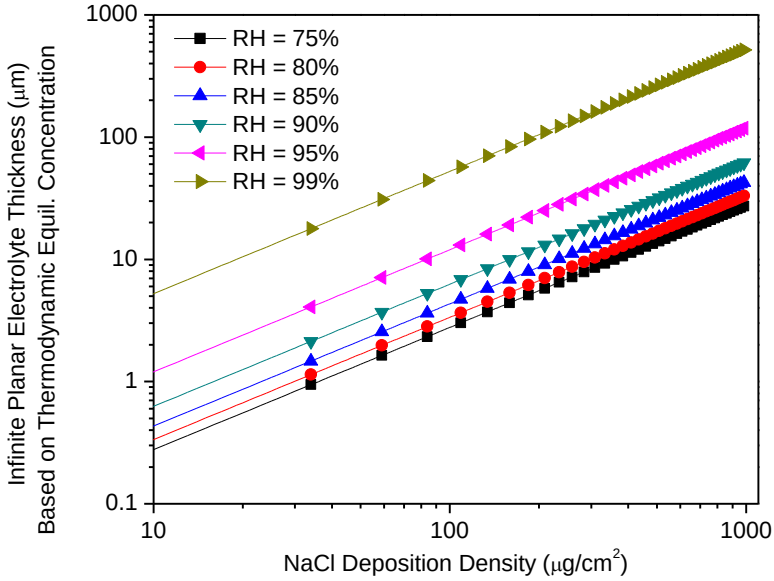

(b)

Figure 6.3. (a) Uniform, planar electrolyte layer thickness based on thermodynamic equilibrium concentration of NaCl with respect to ambient RH and initial deposition density at 25 °C. (b) Planar electrolyte thickness vs. NaCl deposition density. Calculated by OLI.

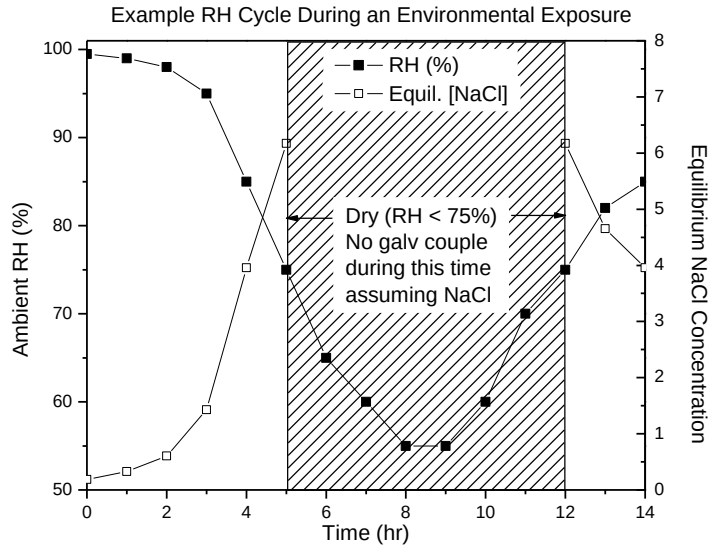

(a)

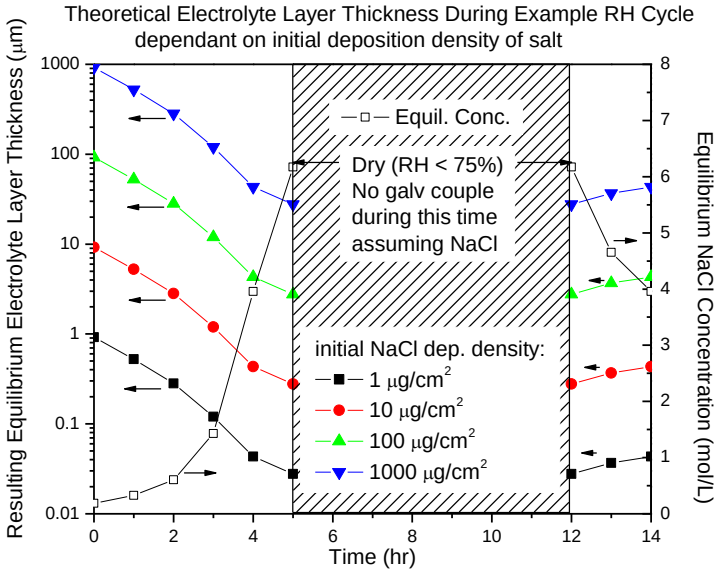

(b)

Figure 6.4. Hypothetical RH cycle and resulting (a) thermodynamic equilibrium NaCl electrolyte concentration and (b) resulting electrolyte layer thickness for various NaCl surface deposition densities.

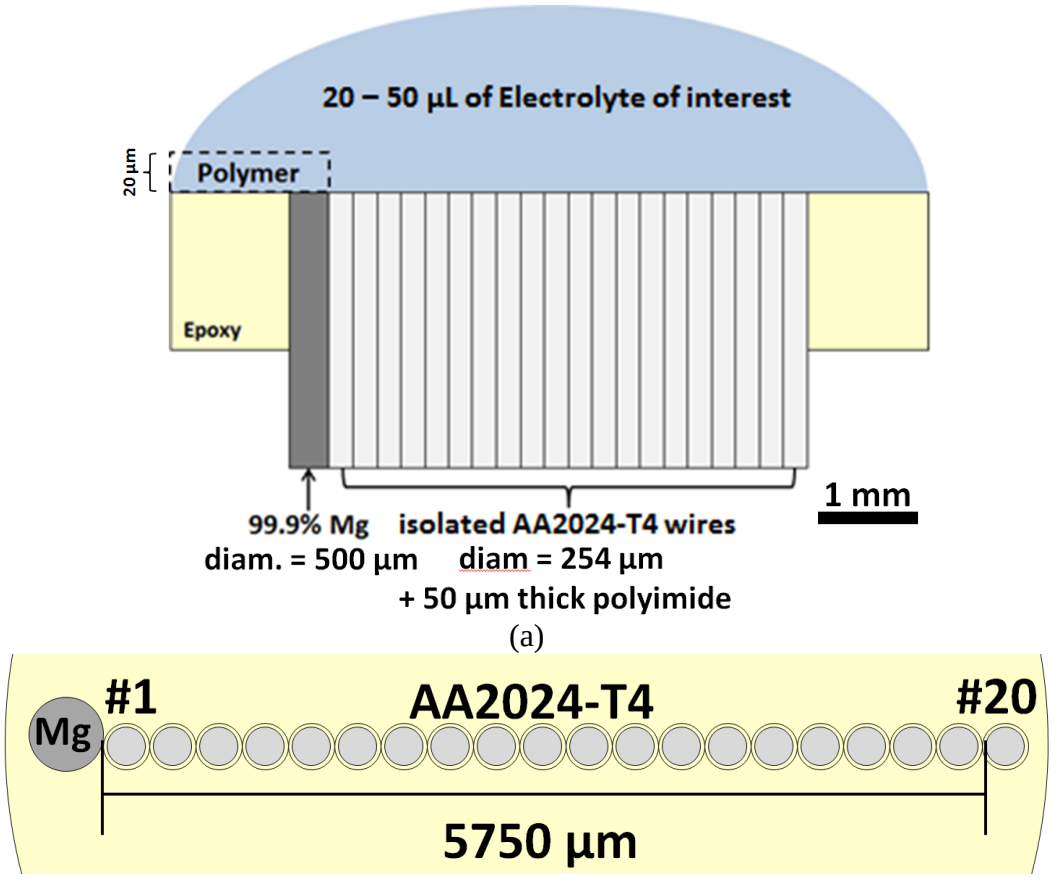

Figure 6.5. Schematic cross-section (a) and planar (b) illustration of the Mg/AA2024-T4 microelectrode array used to diagnostically assess the throwing power of Mg over a representative bare AA2024-T4 scratch in an RH controlled cabinet. The array mimics the geometric arrangement of a coating scratch.

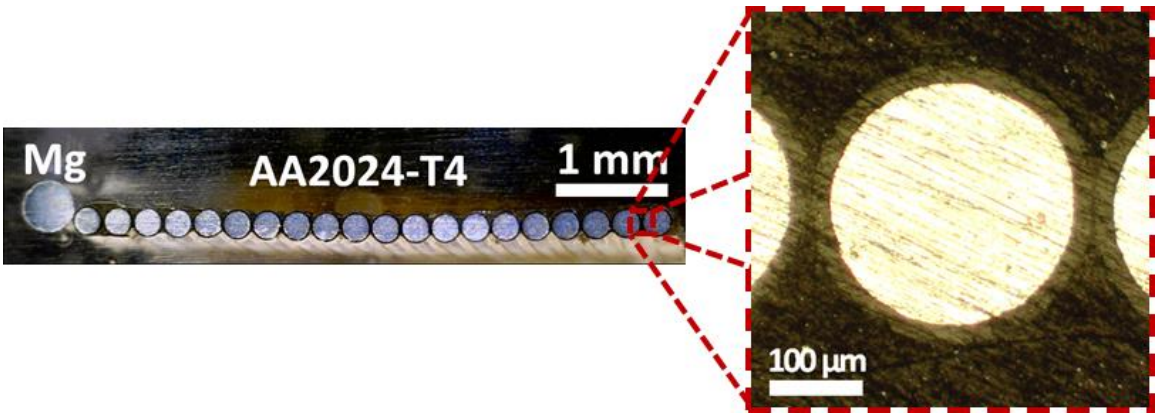

Figure 6.6. Optical images of the bare Mg/AA2024-T4 microelectrode array used to diagnostically assess the throwing power of Mg over a representative bare AA2024-T4 scratch in an RH controlled cabinet.

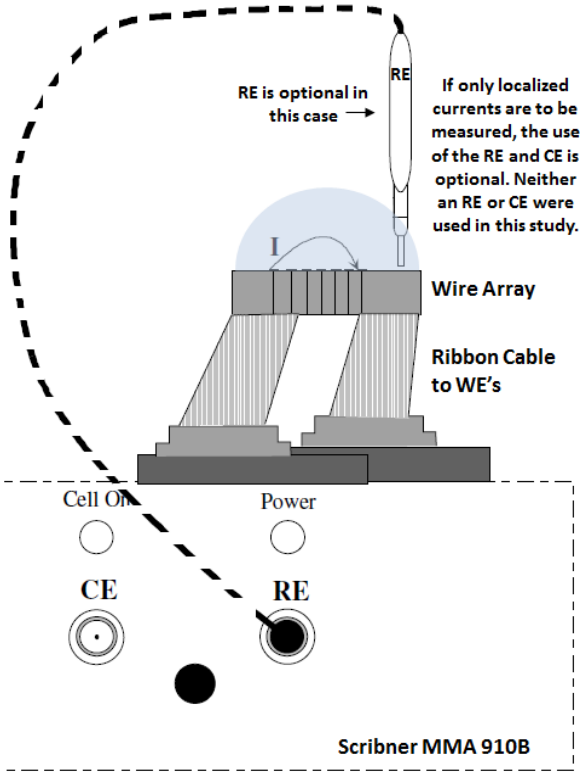

Figure 6.7. Schematic illustration of microelectrode array electrode connections to Scribner MMA 900B. Schematic adapted from MMA910B operator manual. Scribner Associates 2011.

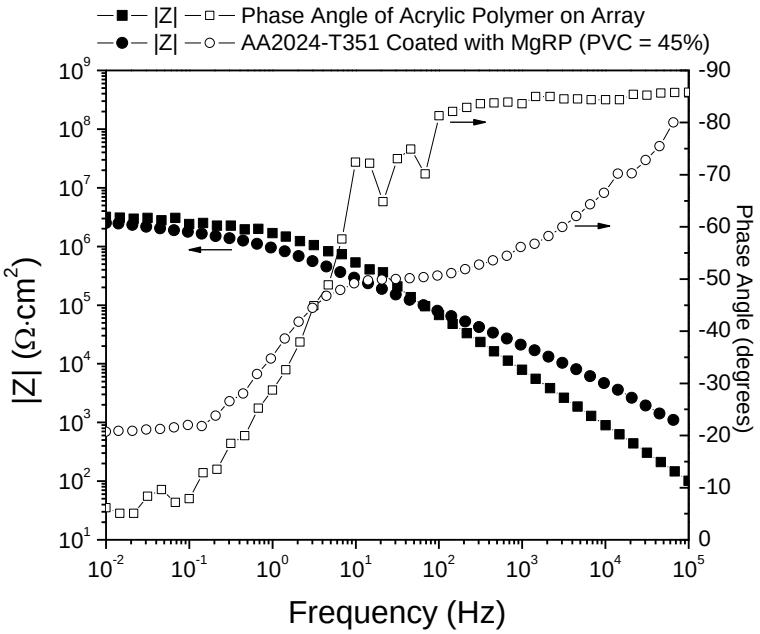

Figure 6.8. Electrochemical impedance spectroscopy of the clear, quick drying acrylic polymer applied to surface of Mg microelectrode in coated Mg/bare AA2024-T351 microelectrode galvanic array.

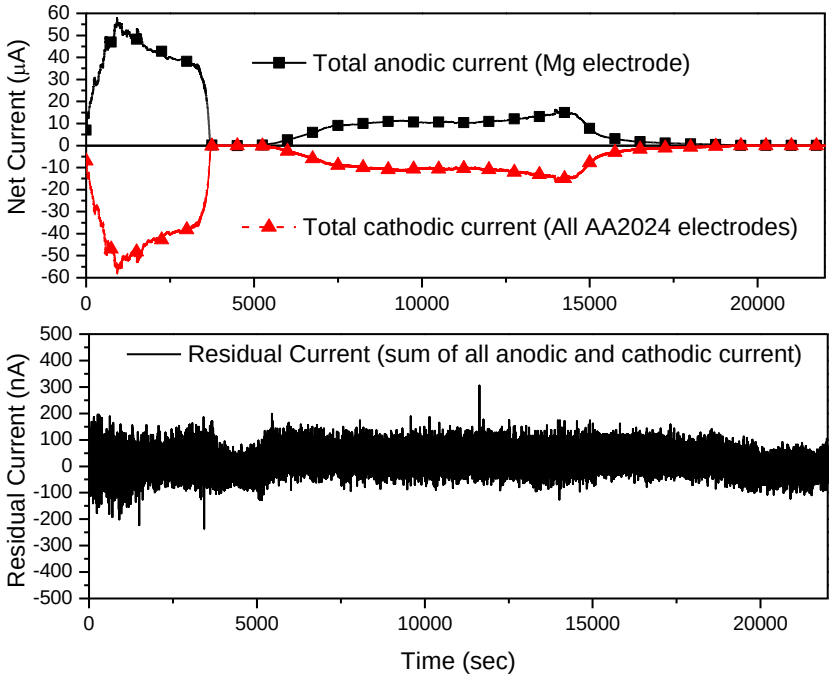

Figure 6.9.Sum of anodic and cathodic current passing through each electrode vs. time of the bare Mg/AA2024-T4 microelectrode array during an episodic wetting and drying event under ASTM Artificial Sea Water shown in Figure 6.16

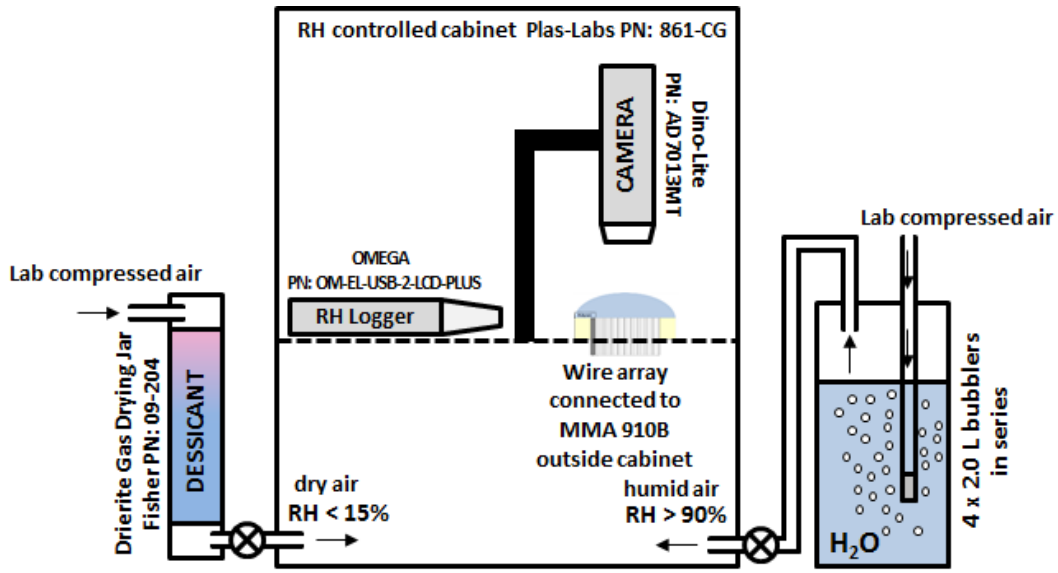

Figure 6.10. Schematic illustration of RH controlled cabinet and camera setup used to environmentally expose Mg/AA2024-T4 microelectrode arrays to high and low RH.

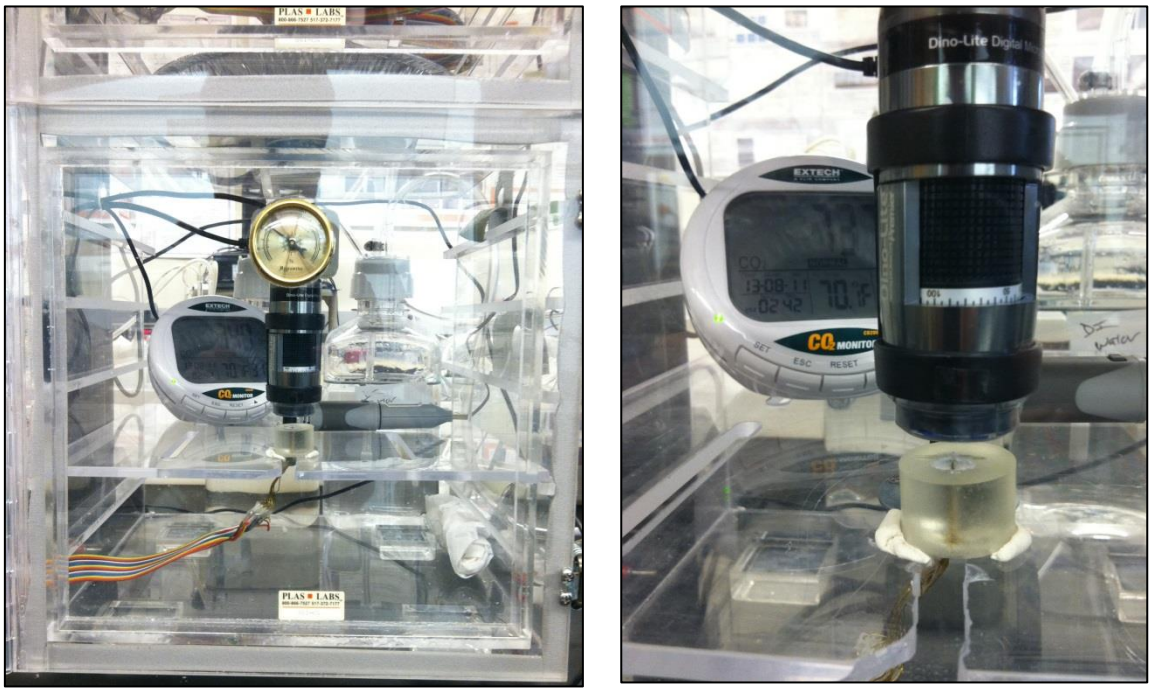

(a) (b)

Figure 6.11. Optical images of of RH controlled cabinet and camera setup used to environmentally expose Mg/AA2024-T4 microelectrode arrays to high and low RH.

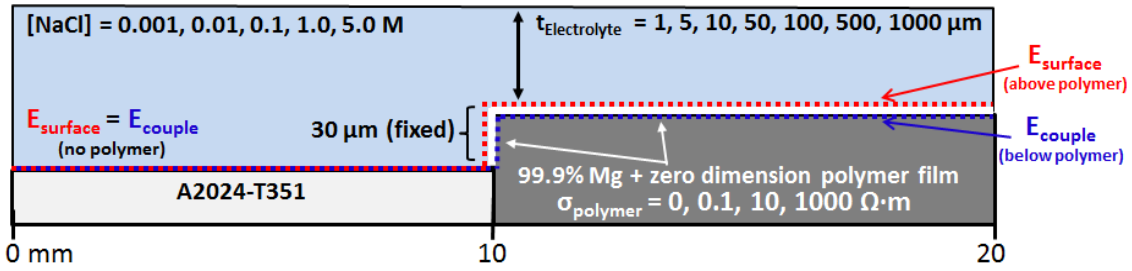

Figure 6.12. Schematic of geometric model developed in finite element computational modeling software (COMSOL).

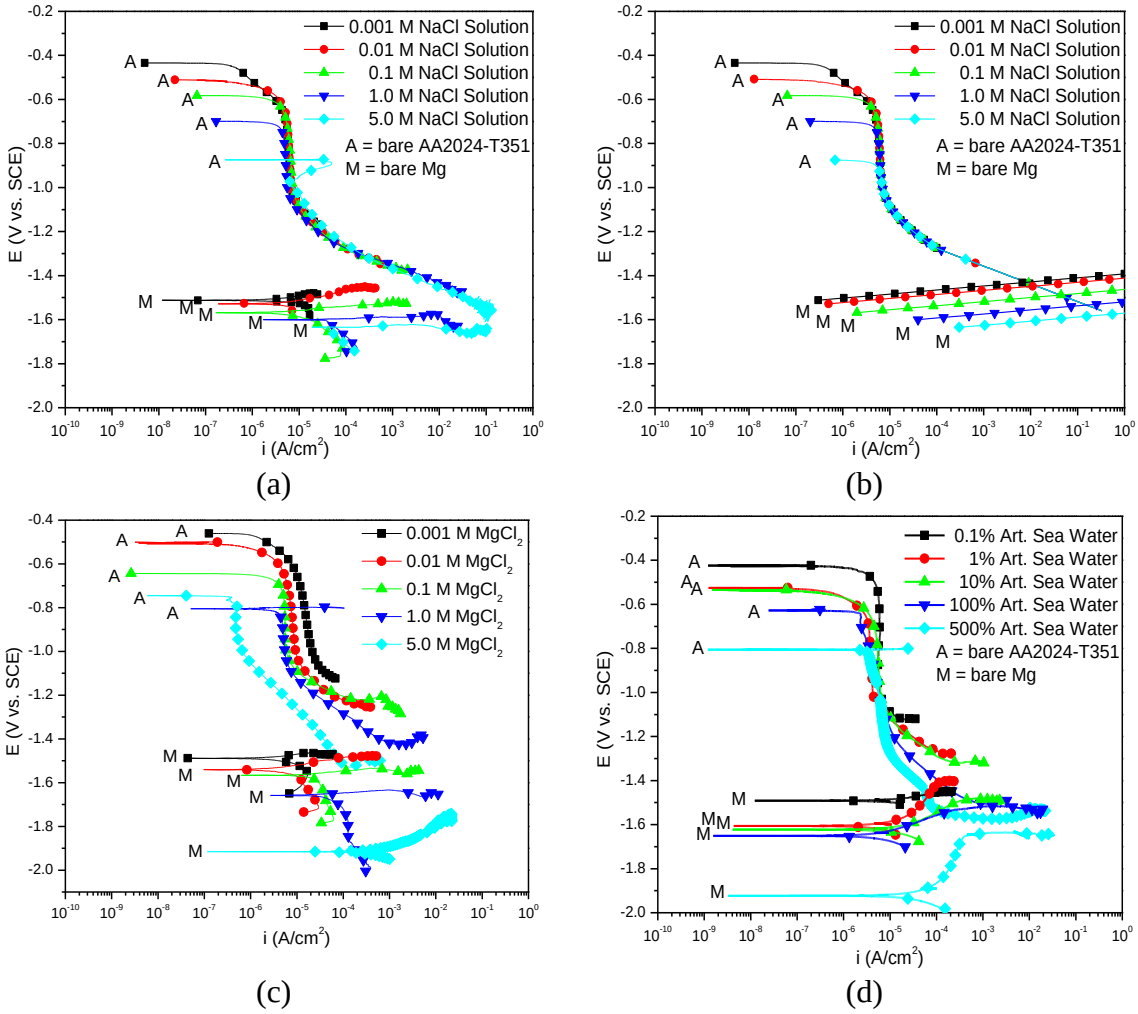

Figure 6.13. E-log(i) boundary condition data for bare high purity Mg and bare AA2024-T351 sheet in various concentrations of ambiently aerated NaCl solution utilized as inputs in finite element computational modeling. The E-log(i) data has been IR corrected. (a) experimentally obtained, full immersion polarization data in ambiently aerated NaCl solution (b) boundary conditions used for computational modeling in NaCl as fitted from a (c) experimentally obtained, full immersion polarization data in ambiently aerated $MgCl_2$ solution (d) experimentally obtained, full immersion polarization data in ambiently aerated ASTM Artifical Sea Water solution. The E-log(i) data has been IR corrected.

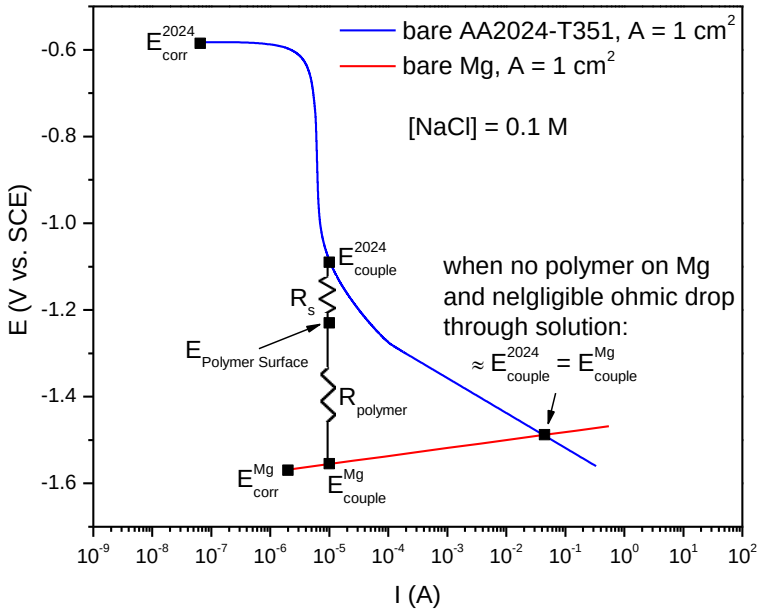

Figure 6.14. Mixed potential model depicting $E_{Surface}$ and E_{couple} as they pertain to a galvanic couple between AA2024-T351 and polymer coated Mg.

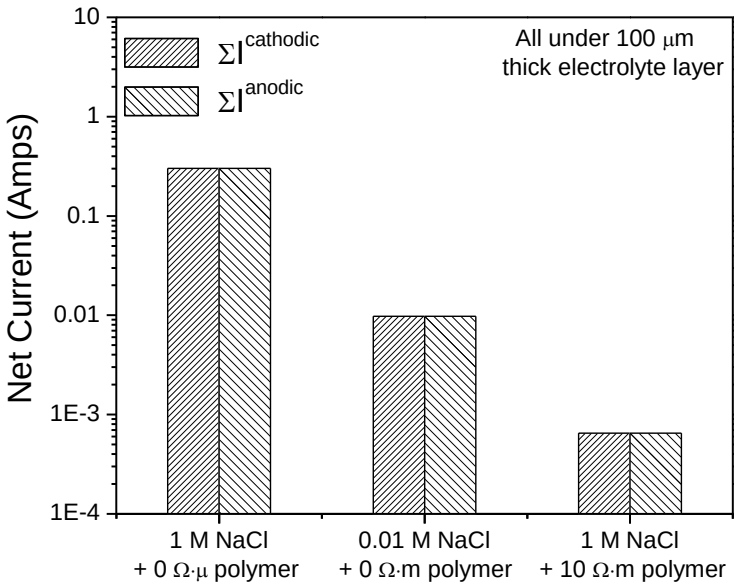

Figure 6.15. Comparison of net cathodic and anodic current from various configurations of a galvanic couple between AA2024-T351 and polymer coated 99.9% Mg as predicted by finite element computational modeling (COMSOL) under a 100 μm thick NaCl electrolyte layer
(a) under 100 μm of 1.0 M NaCl with no polymer covering the Mg (b) under 100 μm of 0.01 M NaCl with no polymer covering the Mg and (c) under 100 μm of 1.0 M NaCl with 10 $\Omega \cdot m^2$ polymer covering the Mg

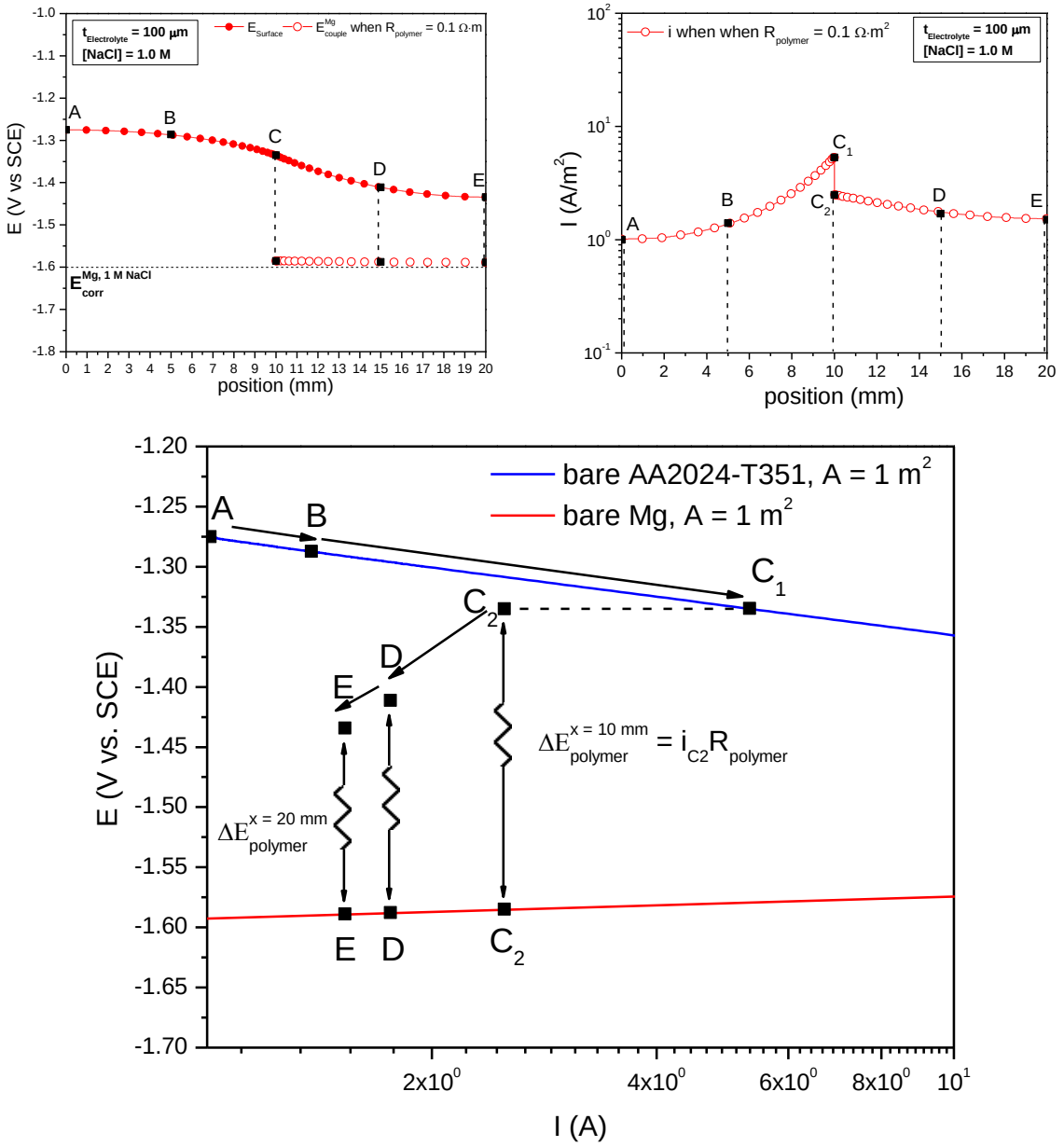

Figure 6.16. Mapping of finite element analysis potential and current distribution results to electrochemical boundary conditions presented on a mixed potential model of a galvanic couple between bare AA2024-T351 and polymer coated Mg.
Area of each electrode is assumed 1 m^2. Mg coated with a polymer of resistance 0.1 $\Omega \cdot m^2$ under a 100 µm thick electrolyte layer of 1.0 M NaCl solution. Assuming a 1 m deep sample geometry.

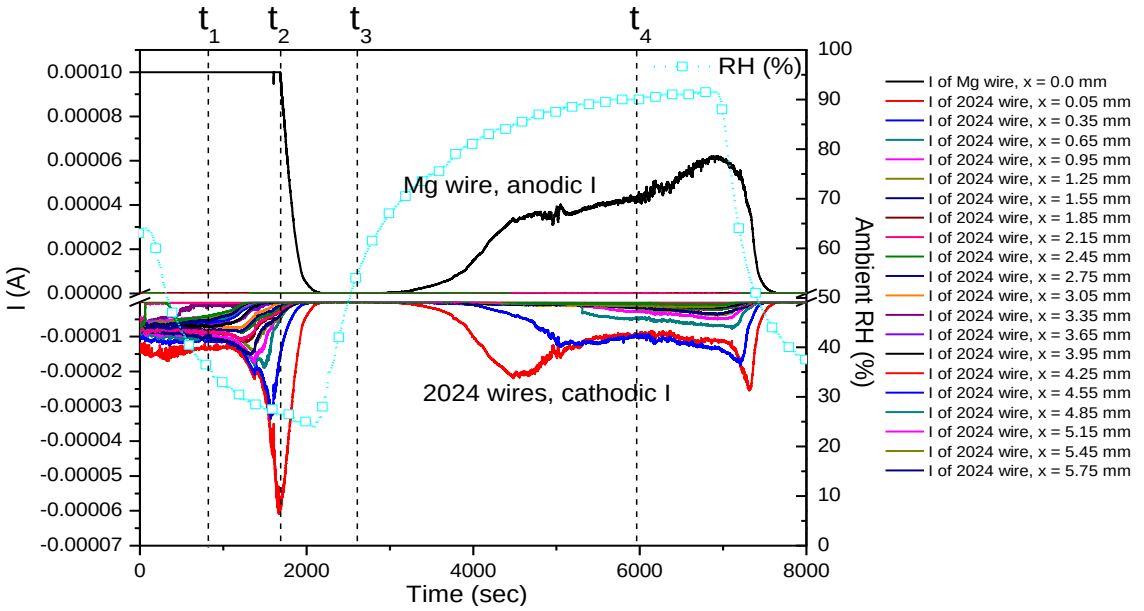

(a)

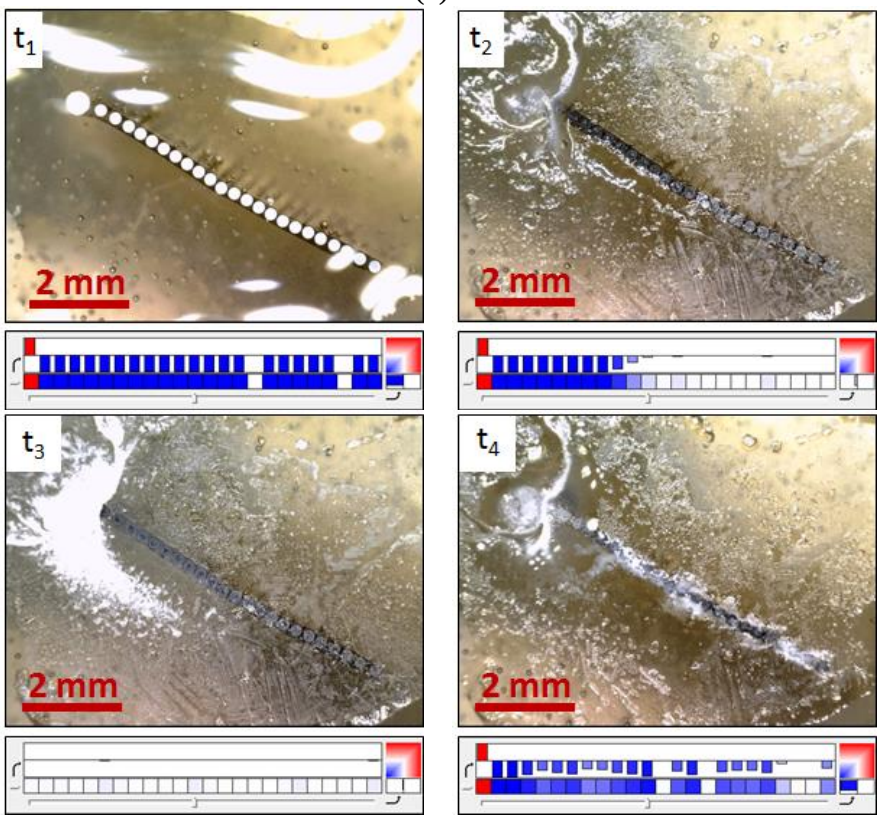

(b)

Figure 6.17. Current, RH, and time-lapse optical images of the bare Mg/AA2024-T4 microelectrode array during an episodic wetting and drying event under 0.9 M NaCl. In the color map dark red indicates an anodic current $\geq 1 \times 10^{-7}$ A and dark blue indicates a cathodic current of $\leq -1 \times 10^{-7}$ A. White color indicates a net current of zero.

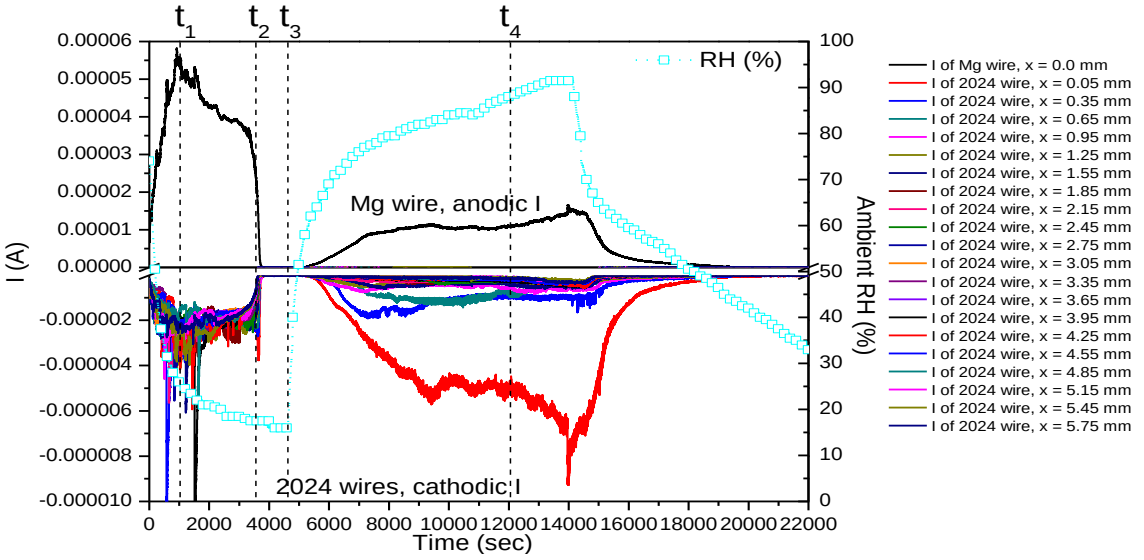

(a)

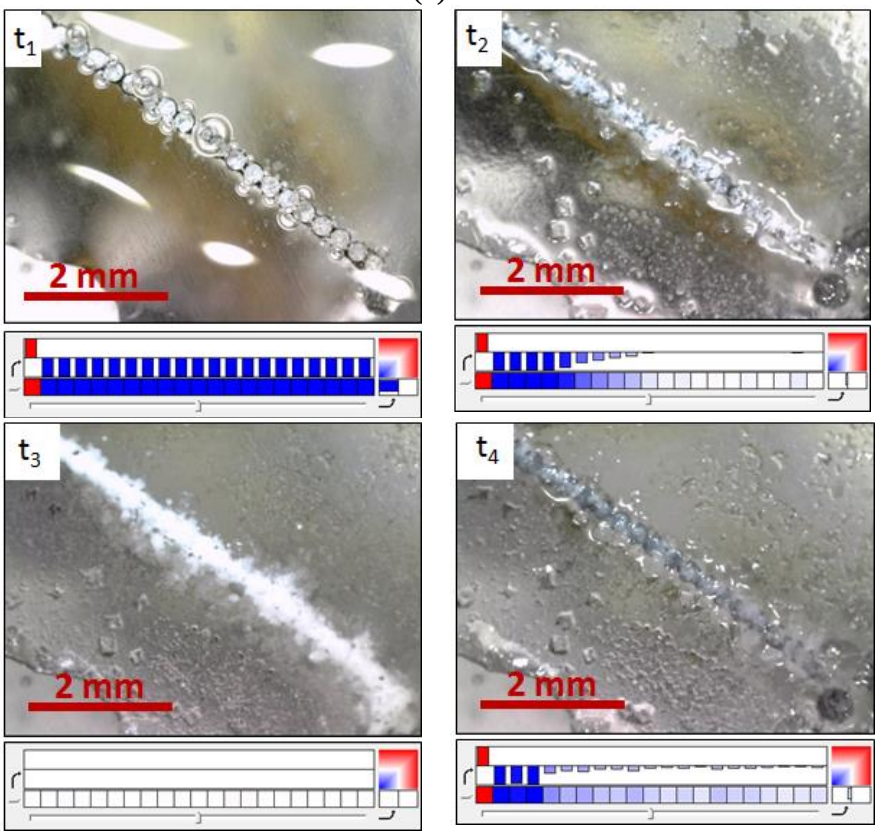

(b)

Figure 6.18. Current, RH, and time-lapse optical images of the bare Mg/AA2024-T4 microelectrode array during an episodic wetting and drying event under ASTM Artificial Sea Water. In the color map dark red indicates an anodic current $\geq 1 \times 10^{-7}$ A and dark blue indicates a cathodic current of $\leq -1 \times 10^{-7}$ A. White color indicates a net current of zero.

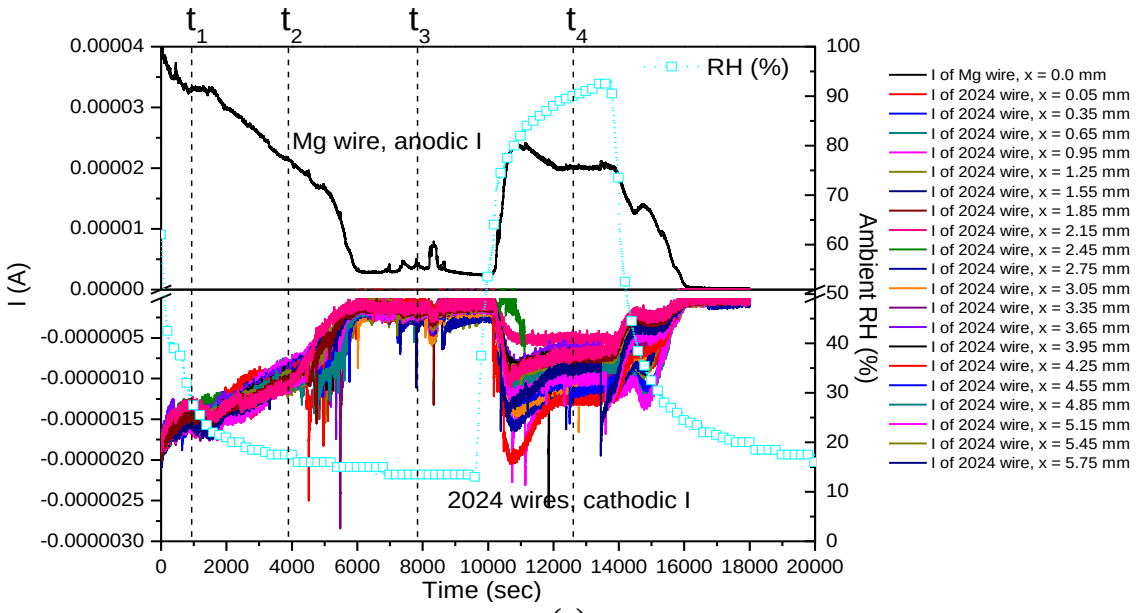

(a)

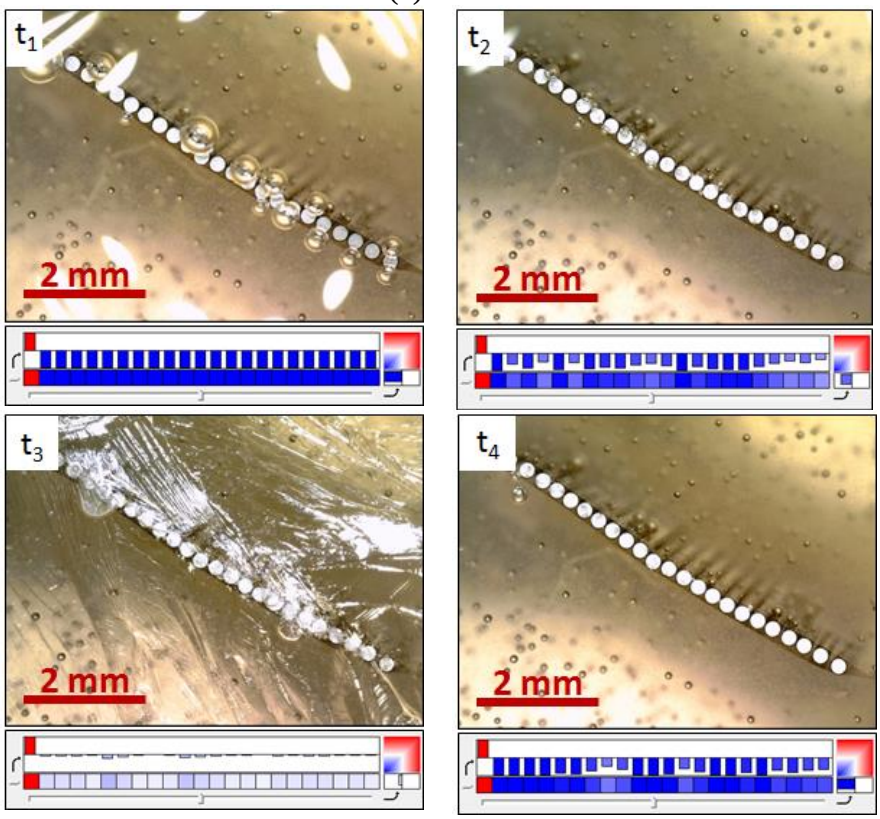

(b)

Figure 6.19. Current, RH, and time-lapse optical images of the bare Mg/AA2024-T4 microelectrode array during an episodic wetting and drying event under 0.6 M $MgCl_2$ solution. In the color map dark red indicates an anodic current $\geq 1 \times 10^{-7}$ A and dark blue indicates a cathodic current of $\leq -1 \times 10^{-7}$ A. White color indicates a net current of zero.

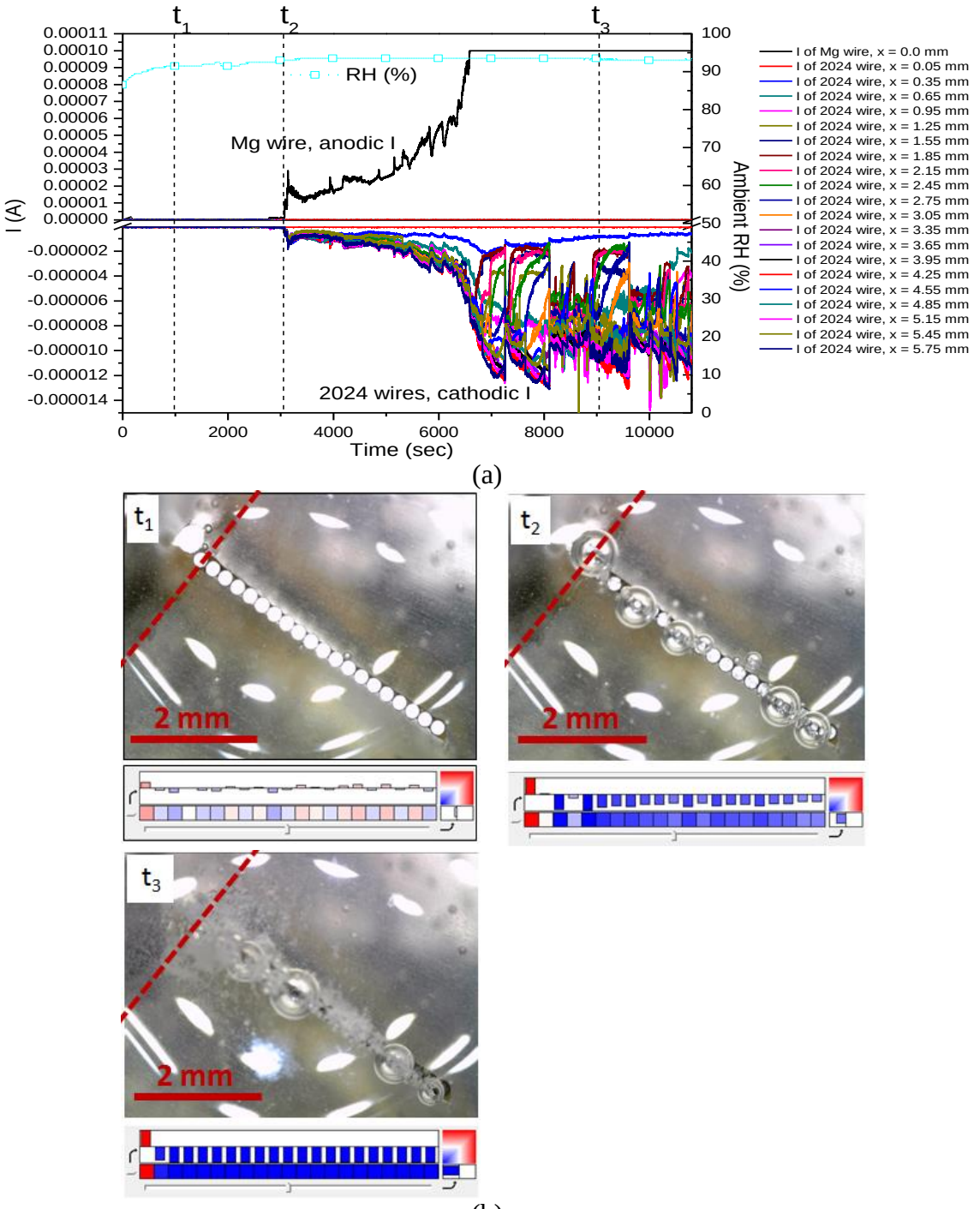

Figure 6.20. Current, RH, and time-lapse optical images of the polymer-coated-Mg/ bare AA2024-T4 microelectrode array exposed to 93% RH under 0.9 M NaCl solution. The polymer developed defect after t_2. In the color map dark red indicates an anodic current $\geq$ 1 x 10^{-7} A and dark blue indicates a cathodic current of $\leq$ -1 x 10^{-7} A. White color indicates a net current of zero.

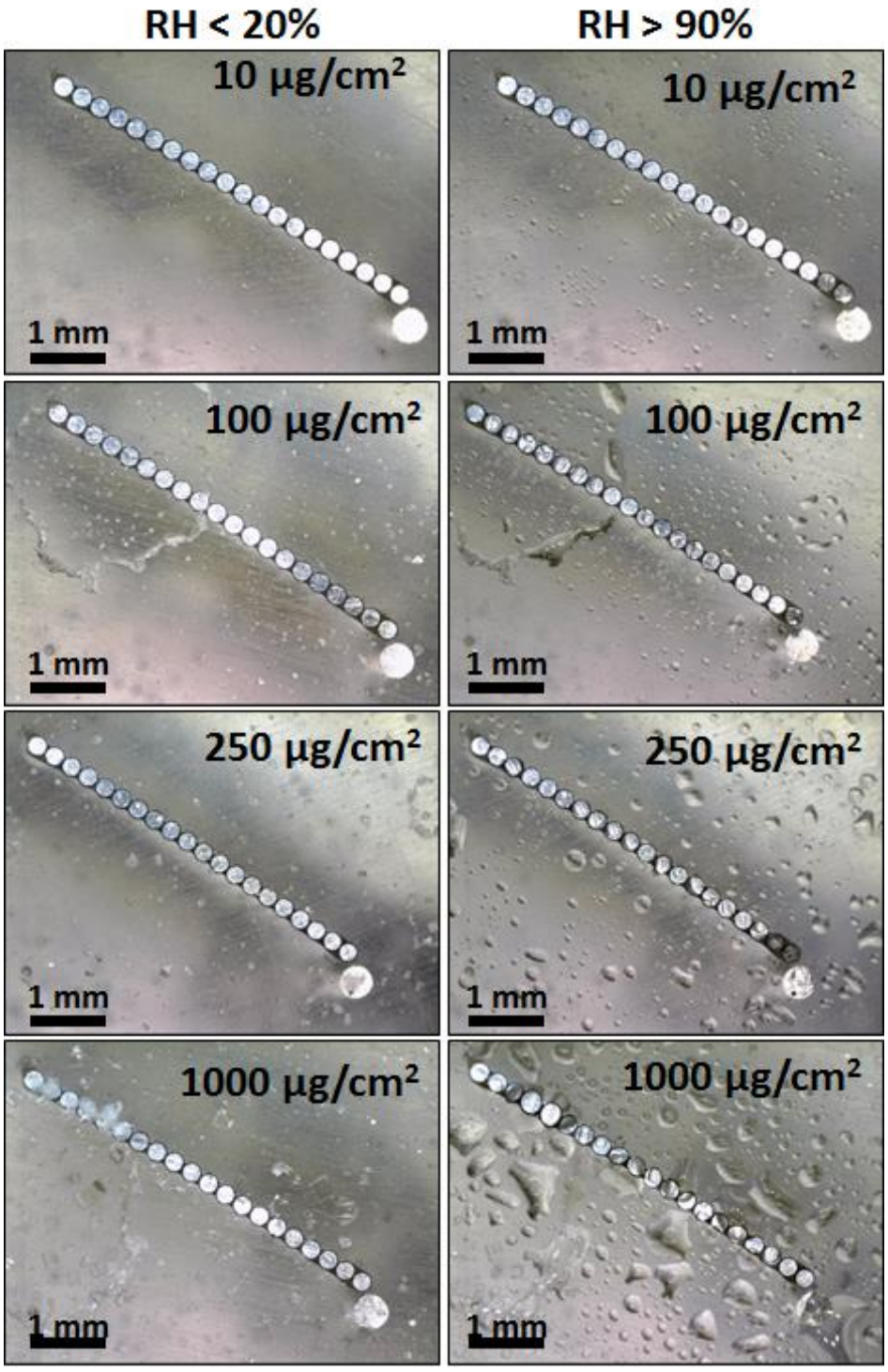

Figure 6.21.Optical micrographs of various deposition densities of NaCl on a microelectrode microelectrode array consisting of one 500 µm diameter 99.9% Mg wire and twenty isolated, 254 µm diameter AA2024-T4 wires in the dry (RH < 20%) and wet (RH > 90%) condition.

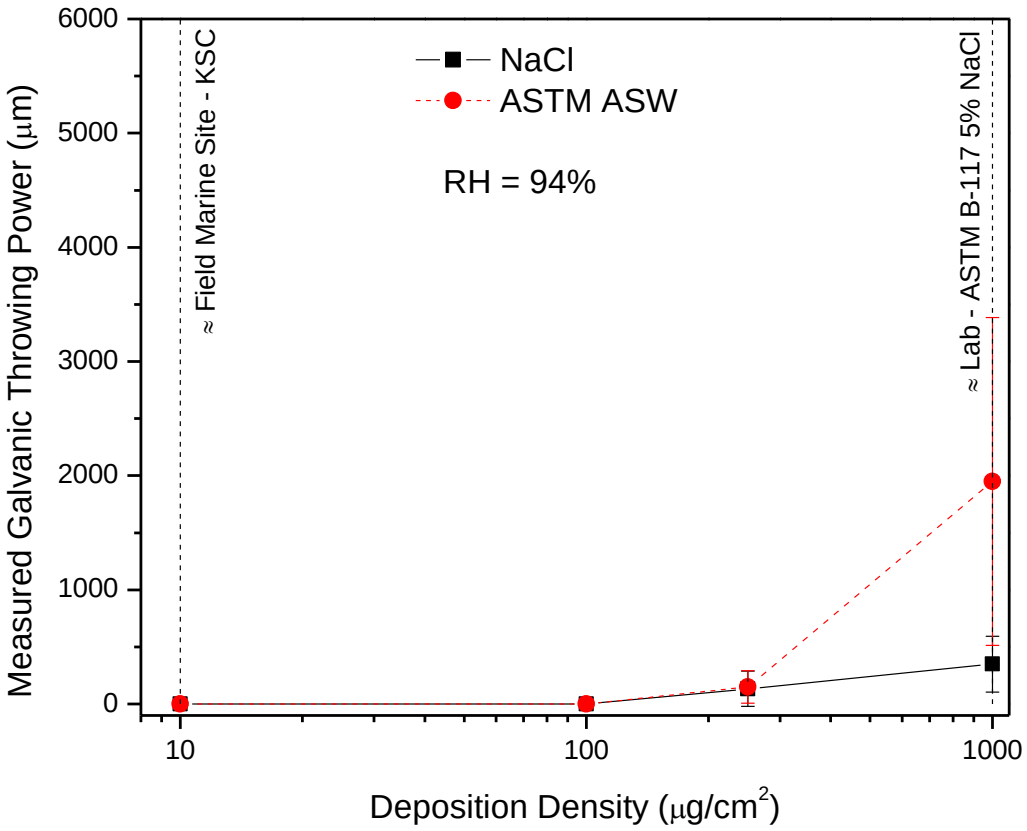

Figure 6.22. Observed throwing power of Mg under various deposition densities of NaCl and ASTM ASW applied via a spray bottle application method at equilibrium in 94% RH.

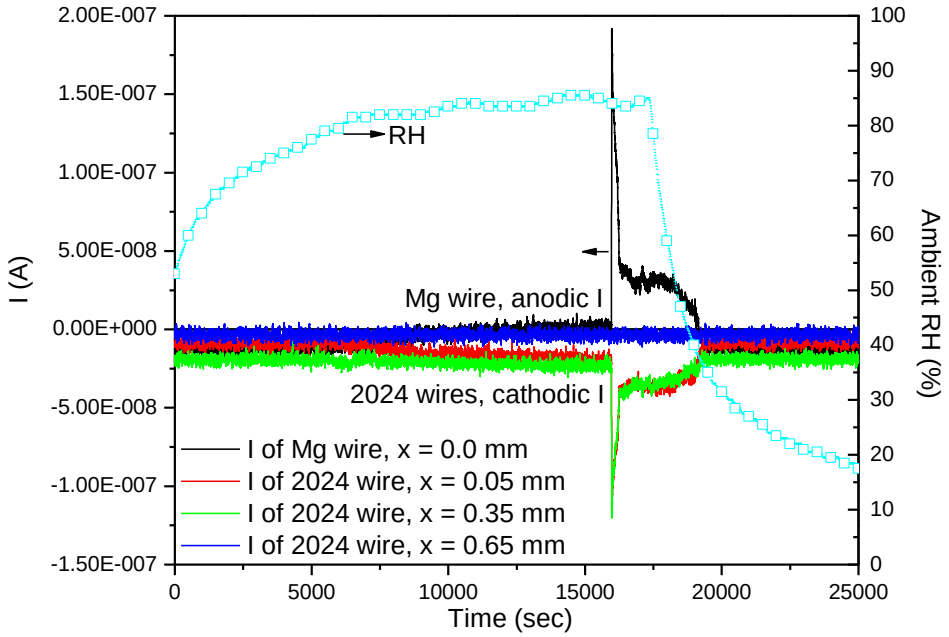

(a)

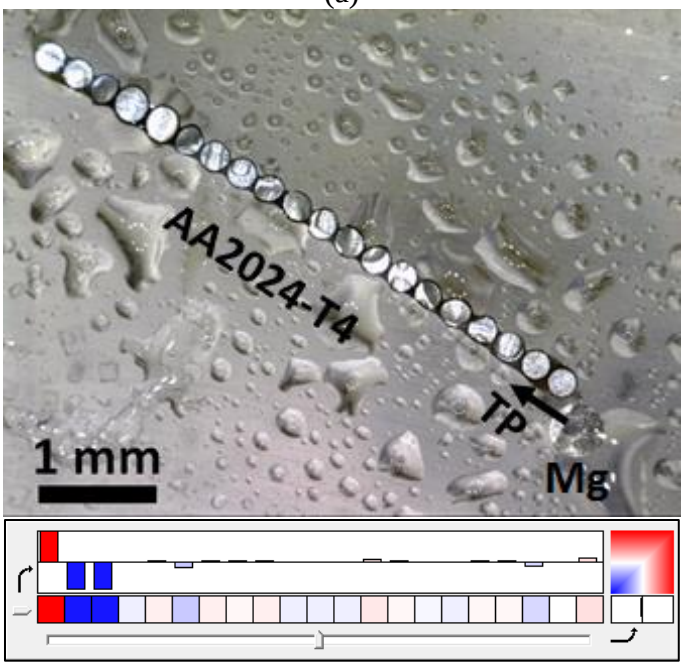

(b)

Figure 6.23. Current, RH, and time-lapse optical images of the bare-Mg/ bare AA2024-T4 microelectrode array with 1000 μg/cm^2 NaCl deposited by salt spray and allowed to equilibrate at 94% RH for at least 3 h. In the color map dark red indicates an anodic current ≥ 1 x 10^{-7} A and dark blue indicates a cathodic current of ≤ -1 x 10^{-7} A. White color indicates a net current of zero.

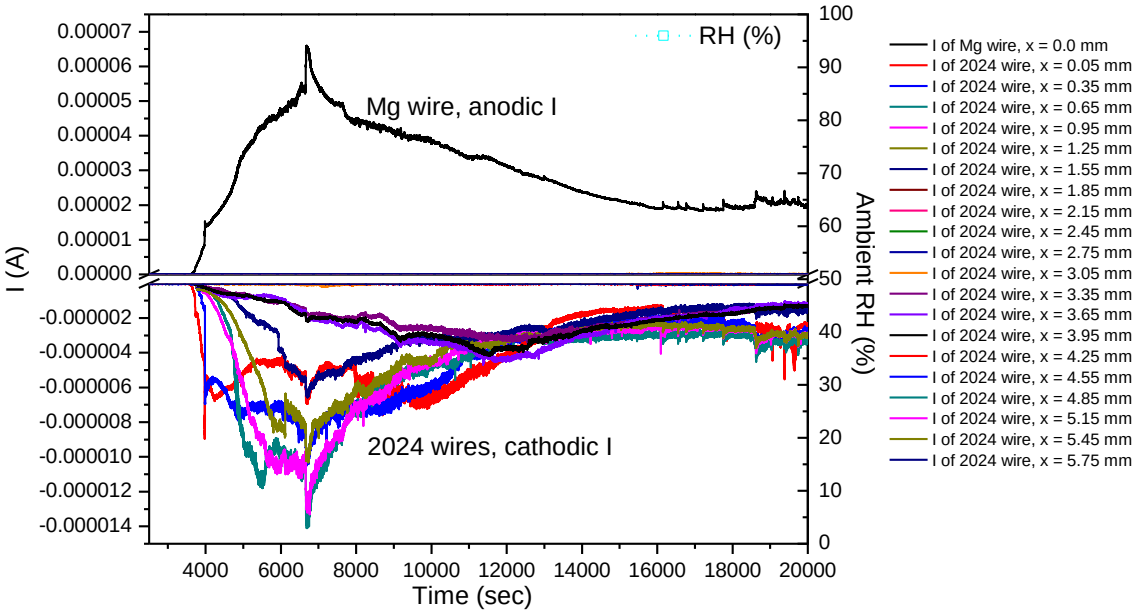

(a)

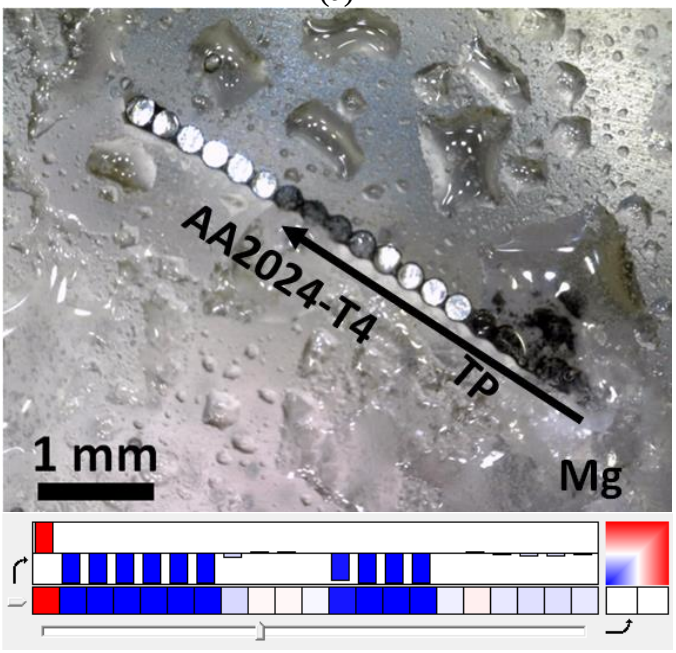

(b)

Figure 6.24. Current, RH, and time-lapse optical images of the bare-Mg/ bare AA2024-T4 microelectrode array with 1000 µg/cm^2 ASTM ASW salt deposited by salt spray and allowed to equilibrate at 94% RH for at least 3 h. In the color map dark red indicates an anodic current ≥ 1 x 10^{-7} A and dark blue indicates a cathodic current of ≤ -1 x 10^{-7} A. White color indicates a net current of zero.

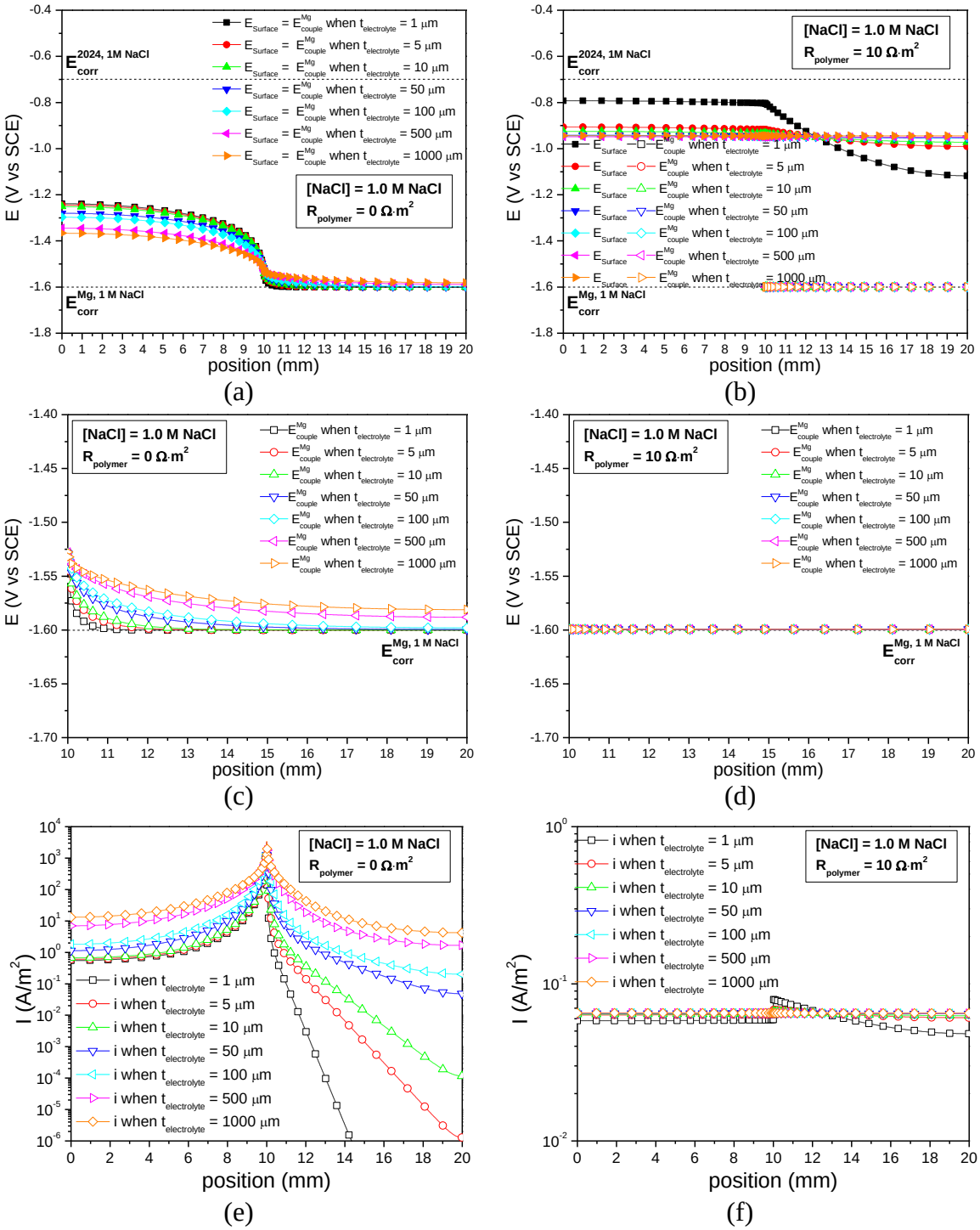

Figure 6.25. Potential ($E_{Surface}$ and E_{couple}) and current profiles over a galvanic couple between AA2024-T351 and polymer coated 99.9% Mg as predicted by finite element computational modeling (COMSOL) under 1.0 M NaCl electrolyte layers of various thickness with polymer layer resistances of (a, c, e) 0 $\Omega \cdot m^2$ (b, d, f) 10 $\Omega \cdot m^2$.

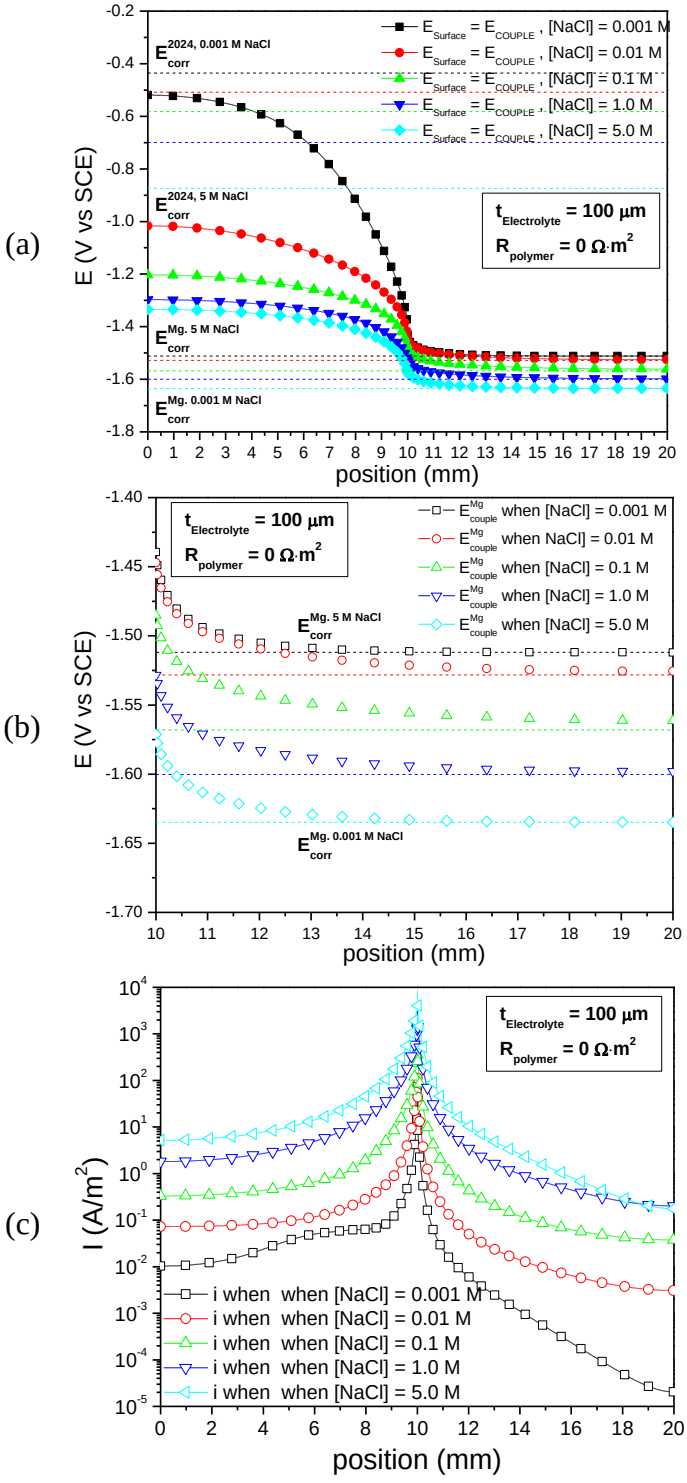

Figure 6.26. Potential ($E_{Surface}$ and E_{couple}) and current profiles over a galvanic couple between AA2024-T351 and polymer coated 99.9% Mg as predicted by finite element computational modeling (COMSOL) under a 100 µm thick NaCl electrolyte layer of varying concentration.

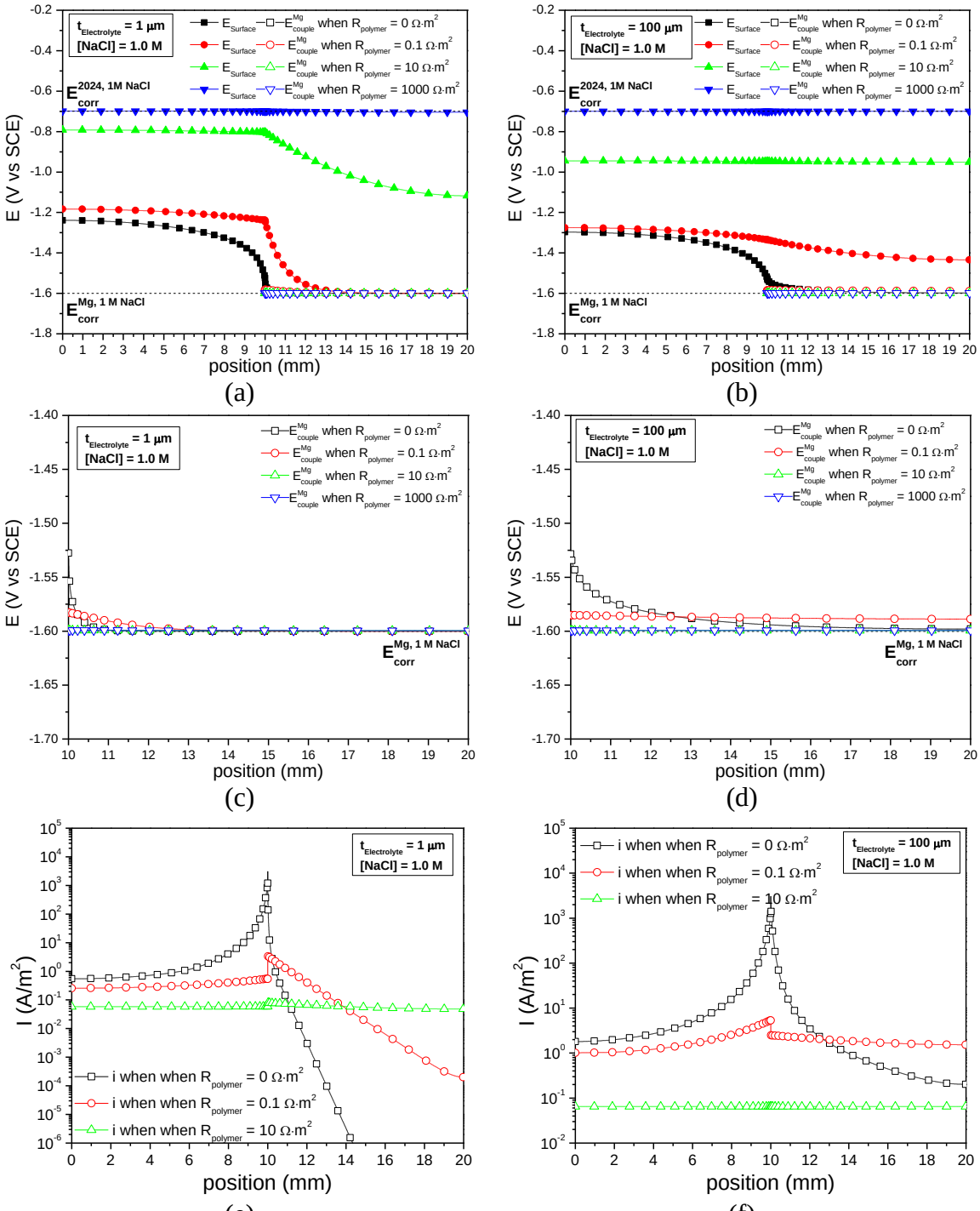

Figure 6.27. Potential ($E_{Surface}$ and E_{couple}) and current profiles over a galvanic couple between AA2024-T351 and polymer coated 99.9% Mg as predicted by finite element computational modeling (COMSOL) with various polymer layer resistances under 1.0 M NaCl electrolyte layers of thickness of (a, c, e) 1 µm (b, d, f) 100 µm.

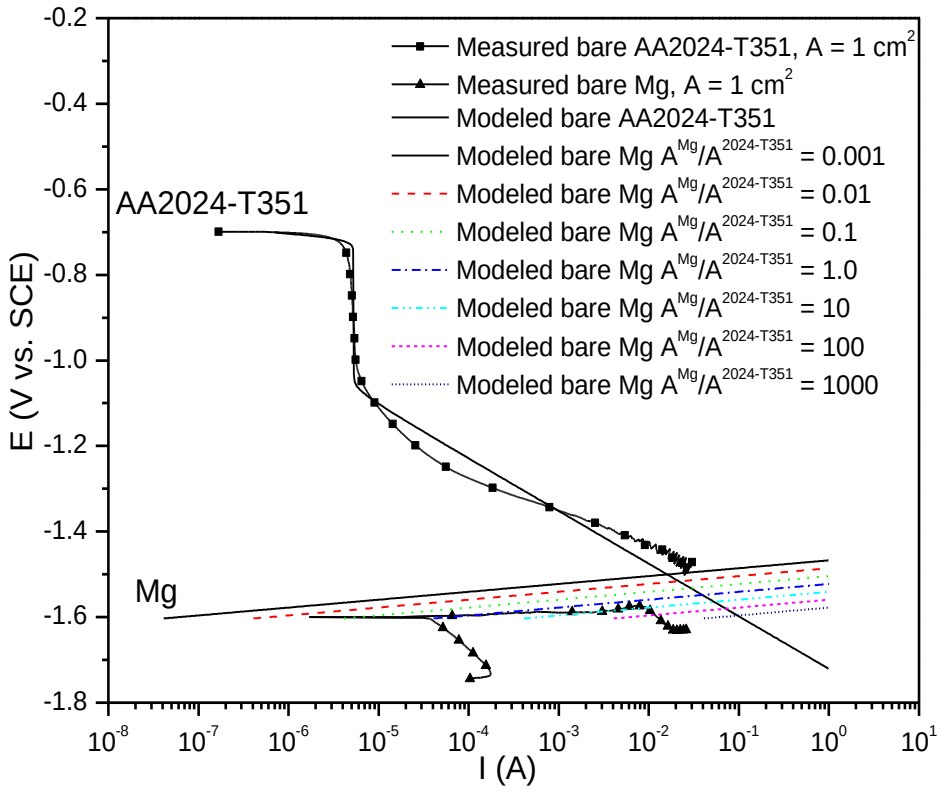

Figure 6.28. Mixed potential model of a galvanic couple between various area ratios of bare Mg to bare AA2024-T351 in 1.0 M NaCl solution.

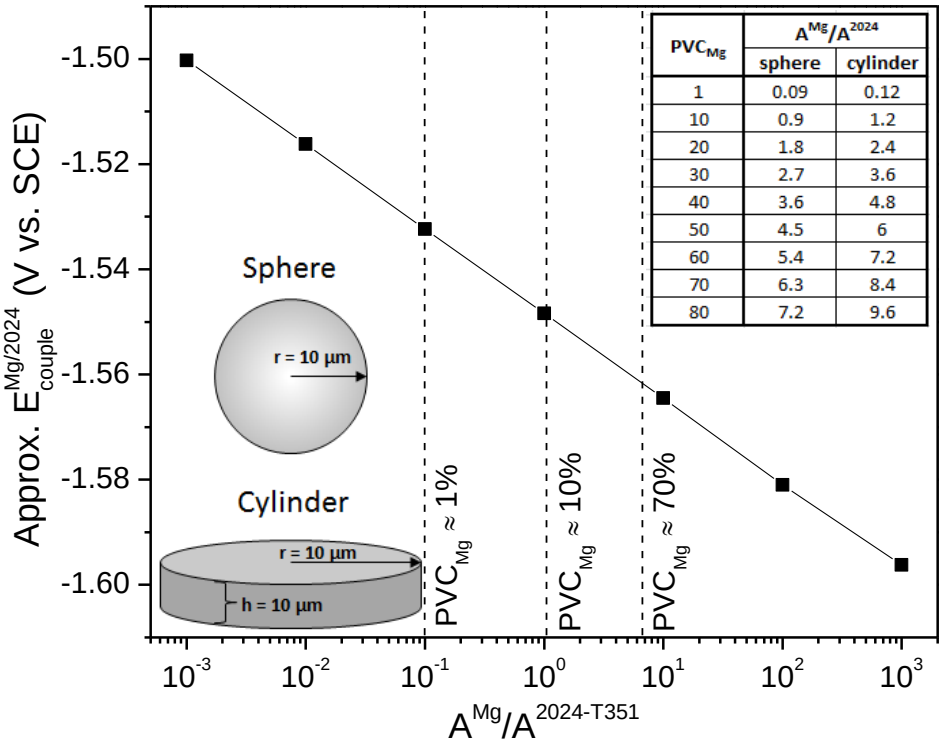

PVC_{Mg}	A^{Mg}/A^{2024}	
	sphere	cylinder
1	0.09	0.12
10	0.9	1.2
20	1.8	2.4
30	2.7	3.6
40	3.6	4.8
50	4.5	6
60	5.4	7.2
70	6.3	8.4
80	7.2	9.6

Figure 6.29. Approximate E_{couple} from mixed potential model between various area ratios of Mg to AA2024-T351 in 1.0 M NaCl solution relevant to a wetted PVC_{Mg} range of 1% to 70% assuming simplified Mg pigment geometries of a sphere or a cylinder and a 30 µm primer layer thickness and no polymer or voltage ohmic drop in solution.

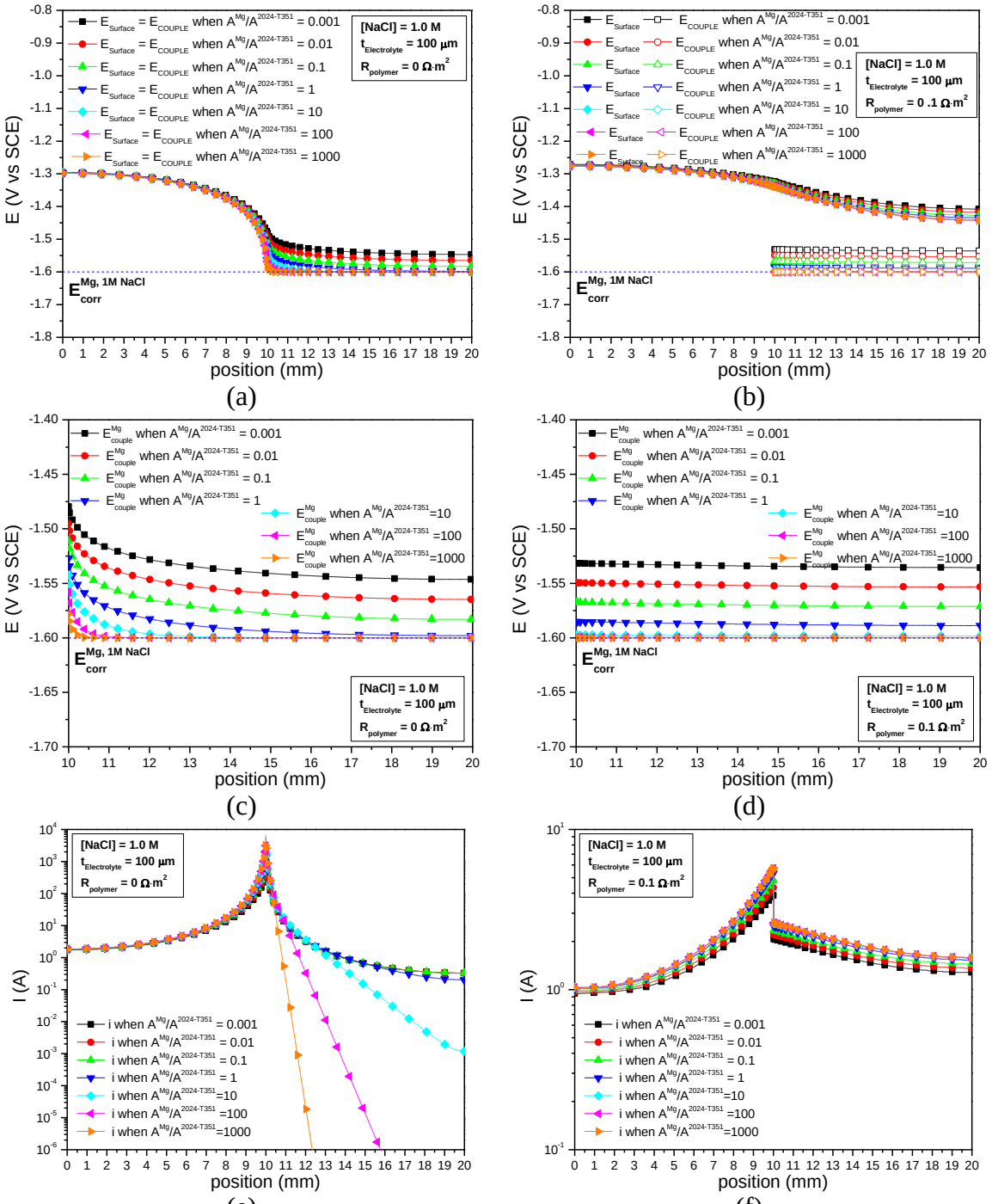

Figure 6.30. Potential ($E_{Surface}$ and E_{couple}) and current profiles over a galvanic couple between AA2024-T351 and various area ratios of polymer coated 99.9% Mg as predicted by finite element computational modeling (COMSOL) under a 100 µm thick, 1.0 M NaCl electrolyte layer with polymer layer resistance of (a, c, e) 0 $\Omega \cdot m^2$ (b, d, f) 0.1 $\Omega \cdot m^2$.

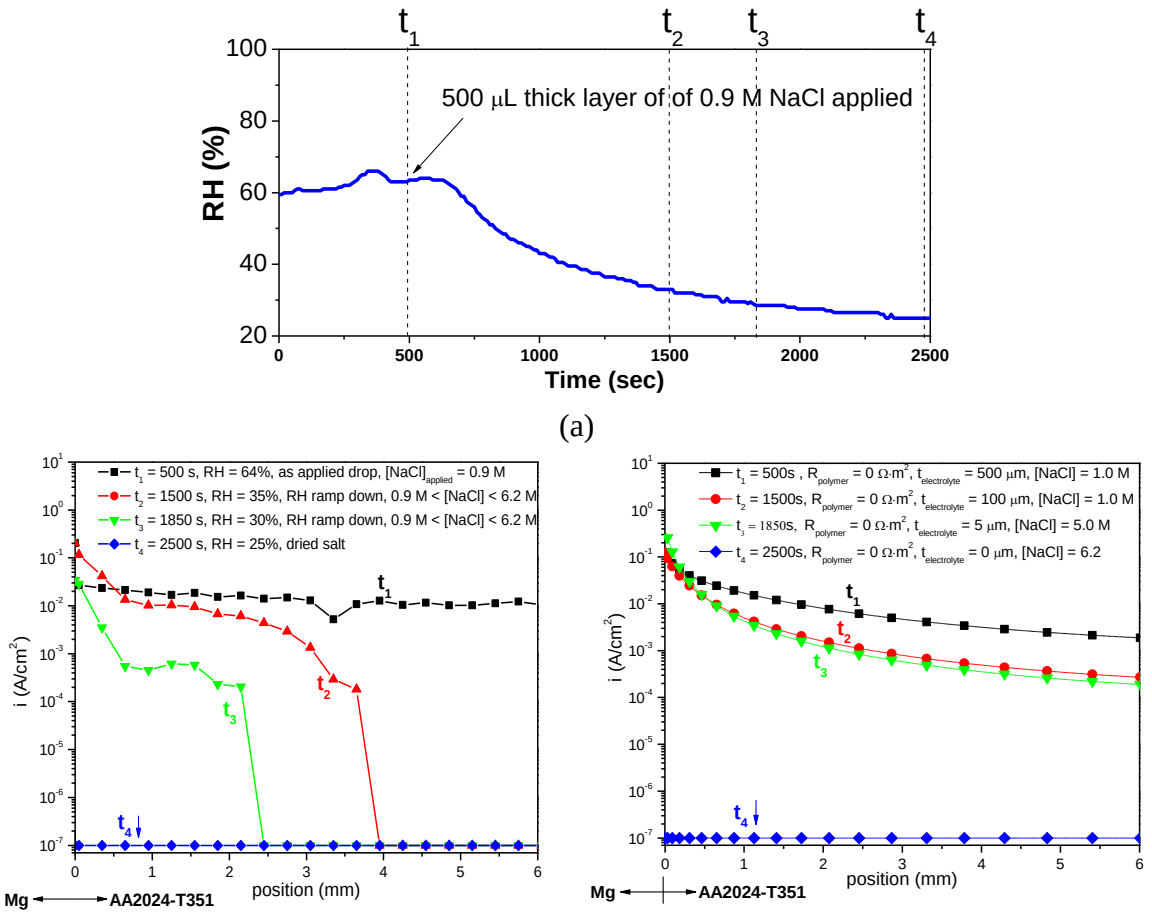

Figure 6.31. Comparison of select cathodic current profiles (over bare AA2024-T351) obtained experimentally from a microelectrode galvanic array and computationally from a finite element computational model of a galvanic couple between bare Mg and bare AA2024-T351. The Mg electrode is to the left of position zero.
(a) RH profile of exposure (b) current profile obtained experimentally from a microelectrode galvanic array and (c) computationally from a finite element computational model

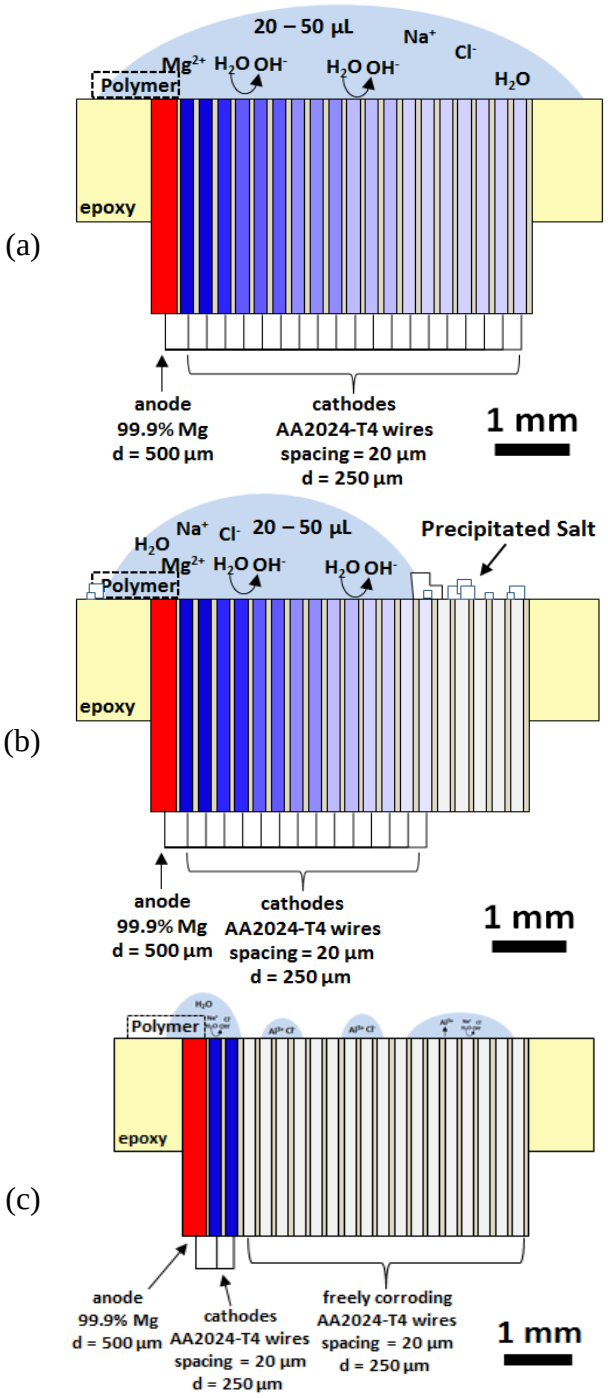

Figure 6.32. Hypothetical schematic depicting the galvanic couple interaction between microelectrodes in the Mg/AA2024-T4 array under (a) continuous (thin layer) and (b) drying (shrinking) continuous thin-layer and (c) discontinuous electrolyte (droplet) layer which can occur during re-wetting of deposited dried salts or droplet deposition.

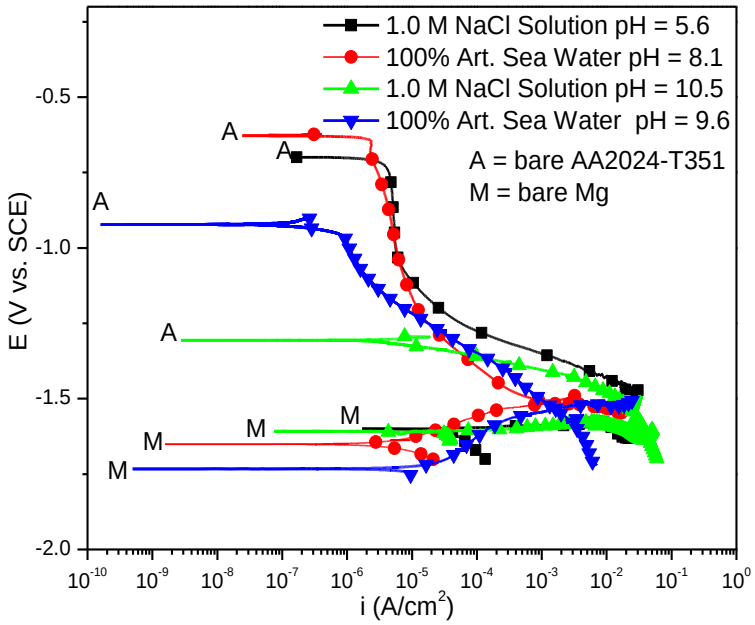

Figure 6.33. E-log(i) boundary condition data for bare high purity Mg and bare AA2024-T351 sheet in

7 Thesis Conclusions and Suggested Future Work

7.1 Conclusions

This work further validates MgRP as an emerging, promising technology to replace chromated corrosion inhibiting technology as a mitigation strategy for a precipitation hardened Al-Cu-Mg alloy. The primary sacrificial and barrier mechanisms of protection afforded to the AA2024-T351 substrate by the magnesium rich primer (MgRP) were demonstrated and investigated. When galvanically coupled to the substrate, the MgRP can afford couple potentials for sacrificial corrosion prevention of the AA2024-T351. This work provides information on the degradation process of the MgRP coating, with and without a topcoat, in various, relevant, field and lab environments and further shows that newer generation MgRP formulations tend to degrade predictably and reliably in the environments investigated in this study when used to protect Prekote pretreated AA2024-T351. The general degradation mechanism in LALT environments was similar to field exposures (except in acidified ASTM B-117 which is presented in Appendix B).

This work has further illuminated and verified test methods to assess MgRP that could be used in the laboratory and in the field and could also be applied to the characterization and performance on other substrates. Mg pigment depletion rate, galvanic protection potential and coating barrier properties were tracked throughout exposure periods in both field and laboratory accelerated life environments. Preliminary acceleration factors with

respect to pigment depletion and residual barrier properties were developed in field vs. lab exposures. Post-mortem characterization with SEM/EDS was conducted to elucidate coating and scribe morphology, corrosion products present, corrosion of the AA2024-T351 substrate, as well as in an attempt to determine the "galvanic throwing power" of the MgRP coating system based on cathodic protection of a scratch exposing bare AA2024-T351. The topcoat was observed to severely mediate the depletion of Mg pigment from the primer otherwise occurring due to high self-corrosion of unprotected Mg pigment in the MgRP. The Mg pigment was depleted monotonically in all environments but the differences in rate of Mg depletion from the coating and of polymer degradation, specifically resistivity, upon environmental exposure were rationalized to be traceable to from differences in time-of-wetness, Cl^- content, electrolyte acidity (pH), and UV exposure. Mg pigment was observed to deplete the fastest in field and lab environments with lowest pH levels and the barrier properties of the epoxy polymer were shown to severely degrade at sites which include UV radiation. A key result from these studies is that the newer generation coating formulations, with and without a topcoat, display consistent degradation characteristics in lab and field environments without blistering, albeit at different rates.

In addition to post-mortem sample evaluation, the galvanic throwing power of the MgRP was studied via finite element analysis modeling in conjunction with diagnostic multi-electrode arrays (MEAs), which enable the spatial distribution of cathodic protection to be elucidated in wet/dry conditions, under thin layers, or droplets. The galvanic protection capabilities of the coating in various full immersion, thin layer, and droplet

electrolyte geometries relevant to field service explain long misunderstood field behavior. Current and potential distributions extended across simulated defects when electrolyte layer was thick, continuous and more conductive (higher concentration) and in the absence of a polymer coating. Current and potential distributions did not extend across simulated defects when the electrolyte became discontinuous or the ionic path became tortuous due to drying or the addition of a polymer coating. Additionally, galvanic protection is shown to intensify during drying and re-wetting over short distances rationalized to be caused by changing solution conductivity, E-i behavior, and electrode area effects. The drying characteristics of individual salts was also shown to have an effect on the evolution of throwing power as $MgCl_2$ (due to its low deliquescence point of ~35% at STP) was shown to be less susceptible to drying at low RH, thus extending the time of which the galvanic couple was active compared to pure NaCl or ASTM Artifical Sea Water.

Significant insight into the corrosion mechanisms of pure Mg regarding valence state and the so called “negative difference effect” were illucidated in this work. Full immersion polarization tests, in corroboration with multiple independent measurement techniques, of the dissolution of bare, commercially pure Mg at open circuit as well as under anodic polarization support the notion that Mg is primarily oxidized to Mg^{+2} in saline solutions. This issue was hotly debated in the literature and these findings provided significant clarification for the corrosion community. An important clarification highlighted in these studies is that the applied current measured on the Mg anode by traditional electrochemical techniques accurately accounts for the current available for protection of

the AA2024-T351 cathode, and is appropriate to use as E-i electrochemical boundary conditions for mixed potential and finite element modeling of the galvanic couple and throwing power of the MgRP system. Also, this clarifies the charge capacity present in MgRP at various pigment loadings. Moreover, in order to accurately predict the physical depletion of the Mg anode material from the MgRP coating, the actual anodic dissolution behavior was characterized.

7.2 Suggested Future Work

7.2.1 Suggested Future Work to Study Effects of Various AA2024-T351 Pretreatments

This project does serve to provide some information on the degradation process of the MgRP coating in various, relevant, field and lab environments and further shows that newer generation MgRP formulations tend to degrade predictably and reliably in the environments investigated in this study when used to protect Prekote^{TM} pretreated AA2024-T351. This project has illuminated test methods to assess MgRP that could be used in the laboratory and in the field and could be applied to the characterization and performance on other substrates (such as 5XXX or 7XXX) or over other pretreatments (such as conversion coatings or anodizations). Should MgRP be employed on other substrates, pretreatments or in a significantly different environment, variations in degradation (still yet unknown) may occur. In service, there is an interest by end-users to apply Mg-rich primers above many different pretreatments or conversion coatings, which

are more resistive in nature than Prekote™. The addition of such resistances into the coating system stackup is presumed to mediate the sacrificial galvanic protection function afforded by the MgRP. Very little is reported in the literature about the performance or function of an MgRP above resistive pretreatments and conversion coatings that might add resistances to the galavanic couple scenario. This topic remains an area of significant need to the DoD, corrosion, and aerospace communities. Future work conducted by fellow researchers at UVa will study the effects of utilizing MgRP for the corrosion protection of AA2024-T351 over various pretreatments other than Prekote™. Exmaples include chromate conversion coatings (Alodine 1200s or Surtec 650) and anodization with and without sealing.

7.2.2 Suggested Future Work to Further Develop Field Deployable Assessment Capabilities

This work demonstrates a suite of field deployable electrochemical and characterization techniques which can be used to track coating degradation with respect to Mg pigment depletion rate, global galvanic protection potential and coating barrier properties throughout exposure periods in both field and laboratory environments. These include standoff methods in air such as XRD and electrochemical methods that require a cell or conductive tape leads. Should the decision be made to deploy a MgRP coating system on a DoD or commercial asset based on other information such as more extensive field exposures, a field deployable XRD method for remaining Mg pigment assessment and

field deployable electrochemical assessment tools should be deployed and would be ready to pursue in follow-up research with the goal of deployment of a portable unit. Commercial, portable XRD units are available mainly for residual stress measurement. The DoD and industry should consider the pursuit of a field deployable device made available to repair depo facilities through the issuance of an SBIR program to build, or otherwise acquire and demonstrate a field deployable instrument. After this is done, we recommend conducting remaining lifetime assessments of MgRP exposed in the field, corroborate the residual MgRP assayed by other means and develop calibration standards that can be used to accompany field measurements. Calibration standards would be necessary for quantitative measurements with different topcoat thicknesses.

7.2.3 Suggested Future Work to Improve Corrosion Properties of Mg Pigment

In light of recent advancements in Mg-alloy development and the improved corrosion resistance of such materials compared to commercially pure Mg, there exists an opportunity to develop an “advanced life” MgRP which utilizes a corrosion resistant Mg alloy as pigment. In this way, the self-corrosion rate of the pigment would be lowered so that the anode capacity would not be depleted as quickly. Improving the corrosion performance of the Mg pigment, while maintaining a sufficient electrochemical driving force for cathodic protection, would serve to prolong the lifetime of both the sacrifical cathodic protection and the barrier protection function afforded by the MgRP. It is suggested that the development of an improved primer pigment be explored in future

work. Several ideas include inhibition of the cathodic reaction, but leaving the anodic kinetics unaltered. Alternatively, anodic kinetics could be slowed. Moreover, the primer polymer could be altered to include a conductive polymer to decrease the electrical resistance between pigment particles while continuing to serve as a suitable barrier to self-corrosion. These options should be considered in the throwing power model to understand the ramifications for protecting a scribe or scratch.

7.2.4 Suggested Future Work to Improve Microeletrode Galvanic Array and Finite Element Computational Modeling

The microelectrode galvanic array and finite element computational modeling both proved to be extremely useful tools in helping to examine the galvanic throwing power of a simulated MgRP / AA2024-T351 system across a simulated planar defect (scribe). These tools allowed for the study of how specific variables, such as electrolyte layer thickness, chemistry, or polymer layers play a role in dictating the galvanic throwing power of Mg over AA2024-T351 in a geometric scenario designed to simulate the bare AA2024-T351 perpendicular to the scribe length on a typical test panel. However, there are many improvements which could be made to both the microelectrode array and the finite element computational model that would improve the correlation to real environmental exposure.

The microelectrode array could be designed to be more analogous to the real MgRP/AA2024-T351 system if the microelectrodes were embedded in AA2024-T351 sheet instead of mounted in epoxy polymer or an MgRP-coated AA2024 electrode could be utilized in place of the Mg electrode. Additionally, a finer scale printed circuit board or a miniaturized microelectrode array would allow for more precise measurement under lower salt deposition or lower RH scenarios where the throwing power may be smaller than the 50 μm limit studied here. Moreover, it would be useful to simultaneously track the real-time electrolyte concentration over the microelectrode galvanic array throughout an environmental exposure. This could be accomplished by monitoring the electrochemical impedance between two close spaced electrodes added to the array.

The finite element computational model could be made more robust by including the consideration of evolving electrolyte chemistry and electrolyte geometry. For example, in the MgRP/AA2024-T351 system, when Mg pigment corrodes, the the electrolyte becomes saturated with $Mg(OH)_2$. When this occurs the pH rises locally and can reach values as high as 10.5. This will have a dramatic effect on the electrochemical boundary conditions of the AA2024-T351 and Mg electrodes. Additionally, the increased hydrogen evolution at sites of cathodic polarization can produce hydrogen bubbles. These hydrogen bubbles are a source of IR drop through the electrolyte layer. Such affects were not accounted for in this work and would prove valuable in furthering the predictive capabilities of the model. Additionally, the lack of ability of the model to predict the shrinking of the geometric boundary of a droplet as it dries is highlighted in Figure 1.31. As an electrolyte layer dries during an atmospheric exposure, not only does the layer thin

but the geometric boundaries of the electrolyte layer shrink as the surface tension of the electrolyte draw the edges of the shrinking droplet inwards. To date, only a uniform electrolyte layer was considered in the model. This change in geometric boundaries causes the ionic pathway between the outermost microelectrodes to be cut off and the observed throwing power to be limited to within the geometric boundaries of the droplet. Similar geometric boundary effects occur when isolated droplets are deposited or form from deliquesced salts on the surface of the coating during environmental exposure. A valuable addition to the model would be the ability to predict and account for this changing electrolyte geometry.

8 APPENDIX A: Blistering Phenomena in Early Generation Mg-Rich Primer Coatings on AA2024-T351 and the Effects of CO_2

UPDATE Jan. 1, 2014: This chapter represents a brief study into the origins of blistering phenomena and the effects of increased CO_2 levels during environmental exposure of early-generation MgRP systems. This work was presented at the 2011NACE DoD Conference in Palm Springs, CA as questions remained in the DoD community about performance discrepancies of early generation MgRP products in lab and field environments. In light of the improved, more uniform performance of newer generation commercial products, this topic was not pursued further.

8.1 Abstract

Two different types of coating blistering on the coating system AA2024-T351/PreKote™/MgRP/with or without Aerodur 5000 Topcoat occurred in early generations of MgRP exposed in ASTM B-117 laboratory tests but are not typically seen during exposures in the field at sites such as Daytona Beach, FL [1-3]. The most common type of blistering on AA2024-T351 was observed to occur proximate to scribe lines and is characterized by large blisters underneath the primer and topcoat layers of the coating system. The blisters are shown to form over thick, relatively uniform layers of aluminum corrosion product. This type of blistering is shown to be caused by anodic coating disbondment through an anodic undermining mechanism aided by H_2 generation and modest coating adhesion. A second type of blistering, or rupturing, was observed to occur

more randomly over the coated surface and is characterized by small pinholes that penetrate deep into (or in some cases through) the AA2024-T351 substrate. This type of blistering or "rupturing" is shown to be caused by localized cathodic (or basic) corrosion of the AA2024-T351 substrate triggered by a local rise in solution pH. This rise in pH can be due to increased cathodic reaction rates on the surface of the Al substrate due to severe cathodic polarization of the AA2024-T351 and/or the formation of $Mg(OH)_2$ at sites of Mg pigment dissolution which when dissolved in an aqueous environment has an equilibrium pH of approximately 10.5.

The effect of increasing the CO_2 concentration, from ambient levels of 400 ppm to concentrations of 5000-6000 ppm, on the occurrence of each blistering phenomena was also studied. Elevated concentrations of CO_2 in the exposure environment suppress the occurrence of each type of blistering by different but related mechanisms. CO_2 does not substantially affect the depletion rate of the Mg pigment in the coating during an environmental exposure. The CO_2 effect does not explain the high severity of the ASTM B-117 lab exposure which is believed to be due to high time of wetness and chloride levels.

8.2 Introduction and Background

There has been significant interest in an organic coating system containing a Mg-pigmented organic primer (MgRP) on precipitation age hardened Al alloy 2024-T351 as well as others [4-9]. Other alloys of interest include AA7075-T6, AA2219-T87, and AA2024-Alclad [1, 2]. One such AA2024-T351/Mg-rich coating system is comprised of AA2024-T351 sheet pretreated with Prekote© surface pretreatment, a 30-40 μm primer

layer of magnesium rich primer with a Mg pigment volume concentration (PVC) of 45% and a 50-60 μm thick topcoat of high performance advanced life polyurethane coating. The Mg-rich primer consists of a 1-part epoxy matrix with Mg metal flake pigment with an average diameter of 20 μm. The high performance topcoat is a two-component polyurethane topcoat developed for military applications in a variety of exposure environments.

This system has been proposed as a candidate coating system to replace chromate type surface pretreatments as well as chromate pigmented primers [4, 10, 11]. One of the corrosion inhibition mechanisms, afforded by the MgRP, has been shown to be sacrificial anode based cathodic protection of the aluminum alloy [5-7, 12-15]. The MgRP is designed to galvanically couple the metallic Mg pigment in the primer to the substrate and provide sacrificial anode based cathodic protection to the aluminum alloy (AA2024-T351). This concept has been successful in the design of zinc-rich primers for use on various steels which have been used for decades in the field [12, 16-31]. Protection by these Zn-rich primers is afforded primarily by sacrificial anode based cathodic protection and secondarily by precipitation of $Zn(OH)_2$ at bare sites after migration of Zn^{+2} [25, 26]. Zinc also has a low self-corrosion rate. In this case, magnesium is also less noble than almost all of the precipitation age hardened aluminum alloys it might be used to protect and is readily available and actively corrodes in most electrolytes [6, 9, 32]. Alclad™ also protects by sacrificial cathodic protection but pits locally and thus is an inefficient anode [33-36]. When coupled to the AA2024-T351 substrate, the Mg pigment becomes an electron donor, and mixed potential theory can be used to explain the galvanic couple potential of the system

when exposed to full immersion. Results support the notion of mixed potential theory describing the galvanic coupling behavior of the primer and substrate [3, 5-9, 12, 32, 37]. Mediation of cathodic protection level is aided by resistive layers associated with pretreatments, epoxy resin or polymer type, PVC, and topcoat [12].

In an effort to gauge performance in a short term test for this coating system, in terms of ability to afford protection, accelerated laboratory cabinet testing has been conducted [3, 37-39]. Interestingly, there are often differences in corrosion behavior of the MgRP between field and laboratory environmental exposures, at least in early generations of commercial products. For example, in ASTM B-117 exposures, scribes through topcoated MgRP systems, exposing AA2024-T351, exhibit noticeably more corrosion product when compared to the relatively clean scribes on samples exposed at Daytona Beach, FL and more benign environments. Moreover, blistering of the coating system is sometimes seen in ASTM B-117 laboratory tests but is typically not seen in field exposures such as at Daytona Beach or Kennedy Space Center [1, 2]. Therefore, it is important for us to understand this blistering phenomenon in order to predict whether it will be seen in any field environments as well as to reassess the relevancy of the ASTM B-117 test to field conditions.

In the lab, two, distinct types of blisters have been observed on the MgRP coating system; each is discussed in this publication. The most common type of blister is shown to be caused by a localized failure of the MgRP to provide adequate local sacrificial anodic protection of the underlying Al substrate. This may be due to a localized depletion of Mg in the primer or simply an area of delamination of the coating system proximate to

a scribe line which can support cathodic reactions. This delamination is also aided by poor adhesion of the polymer organic coating. This lack of protection leads to anodic coating disbondment aided by H_2 gas produced by Al dissolution, is more prevalent in MgRP lean or non-MgRP organic polymer coatings, and the formation of blisters along the defect or scribe [40, 41]. These blisters are characterized by large, round areas of delamination over top of thick, relatively uniform layers of aluminum corrosion product associated with shallow penetration.

A second, much less prevalent type of blister is shown to be caused by a local increase in solution pH due to the corrosion of the Mg pigment and/or increased cathodic reaction rates at sites of severe cathodic polarization of the Al substrate. The local rise in pH results in basic, or cathodic corrosion of the underlying Al substrate due to its amphoteric nature [42-47]. This type of attack is characterized by narrow, deep pinholes which penetrate into the AA2024-T31 substrate. The observation of these performance differences between exposure environments is presumed to stem from fundamental differences in time of wetness, chloride concentration, and ambient CO_2 levels.

It has been shown in the past that CO_2 acts to reduce the cathodic reaction rates on aluminum alloys with Cu-rich secondary phases acting as cathode sites [48]. This is accomplished by minimizing Al dissolution such that a defect free Al oxide is formed without Cu-rich ligaments which could support cathodic reactions. This passivation of cathodic sites leads to more uniform corrosion of the aluminum alloy and a reduction in pitting. Moreover, the presence of high concentrations of CO_2 may also act to prevent cathodic corrosion of the aluminum alloy by moderating the pH at the surface of the alloy

since the equilibrium pH of CO_2 sparged NaCl solution at 1 atm. partial pressure is 4 [48]. It has also been proposed that high CO_2 concentrations will result in the formation of dense magnesium carbonate as a corrosion product of Mg rather than porous magnesium hydroxide, arguing that it offers more effective barrier protection of the Al 2024-T351 substrate [3].

This paper will characterize blisters observed in the field and in lab accelerated weathering exposures and identify similarities and differences. Two distinct types of blisters are distinguished. The fundamental processes that lead to the formation of each type of blister are outlined and reproduced experimentally in controlled laboratory experiments that simulate blisters and diagnostic electrochemical experiments. The performance of the MgRP coating system, with respect to Mg depletion and blister formation, in lab accelerated exposures (ASTM B-117) with ambient CO_2 and CO_2-rich environments is also compared. Thermodynamic and kinetic information is used to interpret findings and mitigation strategies are discussed.

8.3 Experimental Procedures

8.3.1 Materials

1.6 mm thick AA2024-T351 sheet, 99.9% pure magnesium rod, 99.9% pure Mg powder with a flake geometry and an average diameter of 20 µm, as well as 1.6 mm thick AA2024-T351 panels coated with commercial Mg-rich primer (MgRP) were studied in these investigations. The Mg rod was 8.0 mm in diameter and about 2.50 cm long. The Mg rod and AA2024-T351 sheet were used as bare electrodes in full immersion

electrochemical tests. The Mg rod had a measured purity of over 99.9% and was substantially similar to the powder used in the MgRP.

Samples were mounted in epoxy resin, when necessary, in order to make clamping the sample to an electrochemical flat cell easier. The bare electrodes were used in electrochemical analysis and were prepared by alternating polishing with silicon-carbide paper and rinsing with 18.2 MΩ deionized water to a final polishing grit of 1200. The samples were then dried with lab tissue before use.

The MgRP-coated panels studied comprised of a 1.6 mm thick AA2024-T351 sheet with a 30 μm primer layer of magnesium rich primer of various pigment volume concentrations and a 50 μm thick topcoat of a commercial high performance advanced life polyurethane coating. The MgRP-coated AA2024 panels were pretreated with a non-toxic, non-corrosive, non-flammable, CFC free, ODS free, and chromate free surface pretreatment before the MgRp was applied. The pretreatment does not contain any corrosion inhibitors and is not a conversion coating; but promotes adhesion between the primer and substrate. The high performance advanced polymer topcoat is a two-component polyurethane topcoat developed for military applications in a variety of exposure environments. The magnesium rich primer consists of a 1-part epoxy matrix with Mg metal flake pigment mixed in at various volume concentrations (PVC). The Mg pigment itself has flake geometry with an average diameter of 20 μm. All of our coated panels were provided and painted by collaborators [1, 2].

8.3.2 ASTM B-117 Salt Fog Exposure

Mg-rich primer-coated AA2024-T351 panels with Mg PVC ≥ 0% were exposed in a QFog Cyclic Corrosion Chamber according to ASTM B-117 [38]. ASTM B-117 covers the apparatus, procedure and conditions required to create and maintain the salt spray (fog) test environment. Ambient CO_2 concentration was monitored during the exposure in-situ with a CO_2 sensor with a sensing range of 0-10,000 ppm to be 425 ppm (Table 8.1).

During some salt fog exposures CO_2 was introduced into the exposure chamber via a regulated gas cylinder in order to increase the concentration of CO_2 in the exposure chamber to greater-than-ambient levels. During these exposures of increased CO_2 concentrations, a constant flow rate of CO_2 was utilized such that the concentration of CO_2 stabilized to approximately 6000 ppm (Table 8.1).

8.3.3 Field Exposures at Daytona Beach, FL

Natural weathering exposures of Mg-rich primer-coated AA2024-T351 panels with Mg PVC ≥ 0% were conducted at the Battelle Florida Materials Research Facility which is a marine atmospheric testing site located beach-front on the Atlantic Ocean. The Battelle Florida Materials Research Facility is located on the Ponce de Leon Peninsula, 10 miles south of the city of Daytona Beach, Florida, and is used primarily for the testing and evaluation of materials in a subtropical marine environment. During exposure, AA2024-T351 panels coated with MgRP with Mg PVC ≥ 0% and a topcoat of commercial high performance advanced life polyurethane coating were mounted on atmospheric test racks with full exposure to natural elements.

8.3.4 Full Immersion Electrochemical Analysis

Potential control during electrochemical experiments was maintained using a potentiostat with computer interface software. Saturated Calomel reference electrodes (SCE) were used in full immersion testing. Particular potentiostat models were selected because they enable electrochemical impedance spectroscopy (EIS) measurements along with traditional electrochemical measurements.

8.3.5 Anodic Potentiodynamic Scans

Anodic potentiodynamic scans were conducted on 99.9% pure, 8.0 mm diameter bare Mg electrodes as well as the prepared Mg-rich primer-coated AA2024-T351 panels with Mg PVC $\geq$ 25%. Both topcoated and non-topcoated panels were tested. The bare Mg electrodes were polished to 1200 grit silicon carbide paper until a mirror finish was obtained. The potentiodynamic scans were conducted after a 10 minute OCP. A typical anodic scan started at -0.2 V vs OCP up to +0.7 V vs. OCP and scanned at 0.1667 mV per second for bare electrodes and 2.0 mV per second for the coated panels.

8.3.6 Cathodic Potentiodynamic Scans

Cathodic potentiodynamic scans were conducted on bare AA2024-T351 electrodes as well as Mg-rich primer coated AA2024-T351 panels with Mg PVC = 0%. Both topcoated and non-topcoated panels were tested. The bare AA2024-T351 electrodes were ground to 1200 grit silicon carbide paper until a mirror finish was obtained. The potentiodynamic scans were conducted after a 10 minute OCP. A typical cathodic scan started at +0.2 V vs OCP and scanned down to -1.0 V vs. OCP at 0.1667 mV per second.

8.3.7 Electrochemical Impedance Spectroscopy (EIS)

EIS was conducted on bare Mg and AA2024-T351 electrodes as well as the prepared Mg-rich primer-coated AA2024-T351 panels. A typical EIS scan was acquired in sine sweep mode from 100 kHz to 0.01 Hz with 6 points per decade. Bare electrodes were scanned with an AC amplitude of 20 mV while coated panels were scanned with an AC amplitude of 60 or 80 mV to reduce noise. The bare Mg and AA2024-T351 electrodes were polished to 1200 grit silicon carbide paper until a mirror finish was obtained.

8.3.8 Full Immersion, Electrochemical Testing Protocol (Cycle Test)

A full immersion, electrochemical testing regimen was designed to monitor selected coating characteristics over time. This test included a 10 minute OCP followed by an EIS measurement to assess, nondestructively, the galvanic couple potential of the primer coated AA2024-T351 substrate in order to later interpret cathodic protection and the residual barrier properties of the coating. These were followed by a potentiostatic hold at -0.8 V vs. SCE to accelerate the Mg dissolution rate and measure the anodic charge supplied by the MgRP. The test always started and ended with a 10 minute OCP measurement followed by EIS. The cycle test was run under full immersion in 50 mM sodium chloride solution with ambient aeration and used a saturated calomel reference electrode. These three steps were repeated for a specified number of cycles. The cycles of exposure in full immersion cannot as yet be related to hours of exposure in natural environments.

8.3.9 X-Ray Diffraction

X-Ray diffraction was conducted on a powder diffractometer utilizing a Cu-Kα source. The samples investigated included bare AA2024-T351 and the prepared, Mg-rich primer-coated AA2024-T351 panels of all PVC's. All samples were scanned continuously from 10 to 120 degrees. Scans were run at a scan rate of 1.0 degrees per minute on bare electrodes and non-topcoated coatings and 2.0 degrees per minute on topcoated coatings. Both fresh Mg-rich coated panels and panels exposed in full immersion were examined with XRD. XRD Spectra obtained from bare AA2024-T351 and AA2024-T351 coated with MgRP were normalized against the fcc Al <200> $2\theta=44.7384^{o}$ peak. Samples of bare Mg electrodes were normalized against the Mg <101> $2\theta=36.6190^{o}$ peak.

8.3.10 Scanning Electron Microscopy and Energy Dispersive Spectroscopy

Scanning electron microscopy and energy dispersive spectroscopy were used for coating characterization and post-mortem analysis. A field emission SEM with EDS analytical software was used to conduct these investigations. Various accelerating voltages and working distances were used depending on the samples and information being investigated. In general, for EDS, a working distance of 15 mm and an accelerating voltage of at least 3 times the energy of the maximum characteristic peak of interest were used. Signals for Mg and Al K_{α} energies were obtained.

8.4 Results

8.4.1 Initial Characterization of MgRP Coating System

SEM micrographs of two cross sectioned AA2024-T351 panels coated with MgRP are shown in Figure 8.1. EDS spot scans of the substrate show elemental Al. EDS spot scans conducted on magnesium pigment particles in the primer indicated low O levels which suggest the magnesium was largely unoxidized prior to weathering. The thickness of the primer layer was about 30 μm. For topcoated samples, the topcoat was about 50 μm thick. The total coating system thickness was about 80 μm. X-Ray diffraction spectra of the as-received panels of AA2024-T351 coated with MgRP with and without topcoat, were discussed in a previous publication and also indicated the Mg pigment in the primer coating is largely unoxidized prior to weathering and showed that the polymer topcoat contains rutile as a pigment (unknown PVC) [12].

8.4.2 Type 1 Blisters: Disbondment of the Organic Polymer Due to Anodic Undermining and H_2 Production

Panels of AA2024-T351 coated with MgRP (PVC = 0% and 45%) and a topcoat of high performance advanced life polyurethane coating were exposed in a salt fog chamber according to ASTM B-117 [38] under ambient aeration for 840 hours. The CO_2 levels inside the salt fog chamber during exposure were measured to be approximately 425 ppm. This does not vary significantly from accepted ambient concentrations globally (Table 8.1). After exposure the panels were compared to similar panels exposed outdoors at Daytona Beach for approximately 1 year (Figure 8.2). All panels exposed in the salt fog chamber according to ASTM B-117 exhibited large amounts of corrosion product

within the scribe lines and exhibited coating blisters proximate-to, or along the scribe lines. Moreover, the panels without any Mg in the primer (Figure 8.2a) exhibited much larger blisters than panels with a PVC of Mg of 45% (Figure 8.2b). In contrast, panels exposed at Daytona Beach exhibited little-to-no corrosion product build-up within the scribe lines and appeared to be relatively defect free. Furthermore, the only panels from the field that exhibited visible blisters were panels without any Mg in the primer (Figure 8.2c). An interesting feature was the blisters' hemispherical or disc-like nature suggesting relatively uniform pressurization in addition to corrosion products.

Blistered areas along the scribes from each sample visible in Figure 8.2 were cross sectioned and examined in a field emission SEM with EDS capabilities (Figure 8.3 and Figure 8.4). EDS area scans were taken in three areas of each cross sectioned blister: 1) the substrate, 2) the corrosion product, and 3) the coating system and are indicated by the numbered boxes (1-3) in each micrograph in Figure 8.4. Figure 8.4d summarizes the results of the EDS measurements. There were striking similarities found between the blisters sectioned on each sample. They could be characterized by large areas of organic coating delamination over top of thick, relatively uniform layers of fractured corrosion product associated with shallow penetration. It was found that the corrosion product layer in each blister was located underneath both the primer and topcoat layers of the coating system, was approximately 50-80 μm thick, and was relatively uniform. Each corrosion product layer appeared to follow the Al substrate morphology perfectly, suggesting that they grew from the substrate and that they have a Pilling-Bedworth ratio of approximately 1 [49]. Furthermore, EDS analysis showed that the corrosion product layer in

each blister consisted solely of Al and O. EDS analysis of the coating systems over top of each blister were also very similar, each exhibiting strong C, O, Al, Cl and Si peaks. Elemental Mg only appeared in the EDS area scans of the coating system which contained Mg pigment in the primer.

8.4.3 Diagnostic Testing for Type I Blisters

Coupons of AA2024-T351 were coated with a model organic polymer epoxy coating which was clear in color and lacked any pigmentation. After curing, the samples were then scribed with a diamond tipped scribe and exposed to the ASTM B-117 test for 72 hours. After exposure the coupons exhibited coating blisters proximate-to, or along the scribe lines (Figure 8.5a). The model organic polymer epoxy coating was observed to change color from clear to white during exposure due to hydration. Universal pH indicator solution was injected via syringe into a blister immediately upon removing the coupons from the salt fog chamber. The indicator solution which seeped from the punctured blister was observed to be bright red in color indicating a pH of 4.0 or below (Figure 8.5b). In summary the blister could be characterized as an acidic site. Other regions on the unpainted back side of the coupon were blue, indicative of pH greater than or equal to 10.0.

8.4.4 Type 2 Blisters: Ruptures Caused by Cathodic Corrosion of Al

A second, much less prevalent type of blister (or rupture), which is characterized by narrow, deep pinholes in the aluminum substrate which can sometimes penetrate through the panel, has been reported in AA2024-T351 panels pretreated with prekote^{TM} and

coated with commercial MgRP (PVC = 45%) exposed to ASTM B-117 salt fog accelerated weathering by various researchers [1, 2]. We have observed such a phenomenon under full immersion testing of AA2024-T351 panels coated with MgRP without a topcoat. The exposure consisted of a full immersion electrochemical testing protocol in which an AA2024-T351 panel pretreated with prekote™ and coated with commercial MgRP (PVC = 45%) was immersed in aerated 50 mM NaCl and primarily subjected to a potentiostatic hold at -0.8 V vs. SCE with numerous cycles of nondestructive open circuit hold and electrochemical impedance measurements in order to track the coatings degradation [12]. It should be noted, however, that this test protocol did not change impedance barrier properties, i.e. did not damage the polymer away from the rupture site. After about 90 hours of total exposure to this cyclic test, the panels were cross sectioned and examined in a field emission SEM with EDS capabilities. Pinholes were observed to be forming in the AA2024-T351 substrate below areas that appear to be sites of Mg pigment dissolution (Figure 8.6). The coating was ruptured. EDS analysis showed evidence of Al, Mg and O in the pinhole and Mg, O, C, and Cl in the primer layer directly above the hole.

8.4.5 Diagnostic Testing for Type 2 Ruptures

Cathodic, or basic, corrosion of the AA2024-T351 substrate has been suggested to be the mechanism for this type of blistering or rupturing. To test if cathodic, or basic, corrosion of AA2024-T351 is possible in chemical environments relevant to the AA2024-T351/MgRP system, 1” by 1” AA2024-T315 coupons were exposed in full immersion for 1 week to 200 mL of 50 mM NaCl along with 0.55 g of Mg shavings. The Mg shavings

were observed to quickly dissolve within 24-48 hours and produce a fine white product which was shown to be primarily $Mg(OH)_2$ by X-ray diffraction. The pH of the solution was initially 5.6 but rose to 11 during the first 24 hours and declined to 10.6 over the rest of the exposure period. The AA2024-T351 coupon displayed a fairly thick layer of dark corrosion product (Figure 8.7) and after cleaning with nitric acid exhibited a mass loss of approximately 2%.

A similar experiment was conducted by placing a small pile (approximately 0.2 g) of Mg powder directly on a coupon of bare AA2024-T351. Then approximately 0.3 mL of 50 mM NaCl was applied to the surface and the sample was placed in a 100% relative humidity chamber for 24 hours to prevent evaporation of the electrolyte. After exposure, the pile of Mg was observed to have spread out over the entire surface of the AA2024-T351 coupon and the pH of the solution was measured by pH paper to be 10.0 or above. Severe corrosion of the Mg powder and the AA2024-T351 surface was observed. The coupon was rinsed with deionized water after exposure and is shown in Figure 8.8.

To investigate whether cathodic corrosion of AA2024-T351 is possible at potentials relevant to the Mg/Al galvanic couple system, a sample of bare AA2024-T351 polished to 1200 grit paper was potentiostatically held at -1.5 V vs. SCE for 1 hour in full immersion in 300 mL of aerated 50 mM NaCl. After exposure the sample showed significant corrosion (Figure 8.9a). Similarly a sample of bare AA2024-T351 was galvanically coupled to bare Mg in 300 mL of aerated 50 mM NaCl for 1 hour. The galvanic couple potential was measured to be fairly stable at -1.5 V vs SCE for the

entirety of the test. This sample also showed significant AA2024-T351 corrosion after the exposure (Figure 8.9b).

Similar polarization tests were run on samples of AA2024-T351 with cross-sectional dimensions of 6.1 mm by 1.7 mm in approximately 0.3-0.4 mL of NaCl. The samples were constructed by mounting pieces of AA2024-T351 and Mg rod (with a cross sectional diameter of 8.0 mm) in epoxy resin utilizing a cylindrical mold with a diameter of 32 mm. Then, after polishing the samples to 1200 grit paper, the epoxy mold was used as a vertical, cylindrical cell in which approximately a 1-1.5 mm thick electrolyte layer was filled (Figure 8.10). The small volume and geometry of the cell allowed the pH of solution just above the AA2024-T351 electrode's surface to be measured with pH indicator paper during the electrochemical tests. A sample of bare AA2024-T351 was potentiostatically held at -1.5 V vs. SCE for 1 hour in full immersion in aerated 50 mM NaCl. During exposure, bubbles were observed emanating from the AA2024-T351 surface (Figure 8.10a) and the pH over the AA2024-T351 electrode was measured with pH indicator paper to be equal to or greater than 9.5 (Figure 8.10c). Similarly a sample of bare AA2024-T351 was galvanically coupled to bare Mg in full immersion in aerated 50 mM NaCl. The galvanic couple potential was measured to be relatively steady at -1.5 V vs. SCE for the length of the exposure period. During exposure, bubbles were observed emanating from the AA2024-T351 surface (Figure 8.10b) and the pH over the AA2024-T351 electrode was measured with pH indicator paper to be equal to or greater than 9.5 (Figure 8.10d). These results indicate that alkaline pH is the cause for dissolution of Al during exposure, not the presence of Mg.

The effect of severe cathodic polarization is also experimentally shown in Figure 8.11. AA2024-T351 coated with an epoxy resin was galvanically coupled in aerated 50 mM NaCl to a piece of Mg coated with the same epoxy resin. The potential of the AA2024-T351 electrode with respect to a SCE reference electrode was measured throughout the experiment. With both electrodes coated the galvanic couple potential was approximately -1.0 V vs. SCE and no corrosion of the AA2024 surface was visible after 1 hour (Figure 8.11a). The coated AA2024-T351 was then scratched which produced a galvanic couple potential equal to that of bare AA2024-T351 (-0.55 V vs. SCE). After an hour of exposure while being galvanically coupled to the coated Mg electrode the scratch on the AA2024-T351 electrode showed no significant corrosion (Figure 8.11b). Finally when the coated Mg electrode was also scratched, the galvanic couple potential of the AA2024-T351 dropped to -1.5 V vs. SCE which slowly rose to -1.4 V vs. SCE by the end of an hour of exposure. After an hour of exposure while being coupled to the scratched Mg electrode, the scratch on the AA024-T351 electrode showed significant corrosion product (Figure 8.11c).

8.4.6 The Mitigation of Type 1 and Type 2 Blisters by CO_2

Two separate laboratory environmental exposures were conducted in a salt fog cabinet according to ASTM B-117 for approximately 800 hours. The exposures were conducted on two identical groups of panels of AA2024-T351 coated with MgRP. Panels with and without a topcoat of high performance advanced life polyurethane coating were included in each exposure. The first exposure was under ambient CO_2 concentrations which were measured in the salt fog chamber by a CO_2 sensor connected to a PC with data logging

capabilities to be approximately 400 ppm. During the second exposure CO_2 was fed into the salt fog chamber at a constant flow rate from a regulated gas cylinder. During the second exposure the CO_2 concentration in the salt fog chamber was observed to reach a steady state of approximately 6000 ppm. After exposure to salt fog according to ASTM B-117 under ambient CO_2 concentrations (400 ppm) "type 1" blisters could be seen adjacent to the scribe lines on the topcoated samples (circled in Figure 8.12a). After exposure to salt fog according to ASTM B-117 under increased CO_2 concentrations (6000 ppm) only one "type 1" blister could be seen adjacent to the scribe lines on the topcoated samples (circled in Figure 8.12a). This indicates that increasing the CO_2 during the exposure resulted in a decreased occurrence of blistering phenomena. Non-topcoated panels were observed to show a general degradation of the coating but no blistering phenomena were observed after either exposure.

The Mg depletion rate in the MgRP was monitored throughout each exposure in the salt fog chamber with X-ray diffraction measurements (Figure 8.13 and Figure 8.14). The intensities of three prominent magnesium peaks were normalized against the Al <111> peak which appeared in each spectrum due to the underlying AA2024-T351 substrate. The relative intensities of the Mg peaks decreased with increasing exposure time due to the depletion of Mg from the coating system. It was observed that the Mg peak intensities decreased at approximately equal rates in each exposure, suggesting that increasing the CO_2 concentration during the exposure did not have a significant effect on the Mg depletion rates of non-topcoated or topcoated samples. For this reason it appears that

increased concentrations of CO_2 do not lead to increased barrier protection of the Mg pigment by the formation of $MgCO_3$ or other compound.

The equilibrium concentrations of CO_3^{2-} dissolved in solution according to various ambient partial pressures of CO_2 are shown in Table 8.2. The equilibrium concentrations of CO_3^{2-} dissolved in solution were calculated utilizing Henry's Law with a Henry's Law coefficient of 0.034 for CO_2 [50, 51]. The subsequent calculated E-pH diagrams of the Mg-CO_2-H_2O system (Figure 8.15) do not predict any stability of the $MgCO_3$ compound at concentrations of CO_2 relevant to ambient (P_{CO_2} = 0.0005 atm) or CO_2-rich (P_{CO_2} = 0.005 atm) environments. However, when an aqueous environment is sparged with CO_2 (P_{CO_2} = 1.0 atm), $MgCO_3$ becomes stable at a pH range of approximately 9 to 13 and above potentials of about -0.7 V vs. SCE.

In an effort to understand the mechanisms by which CO_2 may have mitigated blistering in topcoated systems during salt fog exposure, some model experiments were developed. pH measurements of various solutions of NaCl relevant to the AA2024-T351/MgRP system are shown inFigure 8.16. NaCl under ambient aeration was observed to have a pH of approximately 5.6. Aerated NaCl sparged with CO_2 was observed to have a pH of 4.5. When 0.55 g of Mg shavings were dissolved in aerated NaCl the pH equilibrated to approximately 11 while the same solution sparged with CO_2 equilibrated to a pH of approximately 7.

1" by 1" AA2024-T315 coupons were exposed in full immersion for 1 week to 200 mL of 50 mM NaCl along with 0.55 g of Mg shavings similar to the experiment conducted

for Figure 8.7 however the solution was sparged with CO_2 throughout the exposure. The Mg shavings were observed to quickly dissolve and produce a fine white product which was shown to be primarily $Mg(OH)_2$ by X-ray diffraction. The pH of the solution was initially 4.5 but rose to 7.2 during the first 24 hours and remained approximately 7 for the rest of the exposure period. After exposure the AA2024-T351 coupon displayed almost no corrosion product (Figure 8.17) and after cleaning with nitric acid exhibited a mass loss of less than 1%.

8.4.7 Electrochemical Diagnostics

Potentiodynamic scans of AA2024-T351 were conducted in various solutions of 50 mM NaCl and are shown inFigure 8.18. AA2024-T351 is shown to have an open circuit potential of approximately -0.55 V vs. SCE in aerated 50 mM NaCl and upon anodic polarization immediately pits. In aerated NaCl sparged with CO_2 AA2024-T351 is shown to have an open circuit potential of approximately -0.57 V vs. SCE with lower cathodic reaction rates (as compared to polarization in aerated 50 mM NaCl without CO_2 sparging) and slightly increased anodic dissolution rates with no change in pitting potential. In a basic solution (50 mM NaCl + 50 mM Na_2CO_3, pH = 11.3) AA2024-T351's open circuit potential is dramatically decreased to -1.2 V vs. SCE and the anodic dissolution of AA2024-T351 dramatically increases as compared to polarization in aerated 50 mM NaCl. When CO_2 is bubbled through the basic solution of 50 mM NaCl + 50 mM Na_2CO_3 the pH is mediated to 6.7 and AA2024-T351 is shown to have an open circuit potential of -0.45 V vs. SCE.

A sample of bare AA2024-T351 polished to 1200 grit paper was potentiostatically held at -1.5 V vs. SCE for 1 hour in full immersion in aerated 50 mM NaCl similar to Figure 8.9a however the NaCl was sparged with CO_2 for the entirety of the exposure. After exposure the sample showed very little corrosion (Figure 8.19a). Similarly a sample of bare AA2024-T351 was galvanically coupled to bare Mg in aerated 50 mM NaCl sparged with CO_2 for 1 hour. The galvanic couple potential was measured to be fairly stable at -1.6 V vs SCE for the entirety of the test. This sample also showed significantly less corrosion after the exposure (Figure 8.19b) than in aerated NaCl which was shown earlier in Figure 8.9b.

8.5 Discussion

8.5.1 Type 1 Blisters

Type 1 blisters are characterized by large areas of delamination over top of thick, relatively uniform layers of aluminum corrosion product with shallow penetration and occur solely along or proximate to scribe lines. Type 1 blisters were observed in coating systems with and without Mg pigment in the primer. The shape of the blister is consistent with osmotic blistering, in which de-adhesion is obtained by exceeding the adhesion strength of the coating with forces caused by osmotic pressurization. However a significant amount of corrosion product is seen inside the blister upon investigation with SEM. The corrosion product in these blisters was shown to consist solely of Al and O (Figure 8.4). Moreover, model diagnostics indicated an acidic pH at such sites (Figure 8.5). All of these observations strongly suggest that this phenomenon is not caused by osmotic blistering or the corrosion of Mg. It is proposed that Type 1 blisters are caused

by a more classical mechanism, often associated with organic polymer coatings, involving anodic disbondment of the organic polymer [40, 41]. The primary mechanism for this phenomenon on aluminum alloys, particularly those containing Cu such as AA2024, has been proposed for years to be anodic coating disbondment through anodic undermining aided in this case by H_2 production according to Equation 1 below [41].

$$2Al + 6H_2O \leftrightarrow 2Al(OH)_3 + 3H_2 \qquad \text{Equation 1}$$

Figure 8.20 shows a schematic of the corrosion mechanism behind anodic disbondment. For this mechanism to be operative the Mg pigment surrounding a coating defect or scribe must be, for some reason, unable to locally prevent the dissolution of Al via cathodic polarization. This may be because the Mg pigment is simply absent from the primer (supported by PVC = 0%, Figure 8.4), depleted from the primer due to environmental exposure, or the primer coating is locally delaminated from the substrate at a site that lacks sufficient electrical or ionic conductivity to other Mg pigment particles in the primer. This theory is supported by the fact that the coating systems without any Mg in the primer coating exhibited much larger blisters of this type than samples which had Mg in the primer coating (Figure 8.2**).** The primary corrosion mechanism is the creation of a differential aeration cell within the defect, between the coating system and substrate, which leads to a galvanic couple between the more active, oxygen depleted head and the scribe [40, 41]. This galvanic couple is quickly exacerbated by an acidic shift in pH and an increase in Cl^- concentration at the head of the blister (exhibited in Figure 8.5b) and a shift to high pH at the tail [40, 41]. The growth of the blister is due to the combination of anodic undercutting and hydrogen production at the outer edges of the

blister where anodic dissolution of the AA2024-T351 substrate is taking place (Equation 1). The galvanic corrosion is eventually mediated by Ohmic resistances created by increased distance between anode and cathode and ionic resistances created by the deposition of corrosion product between the anode and cathode [40].

8.5.2 Type 2 Blisters

Type 2 blisters are characterized by narrow, deep pinholes which penetrate into the AA2024-T31 substrate. Observations of these blisters have been made on panels of AA2024-T351 coated with MgRP (PVC = 45%) without a topcoat exposed in laboratory salt fog exposures [2] and in laboratory full immersion exposures (Figure 8.6). The observation of Type 2 blisters after full immersion testing is particularly interesting because they occurred during an exposure where the panel was potentiostatically held at a potential below AA2024-T351's open circuit potential of -0.55 V vs. SCE in 50 mM NaCl for the majority of the exposure period. Due to the fact that these blisters have been observed to form while AA2024-T351 was cathodically polarized, it has been suggested that the pinholes are caused by the cathodic, or basic, corrosion of Al which is possible due to Al's amphoteric nature [43, 44, 47, 52-56]. In aqueous environments the Al oxide layer is thermodynamically stable in only a narrow window of neutral pH ranges as shown by the E-pH diagram in Figure 8.21. For cathodic corrosion to be the mechanism to form a Type 2 blister, or rupture, there must be a local increase in solution pH at the surface of the AA2024-T351 substrate. There exist various scenarios in the AA2024-T351/MgRP system that could provide for this local pH rise. The rise in pH may be caused by the formation of $Mg(OH)_2$ at sites of Mg pigment dissolution which when dissolved in an

aqueous environment at 25 ^{o}C has an equilibrium pH of approximately 10.45 (Equation 2) [42]. Such an environment was shown experimentally to cause severe corrosion of AA2024-T351 (Figure 8.7).

$$Mg + 2H_2O \leftrightarrow Mg^{2+} + 2OH^- + H_2$$ Equation 2

Another possibility for localized pH increase is increased cathodic reaction rates at sites of severe cathodic polarization of the Al substrate which will lead to the cathodic dissolution of Al at such sites (Equation 3) [42]. In galvanic couples between Mg and AA2024-T351, there exists the possibility for the AA2024-T351 substrates to be polarized as negatively as -1.5 V vs. SCE as evidenced by the polarization scans of bare Mg and bare AA2024-T351 in Figure 8.22. Such severe cathodic polarization was shown experimentally to cause severe corrosion of AA2024-T351 (Figure 8.7).

$$Al + 2H_2O \rightarrow AlO_2^- + 4H^+ + 3e^-$$ Equation 3

However, it has been shown by King schematically (Figure 8.23) and with mixed potential modeling (Figure 8.24) that it is likely that such polarizations in atmospheric exposures are mediated by Ohmic resistances added by primer and topcoat polymers [12]. The primer and topcoat polymers act to add both ionic and electrical resistances between the Mg pigment and the AA2024-T351 substrate. The effect of such electrical resistances is demonstrated experimentally in Figure 8.25a by observing the galvanic couple potential between bare Mg and AA2024-T351 galvanically coupled in aerated 50 mM NaCl with a variable resistor in series between the two electrodes. When the electrical

resistance in the galvanic couple is increased, the galvanic couple potential is mediated. Figure 8.25b shows the effect of adding ionic resistance by coating a bare AA2024-T351 exposed in full immersion to aerated 50 mM NaCl with an epoxy resin. This added ionic resistance also acts to mediate the galvanic potential. However, the possibility remains that there exists local sites of severe cathodic polarization at coating defects or scribe lines where there exists little or no ionic and electrical resistance between anode and cathode. The ASTM B-117 salt spray test is regarded to have a high time-of wetness (TOW) and NaCl concentration to trigger such attack.

8.5.3 The Mitigation of Type 1 and Type 2 Blisters by CO_2

It has been reported [1, 3, 57] and shown experimentally that higher than ambient concentrations of CO_2 act to reduce the occurrence of Type 1 and Type 2 blisters during accelerated laboratory exposures. The addition of high concentrations of CO_2 to accelerated laboratory exposures of AA2024-T351 panels coated with MgRP has a two-fold effect: passivating the Cu-rich cathodic sites on the surface of the Al alloy at defect sites and moderating the pH of the aqueous exposure environment. However, due to the lack of stability of $MgCO_3$ in aqueous environments across the span of partial pressures of atmospheric CO_2 and negative potentials relevant to the various exposure environments utilized in this and similar works (as shown by the calculated E-pH diagrams of the Mg-CO_2-H_2O system in Figure 8.15) it is very unlikely that any realistic increase in atmospheric CO_2 concentration leads to an increased barrier protection brought about by the formation of $Mg(CO)_3$. Furthermore, even under conditions of extremely high concentrations of atmospheric CO_2 (such as P_{CO_2} = 1 atm) $Mg(CO)_3$ is not

stable (Figure 8.15c) at potentials relevant to Mg metal corroding in aqueous NaCl (Figure 8.22) or the pH of NaCl sparged with CO_2 with corroding Mg metal (Figure 8.16). $Mg(OH)_2$ which is electrically isolated from the MgRP may convert to $MgCO_3$. However this process does not govern MgRP performance as XRD shows (Figure 8.13 and Figure 8.14).

Moreover there is a second mechanism of CO_2 operation. Scully and Frankethal have shown that a high concentration of CO_2 acts to reduce the cathodic reaction rates on aluminum alloys with Cu-rich secondary phases acting as cathode sites [48]. This is accomplished by producing a thinner, more homogeneous, defect-free Al oxide film on the Cu-rich, second phase precipitates. This minimizes Al de-alloying in the alloy. As shown in Figure 8.16, high concentrations of CO_2 also mediate the pH of the aqueous environment such that the solubility of the Al oxide layer is minimized (Figure 8.26). For instance the pH of aerated 50 mM NaCl with CO_2 bubbling is 4.5 (Figure 8.16). This passivation of cathodic sites reduced ORR on intermetallic compounds and a reduction in the coupled anodic process or pitting. Type 1 blisters were shown to be caused by the creation of a differential aeration cell within the defect, between the coating system and substrate, which leads to a galvanic couple between the more active, oxygen depleted head and the scribe [40]. In high CO_2 environments, the Cu-rich cathodic sites in the scribe or defect become deaerated and passivated towards cathodic reactions, limiting the cathodic reaction rates in the defect. Limiting the cathodic reaction rates in the defect, in turn, limits the galvanic current between the blister and defect, reducing the anodic

dissolution reactions of Al in the blister. Thus the driving forces for the growth of the blister, anodic undermining and hydrogen production, are reduced.

The presence of a high concentration of CO_2 also acts to moderate the pH of an aqueous environment in which Mg and AA2024-T351 are corroding by buffering (Figure 8.16). CO_2 dissolves in water and forms H_2CO_3 which dissociates into HCO_3^- and CO_3^{2-} according to Equation 4 and Equation 5.[3, 48]

$$CO_2(aq) + H_2O \leftrightarrow HCO_3^- + H^+ \qquad \text{Equation 4}$$

$$HCO_3^- \leftrightarrow CO_3^{2-} + H^+ \qquad \text{Equation 5}$$

This acidification affect can prevent the formation of Type 2 blisters or ruptures which were shown to be caused by the cathodic, or basic, corrosion of the aluminum alloy. This effect is evidenced by cathodic polarization and galvanic couple experiments reported earlier (Figure 8.17, Figure 8.18,Figure 8.19).

However Figure 8.18e indicates the adverse effect of alkalinity and NaCl on Al corrosion. The addition of Na_2CO_3 shifts the pH of the electrolyte alkaline with the Na cation acting as a spectator via Equation 6 below.

$$Na_2CO_3 + H_2O \leftrightarrow Na^+ + HCO_3^- + OH^- \qquad \text{Equation 6}$$

Thus Na_2CO_3 forms a solution with an approximate pH of 11.0 and results in significant corrosion of AA2024-T351.

8.5.4 The ASTM B-117 Test

The ASTM B-117 test is quite severe. Speculatively, differences in corrosion behavior between field and ASTM B-117 exposures are believed to be associated with high TOW and high NaCl concentrations in the ASTM B-117 environment. CO_2 level differences are not the cause as they were shown to be approximately equal in both environments. It should also be noted that high concentrations of CO_2 can suppress both blister types but does not affect Mg pigment depletion nor passivate Mg as speculated elsewhere [3, 57].

8.6 Conclusions

- There are 2 distinct blistering phenomena observed in early generations of the commercial MgRP coating system on AA2024-T351:
  - Type 1 Blisters: Disbondment of the Organic Polymer Due to Anodic Undermining and H_2 Production
    - Have been observed on topcoated systems in ASTM B-117 and field sites at Daytona Beach (only on PVC_{Mg} = 0% in field)
    - characterized by large areas of hemispherical delamination over top of thick, relatively uniform layers of aluminum corrosion product with shallow penetration and occur solely along or proximate to scribe lines.
    - observed in topcoated systems with and without Mg pigment in the primer.
    - caused by anodic coating disbondment through anodic undermining aided in this case by H_2 production
  - Type 2 Blisters: Ruptures Caused by Cathodic Corrosion of Al
    - Have been observed on non-topcoated systems in ASTM B-117
    - characterized by narrow, deep pinholes which penetrate into the AA2024-T31 substrate
    - observed on panels of AA2024-T351 coated with MgRP (PVC = 45%) exposed in laboratory salt fog exposures and in laboratory full immersion exposures where the AA2024-T351 is cathodically polarized

- due the cathodic, or basic, corrosion of Al caused by cathodic polarization of AA2024-T351 substrate and formation of $Mg(OH)_2$ at sites of Mg pigment dissolution.
- Increasing the concentration of CO_2 to levels of 6000 ppm or higher (by sparging for example) during full immersion testing or accelerated lab exposures:
  - Reduces the occurrence of Type 1 blisters by passivating the cu-rich cathodic sites on the surface of the Al alloy at defect sites limiting the galvanic current between cathodic defect sites and anodic sites of coating disbondment.
  - Reduces the occurrence of Type 2 ruptures by moderating the pH of the aqueous exposure environment preventing the cathodic corrosion of the AA2024-T351 substrate.
  - Does not have a significant effect on the Mg depletion rates of non-topcoated or topcoated samples. For this reason it appears that increased concentrations of CO_2 do not lead to increased barrier protection of the Mg pigment by $MgCO_3$ or otherwise.
  - Is not responsible for the difference in corrosion behavior between ASTM B-117 and field exposures.

8.7 Acknowledgements

This work was supported by the Office of the Undersecretary of Defense Corrosion University Pilot Program under the direction of Mr. Daniel Dunmire. Akzo-Nobel™ Corporation is gratefully acknowledged for helpful suggestions and the supply of Mg-rich primers specifically: Pat Adams, Scott Hayes, Michael Chapman, and Roger Brown. Mr. William Abbott of Battelle and Mr. Craig Matzdorf of NAVAIR are acknowledged for correspondence and supply of primer and primer/topcoat specimens. Dr. Marta Jakob of Southwest Research Institute is acknowledged for the supply of bare AA2024-T351 panels.

8.8 References

1. W. H. Abbott, Personal correspondence with Mr. William Abbott of Battelle Memorial Institute, (2009).
2. C. Matzdorf, Personal correspondence with Mr. Craig Matzdorf of NAVAIR, (2009).
3. S. S. Pathak, M. D. Blanton, S. K. Mendon and J. W. Rawlins, Investigation on dual corrosion performance of magnesium-rich primer for aluminum alloys under salt spray test (ASTM B117) and natural exposure, Corros Sci, 52, 4 (2010), pp. 1453-1463.
4. G. P. Bierwagen, D. E. Tallman, M. Nanna, D. Battocchi, A. Stamness and V. J. Gelling, New developments in Cr-free primers for aerospace alloys., Abstr Pap Am Chem S, 228, (2004), pp. U360-U360.
5. D. Battocchi, A. M. Simoes, D. E. Tallman and G. P. Bierwagen, Comparison of testing solutions on the protection of Al-alloys using a Mg-rich primer, Corros Sci, 48, 8 (2006), pp. 2226-2240.
6. D. Battocchi, A. M. Simoes, D. E. Tallman and G. P. Bierwagen, Electrochemical behaviour of a Mg-rich primer in the protection of Al alloys, Corros Sci, 48, 5 (2006), pp. 1292-1306.
7. G. Bierwagen, D. Battocchi, A. Simoes, A. Stamness and D. Tallman, The use of multiple electrochemical techniques to characterize Mg-rich primers for A1 alloys, Prog Org Coat, 59, 3 (2007), pp. 172-178.
8. A. Simoes, D. Battocchi, D. Tallman and G. Bierwagen, Assessment of the corrosion protection of aluminium substrates by a Mg-rich primer: EIS, SVET and SECM study, Prog Org Coat, 63, 3 (2008), pp. 260-266.
9. H. Xu, D. Battocchi, D. E. Tallman and G. P. Bierwagen, Use of Magnesium Alloys as Pigments in Magnesium-Rich Primers for Protecting Aluminum Alloys, Corrosion, 65, 5 (2009), pp. 318-325.
10. U.S. Department of Health and Human Services., Report on Carcinogens, 12th Edition, U.S. Department of Health and Human Services, Public Health Services, National Toxicology Program, 2011.
11. R. G. Buchheit, Chromate and Chromate-Free Conversion Coatings, vol. 13A, ASM Handbook Volume 13A, Corrosion: Fundamentals, Testing, and Protection (ASM International) (Materials Park, Ohio, ASM International, 2003).
12. A. D. King and J. Scully, Sacrificial Anode based Galvanic and Barrier Corrosion Protection of AA2024-T351 by a Mg-Rich Primer and Development of Test Methods for Remaining Life Assessment Corrosion, 67, 5 (2011), p. 055004.
13. K. N. Allahar, D. Battocchi, G. P. Bierwagen and D. E. Tallman, Transmission Line Modeling of EIS Data for a Mg-Rich Primer on AA 2024-T3, J Electrochem Soc, 157, 3 (2010), pp. C95-C101.
14. K. N. Allahar, D. Battocchi, M. E. Orazem, G. P. Bierwagen and D. E. Tallman, Modeling of electrochemical impedance data of a magnesium-rich primer, J Electrochem Soc, 155, 10 (2008), pp. E143-E149.

15. K. N. Allahar, D. Wang, D. Battocchi, G. P. Bierwagen and S. Balbyshev, Real-Time Monitoring of a United States Air Force Topcoat/Mg-Rich Primer System in ASTM B117 Exposure by Embedded Electrodes, Corrosion, 66, 7 (2010).
16. S. Feliu, R. Barajas, J. M. Bastidas and M. Morcillo, Ac Impedance Study About the Protection Mechanisms of Zinc-Rich Primers, Abstr Pap Am Chem S, 195, (1988), pp. 58-Pmse.
17. D. Pereira, J. D. Scantlebury, M. G. S. Ferreira and M. E. Almeida, The Application of Electrochemical Measurements to the Study and Behavior of Zinc-Rich Coatings, Corros Sci, 30, 11 (1990), pp. 1135-1147.
18. S. Feliu, M. Morcillo and S. Feliu, Deterioration of cathodic protection action of zinc-rich paint coatings in atmospheric exposure, Corrosion, 57, 7 (2001), pp. 591-597.
19. V. M. Rudoi, O. V. Yaroslavtseva, T. N. Ostanina, L. P. Yurkina and O. Y. Subbotina, Electrochemical behavior of protective anodic primers, Protection of Metals, 35, 3 (1999), pp. 277-281.
20. H. Marchebois, C. Savall, J. Bernard and S. Touzain, Electrochemical behavior of zinc-rich powder coatings in artificial sea water, Electrochim Acta, 49, 17-18 (2004), pp. 2945-2954.
21. C. M. Abreu, M. Izquierdo, M. Keddam, X. R. Novoa and H. Takenouti, Electrochemical behaviour of zinc-rich epoxy paints in 3% NaCl solution, Electrochim Acta, 41, 15 (1996), pp. 2405-2415.
22. S. G. Real, A. C. Elias, J. R. Vilche, C. A. Gervasi and A. Disarli, An Electrochemical Impedance Spectroscopy Study of Zinc Rich Paints on Steels in Artificial Sea-Water by a Transmission-Line Model, Electrochim Acta, 38, 14 (1993), pp. 2029-2035.
23. C. M. Abreu, M. Izquierdo, X. R. Novoa, C. Perez and A. Sanchez, Influence of different aggressive media on the protective behaviour of zinc rich paints, Rev Metal Madrid, 35, 3 (1999), pp. 182-189.
24. N. V. Kondrashova, S. A. Nesterenko, O. V. Naumenko and L. I. Antropov, Influence of Zinc and Magnesium Cations on the Electrochemical-Behavior of Steel with a Polymer Primer, Protection of Metals, 25, 1 (1989), pp. 73-75.
25. S. Feliu, R. Barajas, J. M. Bastidas and M. Morcillo, Mechanism of Cathodic Protection of Zinc-Rich Paints by Electrochemical Impedance Spectroscopy .1. Galvanic Stage, J Coating Technol, 61, 775 (1989), pp. 63-69.
26. S. Feliu, R. Barajas, J. M. Bastidas and M. Morcillo, Mechanism of Cathodic Protection of Zinc-Rich Paints by Electrochemical Impedance Spectroscopy .2. Barrier Stage, J Coating Technol, 61, 775 (1989), pp. 71-76.
27. C. M. Abreu, M. Izquierdo, P. Merino, X. R. Novoa and C. Perez, A new approach to the determination of the cathodic protection period in zinc-rich paints, Corrosion, 55, 12 (1999), pp. 1173-1181.
28. M. Morcillo, R. Barajas, S. Feliu and J. M. Bastidas, A-Sem Study on the Galvanic Protection of Zinc-Rich Paints, J Mater Sci, 25, 5 (1990), pp. 2441-2446.

29. R. A. Armas, C. A. Gervasi, A. Disarli, S. G. Real and J. R. Vilche, Zinc-Rich Paints on Steels in Artificial Seawater by Electrochemical Impedance Spectroscopy, Corrosion, 48, 5 (1992), pp. 379-383.
30. H. Marchebois, M. Keddam, C. Savall, J. Bernard and S. Touzain, Zinc-rich powder coatings characterisation in artificial sea water - EIS analysis of the galvanic action, Electrochim Acta, 49, 11 (2004), pp. 1719-1729.
31. O. O. Knudsen, U. Steinsmo and M. Bjordal, Zinc-rich primers - Test performance and electrochemical properties, Prog Org Coat, 54, 3 (2005), pp. 224-229.
32. M. E. Nanna and G. P. Bierwagen, Mg-rich coatings: A new paradigm for Cr-free corrosion protection of al aerospace alloys, Jct Research, 1, 2 (2004), pp. 69-80.
33. J. R. Scully, F. Presuel-Moreno, M. Goldman, R. G. Kelly and N. Tailleart, User-selectable barrier, sacrificial anode, and active corrosion inhibiting properties of Al-Co-Ce alloys for coating applications, Corrosion, 64, 3 (2008), pp. 210-229.
34. F. J. Presuel-Moreno, M. E. Goldman, R. G. Kelly and J. R. Scully, Electrochemical sacrificial cathodic prevention provided by an Al-Co-Ce metal coating coupled to AA2024-T3, J Electrochem Soc, 152, 8 (2005), pp. B302-B310.
35. F. J. Presuel-Moreno, H. Wang, M. A. Jakab, R. G. Kelly and J. R. Scully, Computational modeling of active corrosion inhibitor release from an Al-Co-Ce metallic coating - Protection of exposed AA2024-T3, J Electrochem Soc, 153, 11 (2006), pp. B486-B498.
36. F. Presuel-Moreno, M. A. Jakab, N. Tailleart, M. Goldman and J. R. Scully, Corrosion-resistant metallic coatings, Mater Today, 11, 10 (2008), pp. 14-23.
37. D. H. Wang, D. Battocchi, K. N. Allahar, S. Balbyshev and G. P. Bierwagen, In situ monitoring of a Mg-rich primer beneath a topcoat exposed to Prohesion conditions, Corros Sci, 52, 2 (2010), pp. 441-448.
38. Astm, Standard Practice for Operating Salt Spray (Fog) Apparatus, ASTM B117 - 09, DOI: 10.1520/C0033-03, (2009).
39. G. P. Bierwagen, C. S. Jeffcoate, J. P. Li, S. Balbyshev, D. E. Tallman and D. J. Mills, The use of electrochemical noise methods (ENM) to study thick, high impedance coatings, Prog Org Coat, 29, 1-4 (1996), pp. 21-29.
40. D. A. Little, M. A. Jakab and J. R. Scully, Effect of surface pretreatment on the underpaint corrosion of AA2024-T3 at various temperatures, Corrosion, 62, 4 (2006), pp. 300-315.
41. E. L. Koehler, U. R. Evans, B. F. Brown, J. Kruger, R. W. Staehle and National Association of Corrosion Engineers. Research Committee., Corrosion Under Organic Coatings, Localized Corrosion (Houston, Tex., National Association of Corrosion Engineers, 1974, p. 117-133).
42. M. Pourbaix, Atlas of electrochemical equilibria in aqueous solutions, 2d English, vol. (Houston, Tex.: National Association of Corrosion Engineers, 1974), p. 644.
43. G. S. Frankel and Y. Baek, Electrochemical quartz crystal microbalance study of corrosion of phases in AA2024, J Electrochem Soc, 150, 1 (2003), pp. B1-B9.
44. H. Kaesche, Studies on the Corrosion of Aluminum, Zeitschrift für physikalische Chemie, 14, 7 (1963), pp. 557-566.

45. A. R. Despic, J. Radosevic, P. Dabic and M. Kliskic, Abnormal Yields of Hydrogen and the Mechanism of Its Evolution during Cathodic Polarization of Aluminum, Electrochim Acta, 35, 11-12 (1990), pp. 1743-1746.
46. E. P. G. T. Vandeven and H. Koelmans, Cathodic Corrosion of Aluminum, J Electrochem Soc, 123, 1 (1976), pp. 143-144.
47. S. M. Moon and S. I. Pyun, The corrosion of pure aluminium during cathodic polarization in aqueous solutions, Corros Sci, 39, 2 (1997), pp. 399-408.
48. J. R. Scully, R. P. Frankenthal, K. J. Hanson, D. J. Siconolfi and J. D. Sinclair, Localized Corrosion of Sputtered Aluminum and Al-0.5-Percent Cu Alloy Thin-Films in Aqueous Hf Solution .2. Inhibition by CO_2, J Electrochem Soc, 137, 5 (1990), pp. 1373-1377.
49. N. B. Pilling and R. E. Bedworth, The Oxidation of Metals at High Temperatures, Journal Institute of Metals, 29, (1923), pp. 529-591.
50. I. S. Cole, N. S. Azmat, A. Kanta and M. Venkatraman, What really controls the atmospheric corrosion of zinc? Effect of marine aerosols on atmospheric corrosion of zinc, Int Mater Rev, 54, 3 (2009), pp. 117-133.
51. C. Leygraf and T. E. Graedel, Atmospheric corrosion, The Electrochemical Society series, vol. (New York: Wiley-Interscience, 2000), p. xii, 354 p.
52. S. I. Pyun and S. M. Moon, Corrosion mechanism of pure aluminium in aqueous alkaline solution, J Solid State Electr, 4, 5 (2000), pp. 267-272.
53. M. Mokaddem, P. Volovitch, F. Rechou, R. Oltra and K. Ogle, The anodic and cathodic dissolution of Al and Al-Cu-Mg alloy, Electrochim Acta, 55, 11 (2010), pp. 3779-3786.
54. H. Kaesche, Zeitschrift für physikalische Chemie, 34, (1962), pp. 87-108.
55. R. D. Armstrong and V. J. Braham, The mechanism of aluminium corrosion in alkaline solutions, Corros Sci, 38, 9 (1996), pp. 1463-1471.
56. J. S. Zhang, M. Klasky and B. C. Letellier, The aluminum chemistry and corrosion in alkaline solutions, J Nucl Mater, 384, 2 (2009), pp. 175-189.
57. S. S. Pathak, M. D. Blanton, S. K. Mendon and J. W. Rawlins, Carbonation of Mg powder to enhance the corrosion resistance of Mg-rich primers, Corros Sci, 52, 11 (2010), pp. 3782-3792.

8.9 Tables

Table 8.1: Ambient Concentrations of CO_2 in Various Environments

Environment	[CO2] (ppm)
Ambient Global Outdoors	400
Ambient Global Indoors	600
Ambient ASTM B-117 at Uva	425
CO2-rich ASTM B-117 at Uva	6000

Table 8.2: Equilibrium Concentrations of CO_3^{2-}, according to Henry's Law, in an Aqueous Environment under various partial pressures of CO_2.

P_{CO2} atm	$[CO_2]$ vppm	$[CO_3^{2-}]$ mol/L
0.0005	500	0.000017
0.005	5000	0.00017
1	1000000	0.034

8.10 Figures

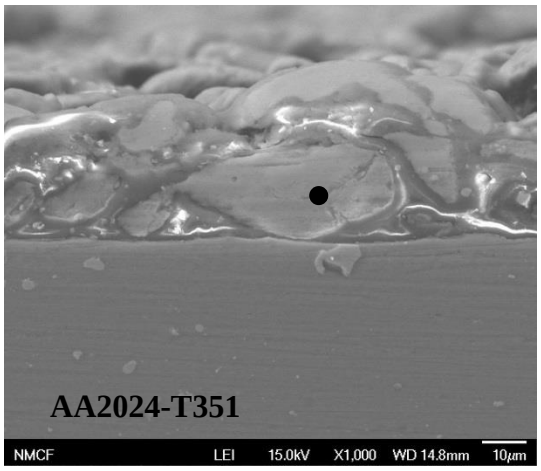

(a)

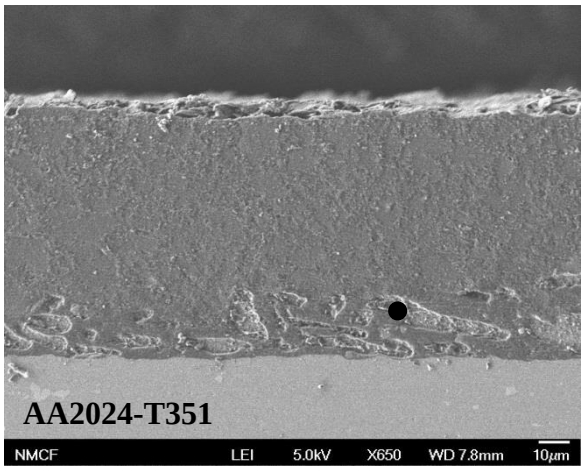

(b)

Figure 8.1 Scanning electron micrograph of cross sectioned AA2024-T351 coated with (a) MgRP Sample ID:493-039-A-P-P22 (b) MgRP + Topcoat Sample ID: T65f. Spot markers indicate approximate location of EDS analysis. For EDS: accelerating voltage = 15.0 KV, working distance = 15 mm.

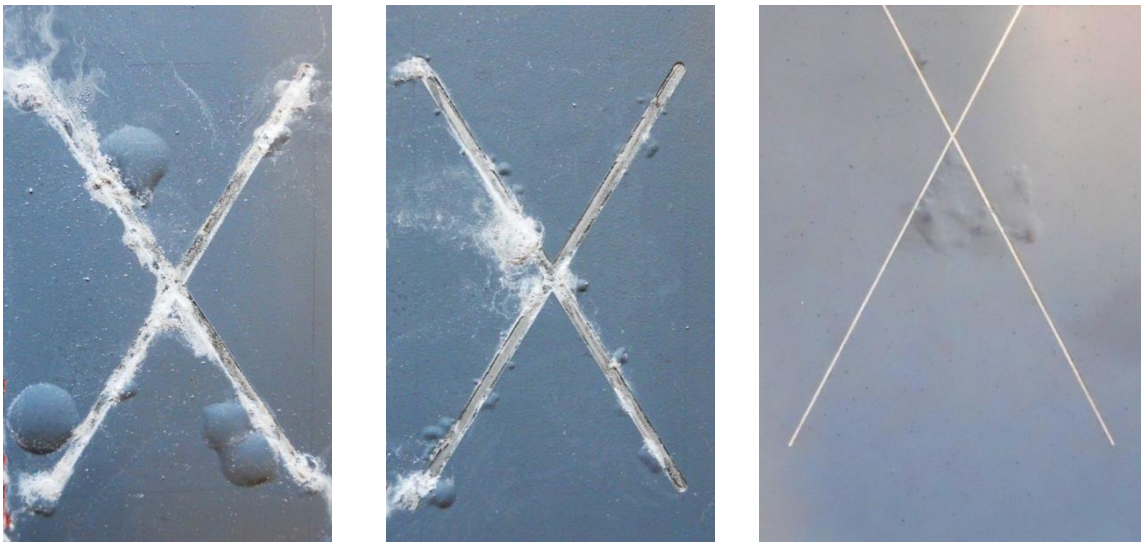

(a) (b) (c)

Figure 8.2. **(a)** AA2024-T351 coated with MgRP (PVC = 0%) and Aerodur 5000 Topcoat after 840 hrs in ASTM B-117 Sample ID:493-039-B-T-P22 (b) AA2024-T351 coated with MgRP (PVC = 45%) and Aerodur 5000 Topcoat after 840 hrs in ASTM B-117 Sample ID:493-039-A-T-P22 (c) AA2024-T351 coated with MgRP (PVC = 0%) and Aerodur 5000 Topcoat after 1 yr exposure at Daytona Beach, Fl Sample ID: unknown.

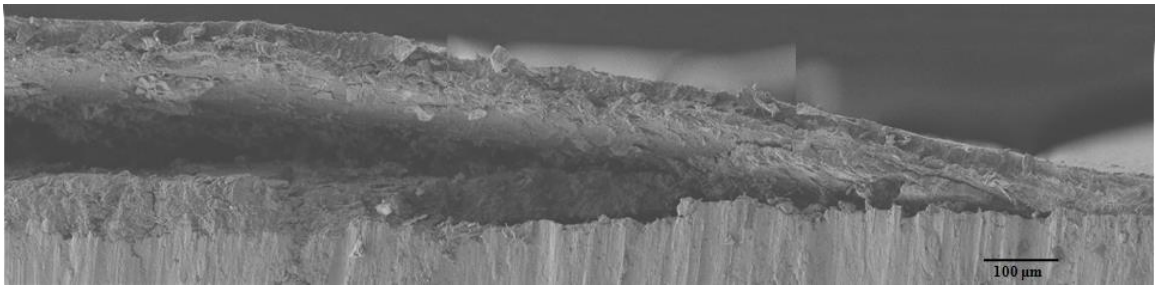

Figure 8.3.. Montage of SEM cross-sections of blisters on AA2024-T351 coated with Akzo Nobel MgRP (PVC = 0%) and Aerodur 5000 Topcoat after environmental exposure at Dayton Beach, FL for 1 yr. Sample ID: unknown

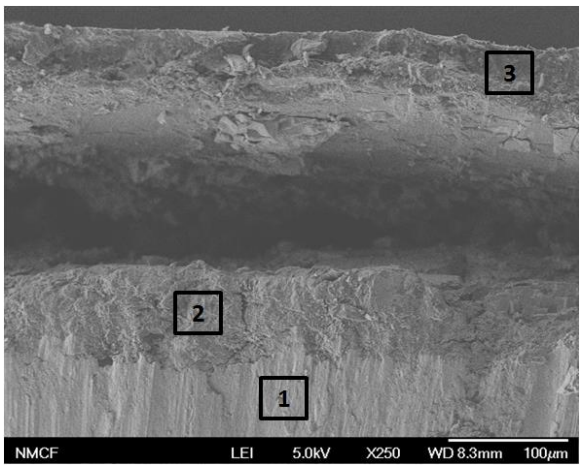

(a)

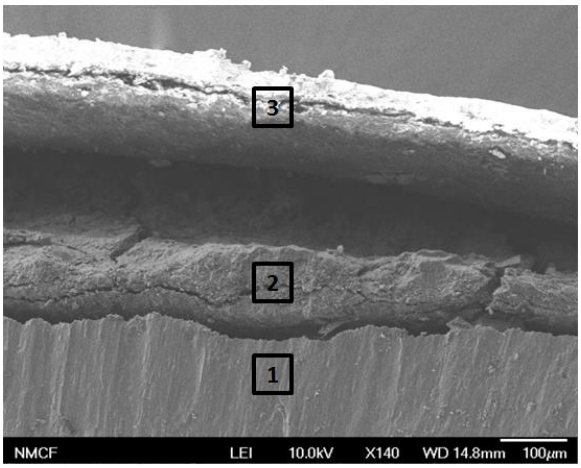

(b)

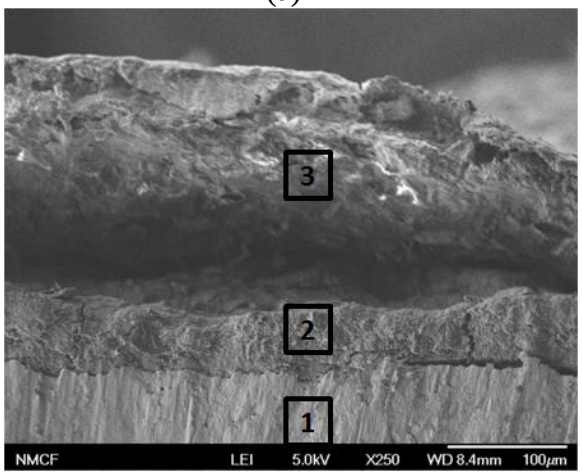

(c)

			Species Present in EDS		
Sample	PVC_{Mg}	Environment	1: Substrate	2: Corrosion Product	3: Coating System
a	0	Daytona	Al	Al, O, Cl	C, O, Al, Si. Cl
b	0	ASTM B-117	Al	Al, O, Cl	C, O, Al, Si. Cl
c	45	ASTM B-117	Al	Al, O, Cl	Mg, C, O, Al, Si. Cl

(d)

Figure 8.4.. SEM cross-section and EDS analysis of blisters on AA2024-T351 coated with Akzo Nobel MgRP and Aerodur 5000 Topcoat after environmental exposure. EDS area scans conducted approximately over black outlined areas. (a) PVC_{Mg} = 0% exposed at Dayton Beach, FL for 1 yr. Sample ID: unknown (b) PVC_{Mg} = 0% exposed in ASTM B-117 for 840 hrs Sample ID:493-039-B-T-P22 (c) PVC_{Mg} = 45% exposed in ASTM B-117 for 840 hrs Sample ID:493-039-A-T-P22

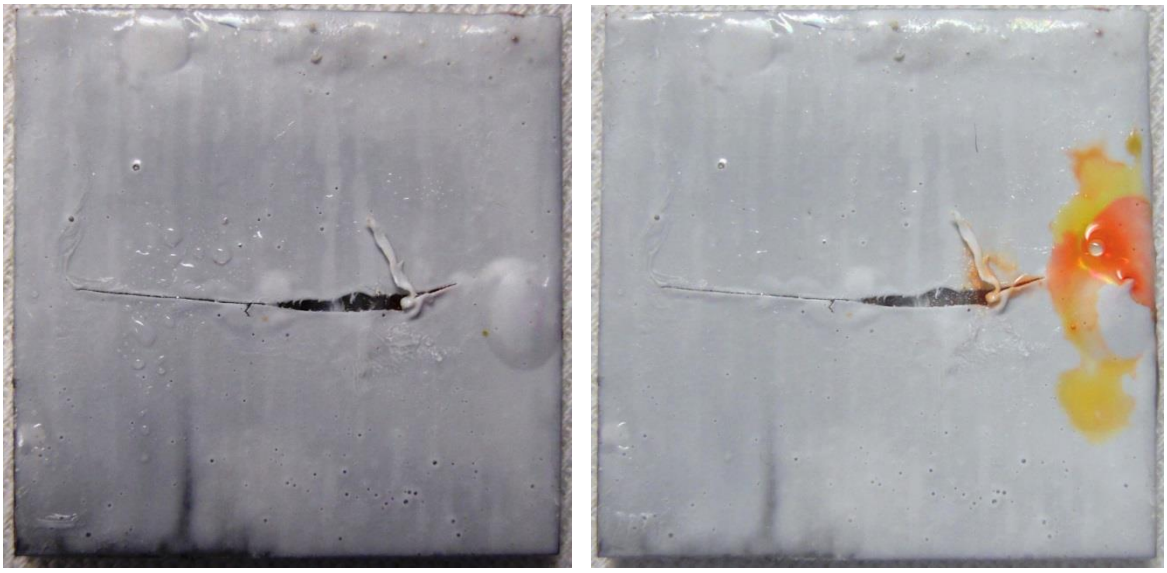

(a) (b)

Figure 8.5. Optical images of AA2024-T351 coated with a model organic epoxy polymer coating after 72 hours exposure in ASTM B-117 with ambient aeration. (a) immediately after environmental exposure (b) universal pH indicator has been injected into a blister located at the base of the scribe.

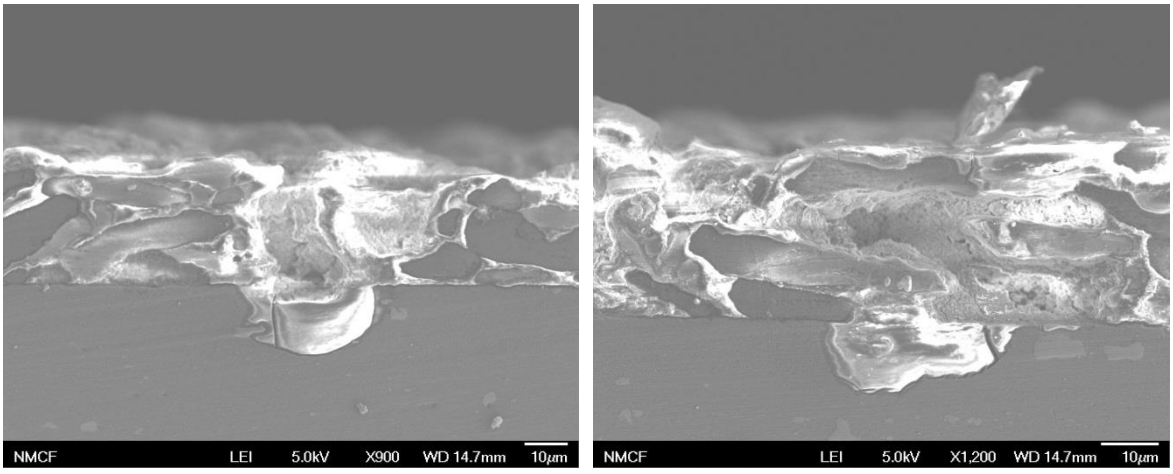

(a) (b)

Figure 8.6. SEM cross-section and EDS analysis of AA2024-T351 coated with Akzo Nobel MgRP after potentiostatic hold at -0.8 V vs. SCE in 50 mM NaCl with ambient aeration for approximately 90 hours. EDS spot scans inside pinhole show presence of Al, Mg, and O. Sample ID:493-039-A-P-P22

Figure 8.7. Optical images of AA2024-T351 after 1 week immersion in 50 mM NaCl with ambient aeration and Mg shavings.

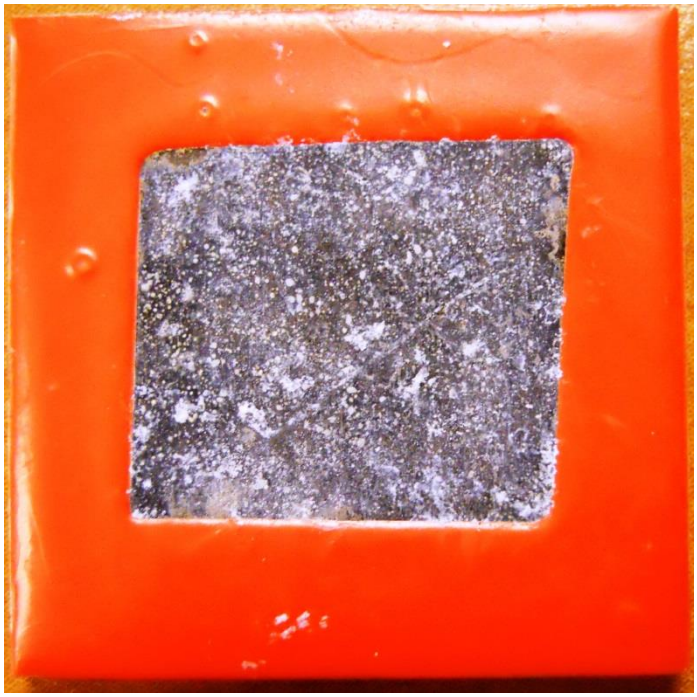

Figure 8.8. Optical images of AA2024-T351 after 72 hours immersion in 50 mM NaCl with ambient aeration and Mg powder.

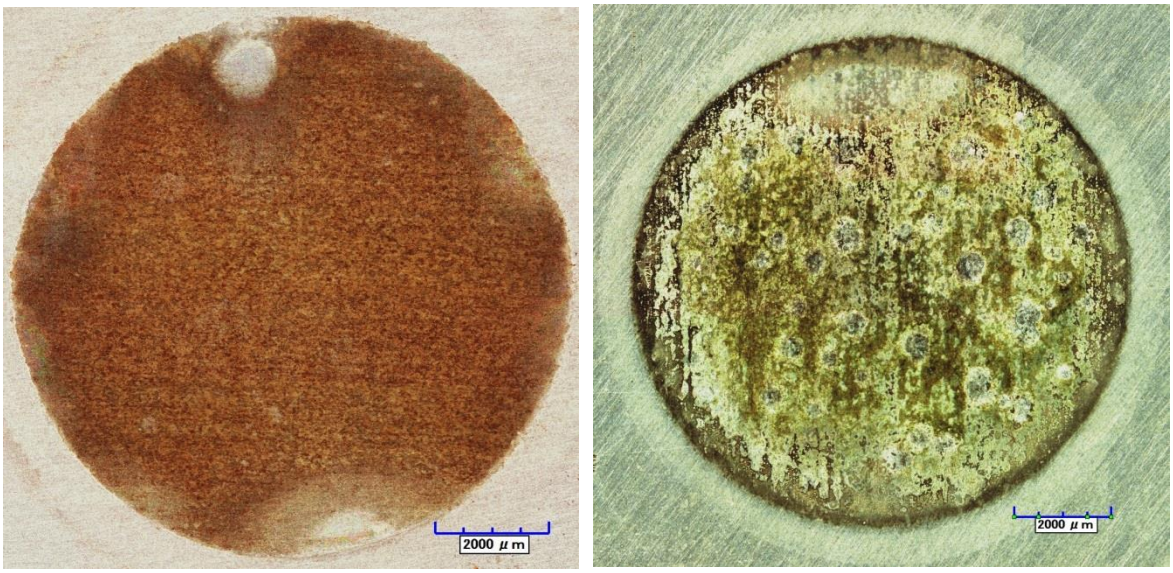

(a) (b)

Figure 8.9. Optical images of AA2024-T351 after (a) 1 hour potentiostatic hold at -1.5 V vs. SCE in 50 mM NaCl with ambient aeration. (b) 1 hour galvanic couple with Mg in 50 mM NaCl solution with ambient aeration

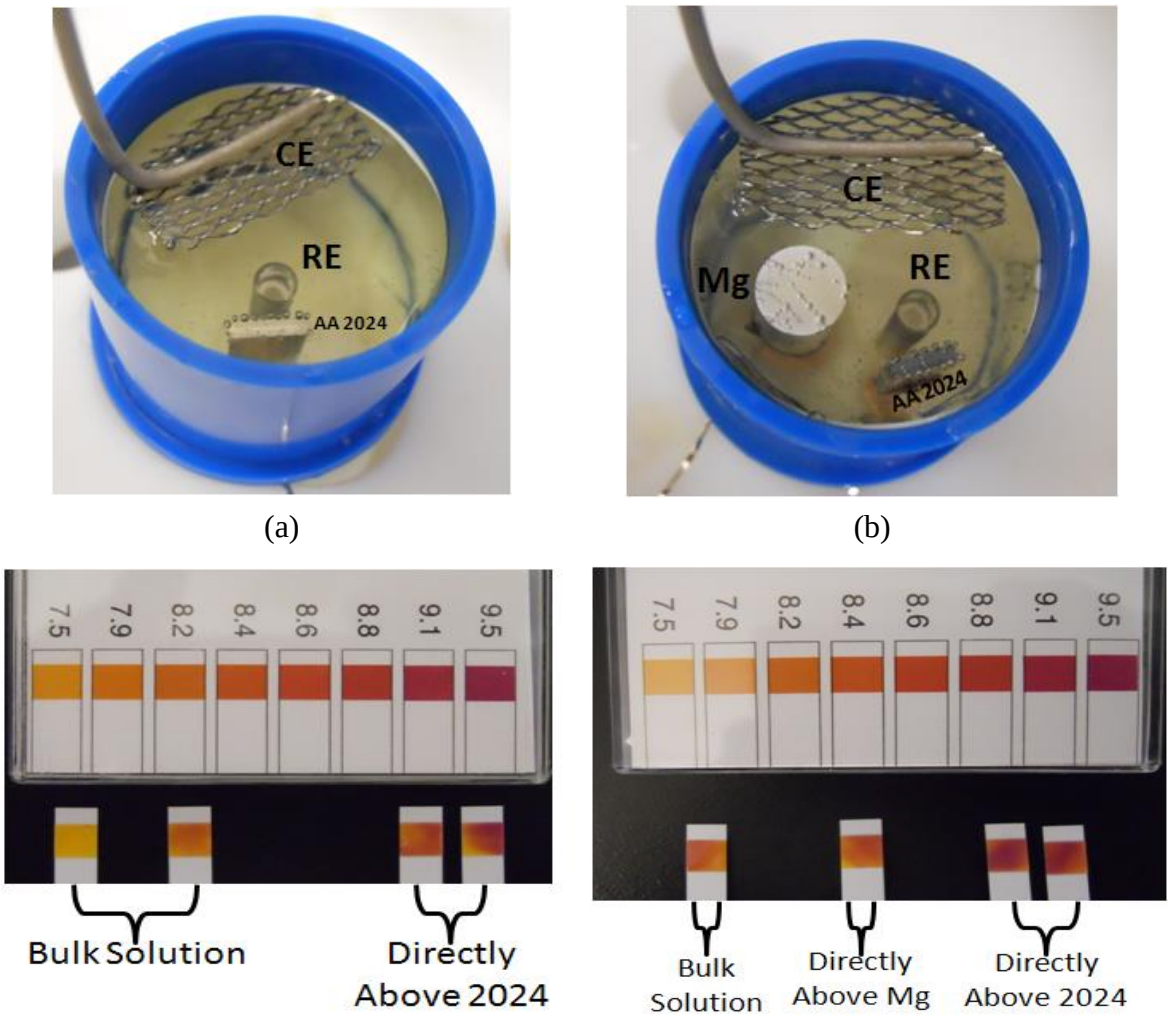

(a) (b)

(c) (d)

Figure 8.10.. Small electrolyte cell setup. (a & b) schematic of sample setup (b & c) optical images of cell setup during experiment (e & f) pH indicator paper measurements, labels indicate location of measurement.

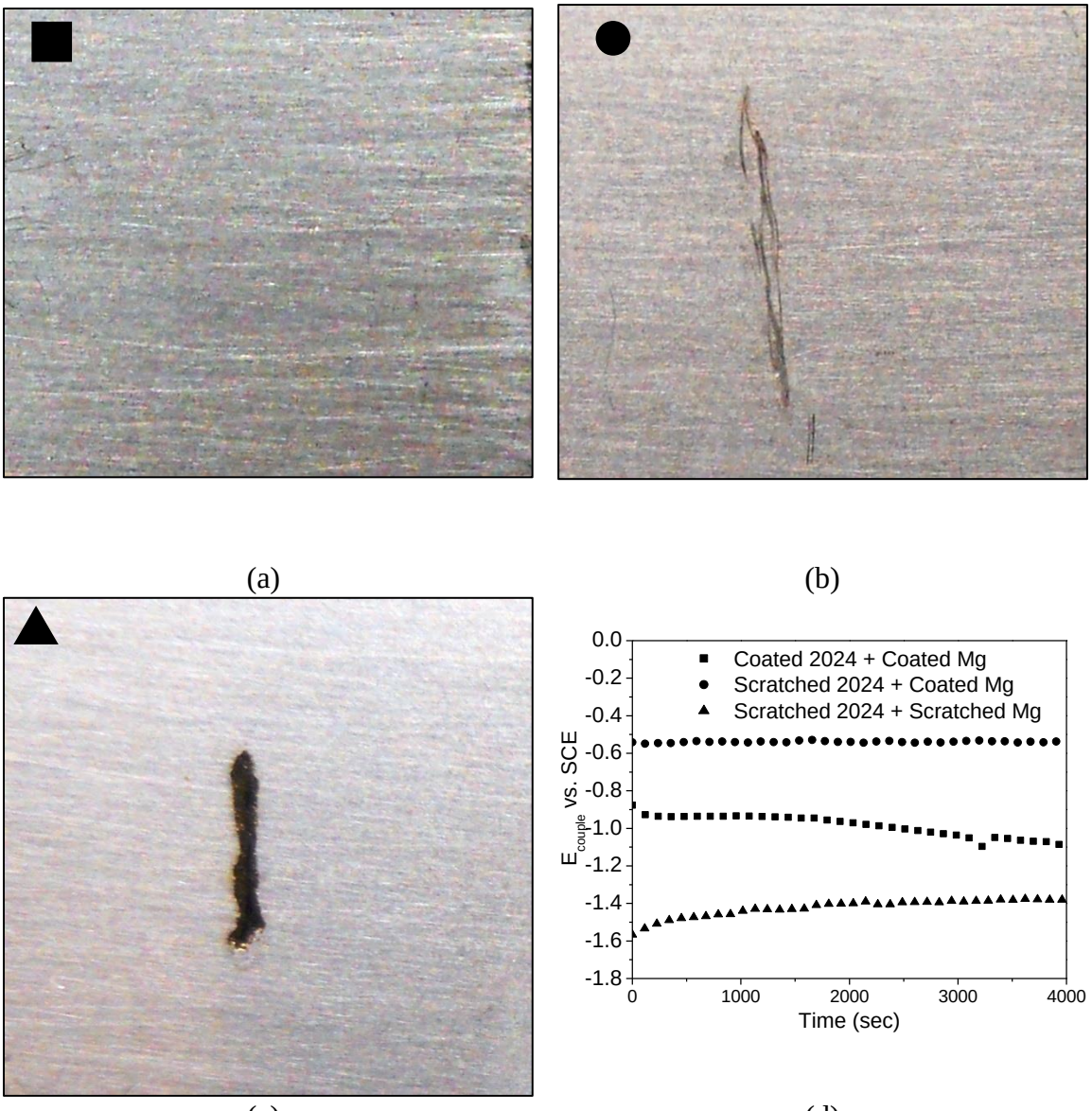

Figure 8.11. E_{couple} data and Optical images of AA2024-T351 after 1 hour galvanic couple between AA2024-T351 coated with Eponol and Mg coated with Eponol (a) both electrodes coated with Eponol (b) AA2024-T351 scratched (c) both electrodes scratched (d) E_{couple} for conditions a-c.

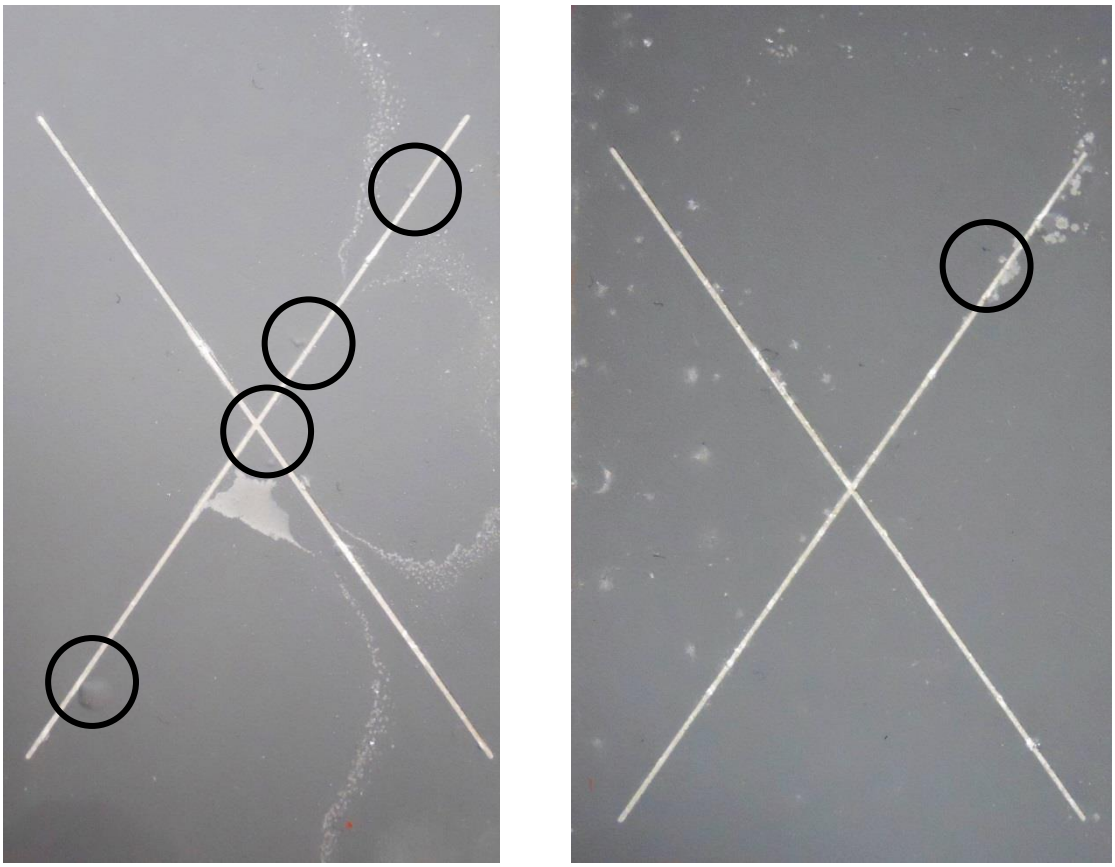

(a) (b)

Figure 8.12.. Optical images of panels of AA2024-T351 coated with MgRP and Aerodur 5000 Topcoat PVC = 45% after about 800 hours of environmental exposure in ASTM B-117. Blisters are circled. (a) in ambient CO_2 environment 450 ppm Sample ID: 510A-1 (b) in CO_2-rich environment 6000 ppm Sample ID: 510A-2

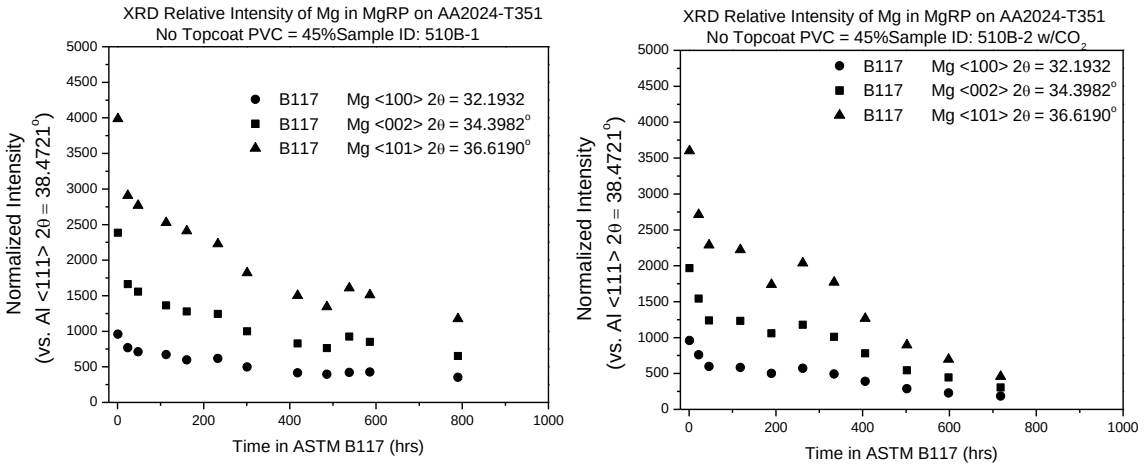

(a) (b)

Figure 8.13. XRD Normalized Mg Peak Intensities vs. environmental exposure time in ASTM B-117 for panels of AA2024-T351 coated with MgRP PVC = 45% (a) in ambient CO_2 environment 450 ppm (b) in CO_2-rich environment 6000 ppm

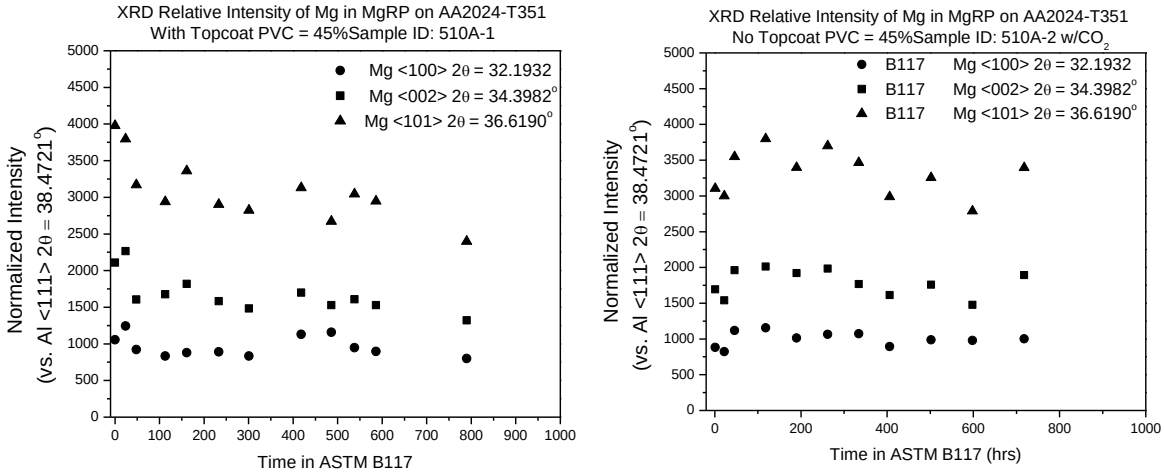

(a) (b)

Figure 8.14. XRD Normalized Mg Peak Intensities vs. environmental exposure time in ASTM B-117 for panels of AA2024-T351 coated with MgRP and Aerodur 5000 Topcoat PVC = 45% (a) in ambient CO_2 environment 450 ppm (b) in CO_2-rich environment 6000 ppm

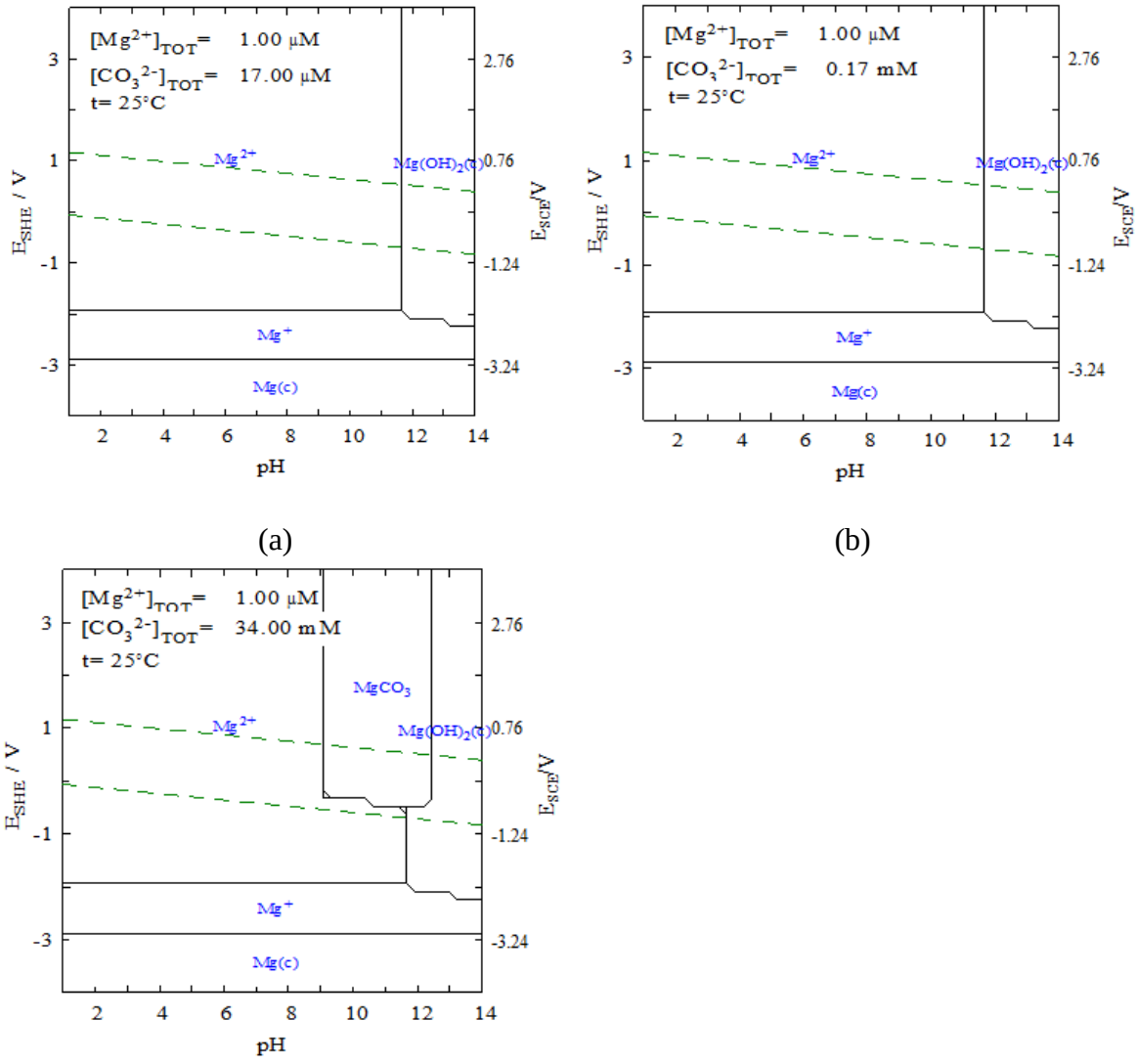

Figure 8.15. The E-pH diagrams for carbonate with metal ion concentration of 10^{-6} M and 3 different partial pressures of atmospheric CO_2.

(a) P_{CO_2} = 0.0005 atm therefore $[CO_3^{2-}]$ = 0.000017 M (b) P_{CO_2} = .005 atm therefore $[CO_3^{2-}]$ = 0.00017 M and (c) P_{CO_2} = 1 atm therefore $[CO_3^{2-}]$ = 0.034 M

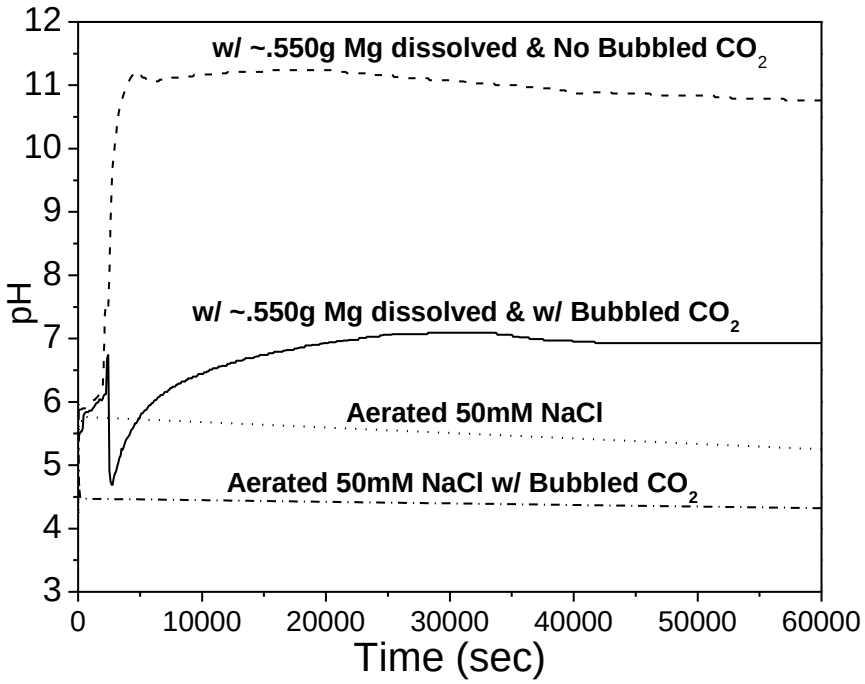

Figure 8.16. Solution pH of 50 mM NaCl with and without dissolved Mg and CO_2 sparging.

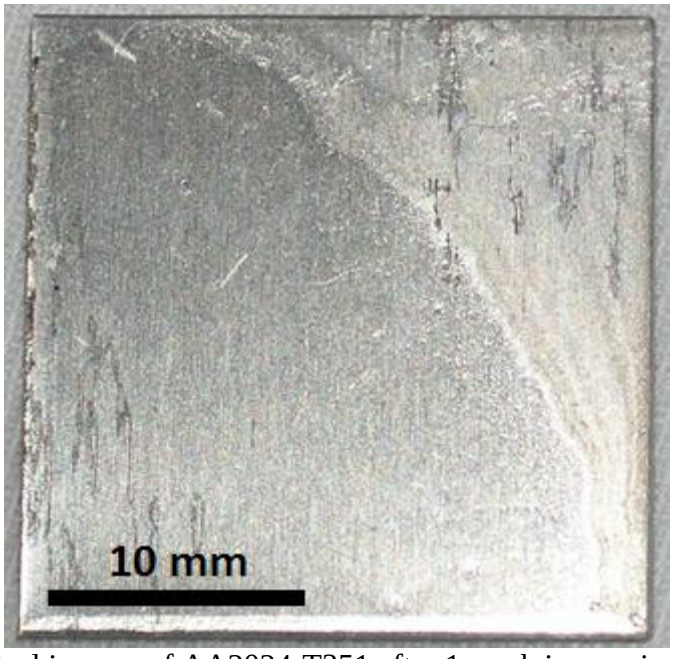

Figure 8.17. Optical images of AA2024-T351 after 1 week immersion in 50 mM NaCl

with Mg shavings and bubbled CO_2.

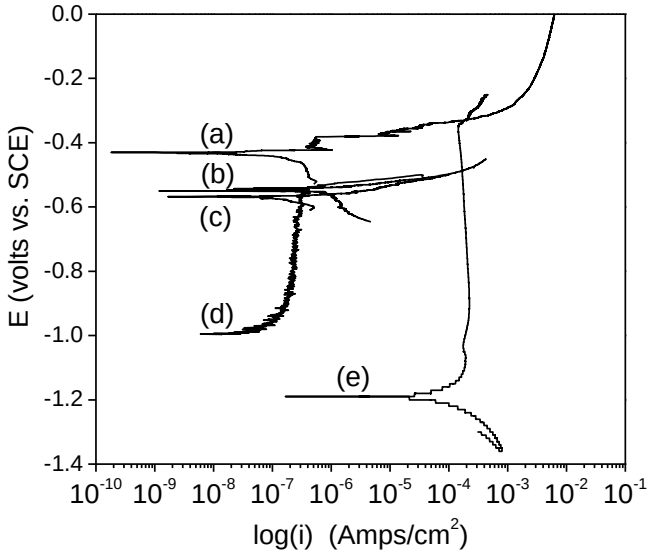

Figure 8.18. Anodic potentiodynamic scans of AA2024-T351 in various solutions. (a) aerated 50 mM NaCl solution + 50 mM Na_2CO_3 + bubbled CO_2 pH = 6.7 (b) aerated 50 mM NaCl solution pH = 5.6 (c) aerated 50 mM NaCl solution + bubbled CO_2 pH = 4.3 (d) deaerated 50 mM NaCl solution (e) aerated 50 mM NaCl solution + 50 mM Na_2CO_3 pH = 11.3

(a) (b)

Figure 8.19. Optical images of AA2024-T351 after (a) 1 hour galvanic couple with Mg in 50 mM NaCl solution with bubbled CO_2 (b) 1 hr potentiostatic hold at -1.5 V vs. SCE in 50 mM NaCl with bubbled CO_2

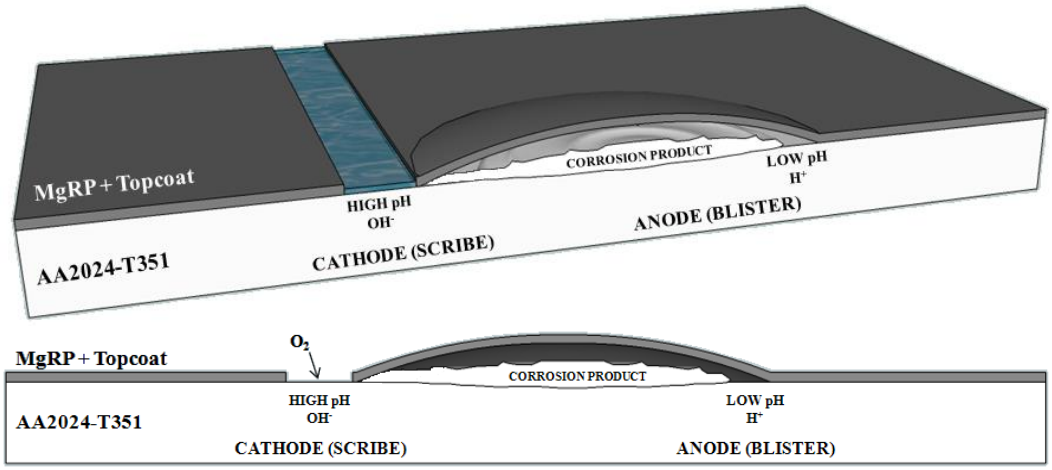

Figure 8.20. Schematic of proposed blistering mechanism: anodic disbondment through anodic undermining and hydrogen production.

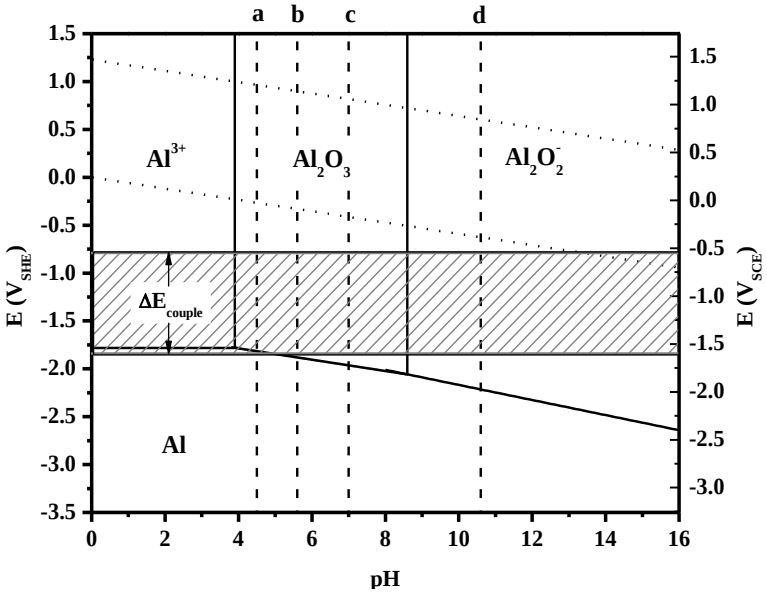

Figure 8.21. Potential-pH equilibrium diagram for Al-H_2O system at 25°C assuming an ion concentration of 10^{-6} pH indications:
(a) pH = 4.5 Aerated 50 mM NaCl with CO_2 sparge (b) pH = 5.6 Aerated 50 mM NaCl (c) pH = 7.0 Aerated 50 mM NaCl with dissolved Mg shavings and CO_2 sparge (d) pH = 10.6 Aerated 50 mM NaCl with dissolved Mg shavings
M. Pourbaix, Atlas of Electrochemical Equilibria in Aqueous Solutions, 2d English, vol. (Houston, Tex.: National Association of Corrosion Engineers, 1974), p. 644 p.

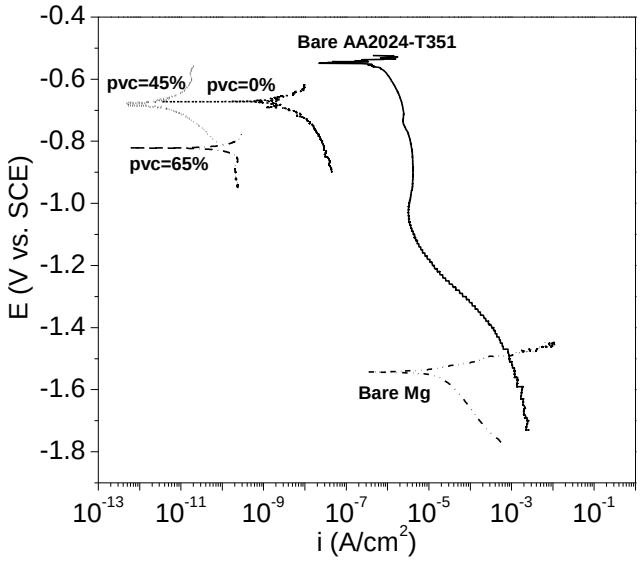

Figure 8.22. Potentiodynamic scans of bare electrodes and AA2024-T351 coated with Akzo Nobel MgRP + Aerodur 5000 topcoat exposed in 50 mM NaCl solution for 10 min, ambient aeration.
——— = Bare AA2024-T351, ━ · · ━ = Bare Mg Rod 99.9% Pure, - - - - = Topcoated MgRP PVC = 0% ID: 493-039-B-T-P22, · · · · = Topcoated MgRP PVC = 45% ID: T45F, ━ · ━ = Topcoated MgRP PVC = 65% ID: T65F.

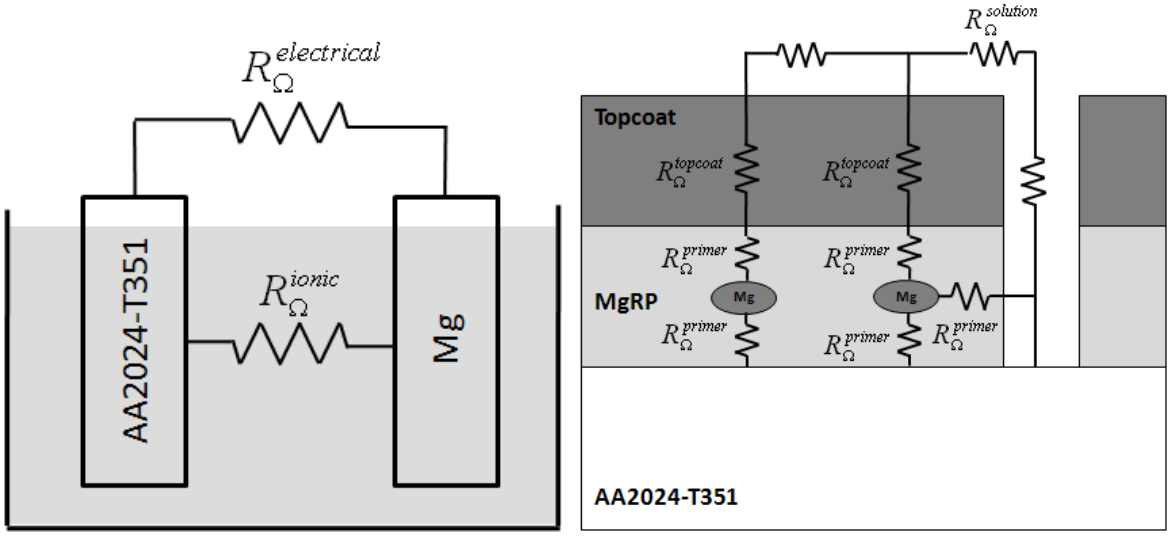

(a) (b)

Figure 8.23. Schematic showing the Ohmic resistances that exist between the Mg

pigment and the electrolyte (ionic) as well as between the Mg pigment and the substrate (electrical).(Interfacial resistances are omitted)

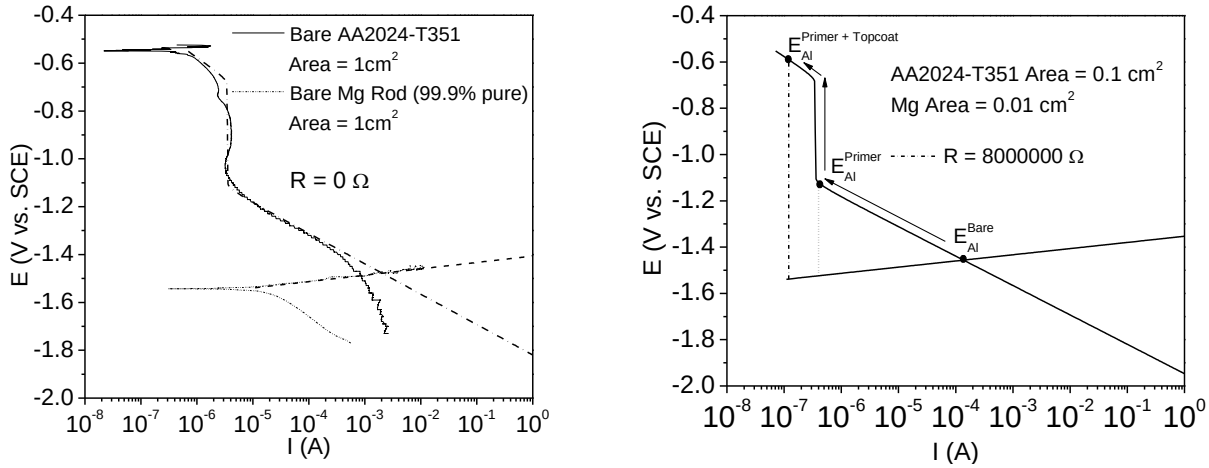

(a) (b)

Figure 8.24. Mixed potential theory modeling based upon polarization scans of bare Mg and bare AA2024-T351.
(a) Polarization scans of bare AA2024-T351 and bare Mg with mixed potential model overlaid. (b) Hypothetically depicts the galvanic coupling of Mg pigment in the MgRP and the AA2024-T351 substrate, incorporating the potential drop due to ionic resistances through both the primer and topcoat polymers to the electrolyte and Ohmic resistances through the primer polymer to the AA2024-T351 substrate.

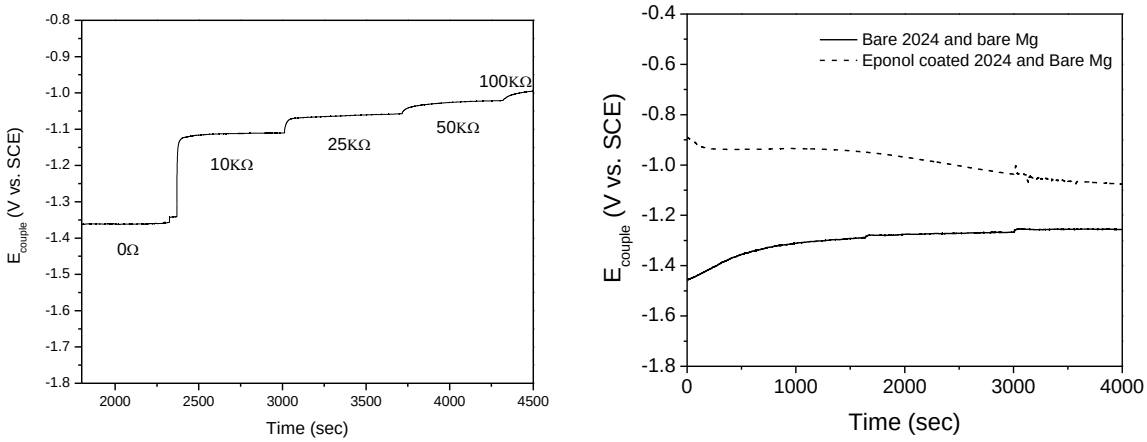

(a) (b)

Figure 8.25. Galvanic couple potential (E_{couple}) of bare AA2024 in a galvanic couple with bare Mg (a) Effect on E_{couple} by adding electrical resistance using a variable resistor. (b) Effect on E_{couple} by adding ionic resistance using an organic polymer coating of Eponol.

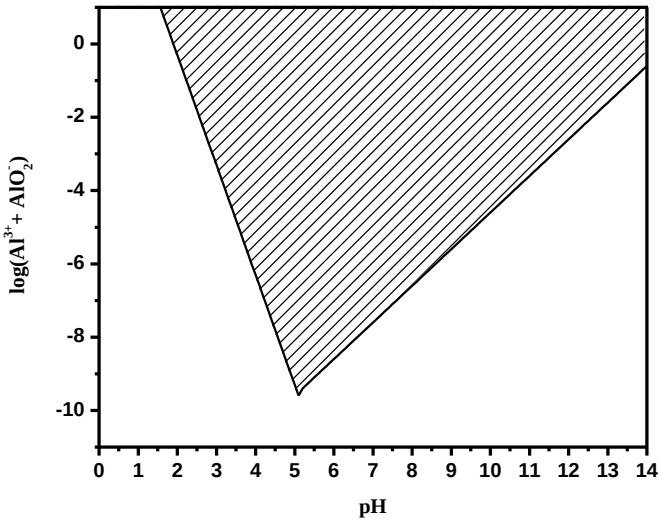

Figure 8.26. Al oxide stability diagram in water

M. Pourbaix, Atlas of Electrochemical Equilibria in Aqueous Solutions, 2d English, vol. (Houston, Tex.: National Association of Corrosion Engineers, 1974), p. 644 p.

9 APPENDIX B: Extensions of Environmental Degradation of a Mg-Rich Primer in Selected Laboratory Environments – Part III. In ASTM B-117 Modified with UV Light and Acidified Artificial Sea Water – FIGURES ONLY

9.1 Introduction

Two additional laboratory accelerated life tests (laboratory salt fog exposures) similar to those presented in Chapters 3 and 4 were conducted to study the effect of adding 1) ASTM artificial sea water + UV light and 2) acidified ASTM artificial sea water + UV light to the salt fog exposure environment. The salt fog exposure cabinet was modified to include four hanging ultraviolet A (UVA), fluorescent lights. The UVA lamps (Q-Lab Corporation model UVA-340) were chosen to simulate sunlight in the critical short-wave UV region from 365 nm down to the solar cutoff of 295 nm.[1] The ASTM artificial seawater was acidified with acetic acid per ASTM G85 A3, wherein artificial seawater was produced according to ASTM D1141 and acidified by the addition of 10 mL of glacial acetic acid per 1 L of salt solution.

9.2 References

1. Y. Wan, E. N. Macha and R. G. Kelly, Modification of ASTM B117 Salt Spray Corrosion Test and Its Correlation to Field Measurements of Silver Corrosion, Corrosion, 68, 3 (2012).

9.3 TABLES

Table 9.1. Exposure conditions in field and lab accelerated life testing environments.

Environment	Mean Temp (°C)				Mean RH (%)				Mean Dew Point (°C)			
	Win.	Spr.	Sum.	Fall	Win.	Spr.	Sum.	Fall	Win.	Spr.	Sum.	Fall
KSC	18.7	23.3	28.2	24.2	71.7	69.7	74	72.7	13.5	17.4	23.1	19
Birdwood	8.1	19.9	24	10.2	59.3	58.3	75.2	65.5	0.6	11	19.3	4
B-117	35				95				34			
B-117 w/ ASW	35				95				34			
B-117 w/ ASW + UV	35				95				34			
B-117 w/ Acid ASW + UV	35				95				34			

Environment	Mean Precipitation (mm/hr)				Precip. pH	Mean Cl^- ($\mu g/cm^2/hr$)
	Win.	Spr.	Sum.	Fall		
KSC	0.066	0.154	0.245	0.184	5.4 ± 0.4	0.8
Birdwood	0.102	0.102	0.135	0.139	4.9 ± 0.3	0.002
B-117	0.19				6.9 ± 0.4	600
B-117 w/ ASW	0.19				8.2 ± 0.3	390
B-117 w/ ASW + UV	0.19				8.2 ± 0.3	390
B-117 w/ Acid ASW + UV	0.19				3.2 ± 0.2	390

Table 9.2. Fitting results of EIS measured on AA2024-T351 panels coated with MgRP (MgPVC = 45%) after LALT in ASTM B-117 modified with artificial sea water and UV light for 0, 192, 408, 698 and 1000 hours.
Tested in ambiently aerated 5% NaCl Solution. Equivalent electric circuit model used shown in Chapter 3.

	units	0 hrs	192 hrs	400 hrs	696 hrs	1000 hrs
R_s	(Ω-cm^2)	10.000	10.000	10.000	10.000	10.000
C_{coat}-Y^o	(μF/cm^2)	0.007	1.611	0.605	1.471	3.783
C_{coat}-n	-	0.357	0.604	0.623	0.614	0.591
R_{coat}	(kΩ-cm^2)	0.003	21.040	85.440	9.330	4.603
C_{dl}-Y^o	(μF/cm^2)	0.005	3.335	2.556	11.090	15.760
C_{dl}-n	-	0.863	0.811	0.609	0.591	0.694
R_{corr}	(GΩ-cm^2)	10.000	10.000	10.000	10.000	10.000

Table 9.3. Fitting results of EIS measured on AA2024-T351 panels coated with MgRP (MgPVC = 45%) after LALT in ASTM B-117 modified with acidified artificial sea water and UV light for 0, 192, 408, 698 and 1000 hours.
Tested in ambiently aerated 5% NaCl Solution. Equivalent electric circuit model used shown in Chapter 3.

	units	0 hrs	192 hrs	400 hrs	696 hrs	1000 hrs
R_s	(Ω-cm^2)	10.000	9.899	10.000	10.000	10.000
C_{coat}-Y^o	(μF/cm^2)	0.007	0.003	53.410	46.210	48.930
C_{coat}-n	-	0.357	0.283	0.542	0.563	0.546
R_{coat}	(kΩ-cm^2)	0.003	0.011	0.015	0.013	0.008
C_{dl}-Y^o	(μF/cm^2)	0.005	66.080	753.400	461.700	1644.000
C_{dl}-n	-	0.863	0.669	0.759	0.639	0.828
R_{corr}	(MΩ-cm^2)	10000.000	0.025	0.007	0.007	0.004

Table 9.4. Fitting results of EIS measured on AA2024-T351 panels coated with MgRP (MgPVC = 45%) and polyurethane topcoat after LALT in ASTM B-117 modified with artificial sea water and UV light for 0, 192, 408, 698 and 1000 hours.
Tested in ambiently aerated 5% NaCl Solution. Equivalent electric circuit model used shown in Chapter 3.

	units	0 hrs	192 hrs	400 hrs	696 hrs	1000 hrs
R_s	(Ω-cm^2)	10.000	10.000	10.000	10.000	10.000
C_{coat}-Y^o	(nF/cm^2)	0.164	0.338	0.492	0.387	0.516
C_{coat}-n	-	0.966	0.945	0.888	0.932	0.891
R_{coat}	(MΩ-cm^2)	10.000	0.460	37.120	6.890	70.870
C_{dl}-Y^o	(nF/cm^2)	0.201	0.172	17.850	585.800	6.262
C_{dl}-n	-	0.607	0.544	0.053	0.337	0.135
R_{corr}	(GΩ-cm^2)	152.000	46.870	0.389	0.006	0.107

Table 9.5. Fitting results of EIS measured on AA2024-T351 panels coated with MgRP (MgPVC = 45%) and polyurethane topcoat after LALT in ASTM B-117 modified with acidified artificial sea water and UV light for 0, 192, 408, 698 and 1000 hours.
Tested in ambiently aerated 5% NaCl Solution. Equivalent electric circuit model used shown in Chapter 3.

	units	0 hrs	48	384	696 hrs	1000 hrs
R_s	(Ω-cm^2)	10.000	10.000	10.000	10.000	10.000
C_{coat}-Y^o	(nF/cm^2)	0.164	0.178	0.271	0.523	0.626
C_{coat}-n	-	0.966	0.941	0.918	0.938	0.901
R_{coat}	(MΩ-cm^2)	10.000	114.800	0.004	0.009	0.104
C_{dl}-Y^o	(nF/cm^2)	0.201	8.987	37.090	21170.000	4356.000
C_{dl}-n	-	0.607	0.596	0.085	0.397	0.368
R_{corr}	(GΩ-cm^2)	152.000	3461.000	8087.000	19820.000	4.322

Table 9.6. Summary of observations made after environmental exposure in various environments.

Environment	UV?	Macroscopic Blistering	Underpaint Corrosion	Cathodic Corrosion	Throwing Power
Kennedy Space Center, FL – 24 wks	YES	NO	NO	NO	200 - 300 μm
Charlottesville, VA – 24 wks	YES	NO	NO	NO	n/a
ASTM B-117 w/ 5% NaCl – 1000 h	NO	NO	NO	NO	≥ 350 μm
ASTM B-117 w/ ASW – 1000 h	NO	NO	NO	NO	≥ 350 μm
ASTM B-117 w/ ASW + UV – 1000h	YES	NO	NO	NO	≥ 350 μm
B-117 w/ acid ASW + UV – 1000 h	YES	YES	YES	NO	n/a
Full Immersion in ambiently aerated 5% NaCl – 170 h	NO	NO	NO	NO	No scribe*

*a non-scribed area of MgRP-coated AA2024-T351 was exposed in a flat cell to 5% NaCl to study the representative global degradation of the coating. Follow up experiments include the same exposure and include variations in the area of bare AA2024-T351.

9.4 FIGURES

9.4.1 No Topcoat

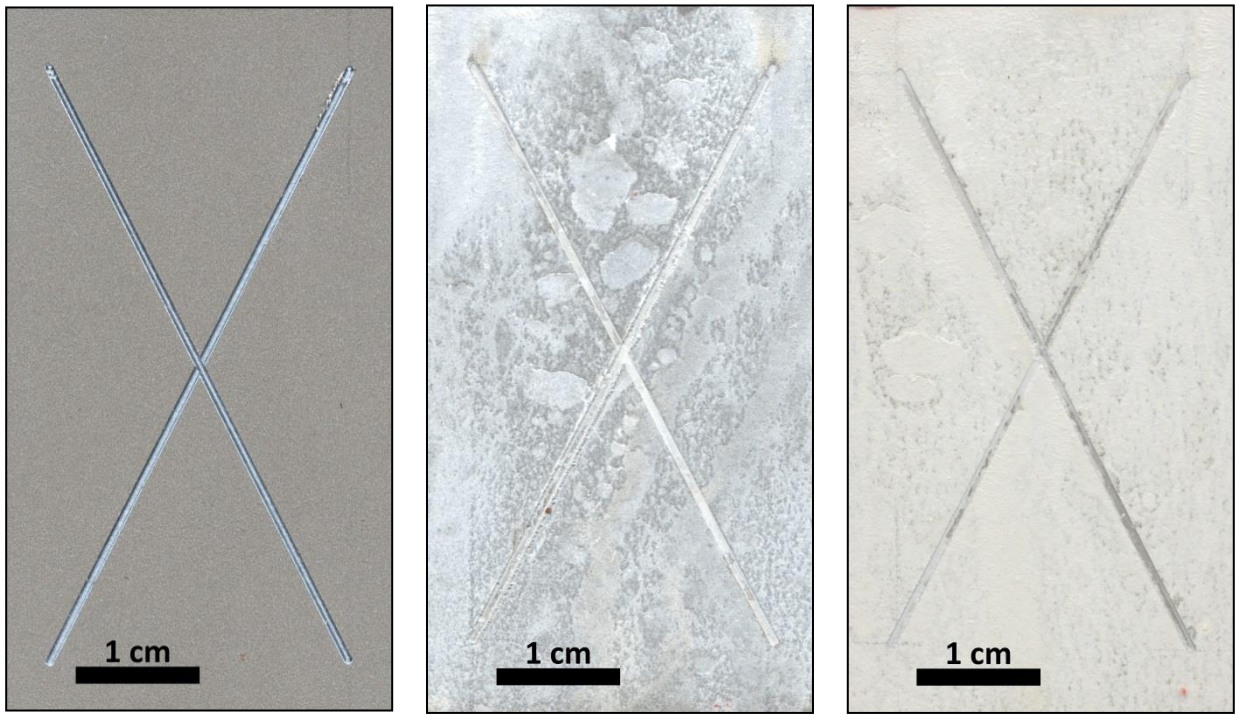

(a) (b) (c)

Figure 9.1. Optical micrograph of AA2024-T351 panels coated with MgRP (initial MgPVC = 45%) after lab accelerated life testing in ASTM B-117 modified with ASTM artificial sea water and UV light for (a) T = 0 hrs (b) T = 400 hrs (c) T = 1000 hrs

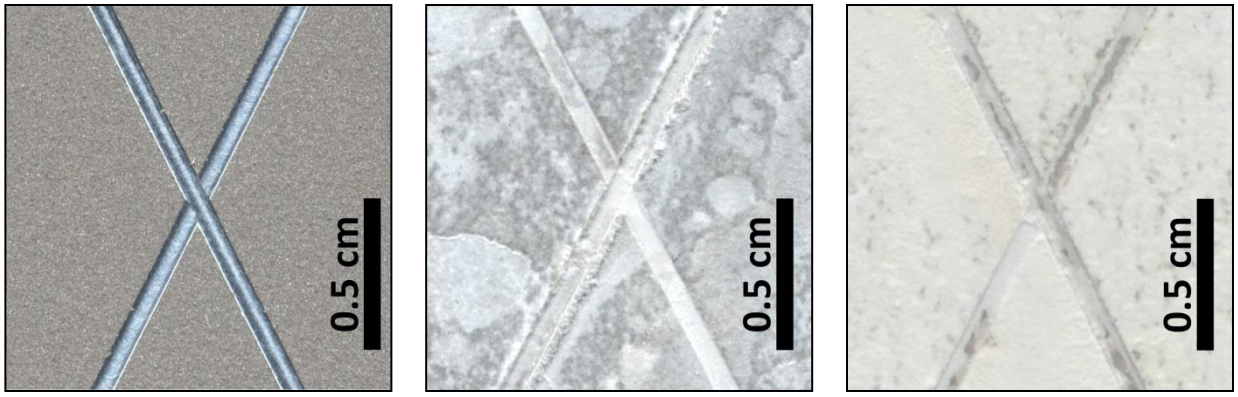

(a) T = 0 hrs in B-117 w/ ASW + UV

(b) T = 400 hrs in B-117 w/ ASW + UV

(c) T = 1000 hrs in B-117 w/ ASW + UV

Figure 9.2. Optical micrograph of AA2024-T351 panels coated with MgRP (initial MgPVC = 45%) after lab accelerated life testing in ASTM B-117 modified with ASTM artificial sea water and UV light for (a) T = 0 hrs (b) T = 400 hrs (c) T = 1000 hrs

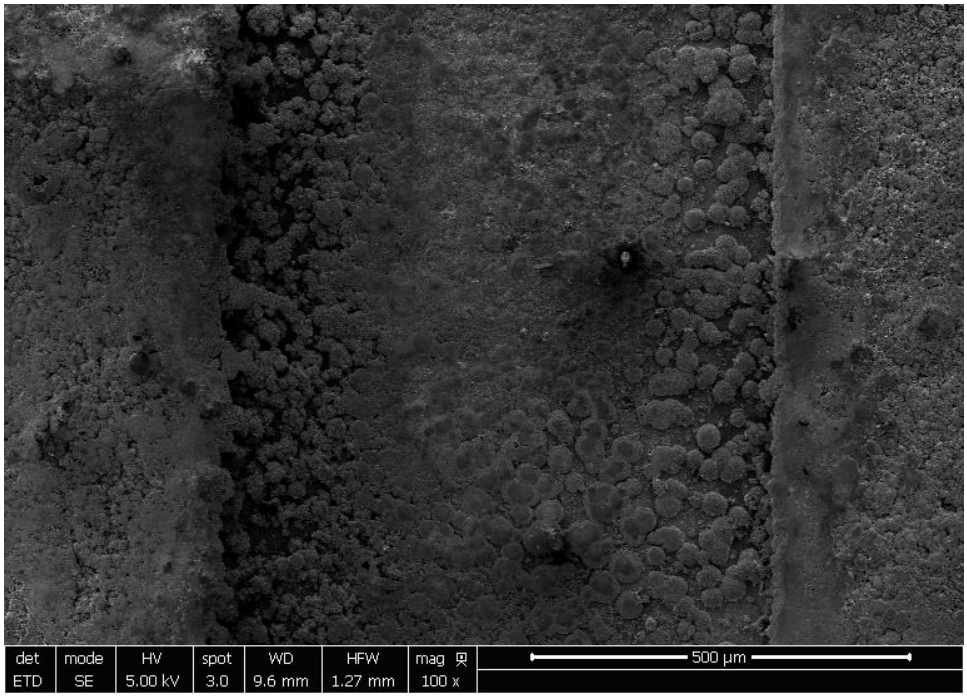

Figure 9.3. Planar-view SEM micrograph of scribed AA2024-T351 pretreated with Prekote and coated with MgRP (initial MgPVC = 45%) after after lab accelerated life testing in ASTM B-117 modified with ASTM artificial sea water and UV for 400 h.

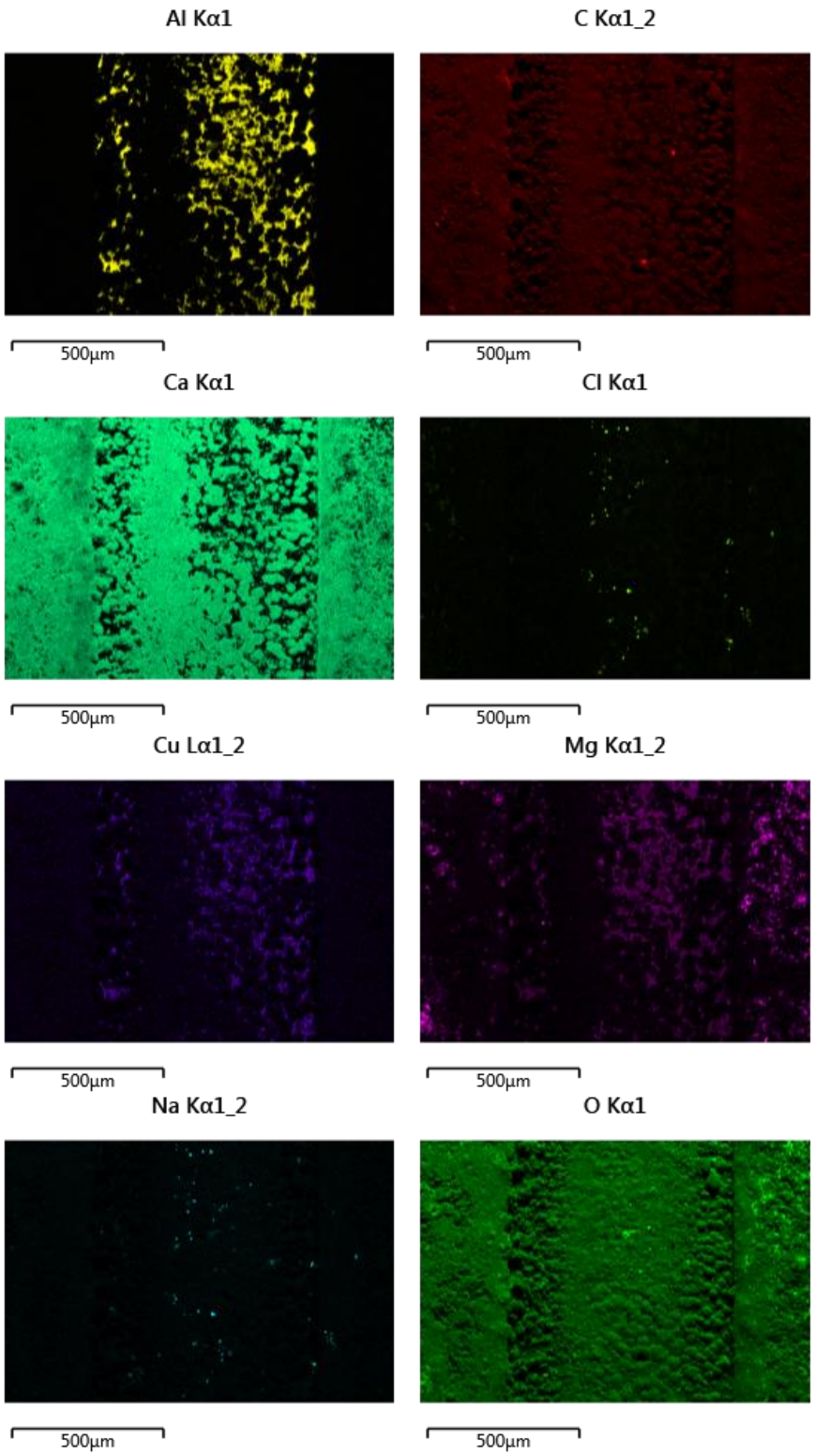

Figure 9.4. Planar-view EDS maps of scribed AA2024-T351 pretreated with Prekote and coated with MgRP (initial MgPVC = 45%) after lab accelerated life testing in ASTM B-117 modified with ASTM artificial sea water and UV for 400 h.

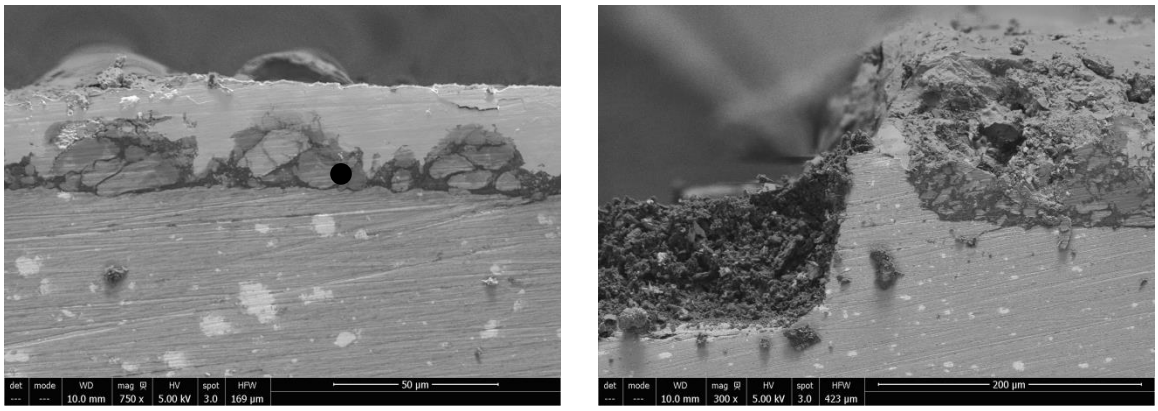

(a) (b)

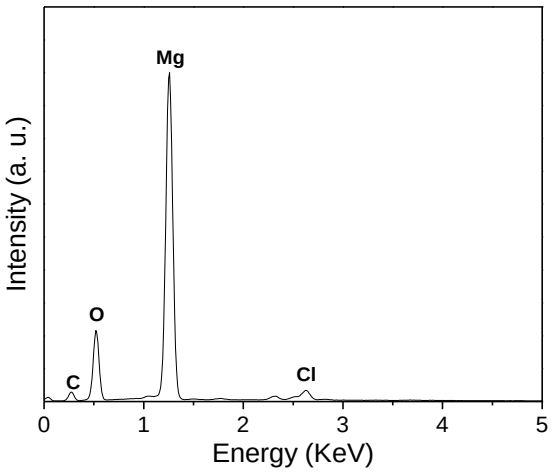

(c)

Figure 9.5. Cross-section SEM micrograph (a) far away from and (b) near to the scribe and (c) EDS spectra of scribed AA2024-T351 pretreated with Prekote and coated with MgRP (initial MgPVC = 45%) after lab accelerated life testing in ASTM B-117 modified with ASTM artificial sea water and UV for 400 h.
Spot marker in (a) indicates approximate location of EDS analysis shown in (c)

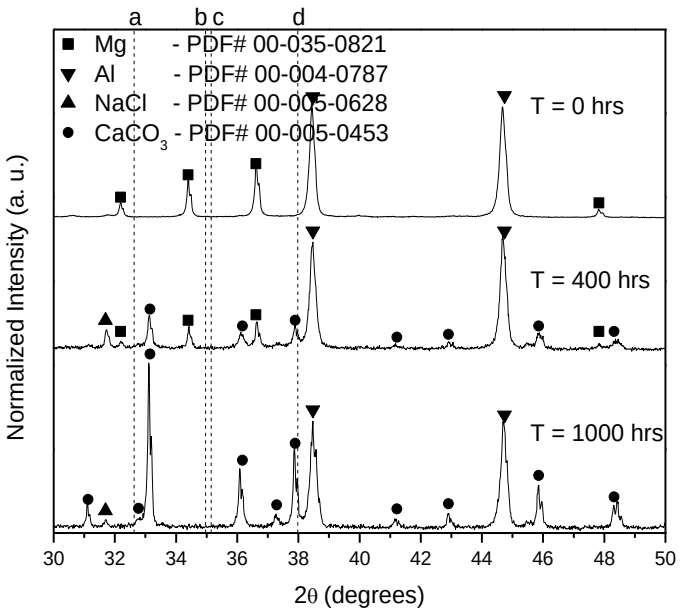

Figure 9.6. X-Ray diffraction spectra of AA2024-T351 panels coated with MgRP (initial MgPVC = 45%) that have been environmentally exposed in ASTM B-117 with ASTM Artificial Seawater and UV for 0, 400 and 1000 hours. Dotted lines indicate the position of the most intense diffraction peak for (a) $MgCO_3$ (b) $MgCl_2$(c) Al_2O_3 and (d) $Mg(OH)_2$.

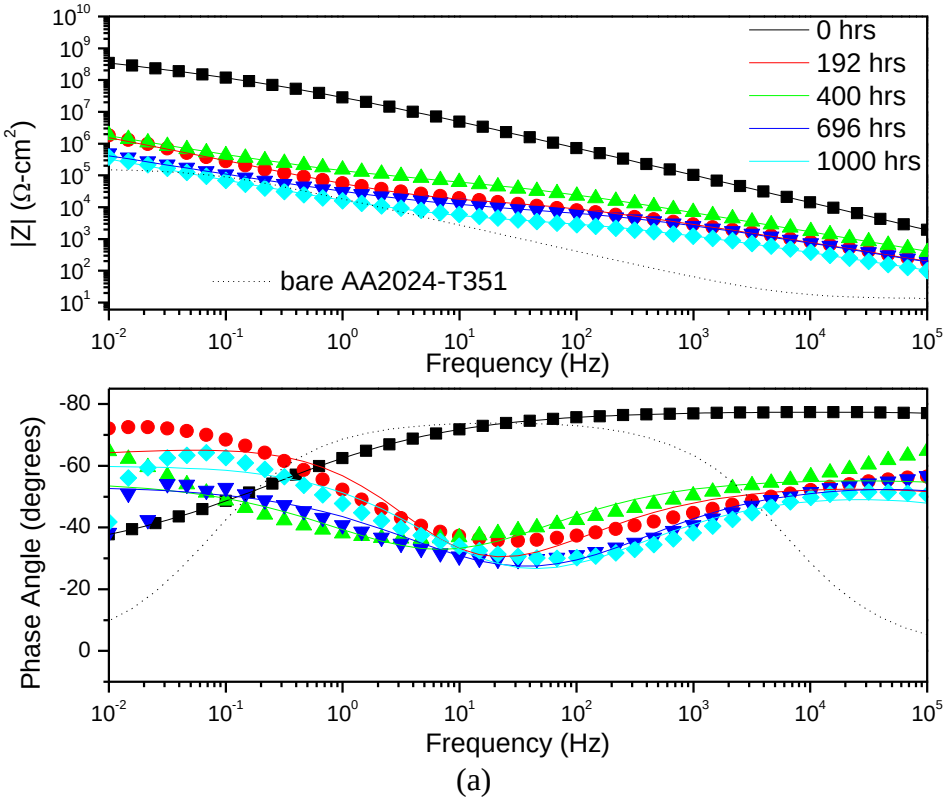

(a)

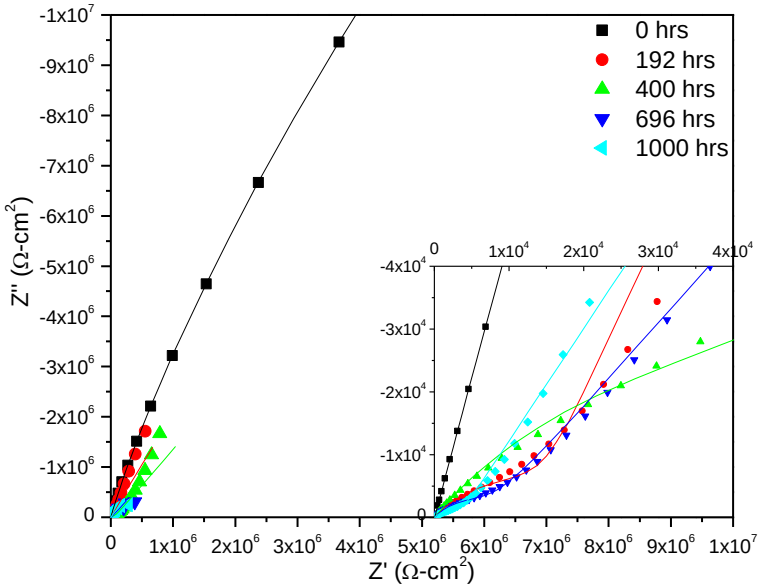

(b)

Figure 9.7. (a) Bode and (b) Nyquist plots of EIS of AA2024-T351 panels coated with MgRP (initial MgPVC = 45%) that have been environmentally exposed in ASTM B-117 modified with ASTM artificial sea water and UV light for 0, 192, 400, 696, and 1000 hours. Tested in ambiently aerated 5% NaCl solution. Fit results tabulated in Table 3.2

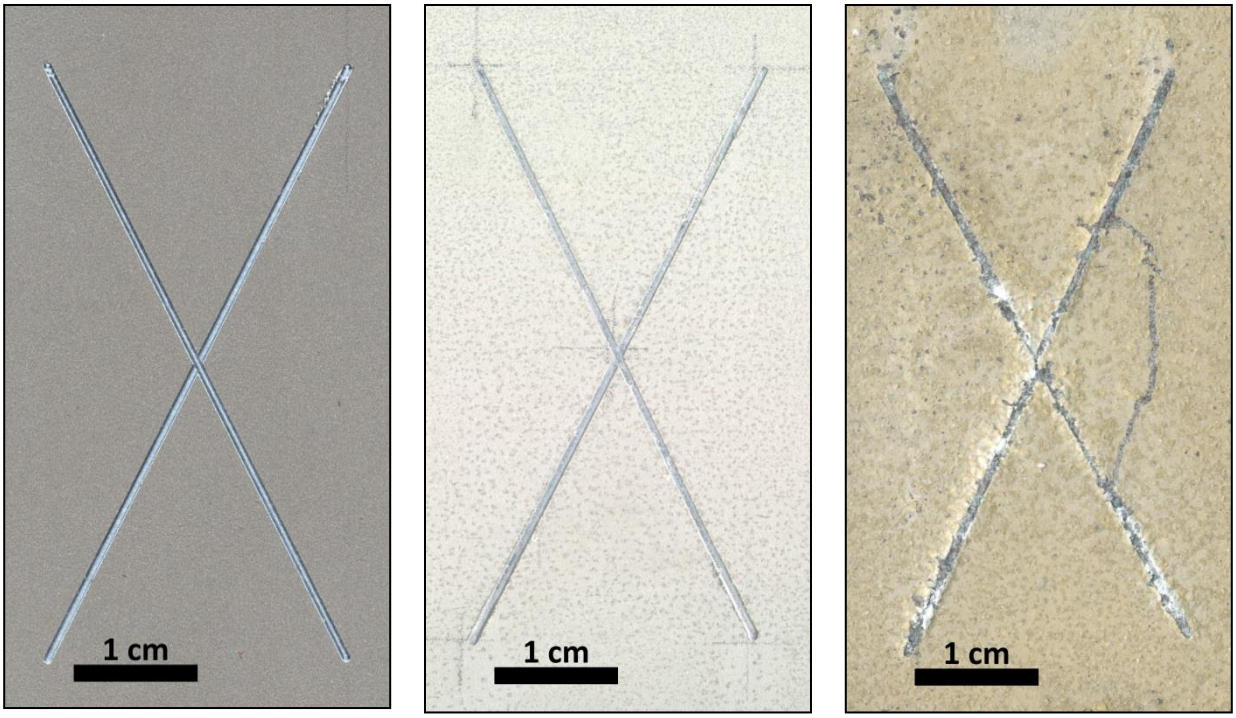

(a) (b) (c)

Figure 9.8. Optical micrograph of AA2024-T351 panels coated with MgRP (initial MgPVC = 45%) after lab accelerated life testing in ASTM B-117 modified with acidified ASTM artificial sea water and UV light. (a) T = 0 hrs (b) T = 384 hrs (c) T = 1000 hrs

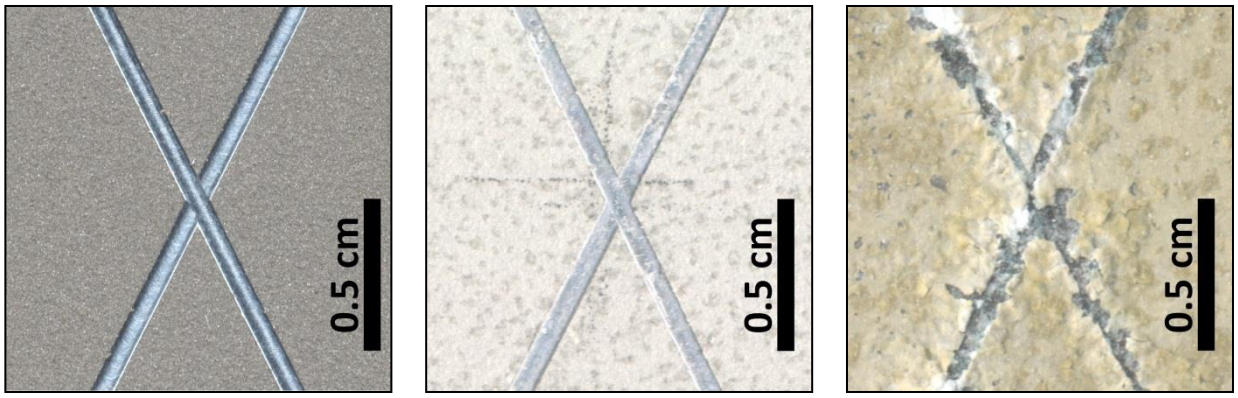

(a) T = 0 hrs in ASTM B-117 w/ ASW

(b) T = 384 hrs in ASTM B-117 w/ ASW

(c) T = 1000 hrs in ASTM B-117 w/ ASW

Figure 9.9. Optical micrograph of AA2024-T351 panels coated with MgRP (initial MgPVC = 45%) after lab accelerated life testing in ASTM B-117 modified with acidified ASTM artificial sea water and UV light (a) T = 0 hrs (b) T = 384 hrs (c) T = 1000 hrs

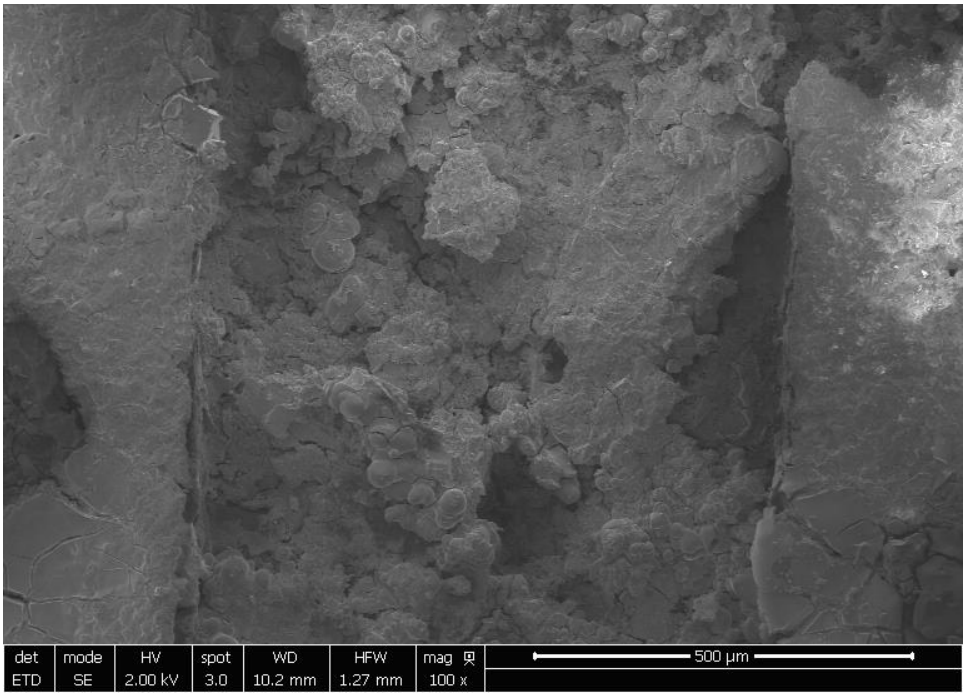

Figure 9.10. Planar-view SEM micrograph (a) of scribed AA2024-T351 pretreated with Prekote and coated with MgRP (initial MgPVC = 45%) after after lab accelerated life testing in ASTM B-117 modified with acidified ASTM artificial sea water and UV light for 408 h.

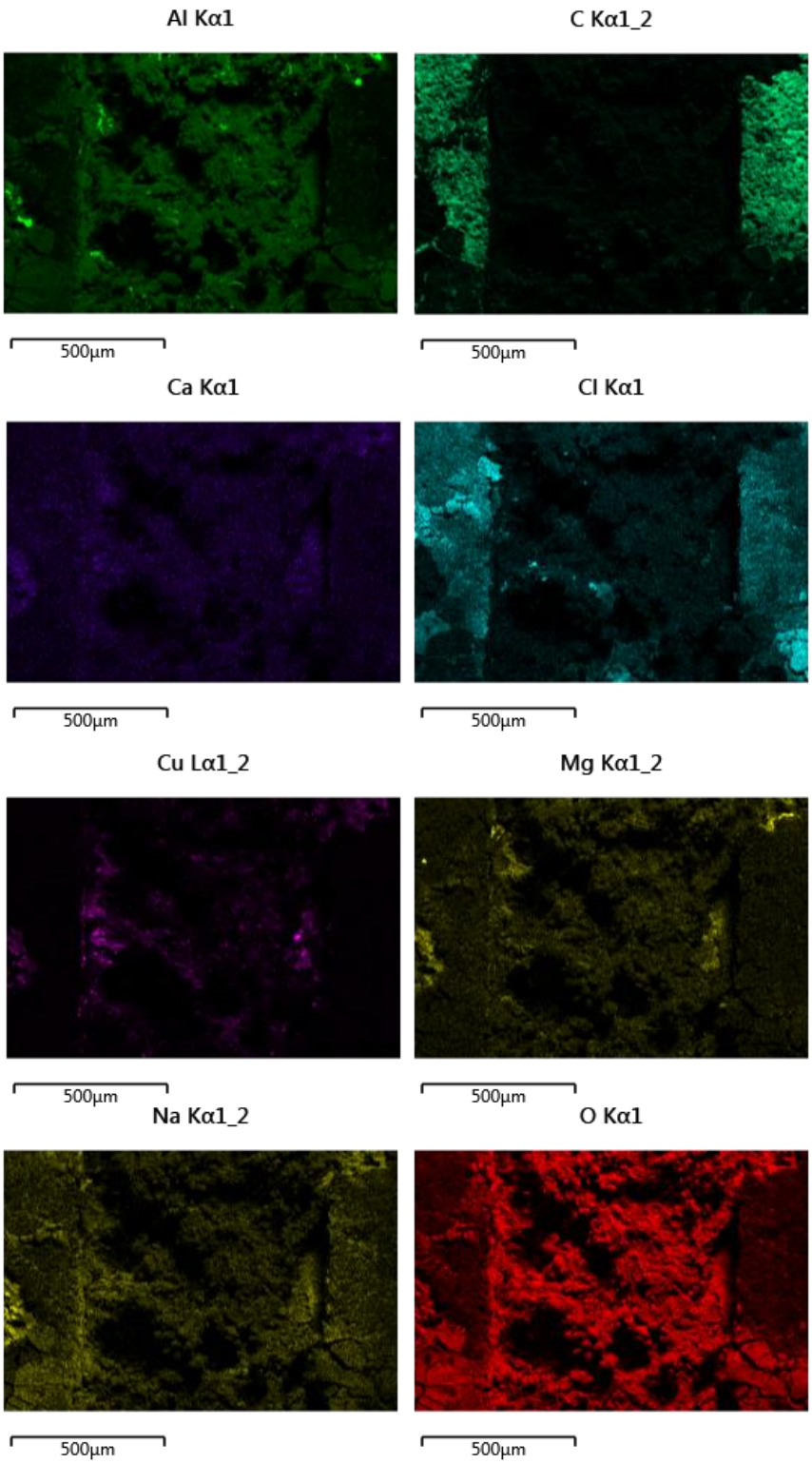

Figure 9.11. Planar-view EDS maps of scribed AA2024-T351 pretreated with Prekote and coated with MgRP (initial MgPVC = 45%) after lab accelerated life testing in ASTM B-117 modified with acidified ASTM artificial sea water and UV light 408 h.

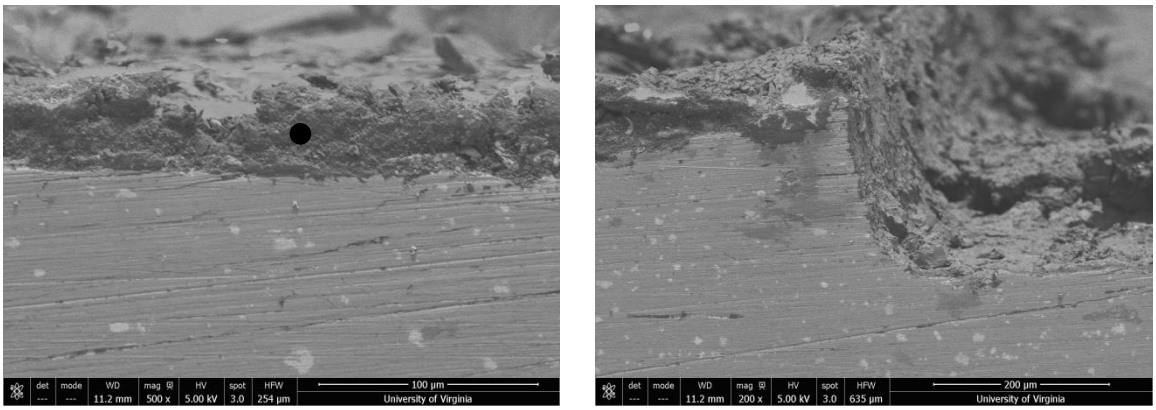

(a) (b)

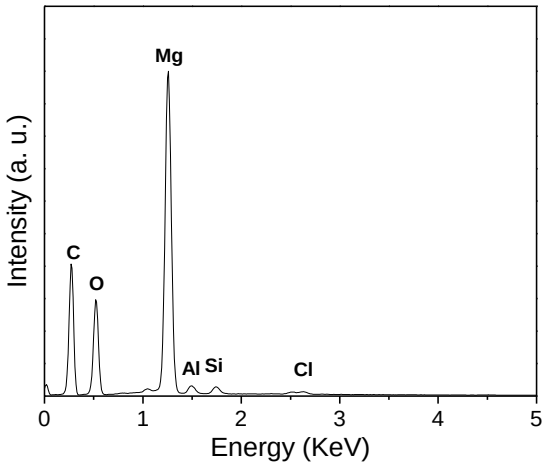

(c)

Figure 9.12. Cross-section SEM micrograph (a) far away from and (b) near to the scribe and (c) EDS spectra of scribed AA2024-T351 pretreated with Prekote and coated with MgRP (initial MgPVC = 45%) after lab accelerated life testing in ASTM B-117 modified with ASTM artificial sea water and UV for 400 h.
Spot marker in (a) indicates approximate location of EDS analysis shown in (c)

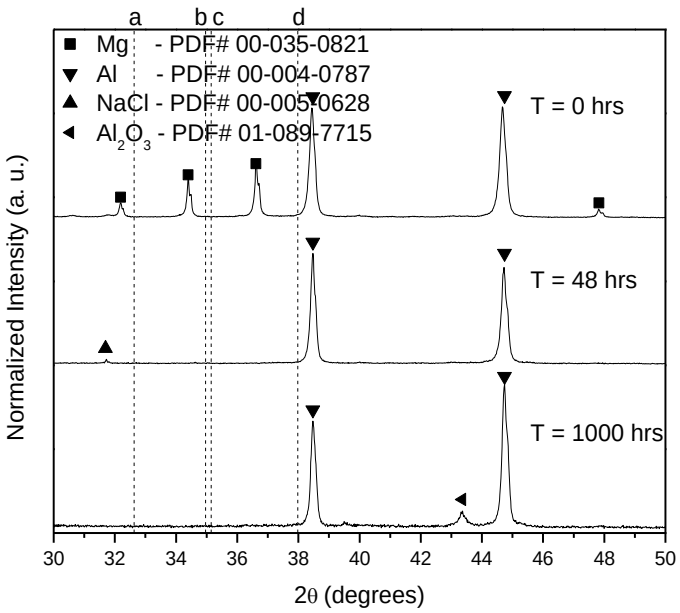

Figure 9.13. X-Ray diffraction spectra of AA2024-T351 panels coated with MgRP (initial MgPVC = 45%) after lab accelerated life testing in ASTM B-117 modified with acidified ASTM artificial sea water and UV light for 0, 48 and 1000 hours. Dotted lines indicate the position of the most intense diffraction peak for (a) $MgCO_3$ (b) $MgCl_2$(c) Al_2O_3 and (d) $Mg(OH)_2$.

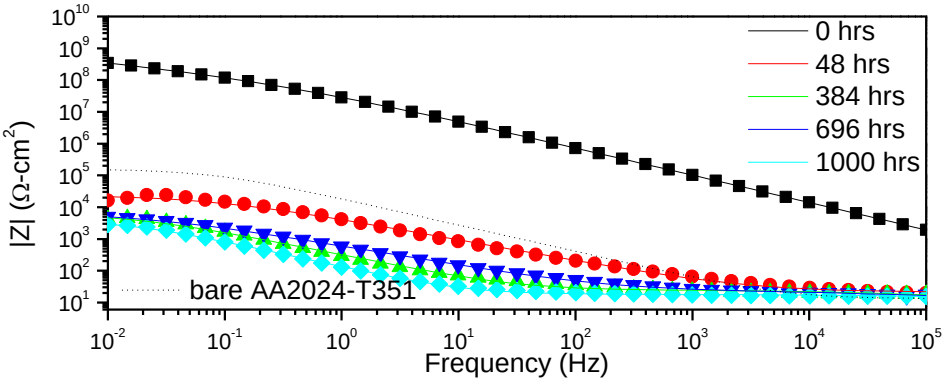

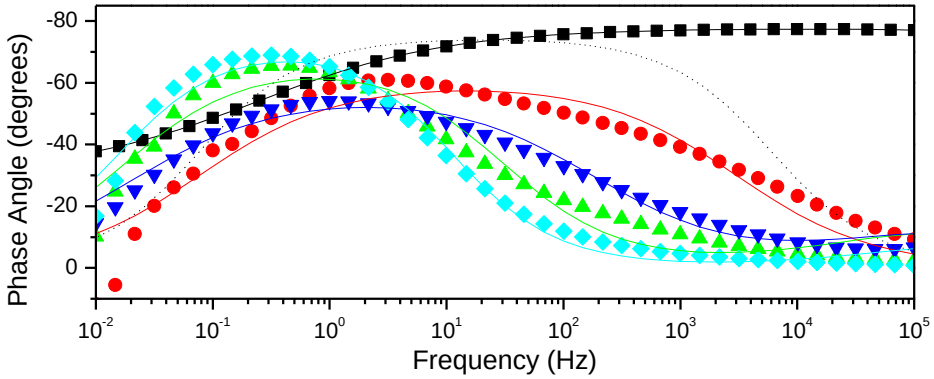

(a)

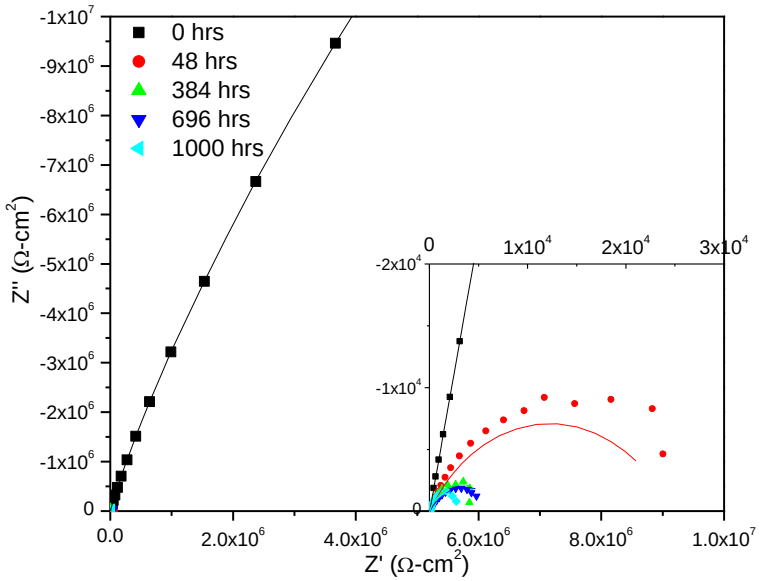

(b)

Figure 9.14. (a) Bode and (b) Nyquist plots of EIS of AA2024-T351 panels coated with MgRP (initial MgPVC = 45%) after lab accelerated life testing in ASTM B-117 modified with acidified ASTM artificial sea water and UV light for 0, 48, 384, 696, and 1000 hours. Tested in ambiently aerated 5% NaCl solution. Fit results tabulated in Table 3.3.

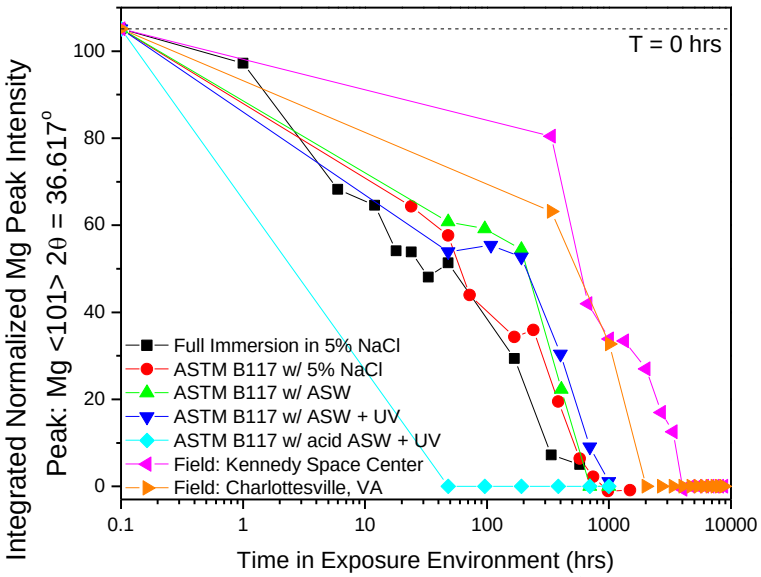

Figure 9.15. Integrated Mg peak (Mg <200> 2θ = 36.6170°) intensity vs. environmental exposure time in various lab and field exposure environments for panels of AA2024-T351 coated with MgRP (initial MgPVC = 45%). Dotted line indicates initial integrated Mg peak intensity of an unexposed panel. XRD Detection limit is estimated to be 3 – 5% of samples by volume.[1]

[1] V. K. Pecharsky and P. Y. Zavalij, Fundamentals of Powder Diffraction and Structural Characterization of Materials, 2nd, vol. (New York: Springer, 2009), p. xxiii, 741 p.

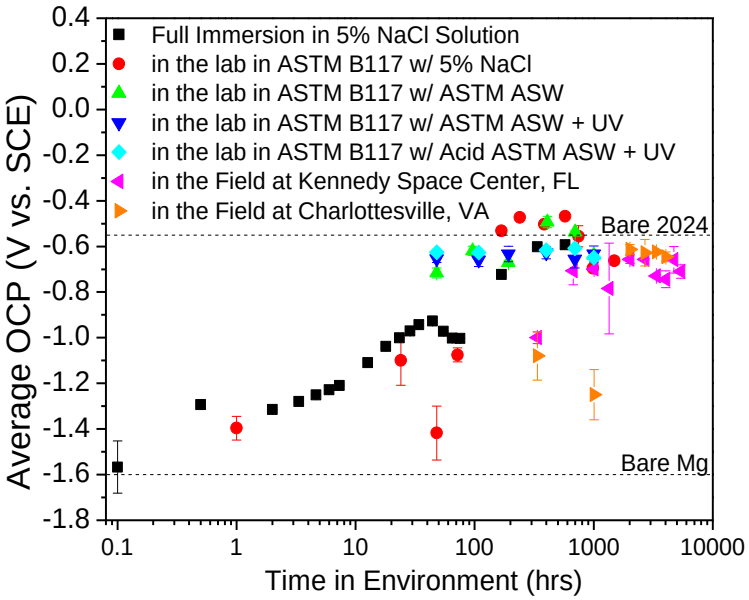

Figure 9.16. Galvanic protection potential of AA2024-T351 coated with MgRP (initial MgPVC = 45%) in ambiently aerated 5% NaCl solution vs. environmental exposure time in various lab and field exposure environments.

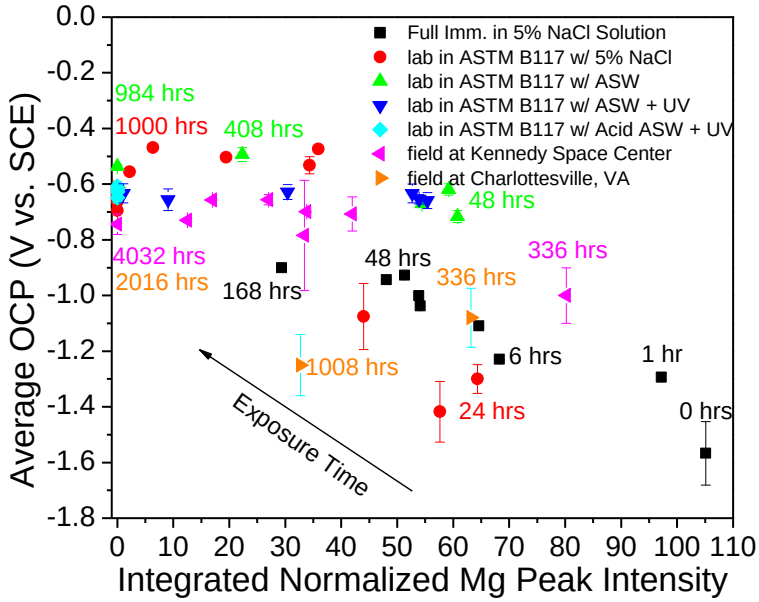

Figure 9.17. Correlation between integrated Mg peak (Mg <200> 2θ = 36.6170°) intensity vs. galvanic protection potential of AA2024-T351 coated with MgRP (initial MgPVC = 45%) in ambiently aerated 5% NaCl solution after exposure in various environments.

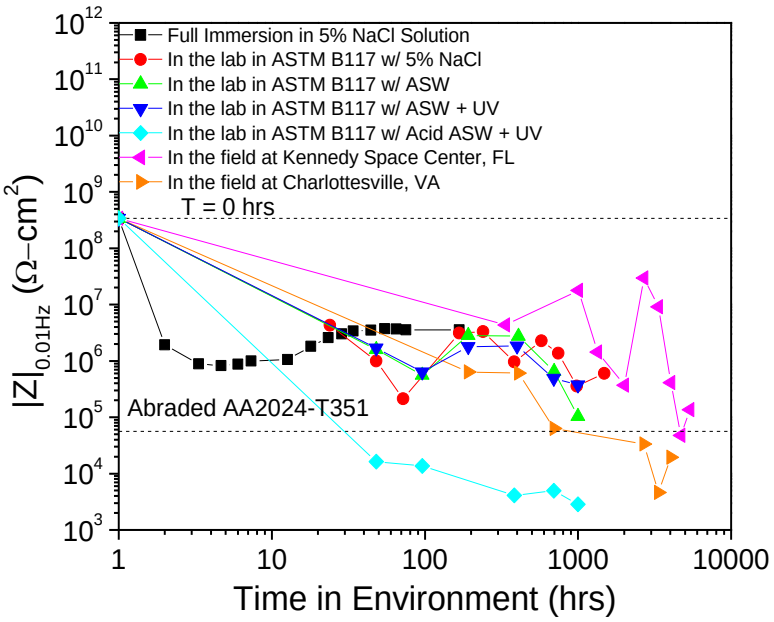

Figure 9.18. Magnitude of electrochemical impedance at 0.01 Hz in ambiently aerated 5% NaCl solution vs. environmental exposure time in various exposure environments for panels of AA2024-T351 coated with MgRP (initial MgPVC = 45%).

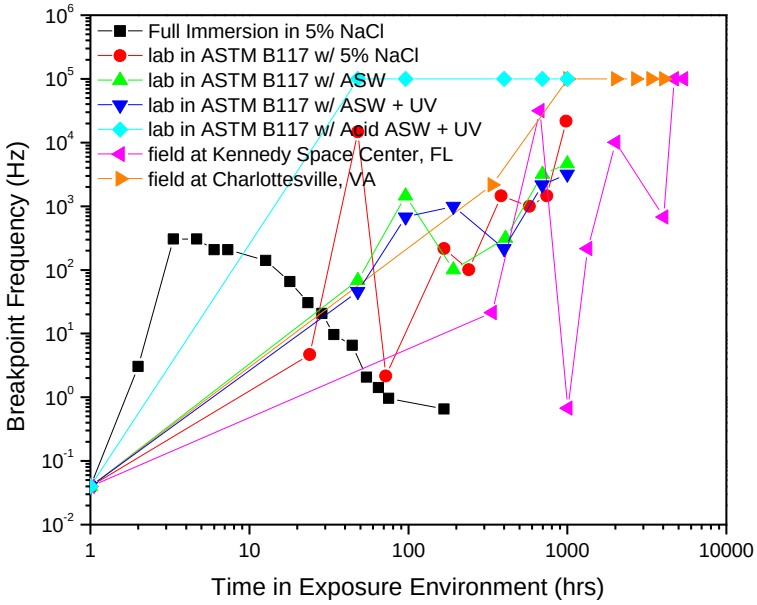

Figure 9.19. Breakpoint frequency in ambiently aerated 5% NaCl solution vs. environmental exposure time in various exposure environments for panels of AA2024-T351 coated with MgRP (initial MgPVC = 45%).

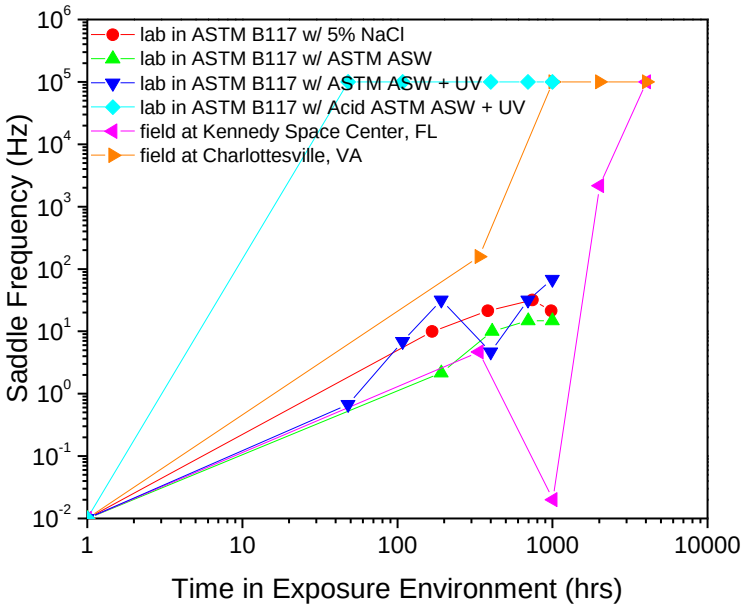

Figure 9.20. Saddle Frequency in ambiently aerated 5% NaCl solution vs. environmental exposure time in various exposure environments for panels of AA2024-T351 coated with MgRP (initial MgPVC = 45%).

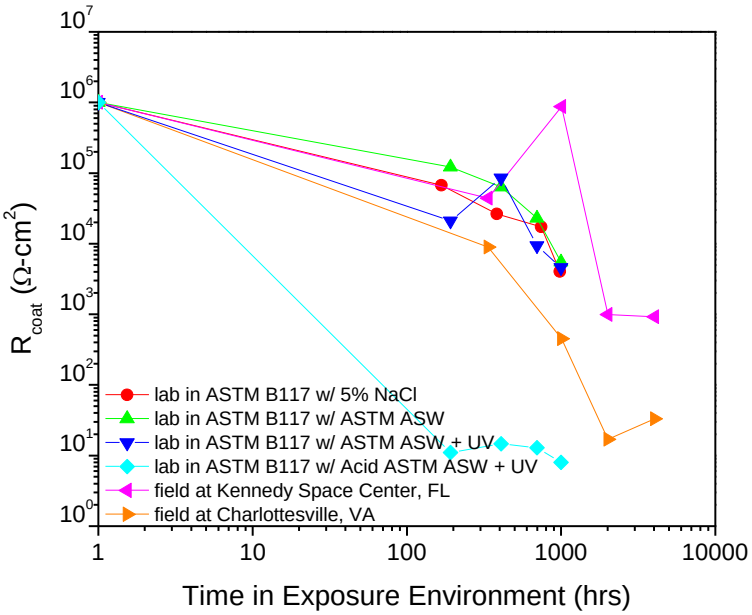

Figure 9.21. R_{coat} in ambiently aerated 5% NaCl solution vs. environmental exposure time in various exposure environments for panels of AA2024-T351 coated with MgRP (initial MgPVC = 45%).

9.4.2 With Topcoat

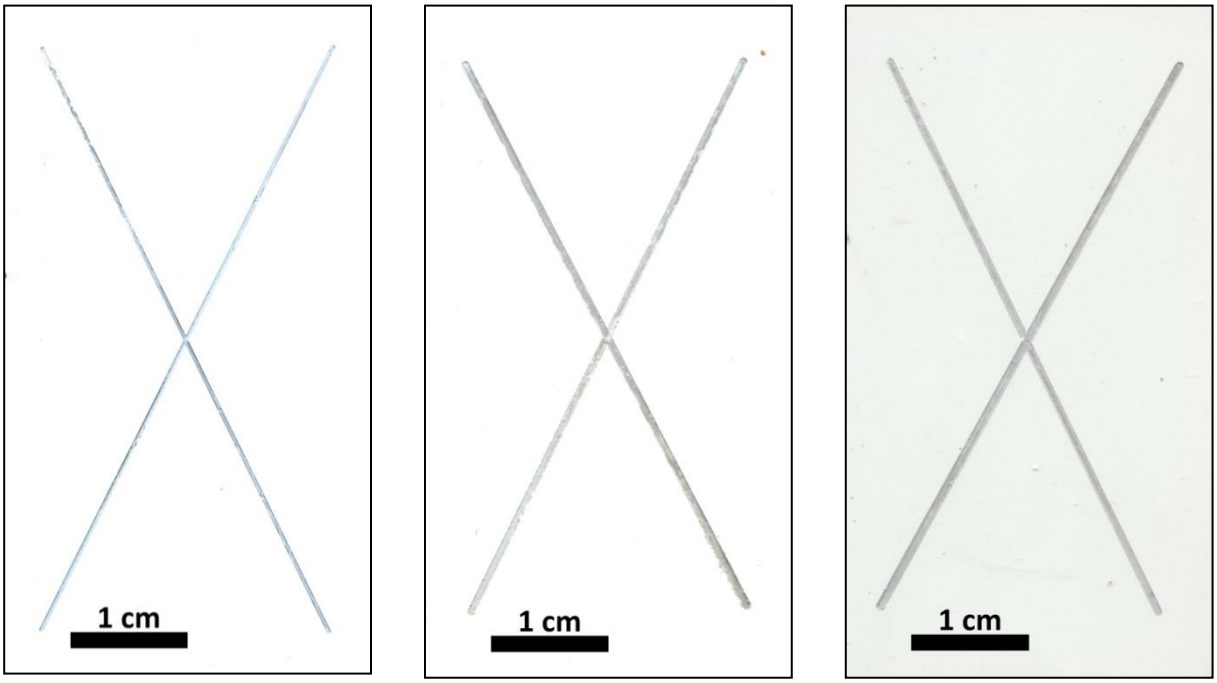

(a) (b) (c)

Figure 9.22. Optical micrograph of AA2024-T351 panels coated with Mg-rich primer (initial MgPVC = 45%) and polyurethane topcoat that have been environmentally exposed in ASTM B-117 with ASTM ASW and UV light for (a) T = 0 hrs (b) T = 384 hrs (c) T = 984 hrs

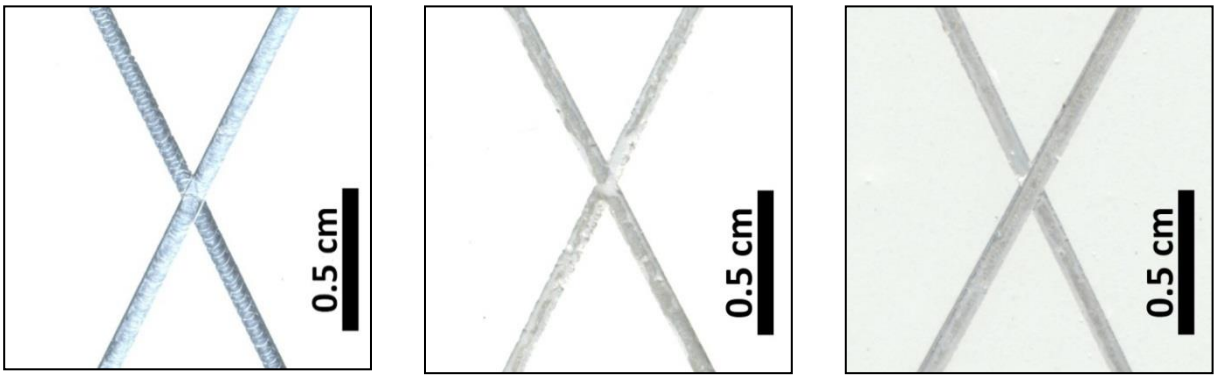

(a) T = 0 hrs in ASTM B-117 (b) T = 384 hrs in ASTM B-117 (c) T = 984 hrs in ASTM B-117

Figure 9.23. Optical micrograph of AA2024-T351 panels coated with Mg-rich primer (initial MgPVC = 45%) and polyurethane topcoat that have been environmentally exposed in ASTM B-117 modified with ASTM artificial sea water and UV light for (a) T = 0 hrs (b) T = 384 hrs (c) T = 984 hrs

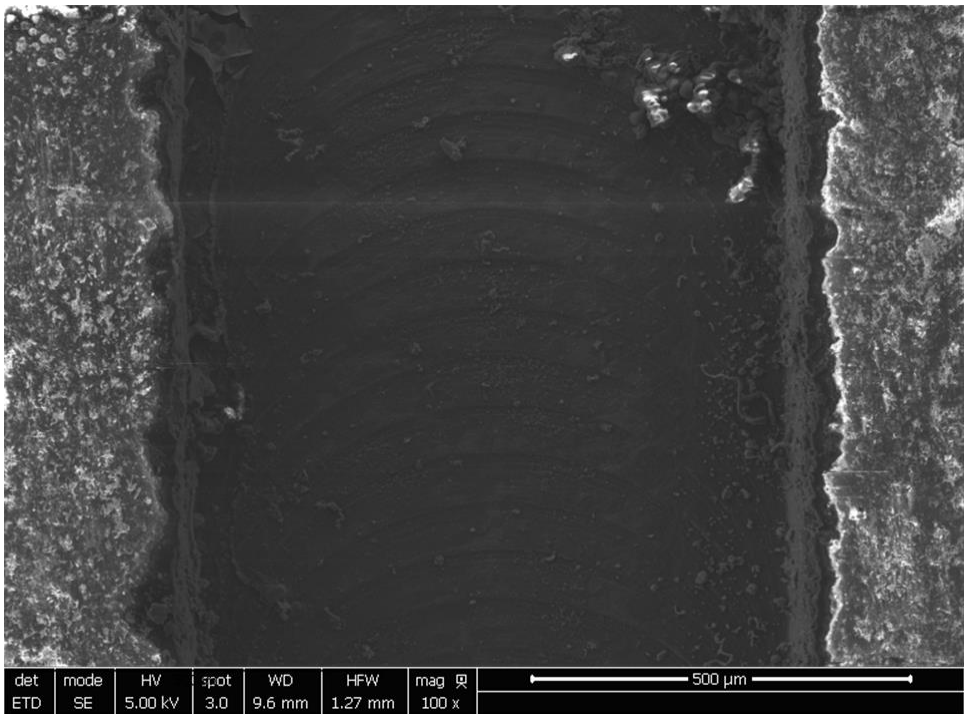

Figure 9.24. Planar-view SEM micrograph of scribed AA2024-T351 pretreated with Prekote and coated with MgRP (initial MgPVC = 45%) and polyurethane topcoat after after lab accelerated life testing in ASTM B-117 modified with ASTM artificial sea water and UV for 400 h.

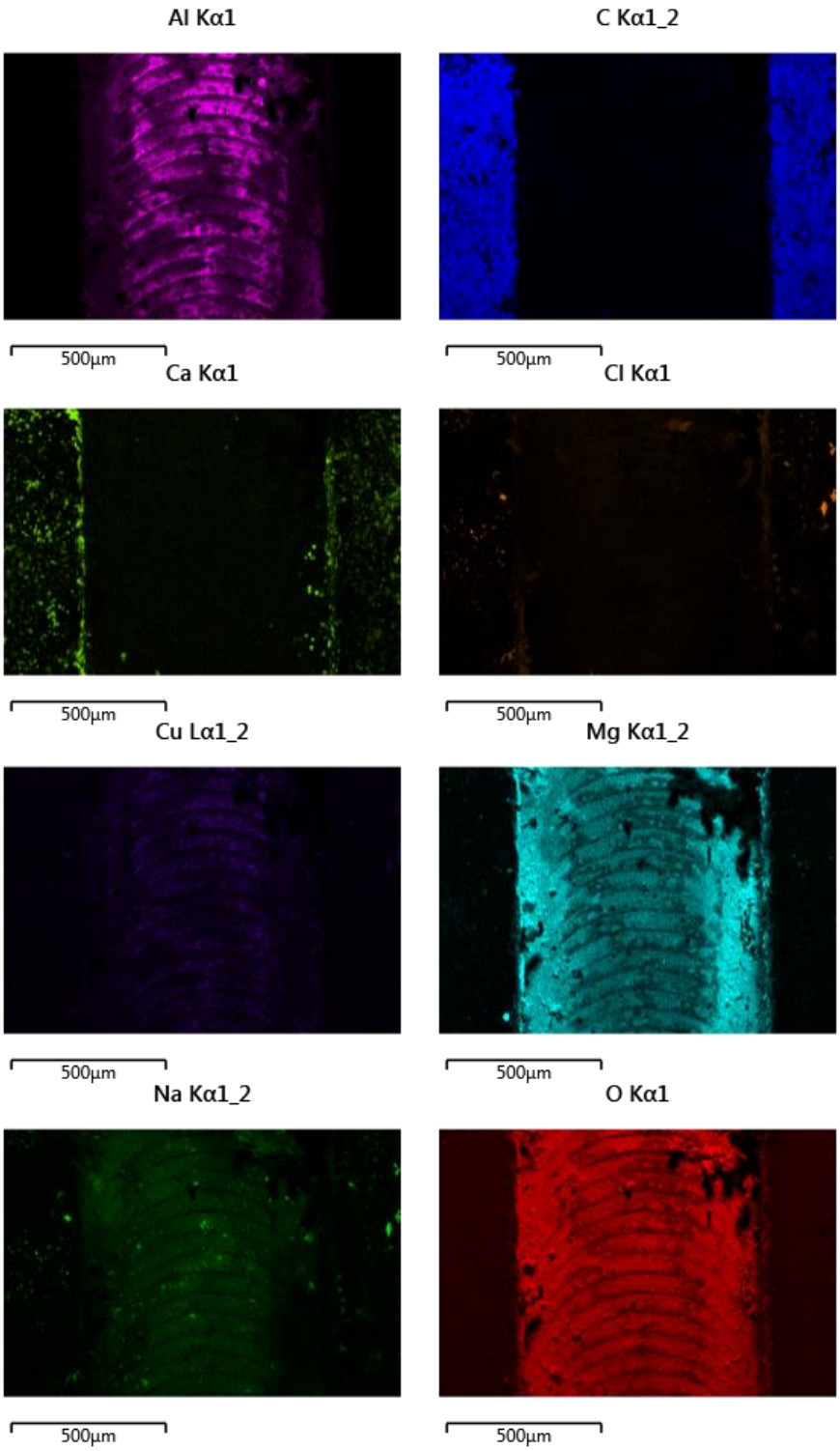

Figure 9.25. Planar-view EDS maps of scribed AA2024-T351 pretreated with Prekote and coated with MgRP (initial MgPVC = 45%) and polyurethane topcoat after lab accelerated life testing in ASTM B-117 modified with ASTM artificial sea water and UV for 400 h.

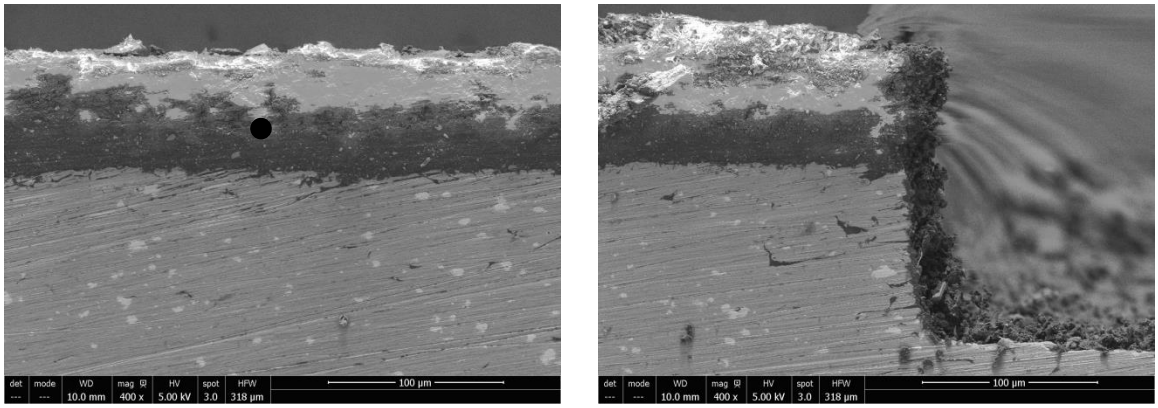

(a) (b)

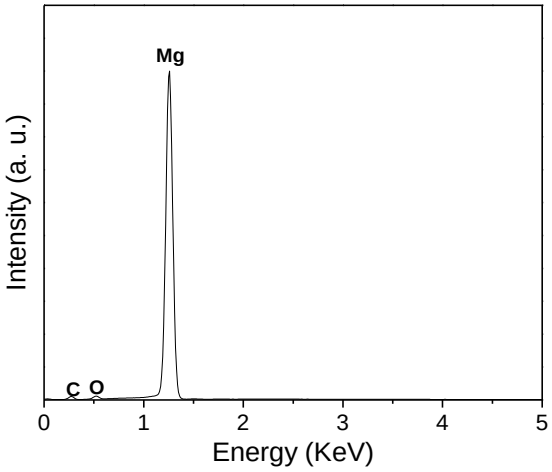

(c)

Figure 9.26. SEM micrograph (a) far away from and (b) near the scribe and (c) EDS of cross-sectioned AA2024-T351 panels coated with Mg-rich primer (initial MgPVC = 45%) and polyurethane topcoat after environmental exposure in ASTM B-117 modified with ASTM artificial sea water and UV light for 984 h. Spot markers in (a) indicate approximate location of EDS analysis shown in (c).

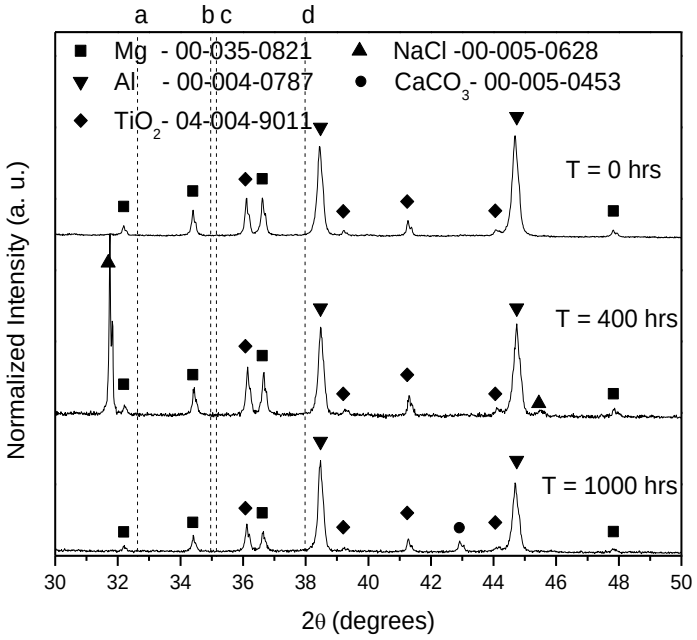

Figure 9.27. X-Ray diffraction spectra of AA2024-T351 panels coated with Mg-rich primer (initial MgPVC = 45%) and polyurethane topcoat that have been environmentally exposed in ASTM B-117 modified with ASTM artificial sea water and UV light for 0, 384, and 984 hours. Dotted lines indicate the position of the most intense diffraction peak for (a) $MgCO_3$, (b) $MgCl_2$, (c) Al_2O_3, and (d) $Mg(OH)_2$.

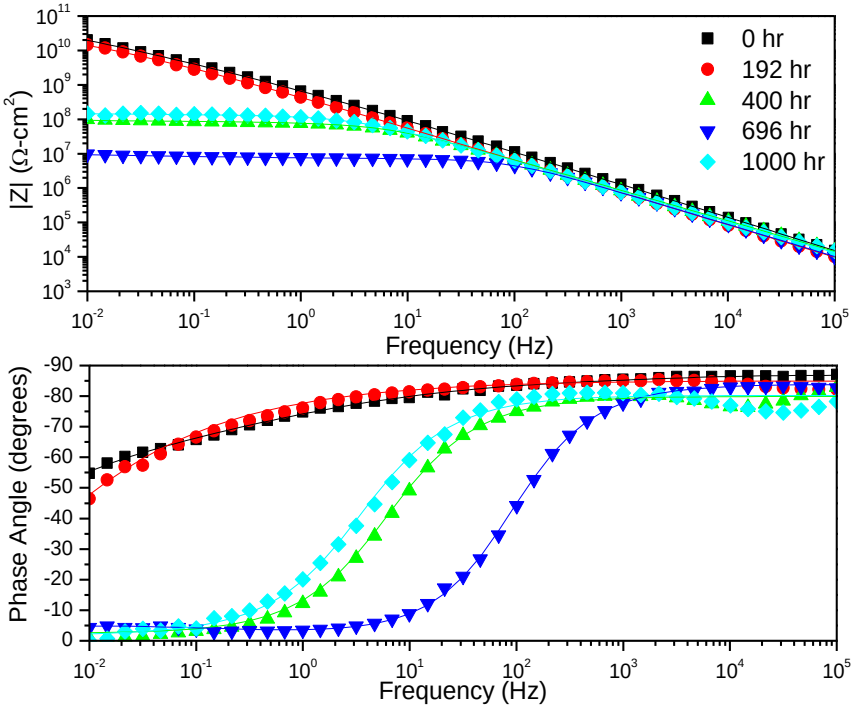

(a)

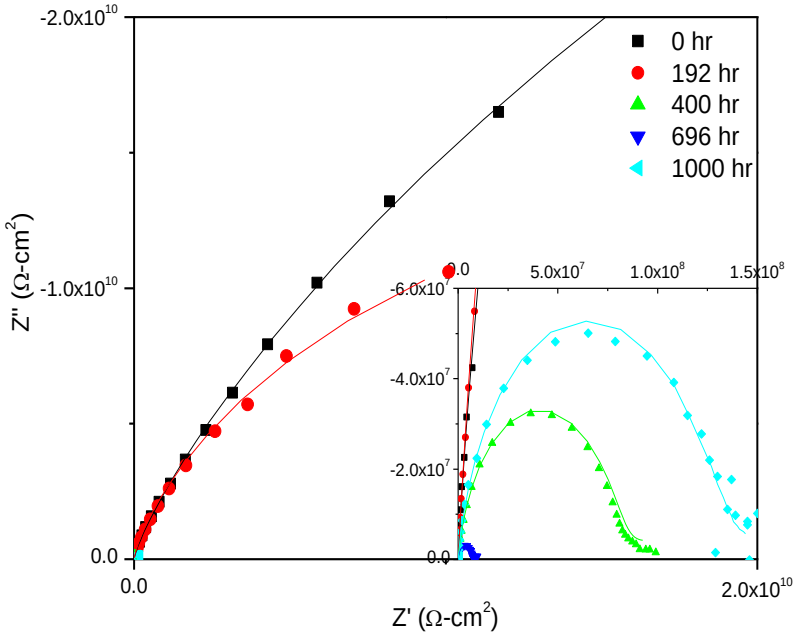

(b)

Figure 9.28. (a) Bode and (b) Nyquist plots of EIS of AA2024-T351 panels coated with Mg-rich primer (initial MgPVC = 45%) and polyurethane topcoat after exposure in ASTM B-117 modified with ASTM artificial sea water and UV light for 0, 168, 384, 744, and 984 hours. Tested in ambiently aerated 5% NaCl solution. Fit results reported in Table 3.4.

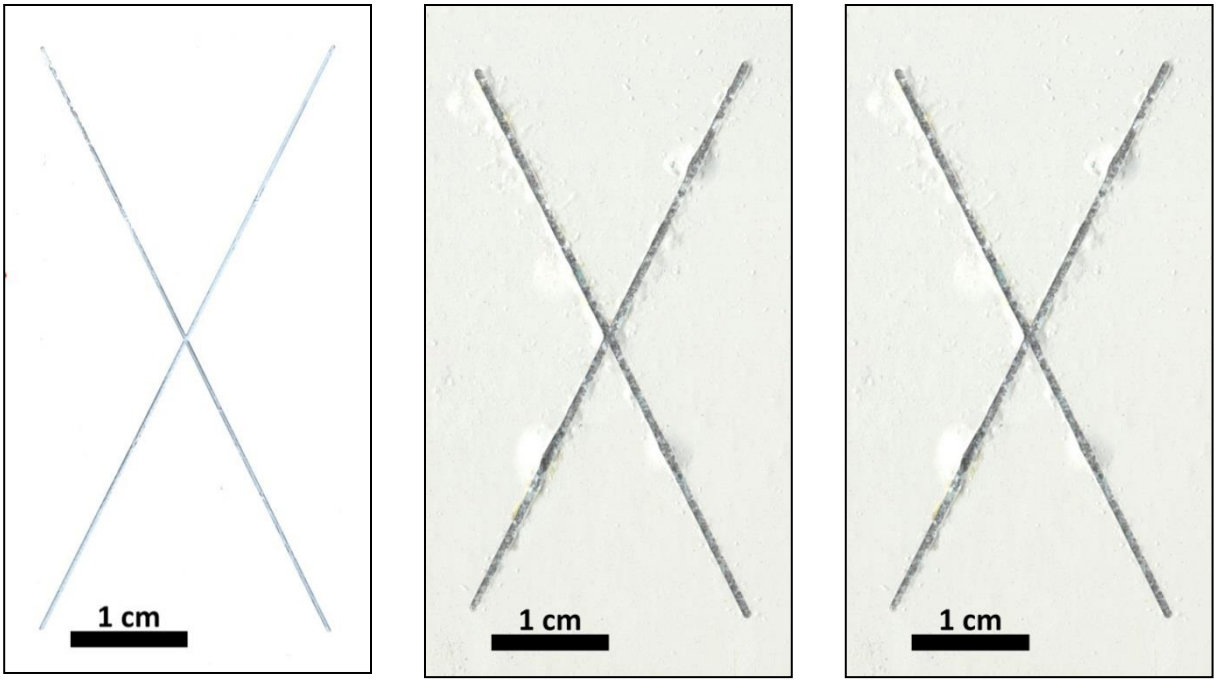

(a) T = 0 hrs in ASTM B-117 w/ ASW (b) T = 408 hrs in ASTM B-117 w/ ASW (c) T = 1000 hrs in ASTM B-117 w/ ASW

Figure 9.29. Optical micrograph of AA2024-T351 panels coated with Mg-rich primer (initial MgPVC = 45%) and polyurethane topcoat that have been environmentally exposed in ASTM B-117 with acidified ASTM ASW and UV light (a) T = 0 hrs (b) T = 48 hrs (c) T = 1000 hrs

(a) T = 0 hrs in ASTM B-117 w/ ASW (b) T = 408 hrs in ASTM B-117 w/ ASW (c) T = 1000 hrs in ASTM B-117 w/ ASW

Figure 9.30. Optical micrograph of AA2024-T351 panels coated with Mg-rich primer (initial MgPVC = 45%) and polyurethane topcoat that have been environmentally exposed in ASTM B-117 modified with acidified ASTM artificial sea water and UV light (a) T = 0 hrs (b) T = 48 hrs (c) T = 1000 hrs

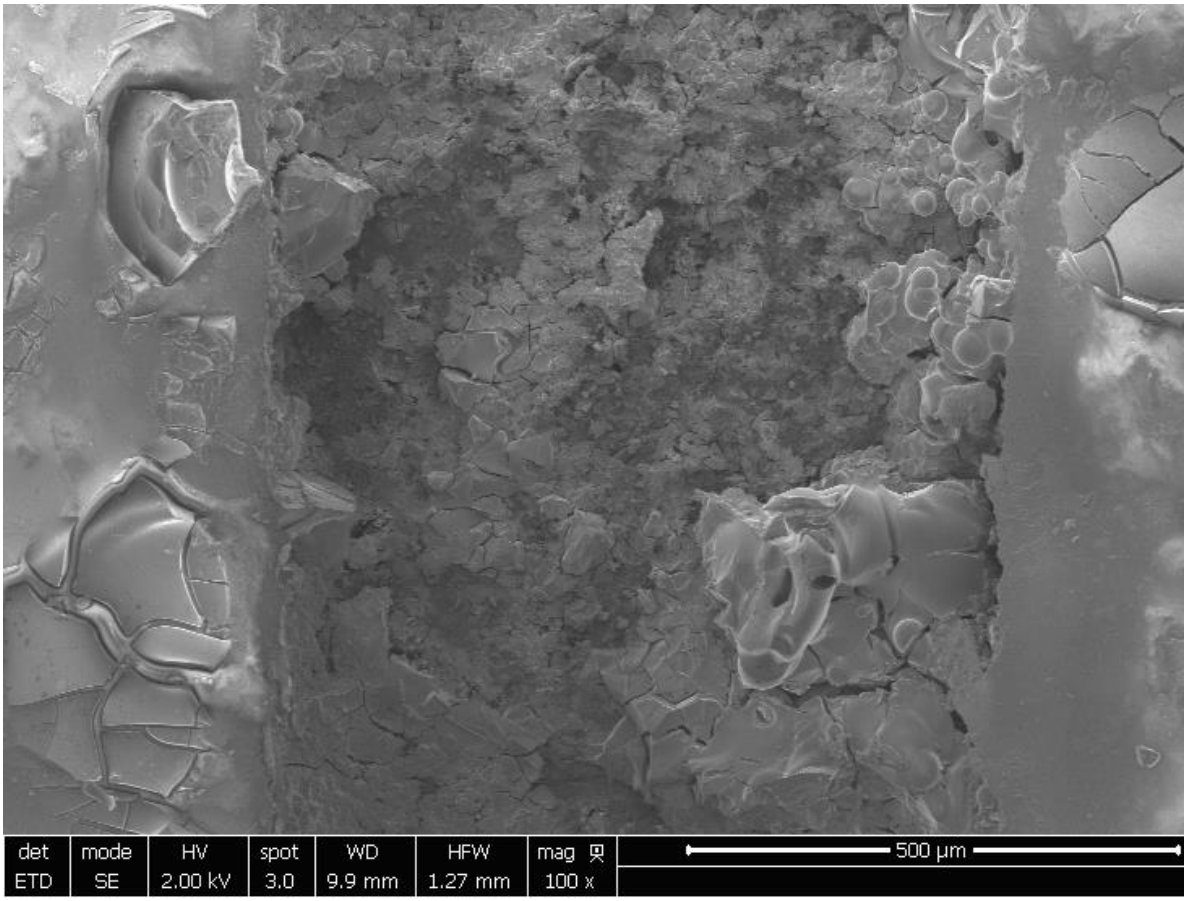

(a)

(b)

Figure 9.31. Planar-view SEM micrograph (a) of scribed AA2024-T351 panels coated with Mg-rich primer (initial MgPVC = 45%) and polyurethane topcoat after exposure in ASTM B-117 modified with acidified ASTM artificial sea water and UV light for 1000 h. Spot markers indicate approximate location of EDS analysis shown in (b).

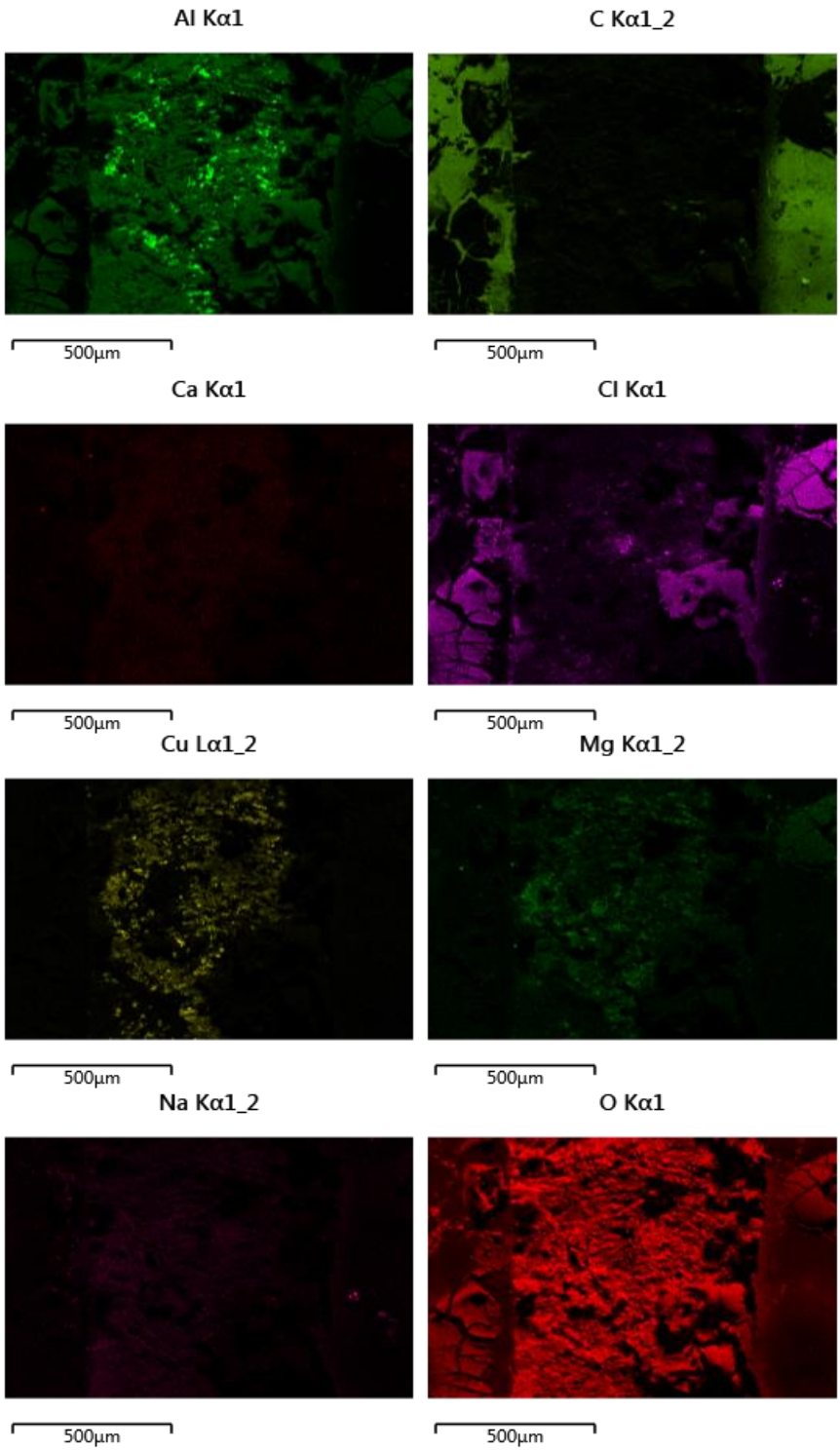

Figure 9.32. Planar-view EDS maps of scribed AA2024-T351 pretreated with Prekote and coated with MgRP (initial MgPVC = 45%) and polyurethane topcoat after lab accelerated life testing in ASTM B-117 modified with acidified ASTM artificial sea water and UV light for 400 h.

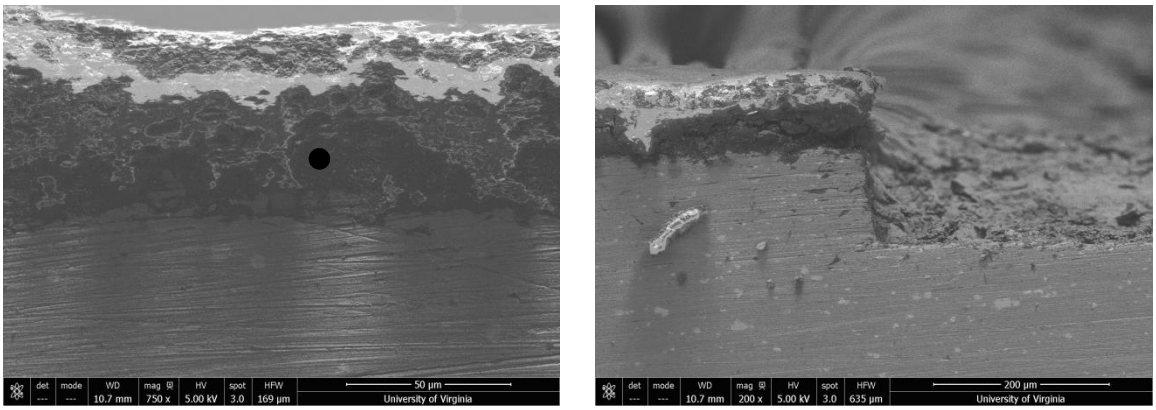

(a) (b)

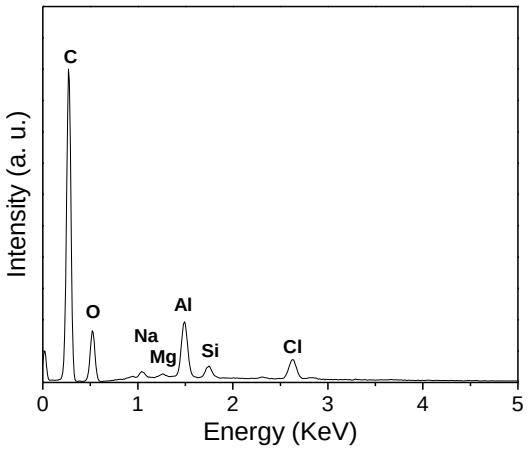

(c)

Figure 9.33. SEM micrograph (a) far away from and (b) near the scribe and (c) EDS of cross-sectioned AA2024-T351 panels coated with Mg-rich primer (initial MgPVC = 45%) and polyurethane topcoat after environmental exposure in ASTM B- modified with acidified ASTM artificial sea water and UV light for 1000 h. Spot markers in (a) indicate approximate location of EDS analysis shown in (c).

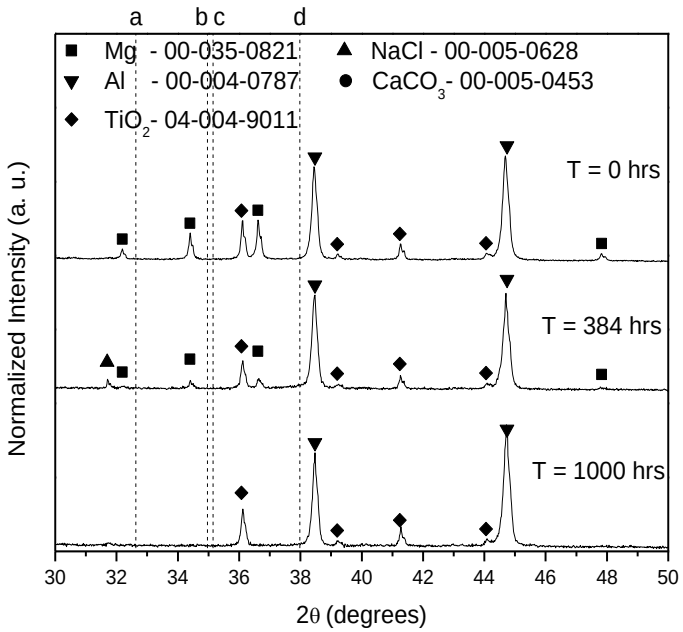

Figure 9.34. X-Ray diffraction spectra of AA2024-T351 panels coated with Mg-rich primer (initial MgPVC = 45%) and polyurethane topcoat that have been environmentally exposed in ASTM B-117 modified with acidified ASTM artificial sea water and UV light for 0, 408, and 1000 hours. Dotted lines indicate the position of the most intense diffraction peak for (a) $MgCO_3$, (b) $MgCl_2$, (c) Al_2O_3, and (d) $Mg(OH)_2$.

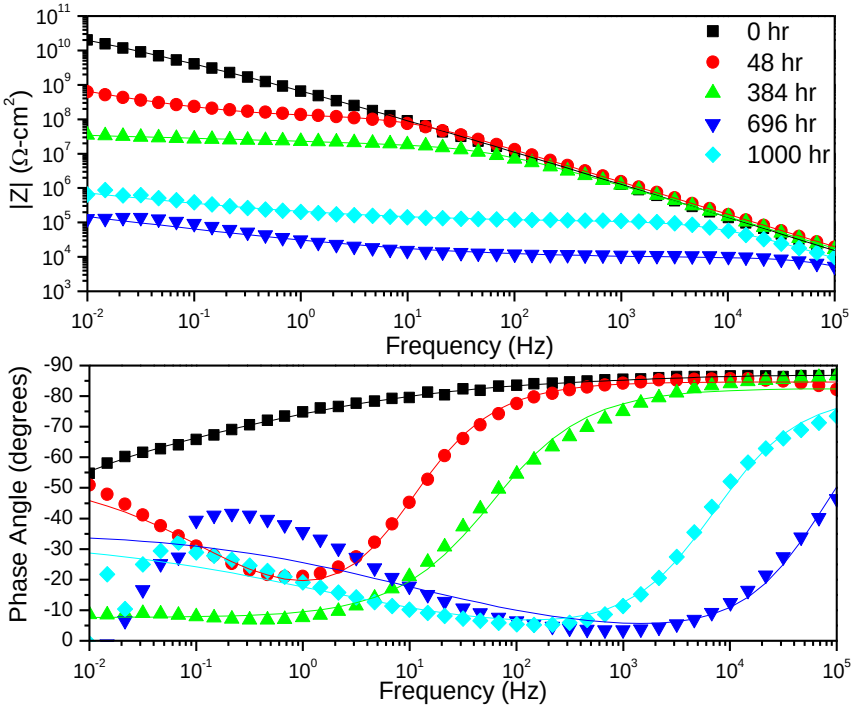

(a)

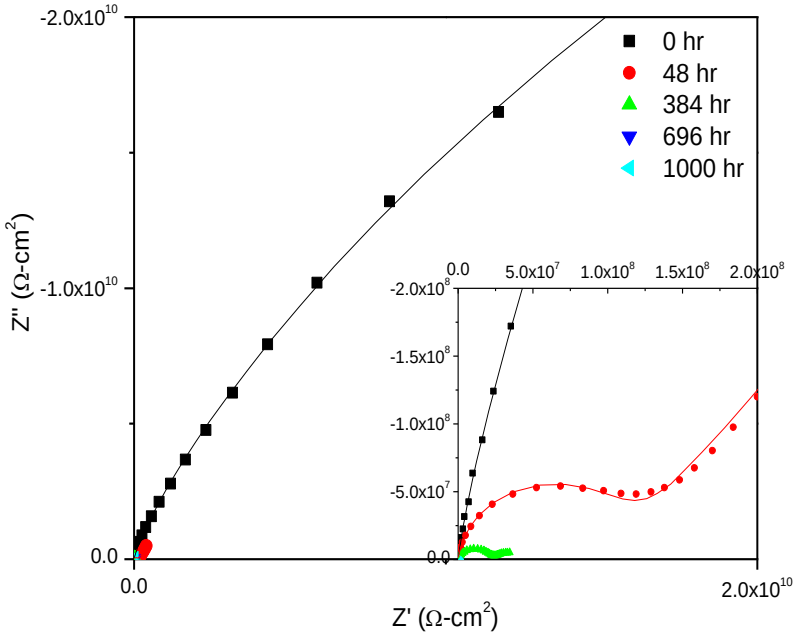

(b)

Figure 9.35. (a) Bode and (b) Nyquist plots of EIS AA2024-T351 panels coated with Mg-rich primer (initial MgPVC = 45%) and polyurethane topcoat after exposure in ASTM B-117 modified with acidified ASTM artificial sea water and UV light for 0, 192, 408, 698, and 1000 hours. Tested in ambiently aerated 5% NaCl Solution. Fit results reported in Table 3.5.

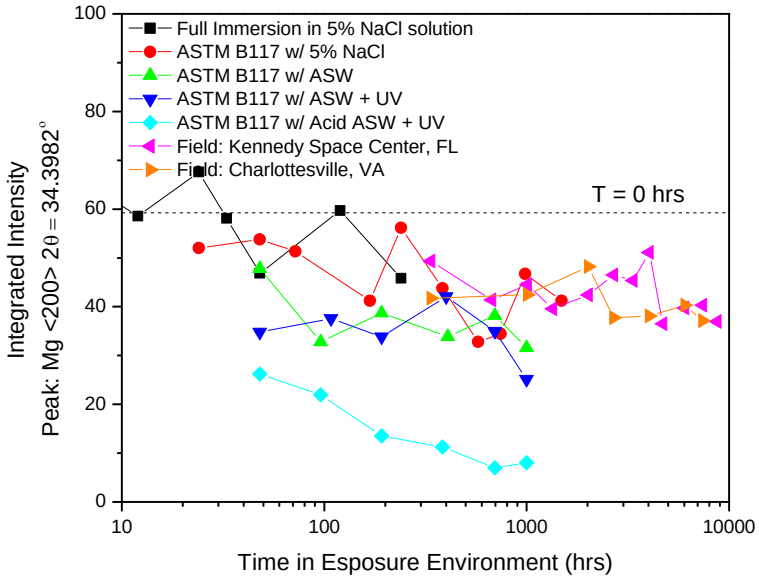

Figure 9.36. Integrated peak intensity vs. environmental exposure time in various exposure environments for AA2024-T351 panels coated with Mg-rich primer (initial MgPVC = 45%) and polyurethane topcoat.

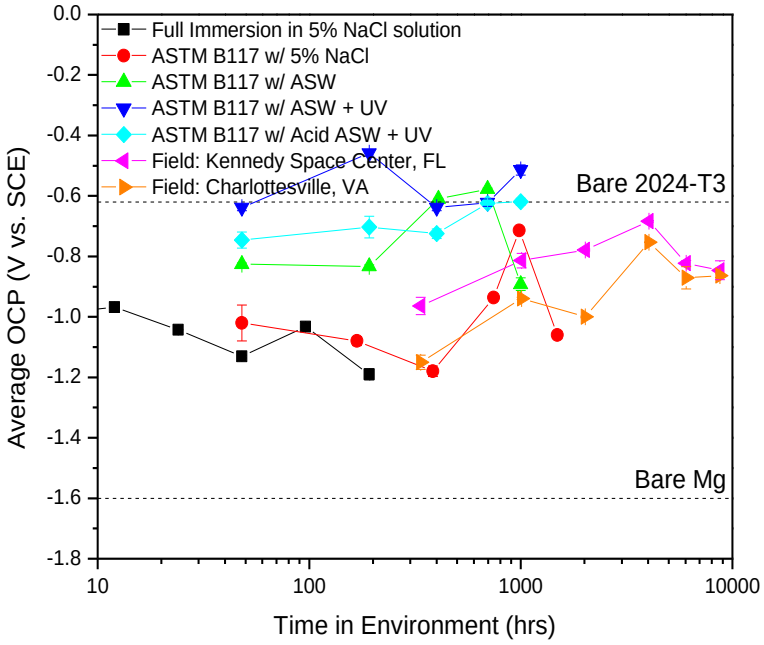

Figure 9.37. Galvanic protection potential in ambiently aerated 5% NaCl vs. environmental exposure time in various exposure environments for AA2024-T351 panels coated with Mg-rich primer (initial MgPVC = 45%) and polyurethane topcoat.

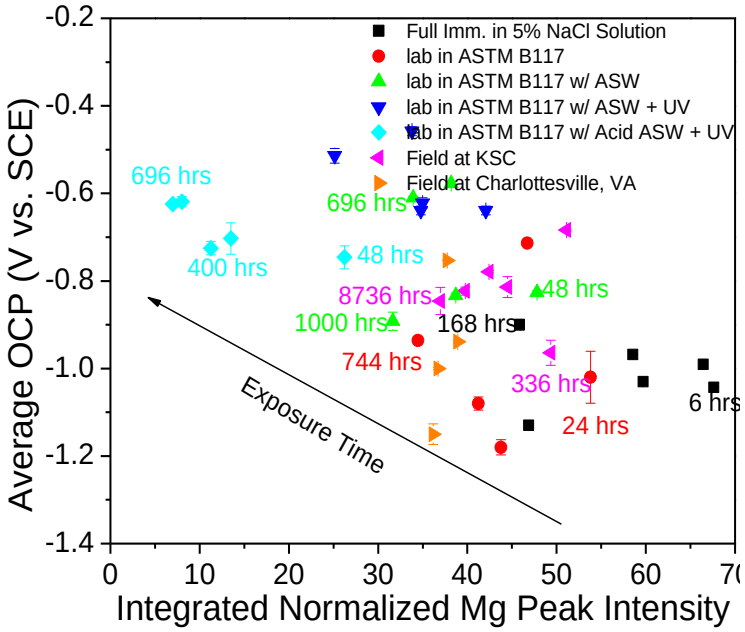

Figure 9.38. Correlation between integrated Mg peak (Mg <200> 2θ = 36.6170°) intensity vs. galvanic protection potential of AA2024-T351 panels coated with Mg-rich primer (initial MgPVC = 45%) and polyurethane topcoat in ambiently aerated 5% NaCl solution after exposure in various environments.

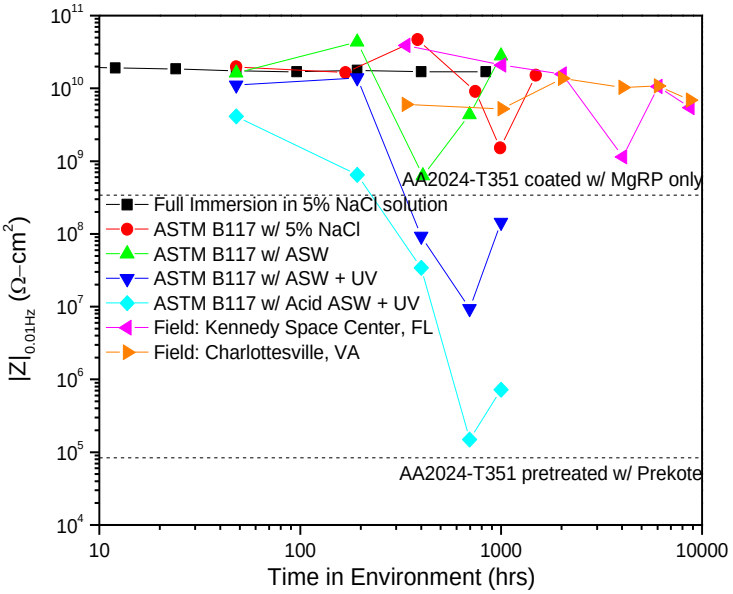

Figure 9.39. Magnitude of electrochemical impedance at 0.01 Hz in ambiently aerated 5% NaCl vs. environmental exposure time in various exposure environments for AA2024-T351 panels coated with Mg-rich primer (initial MgPVC = 45%) and polyurethane topcoat.

10 APPENDIX C: Directions for conducting simultaneous H_2 collection, EIS, and gravimetric mass loss for determination of anodic charge consumption in full immersion

1. Measure and record the pH of the electrolyte you are going to use.
2. Mount Mg rod (or metal of interest) in EpoThin epoxy electrically connected to ~6" of 10-12 gauge solid-core, insulated Cu wire. The insulated Cu wire will serve as the support structure for the mounted sample during the experiment

3. Polish face of sample to 1200 grit.
4. Dry sample in dry box for at least 24 hrs. (48 hrs preferred)
5. Measure the mass of the sample on the high precision balance in MSE 3rd floor (room with TDS and optical scope).
6. Fill the cell with solution and charge the solution with H_2 gas by cathodically polarizing a large piece of Pt mesh to -1.5 V vs. SCE for at least 1 hr, preferably 1.5 hr. You may need to polarize to as low as 2 V vs. SCE before you can observe H_2 bubbles. You may need to use a potentiostat with a high current limit. You do this because H_2 gas dissolves in aqueous solutions up to a solubility limit. We want to capture all of the H_2 gas formed when the Mg is corroding so we want to saturate the solution ahead of time so that all of the H_2 gas produced by Mg is collected in the buret, not dissolved in solution.

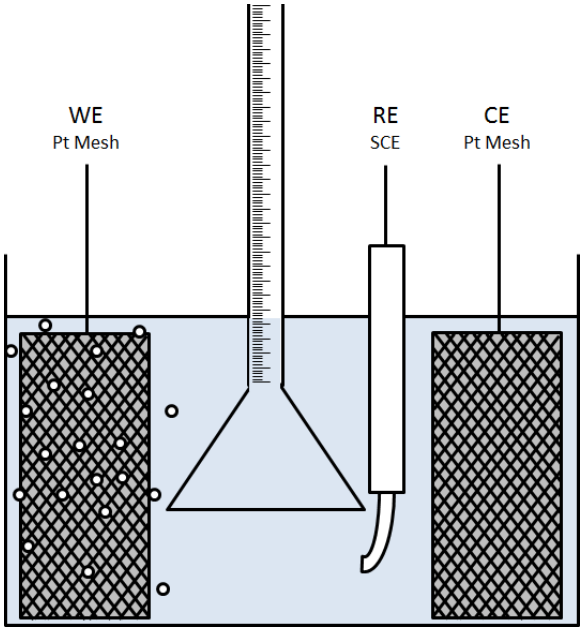

7. Start the Mg exposure. Do the following as quickly as possible while remaining careful and safe.

a. Prepare the computer so that it is ready to start EIS and OCP measurements. DO NOT START THE MEASUREMENT.

b. Pick up lid of cell and Replace the Pt mesh WE with the Mg sample such that the Mg is directly under the funnel to the buret. Replace the lid/RE/buret assembly back on the cell.

c. Suck solution up through the top of the collection buret. Close the valve to the buret so that the buret remains full of solution.

d. START the potentiostat measuring a repeated cycle of EIS and OCP.

e. Record the time you started the experiment.

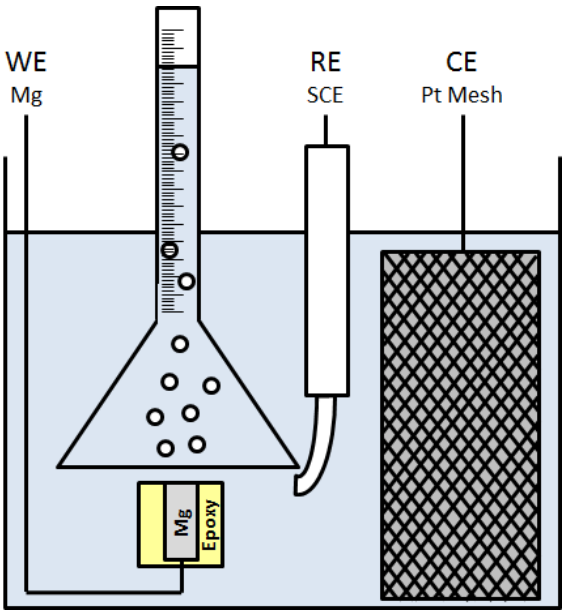
WE
Mg
RE
SCE
CE
Pt Mesh
Mg
Epoxy

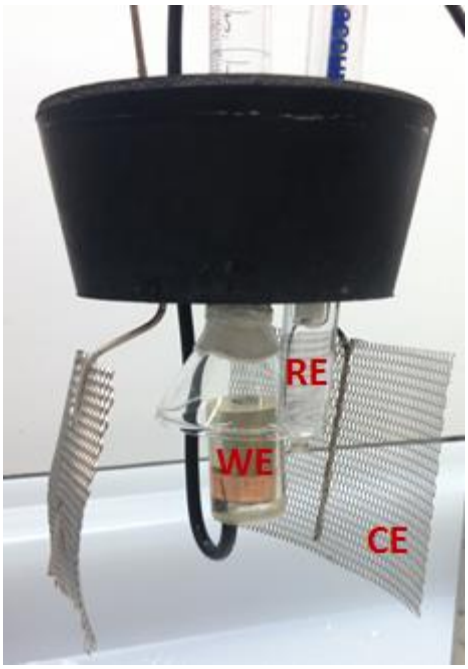
RE
WE
CE

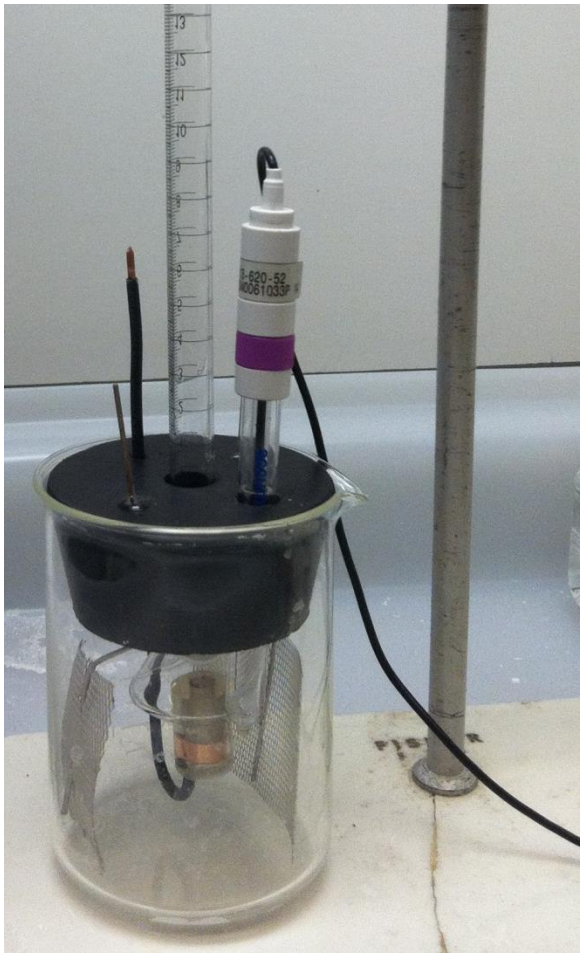

8. At the required time:

a. stop the potentiostat software

b. record the level of H_2 gas collected in the buret. You can mark the buret with a sharpie if you want.

c. promptly remove the Mg from the cell and dry with chemwipe and air. Store the cell solution in a well labeled bottle for future analysis.

9. Clean the surface of the Mg sample with chromic acid (200g of CrO_3 per 1000 mL total solution per ASTM G1), collecting all of the solution to include for future analysis. You only need to make 20 mL of cleaning solution.

10. Dry the Mg sample in a dry box for at least 24 hrs (48 hrs preferred)

11. Weigh the dry, cleaned sample on the high precision scale in MSE 3rd floor. Record the average mass of the sample.